AGRICULTURAL UNIVERSITY OF ATHENS
SCHOOL OF ENVIRONMENT & AGRICULTURAL ENGINEERING
DEPARTMENT OF NATURAL RESOURCES DEVELOPMENT & AGRICULTURAL ENGINEERING
MINERALOGY – GEOLOGY LABORATORY

Doctoral Thesis

Seismic hazard assessment and development of earthquake catastrophe model based on geological data and tectonic geomorphology

Georgios D. Deligiannakis

Supervisor:
Ioannis D. Papanikolaou, Associate Professor, AUA

Supervisory committee:
Ioannis Papanikolaou, Associate Professor, AUA (Lead Supervisor)
Efthimios Lekkas, Professor, NKUA
Alexandros Zimbidis, Assistant Professor, AUEB

ATHENS
2021

AGRICULTURAL UNIVERSITY OF ATHENS
SCHOOL OF ENVIRONMENT & AGRICULTURAL ENGINEERING
DEPARTMENT OF NATURAL RESOURCES DEVELOPMENT & AGRICULTURAL ENGINEERING
MINERALOGY – GEOLOGY LABORATORY

Doctoral Thesis

Seismic hazard assessment and development of earthquake catastrophe model based on geological data and tectonic geomorphology

Εκτίμηση σεισμικού κινδύνου και ανάπτυξη μοντέλου καταστροφικού σεισμού με χρήση γεωλογικών δεδομένων και τεκτονικής γεωμορφολογίας

Georgios D. Deligiannakis

<u>Examination committee:</u>

Ioannis Papanikolaou, Associate Professor, AUA (Supervisor)
Efthimios Lekkas, Professor, NKUA
Alexandros Zimbidis, Assistant Professor, AUEB
Ioannis Koukouvelas, Professor, University of Patras
Christos Karavitis, Associate Professor, AUA
Alexandros Chatzipetros, Associate Professor, AUTH
Emmanuel Vassilakis, Associate Professor, NKUA

Seismic Hazard Assessment and Development of Earthquake Catastrophe Model Based on Geological Data and Tectonic Geomorphology

Department of Natural Resources Development & Agricultural Engineering
Mineralogy – Geology Laboratory

Abstract

Traditional seismic hazard assessment methods are based on the earthquake catalogues for the calculation of an annual probability of exceedance for a particular ground motion level, but suffer from large uncertainty and incompleteness problems. Thus, new seismic hazard assessment methodologies follow fault specific approaches where seismic sources are geologically constrained active faults. This approach aims to address problems related to the incompleteness and the inhomogeneity of the historical records and to obtain a higher spatial resolution of hazard assessment. This method is applied in Greece and offers high-resolution fault-specific seismic hazard maps for the Attica Region for the first time. In addition, a new Earthquake Catastrophe model, based on fault specific seismic hazard assessment, is developed for the first time and is applied in the Attica Region, which is the most densely populated region in Greece.

First, a database of 24 active faults is developed, including information regarding fault characteristics, such as expected magnitudes (Mw 6.1 – Mw 6.7), fault lengths and slip – rates (0.1 mm/y – 2.3 mm/y). It comprises onshore and offshore faults that lie within or in short distances from the Attica region boundaries and can cause damage to the region in case of earthquake rupture. Fault information is obtained with the use of tectonic geomorphology and geological data. Fault parallel and fault perpendicular swath topographic profiles are used, along with tectonic geomorphological indices, such as the enhanced transverse hypsometry index (THi*), the Asymmetry factor (Af) and the Valley floor to valley high ratio (Vf), for the confirmation of active landscapes. Detailed fault scarp profiles, geological cross-sections, paleoseismological methods and SfM photogrammetry are also used to determine fault slip – rates and expected magnitudes. The low average fault slip rate of 0.35 mm/y for these faults implies large intervals between earthquakes in Attica and highlights the importance of the use of geological data in seismic hazard assessment.

Four fault specific seismic hazard maps are developed for the Attica region, one for each of the intensities VII – X (MM), showing their recurrence at each locality in the map. These maps offer a high spatial resolution, as they consider surface geology. The highest recurrence for intensity VII (151-156 times over 15 kyrs, or up to 96 year return period) is observed in the central part of the Athens basin. The maximum intensity VIII recurrence (115 times over 15 kyrs, or up to 130 year return period) is observed in the western part of Attica, while the maximum intensity IX (73-77/15kyrs, or 195 year return period) and X (25-29/15kyrs, or 517 year return period) recurrences are observed near the South Alkyonides fault system.

Based on the above, a method for the Insured Loss estimation is developed, using the high spatial resolution fault specific seismic hazard maps of Attica. This method allows the calculation of the expected earthquake losses over different return periods. More importantly, an earthquake catastrophe model is presented, which combines a

fault specific hazard module with vulnerability, exposure and loss modules, to estimate the Solvency Capital Requirements for insurance companies.

Scientific area: Seismic hazard assessment

Keywords: Active faults, Slip-rate, Fault specific seismic hazard maps, Solvency Capital Requirements, Attica

Εκτίμηση Σεισμικού Κινδύνου και Ανάπτυξη Μοντέλου Καταστροφικού Σεισμού με Χρήση Γεωλογικών Δεδομένων και Τεκτονικής Γεωμορφολογίας

Τμήμα Αξιοποίησης Φυσικών Πόρων και Γεωργικής Μηχανικής
Εργαστήριο Ορυκτολογίας – Γεωλογίας

Περίληψη

Οι παραδοσιακές μέθοδοι εκτίμησης σεισμικού κινδύνου βασίζονται σε σεισμικούς καταλόγους για τον υπολογισμό της ετήσιας πιθανότητας υπέρβασης καθορισμένων μεγεθών εδαφικών κινήσεων, κάτι που συνεπάγεται σημαντικούς περιορισμούς λόγω της αβεβαιότητας και της ελλειπούς πληρότητας των καταλόγων. Οι νέες μέθοδοι εκτίμησης σεισμικού κινδύνου βασίζονται στην ανάλυση ενεργών ρηγμάτων για τον καθορισμό σεισμικών πηγών, επιτυγχάνοντας την αντιμετώπιση των περιορισμών των καταλόγων, καθώς επίσης και υψηλή χωρική ανάλυση στην εκτίμηση του σεισμικού κινδύνου. Η μέθοδος αυτή εφαρμόζεται στην Ελλάδα και παρέχει για πρώτη φορά χάρτες σεισμικού κινδύνου υψηλής χωρικής ανάλυσης με βάση τα ενεργά ρήγματα για την περιοχή της Αττικής. Επιπροσθέτως, στην παρούσα διατριβή αναπτύσσεται για πρώτη φορά μοντέλο καταστροφικού σεισμού με βάση τα ενεργά ρήγματα, στην Αττική, η οποία είναι η πιο πυκνοκατοικημένη περιοχής της Ελλάδας.

Σε πρώτο στάδιο, αναπτύχθηκε βάση δεδομένων ενεργών ρηγμάτων με 24 συνολικά ρήγματα, στην οποία συμπεριλαμβάνονται πληροφορίες για χαρακτηριστικά των ρηγμάτων, όπως αναμενόμενο μέγεθος (Mw 6.1 – Mw 6.7), μήκη και ρυθμοί ολίσθησης ρηγμάτων (0.1 mm/y – 2.3 mm/y). Η βάση αποτελείται από χερσαία και υποθαλάσσια ρήγματα, τα οποία βρίσκονται εντός της Περιφέρειας Αττικής, ή σε τέτοια απόσταση από τα όριά της, ώστε σε περίπτωση ενεργοποίησής τους να προκαλέσουν ζημιές εντός της Περιφέρειας. Οι πληροφορίες για τα χαρακτηριστικά των ρηγμάτων βασίζονται στην χρήση τεκτονικής γεωμορφολογίας και γεωλογικών δεδομένων. Πολλαπλά τοπογραφικά προφίλ ευρείας ζώνης (swath profiles) τόσο παράλληλα όσο και κάθετα προς το ρήγμα, σε συνδυασμό με μορφομετρικούς δείκτες όπως ο Ενισχυμένος Δείκτης Εγκάρσιας Υψομετρίας (THi*), ο Δείκτης Ασυμμετρίας (Af) και ο Δείκτης Λόγου Πλάτους Κοιλάδας προς το Ύψος Κοιλάδας (Vf), χρησιμοποιήθηκαν για την επιβεβαίωση της τεκτονικής ενεργότητας σε κάθε περιοχή. Λεπτομερή τοπογραφικά προφίλ κάθετα στους κρημνούς των ρηγμάτων, γεωλογικές τομές, παλαιοσεισμικές μέθοδοι και φωτογραμμετρικές μέθοδοι (Δομή από Κίνηση – Structure from Motion) χρησιμοποιήθηκαν για την ποσοτικοποίηση του ρυθμού ολίσθησης των ρηγμάτων και των αναμενόμενων μεγεθών. Ο χαμηλός μέσος όρος ρυθμού ολίσθησης (0.35 mm/y) συνεπάγεται μεγάλες περιόδους επαναδραστηριοποίησης των ρηγμάτων στην περιοχή της Αττικής και αναδεικνύει την σημασία της χρήσης γεωλογικών δεδομένων στην εκτίμηση σεισμικού κινδύνου.

Τέσσερεις χάρτες σεισμικού κινδύνου με βάση ενεργά ρήγματα δημιουργήθηκαν για την περιοχή της Αττικής, ένας για κάθε μια από τις εντάσεις VII – X της κλίμακας Modified Mercalli (MM). Κάθε ένας από τους χάρτες αυτούς απεικονίζει σε κάθε

σημείο του την επαναληψιμότητα της εκάστοτε έντασης. Οι χάρτες αυτοί είναι υψηλής χωρικής ανάλυσης, διότι λαμβάνουν υπόψη την επιφανειακή γεωλογία. Η μεγαλύτερη επαναληψιμότητα της έντασης VII (151-156 φορές σε περίοδο 15 χιλιάδων ετών, ή περίοδος επαναφοράς έως 96 έτη) παρατηρείται στις κεντρικές περιοχές του Λεκανοπεδίου Αττικής. Η μέγιστη επαναληψιμότητα της έντασης VIII (115 φορές σε περίοδο 15 χιλιάδων ετών, ή περίοδος επαναφοράς έως 130 έτη) παρατηρείται στο δυτικό τμήμα της Αττικής, ενώ οι μέγιστες τιμές επαναληψιμότητας για τις εντάσεις IX (73-77 φορές σε περίοδο 15 χιλιάδων ετών, ή περίοδος επαναφοράς έως 195 έτη) και X (25-29 φορές, ή περίοδος επαναφοράς έως 517 έτη) παρατηρούνται κοντά στην Νότια Ρηξιγενή Ζώνη των Αλκυονίδων.

Τέλος, στην παρούσα διατριβή αναπτύχθηκε μέθοδος για τον υπολογισμό των απαιτήσεων αποζημιώσεων προς την ασφαλιστική αγορά, με την χρήση των χαρτών σεισμικού κινδύνου της Αττικής βάσει ενεργών ρηγμάτων. Η μέθοδος αυτή προσφέρει τον υπολογισμό των αναμενόμενων ζημιών λόγω σεισμού σε επιθυμητές περιόδους επαναφοράς. Επιπροσθέτως, αναπτύχθηκε μοντέλο καταστροφικού σεισμού, το οποίο υπολογίζει τις κεφαλαιακές απαιτήσεις φερεγγυότητας των ασφαλιστικών επιχειρήσεων με βάση την Ευρωπαϊκή Οδηγία Solvency II. Το μοντέλο αυτό αποτελείται από επιμέρους ενότητες (modules) που σχετίζονται με την εκτίμηση κινδύνου με βάση τα ενεργά ρήγματα, την τρωτότητα των κατασκευών, την έκθεση στον κίνδυνο και τον υπολογισμό του αναμενόμενου κόστους.

Επιστημονική περιοχή: Εκτίμηση σεισμικού κινδύνου

Λέξεις κλειδιά: Ενεργά ρήγματα, Ρυθμός ολίσθησης, Χάρτες σεισμικού κινδύνου με βάση ενεργά ρήγματα, Κεφαλαιακές απαιτήσεις φερεγγυότητας ασφαλιστικών εταιριών, Αττική

To my parents and my brother

To Marianthi and our little Andriani

To Mrs Lemonia

Acknowledgements

The completion of this thesis marks an end to a long journey as a student geologist. A journey that was full of intense experiences, joy, curiosity and knowledge of the geo-environment surrounding us. I was lucky to have the appropriate people next to me, to guide me, help me in difficult circumstances, push me when necessary, and trust me with their knowledge.

First and foremost, I would like to thank my supervisor, Associate Professor I. Papanikolaou, for the assignment of this PhD. I know how important this topic has always been for him, and I felt honoured from the first moment that I was entrusted with developing it and pushing it a little further. I can't thank him enough for his support all these years, his guidance in all critical turns of my research, his patience and inspiration when circumstances diverted my focus on my thesis, his encouragement and support to any professional decisions I had to make. I know that if it wasn't for him, I would not evolve as a researcher, nor as a professional geologist and for that, I will always be grateful. I feel privileged that he was my tutor and supervisor all these years, and I really wish that we could continue to work together for the years to come.

I would also like to express my gratitude to Professor Efthymios Lekkas for being my co-supervisor in my thesis. I have known Professor Lekkas since my undergraduate studies as a geologist, and I was always impressed with his knowledge and experience in natural disasters globally, especially in large earthquakes. All these years that I know him, he was supportive and always available to help.

Assistant Professor Alexandros Zimbidis supervised my insurance-related work in the early steps of my PhD studies, during my occupation in the Bank of Greece – Department Of Private Insurance Supervision and introduced me to all aspects of the insurance industry. Until the completion of this thesis, he never stopped helping me with every task related to earthquake insurance. His guidance was critical, and without him, the Earthquake Catastrophe model would not have been developed. I feel privileged to have such a talented, experienced and established scientist as a co-supervisor to my thesis.

Special thanks go to Professor Ioannis Koukouvelas, Associate Professor Christos Karavitis, Associate Professor Alexandros Chatzipetros and Associate Professor Emmanuel Vassilakis. They reviewed this thesis thoroughly despite their limited time, and their questions and comments gave me the opportunity to display advances and limitations of this Thesis that may add value to future applications. I really appreciate their discernment and sound judgement, and I am honoured now that my PhD has their approval.

Because this work took many years to complete, I had to change my supervising committee in the middle of my PhD studies. I owe a special thanks to Professor Emeritus Dimitrios Papanikolaou and Professor Emeritus Georgios Migiros. They honoured me by supervising my work during the first and most important steps of my

PhD research and added value to the work that followed. Before I started my PhD, I would never have thought that I could ever work with two of the best geologists in Greece, with such an enormous footprint on the geologic research in Greece and abroad. It is an honour that I will never forget.

During the years I spent in my office in the Mineralogy – Geology Laboratory of the Agricultural University of Athens, I had the chance to meet Professor Georgios Stamatis. He is a special kind of person that always worked relentlessly to make sure that all PhD students had all the means to conduct their research. For that, for all his continuous support, his eagerness to help, his precious advice and for accepting my PhD application as the Director of the Laboratory, I truly thank him.

Throughout my student years, I had the privilege of meeting and working together with exceptional geologists from abroad. These collaborations provided me with innovative methods, additional knowledge and different way of thinking. I would like to thank Professors Gerald Roberts and Klaus Reicherter for all these years of collaboration in research projects in Greece and for their invaluable advice. I would also like to thank Dr Christoph Grützner and Dr Sascha Schneiderwind for sharing their knowledge in paleoseismic trench techniques, Ground Penetration Radar, t-LiDAR and Structure from Motion software, and for inviting me to work together at the Milesi fault. Also, I would like to thank Prof. Dr. Tomás Manuel Fernandez-Steeger for introducing me to SfM freeware.

Special thanks go to Dr Silke Mechernich for inviting me to fieldwork in Crete (Gramvoussa, Kera, Kasteli, Lastros, Kavoussi, Thripti and Mouliana faults) and in Attica (Pissia and Loutraki faults). I also thank her for giving me the opportunity to sample Lastros, Mouliana and Pissia fault scarps for cosmogenic ^{36}Cl dating.

Earthquake insurance was a discipline that always intrigued me, even from my Master's Degree. I am grateful to the personnel of the Department of Private Insurance Supervision of the Bank of Greece (Charalampos Vogiatzis, Ioanna Seliniotaki, Stella Adamopoulou, Ioannis Chatzivasiloglou, Thodoris Alexandris, Georgios Pastras, Gregorios Mourtzos, Nikos Zacharopoulos, Stavros Athanasiadis, Georgios Patras, Konstantinos Papistas, Nicolaos Vlachos, Nicolaos Tsagakis, Georgios Memmos) who shared all their knowledge and helped me understand all critical aspects of insurance and re-insurance in Greece, especially under the Solvency II directive. Special thanks go to my colleagues in the "Workgroup Solvency II", Christos Argyropoulos and Ioannis Badounas. I also want to thank Mr Vassileios Marghios, Kostantinos Nikolaou and Iraklis Kakouris from Prudential B. Marghios and Partners, for their support.

The Antonios Papadakis Legacy Postgraduate Scholar from the National and Kapodistrian University of Athens is also thanked for the scholarship during the first four years of my postgraduate studies.

I am really thankful to Dr Aggelos Pallikarakis for his outstanding support and to Dr Michalis Diakakis, who also helped me develop my research skills. Special thanks go to Dr Emmanuel Psomiadis for being always available to help me, both in the field and the office.

I would also like to thank Dr Elena Vassileiou for providing critical data at the beginning of my PhD studies, Simoni Alexiou and Dimitris Skrombolas and for helping me in the field.

I am grateful to Dr James Hengesh for supporting me during the last years of my PhD studies and for his understanding and encouragement during these last months.

I am also thankful to the Hellenic Survey of Geology and Mineral Exploration, especially to Dr Adonis Fotiadis, Dr Irene Zananiri, Mrs Alexandra Zervakou, Dr Dimitrios Galanakis, Dr Charalambos Georgiou, and Dr Vassileios Tselepidis. My colleagues in the GEOINFRA project, Dr Christos Kanellopoulos, Leonidas Moforis, Filomila Statha and Dr Ioannis Vakalas encouraged me and supported me during the last two years, and I am grateful to them. Special thanks go to Dr Sotirios Sboras for his support, his willingness to help, his generosity and for our fruitful discussions regarding tectonics and tectonic geomorphology.

Special thanks go to Ioanna and Mrs Lemonia, who supported me by keeping little Andriani away from my laptop! I simply would not finish the writing of this Thesis without their help.

My parents' support was the cornerstone for completing not only my PhD, but all my studies, and I find it hard to thank them separately without being unfair. My Father introduced me to physical sciences from the first day I started speaking, and he has always been right next to me with all his heart, knowledge, wisdom, and kindness in any trouble I had to resolve or any decisions I needed to make. My Mother has always been my support, no matter what the circumstances were, with her patience, kindness, and willingness to help, always trying to make me a better person. I owe them more than an acknowledgement for making me the person I now am, and I know that I will never be able to give them back all the love and support they have offered me. I understand that completing this thesis will make them happy, and the least I can do to thank them is to dedicate my PhD to them. The same goes for my brother Stelios, for being my best friend, helping me overpass all difficulties and standing next to me from the very first day of my life.

Last but not least, I owe much more than thanks and gratitude to my wife, Marianthi. She is my everyday strength, my other half, my fellow geologist, my everyday happiness, who supports me in all research or professional decisions I need to make. Since we became parents a year ago, I would not even think of completing this thesis without her outstanding support. To her and our daughter Andriani, I would also like to dedicate this thesis.

With my consent, the validity and originality of this Thesis were confirmed by the Examining Committee through plagiarism detection software provided by the Agricultural University of Athens.

TABLE OF CONTENTS

Abstract **1**

Περίληψη **3**

Acknowledgements **5**

1. Introduction **15**

1.1. Earthquakes and Seismic hazard 15
1.2. Earthquakes and Seismic Hazard in Greece 20
1.3. Scope of study 23
1.3.1. Existing situation and associated problems 23
1.3.2. Aims and objectives 24
1.3.3. Importance of this research 25
1.4. Thesis layout 26

2. Seismic hazard assessment **29**

2.1. Existing seismic hazard assessment methods 29
2.2. Seismic hazard assessment in Greece 33
2.3. Disadvantages of traditional seismic hazard assessment methods 41

3. Study area **47**

3.1. Geology – Geomorphology – Active faulting in the Region of Attica 47
3.1.1. Geotectonic setting 47
3.1.2. Geomorphology of the Attica region 52
3.2. Major recent earthquakes in the Attica Region 56
3.2.1. The Alkyonides 1981 earthquake sequence 56
3.2.2. The Athens 1999 Mw5.9 earthquake 59

4. Earthquake catastrophe insurance **63**

4.1. The economic impact of earthquakes 63
4.2. Catastrophe models 65
4.2.1. Brief history of catastrophe models 66
4.2.2. Structure of catastrophe models 67
4.2.3. Problems with existing Earthquake Catastrophe models 68
4.3. Solvency II requirements – EIOPA Standard Approach 70
4.4. Insurance companies' practices 70

5. Methodology **71**

5.1. Tectonic geomorphology and geomorphic indices 71
5.1.1. Background 71
5.1.2. Methods used in this thesis 73
5.1.3. Fault scarp profiling 74
5.1.4. Structure from Motion Photogrammetry induced DTMs 75
5.1.5. Paleoseismology (paleoseismic trenching, ^{36}Cl cosmogenic dating) 77

5.2. Development of seismic hazard maps 79
5.2.1. Active faults identification 79
5.2.2. Fault lengths determination 80
5.2.3. Registration of fault throw-rate data 80
5.2.4. Conversion of throw-rates into earthquake frequencies 81
5.2.5. Earthquake distribution along strike the fault 81
5.2.6. Production of isoseismals 82
5.2.7. Counting and contouring the number of times each locality has been shaken. 83
5.2.8. Amplification/Attenuation of intensity with the bedrock geology 84
5.3. Development of earthquake catastrophe model 87
5.3.1. Hazard Module 87
5.3.2. Vulnerability Module 89
5.3.3. Exposure Module 90
5.3.4. Loss Module 90
5.3.5. Development of the demo portfolio 90
5.3.6. Validation method 91

6. Active faults analysis and active fault database for the Attica Region. 93

6.1. The Sparta fault 93
6.2. Active faults in the Attica region 100
6.2.1. The Milesi fault 100
6.2.2. The Malakasa fault 109
6.2.3. The Afidnes fault 117
6.2.4. The Dionysos fault 121
6.2.5. The Kaparelli fault 125
6.2.6. The Erythres fault 129
6.2.7. The Aigosthena fault 133
6.2.8. The South Alkyonides fault zone 138
6.2.9. The Loutraki fault 144
6.2.10. The Kakia Skala fault 147
6.2.11. Thriassio & Fili faults 150
6.2.12. The Kehriai fault 158
6.2.13. The Dafni fault 161
6.3. Active faults database for the Attica mainland 168

7. Fault specific seismic hazard maps 172

7.1. Seismic hazard maps for the Sparta fault 172
7.2. Seismic hazard maps for the Attica region 177
7.2.1. Maximum expected intensity map 177
7.2.2. Intensity X 178
7.2.3. Intensity IX 179
7.2.4. Intensity VIII 181
7.2.5. Intensity VII 182

7.2.6. Maximum recurrences distribution 183

8. Earthquake Catastrophe model 187

8.1. Insured loss estimation (Loss Reserves Calculation) 187

8.2. Earthquake Catastrophe model for the SCR calculation 191

8.2.1. Hazard Module 191

8.2.2. Vulnerability module 194

8.2.3. Exposure module 195

8.2.4. Loss module 195

8.2.5. SCR calculation for a demo portfolio in Attica region 197

9. Discussion 201

9.1. Assessment of the fault specific seismic hazard mapping method 201

9.1.1. Advantages 201

9.1.2. Limitations 202

9.2. Errors and major assumptions in fault specific seismic hazard maps development 203

9.3. Constraints and limitations in the tectonic geomorphological analysis 207

9.4. Comparison with existing macroseismic intensity data from historic earthquake events 209

9.5. Uncertainties in intensity distribution 212

9.6. Historical seismic record compared to geological fault slip data 213

9.7. The role of the Miocene detachment in fault activity and intensities distribution 216

9.8. Topographic amplification factor 218

9.9. Major assumptions on the Catastrophe model 219

9.9.1. Hazard module 219

9.9.2. Vulnerability Module 220

9.9.3. Exposure module 221

9.9.4. Events table 222

9.10. Comparison of the SCR calculation with the EIOPA's SF. 223

10. Conclusions 229

11. References 231

List of Tables 261

List of Figures 263

Annexes 277

Annex I 279

Annex II 291

1. Introduction

1.1.Earthquakes and Seismic hazard

Earthquakes are the most catastrophic natural phenomena worldwide. They cause significant losses on human lives, building inventory and critical infrastructure. They pose a significant threat to countries' economies, and they trigger extremely high insurance claims in countries where private insurance has a noteworthy penetration in the society. Between 1998 and 2017 geophysical and climate-related disasters caused 1.3 million fatalities and left a further 4.4 billion injured, displaced or in need of emergency assistance (Figure 1.1). While 91% of all disasters were caused by floods, storms, droughts, heatwaves and other extreme weather events, the majority of fatalities were due to geophysical events, mainly earthquakes and tsunamis (Figure 1.2). In addition, UN warn that economic losses from natural hazards are out of control, with direct losses from disasters between 2000 and 2012 being in the range of \$2.5 trillion. Furthermore, US\$71 trillion of assets would be exposed to high earthquake risk globally (1 in 250 years) (UNISDR, 2017). More than this, earthquakes are consistently among the costliest and deadliest catastrophes worldwide (Munich Re Group, 2019). Overall, three out of the five costliest natural catastrophes worldwide concern earthquakes (2011 Tohoku Japan, 1995 Kobe Japan, 2008 Sichuan-Wenchuan China), while the 2011 Japan earthquake yielded the second-largest amount of insured losses over the last 30 years (Munich Re Group, 2019).

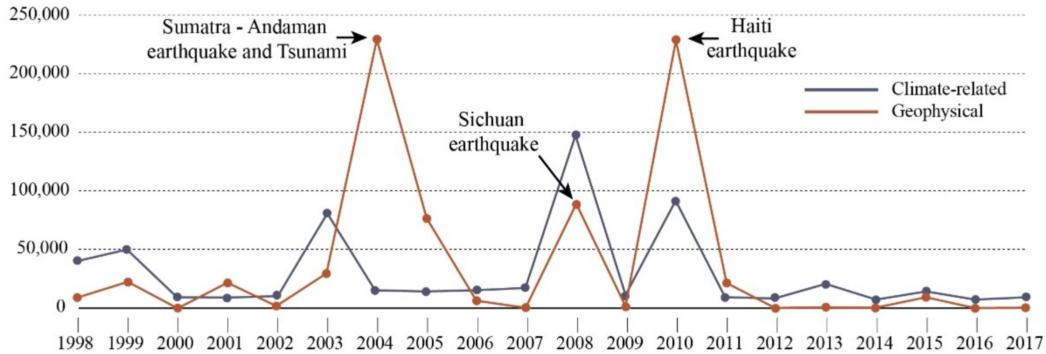

Figure 1.1: Number of fatalities due to geophysical and climate – related natural disasters worldwide, between 1998 and 2017 (reproduced by CRED - UNISDR, 2017). Three major earthquakes (2004 Sumatra – Andaman Mw 9.1earthquake and tsunami, 2008 Sichuan Mw 7.9, 2010 Haiti Mw 7.0 earthquake) resulted in more than 500,000 fatalities.

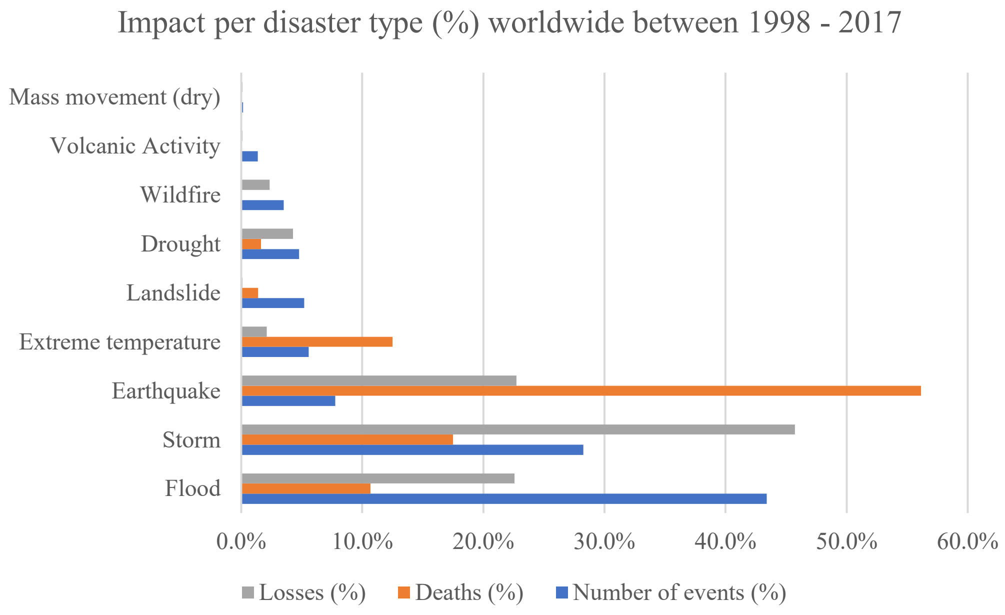

Figure 1.2: Impact of natural disasters worldwide, between 1998 and 2017 (reproduced by CRED - UNISDR, 2017). Although the earthquakes events were considerably less than the climate-related disasters (i.e. floods and storms), they caused the vast majority of fatalities within this period. In addition, in terms of economic loss, earthquakes rank 2nd after storms.

Unlike climatic hazards, earthquakes cannot be predicted in the short term (e.g. Geller et al., 1997; Kerr, 2011). Over the past centuries, several earthquake precursory phenomena have been reported. These phenomena include, among others, abnormal animal behaviour (e.g. Woith et al., 2018), Uranium groundwater anomalies (e.g. Plastino et al., 2010), variations of pH values, and increased As, V, and Fe concentrations in groundwater (e.g. Barberio et al., 2017), pre-earthquake ground displacements using InSAR techniques (e.g. Moro et al., 2017), or anomalies on the ratio of seismic velocities v_p/ v_s (e.g. Scholz et al., 1973). Despite the strong efforts of multiple research teams towards the standardization of these phenomena into a credible earthquake prediction method, none of them appears to be reliable.

Since there is no earthquake prediction method discovered yet, there are two ways to mitigate the effects of these catastrophic phenomena. First, to understand where, when and in what magnitude the next earthquake will occur. Second, to focus on building reliable structures that would withstand the expected strong ground motions after an earthquake event. Although the second is not strictly within the scope of this thesis, it is highly connected to the first way of earthquake effects mitigation, as will be shown below.

Seismic hazard assessment is the necessary tool to provide the best available information regarding the place, time and magnitude of expected ground motions. Its most representative form is expressed in terms of seismic hazard maps, showing the expected ground shaking due to the anticipated future earthquakes.

Apart from ground shaking, earthquake hazards may include liquefaction, landslides, fire, and tsunami. Earthquake risk assessment aims to evaluate the impact of the earthquake hazards on the built environment and population, which would lead to damage and losses. The assessment of earthquake risk represents the first step to support decisions and actions to reduce potential losses. The process involves developing (a) earthquake hazard models characterizing the level of ground shaking and its associated frequency across a region, (b) exposure data sets defining the geographic location and value of the elements exposed to the hazards and (c) vulnerability functions establishing the likelihood of loss conditional on the shaking intensity (UNISDR, 2017). Risk metrics can support decision-makers in developing risk reduction measures that can include emergency response plans, the enforcement of design codes, the establishment of retrofitting campaigns and the development of insurance pools (UNISDR, 2017).

Earthquake mitigation mainly focuses on seismic hazard maps for estimating the consequences of earthquakes offering a long-term prediction of hazard. These maps are essential tools for emergency planning purposes and pre-emergency protection measures such as land-use planning and regulations for earthquake-resistant buildings. The existing seismic hazard maps are usually developed by considering two different approaches of seismic hazard assessment: i) the probabilistic approach, which is the commonest, and ii) the deterministic approach.

In general, seismic hazard maps are usually developed based only the historical and instrumental data regarding past events. Seismic hazard assessment methods that are based on historical earthquakes may either overestimate or underestimate the probability of future earthquakes. Large earthquakes that have already been recorded in the existing earthquake catalogues will lead to an increased probability of future earthquakes, as there would be large magnitudes in the sample used by the traditional models. However, in such cases, the seismic energy would have already been released, and the actual probability for the same fault to rupture in the near future would be, in fact, reduced. On the contrary, in areas where seismogenic faults have not ruptured yet, the traditional seismic hazard models will not have any input for large earthquakes and will inevitably generate decreased probabilities for future earthquakes, although the strain may accumulate over time.

A significant difference over the last decades concerns the introduction of active faults in seismic hazard maps. This is due to our enhanced knowledge of earthquake geology and paleoseismology, where the faults that represent the seismic sources have been well studied, also incorporating slip-rates that govern the earthquake recurrence.

The advances in earthquake-related sciences, especially in earthquake geology, have provided valuable tools to scientists who try to answer where the next earthquake will happen. The key for this answer is that we now know that in general, earthquakes are caused by the sudden slip between the footwall and the hangingwall of active faults. Earthquakes can also be caused mostly by other events such as volcanic activity, landslides, or human activities like hydraulic fracturing for oil and gas extraction, but these are out of the scope of this thesis. As a result, the identification, detailed mapping and determination of faults and their activity are the first steps for every earthquake mitigation procedure.

Fault identification and mapping is the result of various geology-related scientists, such as structural geologists, tectonic geologists, geomorphologists and earthquake geologists. It requires geologic fieldwork and expertise but also the efficient knowledge of different scientific disciplines, such as remote sensing and photogrammetry, and tools, such as Geographic Information Systems and Unmanned Aerial Vehicles (UAV or Drones).

In most cases, the identification of a fault is much easier than the conclusion of whether it is active or not. Various indications may show that a fault is active. Among them are delimitation or even deformation of recent alluvial deposits, a retained postglacial scarp, diversion of the drainage network, asymmetry of drainage basins, abrupt changes in topography along the fault line, etc. For the most part, the estimation of the level of its activity is even more complicated. Usually, it demands the application of a paleoseismic method, such as fault scarp profiling (e.g. Papanikolaou et al., 2013; Mechernich et al., 2018), analysis of the fault plane weathering (e.g. Wiatr et al., 2015; Mason et al., 2016; Mechernich et al., 2018), analysis of the concentration of 36Cl isotopes (e.g. Benedetti et al., 2002; 2003), boreholes analysis or paleoseismic trenching (e.g. Papanikolaou et al., 2015a). In offshore faults, it is often easier to obtain long term fault slip rates if there are seismic data that provide a detailed picture of the subsurface structure, especially the thickness and age of sediments that are cut through active faults (e.g. Foutrakis and Anastasakis, 2020).

The aforementioned methods are significant for the assessment of the seismic hazard potential in an area of interest. New Seismic Hazard Assessment methodologies tend to follow fault specific approaches where seismic sources are geologically constrained active faults (WGCEP, 1990, 1999, 2002, 2007; Ganas and Papoulia, 2000; Boncio et al., 2004; Roberts et al., 2004; Papanikolaou and Papanikolaou, 2007a; Pace et al., 2010; Stein et al., 2012; Papanikolaou et al., 2013). These fault specific approaches are used in order to address the aforementioned problems related to the historical records incompleteness, obtain higher spatial resolution and calculate realistic source locality distances, since seismic sources are very accurately located. Fault specific approaches provide quantitative assessments as they measure fault slip rates from geological data, providing a more reliable estimate of seismic hazard than the historical earthquake record (e.g. Yeats and Prentice, 1996; Papoulia et al., 2001; Michetti et al., 2005).

Geological data have the potential to extend the slip history of an active fault back many thousands of years, a time span that generally encompasses a large number of earthquake cycles (Yeats and Prentice, 1996), and thus explicates the long-term pattern of fault-slip. In addition, geologic fault slip-rate data offer complete spatial coverage, providing higher spatial resolution than traditional seismic hazard maps based on historical/instrumental records (Boncio et al., 2004; Roberts et al., 2004; Pace et al., 2010; Papanikolaou et al., 2013). For land-use planning and critical facilities or insurance risk evaluation purposes, a higher spatial resolution is also desirable (Grützner et al., 2013; Deligiannakis et al., 2018a).

As a result, there is an emerging tendency for incorporating geological data and fault specific information relating both to the identification and mapping of active faults, as well as extracting information regarding the recurrence interval of associated potential earthquakes (Papanikolaou et al., 2015a).

1.2. Earthquakes and Seismic Hazard in Greece

Earthquakes are the most catastrophic events in Greece regarding damages and casualties (PreventionWeb, 2011). In terms of seismic energy, Greece is ranked among the most seismogenic regions in the world, taking sixth place after Japan, the Republic of Vanuatu, Peru, Solomon Islands and Chile. 2% of the seismic energy worldwide and more than 50% of the seismic energy in Europe is released in Greece every year. During the last 500 years, more than 170 destructive earthquakes occurred in Greece and the surrounding area, with mean annual casualties of 17 fatalities and 92 wounded (Papazachos and Papazachou, 2003). According to the Hellenic Association of Insurance Companies, the number of damaging earthquake events with insured claims in Greece is less than 25% of the total number of natural catastrophes since 1993 (EAEE, 2019). Only 6 earthquakes are listed among the 29 most important catastrophic phenomena between 1993 and 2020. However, the number of claims for earthquake damages was similar to the rainfalls' claims, although the latter outnumbered earthquakes, as there were 19 significant rainfall events recorded between 1993 – 2020 (Table 1.1). In terms of insured losses, the worst natural disaster in Greece was the Athens 1999 Mw 5.9 earthquake, which caused more than 4.8 billion euros economic loss and 111 million euros insured loss (Figure 1.3).

Table 1.1: Number of insured claims, claim amount and average claim per disaster type in Greece, from 1993 up to 2018 (reproduced by EAEE, 2019).

Disaster	Number of claims	Claim amount (mil. €)	Average claim (thousand €)
Snowfall	646	2.4	3.7
Rainfall	10,412	128.6	12.4
Forest fire	1,542	45.8	29.7
Earthquake	10,313	133.5	12.9
Riot	1,193	48.5	40.7
Total	24,106	358.8	14.9

Despite the emerging awareness and concern for climate change-related risks, the risk perception among people living in Greece is still connected to this devastating record. A recent questionnaire by Papagiannaki et al. (2019) confirms the above revealing that the average risk perception among Greeks is the highest for earthquakes, compared to wildfires, floods and other meteorological related hazards.

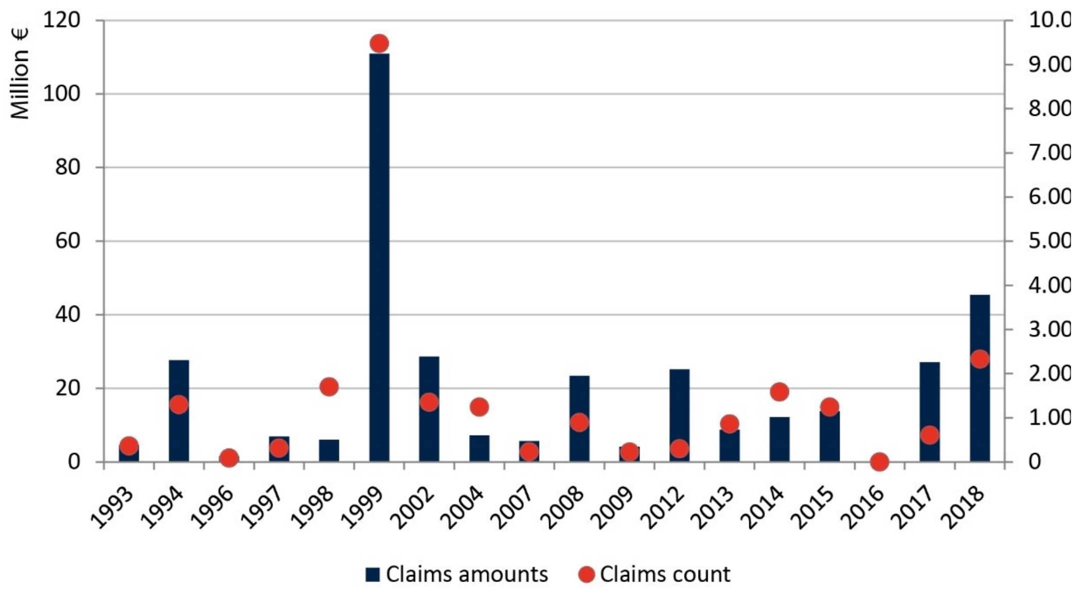

Figure 1.3: Number of claims and the total claim amount per year for all types of natural disasters in Greece, from 1993 up to 2018 (reproduced by (EAEE, 2019). The largest amount of claims and damage compensations were recorded in 1999, when the Athens Mw 5.9 earthquake occurred.

Greece has one of the longest historical catalogues worldwide, with the oldest recorded events in 550 B.C. The historical record of earthquakes in Greece has been compiled by various researchers (Galanopoulos, 1961; Makropoulos and Burton, 1984; Papazachos and Papazachou, 2003), providing useful data on seismic hazard assessment of Greece. However, there is incompleteness and inhomogeneity of geographical and temporal coverage in terms of the seismic record, so that this catalogue is considered complete for events M≥7.3 since 1500 and for M≥6.5 only since 1845 (Papazachos et al., 2000). At the same time, the recurrence interval of particular faults ranges from a few hundred years to several thousands of years (Goes, 1996; Yeats and Prentice, 1996; Machette, 2000).

Regarding the Attica region, recurrence intervals vary from a few hundred years for the highly active South Alkyonides Fault (Collier et al., 1998) up to thousands of years, as shown in the Kaparelli fault, which was reactivated in 1981, after being inactive for several thousands of years (Benedetti et al., 2003; Chatzipetros et al., 2005; Kokkalas et al., 2007). Thus, historical earthquake catalogues are generally too short compared to the recurrence intervals of faults. The latter implies that the sample from the historical record is incomplete and that a large number of faults would not have ruptured during the completeness period of the historical record (e.g. Grützner et al., 2013).

Further uncertainties are related to the epicenters locations, even for instrumentally recorded earthquakes (Papanikolaou et al., 2015b). The errors can reach up to 20 km for the older events (1965-1980) and up to 10 km for the most recent ones (Papazachos et al., 2000). Larger uncertainties result for the older events approximate epicentral locations. For the period 1901-1964 the errors can be up to 30 km, but they can reach up to 50 km for the older events (before 1900) when the number of available macroseismic information points is less than 5 (Papazachos et al., 2000; Stucchi et al., 2012). Indeed, recorded events in the Attica region are an example, as the uncertainty on the epicentral locations for the most recent Athens 1999 Mw 5.9 earthquake, which are derived from different papers and catalogues, exceed 5 km. For the older Oropos 1938 Mw 6.0 event, the epicentres in two different catalogues are located 12 km away from each other.

In that context, the existing earthquake models, which are based mostly on the historical and instrumental earthquake catalogues, are not able to reach the level of accuracy that would be acceptable if they had a representative sample of earthquake events.

This thesis aims on applying a fault specific seismic hazard assessment methodology in Attica, Greece, by incorporating active faults and providing fault specific probabilistic seismic hazard maps. In addition, it incorporates such maps within a hazard module to develop an earthquake catastrophe model. The Attica Region was selected as the study area for the following reasons:

- 40% of the population and 42% of insurance exposure is located in Attica.
- A high-resolution geotechnical map is available for the greater Athens area, offering the possibility to incorporate the effect of bedrock geology to the damage pattern.
- Attica is surrounded by a relatively large number of active faults, many of which have been relatively well studied.
- The vast majority of these faults exhibit low-slip-rates, therefore they are characterized by relatively long recurrence intervals spanning up to several thousands of years.
- Most of these faults have not been activated during the last centuries; therefore they are absent from the historical record and may be ignored in the traditional seismic hazard assessment methods.

1.3. Scope of study

1.3.1. Existing situation and associated problems

The aforementioned problems regarding the incompleteness of seismic catalogues are also inherited in the current seismic hazard maps for the Greek territory. Until now, the seismic hazard assessment studies are based on several procedures and algorithms, which typically require the study area to be divided into seismogenic source zones. These zones are considered to represent seismicity which is homogeneously distributed in space and stationery in time. In addition, the borders of the source zones are based on the historical and instrumental earthquake record (e.g. Vamvakaris et al., 2016).

Apart from the national seismic building code, which separates Greece into three large zones (Zone I - lowest category of seismic risk, Zone II - intermediate risk, Zone III - high risk), there are several seismic hazard assessment studies that separate Greece in numerous seismic source zones (see also Chapter 2, Section 2.2) and as such, they are primarily based on earthquake catalogues. As will be shown in this thesis, the faults that affect Attica are capable of producing earthquakes of magnitude M>6, but in their vast majority, have low slip rates. This implies that there are large time intervals between each event, and many faults may not have ruptured during the past 200 years when the historical and instrumental earthquake catalogues are considered to be complete.

Since such weaknesses regarding the use of earthquake catalogues in seismic hazard assessment are well understood, many researchers have already analyzed active faults that might affect Attica in case of rupture (see also Chapter 3, Section 3.2). However, this information is not assembled in one database for the Attica region. The existing fault databases cover the whole country, and as such, they lack spatial resolution when it comes to smaller areas. In addition to that, there are no GIS-based seismic hazard maps yet based on these databases.

Insurance companies and especially catastrophe model vendors are common users of earthquake catalogues for seismic hazard assessment. The recent EU Directive for the prudential of the insurance companies in Europe, namely Solvency II, demands that the catastrophe models used to calculate the anticipated earthquake losses are based on transparent algorithms and methods. It is common practice for the commercial earthquake catastrophe modellers to use the same earthquake catalogues as input for the Hazard module. However, Petseti and Nektarios (2012) compared four internationally renowned models for the estimation of seismic hazard in Greece and showed that each model generated significantly different results in terms of Probable Maximum Loss (PML) values. Since these models are not fully transparent, there is no way to verify the exact reason for these differences. However, it is evident that in such cases, the seismic hazard assessment depends on the type of earthquake catalogues processing, the vulnerability curves and the loss module, but not the actual seismic potential.

1.3.2. Aims and objectives

This study aims to develop a seismic hazard assessment method that uses active faults characteristics and local geological conditions to estimate the past and future macroseismic intensities distribution in the Attica region. Therefore, an active faults database will be developed, containing essential information for each fault that lies within or in such distance from Attica that could cause damage in case of earthquake rupture.

The most important onshore faults will be analyzed using geologic data interpretation methods to obtain their geometry and length and confirm the level of their activity and extract expected magnitudes and number of past events in a period of 15 ± 3 kyrs. Since active faults data will be used to develop the fault-specific seismic hazard maps, they will be tested against the hypothesis that the current earthquake catalogues for the Greek territory are long enough to be used for earthquake protection planning seismic hazard assessment.

The seismic hazard assessment method will allow for locality specific long term earthquake shaking recurrence record, in contrast to the existing methodologies that usually examine separate homogenous aerial seismic sources and the related short-term seismicity. In addition, the different high spatial resolution seismic hazard maps that will be developed will illustrate the recurrence intervals of macroseismic intensities and not just of the earthquake events. This implies a complex modelling process for multiple faults and their influence on seismic hazard in every location within the Attica region. The seismic hazard maps will also provide a 15 ± 3 kyrs long record of ground shaking in an area that is considered of low seismicity. The whole process will be based on a Geographic Information System (GIS) and will be fully automated in order to reduce errors and processing time and to withstand the complexity of calculations. Overall, the current thesis aims to test whether geological fault slip-rate data, supported by local site-response data and GIS techniques, can provide higher spatial resolution and more reliable representation of seismic hazard than maps based on historical seismicity.

The outcomes of this methodology will be adapted to the requirements/demands of the insurance industry. Therefore, two types of earthquake loss models will be developed. First, a fully transparent functional earthquake loss model that calculates the expected insured loss over a predefined forthcoming time period will be generated. Second, a fully transparent synthetic earthquake catastrophe model will be developed based on a fault specific Hazard Module. This model will be used for the calculation of the Solvency Capital Requirements (SCR) and will be tested against the European Insurance and Occupational Pensions Authority's (EIOPA) Standard Formula, which is the most established model for SCR calculation in the European insurance industry.

Following the above, the results of this thesis are divided into three distinct parts. The first part concerns the collection of fieldwork and literature data regarding the active faults in the Attica Region. This part includes a detailed fault by fault description regarding the fault geometry, kinematics and estimated slip rates. Tectonic geomorphology, paleoseismic trenching, cosmogenic ^{36}Cl dating and geologic cross-sections are among the methods used for the compilation of the active faults database.

The second part presents the methodology and the fault specific seismic hazard maps of the Attica region, providing maps of maximum expected macrosesimic intensity, maximum recurrences distribution, as well as maps with site-specific recurrence for different macroseismic intensities.

The third part incorporates the hazard module within two earthquake catastrophe models for the Attica Region. The first model calculates the expected insured over a desired time period. The second catastrophe model calculates the Solvency Capital Requirements for an insurance company, in compliance with the Solvency II EU Directive.

The detailed layout of the thesis is shown in Section 1.4.

1.3.3. Importance of this research

The importance of this research lies in four major factors:

- First, it aims at providing a solution to the problems connected to the traditional seismic hazard assessment methods, which are the incompletence and uncertainties in earthquake catalogues.
- Second, it is the first time that a fault specific seismic hazard assessment method for multiple faults is applied in Greece.
- Third, it is the first time that fault specific seismic hazard maps are used for the development of an earthquake loss model for the insurance industry.
- Fourth and foremost, it provides useful information regarding the seismic hazard in Attica, which is the most densely populated and built area in Greece.

1.4. Thesis layout

This thesis is divided into 11 Chapters. In particular, Chapter 1 presents the Introduction, the rationale for this research and the scope of the current study. The identification of the importance of this study, the existing research problems and the aims and objectives of this research are presented in Sections 1.3.1-1.3.3, respectively.

Chapter 2 provides a literature review on the existing methods and advances in seismic hazard maps. Section 2.1 describes the existing seismic hazard assessment methods, while Section 2.2 focuses on the existing seismic hazard assessment in Greece. The disadvantages of the existing seismic hazard assessment methods are described in Section 2.3.

Chapter 3 presents information for the study area. Section 3.1 presents geologic, tectonic and geomorphologic characteristics of the Attica region through previous work that has already been conducted. Section 5.1 describes the standard methods used in literature for the analysis of faults, either in the field, or using office-based techniques, or a combination of both. The most important information regarding two recent large earthquakes in Attica is presented in Section 3.2, mainly focusing on the damage patterns and the faults characteristics.

Chapter 4 covers all aspects of the earthquake catastrophe insurance, the Solvency Capital Requirements and the existing situation regarding seismic hazard assessment in the insurance industry. Section 4.1 describes the economic impact of earthquakes on the insurance industry worldwide and in Greece. Section 4.2 presents important aspects regarding the catastrophe models, such as their history, structure, uses and problems. Section 4.3 describes the Solvency II EU directive requirements for the insurance companies and Section 4.4 provides a brief description of the insurance companies practices regarding the use of earthquake catastrophe models.

Chapter 5 presents the methodology used in this thesis. In particular, several different methodologies have been used and they are described in 3 subsections. Section 5.1 introduces the methods used for the active faults analysis and the composition of the fault database. The tectonic geomorphological indices are introduced and the application method is explained. Section 5.2 describes the steps for the development of the seismic hazard maps, including the processing in GIS environment. The methodology for the development of the earthquake catastrophe model is presented in Section 5.3.

The results of this thesis are presented in Chapters 6-8. Chapter 6 presents the active faults database that includes all faults that could produce earthquakes of magnitude M>6 and could affect the Attica region in case of seismic rupture.

The seismic hazard maps showing the site-specific recurrence for intensities VII - IX (MM), as well as the maps showing maximum expected intensities and recurrences distribution, are displayed in Chapter 7.

Chapter 8 presents the results regarding the earthquake catastrophe modelling. The earthquake catastrophe model for the calculation of the insured losses over a certain future time period is shown in Section 8.1, while the earthquake catastrophe model for the calculation of the Solvency Capital Requirements is shown in Section 8.2, along with a detailed description of the Hazard, Vulnerability, Exposure and Loss modules.

Chapter 9 includes discussion over various aspects of this thesis. Section 9.1 presents an assessment of the proposed methodology, with an analysis of advantages and disadvantages. Section 9.2 includes the errors and major assumptions in the development of the seismic hazard maps. Section 9.4 presents a comparison of the fault specific seismic hazard maps with the existing macroseismic intensity data form historic earthquakes in Attica. In Section 9.5 the uncertainties in intensity distribution are discussed, while Section 9.6 presents a comparison of historical seismic record compared to geological fault slip data. Section 9.7 explains the role of a major geological structure, namely the Miocene detachment, in faults activity and intensities distribution, while Section 9.8 discusses the possible impact of the topographic amplification factor in the intensities distribution. Section 9.9 presents the major assumptions underlying the earthquake catastrophe model. Finally, the comparison of the SCR calculation based on the fault specific hazard module, with the EIOPA Standard Formula is presented in Section 9.10.

The results of this thesis are demonstrated in Chapter 10 and the list of references in Chapter 11.

It is important to note that parts of this thesis have already been published or submitted for publication. In particular, Section 5.2 and Chapters 6 and 7 are already published in the following paper:

Deligiannakis, G., Papanikolaou, I.D., Roberts, G., 2018. Fault Specific GIS Based Seismic Hazard Maps for the Attica Region, Greece. *Geomorphology* 306 (2018)

Sections 5.3 and 8.2 have already been submitted in the following publication:

Deligiannakis, G., Zimbidis, A., Papanikolaou, I.D. (submitted for publication). Earthquake loss and Solvency Capital Requirement calculation using a fault specific catastrophe model.

In Chapter 6, work was conducted in collaboration with other colleagues, and is already published, or submitted for publication in the following papers:

Iezzi, F., Roberts, G., Faure Walker, J., Papanikolaou, I., Ganas, A., Deligiannakis, G., Beck, J., Wolfers, S., Gheorghiu, D. (submitted for publication) Temporal and spatial earthquake clustering revealed through comparison of millennial strain-rates from 36Cl cosmogenic exposure dating and decadal GPS strain-rate.

Mechernich, S., Schneiderwind, S., Mason, J., Papanikolaou, I.D., Deligiannakis, G., Pallikarakis, A., Binnie, S.A., Dunai, T.J., Reicherter, K. (2018). The seismic history of the Pisia fault (eastern Corinth rift, Greece) from fault plane weathering features and cosmogenic ^{36}Cl dating. *Journal of Geophysical Research: Solid Earth,* DOI: 10.1029/2017JB014600

Grützner, C., Schneiderwind, S., Papanikolaou, I., Deligiannakis, G., Pallikarakis, A. & Reicherter, K. (2016). New constraints on extensional tectonics and seismic hazard in northern Attica, Greece - the case of the Milesi Fault. *Geophysical Journal International* 204, doi: 10.1093/gji/ggv443.

Papanikolaou, I.D., Roberts, G., Deligiannakis G., Sakellariou, A. and Vassilakis E. (2013). The Sparta Fault, Southern Greece: From segmentation and tectonic geomorphology to seismic hazard mapping and time dependent probabilities. *Tectonophysics*, DOI: http://dx.doi.org/10.1016/j.tecto.2012.08.031

Substantial portions of these papers are the result of work by the present author and thus included in this thesis. Credit for work conducted by others is indicated where appropriate.

2. Seismic hazard assessment

2.1. Existing seismic hazard assessment methods

Typical seismic hazard assessment is divided into two different methodologies: i) the deterministic methodology, and ii) the probabilistic methodology, which is the commonest. An earthquake hazard assessment is deterministic when it specifies a particular earthquake or level of ground shaking in terms of single-valued parameters such as magnitude, location or peak ground acceleration, but without specifying how likely this particular event might be (Yeats et al., 1997). The hazard is expressed in qualitative terms as high, medium and low, showing the variation in the intensity of a hazard from one location to another (Bell, 1999). This approach offers a clear and trackable method of computing seismic hazard whose assumptions and elements are easily discerned, providing understandable scenarios to the end users (Reiter, 1990). However, this approach is problematic in regions of diffuse seismicity, where earthquakes cannot be correlated to a particular seismic source. In addition, it tends to disregard the frequency of earthquake occurrence and can lead to the mistaken assumption that there is no uncertainty (Reiter, 1990).

In probabilistic assessment, numerical probabilities are assigned to earthquake occurrences and their effects during a specific period, such as the life expectancy of a large construction (Yeats et al., 1997). Usually, the results of probabilistic seismic hazard analysis are expressed in the form of maps of different levels of ground motion (intensity, acceleration) at a given level of probability (Main, 1996).

The general procedure followed in probabilistic seismic hazard analysis includes the individual steps of seismic zoning, estimating the recurrence, and fitting a local attenuation law to the ground motion in order to calculate an annual probability of exceedance of a particular level of ground motion (Reiter, 1990). According to Panza et al. (2014), more recent standard zone-based probabilistic seismic hazard assessment (PSHA) requires the definition of the seismic source zones geometry, where seismicity is typically assumed to be rather uniform, and a maximum expected magnitude. Other definitions of sources are also used, including line sources and zoneless approaches (e.g., Frankel, 1995; Woo, 1996).

The standard output of a PSHA is a map displaying the PGA level that has a 10 % exceedance probability in 50 years (or 475 years return period), an input parameter currently required by almost all National Annexes of Eurocode 8 (Bisch et al., 2011). Usually, PSHAs are performed to estimate hazard for a specific location, or they are extended to national or continental scales considering multiple sites (Woessner et al., 2015). In Europe, the first efforts to provide a combined PSHA at the continental scale were completed over 20 years ago (see also Giardini 1999; Jimenez et al. 2001). However, national models or regional models are usually based on similar inputs, yet they are developed under different procedures that are not in agreement and can result in considerable differences at country borders (e.g. Grunthal et al. 1998; Grunthal and Wahlstrom 2000).

The PSHA methodology was first defined by Cornell (1968) and involved four steps:

(1) Earthquake sources are delineated as points, faults or area seismic zones areas. The area source is the most common model used. These areas represent a geographical region of some geological, tectonic and seismological similarity, within which earthquake characteristics are assumed to be uniform (Algermissen et al., 1982). (2) Determination of the frequency-magnitude relationship based on the historical record. The frequency-magnitude relationship that defines the earthquake recurrence is the basis of the probabilistic seismic hazard analysis. This relationship is obtained by regression analysis of the earthquake data. The *b* value is the slope of the regression line that describes the relative frequency of different magnitudes, and indicates the relative number of large and small earthquakes in such way that a low *b* value represents a shallow slope, implying a relatively higher proportion of large earthquakes than a high *b* value (Reiter, 1990). Each of the sources is assigned a recurrence curve based on recorded seismicity with an estimated upper bound earthquake (Yeats et al., 1997) (3) Estimation of earthquake effect, similar to the deterministic procedure, except that the range of earthquake size considered requires a family of earthquake attenuation or ground motion curves (Reiter, 1990). At this step, the attenuation curves are constructed and are then used to estimate intensities and peak accelerations as a function of magnitude and distance (Yeats et al., 1997). In places where a good history of intensity or ground acceleration recording exists, determination of regional attenuation relationships, which depict the local geotectonic and source to site wave propagation condition, are likely to be more representative than worldwide attenuation relationships (Algermissen et al., 1982). (4) Results of the previous two stages are mathematically combined to give one curve, showing the probability of exceedance of given levels of peak acceleration at a site during a specified time period (Yeats et al., 1997).

This approach, although it has served in the seismic hazard assessment for decades, has proved inadequate in many cases, mostly in large earthquake events. The reason is that the existing catalogues are too short, covering a period that is much shorter than the average seismic cycle of the active faults, which rupture at a recurrence interval from a few hundred years to several thousands of years (Scholz, 2019). The completeness period of the earthquake catalogues is usually a tiny fraction of the period covered by the historical record and ranges from only 100 yrs (e.g. central America and New Zealand) up to 500 yrs (in parts of Europe) for earthquakes of magnitude M≥5.8, but is essential since it is used as input data in the traditional seismic hazard assessment methods (Papanikolaou et al., 2015a). Finally, the definition and selection of seismic source boundaries is subjective and depends strongly on expert judgement (Reiter, 1990; Bender and Perkins, 1993; Papanikolaou & Papanikolaou, 2007a, see also Figure 2.1).

In addition, the use of the historical record introduces uncertainties and errors in the exact earthquake locations (Papanikolaou, 2003). The ability to locate earthquakes accurately was improved by the WorldWide Standard Seismograph Network (WWSSN) since 1962, indicating that high-quality earthquake data exists for less than

50 yrs (Bolt, 1999). Still, localities could be tens of kilometres from their assumed sites (e.g. Stuchi et al. 2013). Futhermore, the inclusion of foreshocks and aftershocks in the earthquake catalogue is contrary to the independence assumption proposed by the Poisson model, and thus, these events should be removed from the data set, thus introducing another source of uncertainty (Bender and Perkins, 1993).

Over the last two decades, fault-based hazard models have been developed in Greece (see also Section 2.2), Italy and California (Faure Walker et al., 2021). Fault specific approaches are of decisive value for seismic hazard assessment by providing quantitative assessments through measurement of geologically recorded slip on active faults (WGCEP, 2002; Boncio et al., 2004; Roberts et al., 2004; Pace et al., 2010; Stirling et al., 2012; Papanikolaou et al., 2013). The most commonly used tools infer maximum magnitudes of earthquakes on individual faults from empirical relationships (e.g. Wells and Coppersmith, 1994; Pavlides and Caputo, 2004) and use fault slip-rates to determine average earthquake recurrence rates.

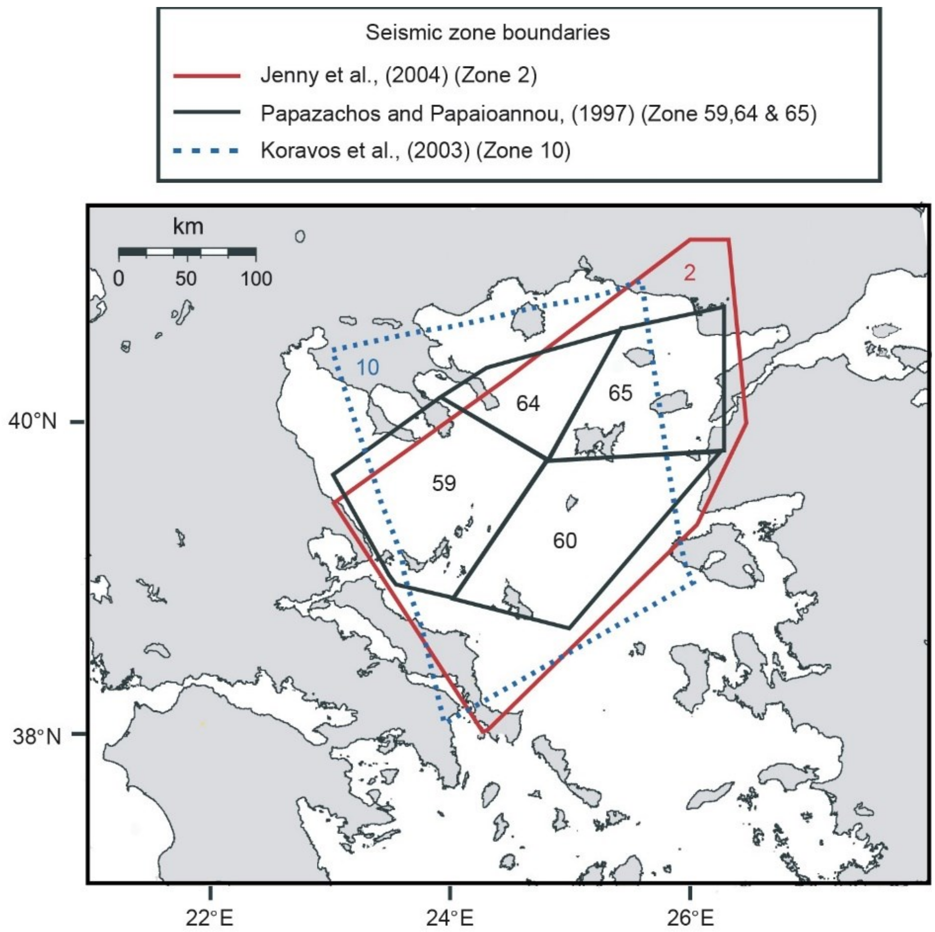

Figure 2.1: A characteristic example of the subjective delination of seismic zones. The spatial distribution of the seismic zones in the North Aegean Basin, Greece, is delineated by different research groups. This figure shows that the definition of zone boundaries, within which seismicity rates are assumed to be uniform, is rather subjective. Image reproduced from Papanikolaou & Papanikolaou (2007).

The first seismic hazard maps developed using purely geological data were introduced by Papanikolaou (2003) and Roberts et al. (2004), who examined 17 active normal faults in the Apennines and provided high spatial resolution seismic hazard maps, showing maximum expected intensity, and intensity recurrence, also taking into account the geological conditions. Several publications regarding seismic hazard assessment using fault characteristics have been published recently, especially in Italy (e.g. Pace et al., 2006, 2010, 2016), Spain (e.g. Rivas-Medina, 2014) and Greece (Papanikolaou et al., 2013; Grützner et al., 2016; Deligiannakis et al., 2018a, also presented in this thesis).

The increasing progress and capability of developing fault specific seismic hazard maps by different research teams, indicated the need to construct the faults databases in a commonly established way. In 2000, Coppersmith and Youngs outlined the method for a Probabilisic of Fault Displacement Hazard Assessment at a specific site and described the type of data needed for this process. More recently, Faure Walker et al. (2021) provided a template database structure that can be easily used as an input to existing software for fault specific seismic hazard models (e.g. Pace et al., 2016; Chartier et al., 2019).

However, although the need for the introduction of active faults in seismic hazard assessment is established, there is a still considerable difference in the number of published papers for seismic hazard assessment using seismicity and active faults. A search in Scopus Database reveals that the publications which had the keywords combination of “seismic hazard assessment” and “earthquake catalogues” or “seismicity” are as much as 11 times more than the ones using the keywords combination of “seismic hazard assessment” and “fault specific”.

2.2. Seismic hazard assessment in Greece

The seismicity of Greece has been extensively and continuously studied by many researchers (e.g. Galanopoulos, 1961; Makropoulos and Burton, 1984; Papazachos and Comninakis, 1986; Papazachos et al., 2000; Makropoulos et al., 2012), who provided seismic catalogues with historical and instrumental earthquakes. These catalogues are constantly used as the primary input for the seismic hazard assessment in Greece, both for research teams and the official state, since they are supposed to provide an accurate description of seismicity in the region and to be sufficiently homogeneous in magnitude (Tselentis and Danciu, 2010).

Since the introduction of the seismic source model as the cornerstone of the probabilistic approach for seismic hazard assessment (see also Cornel, 1968; Esteva, 1970), the seismic catalogues covering the Greek domain were adopted by various researchers as a proxy to constrain seismic zonation for the broader Aegean domain.

Papazachos (1980) divided the Aegean domain (including the Ionian sea) into 19 seismic zones of shallow earthquakes on the basis of several seismotectonic criteria. In fact, he utilized seismicity data from the last 100 years and also incorporated the trend of the main geotectonic zones in Greece for the delineation of the seismic zone borders. In an effort to increase the spatial analysis and to better represent the b values distribution in the Aegean domain, Hatzidimitriou et al. (1985) introduced 21 zones, after revising Papazachos' (1980) map. They also incorporated seismological data, such as the distribution of earthquake foci, the fault mechanisms, and seismicity rates.

A year later, Makropoulos and Burton (1985) used the Peak Ground Acceleration as a hazard measure and provided maps showing maximum expected PGA with 70% probability of not being exceeded in the next 50 years.

Papazachos et al. (1990) considered the macroseismic intensity as a measure of seismic hazard and used instrumental and historical data to compare the application of Cornell's (1968) and the 'mean value' methods. They applied their method to 35 large cities in Greece (see an example for Athens and Corinth in Figure 2.2) and constructed recurrence curves obtained from probabilistic hazard analysis. For example, Athens had a mean return period of 1000 years for Modified Mercalli Intensity VII.

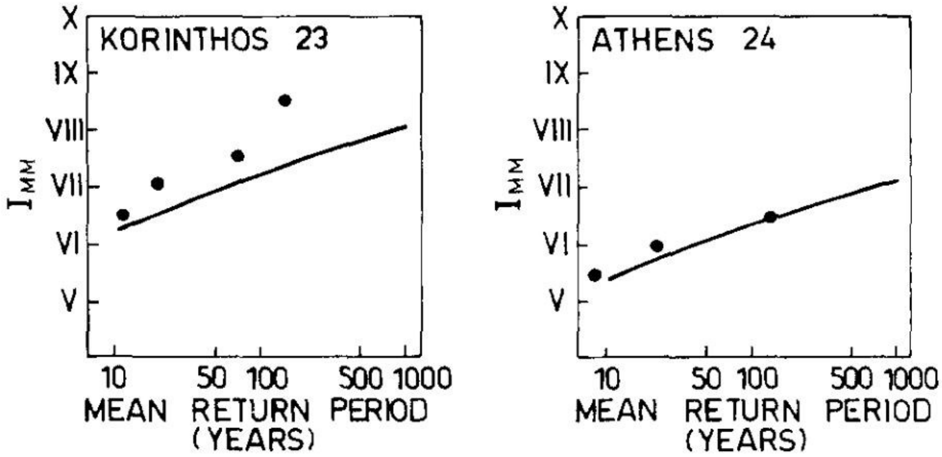

Figure 2.2: Mean-value analysis results (black dots) plotted along with recurrence curves obtained from probabilistic hazard analysis (Cornel, 1968), for Athens and Corinth. The mean-value analysis, which incorporates historical data for macroseismic intensities, results to higher values for the mean-value method. Indeed, at the time of this publication, Corinth had already experienced the 1981 Alkyonides earthquake sequence, but the Athens 1999 Mw5.9 earthquake had not occurred. Image reproduced from Papazachos et al. (1990).

Three years later, Papazachos and Papaioannou (1993) separated the Aegean and the surrounding area in 74 new seismic source zones for shallow and intermediate-depth earthquakes. They used the earthquake magnitude as a hazard measure and introduced empirical relations to calculate the probabilities of occurrence and the magnitude for mainshocks in each seismogenic source for the next ten years. However, large areas were assumed to be aseismic, and thus there were no seismic sources constrained due to the incomplete earthquake catalogues (Figure 2.3).

Papaioannou and Papazachos (2000) redesigned the shallow seismic sources for the Aegean region and concluded to 67 zones without excluding any location (Figure 2.4). They calculated time-independent and time-dependent probabilities of Modified Mercalli intensity occurrence for 144 cities and villages in Greece between 1996 - 2010, using improved source parameters, new attenuation relationships and the local site effects on the strong-ground motion. They showed that Athens would experience intensity VII with a mean return period of 475 years, and the time-dependent probability of occurrence for intensities ≥ VII was relatively low for Athens and Lavrio (south Attica). However, the time-dependent probability method was based on the Papazachos et al. (1997) equation, which uses data from declustered earthquake catalogs.

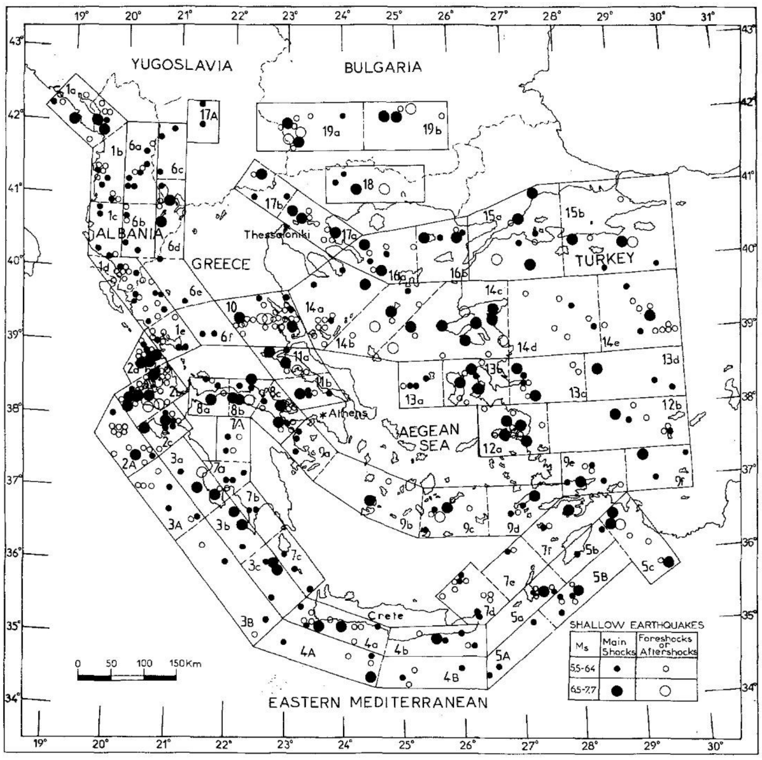

Figure 2.3: The 69 shallow earthquake sources proposed by Papazachos and Papaioannou (1993). Note that there are extended areas in Northern Greece, Attica and the north Cyclades, where no seismic source is constrained, as there was no historical or instrumental seismicity recorded yet. Image reproduced from Papazachos and Papaioannou (1993).

Further analysis of seismicity and the introduction of geodetic data resulted in different seismic source zonations (e.g. Koravos et al., 2003; Jenny et al., 2004), or probabilistic seismic hazard assessment in terms of horizontal PGA values with varying time intervals for important Greek cities (e.g. Tsapanos et al., 2004). Burton et al. (2004) produced isoacceleration maps with PGA variations depending on the different attenuation relationships and return periods, and they suggested that Athens would have a 90% probability of non-exceedance for 0.05 g up to 0.26 g for the next 50 years.

More recently, Tselentis and Danciu (2010) used the 67 source zones proposed by Papaioiannou and Papazachos (2000) as a proxy to build new probabilistic seismic hazard maps for Greece, in terms of Peak Ground Acceleration and Peak Ground Velocity. They assumed homogenous and ideal bedrock site conditions and used a 10% probability of exceedance in 50 years’ time period, which resulted in a mean PGA of 0.26 g. They also produced a seismic hazard map by dividing the Aegean domain into points mesh with an interval of 0.1° and calculated the mean PGA and PGV values for each point (Figure 2.5).

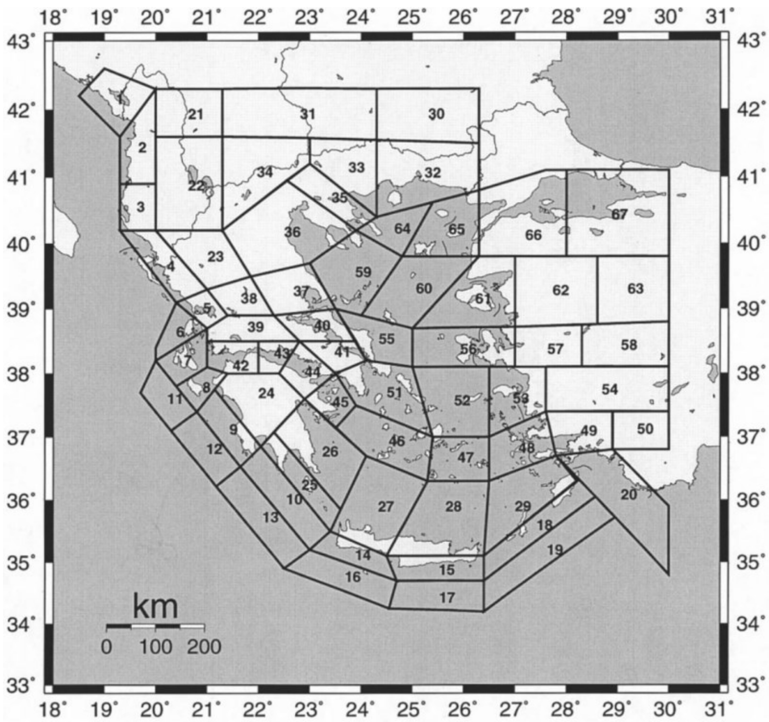

Figure 2.4: The 67 shallow earthquake sources proposed by Papaioannou and Papazachos (2000). Note that after the Kozani Grevena 1996 and Athens 1999 earthquakes, there are no aseismic areas and each location on the map belongs to a source zone. Image reproduced from Papazachos and Papaioannou (2000).

In all the above seismic hazard assessment methods, constrained active faults are usually ignored. Fault slip-rates, expected magnitudes and fault geometry that affect the hazard distribution are not taken into consideration. Instead, when faults are referred as input in the seismic hazard assessment process, they are usually utilized for the depiction of the seismic source borders (Vamvakaris et al., 2016), or they affect predictive equations that use the fault mechanism as an input (e.g., Tselentis and Danciu, 2010). The same holds for the official seismic hazard maps issued for the Greek Earthquake Planning and Protection Organization (EPPO). Indeed, these maps are based on historical and instrumental earthquake catalogs. The first map version was issued in 1984 and divided Greece in 4 seismic hazard zones, showing the expected PGA with a 10% probability of exceedance in 50 years (Figure 2.6). Zone I, with the lowest hazard (0.12 g), covered extended areas in the whole country, including parts of Attica and Western Macedonia. After the 1995 Kozani – Grevena earthquake, which occurred in Zone I, the zone boundaries changed, and a new map was issued in 2000 (EAK, 2000). In this map, Zone I was turned into Zone II, so that areas where large earthquakes had occurred after the 1984 map were included (Figure 2.7). The latest official seismic hazard map was released in 2003 (Figure 2.8; EAK, 2003). In this map, Zone I was abolished, after the recent 1999 Athens devastating earthquake (see also Section 3.3.1), which showed that even areas where there was no historical or instrumental seismicity, could experience large earthquakes if the active fault ruptures have long return periods.

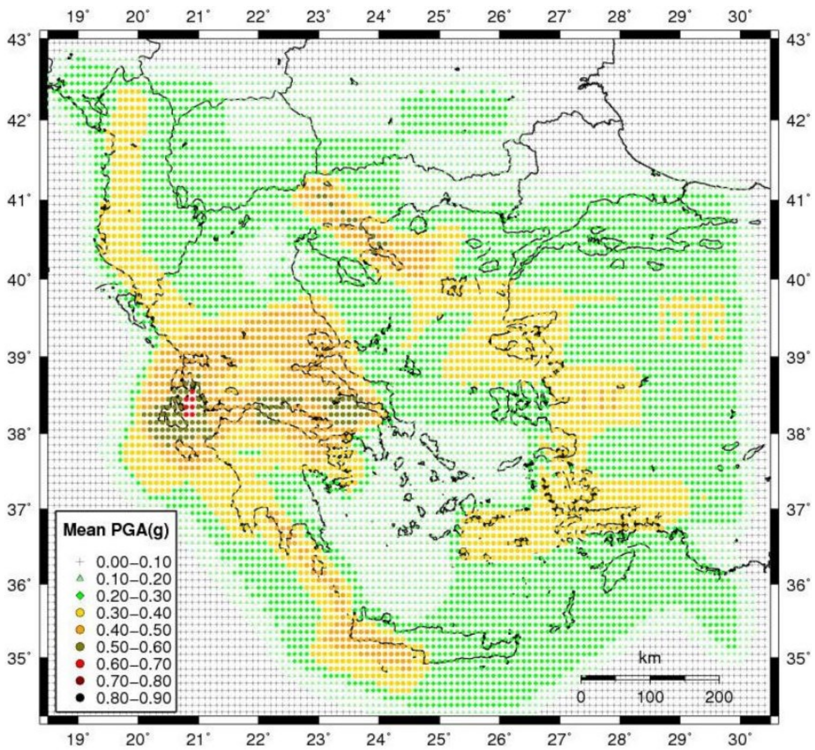

Figure 2.5: Seismic hazard map for the Aegean domain, by Tselentis and Danciu (2010), representing hazard using points mesh with 0.1° interval. Each point corresponds to a PGA value with 10% probability of exceedance for the following 50 years.

The first attempts to provide a more reliable seismic hazard assessment using active fault zones analysis in Greece were held Ganas and Papoulia (2000) and Papoulia et al. (2001). Ganas and Papoulia (2000) applied the FRISK code (McGuire, 1978) to calculate probabilistic estimates of ground motion parameters for six normal fault segments in the Northern Evoikos Gulf in Central Greece. Papoulia et al. (2001) applied the Bayesian extreme-value distribution (see also Cornel, 1972; Stavrakakis and Tselentis, 1987; Stavrakakis and Drakopoulos, 1995), in order to estimate the seismic hazard associated with the Inner Messiniakos fault zone, in terms of probabilities of earthquake occurrence and earthquake magnitude distribution. Their findings showed that the actual seismic hazard was increased in comparison to previous studies that rely only on seismicity and indicated the need to study active faults for seismic hazard assessment.

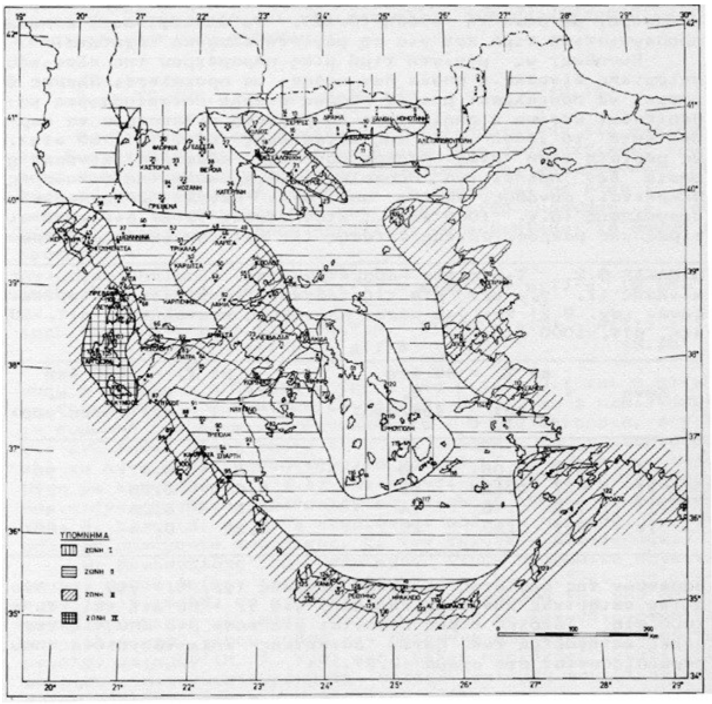

Figure 2.6: The first seismic hazard map issued by the Earthquake Planning and Protection Organization in 1984. It divided Greece into 4 different seismic hazard zones, showing the expected PGA with a 10% probability of exceedance in 50 years. Note that the central Aegean, parts of Attica, Western Macedonia and parts of Thrace belong to the lower hazard zone.

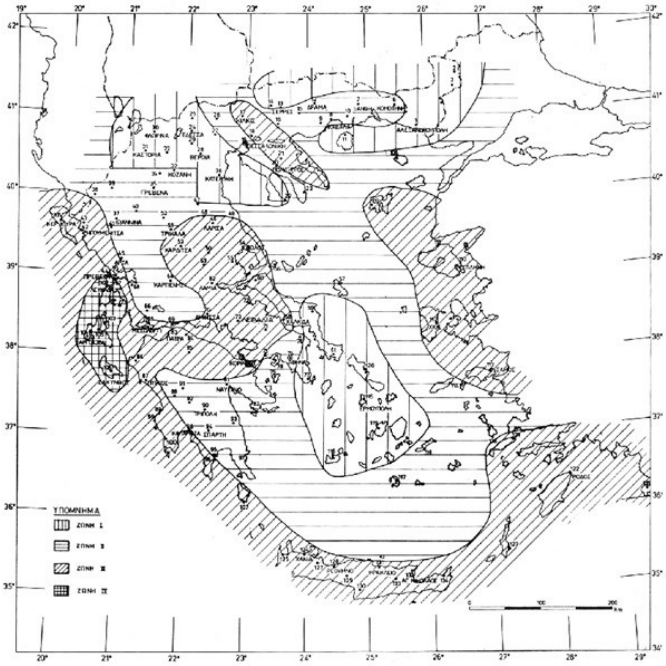

Figure 2.7: The second seismic hazard map issued by the Earthquake Planning and Protection Organization (EAK 2000). Kozani and Grevena cities are now included in Zone II, after the 1995 Kozani-Grevena earthquake.

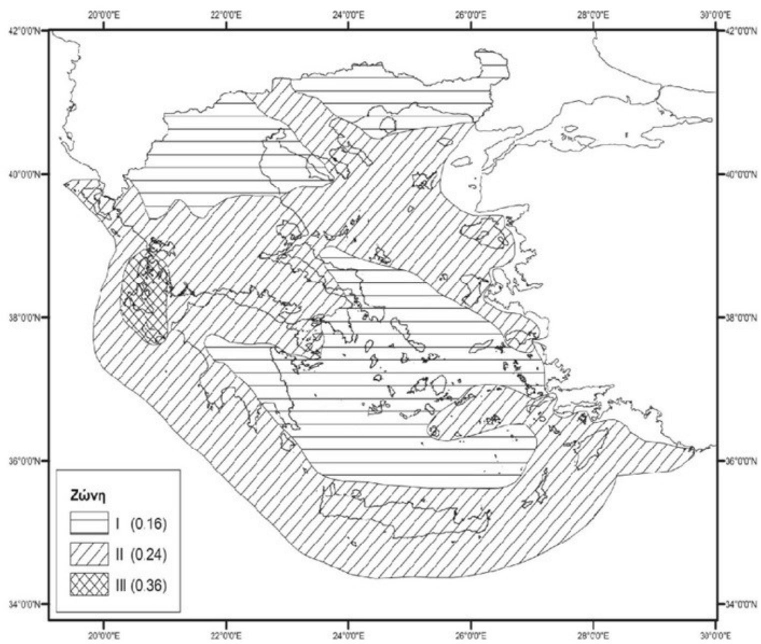

Figure 2.8: The third seismic hazard map issued by the Earthquake Planning and Protection Organization (EAK, 2003). The previous Zone I is now ommited and the lowest hazard Zone (Zone II) represents 0.16g with 10% probability of exceedance in 50 years.

The following research for fault specific seismic hazard assessment in Greece had a similar pattern but used more complex techniques for fault activity identification and subsequent magnitude and ground motions estimation. Papanikolaou and Papanikolaou (2007a) were the first to provide fault specific seismic hazard scenarios using purely geological data. They analyzed the neotectonic structure of the North Aegean Basin fault system and provided deterministic fault specific scenarios of expected earthquake magnitudes, depending on different fault segmentation scenarios. Similarly, Papanikolaou and Papanikolaou (2007b) compiled geological, geomorphological and tectonic structure data to identify active fault structures in NE Attica, Greece. They also indicated the seismic hazard potential of the Afidnes fault, which lies next to the Athens metropolitan area, providing fault slip-rate and expected earthquake magnitude. Pavlides et al (2009) used active faults to assess earthquake potential and ground acceleration in North Aegean islands to confront the culprits of seismogenic sources.

In 2013, Papanikolaou et al. used a fault specific seismic hazard method to develop fault specific seismic hazard assessment maps for the Sparta fault in Peloponnese, Greece. The method was firstly introduced by Papanikolaou (2003) and Roberts et al. (2004) and utilized i) empirical relationships between coseismic slip values, rupture lengths and earthquake magnitudes, ii) empirical relationships between earthquake magnitudes and intensity distributions, and iii) attenuation / amplification functions for seismic shaking on bedrock compared to flysch and basin-filling sediments. The final output was a high-resolution locality specific seismic hazard map for the Sparta Basin, showing intensity ≥ IX recurrence, based on the Sparta Fault postglacial activity (see also Section 7.1). This was the first time this methodology was applied in Greece and was followed by the seismic hazard assessment for the Milesi fault by Grützner et al. (2016). The first approach for multiple faults seismic hazard assessment was conducted by Deligiannakis et al. (2018a), who compiled an active faults database for the Attica region and developed fault specific seismic hazard maps for the Attica region (also presented in this thesis).

2.3. Disadvantages of traditional seismic hazard assessment methods

In general, knowledge of the seismicity of a region is based on the records of past earthquakes retrieved from instrumental or historical data, which constitute the catalogues of earthquakes and they are used for mapping the seismic risk (Papanikolaou, 2003). Thus, seismic hazard maps in their simplest and commonest form are representations of the past historic and instrumentally recorded seismicity of a region (e.g. Scholz, 2019). Moreover, these records, and thus most seismic hazard maps, do not explicitly incorporate active faults as discrete earthquake sources (e.g. Stirling et al., 2012). The data are usually presented as maps of intensity distributions or other forms of ground motion (e.g. PGA, PGV) over stated time periods. The main assumptions are that: i) seismicity in the near-future will follow the same pattern as past activity; ii) past seismicity is representative of the long-term slip-rate variations in one given seismic zone (e.g. McGuire, 1993; Scholz, 2019), and iii) that the seismic activity is uniformly distributed in time so that the probability does not vary in time (Reiter, 1990). The above methods of constructing seismic hazard maps suffer from 5 major disadvantages (Papanikolaou, 2003). In particular:

(1) They have an incompleteness and an inhomogeneity of geographical and temporal coverage in terms of the seismic record. This is because historic catalogues are generally too short (from 100 to 2000 yr depending on the country) compared to the recurrence interval of particular faults (ranging from a few hundred years to tens of thousands of years) (Yeats and Prentice, 1996; Goes, 1996; Machette, 2000).For example, the earthquake history for the San Fransisco Bay is regarded as complete for M≥5.5 only since 1850 (Bacun, 1999), whereas Rikitake (1991) pointed out that a complete catalogue of historical earthquakes in the Tokyo area exists since 1603 and the historical record in New Zealand dates from 1840, when European settlement began (Stirling et al., 2012). On the other hand, fault recurrence intervals range from a few hundred years to tens of thousands of years (e.g. Yeats et al., 1997). Consequently, several faults will not be represented in the historical earthquake record and therefore will be absent from the seismic hazard maps (Papanikolaou, 2003).

This incompleteness can be verified by many examples in Greece, Italy and Japan, despite the fact that Greece and Italy have some of the longest and best-constrained historical catalogues worldwide (Papanikolaou, 2003). Specifically, the damaging earthquakes in Kozani-Grevena Greece 1995 (Ms=6.6) (e.g. Ambraseys, 1999), Belice, Italy, 1968 (Ms=5.9) (Michetti et al., 1995) and on the island of Sakhalin, north of Japan 1995 (M=7.6) (Bolt, 1999) occurred in regions characterized as very low seismic risk or aseismic, according to the historical earthquake records and existing hazard maps, despite the fact that geologic data indicate repeated Late Pleistocene-Holocene slip, but with long (10^3 yrs) recurrence intervals. Even though some of the regions described above were re-assessed as areas of higher risk following these earthquakes, the use of historical and instrumental earthquake catalogues remain the main data source for seismic hazard assessment in the neighbouring region (Papanikolaou, 2003). More recent examples show that even in well-studied areas, significant overprediction or underprediction of hazards can also happen. In Tohoku, 2011 (M=9) (Yomogida et al., 2011), a catastrophic earthquake occurred where the hazard was considered to be low, according to the available earthquake history that appeared to show no record of such mega - earthquakes (Stein et al., 2012) (Figure 2.9).

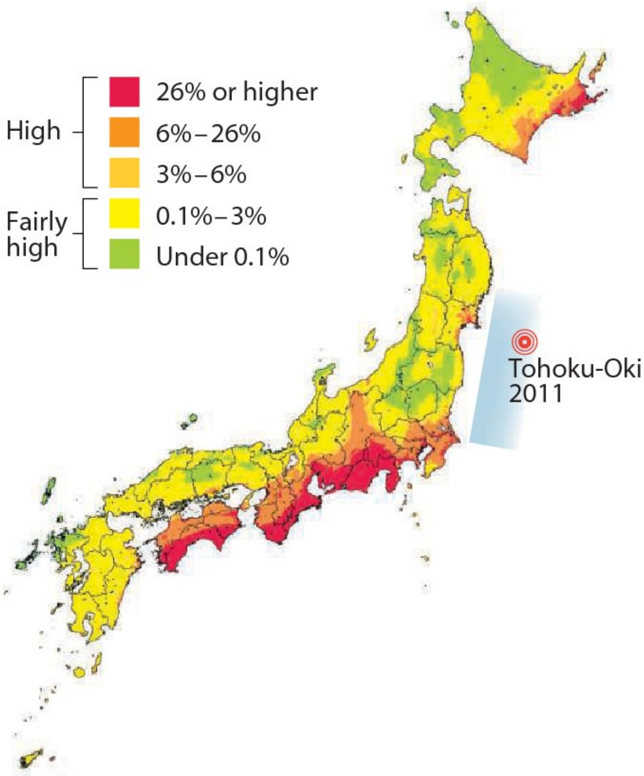

Figure 2.9: The Tohoku 2011 mega-earthquake (star and blue band) struck far north of the zone considered to have the greatest seismic hazard (depicted in red colour). Reproduced by Kerr, 2011.

Similarly, there are cases where seismic hazard is overestimated when using only earthquake catalogues. The example of the different seismic hazard maps of Hungary shows that traditional methods for seismic hazard assessment may predict more concentrated hazard near sites of earlier earthquakes (Figure 2.10, Stein et al., 2012).

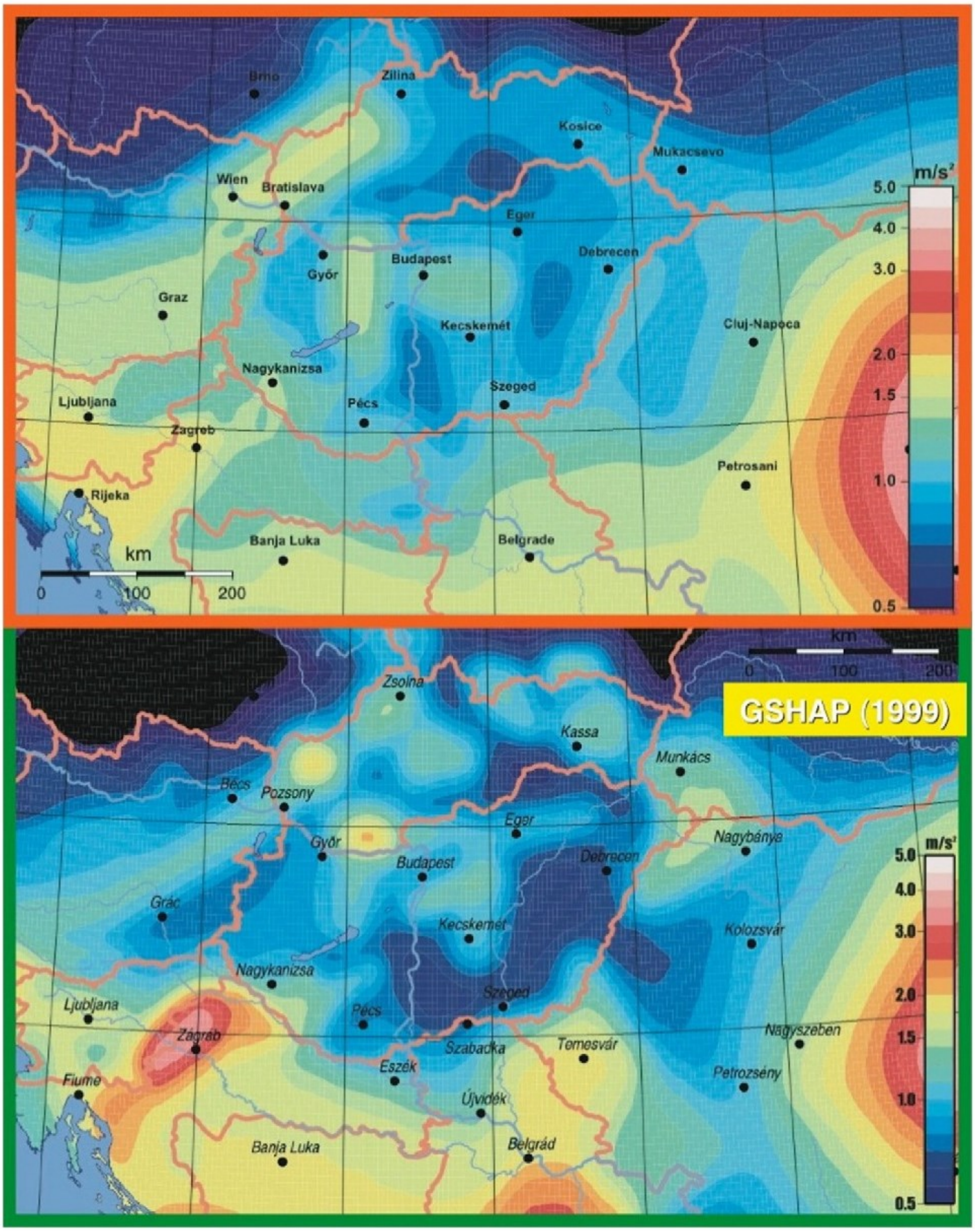

Figure 2.10: Two different seismic hazard maps for Hungary and the surrounding area, showing PGA expected at 10% probability in 50 years (Swafford and Stein, 2007). The GSHAP model (bottom), based only on historic and recorded seismicity, predicts more concentrated hazard near sites of earlier earthquakes, compared to a different model (top) including geological data that predicts more diffuse hazard (Toth et al., 2004). Image reproduced by Stein et al. (2012).

(2) They assume that seismicity per unit time is maintained for different time periods, contrary to evidence from geologically determined slip-rates. The assumption is that the same pattern of seismic activity observed through the historical catalogues in the past, will be valid in the future. However, slip-rates and average recurrence intervals have been proven to be variable over short time-intervals, because earthquake events are often clustered in time and clusters can be separated by relatively long periods of

low activity (Sieh et al., 1989; Marco et al., 1996; Benedetti et al., 2002). If a perceived area of low instrumental/historical seismicity is simply a quiescent interval, then the region sooner or later will enter a period of relatively clustered earthquakes. In that case, the potential seismic hazard is very high.

(3) They lack spatial resolution. Spatial resolution depends on the data input. When source data are poor, the spatial resolution is low. Generally, historical catalogues are short, so they provide a limited number of events and as a result they offer a low spatial resolution map. Indeed, low seismicity regions (e.g. central Europe), or regions of very short historical catalogues (e.g. New Zealand) can not provide high spatial resolution maps.

(4) They fail to consider the influence of bedrock geology on the intensity distribution because most hazard maps incorporate only one specified site condition. However, older [San Francisco 1906, (Reid 1910)] and recent events [Mexico city 1985 (Singh et al., 1988), Spitak Armenia 1988 (Hadjian, 1993), Loma Prieta USA 1989 (Bell, 1999), Pyrgos, Greece 1993 (Lekkas, 1996), Kobe Japan 1995 (Esper and Tachibanac, 1998), Aigion, Greece 1995 (Lekkas et al., 1996), Athens 1999 (Papanikolaou et al., 1999; Lekkas, 2001)] have shown that areas of severe damage are highly localised and that the degree of damage can change abruptly over short distances (Bell, 1999). These differences are frequently due to changes in local geology or soil condition (Bell, 1999).

(5) They can give erroneous pictures of the present day hazard. A low seismicity zone on such a map, representing low hazard, may delineate a seismic gap (i.e. a gap that an impeding earthquake will cover) and actually be a place of high present and future hazard (Scholz, 2002). On the other hand, a region that has recently experienced a damaging earthquake, and hence is represented as high hazard on a map, actually may be a region of low hazard in the near future because it is now at an early stage in a new seismic cycle (Scholz, 2002) or is an area of low fault slip-rate. There is consequently a lack of identification of a time datum upon which to base the hazard estimation. Therefore, these maps fail to incorporate the most basic physics of the earthquake cycle, according to which - following a major earthquake - another earthquake on the same fault segment is unlikely until sufficient time has elapsed for stress to gradually re-accumulate (e.g. Ogata, 1999; Ellsworth et al., 1999; Stein, 2002).

In an attempt to mitigate the effects of incomplete data coverage, the frequency-magnitude relation (Gutenberg and Richer, 1944) has been used. This relation may be determined by recording small earthquakes in a region and then extrapolating them to calculate the recurrence time of potentially damaging earthquakes of larger magnitude (Reiter, 1990; Scholz, 2002). This method has often been used to estimate hazard at regions with no record of destructive earthquakes.

However, this method does not improve the lack of data since:

i) the historical and instrumental records that this method utilizes, are too short to define the repeat time of the largest earthquakes, hence the shape of the magnitude-frequency distribution cannot be defined confidently at the largest magnitude (e.g. Wesnousky 1994);

ii) large potentially damaging earthquakes belong to a different fractal set than small earthquakes, and cannot be predicted accurately with this extrapolation (Scholz, 1990);

iii) there may be areas where the G-R relationship is not applicable, as the seismicity is described by the characteristic earthquake model, implying that characteristic events dominate earthquake recurrence, resulting in nonlinear frequency-magnitude relationships (Schwartz and Coppersmith, 1984; Wesnousky 1994);

iv) near-fault seismicity may not necessarily be a reliable indicator of potentially hazardous normal faults and the 1983 Ms=7.3 Borah Peak, Idaho, earthquake, which produced about 36 km of surface rupture, is a well known example that demonstrates this viewpoint (Crone and Haller, 1991). In the two decades prior to the 1983 Borah Peak earthquake there were no earthquakes of magnitude 3.5 or greater, within 25 km of the main shock (Dewey, 1987). Similarly, in the two months before the mainshock, there were no foreshocks of magnitude 2 or greater, within 50 km of the epicentre (Richins et al., 1987). Even though the region was generally aseismic before 1983, prominent late Pleistocene and Holocene fault scarps are evidence that many large prehistorical surface faulting earthquakes have affected the area in the past (Crone and Haller, 1991).

Speidel and Mattson (1997) suggest that the G-R relationship is still used because: i) political demands require something for probabilistic seismic hazard analysis; ii) it is a variable that is easy to deal with; and iii) no persuasive alternative has come forward. However, the fact that laws and regulations may require such extrapolation adds a political requirement without resolving the scientific one (Speidel and Mattson, 1997).

3. Study area

The following sections present the most important characteristics of the Attica Region in terms of the geological and tectonic setting, geomorphology, and the two most significant earthquakes that hit the area during the last 40 years.

It is important to note that the official Attica Region administrative boundaries include areas that lie far away from the Attica mainland. Distant islands, such as Kythira, Spetses and Hydra, and remote areas in Peloponnese, like Troizina and Methana, are officially included in the Attica Region. However, it is important to clarify that only the Attica mainland is included in the study area when Attica Region is referred to in this thesis.

3.1. Geology – Geomorphology – Active faulting in the Region of Attica

3.1.1. Geotectonic setting

The Hellenic subduction zone is an essential component the active tectonics of the Eastern Mediterranean (Shaw and Jackson, 2010). From Oligocene until late Miocene, extension within the Agean domain produced a series of back-arc to fore-arc extensional basins due to arc-parallel extensional structures (e.g., Mercier et al., 1989; Papanikolaou, 2021). McClusky et al. (2000) integrated nine year's GPS observations, collected from 1988-1997, for a large part of the eastern Mediterranean region in the zone of interaction of the Arabian, African, and Eurasian plates. They suggested that the pattern of regional extension along the Aegean arc does not continue today. Indeed, Mediterranean seafloor subducts northwards beneath Crete at a rate of 35 mm/yr, which greatly exceeds the convergence between Africa and Eurasia (5–10 mm/yr) because of the rapid SW motion of the southern Aegean itself, relative to Eurasia (Reilinger et al., 2006). The motion of the Aegean block is accommodated by a right slip zone in the northern Aegean (see also Papanikolaou and Papanikolaou, 2007a). This zone continues westward into a broad zone of dextral and extensional shear along the Central Hellenic Shear Zone that crosses central Greece, cross-cuts older structures of the Hellenic arc, and bounds a series of neotectonic basins (Papanikolaou and Royden, 2007). As a result, it produces much of the seismicity associated with the extensional deformation of the Aegean region (Ambraseys and Jackson, 1990; Goldsworthy et al., 2002). Active faulting and focal mechanisms of past earthquakes imply that the NE-SW right-lateral strike-slip faulting in the northern Aegean changes into E-W normal faulting in mainland Greece (Taymaz et al. 1991; Hatzfeld 1999; Goldsworthy et al., 2002), while thrust faulting occurs in the Hellenic Trench and the coastal fold belt of NW Greece and Albania (Taymaz et al. 1990).

Two main actively extending basins form part of the Central Hellenic Shear Zone near the Attica region. The Gulf of Corinth, has one of the highest extension rates in the world, with up to 20 mm/yr that diminishes to 8 and 4 mm/yr towards its eastern end (e.g. Billiris et al., 1991; Briole et al., 2000). The Saronikos Gulf is tectonically less active than the Gulf of Corinth, but a number of active faults have been mapped (see also Foutrakis and Anastasakis, 2020), and historical seismicity has been recorded. A number of these faults have been interpreted as being active, capable of producing large magnitude earthquakes, and to pose seismic hazard to the region (Deligiannakis et al., 2018a).

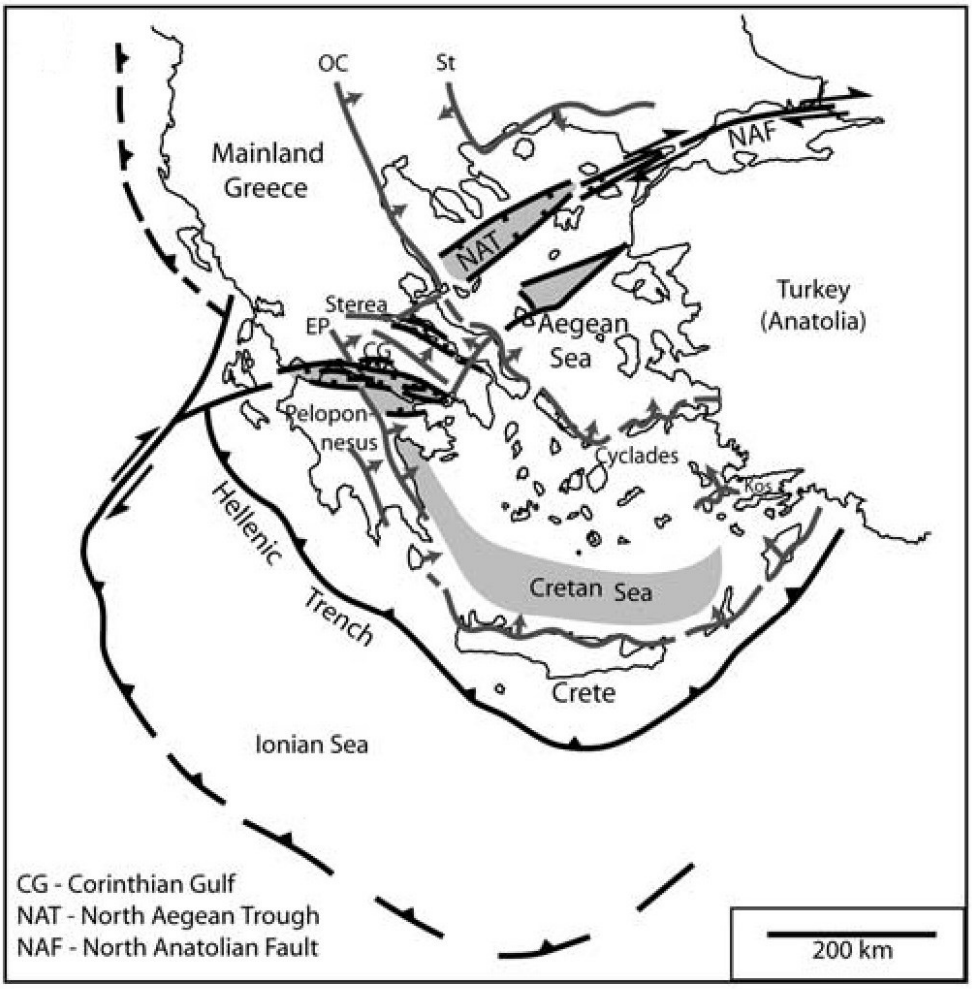

Figure 3.1: Simplified map of the Hellenic system by Papanikolaou and Royden (2007) showing active thrust faults (black lines with barbs), active normal faults (black lines with tick marks), and arc-parallel extensional detachment faults of Miocene age (grey lines with arrows, St, Strymon detachment; OC, Olympos-Cyclades detachment; EP, East Peloponnesus Detachment).

The geological formations that outcrop in Attica region play an important role not only in the understanding of the geological regime and the tectonic setting but also in the earthquake ground motions attenuation or amplification. Attica is characterized by a combination of metamorphic and non-metamorphic geologic formations, which comprise the alpine bedrock. These formations are covered by post-alpine sediments, beginning from the Miocene sediments up to the most recent alluvial - Quaternary deposits that are present in recently formed basins across the whole study area. The alpine formations of the Attica Region are divided into two major groups (Papanikolaou et al., 1999):

a) the upper group, consisting mainly of the Pelagonian zone (s.l.) series, from the Paleozoic phyllites, quartzite, sericite schist, shale, sandstone (Gaitanakis, 1982) to Triassic – Jurassic Limestone, overlain by a tectonically emplaced ophiolitic formation, mostly peridotite, along with a sub-ophiolitic tectonic mélange of shales and radiolarites. Upper Cretaceous shallow-water limestone overly transgressively the ophiolite formations (Dounas, 1971; Bornovas et al.,1981; Katsikatsos et al., 1986; Katsikatsos 1991, 2000, 2002; Parginos et al., 2007). The Pelagonian zone (s.l.) outcrops in the north and western parts of the Attica region, namely Parnitha, Aigaleo, Poikilo and Pateras Mts.

b) the lower group which comprises metamorphic formations, including marble, schist, and crystalline limestone (Papanikolaou et al., 1999). The metamorphic formations outcrop in the eastern part of the Attica region, namely in Penteli and Ymittos mountains, but also in smaller mounts and hills in Mesogeia and Lavrio areas. According to Krohe et al. (2010), the metamorphic basement rocks of Attica region consist of high-pressure formations that are divided into upper and lower tectonic units that differ in lithological formations and pressure-temperature paths (e.g. Marinos and Petraschek, 1956; Katsikatsos et al., 1986). Krohe et al. (2010) propose that the lower tectonic unit consists of marbles, calc-schists and metapelites, metamigmatites, metabasic rocks and antigoritic serpentinites. Moreover, the same authors support that in the area of Hymettus and Panion mountains, Triassic dolomites and a metaclastic sequence from tuffaceous metavolcanic tectonically underlie the lower tectonic unit, implying that they might constitute the para-autochthonus unit of Attica (see also Lekkas and Lozios, 2000; Liati et al., 2013). It is suggested that the lower tectonic unit is correlated with Almyropotamos Unit in Evia (Katsikatsos et al., 1986; Baziotis, 2008; Krohe et al., 2010), though the latter lacks calc-schists and dolomite sequences, which are typical for this unit (Krohe et al., 2010). The upper tectonic unit emerges to the NE side of Penteli Mt, the north side of Hymmetus Mt and in Mesogea and Lavrion areas. Moreover, it consists of marbles, calc-schists, phengite-chlorite schists, phyllites and metabasites (Krohe et al., 2010).

A detachment fault, which was active during the Miocene (Papanikolaou and Royden, 2007), separates the metamorphic units from the non-metamorphic units (Figure 3.2). This detachment passes from the Southern Evia Island, through Aliveri to Kalamos in northeast Attica and continues to the southwest into the Athens Basin, approximately along the Kifissos River (Papanikolaou et al., 1999; Xypolias et al., 2003). High seismic velocities in the central part of the basin are most likely related to this major boundary (Drakatos et al., 2005). According to Papanikolaou and Royden (2007), this boundary has a significant portion of dextral shear, whereas Mariolakos and Fountoulis (2000), and Krohe et al. (2010) propose a right-lateral strike-slip fault zone. The detachment fault was active throughout the Middle to Late Miocene and progressively became inactive during the Early Pliocene (Papanikolaou and Royden, 2007; Royden and Papanikolaou, 2011). It has accommodated more than 25 km of vertical displacement and causes significant local variations of strain rates (Foumelis et al., 2013). Nevertheless, it forms the main boundary that separates the E-W trending higher slip-rate active faults in the western part of Attica from the NW-SE trending lower slip-rate faults in the eastern part (Papanikolaou et al., 2004; Papanikolaou and Papanikolaou, 2007b). It is also thought to be responsible for the formation of the Miocene tectonosedimentary debris flow formation in between the metamorphic and non-metamorphic rocks in NE Attica (Papanikolaou and Papanikolaou, 2007b).

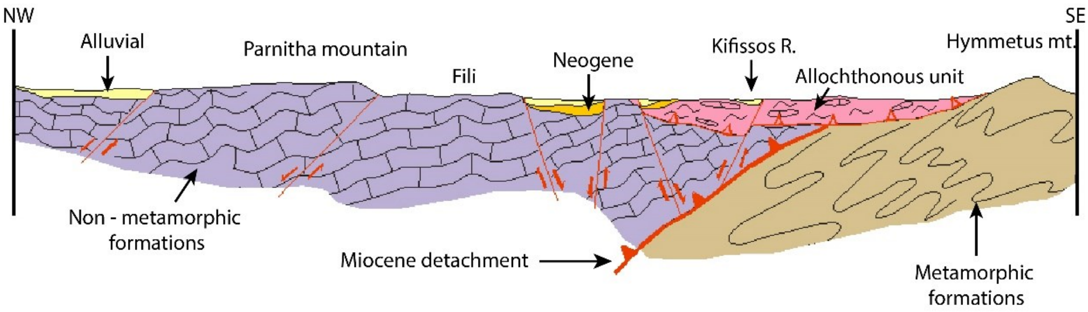

Figure 3.2: Schematic geological cross-section of the central part of Attica, in a NW – SE direction including the Athens basin. The NW dipping Miocene detachment separates the non-metamorphic bedrock in the west, from the metamorphic formations in the east. Image modified from Papanikolaou et al., 1999.

In east Attica, isolated blocks of the Pelagonian zone (s.l.) are preserved (Mposkos et al., 2007) on Lavrion peninsula, where at the top Cretaceous fossiliferous limestones occur and at the base serpentinites and cherts (e.g. Photiades and Carras, 2001), and at the eastern part of Hymmetus Mt, south of Koropi, where Eocene – Oligocene mollassic sediments, such as mudstones, sandstones and limestones, overly the lower tectonic unit marbles (Alexopoulos et al., 1998; Mposkos et al., 2007). Moreover, chert and limestone overlay the Athens schist (Allochthonus Unit) at Acropolis, Lykabettus and Tourkovounia hills (Papanikolaou et al., 2004).

There are four major onshore basins in the Attica region that contain material from the sedimentation that started in the late Miocene until the present; the Athens, Mesogea, Megara and Thriassion basins.

The post-alpine sediments of the Athens basin have Neogene and Quaternary age. The Neogene formations, can be distinguished in marine/coastal facies (mostly found in the south part of the Athens Basin) and lacustrine – fluviolacustrine deposits (northern part of the Athens Basin) (Papanikolaou et al., 2004b). They consist mainly of alternatin beds of marls, marlstones, marly limestones, dolomitic limestones and intercalations of sandstones and conglomerates with frequent lignite occurrences (Marinos et al., 2001). Alluvial deposits, coastal deposits, fluvial terraces, talus cones and scree of Quaternary age overlie the Neogene formations (Papanikolaou et al., 2004b). According to geophysical investigations (see also Papadopoulos et al., 2007;

Dilalos et al., 2019), various faults and fault zones have been buried beneath talus cones and alluvial deposits and some of them seem to have affected the damage distribution during the earthquake of September 7th, 1999. After this event, Marinos et al. (1999a) issued a 1:25,000 geotechnical map of the Athens Metropolitan Area. It provided 5 soil classes for seismic hazard assessment, namely hard rock, coherent or dense soil, medium coherence or low density soil, loose coastal deposits, river and fluivial beds – recent backfills, according to the EAK (2000). According to geophysical investigations (see also Papadopoulos et al., 2007; Dilalos et al., 2019), various faults and fault zones have been buried beneath talus cones and alluvial deposits and some of them seem to have affected the damage distribution during the earthquake of September 7th, 1999.

In the Mesogea basin, the early stages of sediments deposition started in Miocene (e.g. Ioakim et al., 2005) and according to Mposkos et al. (2007) two sedimentation stages are distinguished; the earlier sedimantaiton stage that included material from the Pelagonian zone and the metamorphic underlying units and the later stage, where the sedimentation was controlled by the Miocene detachment which exposed the marble, schist and crystalline limestone of Penteli and Hymmetus Mts. The Upper Miocene sediments consisf ot marl, loam, sandstone, conglomerate, while the Upper Pliocene consists of marine – coastal formations of marl, sandstone, breccio conglomerates, and travertinoid limestone. These formations are covered in places by Pleistocene fluvio-terrestrial deposits and Holocene Alluvial deposits, coastal deposits, scree and talus cones (Latsoudas, 1992; Krohe, 2010).

The Megara basin forms a tectonic semi-graben between the horsts of Mt Gerania (1.351 m) to the SE and Mt Pateras (1.432 m) to the NW. Strata within the basin are titled 10-40o to the NNE so that a WNW-ESE rotating axis is deduced (Mariolakos and Papanikolaou 1982). This rotation relates to the WNW-ESE trending normal fault that bounds northeastwards the Megara Basin. This fault was active during Pliocene and Lower Pleistocene times, but at present, it shows no sign of activity and has been offset by the ENE-WSW Alksyonides fault zone that partly ruptured during the 1981 earthquake sequence (Mariolakos and Papanikolaou 1982, Leeder et al., 1991). The basin sediments are characterized by a Neogene to Pleistocene succession of upwards coarsenind sequensce of 1 km thickness (Bentham et al., 1991). According to Galanakis et al. (2004), it contains mostly Plio-Pleistocene lacustrine, deltaic to fluviatile deposits. The lower part of the central basin fill is comprised of marls, siltstones, sandstones and conglomerates (Dounas, 1971; Bentham et al., 1991). The upper part of the Neogene basin fill largely comprises fluviatile gravels, but with two important marine transgressional horizons and renewed calcareous mar1 deposition (Bentham et al., 1991). The overlying Pleistocene alluvial clastics were deposited by a NW-flowing system (Bentham et al., 1991) and consist of conglomerates, clays, muds, old talus cones and scree (Dounas, 1971). It is overlaid by Holocene alluvial deposits, coastal deposits, scree and fans.

The Thriassion Plain is a NE-SW oriented depression. It has been affected by NE-SW and NW-SE striking active normal faults (e.g. Ganas et al., 2005; Foumelis, 2019) that caused uplift or subsidence of the area during the Pleistocene (Mariolakos and Theocharis, 2001). During the Pleistocene sea-level fluctuations, Thriassio plain was filled with torrential, lacustrine and lagoon sediments, consisting of marls, clay, marly limestone and carbonate breccia/conglomerate (Hermides et al., 2020), as well as torrential fans, and valley deposits of low cohesion (Katsikatsos et al., 1986). The total thickness of the Pleistocene sediments is 300–350 m. Holocene clay, sands and gravels with thickness ranging from 5 to 10 m have filled the basin (Hermides et al., 2020).

3.1.2. Geomorphology of the Attica region

The Attica region is located in the southernmost part of Sterea Hellas province, central Greece. It is a triangular shaped peninsula, which is surrounded by Saronikos Gulf on the SW and South Evoikos Gulf on the SE. The north part of Attica region has a common boundary with Boeotia region, with the borderline roughly following the margin of the Erythres basin. Part of the NW coastline is located in the easternmost end of the Corinth Gulf.

There are several plains, basins and topographical depressions throughout the whole Region. The most important one is the Athens Basin, which is surrounded by Mount Hymmetus on the East, Mounts Penteli and Parnitha in the North, and Mounts Egaleo and Poikilo in the west. The basin ends at the Saronic Gulf in the South. Next to the Athens Basin and east of Mount Hymmetus, the Mesogea basin expands toward the coastline in the East. It accommodates the new Athens city expansion, and it is separated into two sub-basins due to the presence of Merenta, Paneio and Olympus Mts in the south. Thriassio plain is located south of Parnitha Mt., but is separated from the Athens basin due to the Egaleo and Poikilo Mts. It is bounded by the Elefsina Gulf in the south and the Pateras Mt in the west. Northwest of Thriassio plain lie the closed basins of Oinoi and Skourta, which are located between Mount Parnitha on the East, Mount Pateras on the west and Mount Kithaironas in the north. West of Thriassio plain and at the west of Pateras Mt, the Megara basin has a NW-SE direction and is bounded by Geraneia Mt in the west and the Saronic Gulf in the south (Figure 3.3).

The highest mountain of Attica is Mt Parnitha, at the northern part of Attica, with an altitude of 1413 m above sea level. It mainly comprises non-metamorphic limestone of the Triassic age and is bounded by neotectonic faults (Ganas et al., 2004). The most important are the SW dipping Thriassio and Fyli faults in the south and the NE dipping Malakasa and Afidnes faults in the north, which are considered to be active (Ganas et al., 2004; Papanikolaou and Papanikolaou, 2007b). The second highest is Mt Kithaironas in the northern border of the Attica region, with an altitude of 1409 m. Kithaironas is bounded by the active, north-dipping Erythrai and Dafni faults. Mt Geraneia, with an altitude of 1351 m, are laying on the footwall of the Skinos – Pissia faults, which are referred to as the South Alkyonides fault zone in this thesis. This fault zone diminishes towards the east in the Mt Pateras (1132 m). Mt Penteli is the second higher mountain bounding the Athens basin, after Mt Parnitha. With an altitude of 1114 m, it comprises metamorphic rocks (marble and schist), and it lies on the footwall of the NE dipping Dionissos fault. Mt Ymittos (1027 m) also comprises schist and marble, and it separates the Athens basin from the Mesogea basin.

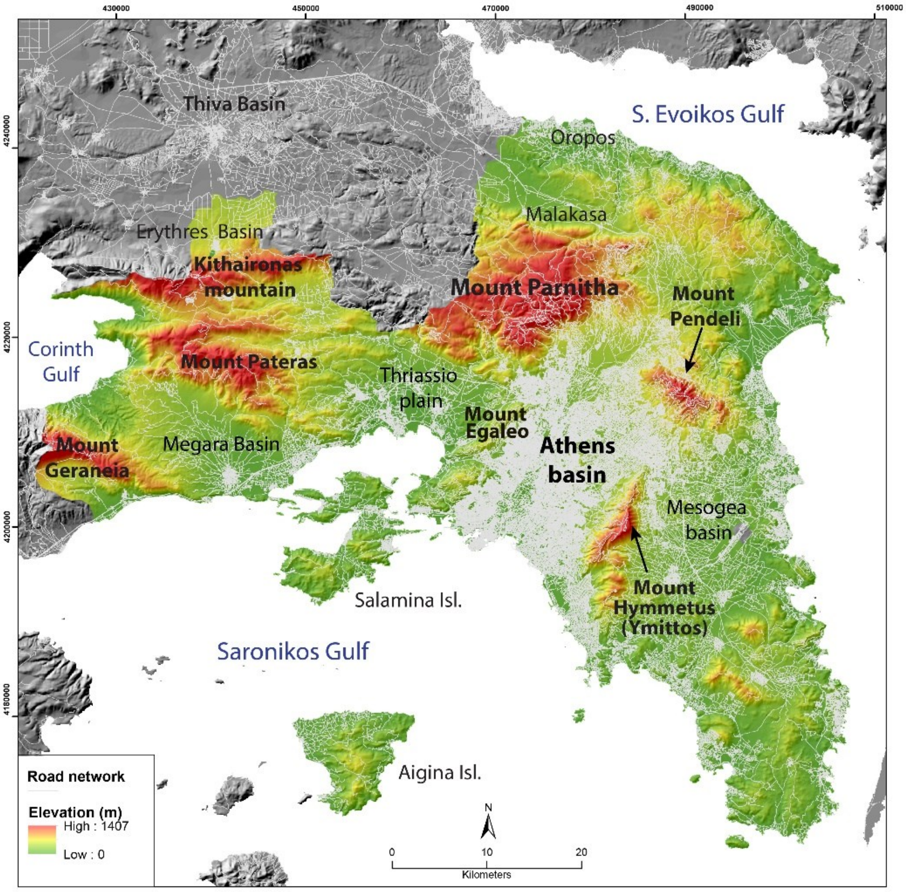

Figure 3.3: Map showing the topography in the Attica Region, including the most important mountains and basins. Road network source: OpenStreetMap 2019.

The Athens basin is characterized by gentle slopes ranging from 1.5% to 6%, apart from the four hills of the basin, Tourkovounia (323 m), Lycabetus (265 m), Acropolis (162 m) and Filopapou (161 m), that have steep slopes (Pavlopoulos et al., 2005). On 100 – 400 m altitudes, deep erosion up to 10 m occurs in areas and valleys, probably attributed to the last Glacial period, where sea level was 120 m lower than today in combination with the upward tectonic movements of Parnitha Mt (Pavlopoulos et al., 2005).

The geomorphology of the Attica region has been studied by various researchers, especially in relation to the tectonic regime. This is because of the proximity to the Greater Athens Area and the risk that this poses to a potential fault rupture. Indeed, research on major active faults in Attica has increased during the last three decades, especially after the 1981 Alkyonides earthquake sequence (Leeder et al., 2005) and the 1999 Athens earthquake event. Ganas et al. (2005) used Digital Elevation Models (DEM) of varying resolutions to map fault structures and display their spatial relationships across the Northwest part of the Attica region. This method is widely used in literature (e.g., Murphy, 1993; Goldsworthy and Jackson, 2001; Ganas et al., 2001; Jordan et al., 2003; Koukouvelas et al., 2018; Hodge et al., 2019) and provides critical information for seismic landscapes. They showed that the normal faults of Attica are more closely spaced in comparison to the Corinth Gulf, which implies lower slip rates (see also Cowie and Roberts, 2001). However, areas proximal to the Athens basin and the Alkyonides fault zone are of high interest in terms of geomorphological findings and the related seismic hazard.

Penteli and Parnitha mountains overshadow the geomorphology of the central and east Attica, as they also act as the north and north-east boundary of the Athens basin. Three major drainage basins are observed in this part of Attica (Papanikolaou and Papanikolaou, 2007b): a) The Kifissos river basin with a NNE-SSW flow direction drains the Athens basin from the southern slopes of Parnitha and the southwestern slopes of Penteli to the Saronic Gulf in the southwest. According to Papanikolaou and Papanikolaou (2007b), Kifissos flows parallel to or near the Miocene detachment trace. b) The Asopos basin, which coincides with the northern border of the Attica region as the river flows westwards, in an east-west direction. As it approaches the Evoikos Gulf it flows northwards, but has a more complex structure due to the existence of the Avlona-Malakasa and the Milesi faults c) The Charadros basin with a W-E flow, starting from the eastern flanks of the Parnitha Mountain, up to the Afidnai plain and the Marathon lake in the Northeast.

At this area, the drainage basins are asymmetric due to the presence of active normal faults (Papanikolaou and Papanikolaou, 2007b). There is a combination of fault parallel and fault perpendicular flow which is typical in active normal faulting regimes (Gawthorpe and Hurst, 1993; Eliet and Gawthorpe, 1995). For example, the footwall of the Afidnai fault is tilted, resulting in a fault perpendicular flow direction, which drains the footwall away from the hangingwall. On the other hand, the headward erosion occurring within the footwall catchments that flow across the fault into the hangingwall, produces fault perpendicular flow directions (e.g. Malakasa fault, Afidnai fault). Finally, in Afidnai, Avlona, and Milesi faults several catchments are clearly deflected into a fault parallel flow direction due to hangingwall subsidence (Papanikolaou and Papanikolaou, 2007b).

The most characteristic seismic landscape of the region lies on the 33 km long South Alkyonides fault zone, where Jackson et al. (1982) identified two parallel faults (Pisia and Skinos faults) from surface ruptures after the 1981 earthquake sequence. These faults have controlled subsidence of the Alkyonides Gulf, at the eastern end of the Gulf of Corinth (e.g. Collier et al., 1998) and uplift Mesozoic limestones, ophiolitic peridotites and poorly-consolidated Plio - Pleistocene sediments of the inactive Megara basin in their footwall (Leeder et al., 1991). According to Cowie and Roberts (2001), coastal uplift occurs within the footwalls of high slip rate active north dipping normal faults, close to the southern shores of the Corinth Gulf. These faults have explicit geomorphic expressions and display evidence for repeated ruptures in the upper

Quaternary and Holocene (Roberts et al., 2009; Mechernich et al., 2018), including the two large earthquakes in 1981 (Ms 6.9, 6.7, Ambraseys and Jackson, 1990), attributed to the Skinos and Pissia faults (Jackson et al., 1982). Pantosti et al. (1996) and Collier et al. (1998) conducted paleoseismic trench analysis in an active alluvial fan where ruptures of the latest 1981 earthquake ruptures were preserved. They discovered multiple Holocene events in each of the three trenches they opened and estimated a maximum slip rate of 2.3mm/y for the Skinos fault and an average recurrence interval of 330 years.

More recently, Mechernich et al. (2018) used terrestrial laser scanning (TLS), together with analyses of colour changes, lichen colonization, and karstic features, to identify potential variations in the weathering extent of the exposed fault scarp of the Pissia fault. They coupled their interpretations with cosmogenic ^{36}Cl dating and suggested varying slip rates over the Holocene, with increased activity in the early Holocene, ranging from 0.8-2.3 mm/y. The slip rate associated with the last 6-8 earthquakes that occurred during the last 7.3 ± 0.7 kyr, including the 1981 rupture, is calculated at 0.5-0.6 mm/y. However, both Skinos and Pissia faults are most likely linked at depth (Roberts, 1996), and since Mechernich et al. (2018) interpreted an age range of 1.4–2.5 kyr for the penultimate event on the Pisia fault, at least three of the reported paleoearthquakes by Collier et al. (1998) on the Skinos fault were not accompanied with surface ruptures of the Pisia fault. The latter implies that the Pissia and Skinos faults do not always rupture simultaneously, as happened in 1981. In such case, the central part of the Skinos fault seems to have increased activity during the Late Holocene, as revealed from the paleoseismic trenching in Vamvakies alluvial fan (Pantosti et al., 1996; Collier et al., 1998), compared to the findings of Mechernich et al. (2018) for the Pissia fault.

3.2. Major recent earthquakes in the Attica Region

3.2.1. The Alkyonides 1981 earthquake sequence

On February 24, 25 and March, 4, 1981, three major earthquakes of magnitudes Ms= 6.7, Ms = 6.4 and Ms = 6.3 occurred in the easternmost part of the Gulf of Corinth. The sequence started on February 24, at 20.53 local time, and the epicentre was located approximately 75 km west of the city of Athens (Papazachos et al., 1984). Three and a half hours later, on February 25, 00.30 local time, the second earthquake, with a magnitude of Ms = 6.4, occurred in the same area. Immediately after the first two earthquakes, and until March 4, 1981, the Universities of Cambridge, Paris and Thessaloniki set up a network of local seismographs in the area, which operated for five weeks in combination with studies of surface faulting and shoreline changes (Jackson et al., 1982). According to the focal mechanisms, these two earthquakes were the result of a NE-SW trending normal fault zone (Billiris et al., 1991), which was also confirmed by the north dipping surface ruptures mapped by Jackson et al. (1982), Abercrombie et al. (1995), and Hubert et al. (1996). The two large earthquakes were followed by a series of aftershocks, which decayed with time (Papazachos et al., 1984). Seven days later, on March 4, the third earthquake, with a magnitude of Ms=6.4, occurred in a south-dipping normal fault in Kaparelli (Jackson et al., 1982). Because the projection of the epicentres fell into the Alkyondies Gulf, next to Alkyonides islets, the earthquakes were named the Alkyonides earthquake sequence.

The first two earthquakes produced several surface ruptures along the Pissia and Skinos postglacial fault scarps, with an average of 60-70 and a maximum 150 cm measured displacement (Jackson et al., 1982; Mariolakos et al., 1981 & 1982). However, Hubert et al. (1996) suggested that displacement values higher than 100 cm probably overestimate the coseismic effect. The third earthquake caused approximately 50-70 cm of displacement along the pre-existing postglacial scarp of the south-dipping Kapareli fault (Jackson et al.,1982; see also Figure 3.4).

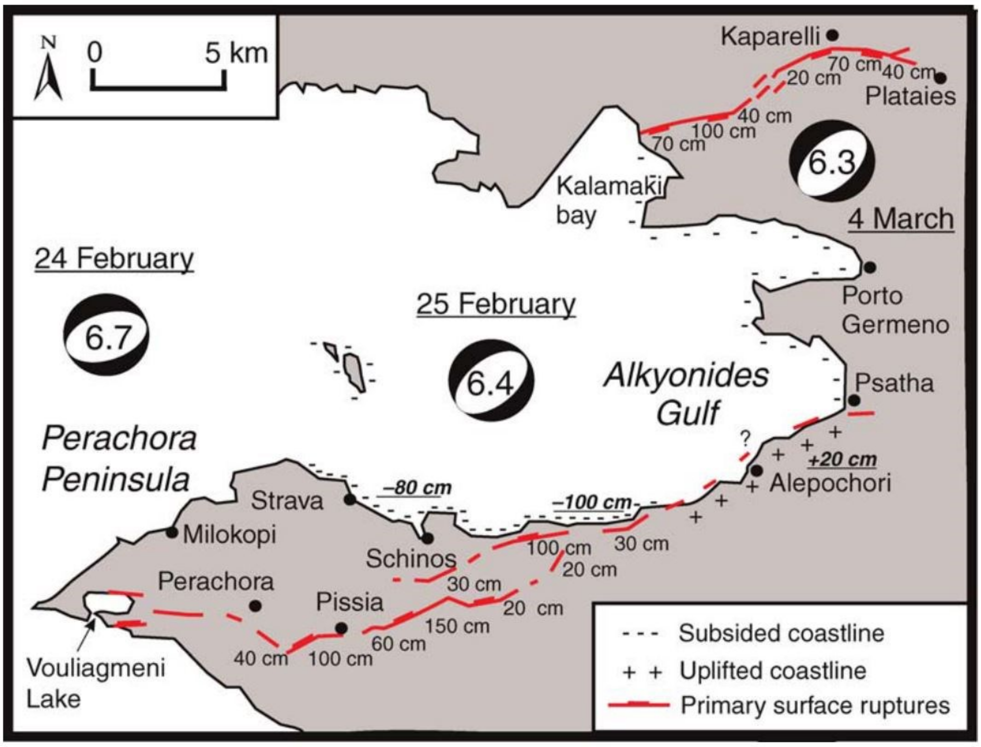

Figure 3.4: Map showing locations of subsided and uplifted coastline, primary surface ruptures and focal mechanisms after the 24 – 25 February and 4 March major earthquakes that struck west Attica in 1981. Sketch reproduced from Papanikolaou et al., 2009).

The series of earthquakes caused extensive damages in three different provinces (Beotia, Attica and Corinth). 7701 buildings collapsed or were damaged beyond repair, and 20954 buildings were severely damaged (Antonaki et al., 1988). Around 20 deaths were attributed to the earthquakes, although not all of them were direct (Trihopoulos et al., 1983). After the first event, many people evacuated the heavily damaged buildings. As a result, the building collapses due to the second earthquake had very low consequences for such a strong event. In addition, most of the tourist facilities along the Skinos coast were closed for the season (Carydis et al, 1982).

According to Carydis et al. (1982) the first event was felt over an area of approximately 250,000 km^2. The inferred Modified Mercalli Intensity reached up to VIII within an area of 1,400 km^2. Parts of Athens experienced intensity VII (Figure 3.5). The same researchers observed that the intensity VII and VIII isoseismals had an elliptical footprint, being elongated in an east-west direction by a factor of two. This elongation appeared to follow the strike of the Skinos and Pissia faults. However, the higher intensity (IX) occurred after the second event, maybe because many already damaged buildings from the first event collapsed. Carydis et al. (1982) noted that the majority of damaged buildings occurred in the towns and villages located around the eastern end of the Gulf of Corinth, next to the Skinos and Pissia faults. Less damage was observed along the coast of the Saronic Gulf west of Athens. In addition, several villages between the Gulf of Corinth and Thebae were devastated by the March 4 event (Carydis et al., 1982). On average, the greater Athens area experienced intensities of

VII and VIII; however, in certain districts, namely Chalandri, Anthoupoli, Moschato, Aigaleo, Nea Ionia and Nikaia, intensities up to IX were also recorded (Antonaki et al. 1988), mainly due to poor local site conditions (mostly fluvial and alluvial deposits) (Papanikolaou et al., 2009; see also Christoulas et al. (2005) for characteristics of Chalandri formations).

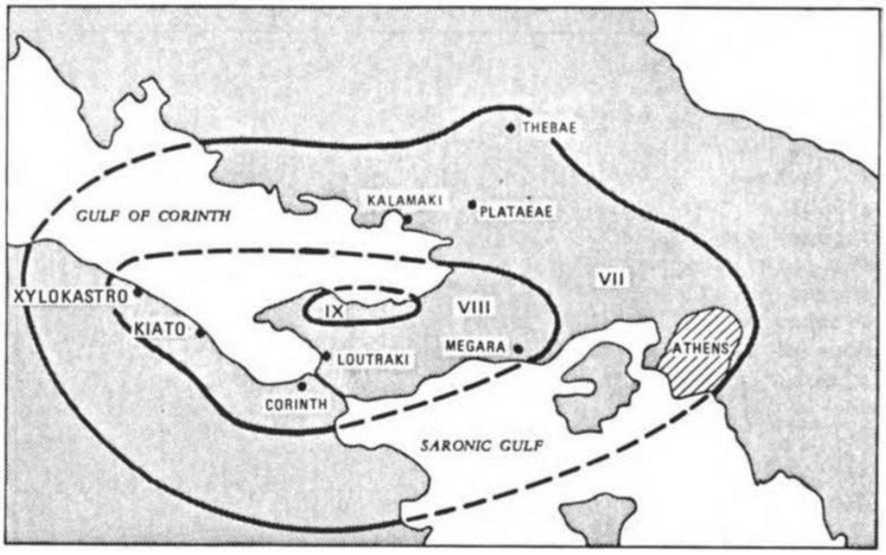

Figure 3.5: Map showing the Modified Mercalli Intensity distribution after the two earthquakes on 24 and 24 of February (reproduced from Carydis et al., 1982)

Apart from the damages in the built environment, the earthquakes caused several severe environmental effects, such as extensive liquefaction at the Kalamaki Bay, in Porto Germeno and in Kineta coastal area (Andronopoulos et al., 1982; Papazachos et al., 1982), ground fissures in Loutraki beach, Vouliagmeni Lake, Porto Germeno, Kiato and Corinth (Papazachos et al. 1982) and submarine slumping and several mass-movement phenomena in the Alkyonides deep basin and in the shelf area (Perissoratis et al. 1984). According to Jackson et al. (1982) people reported a 1 m high tsunami during the main shock in the Alkyonides Gulf, which could be attributed to the reported submarine slumping.

Papanikolaou et al. (2009) examined the recorded environmental effects due to the three events, in order to test the application of the Environmental Seismic Intensity (ESI 2007) scale (Michetti et al., 2007). They determined a maximum intensity X, mainly along the primary surface ruptures along the Skinos and Pissia faults, but also along the coastline from Strava, up to Alepochori (see also Figure 3.4 for locations). They also noted that despite the fact that Maximum MS (Mercalli–Sieberg) intensity values were also recorded in all villages that were in close proximity to the activated faults (Perachora IX–X, Plataies IX–X, Schinos IX, Pissia IX, Kaparelli IX), no intensity X was assigned and most of the epicentral villages recorded an epicentral intensity IX. As a result, the current traditional intensity scales underestimate the severity of this earthquake sequence. This occurs because the epicentral area was sparsely populated but at the same time there where significant EEE were recorded. In addition, several villages located in the epicentral region were founded on bedrock sites and others on the footwall block, experiencing less shaking (Papanikolaou et al., 2009).

3.2.2. The Athens 1999 Mw5.9 earthquake

Although Athens 1999 earthquake is not the largest magnitude event that hit Athens during historical times, it is maybe the most destructive one in terms of human losses and building damages. The latter is supported by Ambraseys and Psycharis (2012), who report that the ancient and historical part of Athens hasn't experienced strong ground motions for the last 2300 years. Even though the magnitude was just below M_w=6, a combination of aggravating factors led to what we now know as one of the most destructive earthquakes of the last 200 years in Attica (Papadopoulos, 2002).

On September 7, 1999, at 14.56 local time, an earthquake of magnitude M_s=5.9 struck Attica. The epicentre was located in the southwestern part of Parnitha mountain, approximately 20 km from the centre of Athens. The earthquake was the result of the rupture of a WNW – ESE trending fault with an average dip of 60^o. The immediate hanging wall area suffered extensive damages, but also large parts of the Athens basin were highly affected. Several buildings collapsed, causing 143 deaths and more than 800 injuries. While most of the damage occurred within a distance of 12 km from the epicentre (Lekkas, 2001; Psycharis et al., 1999), more than 7,500 buildings were heavily damaged, and 24,500 buildings suffered minor damage to structural elements in the broader Athens metropolitan area and its western suburbs. The majority of the reinforced concrete buildings however in the broader area of Athens suffered only minor structural damage because they had strength reserves (Psycharis et al., 1999).

The earthquake occurred close to Athens, and was recorded by a variety of seismograph networks, both local and global (Louvari & Kiratzi, 2001; Papadimitriou et al., 2002; Papadopoulos et al., 2000; Stavrakakis et al., 2002). Additional seismograph networks were deployed close to the epicentre and in the surrounding areas, to monitor the aftershock sequence (e.g. Tselentis & Zahradnik, 2000). The following days after the mainshock, numerous teams of engineers surveyed the damaged buildings. Furthermore, different teams of geologists surveyed the whole area for surface rupture indications, focusing on the two parallel Thriassio and Fyli faults (Pavlides et al., 2002).

There is still a debate regarding the fault that caused the Athens 1999 earthquake, since there were no surface ruptures along any of the two parallel faults. Pavlides et al (2002) set multiple geomorphic and seismotectonic criteria, such as the distance of the epicentre, aftershocks and damage distribution, to decide which one of the Thriassio or Fili faults ruptured during this event. Furthermore, Kontoes et al.(2000), Ganas et al. (2001) and Atzori et al. (2008) analyzed the coseismic deformation of the epicentral area using SAR interferometry. According to Kontoes et al. (2000), the main fault has a N120^o orientation. Similarly, Atzori et al. (2008) suggested that the modelled fault plane intersects the Thriassion normal fault in depth and may reach the surface near the

Fili Fault. However, Papazachos et al. (2001), Baumont et al. (2002) and Roumelioti et al. (2003) suggest that the rupture did not reach the surface.

Papadimitriou et al. (2002) installed six digital three-component continuous recording seismographs and two digital accelerographic instruments one day after the mainshock to define the aftershocks distribution and model the fault plane solution. They also developed an interferogram with three distinct fringes instead of two that Kontoes et al. (2000) interpreted. Although the maximum displacement of 220 mm is in the same order of magnitude as the 300 mm that Kontoes et al. (2000) suggest, the inner fringe lies very close to the inferred relocated epicentre, which is related to the Thriassio (or Parnitha) fault. In addition, the aftershock distribution also indicates that the fault trace at the surface corresponds to the Parnitha fault scarp.

It is not clear which of the two faults ruptured on September 7, 1999. All findings agree that the fault had an NW-SE direction, parallel to Thriassio and Fili faults. Furthermore, the location of the epicentre, although there are 5 different epicentre locations published so far (Figure 3.6), implies that either one of the two faults or a smaller parallel structure caused the Mw 5.9 earthquake. The earthquake magnitude is just below the threshold of Mw=6.0 for surface ruptures (Bonilla et al., 1984; Darragh and Bolt, 1987; Michetti et al., 2000), and as a result, there is no strong evidence for coseismic rupture along any of the faults in question. This is also supported by the fact that Mariolakos et al. (2000) report no surface ruptures with vertical displacement along any of the Thriassio or Fili faults. Nevertheless, there is no other strong evidence in favour of any of these faults.

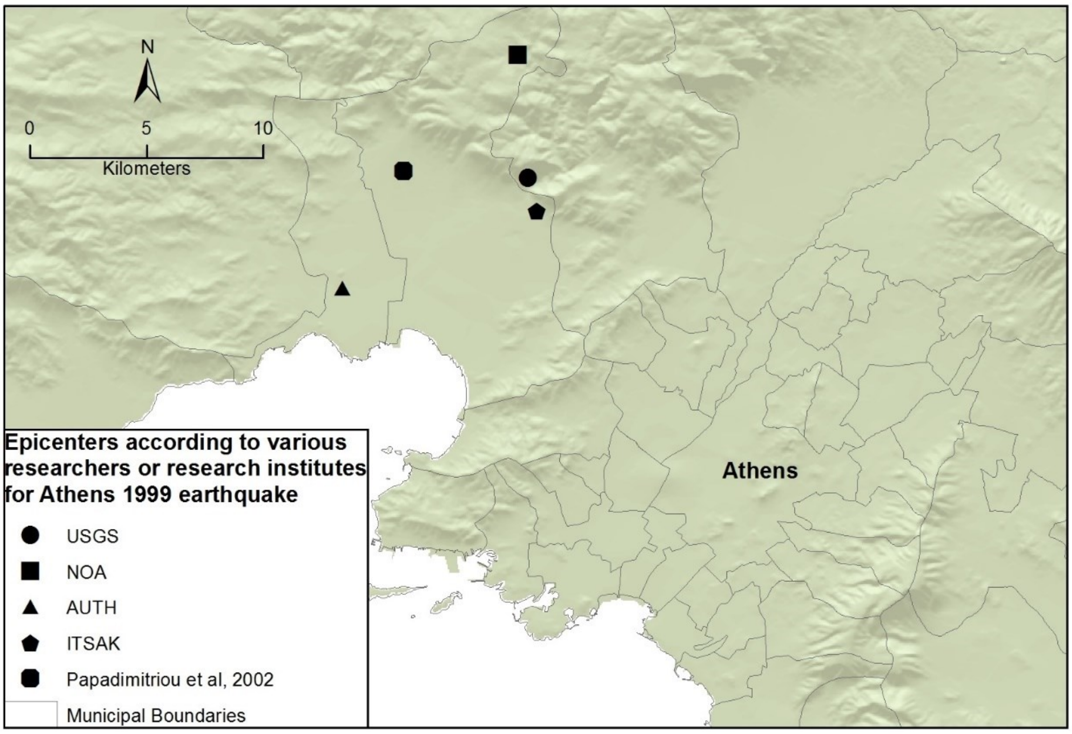

Figure 3.6: The inferred epicentre locations after the Athens 1999 M5.9 earthquake in West Attica. Note that the epicencers of AUTH and NOA lie in a distance of about 12 km apart from each other. Reproduced after Papanikolaou et al., 2015a.

Damage distribution and intensity pattern

Lekkas (2001) was the first to examine the distribution of the macroseismic intensity just after the earthquake event. He suggested that the intensity distribution pattern occurred due to the strike of the seismogenic fault, seismic wave directivity effects and the NNE±SSW Miocene detachment (Figure 3.7). Indeed, several researchers suggest that there was a source directivity towards the Athens Metropolitan Area, east of the epicentral area. Tselentis and Zahradnik (2000b) indicated that the variability of the apparent source duration indicates source directivity. Mylonakis et al. (2003) identified high acceleration pulses in the ground motion, generated by source directivity effects, which were also amplified due to the poor soil properties in the areas of high intensity. The combination of these two factors that affected the damage distribution was also suggested by Roumelioti et al. (2004). Roumelioti et al. (2003) examined several scenarios in regard to the location of the hypocenter and showed that the directivity effect might have contributed to the destructiveness of this earthquake. Papadimitriou et al. (2002) showed that the time difference between the first P-wave and the stop phase arrival times at each station of the Cornet network, together with the InSAR data and the aftershock distribution, implies a source directivity towards east. However, Sargeant et al. (2002) adopted a circular fault model without any elliptical dimensions.

Lekkas (2001) also discovered that site foundation formations, old tectonic structures that were buried under recent formations and morphology played an essential role in the distribution of the damages across the affected area. Bouckovalas and

Kouretzis (2001) highlighted the role of the geological and geotechnical conditions, showing that the very stiff soil conditions amplified the ground motions by approximately 40%. Furthermore, Foumelis et al. (2009) used ERS SAR images to analyze the period from September to December of 1999. They observed a distinct propagation of the ground deformation maxima towards the SE direction. The aforementioned evolution of deformation was also recognized by the observed expansion of the displacement field to the east.

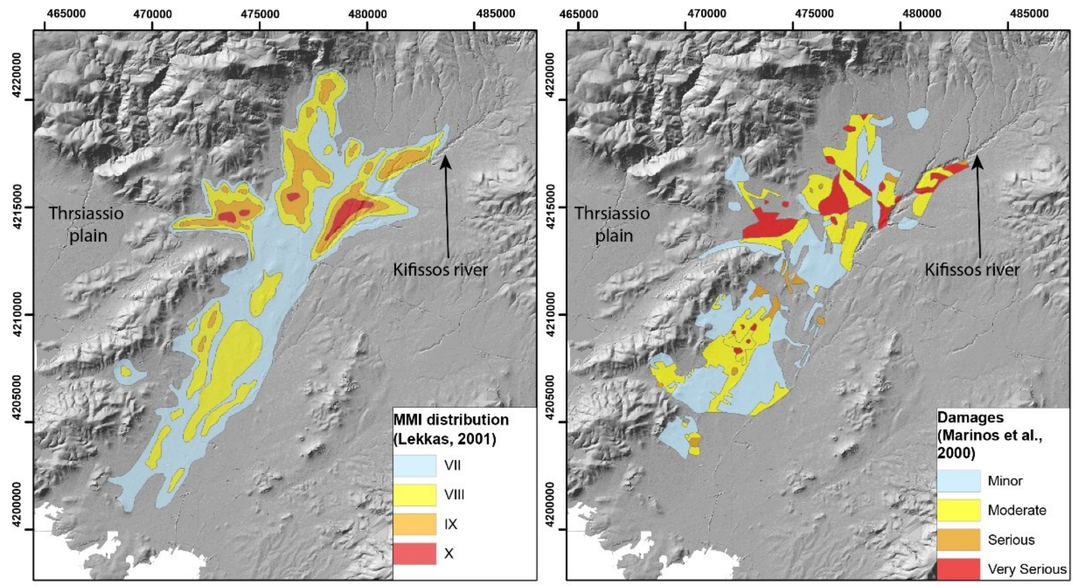

Figure 3.7: Distribution of buildings damages after the Athens 1999 earthquake. Left: MMI distribution after Lekkas (1999), Right: Damages distribution and categorization after Marinos et al., 2000. Note that in both cases damages were constrained by the Kifissos river, which possibly flows over the Miocene detachment.

The importance of this earthquake lies on the fact that it was the first that struck Athens, which had not experienced such strong ground motions for at least 25 centuries (Papazachos and Papazachou, 2003). However, this event occurred in an area considered aseismic because there were no significant earthquakes at a distance of less than 30 km affecting Athens in the historical records (Papazachos & Papazachou, 2003; Pavlides et al., 2002). Gazetas et al. (2002) recorded the highest Modified Mercalli Intensity values (IX) in Menidi, Ano Liosia, Chelidonou and Adames areas. Nevertheless, that damage was non-uniform, especially in the hardest-hit sites, with variations of up to 2 scale units in distances less than 1 km apart.

The 1999 event, however, clearly demonstrated that the low rate of seismicity alone is not a safe criterion to assess the seismic potential of a region. Only a detailed tectonic analysis and mapping of active faults and soil conditions contribute toward a reliable seismic risk assessment. Had such studies been undertaken before 1999, they certainly would have revealed the potential risk of the active tectonic structures that ruptured during the 7 September 1999 seismic crisis (Makris et al., 2004).

4. Earthquake catastrophe insurance

The following sections present the impact of earthquakes from the insurance point of view. Apart from a brief presentation of the latest circumstances in insured losses, a brief history of catastrophe models is presented, along with information on their structure and the problems inherited due to the traditional methods of seismic hazard assessment.

4.1. The economic impact of earthquakes

Catastrophic phenomena are high severity events with a low probability of occurrence yet related to significant fatalities and economic losses. Global annual financial losses due to natural catastrophes are monitored continuously by organizations such as large reinsurance companies (Munich Re Group, 2019; Swiss Re Institute, 2019a) or international foundations like UNISDR (CRED - UNISDR, 2017) and World Bank (Brecht et al., 2013), and their reports show that there is an increase on the number of economic losses each year. Apart from the meteorological disasters, catastrophic earthquakes cause an even larger negative footprint because of their rarity and devastating results to the built environment. Between 1998 and 2017, meteorological disasters and earthquakes resulted in a loss of more than 1.3 million people. Although earthquakes and tsunamis caused the majority of fatalities, the vast majority (91%) of all disasters were caused by extreme weather events (CRED - UNISDR, 2017). The overall economic losses show an uprising trend during the last 20 years (Swiss Re Institute, 2019a), although their frequency has not changed (Shearer and Stark, 2012). This happens because the vulnerability increases and more assets are concentrated in earthquake-prone areas (Ambraseys, 2009; Brecht et al., 2013). Beyond the negative economic footprint, the natural catastrophes have a considerable impact on the liabilities, as the insured losses have soared during the last 20 years around the world (Swiss Re Institute, 2019b).

Greece is prone to various natural disasters, such as wildfires, floods, landslides, and earthquakes, due to the particular environmental and geological conditions dominating in tectonic plate boundaries. Seismic is the leading risk in terms of damages and casualties in the Greek territory (PreventionWeb, 2011). During the last 500 years, more than 170 destructive earthquakes occurred in Greece and the surrounding area, with mean annual casualties of 17 fatalities and 92 wounded (Papazachos & Papazachou, 2003). According to Maccaferri et al. (2012) and Petseti & Nektarios (2013), the two most destructive earthquakes in Greece between 1990 – 2010 were the Athens 1999 Mw5.9, with total losses of 4.83 billion euros and the Kozani – Grevena 1995 Ms6.6 event with 1.16 billion euros. However, the insured losses were negligible for the Kozani-Grevena earthquake and reached only 111 million euros for the Athens 1999 earthquake (EAEE, 2019). This is attributed to the fact that the earthquake insurance penetration rate in Greece is less than 10% (Maccaferri et al., 2012).

Various researchers have published historical records of earthquakes in Greece (e.g., Makropoulos & Burton, 1985; Papazachos & Papazachou, 2003), providing useful data in seismic hazard assessment. Although insured claims are connected to a variety of natural perils in Greece, with numerous flash floods and forest fires in a yearly basis (EAEE, 2019), earthquake is the only material peril that requires to be modelled in order to calculate the Solvency Capital Requirements (SCR) for the Greek Insurance Companies (European Commission, 2010; EIOPA, 2014a). According to the Hellenic Association of Insurance Companies, the number of damaging earthquake events with insured claims in Greece is less than 25% of the total number of natural catastrophes since 1993 (EAEE, 2019). Still, the amount of insured losses from earthquake damages is similar to the summary of insured losses from all other perils during the same period. Overall, claims due to earthquake losses, totaling 133.5 million € since 1993 (EAEE, 2019). These claims originate from 5 earthquake damaging events (111 million € in Athens 1999, 7.8 million € in Kefalonia Island 2014, 2.8 million € in Lefkada Island 2015, 9.5 million € Kos Island 2017, 2.4 million € in Zakynthos Island 2018), implying that there is a significant recurrence of moderate to strong events, that are damaging but not catastrophic.

4.2. Catastrophe models

Catastrophic earthquakes lead to a significant number of losses and insured claims simultaneously, because insured buildings and infrastructure are damaged at the same time when a major earthquake occurs. This leads to spatiotemporally correlated insurance claims and in extreme cases, insolvency of insurance companies (Goda and Hong, 2010). Scientific research addresses risk characterization with the use of catastrophe models (Grossi et al., 1999), which are used to assess and communicate the risk amongst different perspectives and disciplines. This occurs because often the primary scientific research is out of the scope of insurers (Weinkle, 2015) or insurance supervisors. For example, catastrophe risk assessments can be used by various stakeholders, such as insurers, reinsurers, policymakers, and civil protection officials (Mitchell-Wallace et al., 2017). Recently, catastrophe bonds have also been issued in capital markets (e.g., Zimbidis et al., 2007; Cummins, 2008; Hofer et al., 2020), and they are based on catastrophe models estimations for natural hazards and properties at risk.

Catastrophe models are the primary tool for insurance companies for characterizing their decision processes in choosing between competing risk management strategies, reinsurance treaties and Solvency II requirements, regarding the Own Risk and Solvency Assessment (ORSA) and the Solvency Capital Requirements (SCR) (see also European Union, 2009).

The scope of these models is the loss estimation in the built environment and human lives, and as such, the critical element is the identification and quantification of the hazard – vulnerability relationship. Thus, the identification of seismic hazard is the cornerstone of every earthquake catastrophe model because it determines the critical parameters of the modelled earthquakes, such as the location, the severity, and the corresponding probability of occurrence (Grossi et al., 2005).

The most common catastrophe model output is the Exceedance Probability (EP) curve, which represents the probability that a certain amount of loss will be surpassed in a given time period (EP curve example here) for an insured portfolio. The majority of the stakeholders are interested in the right-most tail of the EP curve, where the largest losses are depicted. In contrast with the hazard maps, which display hazard and losses in a spatial manner, EP curves provide the temporal representation of the anticipated losses due to catastrophic events. It is particularly valuable for the insurance and reinsurance industry to be able to accurately determine the size and distribution of their portfolios' potential losses (Figure 4.1). Moreover, it is a powerful tool for underwriting, type of coverage and policy pricing, and determining which proportion of the insured risk must be transferred to reinsurers or capital markets for the insurance companies to be solvent in an acceptable manner level.

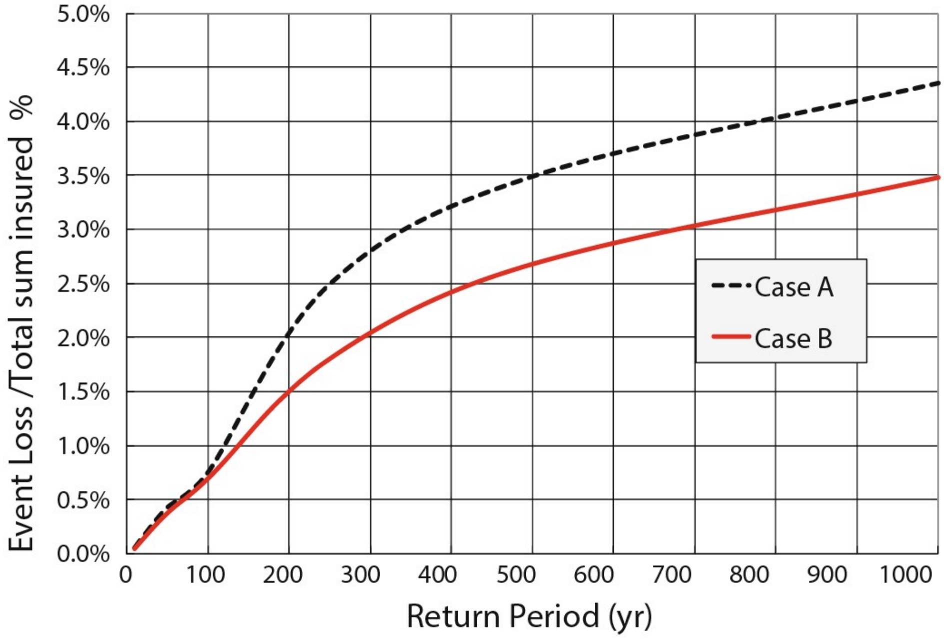

Figure 4.1: An example of an EP (Exceedance Probability) curve from Hsu et al. (2012) which displays the loss loss ratio versus return period. The loss ratio is 3.5 % in case A and greater than 2.65 % in case B for an event loss of 500 return periods. Figure reproduced from Hsu et al. (2012).

The typical earthquake catastrophe model structure includes four different modules: Hazard, Vulnerability, Exposure, and Loss estimation modules (Grossi et al., 2005; Mitchell-Wallace et al., 2017). The last three modules are directly based on the outcome and the related assumptions of the Hazard Module. As a result, the constraints and assumptions made during the Hazard Module development have a strong impact on the actual model quality and reliability.

4.2.1. Brief history of catastrophe models

The term "catastrophe modeling" is connected mostly with the insurance industry, especially property insurance, but it is also a common phrase among geoscientists and natural hazards experts. Catastrophe loss estimation techniques, known collectively as catastrophe modeling, have gained widespread acceptance by the insurance and risk management industries and are now heavily relied upon to support a wide range of financial decisions (Mahdyiar and Porter, 2005). The key advances on catastrophe modeling came from the natural hazards scientists, who provided methods both for mapping risk and measuring the extent, magnitude and recurrence of the natural hazards (Grossi et al., 2005). Steinbrugge’s (1982) compilation of losses from earthquakes, volcanoes, and tsunamis was among the first attempts for developing historical database of losses attributed to earthquake related hazards. The overlay of these two values in a GIS environment was the key advance in hazard and loss and three US based cat modeling vendors emerged between 1986 and 1994. Two major Catastrophic events (Hurricane Hugo and Loma Prieta Earthquake) in 1989 set an alarm in the insurance industry, as the insured losses exceeded 4 billion and 6 billion dollars respectively (Stover and Coffman, 1993). Hurricane Andrew in 1992, was the next hurricane that made landfall after 3 years and it was the first catastrophe where the forthcoming losses were adequately predicted by a commercial catastrophe model (Grossi et al., 2005). Due to the huge losses related to this event, nine US insurance companies became insolvent (Grossi et al., 2005) and the industry realized that an efficient management of their risks and underwritings is only feasible with more precise estimations of the anticipated losses. It was also then that the Federal Emergency Management Agency issued their first report on their earthquake loss assessment methodologies (FEMA, 1992). Since then, at least four commercial catastrophe models have issued global coverage for earthquake hazards. Moreover, the introduction of cloud computing and open source modelling has combined with the increased demand for quantitative risk models from the disaster risk financing community (e.g. Ley-Borrás and Fox, 2015) to generate an increase in model provision, including a much wider community of model developers and users (Mitchell-Wallace et al., 2017). In addition, large re-insurance companies have developed their own proprietary earthquake catastrophe models in order to manage reinsurance treaties, or sponsor open-source software, such as the Global Earthquake Model (GEM) (Crowley and Pinho, 2011). In any case, the need for model completeness and validation of the models use to represent the view of risk will continue to drive demand for increased model resolution and coverage (Mitchell-Wallace et al., 2017).

4.2.2. Structure of catastrophe models

All models are based on four different modules: Hazard, exposure (inventory), vulnerability and loss (Goda et al., 2014; Grossi et al., 2005).

The Hazard module indicates the extent, intensity and frequency of a peril as defined by a specific earthquake hazard metric (Mitchell-Wallace et al., 2017). It estimates the probability that the physical parameters that define the hazard will exceed various levels. In the case of earthquakes, the model estimates the probability that parameters such as intensity, peak ground acceleration or spectral acceleration will exceed various levels at a particular site (Mahdyiar and Porter, 2005). The hazard is often represented as intensity variation across a pre-defined geospatial framework, either in a regular raster (grid cell-based), or in an irregular vector structure (e.g. Postal Code polygons or exact address points).

The Exposure Module handles the particularities of each portfolio that are inserted in the model. Each insurance company adopts a unique database architecture, which includes the locations and details of the insured buildings, along with other policy features, such as the coverage types and limits. As a result, the insured portfolio database is redesigned in a way that can be incorporated into the Vulnerability Module and then transferred into the Loss Module. Exposure is used in two distinct ways in catastrophe models. First, exposure data for the specific objects being modelled are entered by the user into the model. Second, a representation of industry exposure for the region covered by the model is also used in the process of building a catastrophe model. This takes the form of a database of exposure values split by area and by type of object being modeled (Mitchell-Wallace et al., 2017). The most important parameter used to characterize the exposed portfolio is the location of each building construction. Usually, geographic coordinates are assigned to each property at risk, such as postal code, longitude - latitude or another location descriptor. Apart from the property's location in spatial terms, other parameters include such features as its construction type, the number of stories in the structure, and its age (Mahdyiar and Porter, 2005; Grossi et al., 2005).

The Vulnerability module deals with the potential for the hazard to damage structures and their contents (Mitchell-Wallace et al., 2017). It estimates the probability that building damage will exceed various levels as a result of ground motion (Mahdyiar and Porter, 2005). In other words, vulnerability modules quantify the physical impact of the modelled earthquake on the property at risk. There is a diverse approach between models on how this vulnerability is calculated. HAZUS adopts a 4 categories classification system, using descriptions such as Slight, Moderate, Extensive, or Complete damage (Kircher et al., 2006). Other models utilize damage curves or damage tables and relate structural damage to a severity parameter (Grossi et al., 2005), such as peak ground acceleration (PGA), spectral acceleration (SA) or intensity (usually Modified Mercalli Intensity). In all models, damage curves are constructed for the building construction, contents and time related losses, such as business interruption loss.

Within the Loss module, physical damage is translated to total, or ground up losses (Mahdyiar and Porter, 2005), which is the total loss before the application of any insurance or reinsurance financial policies (Mitchell-Wallace et al., 2017). Insured losses are calculated by applying policy conditions to the estimates of total loss. Loss is estimated on the basis of vulnerability assumptions. It calculates both direct (meaning cost to repair or replace construction) and indirect (meaning business interruption) losses but it also integrates other significant policies characteristics, such as deductibles and coverage limits, reinsurance coverage etc. Up to date models also include the Solvency II SCR calculation methods, which differ from the traditional projection of losses in a given future time span.

4.2.3. Problems with existing Earthquake Catastrophe models

Due to their uniqueness and rarity, earthquake catastrophes cannot be easily modelled, because their physical characteristics are not on the same frequency with the meteorological catastrophes, which have much shorter interval periods and can be simulated more effectively. Although there is immense scientific progress on seismic hazard and earthquake modelling, the traditional earthquake catastrophe models which are based on earthquake catalogues often fail (Stein et al., 2012). This is attributed mainly to the rough assumptions that models incorporate because earthquakes are both rare and destructive phenomena.

The designation of seismic hazard for a certain location is affected by considerable epistemic uncertainty, in addition to the randomness inherent in the occurrence of a major earthquake and its ground motions (Gkimprixis et al., 2021). This is reflected in the significant difference in the assessed seismic hazard according to different studies for the same region.

The traditional hazard modules architecture relies on sophisticated statistical approaches and stochastic simulations of the existing seismic catalogues. In fact, the first seismic risk analyses used seismological data in order to identify the spatial distribution of hazard and severity of the underlying risks (Cornell, 1968; McGuire, 1976). At the same time, samples from historical and recorded earthquake events are too small compared to the active faults seismic cycle (Coppersmith and Youngs, 2000; Scholz, 2002), so even the most sophisticated statistical models provide inevitably unsatisfactory results (Stein et al., 2012). The implementation of active faults as seismic sources posed a different point of view in the earthquake risk assessment (e.g. Schwartz & Coppersmith, 1986), by providing a quantitative assessment of fault slip rates, and a more reliable hazard estimation than the historical earthquake record (e.g. Yeats & Prentice, 1996; Papoulia et al., 2001; Boncio et al. 2004, Roberts et al. 2004, Michetti et al., 2005, Pace et al., 2010). Regarding vulnerability, many researchers use FEMA's HAZUS software (FEMA, 2018, 1992, 1989) as a benchmark for the risk and vulnerability assessment methodology (Goda & Hong, 2010; Tripathi, 2001), or apply its methods usually by modifying the building classes within the software (Bommer et al., 2002), since they represent the US building and repair costs.

Because the Hazard module holds the most significant results for any catastrophe model, since it governs earthquake recurrence and spatial distribution, at the same time it is the main reason for the majority of the models' failures, especially after extreme events (e.g., Sumatra 2004, Wenchuan 2008, New Zealand 2011 and Tohoku 2011 catastrophic earthquakes). The errors and assumptions that are incorporated into the Hazard Module propagate and affect the model's outputs. For example, the anticipated losses in case of extreme catastrophic events are still calculated using statistical methods that focus on past events and their corresponding insured losses. This approach has two deficits. Firstly, historical and instrumentally recorded events cover a short period compared to the active faults seismic cycle, providing a largely incomplete statistical sample (Grützner et al., 2016). The second relates to the fact that by considering only the losses, the intention to model earthquake events fails when the physical parameters of the earthquake event are ignored. Both deficits lead to erroneous calculations due to overestimated or underestimated probabilities of occurrence for significant earthquake events, their location, their magnitude and severity. In general, the use of historic and instrumentally recorded events as the sole input for hazard modules can give erroneous pictures of the present-day hazard (Scholz, 2002), by ignoring faults that have not been activated during the completeness period of the historical record. However, these faults could soon approach the end of their cycle, providing a higher earthquake probability. On the other hand, recently recorded events, which occurred on faults that are now at an early stage in a new seismic cycle, may imply low earthquake probability.

4.3. Solvency II requirements – EIOPA Standard Approach

Insurance companies operating in the EU are obliged to calculate the SCR to ensure that economic collapse occurs only once in every 200 years. In other words, they need to ensure that those undertakings will still be able, with a probability of at least 99.5%, to meet their obligations to policyholders and beneficiaries over the next 12 months (European Commission, 2009). These calculations are significant for the Insurance Companies' operation, as they define their credibility and reliability against catastrophic earthquake events. EIOPA's Standard Formula (SF) is an alternative way of assessing the SCR. In fact, Greek Insurance Companies are widely using it to calculate the SCR for their life and non-life undertakings. However, in case that the risk profile of the insurance undertaking is significantly different from the assumptions underlying the SF calculation, it is advised that the insurance companies use an internal catastrophe model. This happens as the Standard Formula is, by its very nature and design, a standardized calculation method, and is therefore not tailored to the individual risk profile of a specific undertaking. For this reason, in some cases, the standard formula might not reflect the risk profile of a specific undertaking and consequently the level of own funds it needs (EIOPA, 2014b).

4.4. Insurance companies' practices

According to the Solvency II regulatory framework, each insurance company needs to accomplish a detailed risk assessment for material perils every year. The results are used for the Own Risk and Solvency Assessment (ORSA), for the more detailed SCR calculation, and the reinsurance treaties. This leads to an immense need for accurate models for the catastrophic earthquake losses (e.g. Gkimprixis et al., 2021), especially in regions of high seismic activity. For the Greek insurance companies, this means that they need to develop their internal model, which usually relies on the existing commercial earthquake models, or they can utilize the SF, which is released by EIOPA. A third option would be that they use both the internal model and SF results, in a solution that is known as a partial internal model (European Commission, 2009). Indeed, EIOPA proposes a standard model using a two-level approach with predefined correlations between the different 'risk modules' on the top level, and between the 'submodules' within each risk module on the base level (Alm, 2013). However, there are plenty of requirements and limitations on using internal models, such as the commitment on transparent modules and algorithms that lead to the SCR calculation, and the full comprehension of how these models work (Mitchell-Wallace et al., 2017).

5. Methodology

This Chapter presents the methods used for the compilation of the active faults database, the compilation of the fault specific seismic hazard maps for the Attica region and the development of the earthquake catastrophe model for the insurance industry.

5.1. Tectonic geomorphology and geomorphic indices

5.1.1. Background

The study of the tectonic geomorphology has made remarkable progress in recent years. The identification and mapping of active faults and the extraction of information regarding the recurrence interval of associated earthquakes progressed since the advance of paleoseismicity in the 1970s (Papanikolaou et al., 2015). Moreover, since the early ’80s, tectonic geomorphology experienced significant evolution due to the advances of the Geographic Information Systems and the Digital Elevation Models (DEMs) (Pérez-Peña et al., 2017) and is being used, among others, for structural analysis, paleoseismology, seismology, and Quaternary science (see also Koukouvelas et al., 2018). To a significant extent, advances in tectonic geomorphology have been enabled by rapid improvements in the digital representation of topography (e.g., Fielding et al., 1994; Kirby and Whipple, 2001; Whipple and Tucker, 2002; Ganas et al., 2004 and 2005; Koukouvelas et al., 2018; Hodge et al., 2019; Konstantinou et al., 2020). The principal goal of tectonic geomorphology is to extract information regarding the rates and patterns of active deformation directly from landscape topography (Kirby and Whipple, 2001).

The longitudinal profiles of bedrock channels constitute a significant component of the relief structure of mountainous drainage basins and therefore limit the elevation of peaks and ridges. In addition, bedrock channels communicate tectonic and climatic signals across the landscape, thus dictating, to first order, the dynamic response of mountainous landscapes to external forcings. For a detachment-limited channel, the steady-state gradient is set by a combination of the river’s ability to erode the bed and the prevailing rate of rock uplift or base-level fall (Whipple & Tucker, 1999).

Whipple and Tucker (2002) explored potentially diagnostic differences in the rates and patterns of transient channel response to changes in rock uplift rate. In addition to general differences between detachment- and transport-limited systems, their analysis identified that ‘‘hybrid’’ channels at the threshold between detachment- and transport-limited conditions are expected to act as detachment-limited systems in response to an increase in rock uplift rate (or base-level fall) and as transport-limited systems in response to a decrease in rock uplift rate, especially during the post-orogenic topographic decline.

In general, the footwall uplift and uplift rate control the maximum elevation and morphology of mountain fronts, as well as the geometry of footwall up-warping

(Wallace, 1978; Armijo et al., 1986). Topographic profiles depict long term landscape balance, whereas river longitudinal profiles represent the short-term response of the landscape to the tectonic, lithological and climatic changes (Pérez-Peña et al., 2017). Stacked swath profiles now allow for topographic assessment at the scale of large normal faults (Fernández-Blanco et al., 2019). Armijo et al. (2015) initially used stacked swath profiles to illustrate the major morphological features of the Central Andes coastal margin, while Pérez-Peña et al. (2017) provided a new add-in tool that works within the ArcGIS 10.x environment and produces stacked swath profiles. A stacked swath profile contains a significant number of consecutive parallel swath profiles derived from topographic data, usually Digital Elevation Models (DEMs), plot together orthogonally to their strike (Pérez-Peña et al., 2017). The end product highlights an explanatory view of structural and morphological features. Pérez-Peña et al. (2017) tested their method in the Sierra Alhamilla mountain range in Spain by producing stacked swath profiles perpendicular to the inferred fault lines, as well as a fault–parallel one (Figure 5.1). The latter was used to examine the local relief curve related to the uplift produced by the Sierra Alhamilla anticlinorium.

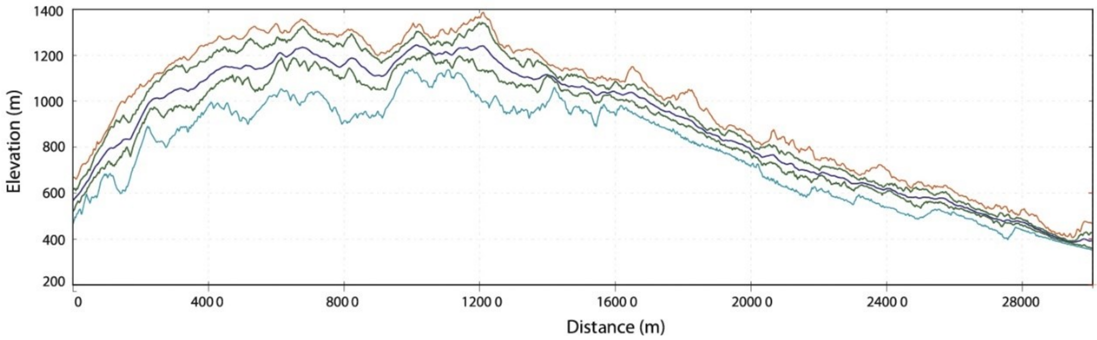

Figure 5.1: 2 km wide swath profiles for Sierra Alhamilla mountain range, modified after Pérez-Peña et al., 2017.

Various geomorphic indices have been widely used to classify active deformation. In a large scale, geomorphic indices tend to have a qualitative approach, but in small scale, they tend to offer also a qualitative point of view (e.g. Koukouvelas et al., 2018). For example, a simple index, the Valley floor/width ratio index (V_f) (Bull and McFadden, 1977; Silva et al., 2003; Bull, 2009), can describe differences in the transverse morphologies of valleys, such as V-shaped canyons and broad-floored pediment embayments (see also Koukouvelas et al., 2018). When calculated for several streams draining a mountain range, or a larger region, the V_f index can reveal spatial variations in incision and uplift. Asymmetry factor (A_f) is another geomorphic index that shows the tectonically induced tilting of drainage basins (Keller and Pinter, 1996). Further analyses on streams longitudinal profiles, such as the Steepness Index k_s and the concavity index θ (Kirby and Whipple, 2001; Kirby et al., 2003; Wobus et al., 2006;), can contribute to the qualitative analysis of the regional uplift rates, which may be attributed to the understanding of fault segmentation and deformation pattern along large faults (see also Papanikolaou et al., 2013).

In addition, Hypsometric Integral (HI) is another index which highlights the deviations between the highest and the mean elevation when assessed with swath topographic profiles (Pérez-Peña et al., 2017). Values of HI near to 1 indicate young transient landscapes, while HI values near to 0 may indicate a mature landscape (Keller and Pinter, 1996). Recently, Pérez-Peña et al. (2017) proposed the use of a transverse hypsometric integral (THi), in which HI values are weighted by the relative local relief, in order to avoid HI artifacts in low elevation areas. They also introduced the enhanced transverse hypsometry index (THi*), which can improve the hypsometry analysis along a swath profile by re-scaling HI values between 0.2 and 0.8.

Regarding fault throw, Hodge et al. (2019) explained the meaning of variations at fault scarp characteristics and proposed an algorithm to examine fault scarp changes using DEMs automatically. They showed that for fault scarp interpretation, the DEM resolution plays an important role, and as a result, the most suitable dataset they used was the Pleiades satellite DEM product. This comes in agreement with Koukouvelas et al. (2018), who tested six different DEMs and concluded that global ALOS data are suitable for tectonic geomorphology applications globally, but the Greek Cadastral DTM was used as a proxy for the comparison of different results in morphometric indices calculation.

5.1.2. Methods used in this thesis

The fault analysis in this thesis firstly focuses on the identification of active faults that are long enough to cause earthquakes with magnitude M ≥ 6.0 and strong ground motions that could pose a threat to the region of Attica in case of rupture. Second, it aims to determine the fault slip rates and maximum expected magnitudes to incorporate them into the seismic hazard assessment and earthquake catastrophe models. Many of the faults are already well described in the literature either in published research in scientific journals, including their slip - rates, or depicted in neotectonic onshore and offshore maps from where slip – rates can be indirectly inferred. However, tectonic geomorphological analysis was carried out for the onshore faults to challenge new techniques and confirm the level of their activity from a qualitative point of view.

The fault activity was qualitatively determined and confirmed using a geomorphological interpretation of high-resolution Digital Terrain Models (DTMs) and their derivatives, namely the shaded relief and slope maps. A combination of techniques and geomorphic indices was used for 14 onshore faults or fault zones. This includes, where applicable, the Valley floor/width ratio index (V_f), and the Asymmetry factor (A_f). Fault – parallel stacked swath profiles, as well as fault perpendicular profiles, were also used to examine deformation pattern on footwall due to uplift. The Steepness Index k_s and the concavity index θ were used only for the Sparta fault, and not for Attica. According to Whittaker et al. (2008), the selected rivers should discharge a drainage basin larger than 10 km^2 above the fault and the upstream length should be at least 5 km. This is not the case for the vast majority of rivers and drainage basins crossing faults in Attica; however, the method was applied in the Sparta fault by Papanikoloaou et al. (2013), and the results are presented here, as this study was carried out within this PhD.

The influence of active faulting on the topography in Attica was assessed by swath topographic profiles along strike the examined faults, as they summarize elevation data into a single profile (Andreani et al., 2014). The aim was primarily to examine the triangular throw pattern along strike the fault and to identify possible indications of fault segmentation or deep channel incision. Nevertheless, the clearest view of the long term throw is obtained with the classic geological cross-sections (as shown in Sections 6.2.1, 6.2.2 and 6.2.11). However, such topographic profiles can demonstrate the level of fault activity both in a qualitative and quantitative way. In addition, the THi* was used in order to test its maximum values along profiles that followed catchments flowing perpendicular to the faults. The application of these techniques was made using the SwatProfiler toolbar, which was developed by Pérez-Peña et al. (2017) and works as an ArcGIS add-in.

For the slip–rate determination, the postglacial throw was measured for the onshore faults. Field measurements were made for five different fault scarps, either directly with scarp profiles, through chain surveying techniques using a ruler (1 meter) and a clinometer, or using Structure from Motion photogrammetry. In some cases, throws associated with scarps were estimated by eye or by evaluating published description of fault scarps offsets. Other techniques used for the determination of fault slip – rate and recent activity were paleoseismic trenching and ^{36}Cl cosmogenic dating. These methods are explained in detail in the following sections.

5.1.3. Fault scarp profiling

All the profiles across post-glacial scarps were constructed using a 1 m ruler and a geological compass or using photogrammetry induced, high-resolution DSM (see Section 5.1.4). The profiles exhibit common features characteristic of fault scarps, such as the upper slope, the degraded scarp, the free face, the colluvial wedge and the lower slope. As the footwall of a normal fault undergoes continued uplift by repeated earthquakes, the original steep fault plane (free face) is dissected by streams and reduced in gradient by erosion, producing a degraded scarp (Yeats et al., 1997). Therefore, it is important to define the upper slope and its contact with the degraded scarp accurately to avoid any throw under-estimation. Finally, new faulting on a pre-existing scarp creates a new free face, followed by scarp degradation. These features are crucial elements to identify in every profile because they impact the throw measurement (Papanikolaou et al., 2015a).

Selection of scarp profile locations that minimize differential incision, deposition and erosion processes, post-dating the surface of known age, is also critical (Papanikolaou, 2003). The profile locations were selected in a way that natural or artificial alterations from the original slope that could lead to misleading post-glacial throw values were avoided. Additionally, scarp profiles on step-up or step-down fault zones were avoided because these zones are sites of increased degradation potential (Stewart and Hancock, 1991). Moreover, scarp profiles on relay ramps where there is a high potential for sediment transport, from footwall to hanging wall (Roberts and Gawthorpe, 1995; Gawthorpe and Leeder, 2000; Childs et al., 2003) were also avoided.

After defining the main characteristics of the scarp profiles in the field, the profiles were reconstructed and interpreted in a graphics package and the throw was calculated. The throw is defined as the height measured between the intersection of the fault plane with the projected positions of the upper and the lower slope, respectively.

5.1.4. Structure from Motion Photogrammetry induced DTMs

View from above, or bird's eye view, is a crucial advantage for landscape detection and identification of active faulting geomorphological structures. Depending on the scale of the formations to be examined, different remote sensing data, equipment and methods of representing the actual elevation pattern can be used. Satellite images or DEMs derived from satellite stereo imagery are used to analyse seismic landscapes, which can be displayed in small scale maps, such as asymmetrical drainage basins, river branches deviation, types of the river network and large-scale anaglyph characteristics. The ability of satellite-derived DEMs to represent fault – induced lineaments or active faulting related anaglyph depends on the fault scarp heights, the fault activity and the spatial resolution of the images acquired. Active tectonic landscapes can be identified using shaded anaglyph derived from various spatial resolution DEMs (e.g. Hodge et al. 2019). However, even if nowadays spatial resolution of satellite-derived DEMs is increased (see also Koukouvelas et al., 2018), active faulting landscapes are not always visible even in such high-resolution products.

Structure from Motion (SfM) generates high-resolution topography from a set of overlapping photographs taken from different viewpoints. Johnson et al. (2014) were the first to use SfM as a tool for mapping fault zone topography in semiarid tectonic landscapes along active faults in southern California, using an unmanned helium balloon (see Figure 5.2 for an example from an initial SfM approach in Lastros fault, Crete) and a motorized glider. They also compared their SfM derived DTMs with airborne Lidar data and concluded that SfM produces even denser topographic and more homogenous spatial coverage than terrestrial LiDAR. Since then, and because of the tremendous development of small drones with camera mounts, an outburst of similar studies proved that on a local scale, the SfM photogrammetry could be of high importance for faults identification and free face measurements (e.g. Bemis et al., 2014; Angster et al., 2016; Corradetti et al., 2017; Grützner et al., 2017; Rao et al., 2020).

Figure 5.2: Helium balloon with a camera mount on the belly side, at the Lastros fault postglacial scarp in Lasithi, Crete.

Indeed, small drones can be utilized to achieve a spatial resolution (or Ground Sample Distance – GSD) of the order of centimetres (see also Alexiou et al., 2021). The absolute accuracy of the derived models can be dramatically increased by surveying Ground Control Points (GCPs) with Real-Time Kinematic (RTK) Global Navigation Satellite System (GNSS) receivers, which provide horizontal and vertical accuracy of the order of 5 – 20 millimetres in real-time (Alexiou et al., 2021 and references therein). However, the relevant accuracy of these models can be achieved by manually setting well-defined distances between known points within the model, provided that the extent of the model is adequate.

SfM photogrammetry with the use of a small drone was applied in order to examine the Dafni fault scarp profile (Section 6.2.13, see also Figure 5.3). GCPs printed on plain A4 paper were used for the registration of relevant distances within the models (Figure 5.3). For that reason, their relevant distances were measured in the field with a conventional tape measure.

In addition, the Dafni and Malakasa fault scarps were modelled using a handheld 12 mp camera and multiple 10 x 10 cm papers as ground control points. Again, their relevant distances were measured with a tape measure in order to increase the relative accuracy of the models. The estimated error is discussed in the relevant Sections.

Figure 5.3: Left: The small drone (DJI Phantom 4) from the Mineralogy – Geology Laboratory (Agricultural University of Athens), which was used to create high resolution DSM. The Dafni fault postglacial scarp is visible in the background. Right: GCP number 7, printed on an A4 paper, and installed in the upper part of the fault scarp, on the profiling axis (thin white line at the center of the image laying in the hanging wall).

5.1.5. Paleoseismology (paleoseismic trenching, ^{36}Cl cosmogenic dating)

Paleoseismic trenches are widely used worldwide, not only for research purposes (e.g. Collier et al., 1998; Chatzipetros et al., 2005; Grützner et al., 2016) but also for the foundation of large and critical infrastructure, such as Nuclear Plants, airports, oil and gas pipelines, etc. According to the (IAEA, 2015), paleoseismic trenches are used for the identification of seismogenic structures based on the recognition of effects of past earthquakes in the region, improvement of the completeness of earthquake catalogues, estimation of the maximum seismic potential and the amount of displacement per event, and rough calibration of probabilistic seismic hazard assessment (PSHA), by using the recurrence interval of large earthquakes detectable by paleoseismic investigations.

Palaeoseismological trenching generally aims at identifying and dating units that are offset by fault rupture and consecutive movement. According to Chatzipetros et al. (2005), because information regarding faults that produced surface ruptures during historical times is scarce (see also Roberts and Koukouvelas, 1996), palaeoseismological studies are rapidly increasing (Pavlides, 1996; Collier et al., 1998; Chatzipetros and Pavlides, 1998; Pavlides et al., 1999; Koukouvelas et al., 2001; Pantosti et al., 2004). Trenches are commonly used to extend the seismic record through geological time and are an essential tool that can provide data regarding prehistoric earthquakes that caused surface rupture (Pavlides et al., 1999; Kokkalas et al., 2007; McCalpin, 2009). A fundamental prerequisite to constrain the previous earthquake ruptures in time is to define the age of characteristic paleosols. Age control is usually done by radiocarbon dating if suitable organic material like charcoals, plant remains, etc., is present. Palaeosols often contain enough bulk organic material to be dated, even if distinct pieces of organic matter cannot be retrieved. Furthermore, palaeosols are excellent markers for reconstructing the horizons that were the surface in the past, later downthrown by fault movement and buried by younger material from the footwall of the fault (Grützner et al., 2016). A paleoseismic trench was cleaned and logged during the study of Milesi fault, and the results are presented in Grützner et al. (2016) and in Section 6.2.

Constraining surface fault displacements can also be achieved by cosmogenic isotopes analysis, either by dating deformed geomorphologic features (e.g. Bellier et al., 1999) or by dating the scarps themselves (e.g. Benedetti et al., 2002). Other methods have also been introduced for the fault scarp sampling and analysis, such as ^{10}Be dating (Hippolyte et al., 2006). The most frequently applied technique for earthquake analysis on limestone bedrock fault scarps is exposure dating using cosmogenic ^{36}Cl (e.g., Zreda & Noller, 1998; Mitchell et al., 2001; Benedetti et al., 2003; Palumbo et al., 2004; Schlagenhauf et al., 2011; Akçar et al., 2012). ^{36}Cl was applied in these studies as the only isotope for exposure dating of carbonates. A regular and dense distribution of ^{36}Cl samples can be used to determine the location of earthquake horizons on the fault plane using probability density functions (e.g., Benedetti et al., 2013; Schlagenhauf et al., 2010; Tesson et al., 2016). The determined location of event horizons allows earthquake event ages to be calculated based on the temporal accumulation of ^{36}Cl concentrations. In Section 6.2.8, paleoearthquake offsets of the Pisia bedrock fault scarp are determined using a range of weathering features, and these earthquake horizons are then dated using ^{36}Cl exposure age dating (after Mechernich et al., 2018).

5.2. Development of seismic hazard maps

The method of seismic hazard mapping from geological fault throw-rate data was firstly introduced by Papanikolaou (2003) and Roberts et al. (2004). It consists of the combination of the following four major factors (Deligiannakis et al., 2018a):

1. compilation of a fault database, that includes the identification of seismic sources, determination of fault lengths and their characteristics regarding their kinematics and slip rates which govern earthquake recurrence.
2. empirical data which combine fault rupture lengths, earthquake magnitudes and coseismic slip relationships (Wells and Coppersmith, 1994; Pavlides and Caputo, 2004).
3. the radii of VI, VII, VIII, and also IX isoseismals on the Modified Mercalli (MM) intensity scale, within which horizontal ground accelerations exceed 500cm/sec^2 in the Greek territory (Theodulidis and Papazachos, 1992) causing damage even to well-constructed buildings (Reiter, 1990).
4. Attenuation - amplification functions for seismic shaking on bedrock compared to basin filling sediments (Sauter and Shah, 1978; Degg, 1992).

In detail, fault specific Seismic Hazard Mapping methodology can be displayed in the following steps (see also Papanikolaou, 2003; Roberts et al., 2004; Papanikolaou et al., 2013; Deligiannakis et al., 2018a):

5.2.1. Active faults identification

When seismic hazard is estimated for a wide region, all the seismic sources must be identified. All active faults that affect the study area must be accurately mapped, as they are going to be analyzed in the next steps. Geological and geomorphological studies are often the primary basis for locating potential seismic sources (Wesnousky, 1987). A large set of data is used for understanding the current tectonic regime and rates of activity, including aerial photographs, remote sensing data (e.g. satellite imagery, drone imagery), GPS and interferometry data, strain rate measurements, mapping and analysis of Quaternary formations and/or landforms (e.g., terrace analysis, investigation of drainage network evolution), and pedological and sedimentological studies. Usually, it is necessary to perform detailed geomorphological-geological mapping, geophysical prospecting, or subsurface investigation to fully characterize the identified structures (Michetti et al., 2005). The usual criteria for identifying active faults are the disruption of Quaternary deposits or river systems and the creation of a characteristic and recognizable set of geomorphologic landscapes.

The detailed data for fault characteristics were derived from scientific articles, onshore and offshore neotectonic maps and fieldwork observations. In general, two types of source were used for the active fault determination:

a) Already published literature regarding location and fault activity.

The published papers of researchers working on the active tectonics of Attica and the surrounding areas were used for the majority of the active faults (17 out of 24) regarding the compilation of the database. For 16 out of the 24 faults (Fault id numbers 1-5, 8-11, 13-15 and 19 of the database), information regarding fault geometry and slip rates were extracted from the existing literature, tectonic geomorphology methods and fieldwork (see Table 6.1 for details on faults numbering and the corresponding literature). Moreover, onshore and offshore neotectonic maps provided information about the fault geometry and slip rate. The depiction of the 8 offshore active faults (Fault id numbers 12, 16-18, 21-24) was predominantly based on the official 1:100.000 offshore neotectonic maps of the Saronikos and the Southern Evoikos Gulfs (Papanikolaou et al., 1989a; Papanikolaou et al., 1989b) and the detailed description of the neotectonic structures in Saronikos Gulf by Papanikolaou et al. (1988), as confirmed and improved by Foutrakis (2016).

b) Fieldwork with in situ geomorphological interpretations.

Field research was conducted for faults 1 (Milesi fault), 2 (Malakasa fault), 7 (Aigosthena fault), 8 (Pissia fault, which is part of the South Alkyonides Fault Zone), 10 (Loutraki fault), 15 (Fili fault) and 20 (Dafni fault), in order to estimate fault lengths, finite throw and slip rate values (see Table 6.1 and Figure 6.92 for faults locations, Sections 6.2.1, 6.2.2, 6.2.7, 6.2.8, 6.2.9, 6.2.11 and 6.2.13 for details).

5.2.2. Fault lengths determination

Since fault length was used to determine the expected earthquake magnitude, each one of the active faults that could affect Attica region in case of earthquake rupture was mapped in a GIS environment (see Chapter 9.2 for constraints based on errors and assumptions).

Despite the fact that 1:50.000 scale geological maps cover nearly the whole Greek territory, fault depiction is usually restricted to small or inactive structures with no contribution to seismic hazard. Fault lengths for the faults 6-7 and 20 were determined using a combination of geomorphological and geological criteria. In addition to the in situ interpretations, hillshade and slope maps were utilized so that the overall topographic imprint would be observed. In addition to that, geological cross-sections in the tips of these faults were used to identity the sediments offset, which allowed a detailed mapping of the fault lengths.

5.2.3. Registration of fault throw-rate data

Throw-rates are measured values derived from geological data, such as postglacial scarp analysis, palaeoseismological research and geomorphological interpretations. Fault throw-rate values are essential for Seismic Hazard Assessment, as high values indicate shorter recurrence intervals between earthquake events, implying increased fault activity (Cowie and Roberts, 2001; Roberts et al., 2004). The determination of fault throw rates was based on the published literature findings where applicable. For faults id 1-3, 5, 8-9 and 14-15 (see Section 6.3 for details on faults numbering) throw rates were extracted from the well – described and constrained values already presented in the literature (e.g. Benedetti et al., 2003; Ganas et al., 2005; Chatzipetros et al., 2005; Papanikolaou and Papanikolaou, 2007b; Sakellariou et al., 2007; Grützner et al., 2016). Faults derived from the neotectonic maps did not have an assigned throw rate value. For these faults we used the average thickness of the sediments versus their age, for the extraction of their long-term slip rate. Slip rate values extracted from fieldwork were attributed to the maximum scarp heights, assuming that they represent the maximum finite throw over a fixed time period (ie since the last glaciation). A post-glacial age of 15 ± 3 kyrs was adopted for this time period, as a widely used hypothesis (e.g. Papanikolaou et al., 2005; Caputo et al., 2006; Papanikolaou et al., 2013; Grützner et al., 2016) that correlates with the transition from glacial to interglacial climate (Tucker et al., 2011) and has been confirmed by absolute dating techniques on active faults in Italy and Greece (Giraudi and Frezzoti, 1997; Benedetti et al., 2002; Palumbo et al., 2004; Schlagenhauf et al., 2011; Tesson et al., 2016). However, for calculation purposes, fault throw rates registration was based on an average value of 15 kyrs for all active faults.

5.2.4. Conversion of throw-rates into earthquake frequencies

Assuming a triangular throw profile for the faults (Cowie and Shipton, 1998) and earthquake surface ruptures, and that the maximum throw is observed at the center of the fault, the number of surface faulting earthquakes of fixed size can be calculated for each one of the faults in a certain time period. Throws in these profiles represent the slip that each fault has accumulated during the last 15 kyrs and most of them have been extracted from geomorphic observations of offset postglacial features. However, for the South Alkyonides Fault, the surface ruptures used (25km) are shorter than the total length of the fault, as the 1981 earthquakes did not rupture the entire length of the South Alkyonides Fault (Roberts, 1996). This results to the assumption that the South Alkyonides fault produces earthquakes of smaller magnitude (e.g. Ms = 6.7) more frequently, rather than larger earthquakes that rupture the total fault length but over a longer recurrence time. Thus, it is assumed that this fault ruptures in floating earthquakes, which are distributed around a mean magnitude of fixed size (e.g. Papanikolaou et al., 2013). As a result, by comparing the areas of triangles for faults and ruptures, the number of earthquakes each fault has experienced during the last 15 kyrs can be calculated (example shown in Figure 5.4a,b).

5.2.5. Earthquake distribution along strike the fault

After calculating how many earthquakes of certain size each fault has experienced during the last 15 kyrs, modelled earthquakes have to be distributed according to the fault throw variation along the strike of each fault trace. The aim is to extract the earthquake density along the strike of the fault. The distribution of the associated hypothetical epicentres along the strike of the fault is made using the mathematical formula of Papanikolaou (2003), as illustrated in Figure 5.4c.

5.2.6. Production of isoseismals

Earthquakes are not uniformly distributed throughout the continental crust, but are overwhelmingly concentrated in the upper 10-15 km, close to the base of the seismogenic layer, with the lower continental crust remaining aseismic (Chen and Molnar, 1983; Sibson, 1984). Moreover, large seismogenic faults on the continents appear to be restricted to a dip range between 30º - 60º (Jackson and White, 1989; Chen and Molnar, 1983). The thickness of the seismogenic layer, as well as the dip angles of normal faults, constrained the placement of the hypothetical epicenters. Assuming 50º - 55º dipping faults and hypocenters at the depth of 10 km, they were plotted 7 - 8.5 km away from the fault in the hanging wall.

The active faults were grouped in two sets, depending on their length, which correlates with the earthquake magnitude they can produce, as shown by Wells and Coppersmith (1994), and Pavlides and Caputo (2004). Even if a fault of a given area ruptures repeatedly, there will be some variation in magnitude about its mean, due to variations in factors such as the earthquake stress drop (e.g. Scholz, 2002). According to the WGCEP (1999, 2002), each fault is assumed to rupture in earthquakes distributed around a mean magnitude. This natural random variability in magnitude is described as a normal distribution around the mean, defined by ± 2 standard deviations (σ), with a standard deviation of 0.12. A similar approach is followed in this thesis, however 1 standard deviation of 0.15 was used, so that faults shorter than 16km will produce earthquakes of magnitude 6.25 ± 0.15. Indeed, according to Wells and Coppersmith (1994) faults from 9.2 km up to 16 km can produce earthquakes that lie within a range of magnitude 6.1 – 6.4. Consequently, following the same empirical regressions of surface rupture length and magnitude, faults longer than 16 km produce earthquakes of magnitudes that exceed Ms=6.5. However, it is possible that faults around 25 km – 40 km length could rupture in sub-events or break parts rather than the entire fault length, thus producing earthquakes around Ms 6.5 – Ms 6.7 (e.g. Roberts, 1996; Roberts et al., 2004). For each group, the Theodulidis (1991) attenuation relationships between earthquake magnitude and intensity distribution were used for the production of the modeled isoseismals (Table 5.1), assuming that the Earth is homogeneous and isotropic so body waves would have spherical wave fronts (Figure 5.4d).

Table 5.1: Radii of the isoseismals for the active faults in Attica, based on the Theodulidis (1991) attenuation relationships. Intensity IX is not expected in firm sediments affected by faults shorter than 16km.

Faults group by earthquake magnitude	**Intensity (MM)**			
	IX	**VIII**	**VII**	**VI**
6.65 ± 0.15 (6.5 – 6.8)	11km	25km	44km	74km
6.25 ± 0.15 (6.1 – 6.4)	-	15km	31km	53km

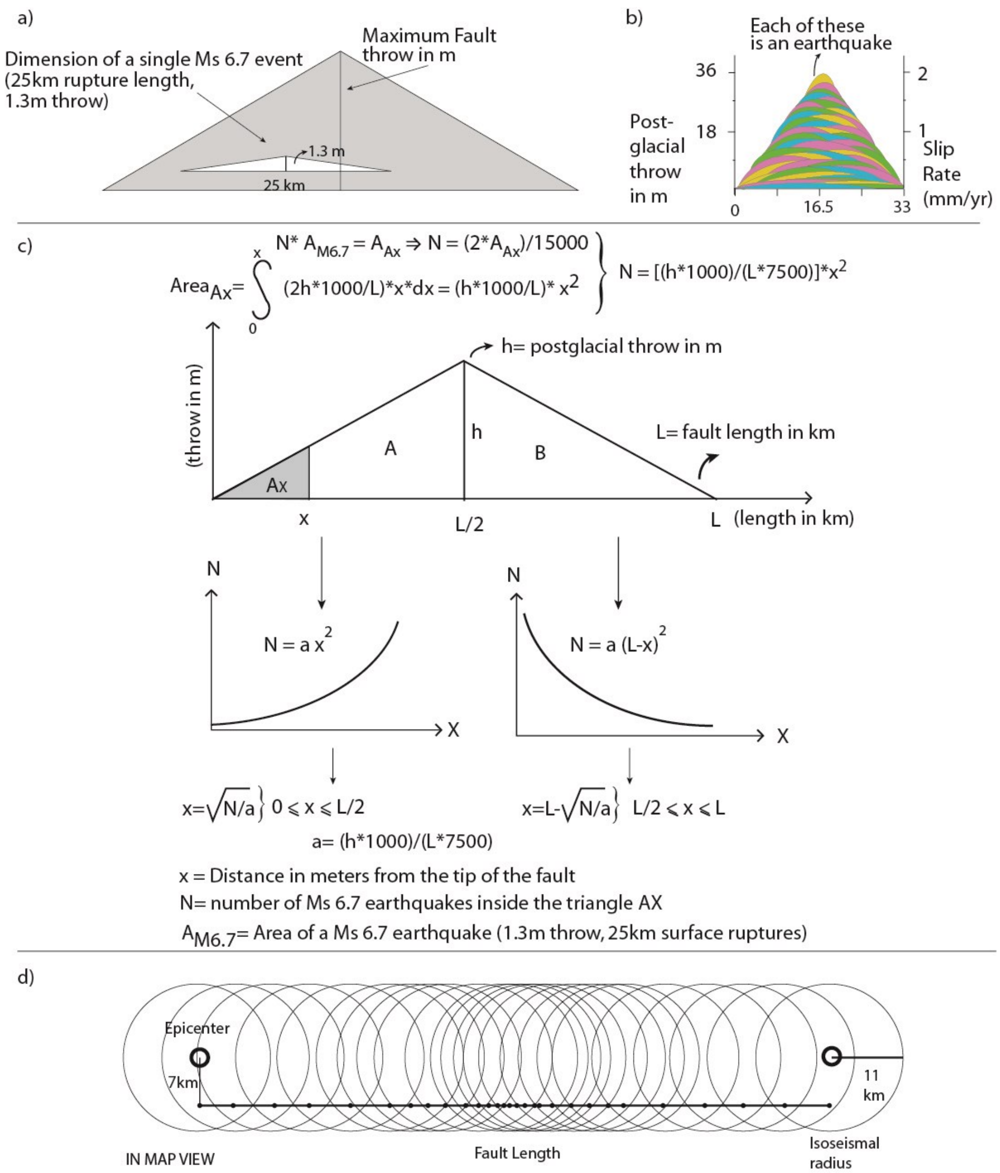

Figure 5.4: Schematic representation for the construction of the hazard map, modified after Papanikolaou (2003) and Roberts et al., (2004). a) The concept of the methodology for one of the 24 faults in Attica (South Alkyonides Fault). Assuming a triangular throw profile for the faults and ruptures and that the maximum throw is observed at the centre of the fault, the number of surface faulting earthquakes of Ms=6.7 can be calculated. b) Throw in this profile represents the slip that the fault has accumulated during the post-glacial period (since 15 kyr ago±3 kyr). c) Mathematical formula describing the earthquake distribution along strike each active fault. The distance (x) of each earthquake point from the tip of the fault is calculated. Each fault is divided in two halves (triangles A and B) and the corresponding formula is applied for each one of them. d) Epicentres are plotted 7 km away from the fault in the hanging wall and circles with 11 km radius of intensity IX (representing "isoseismals") are added. Geology is not yet taken into account.

5.2.7. Counting and contouring the number of times each locality has been shaken.

Every intensity coverage was represented as a separate raster, so that no overlapping occurred between raster coverages of different intensities around the same modeled epicenter. Buffer zones were created around each hypothetical epicenter for every modeled intensity, using the ranges displayed in Table 5.1. These buffer zones were converted to raster coverages and attributed by new values. Then, all these coverages, centered to the hypothetical epicenters, were added in separate map views for each intensity scenario, representing areas that receive enough energy to shake at intensities VI – IX.

This process results in four individual maps, showing how many times each locality receives enough energy to shake at intensities VI - IX in 15kyrs, assuming homogenous bedrock geology, spherical wave fronts for body waves and isoseismal ranges as shown in Table 5.1. The hazard distribution varies along strike each fault, therefore over long time periods the hangingwall center of a fault receives most of the seismic energy, in contrast to fault tips where the hazard is considerably lower.

5.2.8. Amplification/Attenuation of intensity with the bedrock geology

The differences in amplification and attenuation of intensity between soil and rock are well known, even from the Loma Prieta earthquake, where damages were highly correlated to the bedrock geology and local site conditions. However, there is still much uncertainty about the actual values that should be used for different site geologic conditions (Reiter, 1990). For instance, soil formations are connected with enhanced ground motions, both in amplitude and duration compared to those recorded in rock, resulting in higher damages (Bolt, 1999). It is well established (Medvedev, 1965; Evernden and Tomson, 1985; Degg, 1992) that the Quaternary sediments shake at about one intensity degree more than pre-Quaternary sediments (such as Flysch deposits or foredeep sediments). Similarly, pre-Quaternary sediments shake at about one intensity degree more than Mesozoic-Neogene limestones and metamorphic rocks (see also Papanikolaou, 2003). In more recent approaches, scientists have divided the bedrock geology into three units: hard rock, soft rock and alluvium and correlate all Quaternary units as alluvium, Tertiary units as soft rocks and Mesozoic as hard rocks (Petersen et al., 1997; Park and Elrick, 1998).

The modeled intensity coverages are attenuated/amplified according to the surface geologic conditions, providing the expected intensities for each geological formation. The simple attenuation model decreases the intensity by: i) a single value, if two localities are equidistant from an epicenter, but one lies on Mesozoic or Tertiary limestone and the other lies on flysch/foredeep deposits and ii) two single values if two localities are equidistant from an epicenter, but one lies on Mesozoic limestone and the other lies on Quaternary sediments (Table 5.2).

In the case of the Attica Region, the Quaternary deposits increase the intensity by a single value. The flysch/foredeep deposits will cause no alterations in the intensity value, while the bedrock (mostly Mesozoic or Tertiary limestone) will decrease the intensity by one value (Figure 5.5). The input data for the surface geology were extracted from: a) the 1:25,000 Earthquake Planning and Protection Organization (E.P.P.O.) detailed geotechnical map for the Athens Metropolitan Area (Marinos et al., 1999a), b) the 12 1:50,000 geological maps of IGME (Tataris et al., 1966; Dounas, 1971; Gaitanakis, 1982; Bornovas et al., 1984; Gaitanakis et al., 1984, 1985;

Katsikatsos et al., 1986, 1991, 2000, 2002; Latsoudas, 1992; Parginos et al., 2007) for the rest of the Attica mainland.

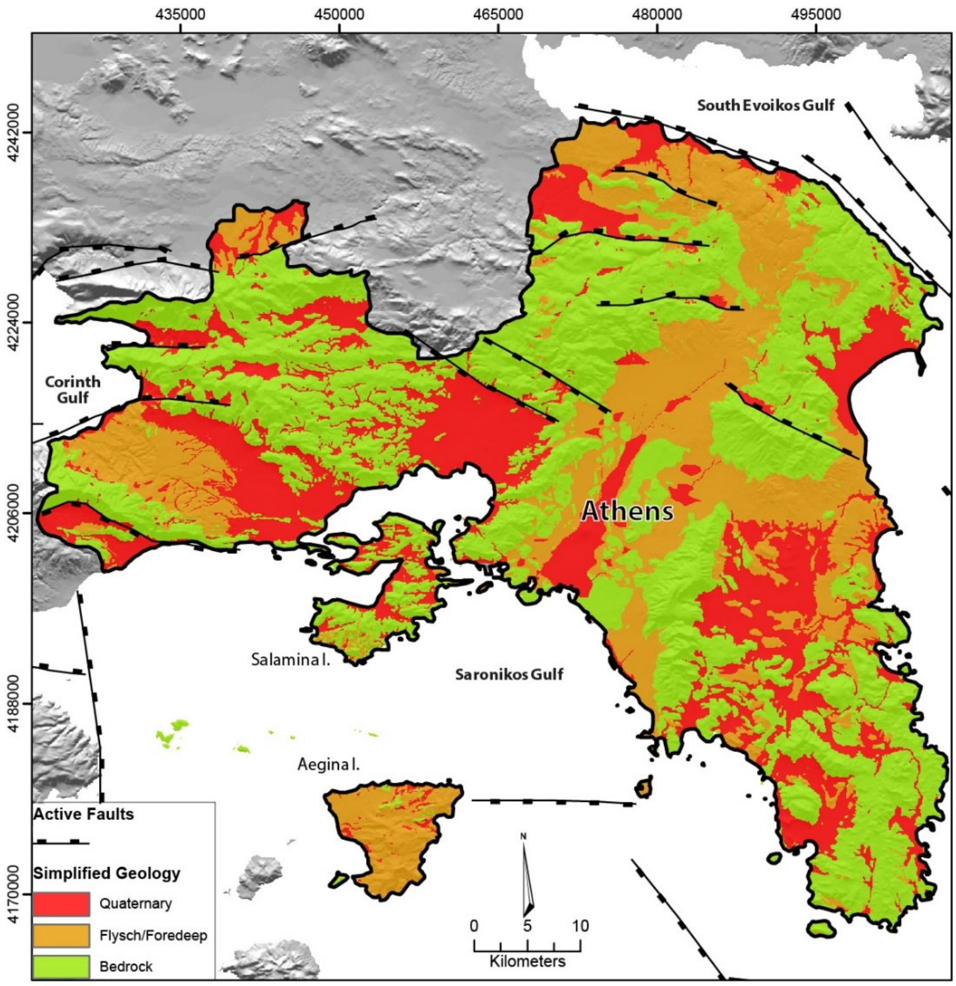

Figure 5.5: Simplified geological map of the area of Attica, based on 1:50,000 scale geological maps of IGME and the 1:25,000 scale Earthquake Planning and Protection Organization (E.P.P.O.) detailed geotechnical map for the Athens Metropolitan Area (Marinos et al., 1999a).

Table 5.2: Average intensity changes depending on different types of surface geology, proposed by Sauter and Shah (1978), and Degg (1992).

Subsoil	**Average change in intensity**
Rock (e.g. limestone, granite, gneiss, basalt)	-1
Firm sediments	0
Loose sediments (e.g. sand, alluvial deposits)	+1

Overall, the produced hazard maps incorporate information on bedrock geology and its contribution to spatial variations in ground shaking intensity.

5.3. Development of earthquake catastrophe model

According to the Solvency II regulatory framework (European Union, 2009), insurance companies are obliged to calculate a specific capital every year, which would cover all unexpected losses due to catastrophic events. This capital should be adequate in order to cover 99,5% of such cases each year, and it is a prerequisite for the insurance companies in order to be solvent. Solvency II characterizes this capital as the "Solvency Capital Requirement" and demands a detailed and transparent calculation process, which is supervised by the insurance supervision authorities in each European country.

This thesis proposes a calculation method for the SCR that is based on an Earthquake Catastrophe Model, which incorporates original research results from different scientific disciplines. The scope of this model is to take advantage of the benefits of Earthquake Geology in seismic hazard assessment by exploiting active faults analysis and combining them with the traditional vulnerability and loss calculation processes.

The differences between the proposed model and the existing ones are that: a) it is based on active faults analysis in order to address the problems with the spatial and temporal incompleteness of the existing catalogues (see also Chapter 2), and b) it is explicitly developed for the calculation of the SCR. It includes four different modules, namely the Hazard, Vulnerability, Exposure and Loss (Figure 5.6).

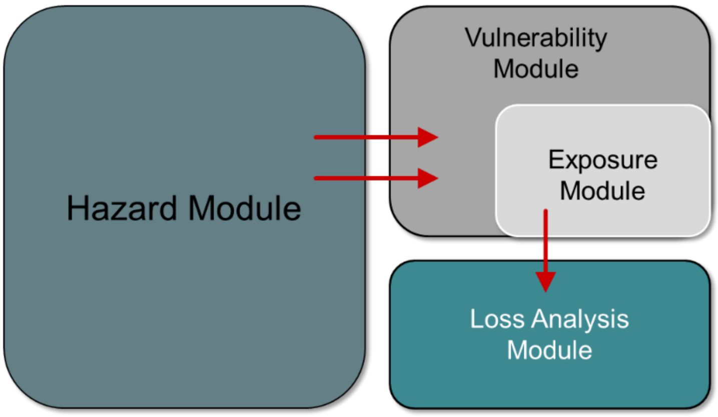

Figure 5.6: The basic modules of the Earthquake Catastrophe model. The Hazard Module has the most critical role, as the whole model is based on its outputs. The final results are extracted from the Loss module, which calculates both direct (meaning cost to repair or replace construction) and indirect (meaning business interruption) losses, but it also integrates other significant policy characteristics, such as deductibles and coverage limits, reinsurance coverage, etc.

5.3.1. Hazard Module

The proposed Hazard Module for the region of Attica consists of 4 sections, briefly described below:

1. Compilation of an active fault database that includes the seismic sources, fault lengths, fault kinematics characteristics, and fault slip rates, which govern

earthquake recurrence. Simulation of earthquake events of magnitude M≥6 during the last 15,000 years, thus incorporating the number of seismic cycles.
2. Evaluation of historic earthquake catalogues in order to include aerial sources, background seismicity and deep earthquakes related to the subduction zone
3. Construction of the final earthquake catalogue. Since it incorporates both the analysis of active faults and seismic catalogues, it is considered complete for the past 15,000 for intraplate earthquakes of magnitude M≥6. These events are considered as potentially catastrophic and are of high importance for the analysis of the extreme events that could cause significant insured losses.
4. Stochastic modelling of future earthquake events in the Region of Attica, using the combination of fault specific seismic hazard assessment and seismic catalogues. The stochastic simulation is applied for the location, magnitude, time and depth of future earthquake events.

The stochastically modelled catalogue of future earthquake events is then imported into the ArcGIS software, in order to simulate the future earthquake events for each stochastically created epicentre. These events are simulated by applying Ground Motion Prediction Equations (GMPEs) on each modelled epicentre, in order to define the spatial distribution of the macroseismic intensity values of each event.

Depending on the depth of the epicentres, two different types of attenuation relationships are applied. The seismicity in Attica relates mostly to shallow events. They are not uniformly distributed throughout the continental crust but are proven to be concentrated in the upper 10-15 km, close to the base of the seismogenic layer (Chen and Molnar, 1983; Sibson, 1984). For these earthquakes, the Theodulidis (1991) attenuation relationships were used (see also Deligiannakis et al., 2018a).

The second type of earthquakes is related to the subduction zone. Since the region of Attica is located in the back-arc area of the Hellenic subduction zone, it is affected by deficient levels of ground motions for intermediate-depth events, as is evident in instrumental recordings (Skarlatoudis et al., 2013) and the recorded damages after large intermediate-depth earthquakes (Papazachos & Comninakis, 1971). This may be attributed to the fact that there is a substantial attenuation of the ground motion that is related to the presence of the volcanic arc and the associated mantle wedge (Papazachos et al., 2005; Boore et al., 2009; Skarlatoudis et al., 2013). However, the Papaioannou (1984) attenuation relationships were used for the earthquakes originating from the subduction zone, as they calculate the intensity attenuation rather than the PGA or SA distribution.

For obtaining more accurate and realistic results, the local site conditions are imported into the model, by using attenuation or amplification functions for seismic shaking depending on surface geology (see also Roberts et al., 2004; Papanikolaou et al., 2013; Deligiannakis et al., 2018a). The whole procedure is automated in a GIS environment so that it is fully customisable for different local site conditions or inputs regarding new inputs in the fault database, attenuation relationships, and surface geology conditions (Figure 5.7).

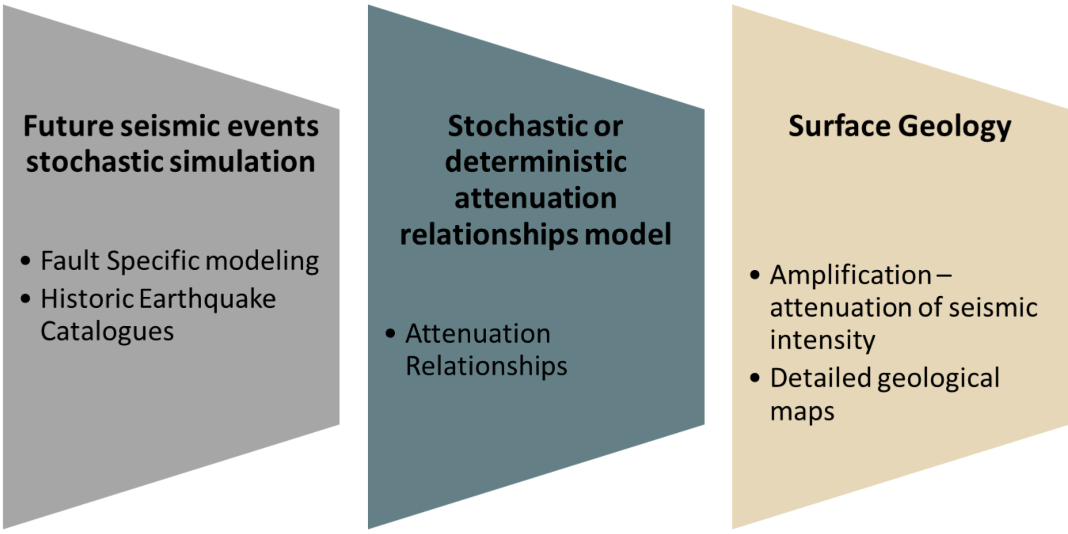

Figure 5.7: The main processes within the proposed Hazard module. The primary input is the fault specific modelling results, which vastly increases the earthquakes sample for magnituted M≥6.

5.3.2. Vulnerability Module

The structural damage in buildings and the corresponding loss that occurs due to the simulated earthquake events is computed using the Vulnerability Module. The extent to which a building will be damaged during a simulated earthquake depends on individual characteristics, such as the building construction type, the age, the number of floors and the building use (Kappos et al., 1998; Chandler et al., 2001). The proposed model relies on eight different building types, related to the construction type and the seismic codes under which they were built.

In general, the Building Vulnerability Tables display the average value of the expected building damage $E[Y_i]$, depending on the seismic intensity and the building characteristics. In the same way, the Building Interior Vulnerability Tables display the average value of the expected building interior damage $E[Z_i]$, depending on the seismic intensity and the building characteristics.

The total damage X_i corresponding to the i_{th} building, is calculated by the sum $\boldsymbol{X_i} = \boldsymbol{Y_i} + \boldsymbol{Z_i}$, where Y_i and Z_i are independent uniformly distributed random variables, described as follows:

$$\boldsymbol{Y_i \sim U(E(Y_i)\text{-}\alpha\%E(Y_i),\ E(Y_i)+\alpha\%E(Y_i)),}$$

$$\boldsymbol{Z_i \sim U(E(Z_i)\text{-}\alpha\%E(Z_i),\ E(Z_i)+\alpha\%E(Z_i))}$$

and a value depends on the range of uncertainty that the model would take into account. A value of 20% is assumed as a more standard approach for contemporary buildings stock.

The model is also capable of using vulnerability functions or vulnerability curves, which are also used for the estimation of the building damage depending on other strong-motion parameters, such as the Peak Ground Acceleration (PGA), the Peak Ground Velocity (PGV) or the Spectral Acceleration (SA) and the building characteristics. In the same way, they are used for the estimation of the building interior damage depending on the PGA, PGV or SA and the building characteristics.

5.3.3. Exposure Module

The Exposure Module handles the particularities of each portfolio that are inserted in the model. Each insurance company adopts a unique database architecture, which includes the locations and details of the insured buildings, along with other policy features, such as the coverage types and limits. As a result, the insured portfolio database is redesigned in a way that can be incorporated into the Vulnerability Module and then transferred into the Loss Module.

5.3.4. Loss Module

The Loss Reserves Calculation module is based on the iteration of the earthquake scenario simulation as follows:

- The stochastic simulation of earthquake events that were simulated during the Hazard module is used for the construction of high spatial resolution intensity maps for the Attica region. The results are then aggregated in order to provide the damage extent in Postal Code level.
- The expected damage per contract is calculated based on the vulnerability module and the building characteristics.
- The expected amount of loss is calculated based on each insurance policy, line of business and insured value.
- The annual own retained losses are calculated after taking into consideration the reinsurance conditions.
- Finally, all policies are summed, and the total loss for the insured portfolio for each earthquake scenario per year is calculated.

This procedure is repeated for a large number of earthquake scenarios (~10,000 iterations).

The total amount of insured claims during a certain period (which is typically one calendar year) is denoted a random variable. Then, according to a standard portfolio of insured risks, we obtain the corresponding total claim amounts for the relevant events.

5.3.5. Development of the demo portfolio

The model was run against the EIOPA’s SF benchmark, in order to analyse similarities and differences regarding the numbers for the SCR between the two models. To this end, a demo database was developed for a hypothetical company that is exposed only in the Attica region. The insured portfolio was modified so that it only includes buildings of the most common construction types in Greece. Out of eight construction types that are available in the Vulnerability module, the test was run assuming that all building types were reinforced concrete under the latest, intermediate, or no seismic design at all. Reinforced concrete structures are the most common construction type in Greece (ELSTAT, 2015). However, since the different Greek seismic designs pose a noticeable variation in the building's response to strong ground motions (Kappos et al., 1998), this diversification was applied to the demo portfolio to simulate the actual exposure more accurately.

Another critical parameter for the development of the demo portfolio was the spatial diversification of the exposure. Since there are no publicly available data regarding the buildings sum insured values, the Industry Exposure Database (IED) were used, as provided by the Catastrophe Risk of the Insurance and Reinsurance Stakeholder Group and the Catastrophe risk work-stream (CAT WS) at the EIOPA, under the cooperation for the validation of the EIOPA SF results for the Greek territory (EIOPA, 2018). The IED was based on data received directly from the largest insurance companies in Greece, covering more than 70% of the insured values across the country. The granularity of the IED reached the postal code level, which is the most common level of spatial analysis used in the Greek insurance market to assign a geographic location for their risks. Even though the SF uses CRESTA zones to determine the geographical divergence of the exposure, it was decided not to aggregate the IED values to this level, because of the anticipated differences related to the granularity of the proposed model, compared to the SF.

5.3.6. Validation method

The simulation of the insured portfolio served two causes: First, to confirm how the model performs using exposure data that are as similar as possible to the actual conditions of the Greek insurance market. The Attica region gathers more than 40% of the total insured value of Greece so that the results would be as representative as possible. Second, to compare the results with the industry standards and the SF, the same model input was needed. Since any parameterisation of Hazard, Vulnerability, and Loss modules is not possible when running the SF, the only way to have a comparable result was to have a similar Exposure module. However, the SF algorithm only uses the CRESTA aggregation standard, which refers to the first two digits of the Postal Codes in the case of Greece. Furthermore, for the whole Attica region and the individual CRESTA Zones calculations, zero relativity values for the rest of Greece were assumed.

6. Active faults analysis and active fault database for the Attica Region

This Chapter presents the tectonic geomorphological analysis of the Sparta fault (Section 6.1), as well as information on the existing literature and details for the faults that were used as input the seismic hazard assessment of the Attica region (Section 6.2). The Attica faults database and maps showing the geometry and other characteristics of the faults are presented in Section 6.3.

6.1. The Sparta fault

The Sparta fault system is a major structure that bounds the eastern flanks of Taygetos Mountain (2.407 m) and shapes the western boundary of Evrotas Basin. It trends NNW-SSE and has a length of 64 km (Figure 6.1). Beyond the main Sparta fault system there is also a significant antithetic structure approximately 5 km eastwards from the main fault. Both structures shape the present-day Sparta basin forming linear features. The Sparta fault was activated in 464 B.C., completely destroying the city of Sparta (~20,000 fatalities) (Papazachos & Papazachou, 2003). Since then, no other major earthquake has been generated by this system, and a future event could be imminent.

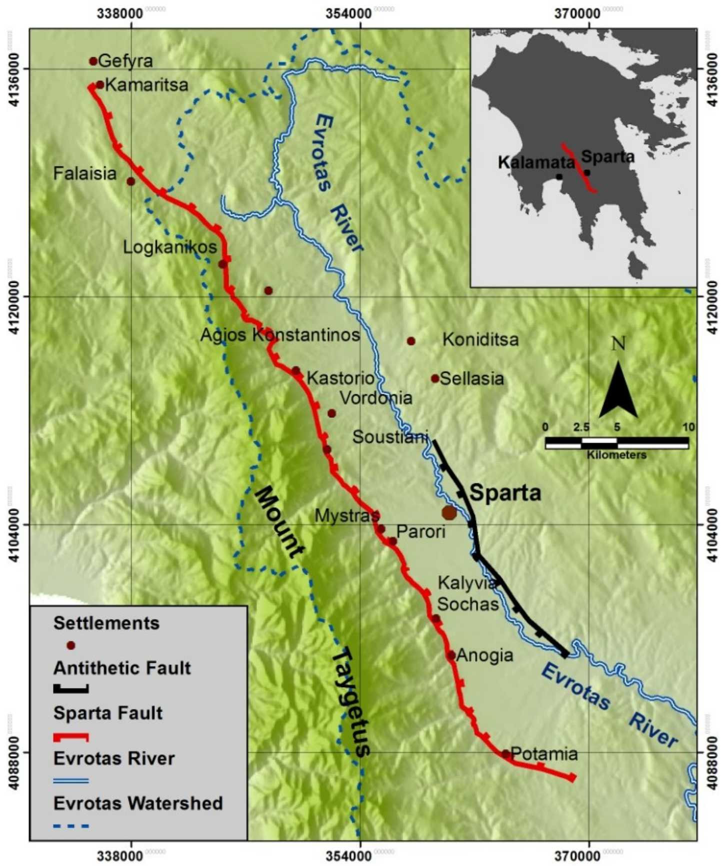

Figure 6.1: Map view of the the Sparta fault. It trends NNW-SSE and has a length of 64km.

Fluvial long profiles of 9 transient rivers crossing different segments of the Sparta fault were constructed in order to examine the longitudinal convexity and its variation along strike. Such profiles were also compared to the longitudinal profiles of 3 neighbouring catchments that are not influenced by any fault and 2 catchments crossing the antithetic fault (Figure 6.2). Geological data of the study area, in conjunction with a 25 m resolution digital elevation model (DEM) were digitized, transformed into raster data and imported in ArcMap. The interpretation and calculation of the Steepness Index - k_{sn} of catchments profiles was rendered by the combination of ArcGIS Profiler Toolbar Version 4.2 and codes in Matlab version 7.10.0.499 (Mathworks, 2010, see also Whipple et al., 2007; Vassilakis et al., 2007).

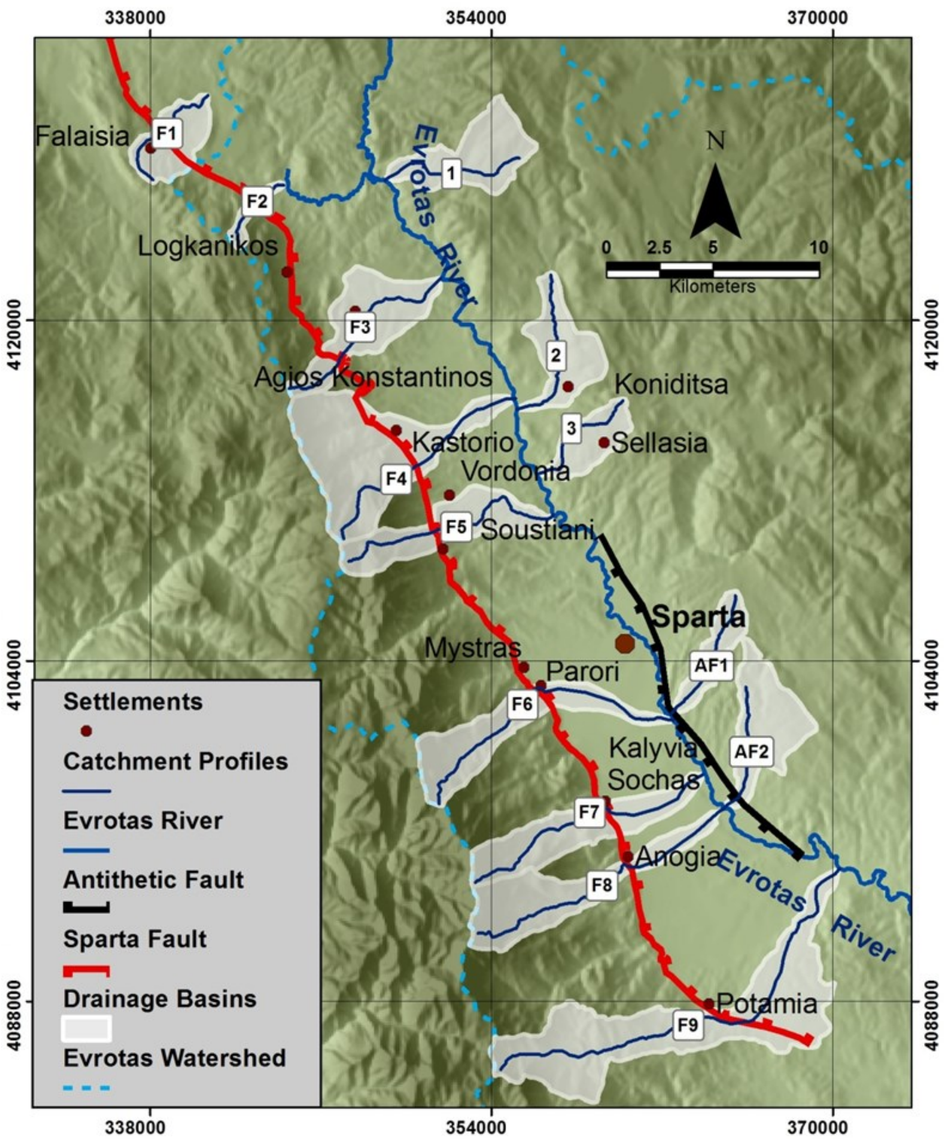

Figure 6.2: Drainage basins and main branches for 9 catchments crossing the Sparta fault, two crossing the antithetic structure and three crossing no fault.

The analysis of long profiles was carried out by the author of this thesis and was published in 2013 (see Papanikolaou et al., 2013). The results are also presented in this thesis.

Qualitative analysis showed a significant difference in longitudinal convexity between the central and both the south and north parts of the fault, leading to the conclusion of varying uplift rate along strike (Figure 6.3). A minor convex reach of 205 m in Potamia catchment long profile (southeast part of the Sparta Fault) can be clearly observed, although it seems to have propagated upstream in relation to the fault. This could happen as the channel successively adjusts to the imposed uplift field (Whipple and Tucker, 2002). On the other hand, Anogia river's flow with significant deviations downstream and through a rapid variation of different geologic formations upstream creates a long profile convexity that appears on a smaller scale (101 m) than the other profiles. The northernmost of the two above catchments, Kalyvia–Sochas catchment long profile, revealed a convex reach of 246 m, which is in contact with the Sparta Fault, in contrast to Potamia catchment's convex reach that is located 3 km away from the present-day fault trace in the footwall. The Parori and Kalyvia–Sochas catchments are the localities where extensive alluvial fans outcrop (Pope et al., 2003).

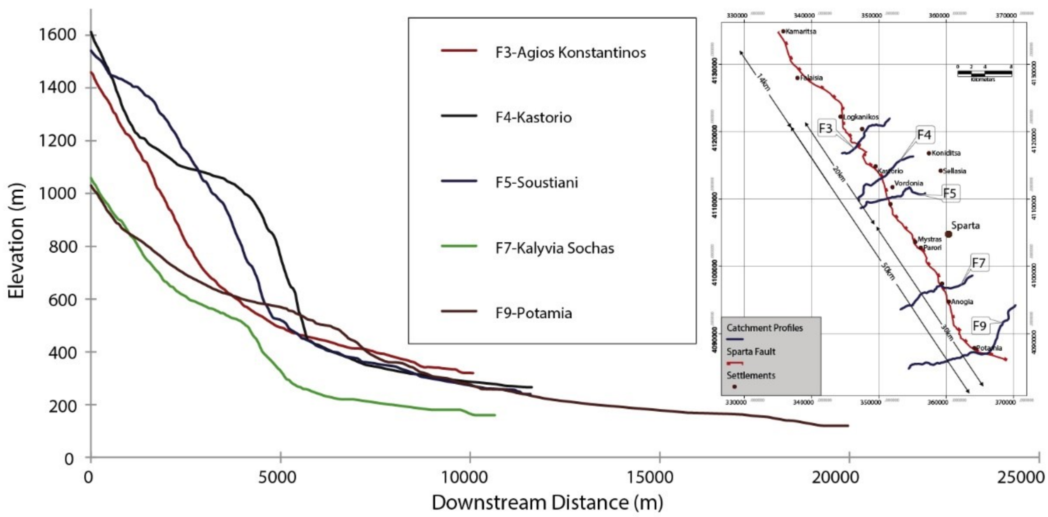

Figure 6.3: Comparison of 5 catchment long profiles crossing the Sparta fault. Agios Konstantinos - F7 (northern part) catchment is the only one to appear with concave up long profile, while Potamia - F9 (southern part) profile is the less steep. Figure reproduced from Papanikolaou et al., 2013.

Parori catchment long profile convex reach appears to consist of three separate knickzones that are possibly related to lithological variations but could be interpreted as cumulative convexity with a height of 536 m. Located in the central part of the Sparta Fault, catchments near Soustianoi and Kastori villages have convex reaches whose downstream ends are in contact with the fault, outreaching 876 m and 590 m, respectively. In the northern part of the Sparta Fault, the Agios Konstantinos catchment seems to have a concave-up channel profile, possibly indicating a constant and low slip rate since it is located towards the northern tip of the fault. The lack of profile convexity of Agios Konstantinos can also be attributed to the lithology factor since it flows through the higher erodible schists rather than the limestones (Figure 6.4). Logkanikos and Falaisia catchment long profiles have significant convexities. However, as previously stated, their drainage basins above the fault are too small and the upstream lengths are too short to extract meaningful results. On the other hand, catchments crossing the antithetic structure as well as neighbouring areas where no active faults are traced display similar characteristics, such as typical concave up profiles with small exceptions related only to differential erosion (Figure 6.5). Such examples form a minor convexity that does not exceed 100 m on a catchment near Koniditsa (Figure 6.5, profile 2), due to profile long alterations in lithology and a 30 m high knickzone appearing in the last few hundred metres downstream Kolliniatiko river, related to the same lithological conditions that mark the transition from limestone to flysch or alluvial deposits. In both cases, the convexity coincides with the transition from limestone to flysch or alluvial deposits, indicating the strong control of the lithological factor.

Finally, the normalised steepness index, k_{sn}, using a reference concavity of 0.45, was calculated for all catchments crossing all Sparta Fault parts and plotted against along strike distance from NNW tip of the Sparta fault (Figure 6.7). This plot demonstrates that the higher values of the k_{sn} outcrop towards the centre of the fault. The k_{sn} values for the catchments closer to the tips of the Sparta Fault (F3-Agios Konstantinos and F9-Potamia) were 90 and 82.7, respectively, while in the central part, the steepness rates are higher and vary from 121 to 138 ($121<k_{sn}<138$). On the other hand, k_{sn} values for the catchments AF1 and AF2, crossing the antithetic structure, were 26.2 and 27.9, respectively, while the same normalised steepness index in catchments 2-Koniditsa and 3-Sellasia were 48 and 31.7, respectively.

In conclusion, the tectonic geomorphological analysis of the Sparta fault implies that its segments are hard linked and thus it could be modelled as a single structure for seismic hazard assessment (see also Section Figure 7.1).

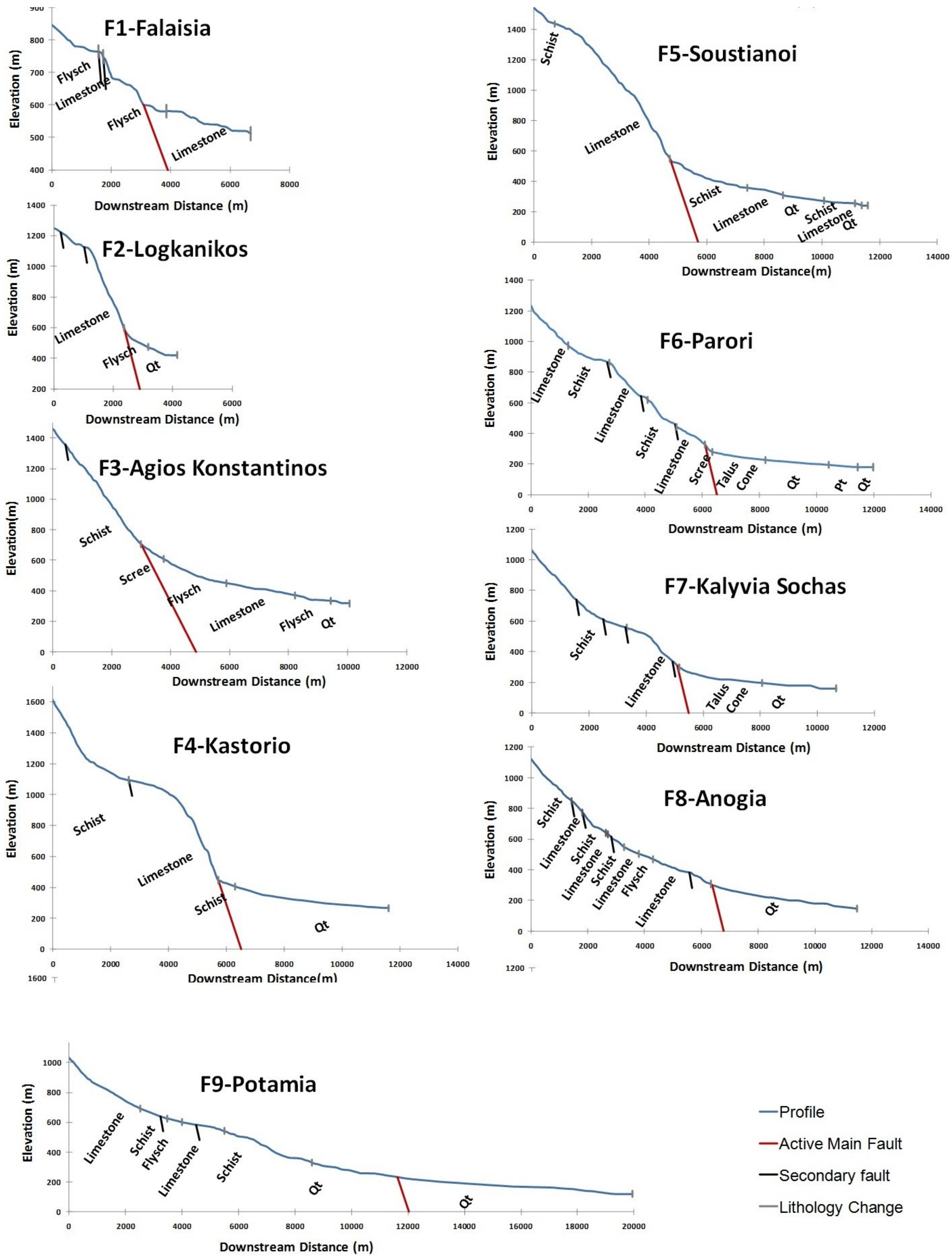

Figure 6.4: Long profiles of rivers crossing perpendicular the Sparta Fault near the Potamia, Anogia, Kalyvia-Sochas, Parori, Soystianoi, Kastorio, Ag. Konstantinos, Logkanikos and Falaisia villages, respectively. Locality names are shown geographically in Figure 6.2. Figure modified from Papanikolaou et al., 2013.

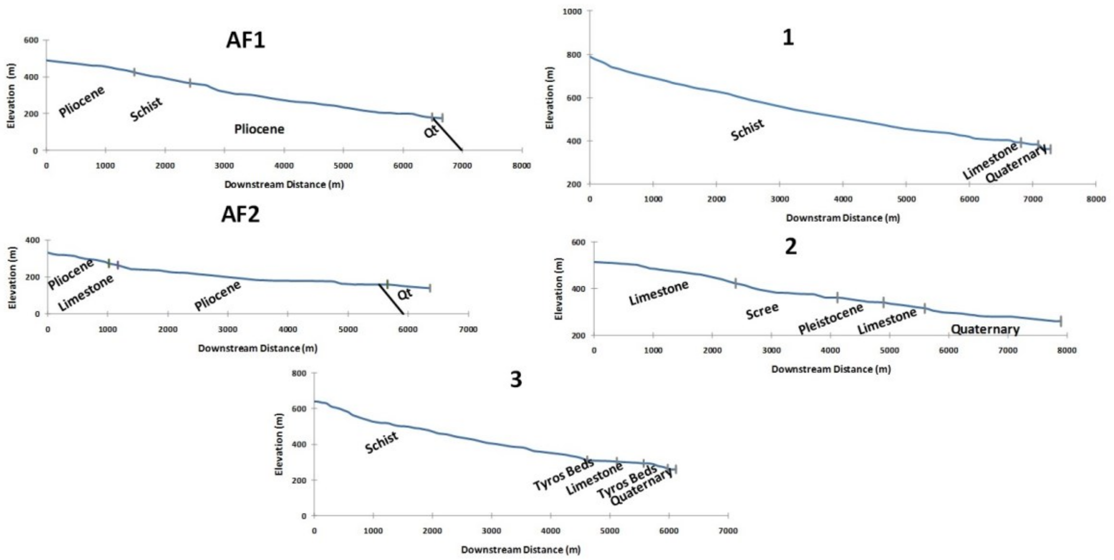

Figure 6.5: Long profiles of rivers crossing the antitethic Sparta Fault as well as rivers that cross no active fault near the Sellasia, Koniditsa and Kollinaitiko villages. Locality names are shown geographically in Figure 6.2. Figure modified after Papanikolaou et al., 2013.

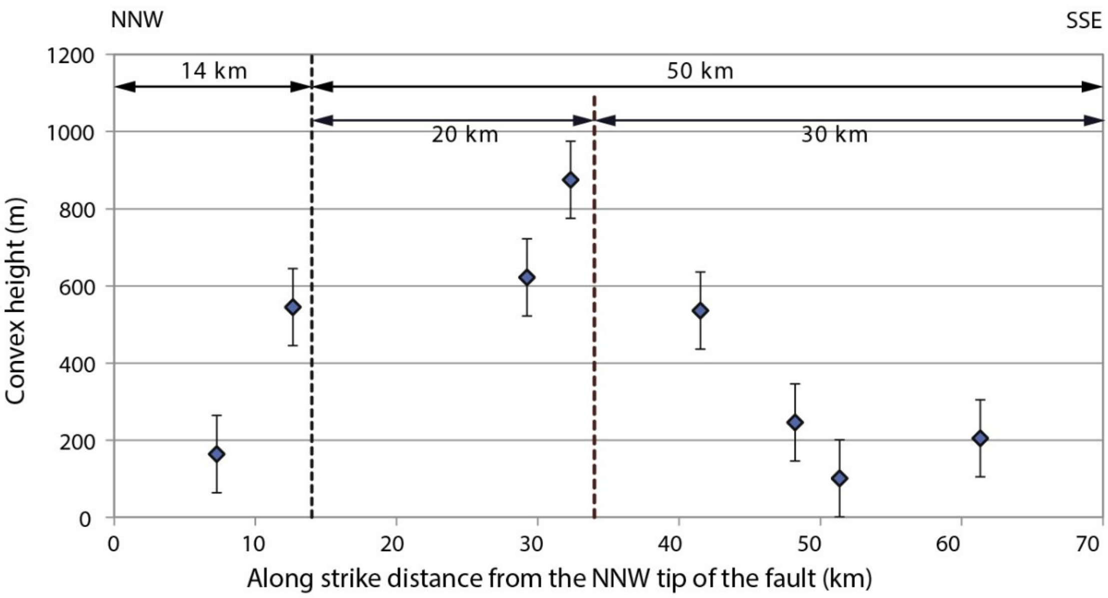

Figure 6.6: Diagram showing the convex height variability of the catchments along strike the fault system, with higher values towards its centre that diminish towards its tips. Error bar represents the 100 m convex height that can be attributed to differential erosion. Agios Konstantinos profile is missing, due to the convexity that is attributed to the lithology. Figure modified after Papanikolaou et al., 2013.

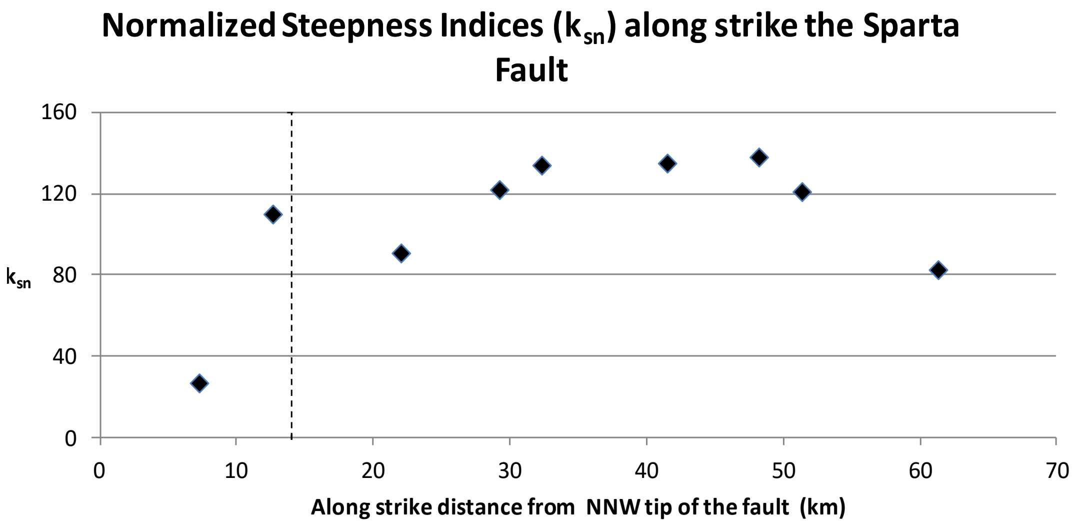

Figure 6.7: Normalized steepness index (k_{sn}) for each of the 9 catchments crossing the Sparta Fault. Higher values appear in the centre of the fault. Dashed line separates the northern 14 km fault segment.

6.2. Active faults in the Attica region

This section offers information on the active faults that lie within or in short distances from the Attica region boundaries, so that they could cause damage in case of earthquake rupture. Published results are presented here with the appropriate references. However, tectonic geomorphological analysis was carried out for the onshore faults to challenge new techniques and confirm their activity level from a qualitative perspective. Apart from traditional geomorphological indices, which are applied where applicable, swath profiles were generated with the Swath Profiler tool (Pérez-Peña et al., 2017) in a GIS environment in order to visualize the deformation pattern both along strike and perpendicular to the studied faults.

6.2.1. The Milesi fault

The Milesi fault was first regarded to be active by Papanikolaou et al. (1988), based on geomorphological observations. Goldsworthy et al. (2002) named it after the Oropos village, which lies in the immediate vicinity of the fault. However, as Oropos most people address today the Skala Oropou that is the coastal town lying 3.6 km northwards the Milesi Fault, which is significantly bigger and corresponds to the ancient Oropos, that served as a port. In addition, the coastal offshore fault is also known as Oropos in the literature. Following the above, the fault is named after the Milesi town, which lies in the immediate hangingwall (see also Grützner et al., 2016).

Goldsworthy et al. (2002) speculated that the Milesi fault was the one that ruptured during the Mw = 6.0 earthquake in 1938 (Ambraseys and Jackson, 1990; see also Papanikolaou and Papanikolaou, 2007b), about 40 km north from the Athens centre. However, there is uncertainty about the exact location of the epicentre (Figure 6.8), while the best candidate for hosting this earthquake is the coastal north dipping Oropos fault, where several ruptures and severe secondary effects were recorded (see also Papanikolaou et al., 2015).

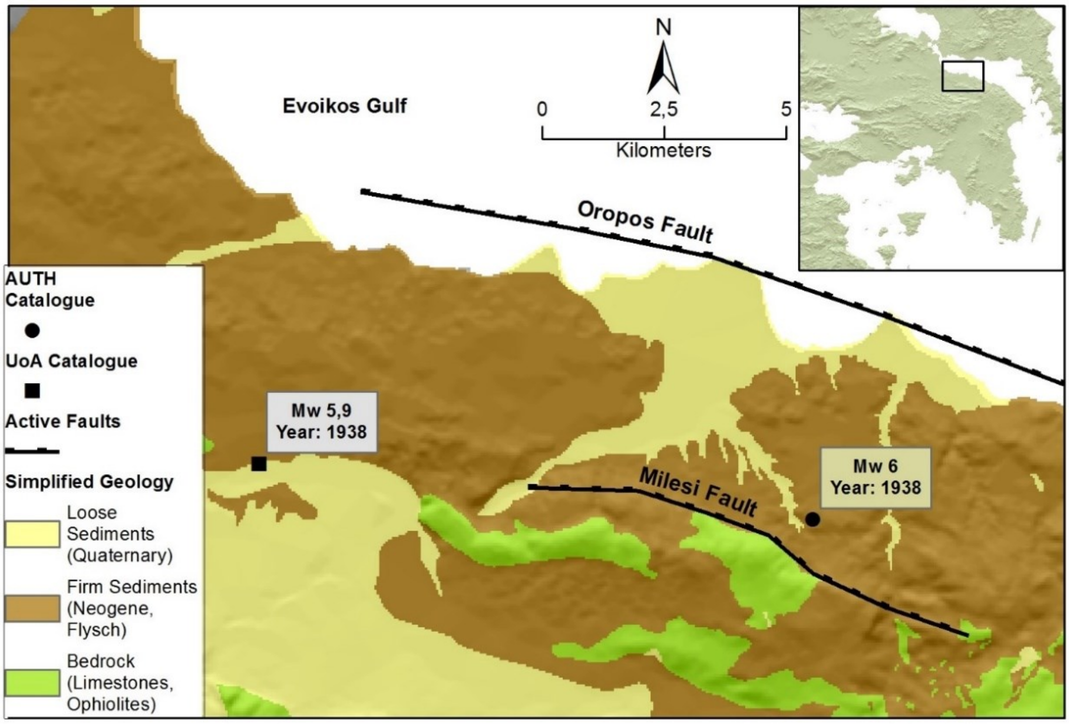

Figure 6.8: The Milesi and Oropos faults plotted against the Mw=6.0, 1938 Oropos event, which is retrieved from the two earthquake catalogues of NOA (UoA) and AUTH. Both epicentres are located 12 km away from each other and on the footwall of the Oropos fault, rather than its hangingwall. Image reproduced from Papanikolaou et al., 2015.

The fault was recently studied by Grützner et al. (2016), who conducted GIS-based geomorphological analyses, field mapping of the postglacial fault scarp, ground-penetrating radar profiling, and palaeoseismological trenching, which allowed the extraction of data on slip rates and palaeoearthquakes.

The Milesi fault is an NW - SE striking, NE dipping normal fault, with a length of approximately 10 km. It is located in North Attica, and it is parallel to the offshore Oropos fault further NE and the Malakasa fault in the SW (Figure 6.9). The footwall of the fault comprises Triassic - Jurassic limestones, with small relicts of the ophiolite nappe of the Pelagonian zone (s.l.), and the hanging wall consists of colluvium, marls, conglomerates and loams (Katsikatsos, 2000; Parginos et al., 2007).

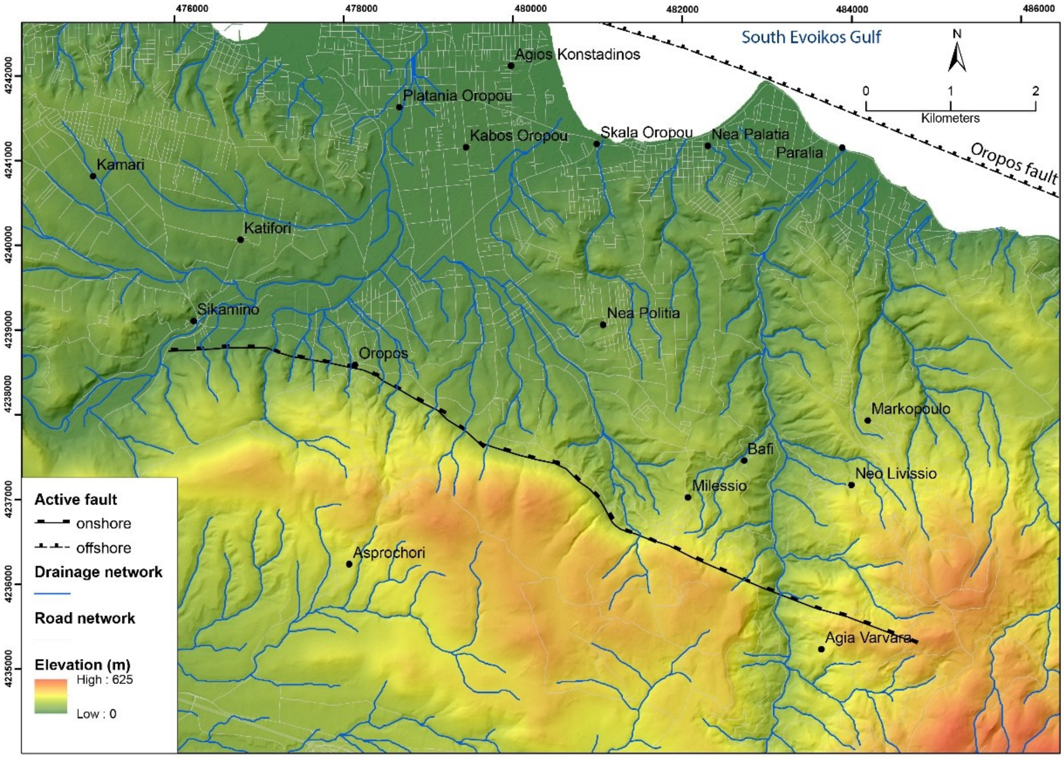

Figure 6.9: The NW-SE striking and NE dipping Milesi fault in NE Attica (id = 1 on Table 6.1) and the main drainage network flowing towards the South Evoikos Gulf. Base map shows the Digital Terrain Model (DTM) from the National Cadastre with 5 m spatial resolution.

Steep slope gradients occur in the immediate footwall, reaching up to 45° in the central part, but they diminish at the fault tips, with an average slope gradient of 10° (Figure 6.10).

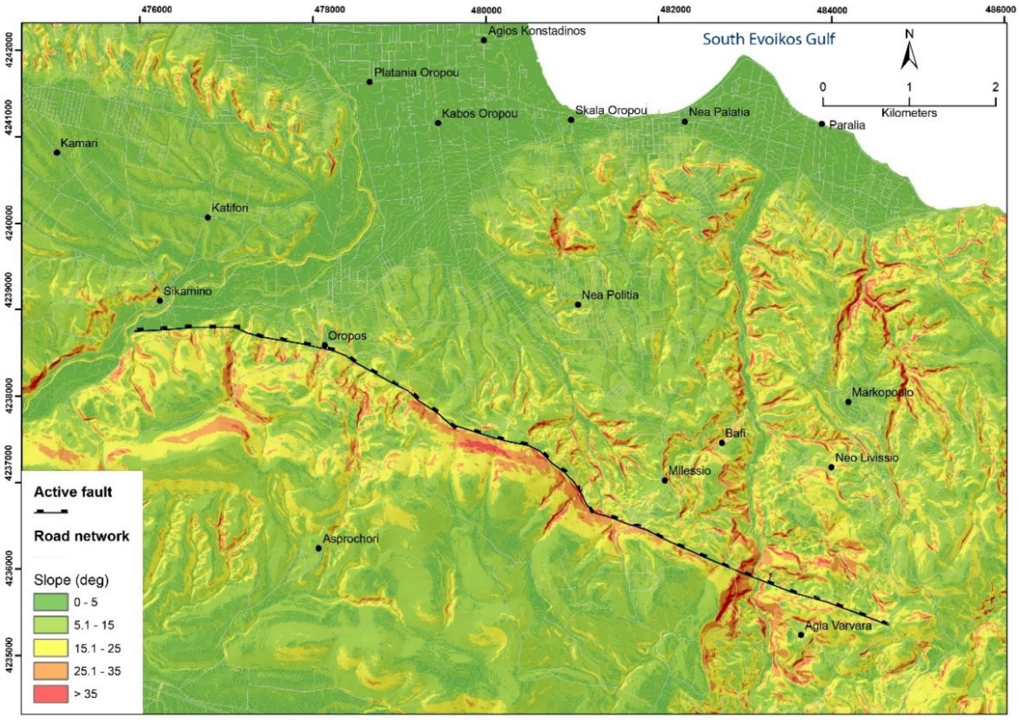

Figure 6.10: Slope map showing the break of slope related to the Milesi fault (id = 1 on Table 6.1). Steeper slopes are observed at the footwall centre, where the maximum displacement is observed.

Deeply incised channels are visible in the footwall, where at least two windgaps are formed close to the centre of the fault (Figure 6.11).

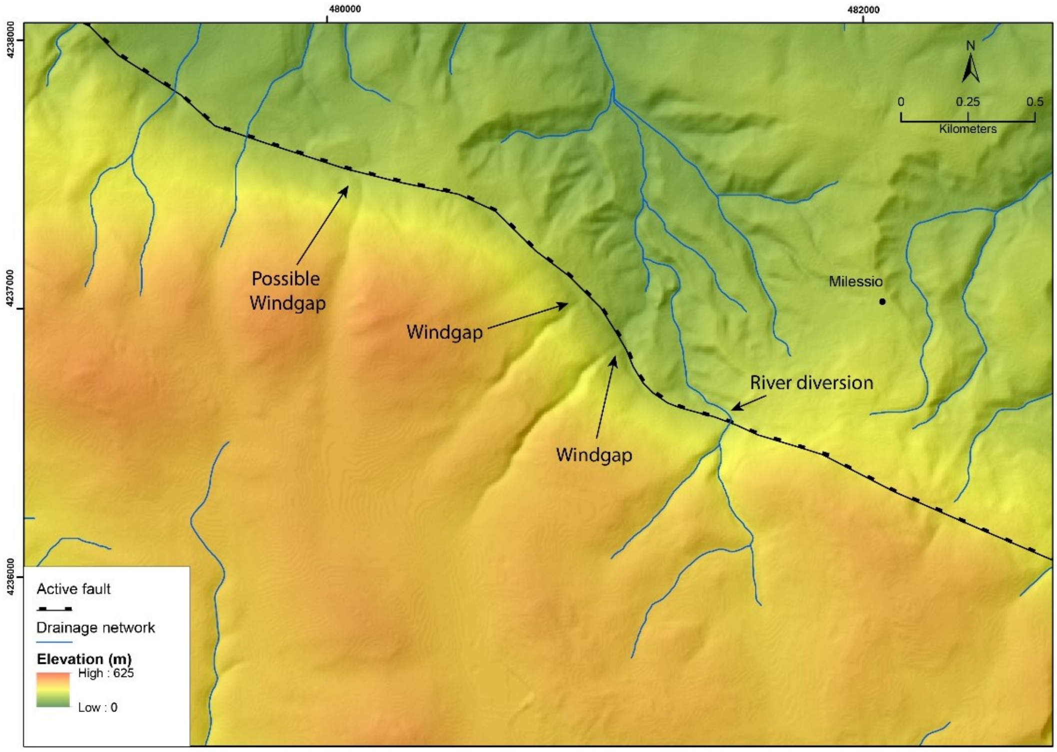

Figure 6.11: Zoomed map showing 2 windgaps and one possible windgap, at the center of the fault. The second order stream in tle lower right part of the map is flowing towards NE but seems to be diverted towards NW, parallel to the fault strike.

A swath profile in a fault-parallel direction, using the SwathProfiler toolbar (Pérez-Peña et al., 2017), shows that the elevation difference between the footwall and the hanging wall is up to 320 m. The greater differences occur in the centre of the fault, which creates a clear triangular throw pattern as shown from the "local relief" curve in Figure 6.12.

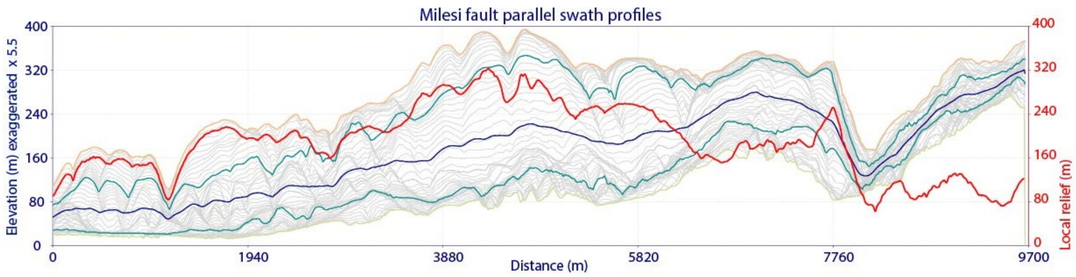

Figure 6.12: Swath topographic profiles within a Milesi fault-parallel stripe. Fault located at the centre of the stripe. Stripe width is 2600 m. Y-axis is exaggerated about 5.5 times. View looking towards NE. Orange line represents the maximum elevation, light green line represents the lower elevation, blue line represents the mean elevation, dark green lines represent the Q1 and Q3 quartiles, red line represents the local relief (maximum elevation minus minimum elevation at the same distance along the fault line).

Three swath topographic profiles within fault perpendicular stripes reveal higher uplift rates at the central part of the fault (Figure 6.13, see Figure 6.14 for profile locations), although part of the topographic differences could be attributed to the different lithology (see also Whittaker et al., 2008).

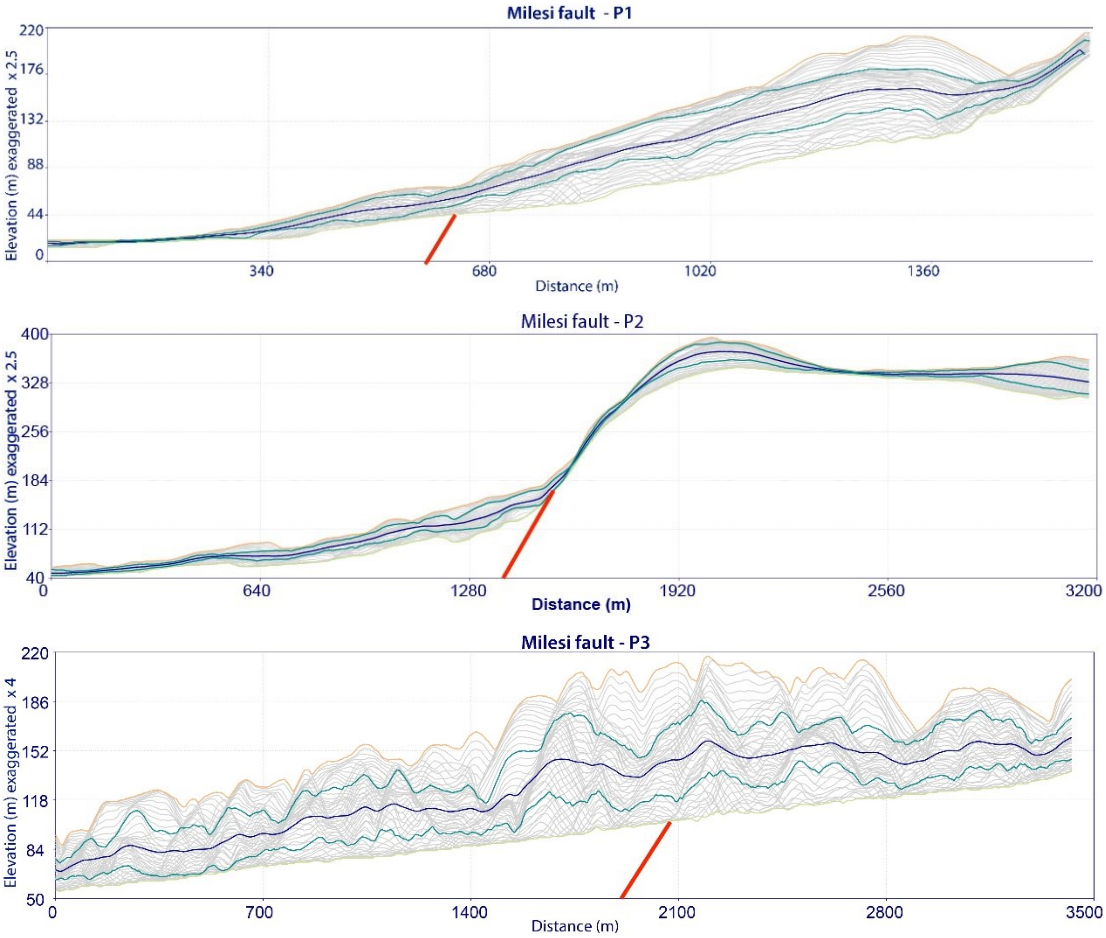

Figure 6.13: Swath topographic profiles within fault perpendicular stripes, following drainage network branches close to the center and both ends of the fault. Stripe axes locations shown in Figure 6.14. Stripe width is 500 m. Y-axis is exaggerated about 2.5 times for P1 & P2, and 4 times for P3. View looking towards E. X-axis is not on the same scale in each profile. Orange line represents the maximum elevation, light green line represents the lower elevation, blue line represents the mean elevation, dark green lines represent the Q1 and Q3 quartiles. The red line represents the Milesi fault. Note the prominent convex profile on the footwall in P2, which indicates higher uplift rates towards the centre of the fault.

Additionally, the enhanced Transverse Hypsometric Integral (THi*) values were calculated using the SwathProfiler toolbar. They reach up to 0.8 for the central profile (P2), while they are still above 0.5 for P1 and P3 (i.e. 0.55 and 0.53, respectively), implying a young transient landscape, with mean elevations closer to maximum elevations (see also Pérez-Peña et al., 2017) and suggesting that the throw decreases towards the tip of the fault, as would be expected.

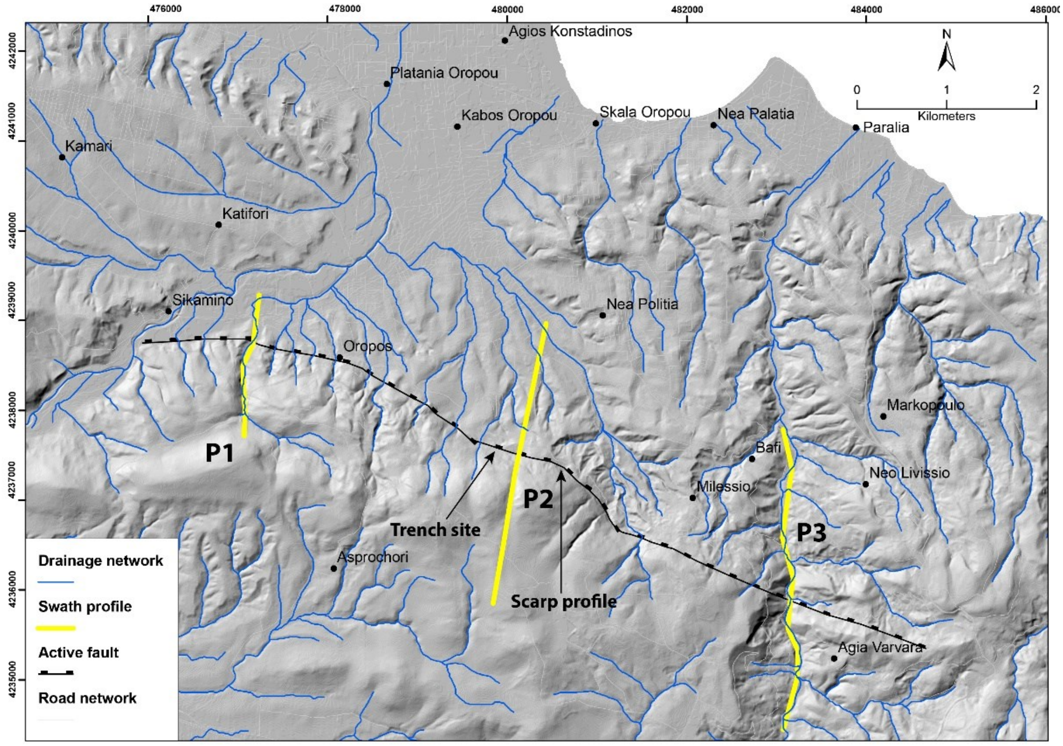

Figure 6.14: Shaded relief map of the Milesi fault, showing tha main drainage network, the locations of paleoseismic trench and fault scarp profile, as well as the location of the fault – perpendicular swath profiles (P1, P2 and P3).

The accumulated net offset of the fault is not precisely known. From cross-sections based on the official 1:50,000 scale geological map (Katsikatsos, 2000), it is clear that its total throw is 1050 ± 500 m see also Figure 6.15). The large error bar stems predominantly from the uncertainty regarding the thickness of the post alpine sediments, which vary significantly over short distances (Grützner et al., 2016).

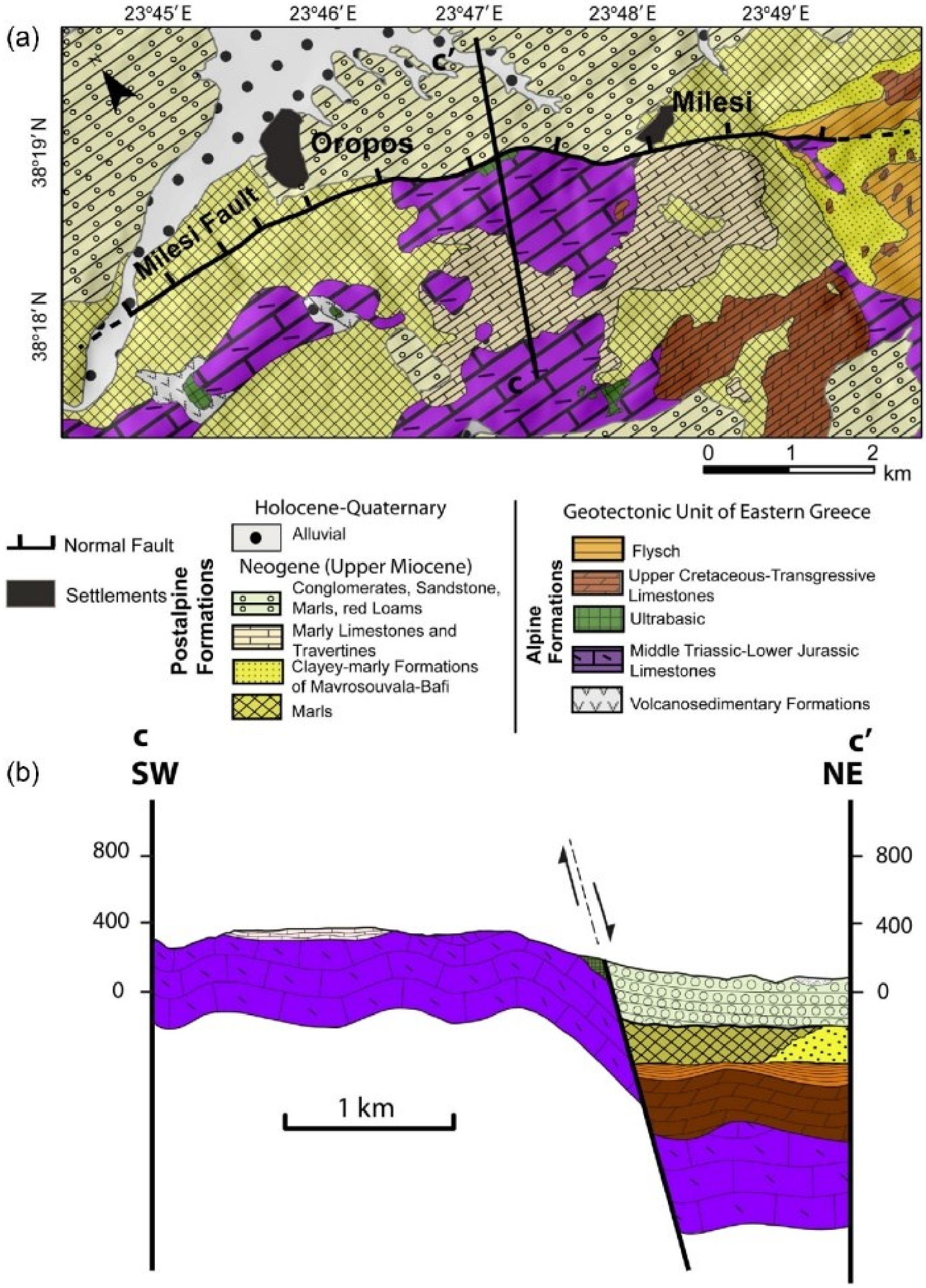

Figure 6.15: a) Geology of the Milesi Fault and the surroundings (geology modified after Katsikatsos 2000; map and cross-section after Grützner et al., 2016). C–C′ marks the cross-section in (b). (b) Cross-section based on the Geological Map (Katsikatsos 2000). The total throw of the Milesi Fault is 1050 ± 500 m.

Grützner et al. (2016) logged an existing outcrop that exposed the contact between the ophiolites of the Pelagonian zone (s.l.) in the footwall and the colluvium in the hanging wall, separated by a shear zone dipping to the North (Figure 6.16). According to their interpretation, an average throw rate of 0.4 mm - 0.45 mm/y was calculated over the last 4000 years, and a 0.28 mm/y was calculated for the last 2000 years. However, an average throw rate of 0.26 mm/y was inferred from a detailed topographic profile of the exposed post-glacial scarp (Figure 6.17). As a result, an average throw rate of 0.3 mm/y was adopted for the Milesi fault.

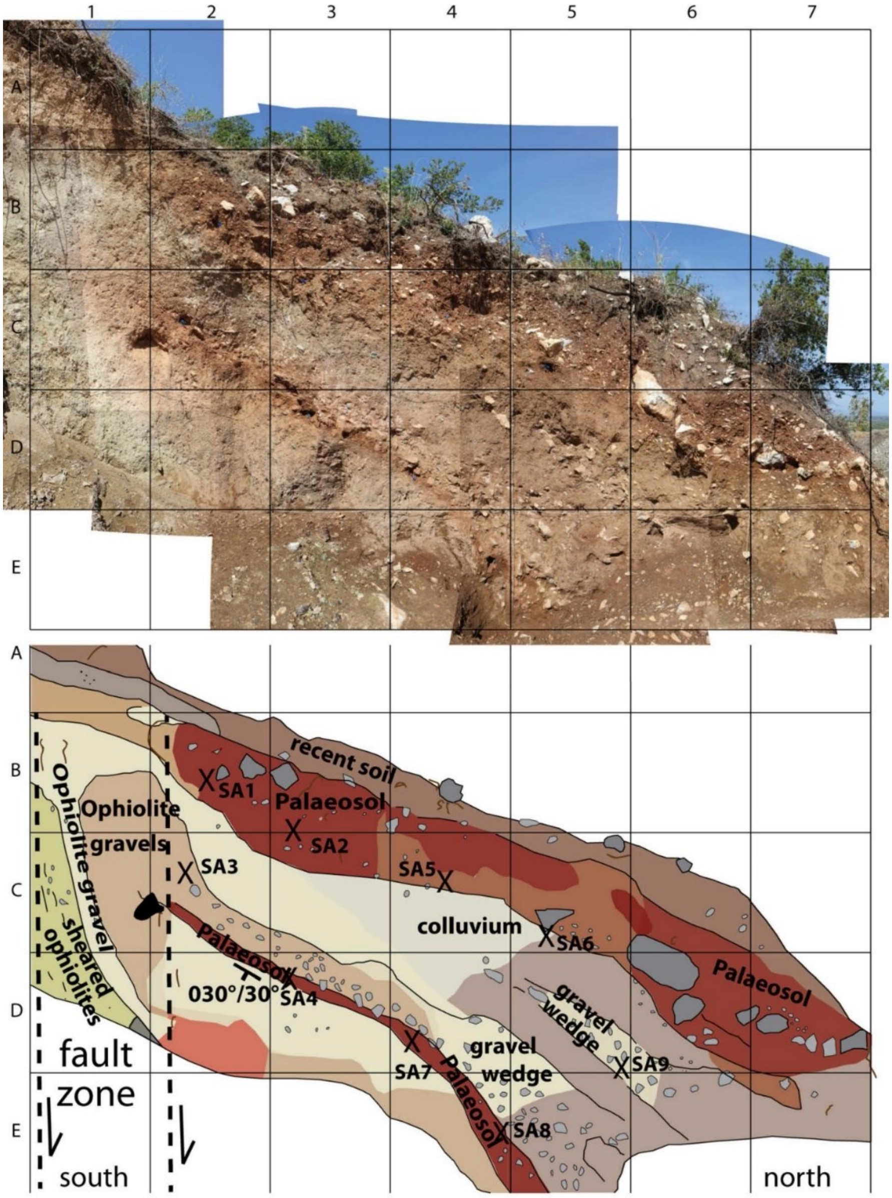

Figure 6.16: Photo mosaic of the trench wall (top) and interpretation of the main units (bottom) after Grützner et al., 2016. Grid width is 1 m. Note the buried palaeosol close to the surface and a second one at 1–2 m depth. SA: Sample location. 30°/30°: dip direction and dip angle of the second palaeosol. A retrodeformation with 4 up to 5 earthquake events that led to the present day geometry, along with the dating results are presented in Grützner et al., 2016.

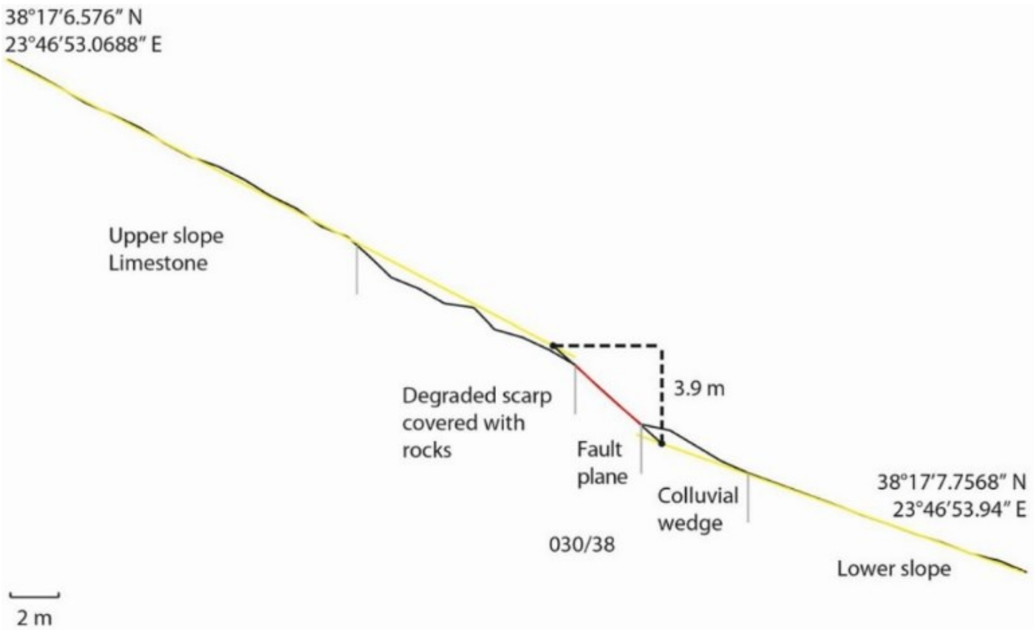

Figure 6.17: Topographic scarp profile of the weathered large fault plane above the trench site, after Grützner et al. (2016). This fault plane dips with 38° to the NNE (30 ° /038°) and has a vertical throw of 3.9 m as derived from the profiling by means of a yardstick and an inclinometer. For methodology see Papanikolaou et al. (2005). Coordinates indicate the upper and lower ends of the profile. Image reproduced from Grützner et al., 2016.

6.2.2. The Malakasa fault

The Malakasa fault was first reported as active by Papanikolaou et al. (1988), based on geomorphological observations. Goldsworthy et al. (2002) and Ganas et al. (2004 & 2005) referred to it as the Avlona (or Avlon) fault, named after a small town that lies near the fault (Figure 6.18). Papanikolaou and Papanikolaou (2007) speculate that, along with the Afidnes fault (Section 6.2.3), it is a candidate fault for the 1705 M~6.4 (according to Papazachos and Papazachou, 2003) event, although the historical catalogues are incomplete regarding the exact magnitude and location.

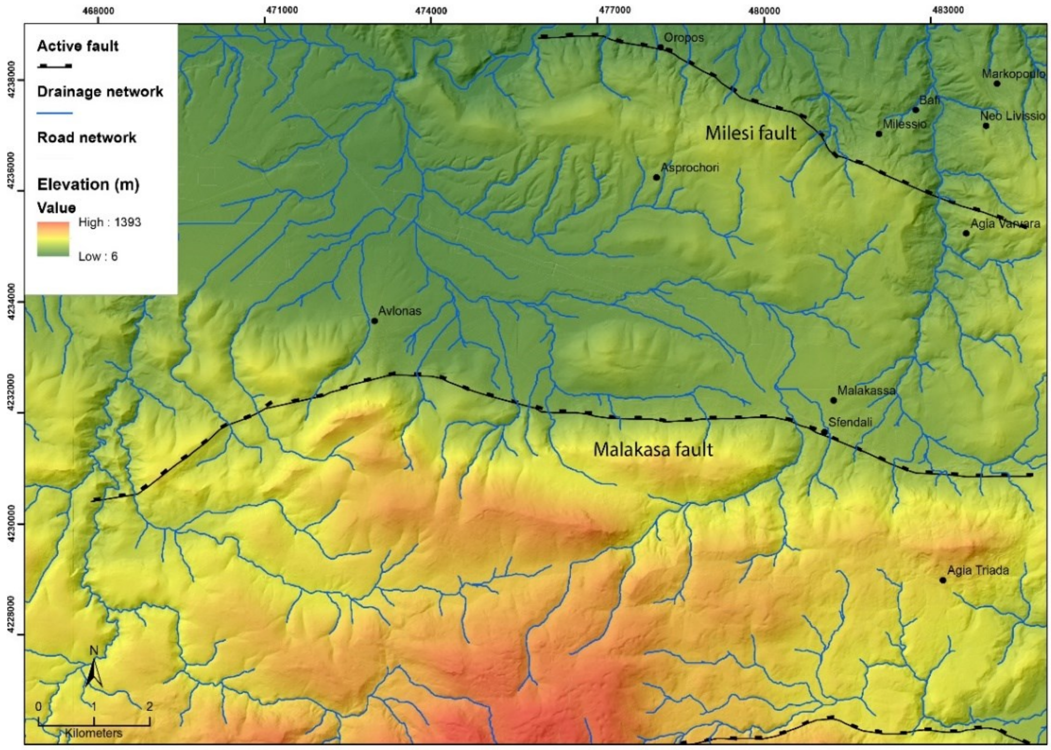

Figure 6.18: The E-W striking and North dipping Malakasa fault in NE Attica (id = 2 on Table 6.1) and the main drainage network of the area.

The Malakasa fault is an ESE–WNW striking, N dipping normal fault, with a length of approximately 18 km. It is located in North Attica, and it is parallel to the Milesi fault further NE (Figure 6.18). The footwall of the fault comprises Triassic – Late Cretaceous limestones of the Pelagonian zone (s.l.), and the hanging wall consists of scree and fluvial deposits, overlaying Miocene marls (Katsikatsos et al., 1986; Parginos et al., 2007).

Steep slope gradients occur in the immediate footwall, reaching up to 58^o in the central part, where deeply incised channels are visible (Figure 6.19).

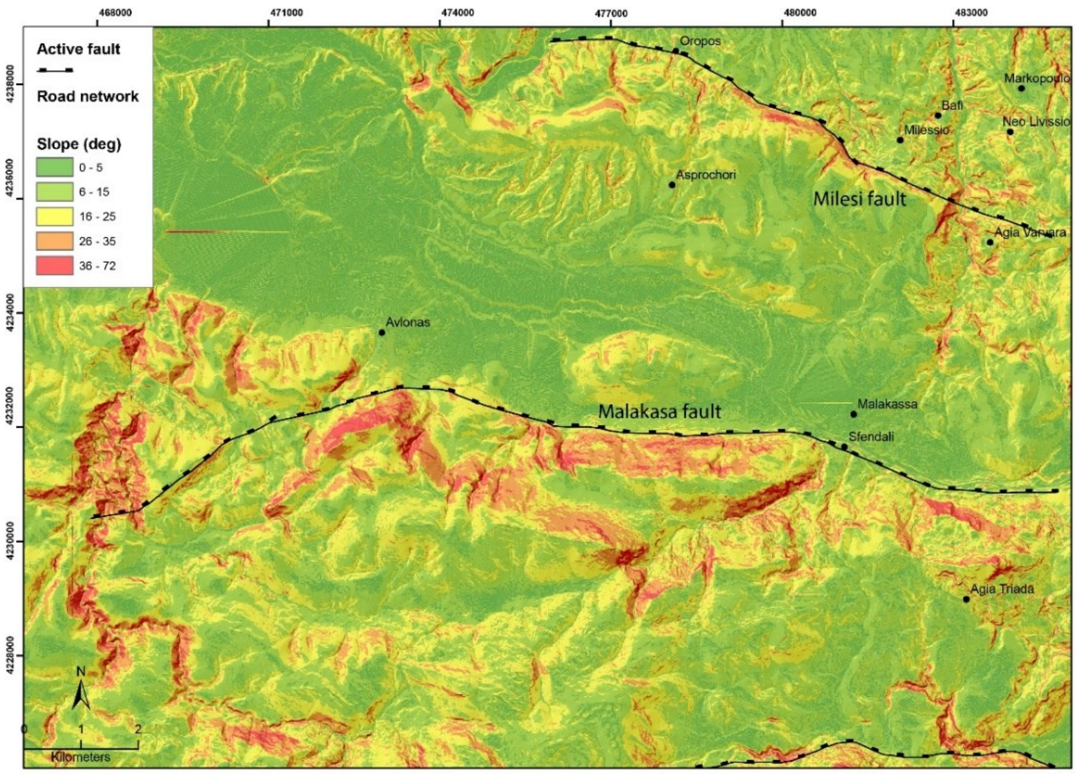

Figure 6.19: Slope map showing the abrupt slopes in the Malakasa fault footwall. Highest slope values (> 45°) appear on the central part of the footwall.

A swath topographic profile in a fault-parallel direction indicates that the elevation difference between the footwall and the hanging wall is up to 400 m. Larger differences occur in the centre of the fault, which creates a triangular throw pattern, as shown from the "local relief" curve in Figure 6.20.

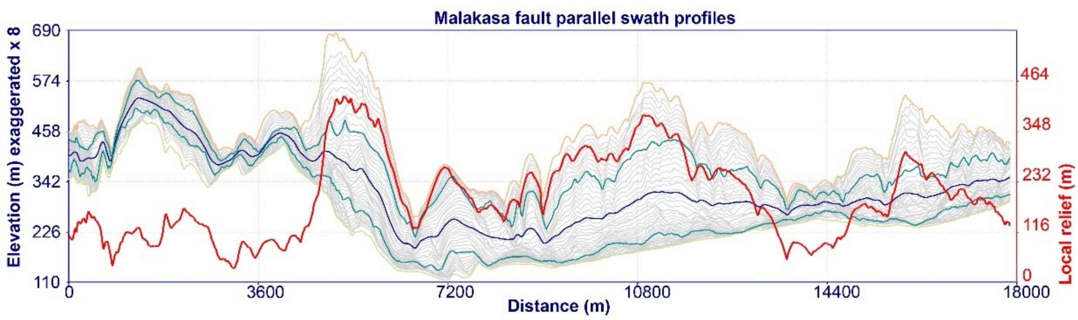

Figure 6.20: Swath topographic profiles within a Malakasa fault parallel stripe. Fault located at the center of the stripe. Stripe width is 2000 m. View looking towards North. Y-axis is exaggerated about 8 times. Orange line represents the maximum elevation, light green line represents the lower elevation, blue line represents the mean elevation, dark green lines represent the Q1 and Q3 quartiles, red line represents the local relief (maximum elevation minus minimum elevation at the same distance along the fault line).

Four swath topographic profiles within fault perpendicular stripes (Figure 6.21) reveal higher uplift rates at the central part of the fault (Figure 6.22) due to the convex shape of the profiles at the fault centre. The enhanced transverse Hypsometric Integral (THi*) values reach up to 0.6 for one of the two central profiles (P2). However, the values decrease to 0.51 for the other three profiles (P1, P3 & P4). This implies a young landscape (see also Pérez-Peña et al., 2017), but the throw decreases towards the tip of the fault.

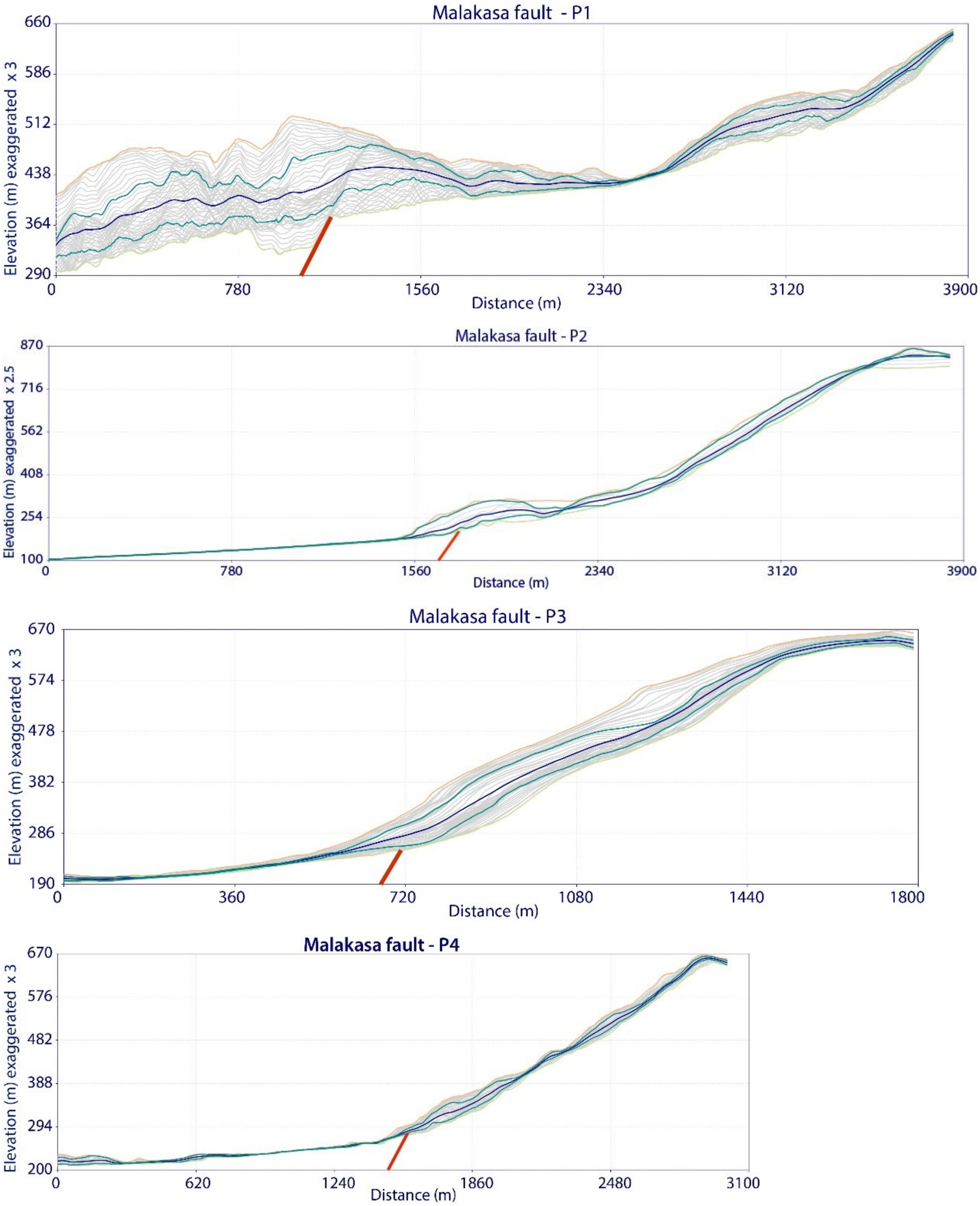

Figure 6.21: Swath topographic profiles within a fault perpendicular stripe, following drainage network branch near the Western tip of the Malakasa fault. Stripe axis location shown in Figure 6.22. Stripe width is 500 m. View looking towards NE. Y-axis is exaggerated. Orange line represents the maximum elevation, light green line represents the lower elevation, blue line represents the mean elevation, dark green lines represent the Q1 and Q3 quartiles. The red line represents the Malakasa fault.

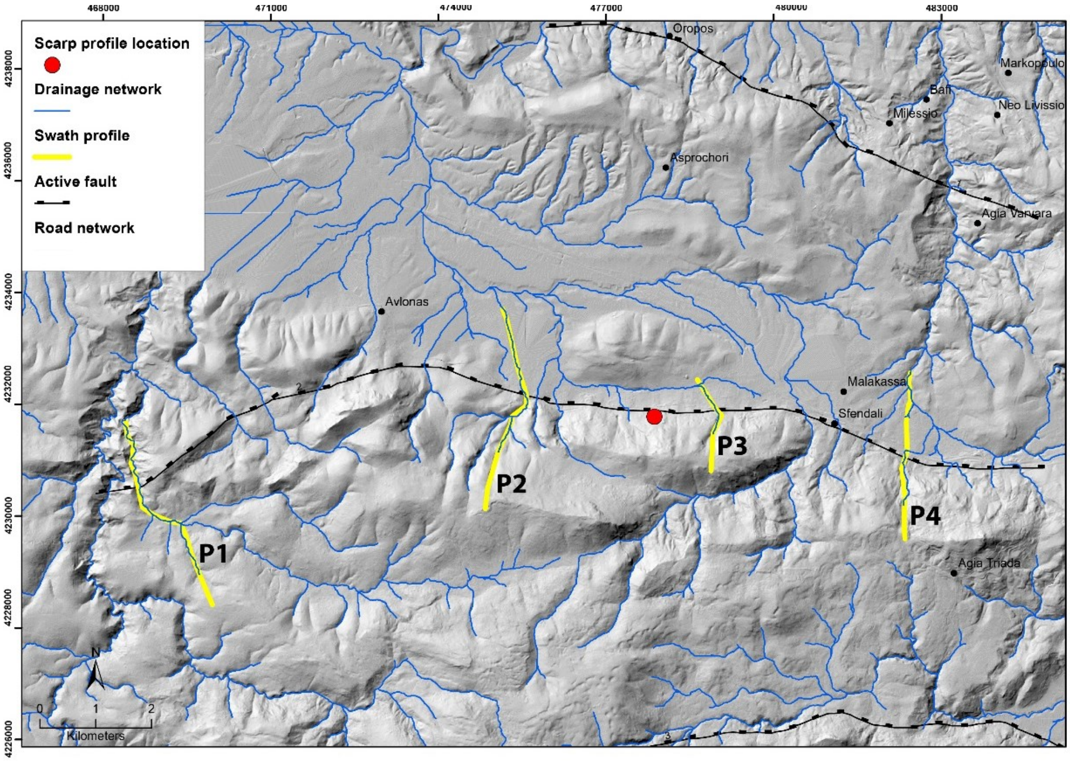

Figure 6.22: Shaded relief map of the Malakasa fault area, showing the main drainage network and the location of the fault – perpendicular swath profiles (P1 - P4).

Ganas et al. (2005) suggested a minimum throw estimate of 718–1400 m during the last 8-10 My based on DEM analysis, which implies a slip rate of 0.14 – 0.18 mm/y. However, the Malakasa fault has a higher rate than the Milesi fault, as it is one of the longest faults in the region, and it has a finite throw of at least 1200 ± 300 m, as inferred from the geological cross-section in Figure 6.23 and Figure 6.24.

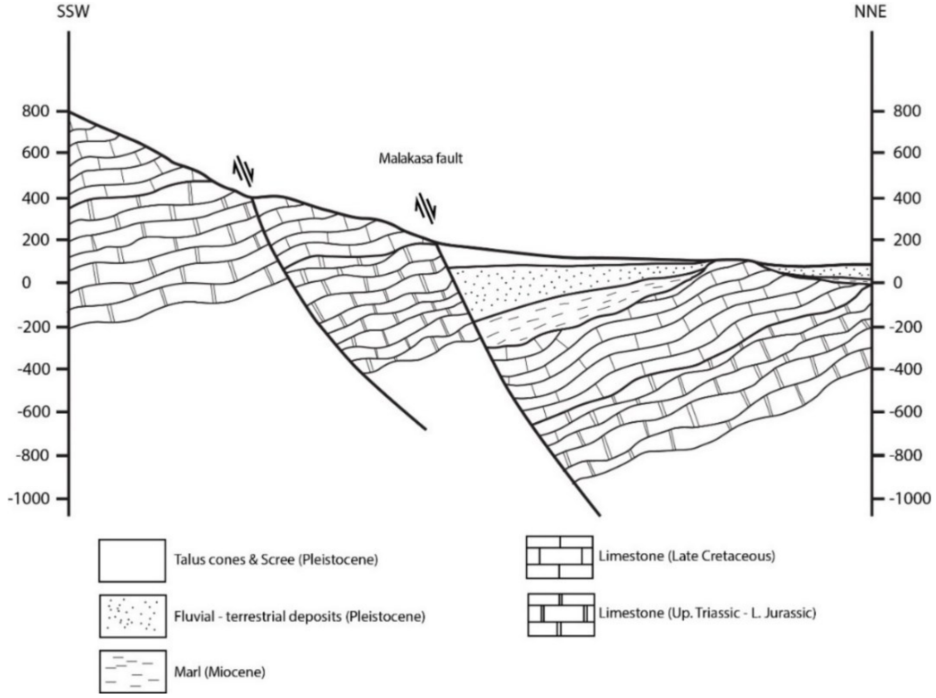

Figure 6.23: Geological cross-section at the central part of the Malakasa fault (previous page), based on the 1:50.000 geological map of HSGME (Figure 6.25) (Gaitanakis, 1982; Parginos et al., 2007). The total throw of the Malakasa Fault 1200+/-300 m. Although it is not depicted in the current 1:50.000 scale geological map, it's clear that there is at least one older structure further upwards because of the limestone sequence that is exposed in the footwall (Late Cretaceous limestone right on the fault, then Triassic - Jurassic limestone and Late Cretaceous limestone again in the upper parts) and of the morphology. The latter is also supported by the swath profile P2. This structure is now inactive, and today′s fault location is an example of fault scarp′s hanging wall migration.

It also has a very clear postglacial scarp (Figure 6.25), which is almost continuous within the forest for about 1.2 km. The scarp height reaches up to 6-7 m in non-disturbed sites (see example in Figure 6.26). Indeed, after the Pisia fault segment (see also Section 6.2.8) and Loutraki upper scarp (see also Section 6.2.9) it displays the best-preserved and third-highest post-glacial scarp height in Attica. As a result, an average slip - rate of 0.4 mm/y was used for the Malakasa fault.

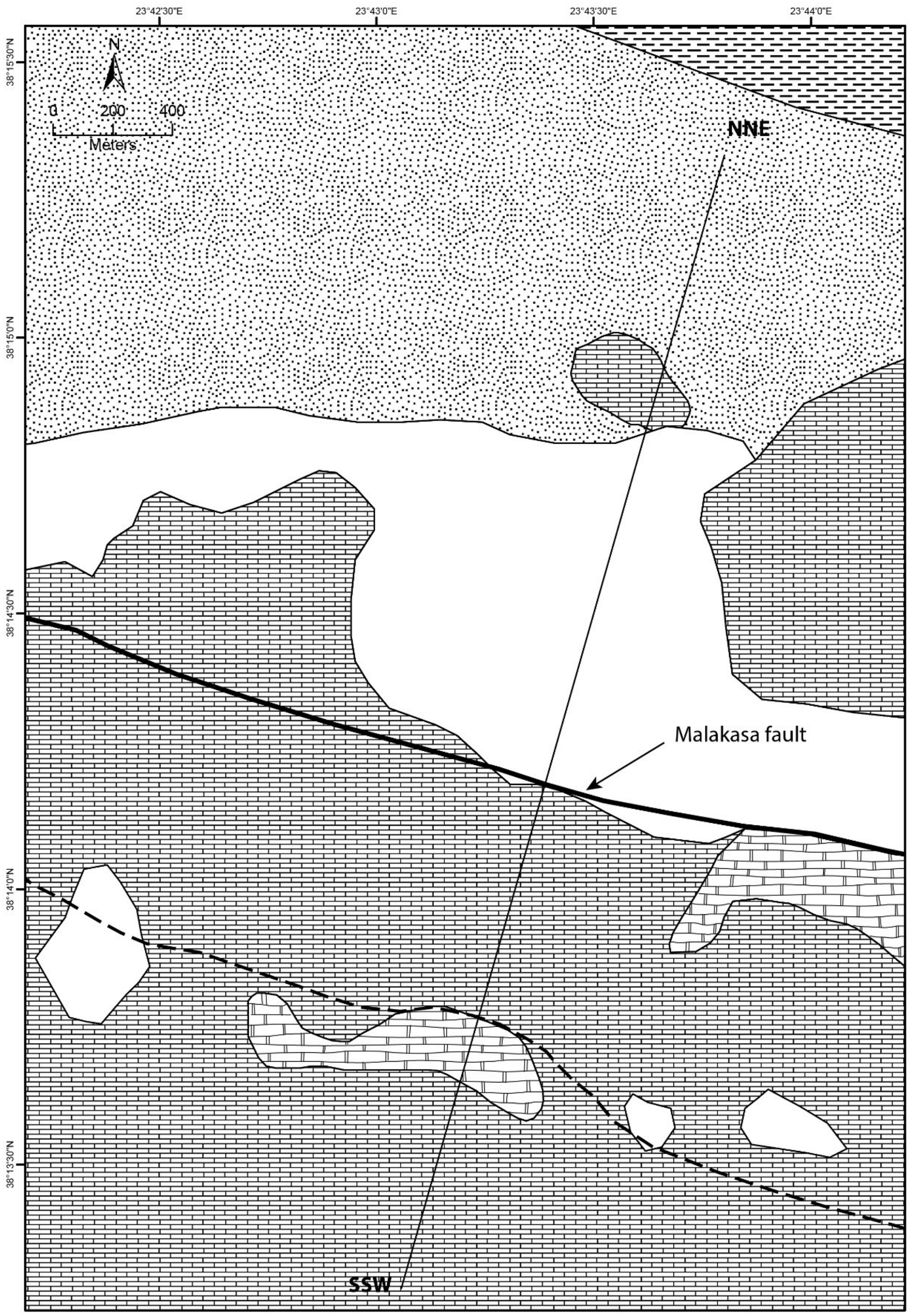

Figure 6.24: Geology of the Malakasa Fault and the surroundings (geological map compiled and modified after Gaitanakis, 1982; Parginos et al., 2007). The dashed line represents the secondary, probably older fault, further upwards. The Straight SSW NNE black line represents the geological cross-section profile (Figure 6.26).

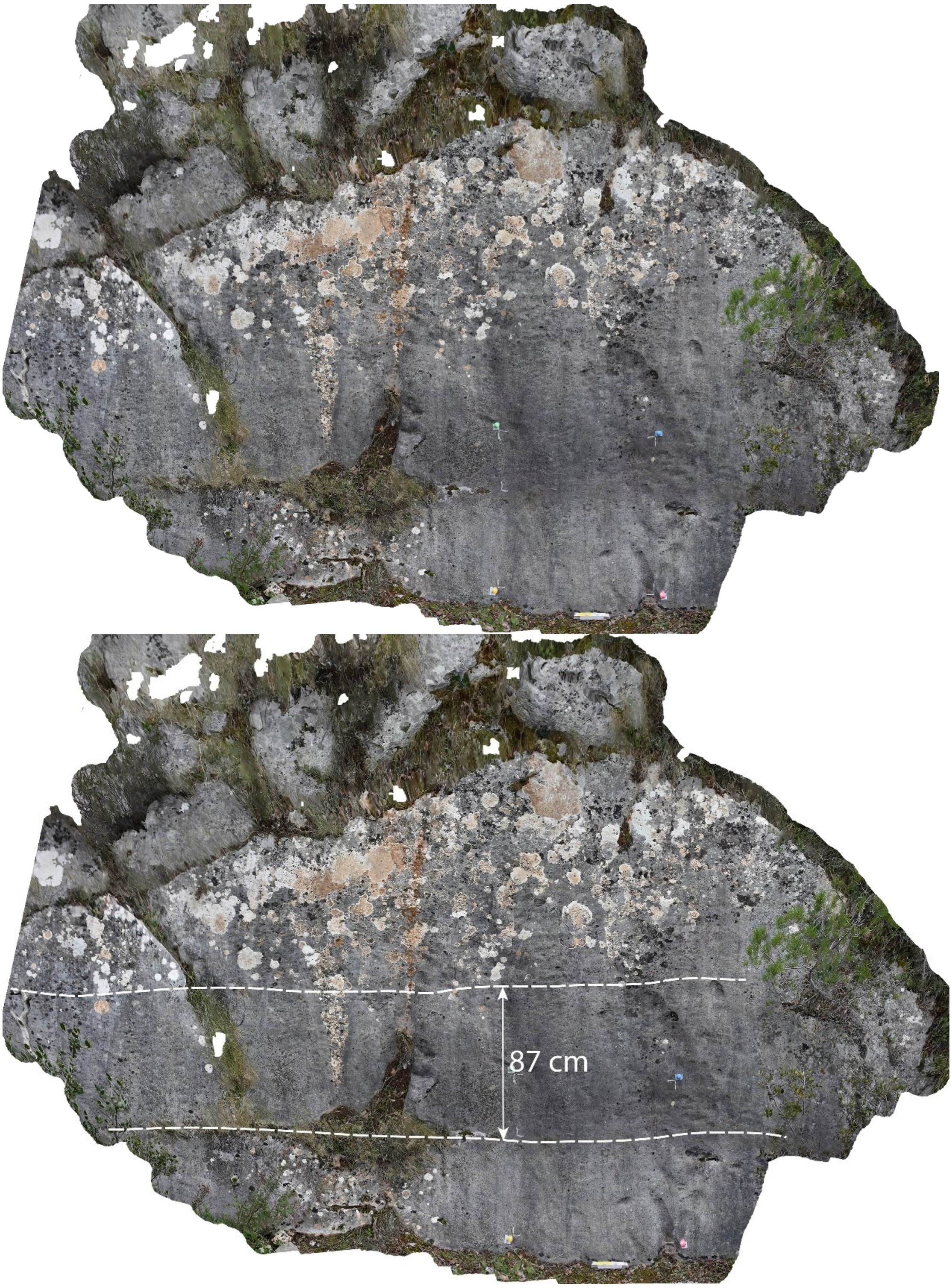

Figure 6.25: Orthomosaic of part of the post-glacial scarp on Malakasa fault. The potential occurrence of differentially weathered horizontal stripes is visible. Stripe thickness is measured at 86 ± 1.6 cm. The orthomosaic was developed using Structure from Motion photogrammetry through Agisoft Metashape Professional. In total, 26 mages were acquired using a Nikon D7200 camera with an 18 mm lens, and were photogrammetrically processed in Agisoft Metashape Professional v1.5.0. Relative accuracy was achieved by setting control points within 1 m distance from each other. Image location is shown in Figure 6.22. It is important to note that the photogrammetric processing at the Malakasa fault aimed on the determination of possible horizontal stripes, and not for the total throw measurement.

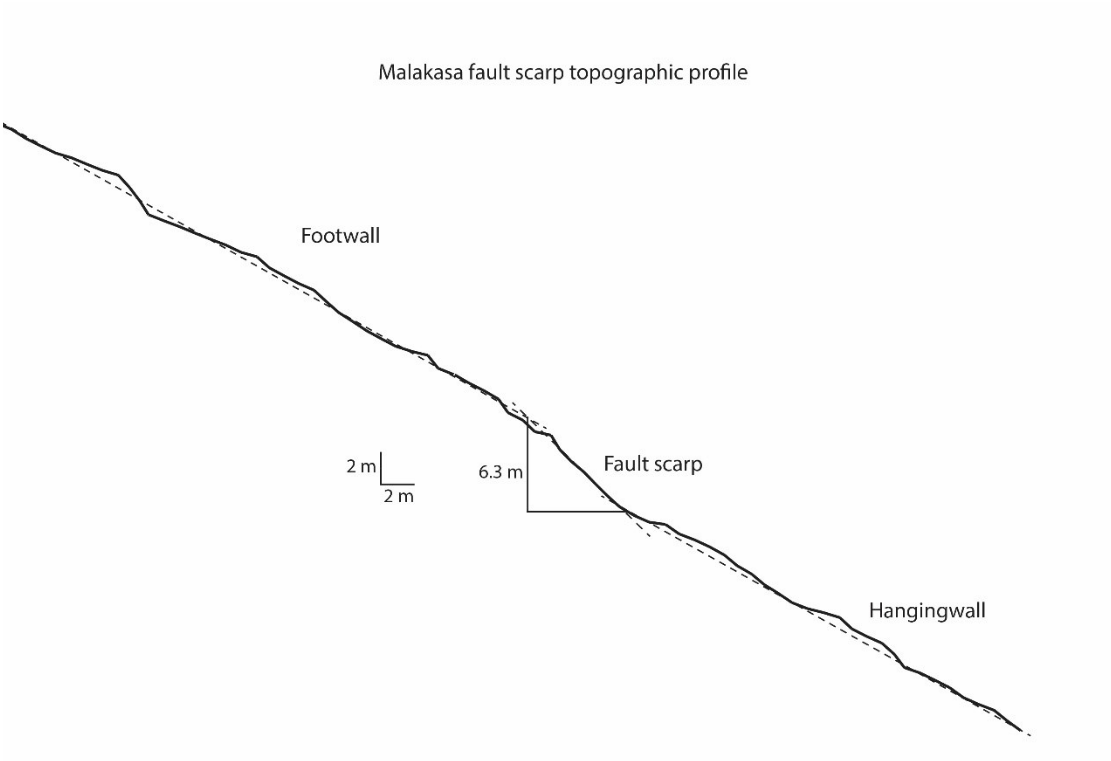

Figure 6.26: Topographic profile crossing the Malakasa fault scarp. Measurements obtained using a clinometer and a foldable meter scale (see also Papanikolaou et al., 2005 for details in methodology). The profiles reveal the fault scarp height and geometry, which are used for the throw rate calculation. Location of the profile is shown in Figure 6.22.

6.2.3. The Afidnes fault

Although the Afidnes (usually referred to as Afidnai) is not well studied in the literature, Ganas et al. (2005) and Papanikolaou and Papanikolaou (2007b) provided data on its activity and the corresponding slip-rate. It is an E-W striking, N dipping normal fault, with an approximate length of 14.2 km (Figure 6.27).

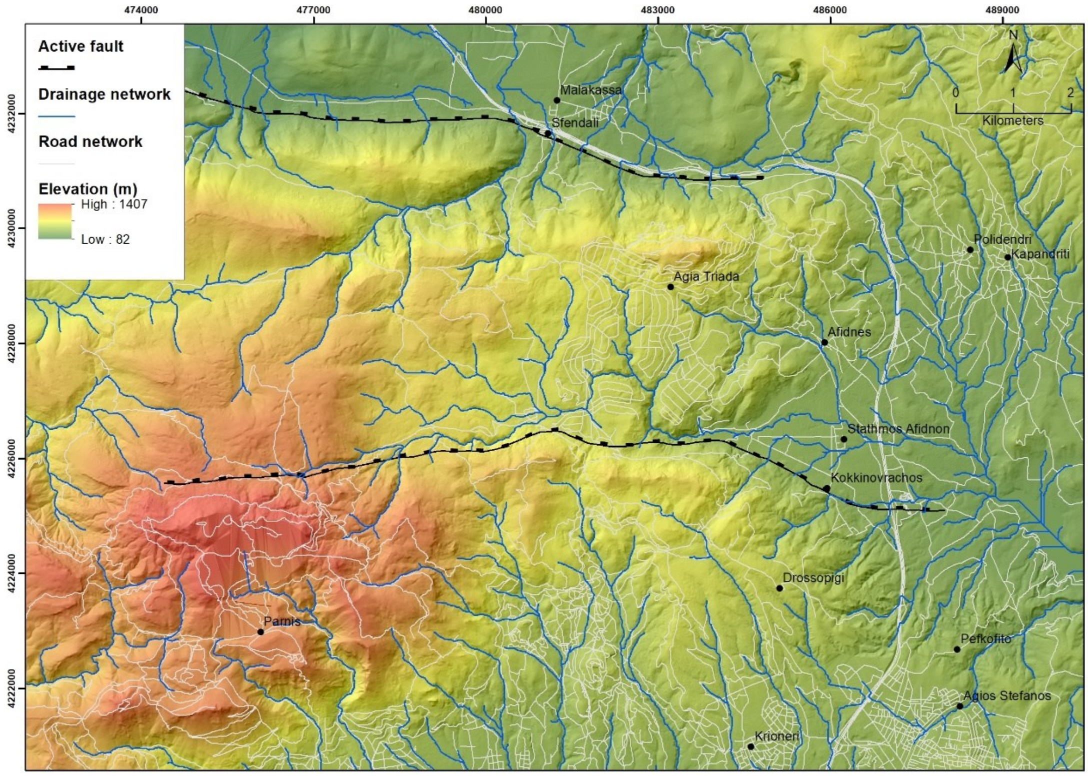

Figure 6.27: The E-W striking and North dipping Afidnes fault in NE Attica (id =3 on Table 6.1) and the main drainage network flowing towards the Athens Basin.

It is located in North Attica, parallel to the Malakasa fault further north and bounds the Athens basin in the north (Papanikolaou and Papanikolaou, 2007b). The footwall comprises the Paleozoic basement of the Pelagonian zone (s.l.), with the Triassic and Upper Cretaceous limestones of the same Unit. The hanging wall comprises recent Holocene deposits in the east (Gaitanakis, 1982; Katsikatsos, 2002). According to Roubanis (1961), the metamorphic basement was drilled at a depth of 47 m in the Afindai plain and the thickness of the Neogene sediments only reached 15 m. This implies that that the Late Pleistocene-Holocene sediments are about 30 m thick (Papanikolau and Papanikolaou, 2007b). The fault's eastern tip seems to stop at the N-S trending Miocene detachment at the east part of the Athens basin. Steep slope gradients occur in the immediate footwall, reaching up to 40º the mostly in the eastern part. However, the steep slopes are not constant through the whole length of the fault (Figure 6.28).

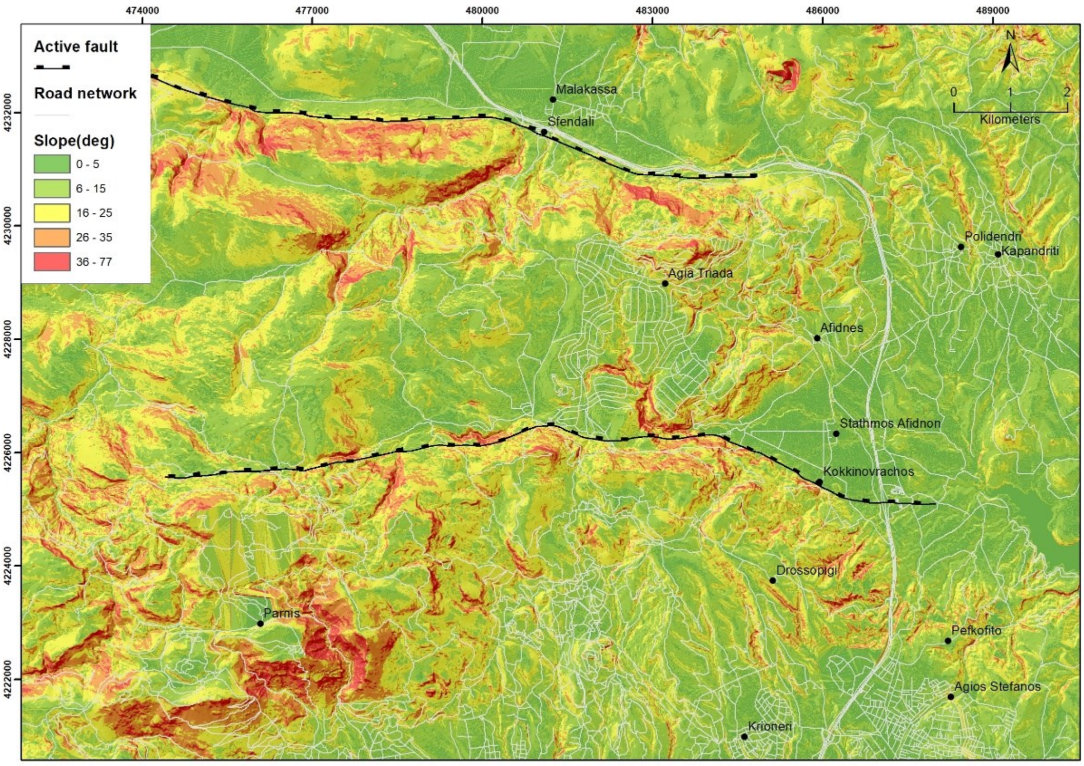

Figure 6.28: Slope map showing the slope changes related to Afidnes fault (id = 3 on Table 6.1). Steeper slopes are observed at the footwall, in parallel to the Afidnes fault.

A swath profile in a fault-parallel direction shows that the elevation difference between the footwall and the hanging wall is up to 190 m. Despite the fact that the fault is backtilted towards the Athens basin, it is evident from the local relief curve that the greater displacement occurs in the fault centre, which forms a clear triangular throw pattern (Figure 6.29).

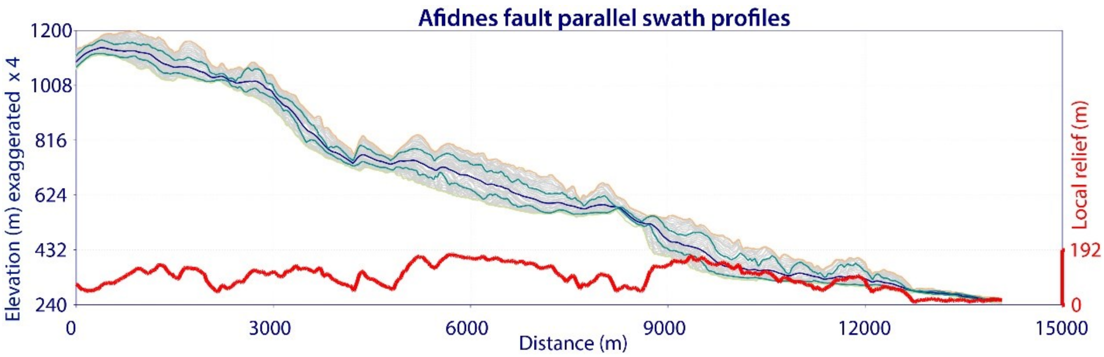

Figure 6.29: Swath topographic profiles within an Afidnes fault parallel stripe. Fault located at the centre of the stripe. Stripe width is 1500 m. Y-axis is exaggerated about 4 times. View looking towards North. The orange line represents the maximum elevation; the light green line represents the lower elevation, the blue line represents the mean elevation, dark green lines represent the Q1 and Q3 quartiles, the red line represents the local relief (maximum elevation minus minimum elevation at the same distance along the fault line).

Three swath topographic profiles within fault perpendicular stripes (Figure 6.30) reveal higher uplift rates at the central part of the fault (see locations of profiles in Figure 6.31).

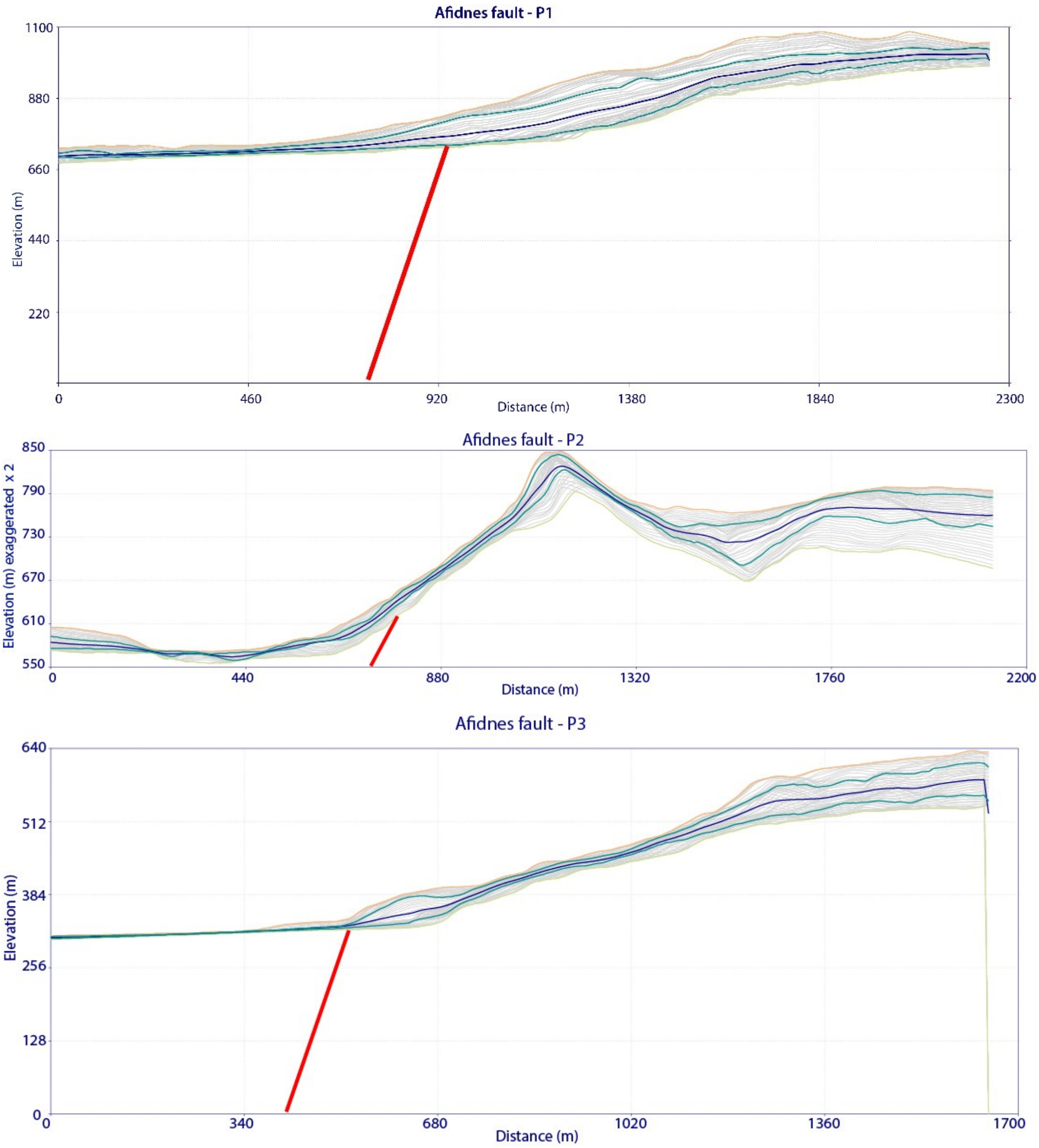

Figure 6.30: Swath topographic profiles within 3 fault perpendicular stripes, following catchments flowing perpendicular to the Afidnes fault. Stripe axis location shown in Figure 6.31. Stripe width is 500 m. Relief is exaggerated about 2 times for P2. View looking towards NE. Y-axis is exaggerated 2 times in P2. Orange line represents the maximum elevation, light green line represents the lower elevation, blue line represents the mean elevation, dark green lines represent the Q1 and Q3 quartiles. The red line represents the Malakasa fault

However, part of the topographic differences could be attributed to the different lithology (see also Whittaker et al., 2008). Additionally, the enhanced transverse Hypsometric Integral (THi*) values were calculated using the SwathProfiler toolbar. They reach up to 0.6 in the central profile (P2), while they are 0.5 for P1 and 0.6 for

P3, implying that the fault is actively deforming the landscape which is in agreement with Papanikolaou and Papanikolaou (2007b). Furthermore, the basin asymmetry factor (Af) value is 35.6, which shows that the drainage network flowing parallel to the fault is diverted, and the basin is tilted towards the south (Figure 6.31).

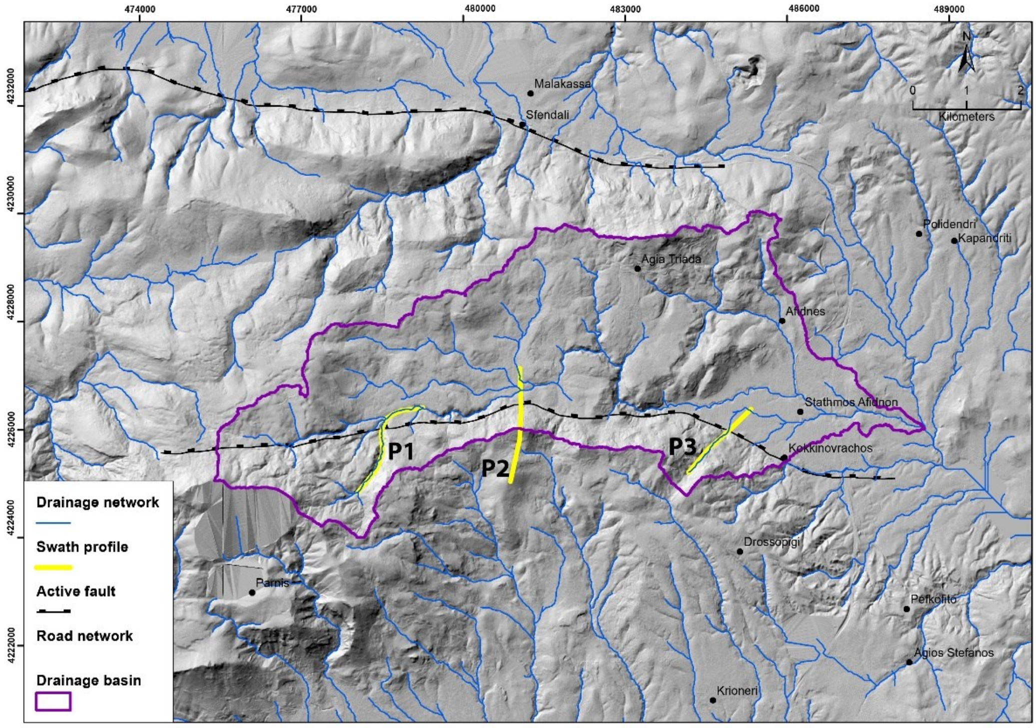

Figure 6.31: Shaded relief map of the Afidnes fault area, showing the main drainage network and the location of the fault – perpendicular swath profiles (P1 - P3). Note the asymmetry on the drainage basin of the river flowing towards the east, parallel to the fault. The Af is calculated at 35.6, indicating a tilt towards the south.

The fact that it has no visible postglacial scarp and the characteristic stratigraphic horizons are absent suggests that the fault throw rate is inferred indirectly, using geomorphic features as a proxy). Indeed, Papanikolaou and Papanikolaou (2007b) estimate a long term throw rate of 0.08 – 0.12 mm/y, extracted towards the eastern tip of the fault, that is in agreement with the maximum slip – rate of 0.3 mm/y estimated by Ganas et al. (2005), extracted for the centre of the fault, which is also used in this thesis.

6.2.4. The Dionysos fault

The Dionysos fault is an NW – SE trending, NE dipping normal fault that bounds the Pendeli mountain in the north (Figure 6.32). The footwall comprises marble and schist of the Autochthonous Unit of Attica, and the hanging wall consists of Pleistocene scree and talus cones (Katsikatsos, 2002).

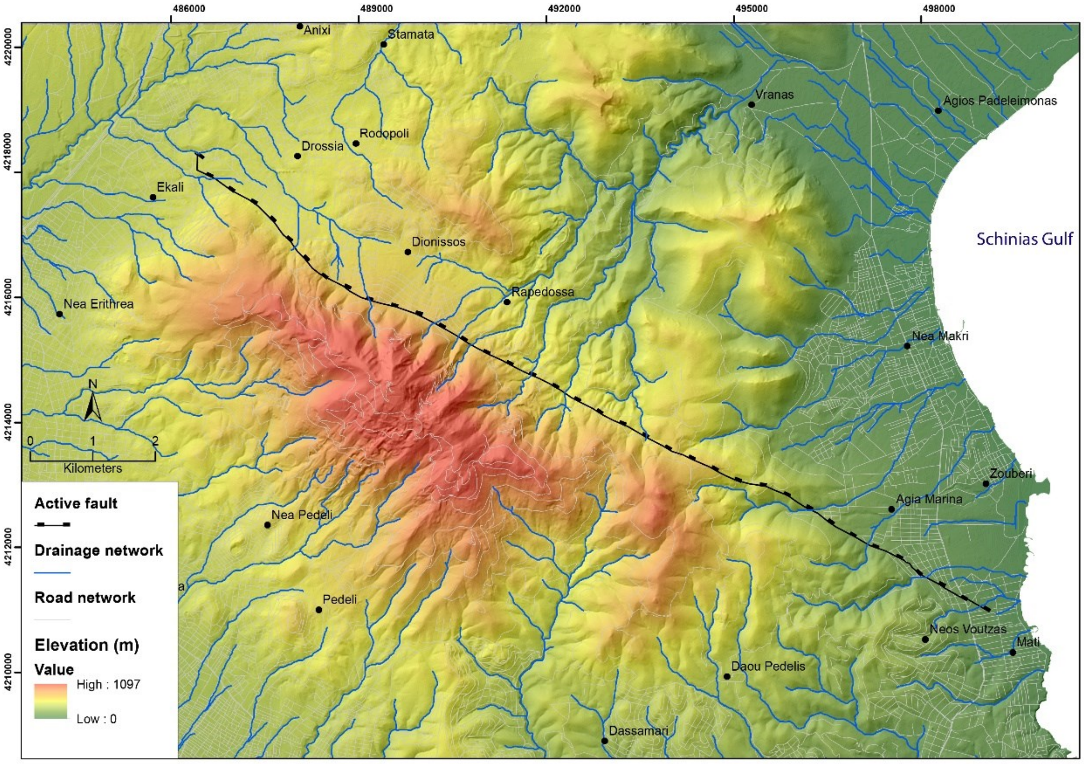

Figure 6.32: The NW-SE striking and NE dipping Dionysos fault in NE Attica (id =4 on Table 6.1) and the main drainage network. The fault bounds the NE facing flanks of the Penteli mountain.

The steepest slope gradients occur mainly in the NW part of the fault, reaching up to 35° (Figure 6.33).

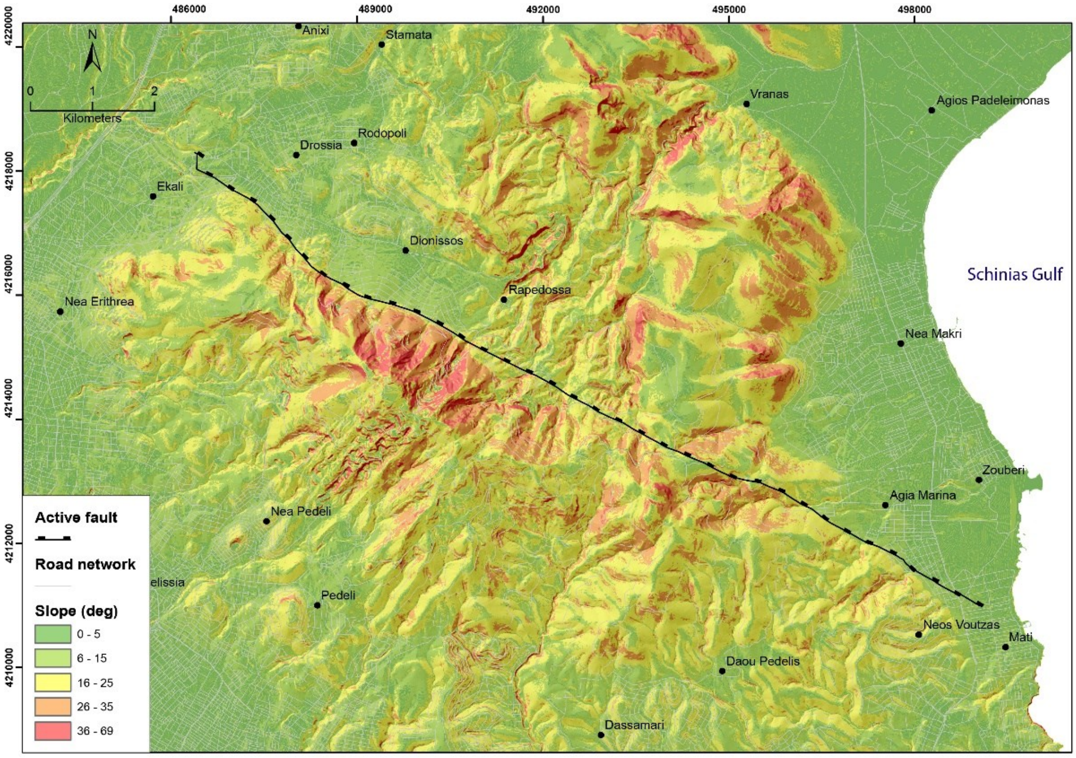

Figure 6.33: Slope map showing the slope changes related to Dionysos fault (id = 4 on Table 6.1). Steeper slopes are observed at the footwall, parallel to the fault, especially in the central and northern part.

A swath topographic profile in a fault-parallel direction reveals an elevation difference between the footwall and the hanging wall 520 m. However, the shape of the local relief curve indicates that the footwall is highly incised by the fluvial network in the central part of the fault (Figure 6.34), probably due to the erodibility of the schists that outcrop in the central part of the fault. It is important to note that the stripe of the swath profiles does not reach the top of Pendeli mountain. However, there are well preserved triangular facets in the uplifted marble in the NW part of the fault (see also the left section of Figure 6.34).

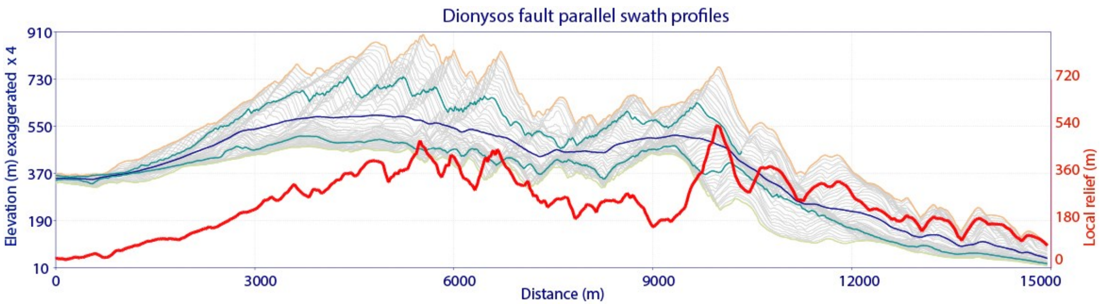

Figure 6.34: Swath topographic profiles within a Dionysos fault parallel stripe. Fault located at the center of the stripe. Stripe width is 1500 m. Y-axis is exaggerated about 4 times. View looking towards NE. Orange line represents the maximum elevation, light green line represents the lower elevation, blue line represents the mean elevation, dark green lines represent the Q1 and Q3 quartiles, red line represents the local relief (maximum elevation minus minimum elevation at the same distance along the fault line).

Three swath topographic profiles within fault perpendicular stripes (Figure 6.35, see Figure 6.36 for the profiles locations) show small convex reaches at the central part of the west and central part of the fault. The enhanced transverse Hypsometric Integral (THi*) was calculated at 0.42 for P1, 0.6 for P2 and 0.48 for P3. This implies an active fault but with a low slip rate.

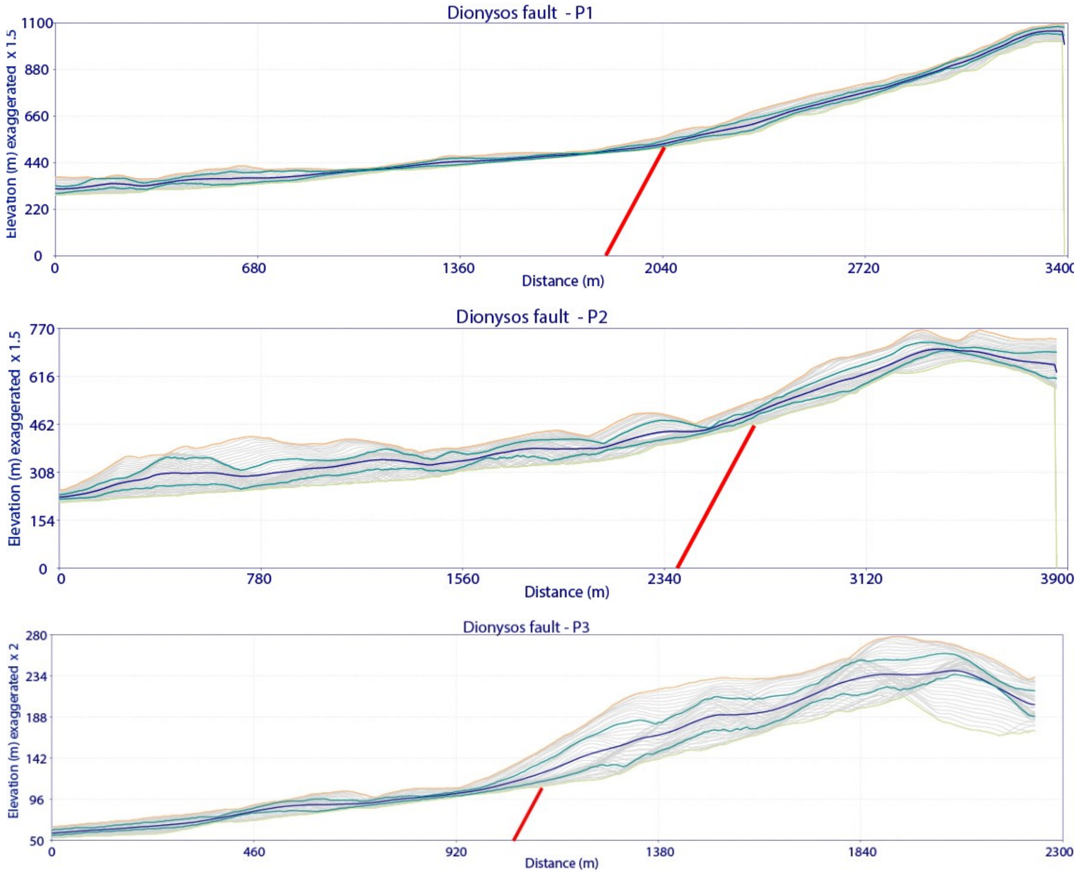

Figure 6.35: Swath topographic profiles within a fault perpendicular stripe, following drainage network flowing perpendicular to the Dionysos fault. Stripe axis location shown in Figure 6.36.Stripe width is 500 m. Y-axis is exaggerated about 1.5 times for P1 and P2 and 2 times for P3 and P2. View looking towards SE. Orange line represents the maximum elevation, light green line represents the lower elevation, blue line represents the mean elevation, dark green lines represent the Q1 and Q3 quartiles. The red line represents the Dionysos fault.

Ganas et al. (2005) refer to this fault with the name Pendeli fault and calculate a slip rate between 0.13 – 0.16 mm/y. A postglacial scarp profile at the NW part of the fault (see Figure 6.36 for the location of the profile) indicates a 1.4 m post glacial throw, which implies a low throw rate of 0.1 mm/y.

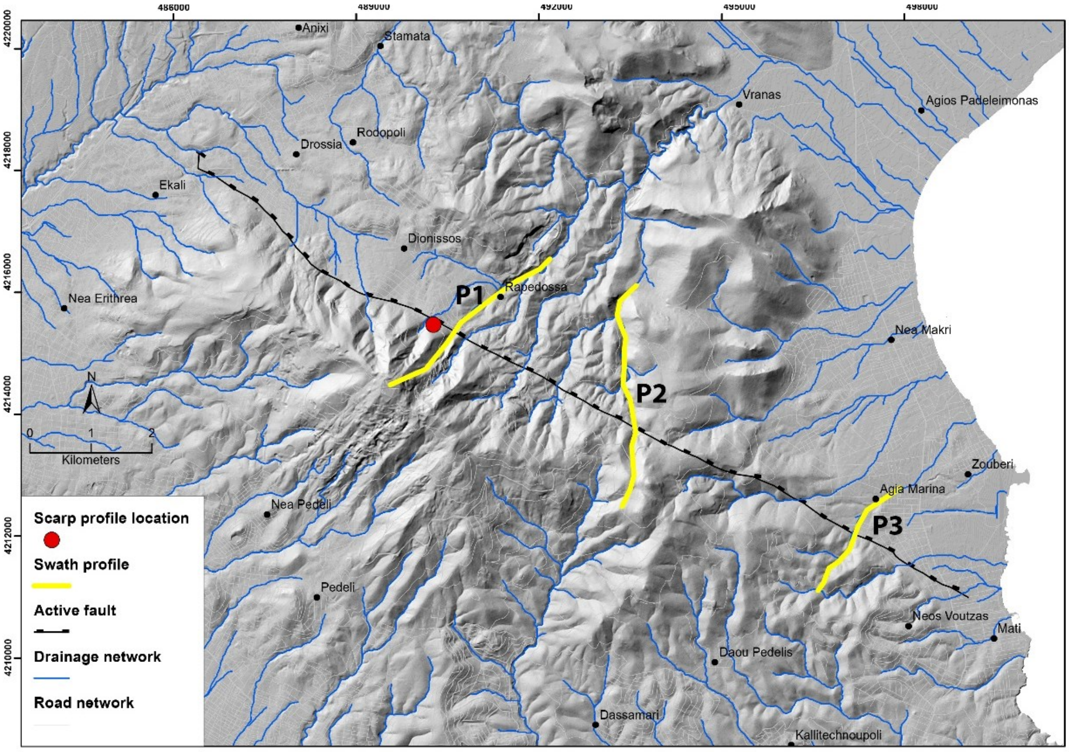

Figure 6.36: Shaded relief map of the Dionysos fault area, showing tha main drainage network and the location of the fault – perpendicular swath profiles (P1 - P3). Note the prominent triangular facets at the NW and the SE tips of the fault.

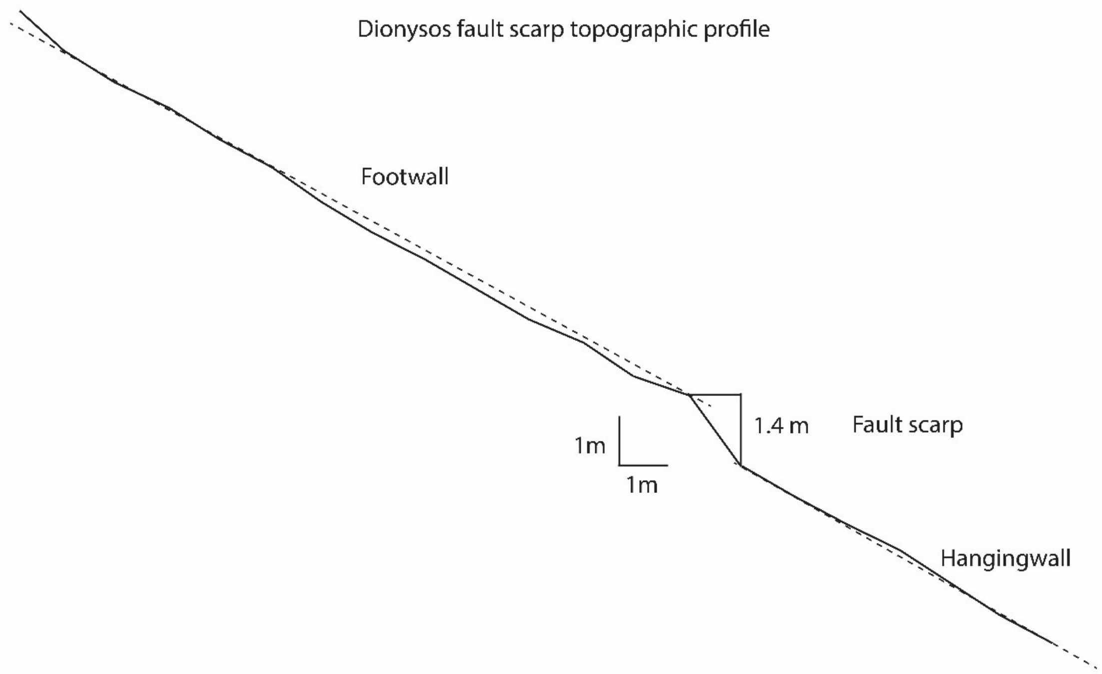

Figure 6.37: Topographic profile crossing the Dionisos fault scarp. Measurements obtained using a clinometer and a foldable meter scale (see also Papanikolaou et al., 2005 for details in methodology). The profiles reveal the fault scarp height and geometry, which are used for the throw rate calculation. Location of the profile is shown in Figure 6.22.

6.2.5. The Kaparelli fault

The Kaparelli fault was activated on March 4, 1981, after the 25 & 25 February 1981 earthquakes in the Alkyonides fault zone (Jackson et al., 1982). It produced an earthquake of magnitude Ms = 6.4, which formed a south-dipping, almost 12 km long surface rupture in the area of Kaparelli and Plataies villages (Jackson et al., 1982), with an approximate displacement of 0.7 m (Chatzipetros et al., 2005), while 40 cm of a limestone fault scarp was exhumed by the earthquake (Benedetti, 2003). The ruptures occurred along the Triassic limestone pre-existing fault scarp, as well as in alluvial fan deposits in the Livadostras river valley (Kokkalas et al., 2007).

The Kaparelli fault is a complex fault zone that consists of multiple different fault strands and segments of different strike (Kokkalas et al., 2007). For the purposes of this thesis, the Kaparelli fault represents the simplified Kaparelli – Livadostras fault zone (see also Morewood and Roberts, 2001; Tsodoulos et al., 2008; Konstantinou et al., 2020), with a total length of 14.5 km (Figure 6.38). It is examined as a single structure and is modelled as such in Section 7.2. The footwall consists of Triassic – Jurassic limestone and dolomite of the Boeotian zone, and the hanging wall comprises Holocene alluvial deposits and scree, which overlay thick fluvioterestrial sediments (Bornovas et al., 1981). Steep slopes of the order of 35° occur in the footwall the NE – SW trending part of the fault zone, as it bounds the Korompilli mountain (Figure 6.39).

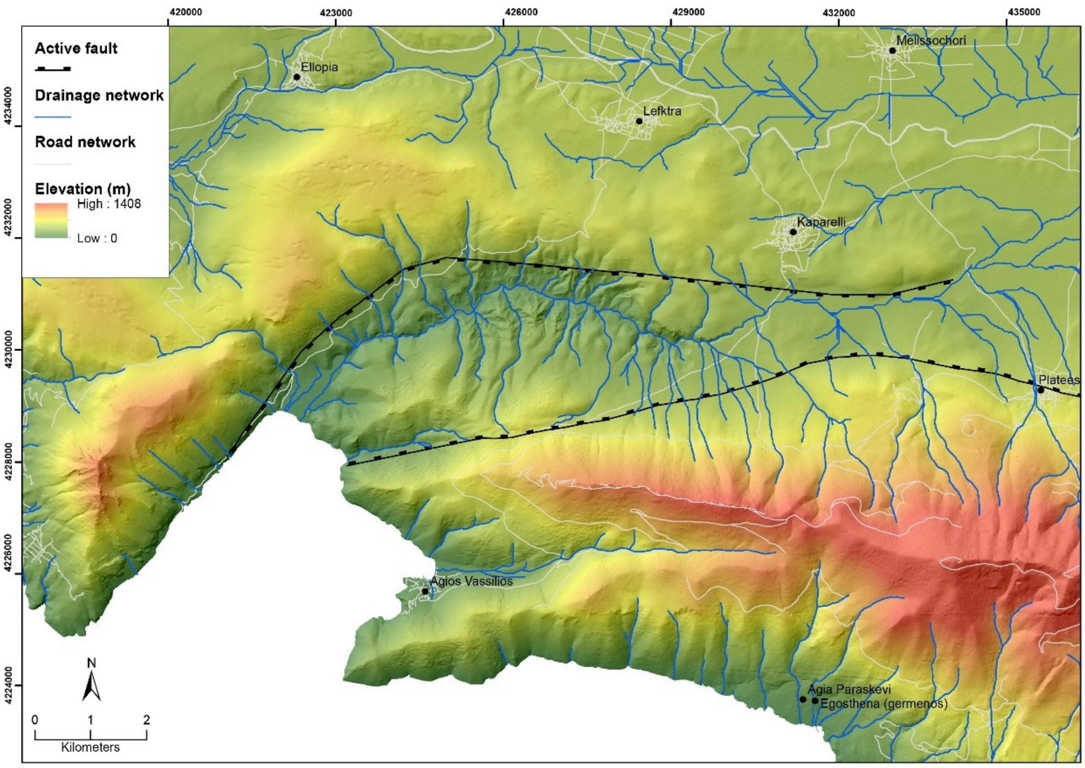

Figure 6.38: The SE dipping Kaparelli fault zone in NW Attica (id = 5 on Table 6.1) and the main drainage network.

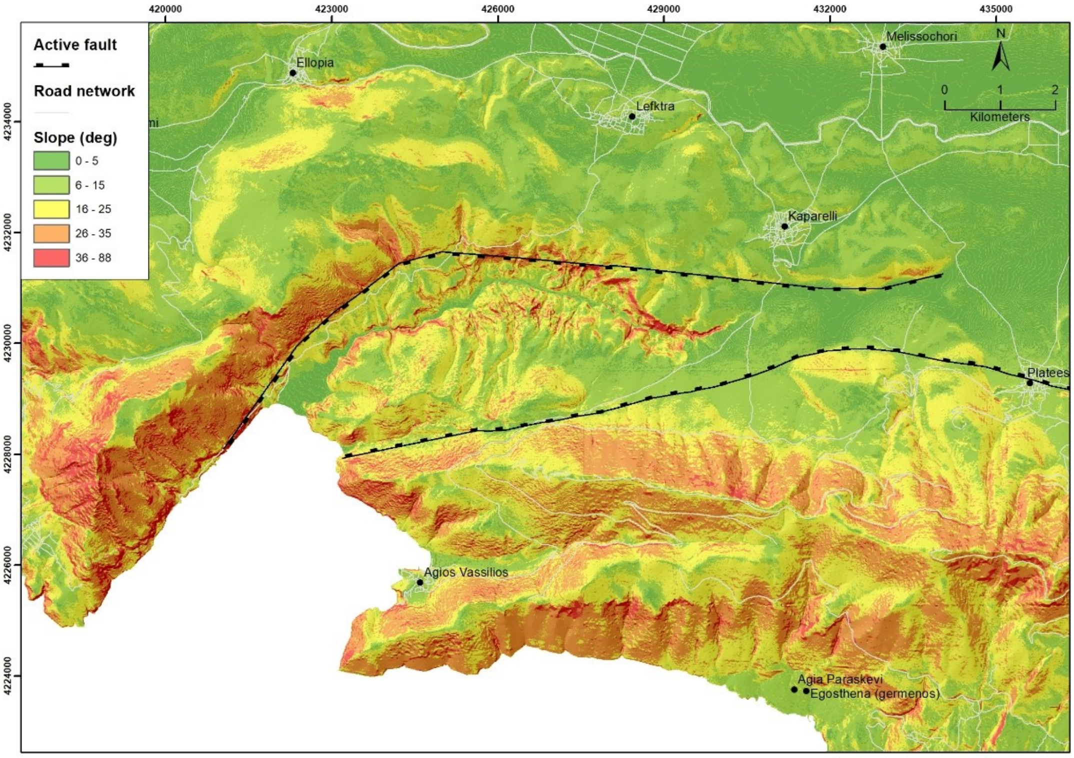

Figure 6.39: Slope map showing the slope changes related to the Kaparelli fault (id = 5 on Table 6.1). Steeper slopes are observed at the footwall in the Livadostras fault segment (see text for explanation).

A swath topographic profile in a fault-parallel direction reveals an elevation difference between the footwall and the hanging wall 600 m. However, the shape of the local relief curve indicates that the maximum displacements and deepest incisions occur in the Livadostras segment (Figure 6.40), which implies that the fault zone may continue offshore (see also Sakellariou et al., 2007; Tsodoulos et al., 2008). The same is observed in the fault perpendicular swath profiles, where the one crossing the Livadostras segment exhibits a convex shape right on the immediate footwall (Figure 6.41, see Figure 6.42 for profiles locations). Interestingly, the THi* index for the P1 is 0.6, and for the P2 is 0.55. This implies active deformation for both areas, although the P1 seems to cross a much smoother anaglyph.

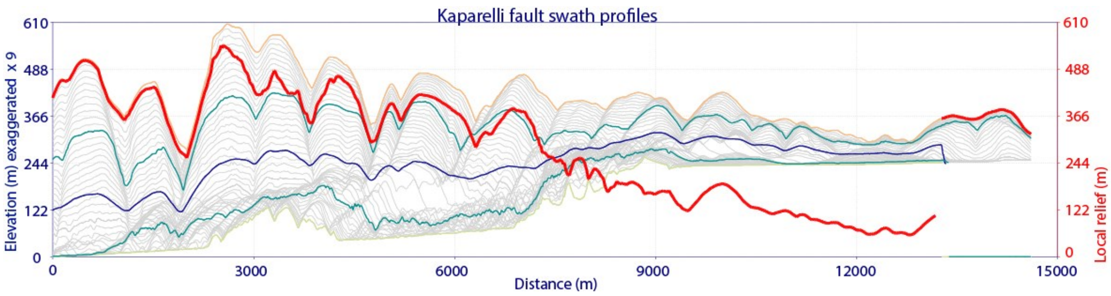

Figure 6.40: Swath topographic profiles within a fault parallel stripe. Fault located at the center of the stripe. Stripe width is 1500 m. Relief is exaggerated about 9 times. View looking towards north. Orange line represents the maximum elevation, light green line represents the lower elevation, blue line represents the mean elevation, dark green lines represent the Q1 and Q3 quartiles, red line represents the local relief (maximum elevation minus minimum elevation at the same distance along the fault line).

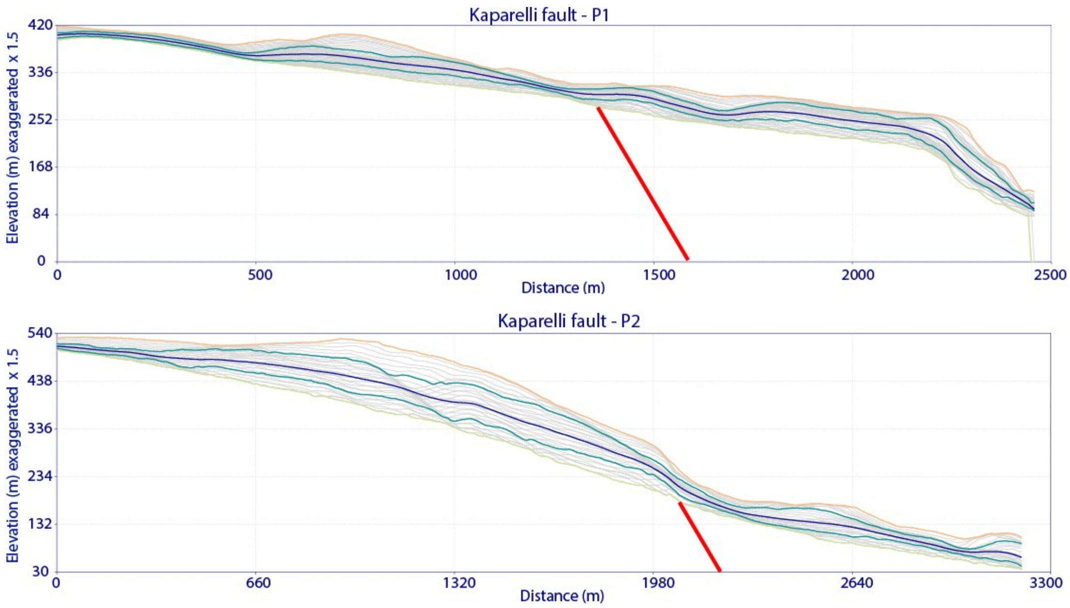

Figure 6.41: Swath topographic profiles within fault perpendicular stripes, following drainage network flowing perpendicular to the Kaparelli fault. Stripe axis location shown in Figure 6.42. Stripe width is 500 m. Relief is exaggerated about 1.5 times. View looking towards East. Orange line represents the maximum elevation, light green line represents the lower elevation, blue line represents the mean elevation, dark green lines represent the Q1 and Q3 quartiles. The red line represents the Kaparelli fault.

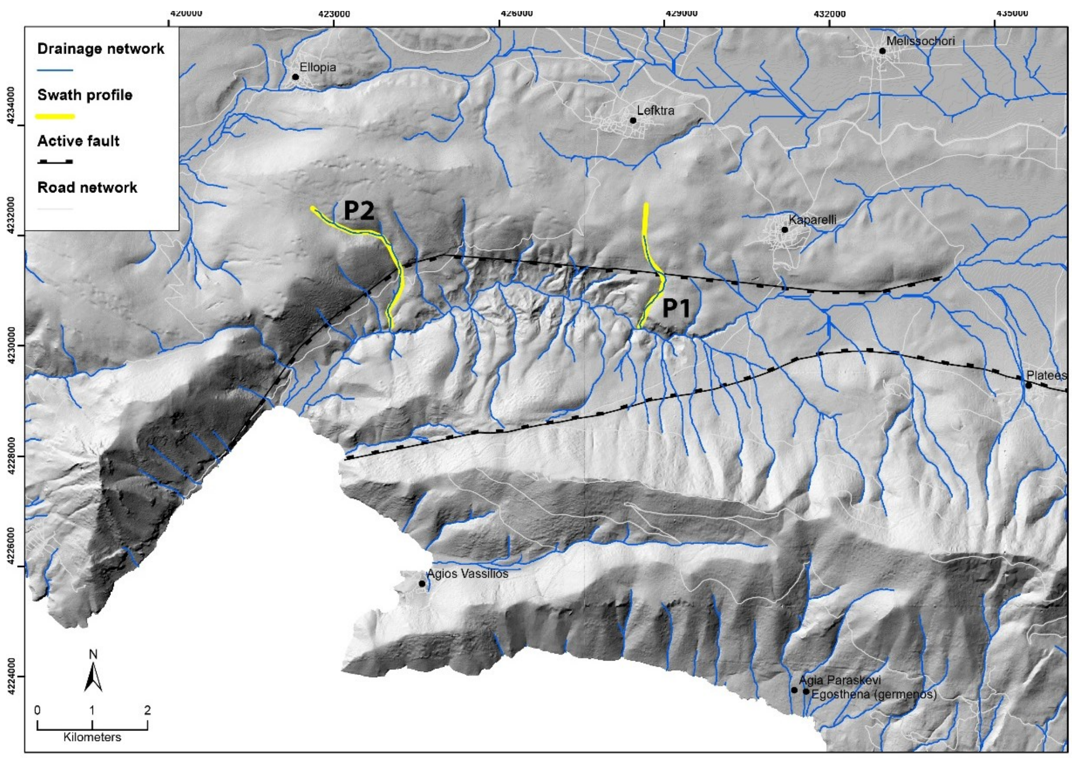

Figure 6.42: Shaded relief map of the Kaparelli fault area, showing the main drainage network and the location of the fault – perpendicular swath profiles (P1 & P2).

The Kaparelli fault was studied by a number of researchers during the years following the 1981 earthquake rupture. Benedetti et al. (2003) sampled the fault's postglacial scarp and analysed the seismic history prior to the 1981 rupture. They found that the fault was inactive 10 kyrs before it ruptured in 1981, and they estimated a slip rate of 0.2 mm/y, with slip amplitudes varying between 0.6 m and 2.1 m, which was also used in this thesis. On the other hand, Kokkalas et al. (2007) performed paleoseismic trenching in 3 locations along the E-W trending Kaparelli fault segment and estimated a maximum slip rate of 0.3 mm/y, with an average 2300 years recurrence interval (see also Chatzipetros et al., 2005).

6.2.6. The Erythres fault

The Erythres fault is an E – W striking, north dipping normal fault, which forms the westward continuation of the adjacent Dafni fault (see Section 6.2.13). It bounds the northern flanks of the Kithaironas Mountain (Figure 6.43), which is the second-highest mountain in the Attica region (1409 m). The Erythres fault trace was firstly depicted as a boundary of the Erythres-Thiva Basin from Roberts and Koukouvelas (1996).

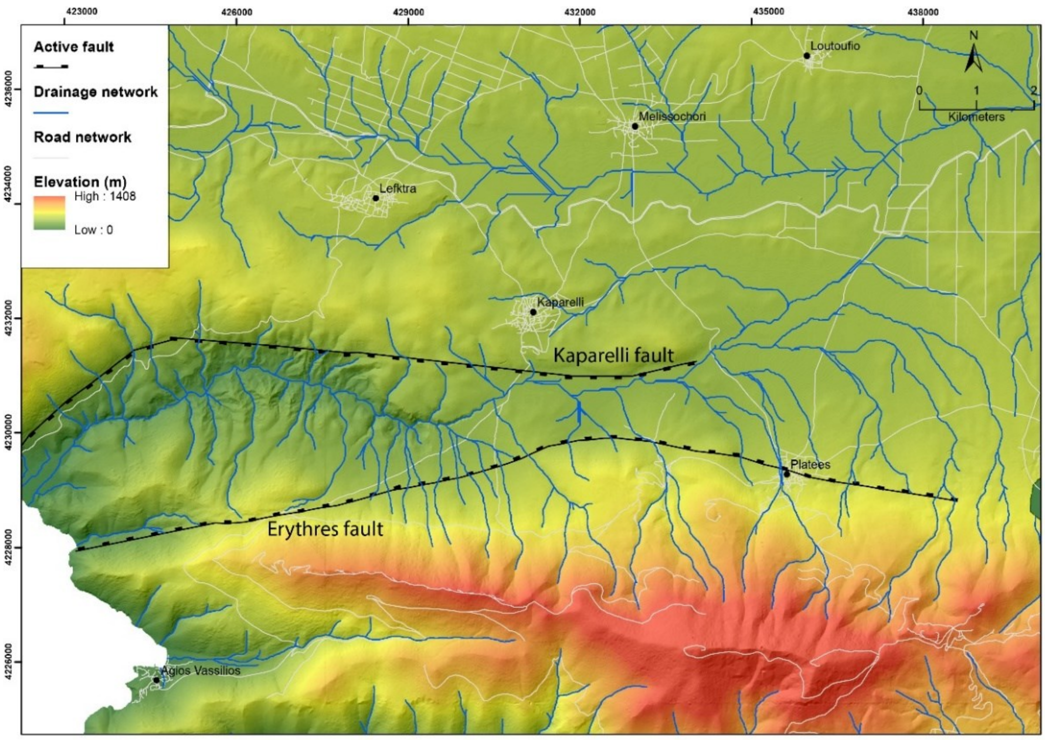

Figure 6.43: The north dipping Erythres fault in NW Attica (id = 6 on Table 6.1) and the main drainage network. Note that first order elongated catchments flow perpendicular to the Erythres fault, which forms the northern flanks of Kithaironas mountain.

Although the slope map reveals only mild gradients along the fault trace (Figure 6.44), there are clear indicators of quaternary tectonic activity spotted at the Kithaironas northern flanks, namely triangular facets and wine glass valleys (Figure 6.45). Swath topographic profiles parallel to the fault reveal a considerable total throw of at least 880 m (lower graph in Figure 6.46), but at the same time, U shaped valleys are present in the western part of the fault. The fault perpendicular swath profiles (see Figure 6.47 for profiles location) have a typical concave-up form. However, small convexities appear in the central profile (P2).

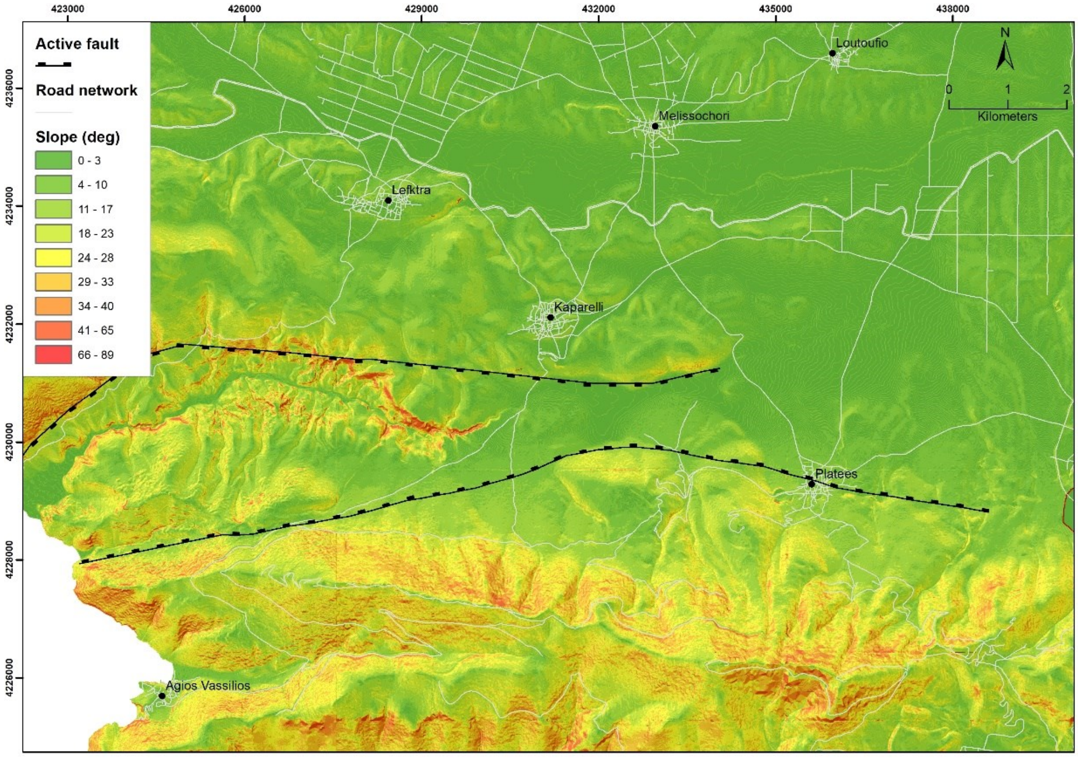

Figure 6.44: Slope map showing the slope changes related to Erythres fault (id = 6 on Table 6.1).

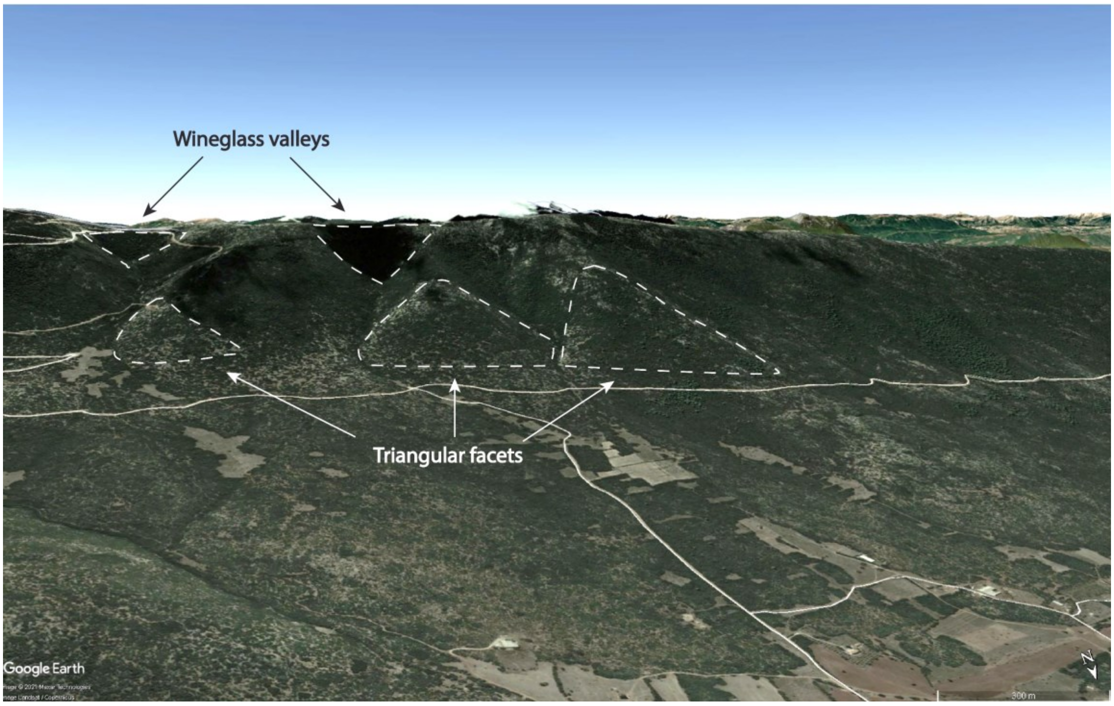

Figure 6.45: Oblique view of the north flanks of Kithaironas mountain, which is bounded by the Erythres fault. Wineglass valleys and triangular facets are visible, implying quaternary tectonic activity (Armijo et al., 1986). Image modified from Goole Earth. View looking South.

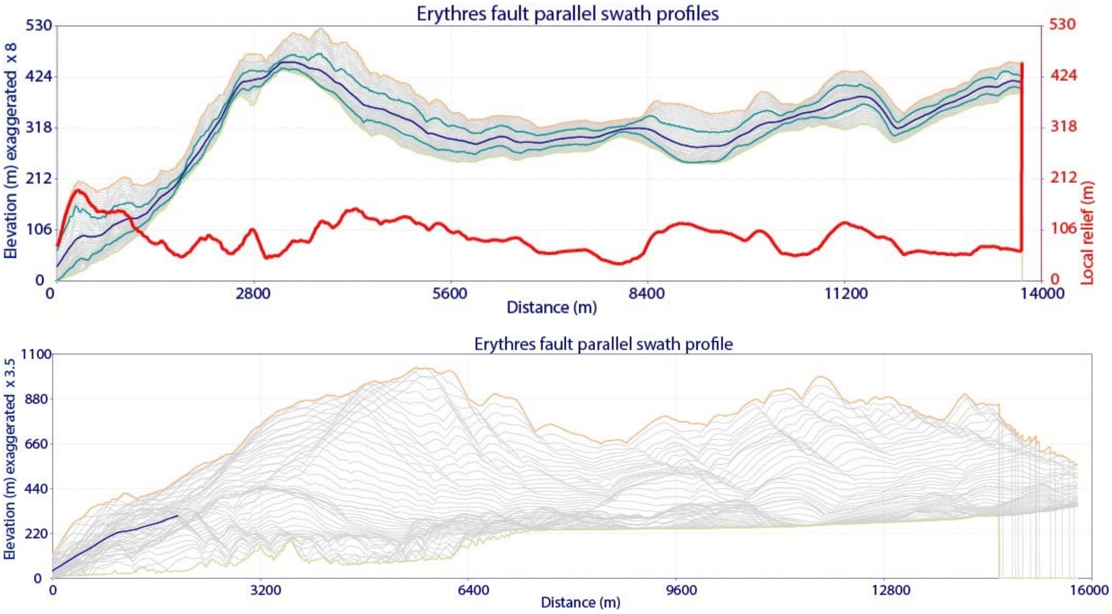

Figure 6.46: Swath topographic profiles within the Erythres fault parallel stripe. Fault located at the center of the stripe. Stripe width is 1000 m for the upper graph and 9000 m for the lower graph. Y-axis is exaggerated 8 times for the upper and 3.5 times for the lower graph. View looking towards South. Orange line represents the maximum elevation, light green line represents the lower elevation, blue line represents the mean elevation, dark green lines represent the Q1 and Q3 quartiles, red line represents the local relief (maximum elevation minus minimum elevation at the same distance along the fault line).

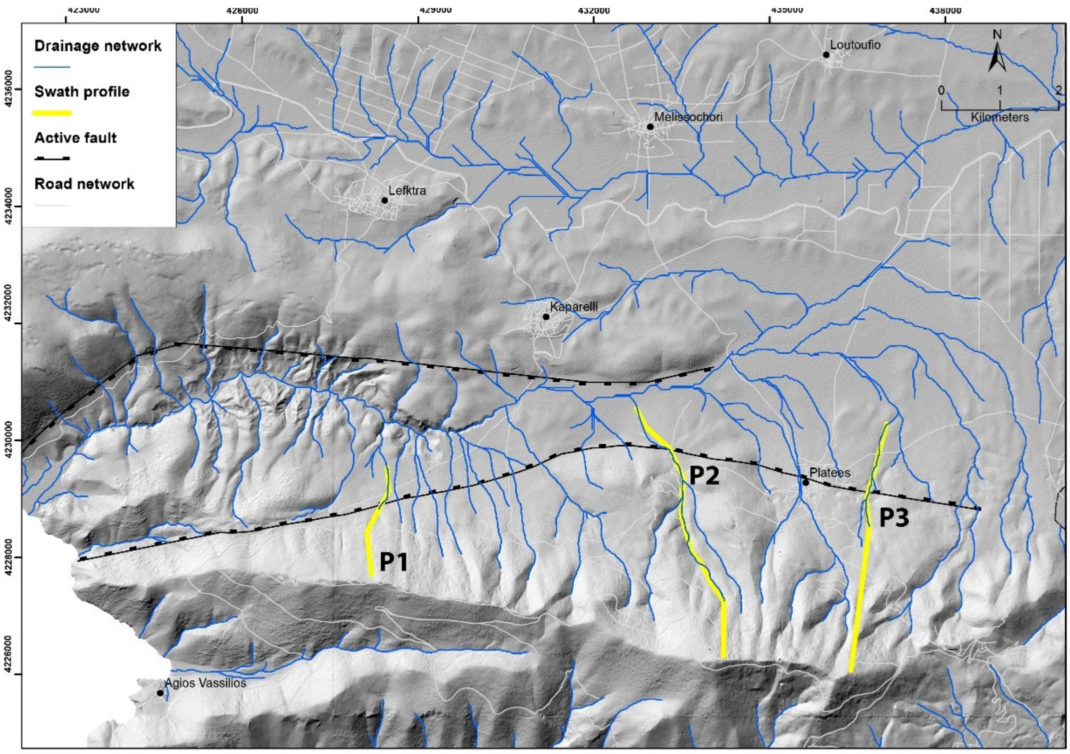

Figure 6.47: Shaded relief map of the Erythres fault area, showing the main drainage network and the location of the fault – perpendicular swath profiles (P1 – P3).

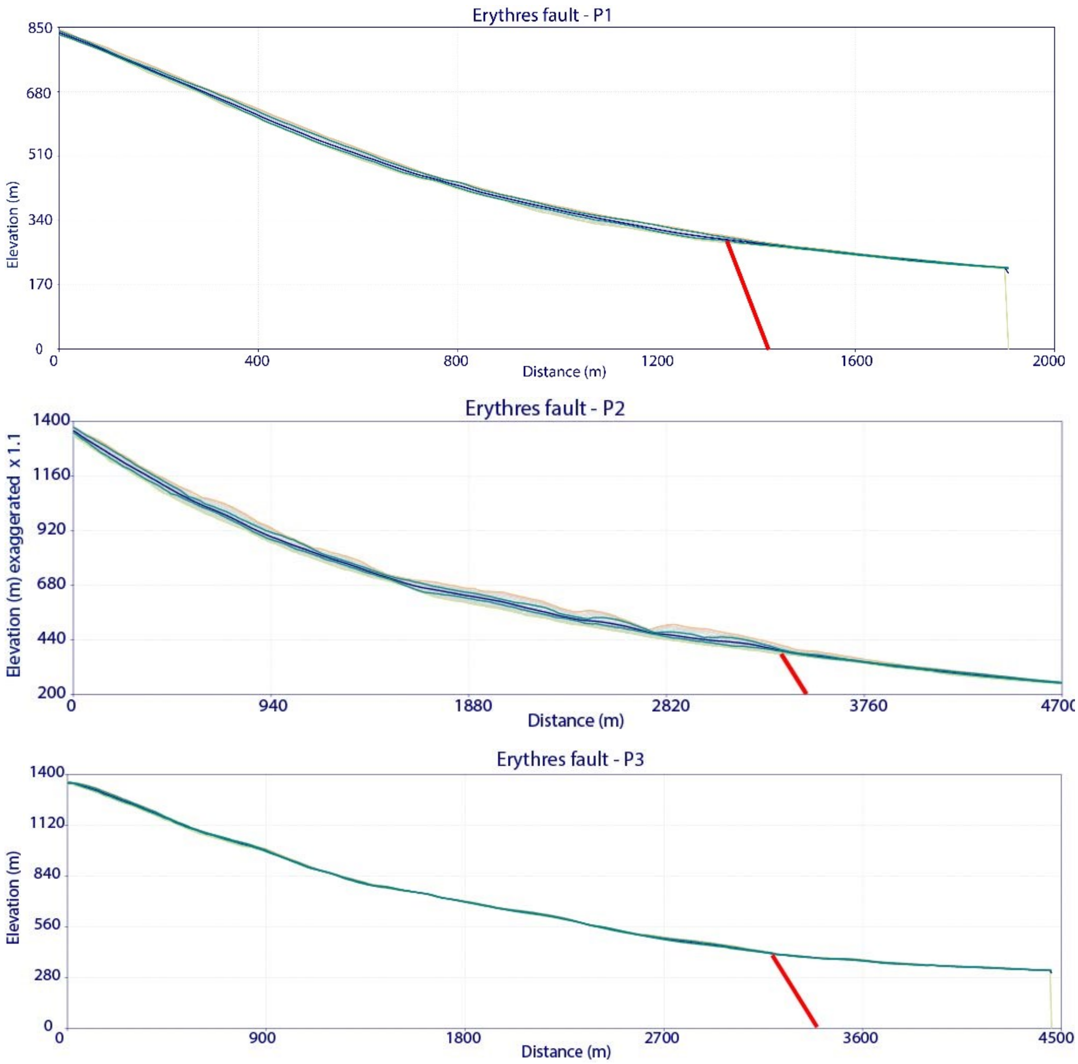

Figure 6.48: Swath topographic profiles within a fault perpendicular stripe, following drainage network flowing perpendicular to the Erythres fault. Stripe axis location shown in Figure 6.47.Stripe width is 200 m. Y-axis is sligthtly exaggerated for P2. View looking towards West. Orange line represents the maximum elevation, light green line represents the lower elevation, blue line represents the mean elevation, dark green lines represent the Q1 and Q3 quartiles. The red line represents the Erythres fault.

Nevertheless, the THi* index values for P1, P2 and P3 are 0.53, 0.51 and 0.6, respectively, implying a transient landscape. Considering that the Erythres fault does not have a postglacial scarp, an average slip-rate of 0.3 mm/y is assigned, taking into account a minimum of 880 m total throw (Figure 6.46, lower graph) and Pleistocene age of fault activity, based on the oldest basin fill (Ganas et al., 2005). This slip-rate value is close to the average slip-rate at the region of Attica (see also Section 6.3). The absence of a postglacial scarp may suggest a fault migration towards lower altitudes, and as a result, it is assumed that the present fault trace is located in the lowest break in slope of the Kithaironas mountain northern flanks.

6.2.7. The Aigosthena fault

The Aigosthena fault is relatively underrepresented in the literature, despite being in the well studied Corinth Gulf. Roberts and Koukouvelas (1996) and Ganas et al. (2005), who also named this fault after the ancient Greek Aigosthena fortress, report the existence of an E-W trending, north dipping normal fault that forms the southern boundary of the Germeno gulf and bounds the northern flanks of the Western Pateras mountain (Figure 6.49). Moreover, Sakellariou et al. (2007) refer to this fault as the N. Mytikas fault and suggest that there is no fault continuation further due west, in the Alkyonides Gulf.

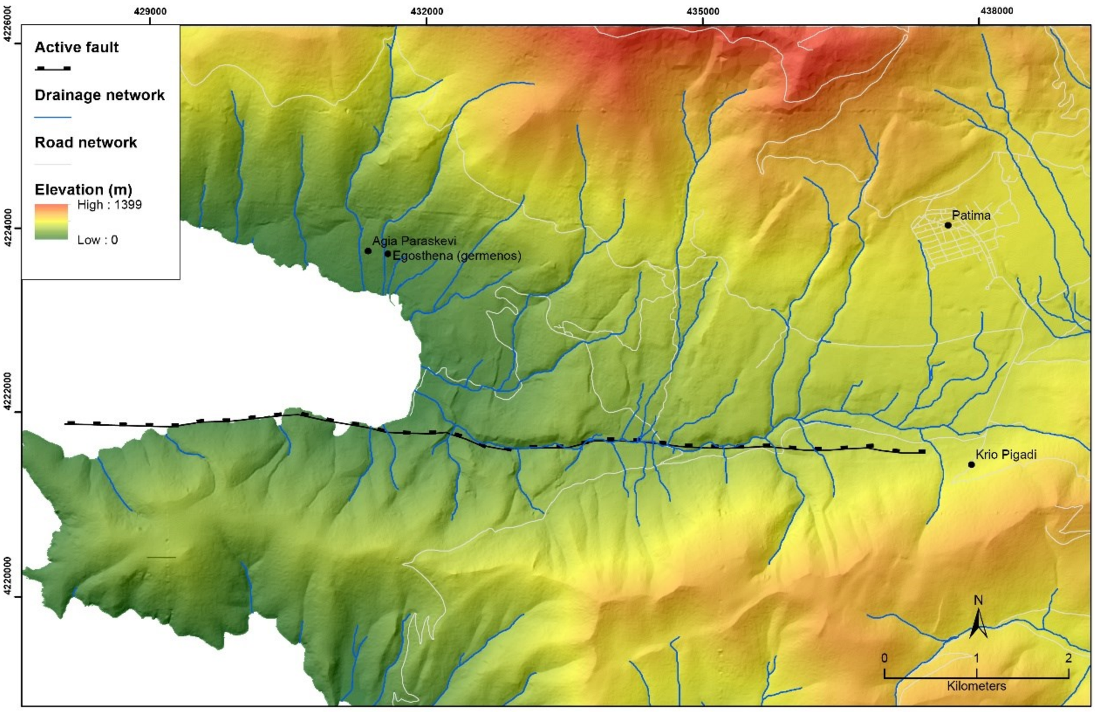

Figure 6.49: The North dipping Aigosthena fault in W Attica (id = 7 on Table 6.1) and the main drainage network. The base map shows the Digital Terrain Model (DTM) from the National Cadastre with 5 m spatial resolution. The fault continues offshore.

The footwall consists of Triassic – Jurassic limestone and dolomite of the Boeotian zone, and the hanging wall comprises Holocene alluvial deposits and scree, which overlay Pleistocene fluvioterestrial sediments and scree (Dounas, 1971; Bornovas et al., 1981). Steep slopes are observed in the central (44°) and western parts (35°) of the footwall (Figure 6.50).

A swath profile in a fault-parallel direction shows that the elevation difference between the footwall and the hanging wall is up to 560 m (Figure 6.51). However, the local relief curve shows a highly incised footwall rather than a triangular shape with higher altitudes toward the centre of the fault.

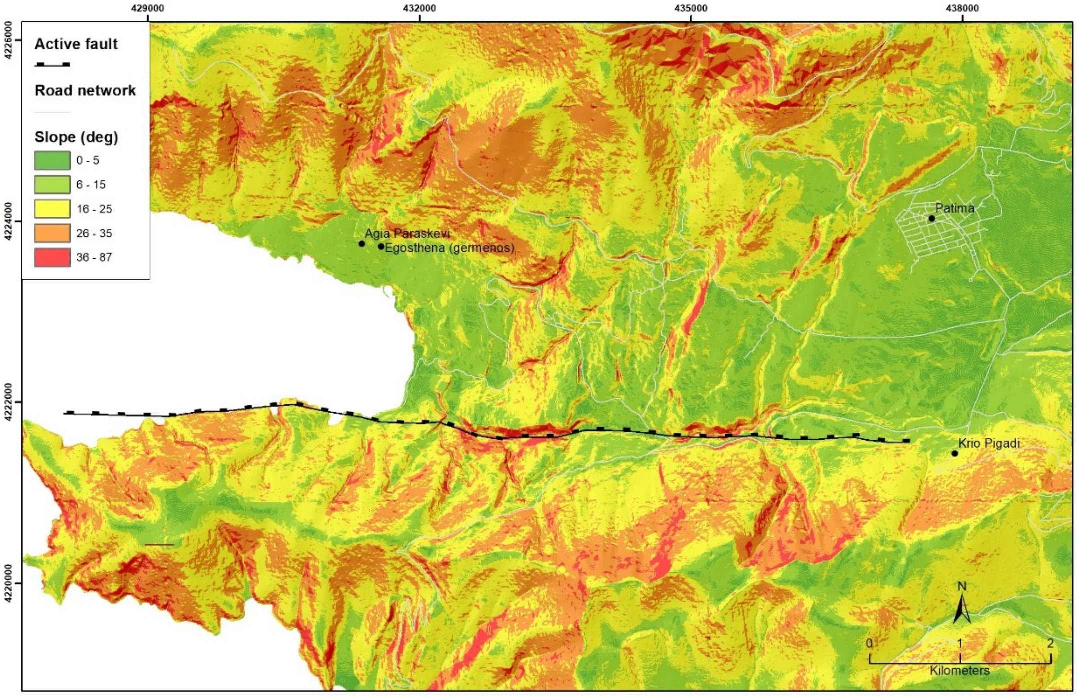

Figure 6.50: Slope map showing the slope changes related to Aigosthena fault (id = 7 on Table 6.1). Steeper slopes are observed at the footwall, in parallel to the Aigosthena fault.

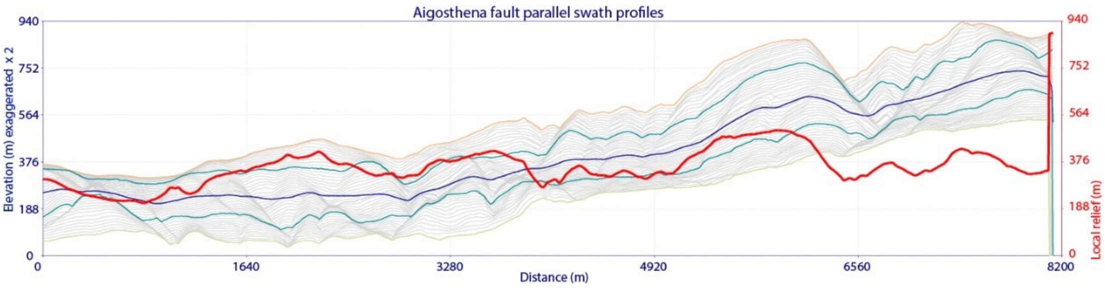

Figure 6.51: Swath topographic profiles within the Aigosthena fault parallel stripe. Fault located at the northern edge of the stripe. The stripe width is 500 m. Y – axis exaggerated about 2 times. View looking towards South. Orange line represents the maximum elevation, the light green line represents the lower elevation, blue line represents the mean elevation, dark green lines represent the Q1 and Q3 quartiles, red line represents the local relief (maximum elevation minus minimum elevation at the same distance along the fault line).

Three swath topographic profiles within fault perpendicular stripes (Figure 6.52) reveal concave up profiles for P1 and P2, while a small concavity is observed right over the fault in P3 (see locations and names of profiles in Figure 6.53). Additionally, the enhanced transverse Hypsometric Integral (THi*) values were calculated using the SwathProfiler toolbar. They reach up to 0.7 in the central profile (P2) right at the fault trace, and then drop to 0.5 for P1 and 0.6 for P3, implying that the fault is actively deforming the landscape. Furthermore, the basin asymmetry factor (Af) value is calculated at 66.6, which shows that the drainage network flowing parallel to the fault is diverted, and the basin is tilted towards the south (Figure 6.53).

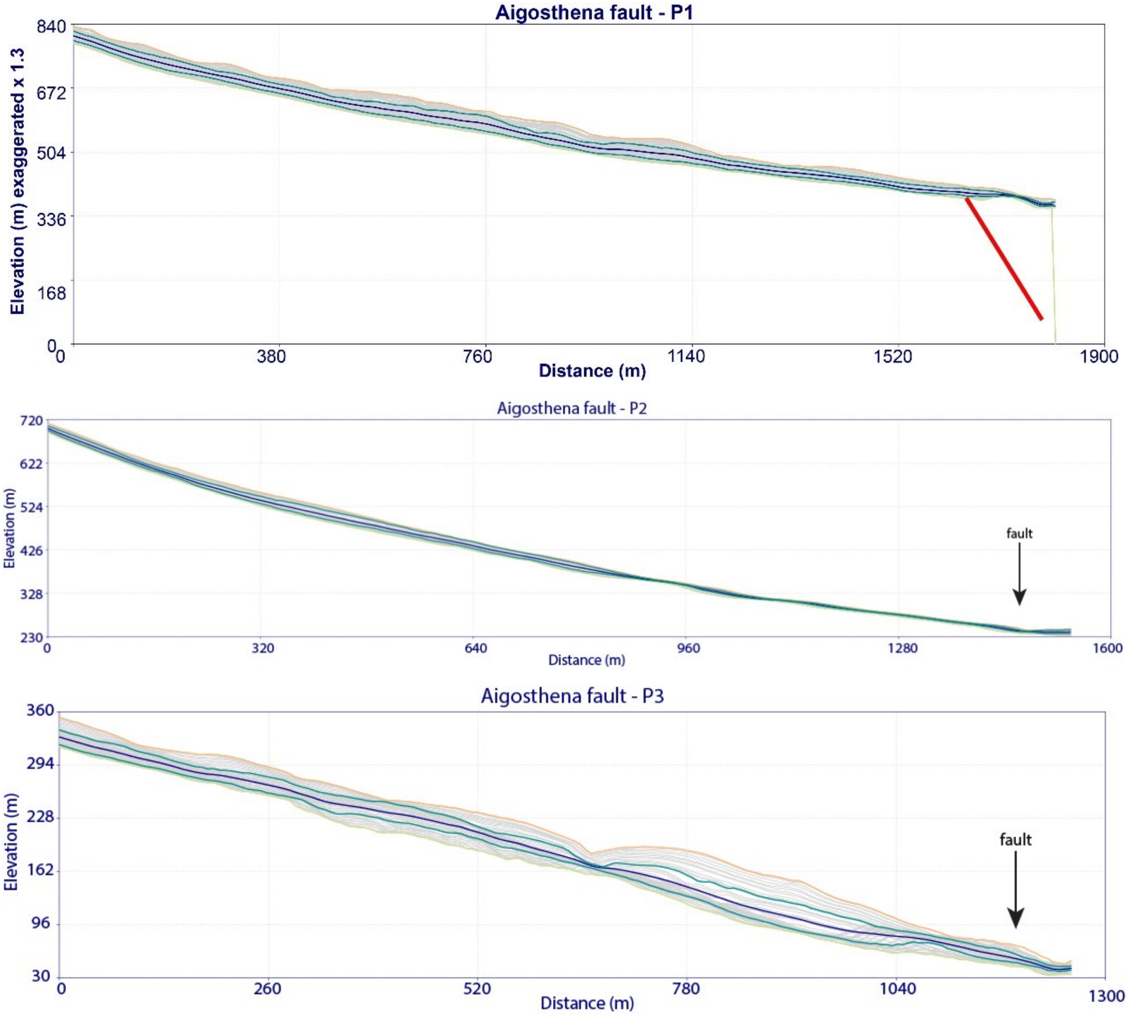

Figure 6.52: Swath topographic profiles within a fault perpendicular stripe, following drainage network flowing perpendicular to the Aigosthena fault. Stripe axes locations shown in Figure 6.53. The stripe width is 200 m. Y-axis is exaggerated about 1.3 times for P1. View looking towards West. The red line represents the Aigosthena fault.

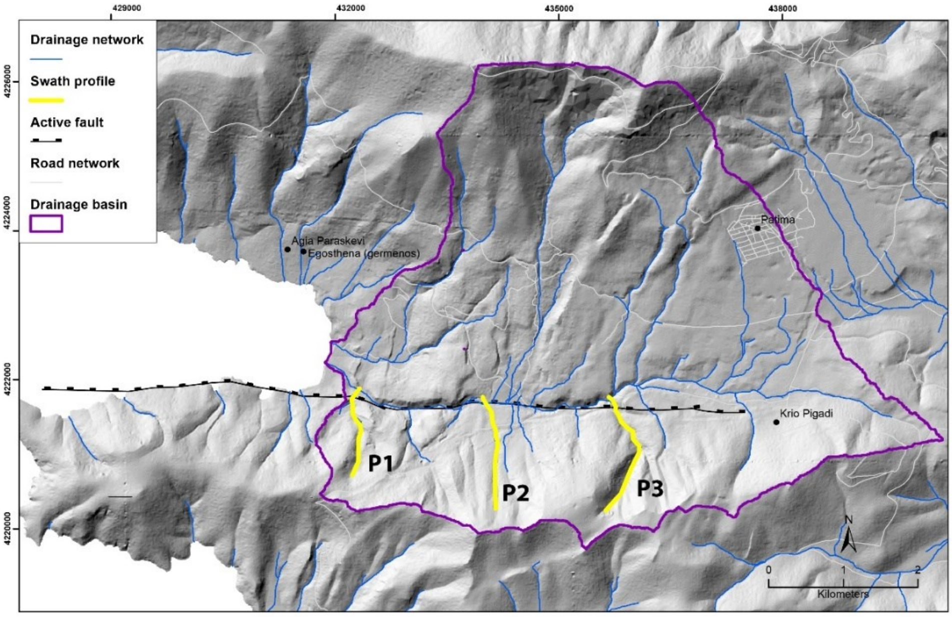

Figure 6.53: Shaded relief map of the Aigosthena fault area, showing the main drainage network and the location of the fault – perpendicular swath profiles (P1 – P3). Note the asymmetry on the drainage basin of the river flowing towards the west, parallel to the fault.

The Aigosthena fault exhibits a non-continuous highly degraded fault scarp, which is exposed at the eastern part of the fault, next to the P3 profile (Figure 6.54). The throw is visually estimated at 7 – 8 m. At the easternmost tip of the fault, a much smaller scarp is exposed (Figure 6.55), with a maximum throw of 1.5 m. As a result, a slip rate of 0.5 mm/y is estimated, assuming 15 kyrs postglacial age for the degraded fault scarp.

Figure 6.54: Distant (top) and close (bottom) view of the degraded fault scarp at the central part of the Aigosthena fault next to P3 profile (see location in Figure 6.53). The visually estimated throw is 7-8 m.

Figure 6.55: The Aigosthena fault scarp remnants, at the easternmost tip of the fault. Scarp height is 1.5 m

6.2.8. The South Alkyonides fault zone

The South Alkyonides fault zone is one of the best studied fault zones in Greece. Since the February 1981 major earthquakes sequence with magnitudes Ms= 6.7 and Ms= 6.4, multiple researchers have mapped the fault zone and the 1981 primary surface ruptures (e.g. Jackson et al., 1982; Papazachos et al., 1984; Biliris et al., 1991; Abercrombie et al., 1995; Hubert et al., 1996; Pantosti et al., 1996; Stewart, 1996; Collier et al., 1998; Morewood and Roberts, 1999 & 2001; Roberts et al., 2009; Roberts et al., 2011; Mechernich et al., 2018). Since most of the fault zone has been ruptured in 1981 (with the exception of the Psatha segment), all recent fault investigations aimed on defining the fault slip rate and the earthquake recurrence interval, since this fault zone is the largest and most active in the Attica region, or in close distance from it.

The NW dipping South Alkyonides fault zone expands from the Perachora peninsula in the West to Psatha gulf in the East (Figure 6.56). This zone includes several faults and fault segments, with the Schinos (north) and Pisia (south) faults being the most important ones (see also Mechernich et al., 2018). The largest part of the fault is onshore. However, it continues offshore from the Vamvakes fan until Psatha further in the East. This is also confirmed by the uplift in the coast line east of the Alepochori village, during the 1981 earthquakes (Papanikolaou et al., 2009). For the seismic hazard assessment process, it was modelled as a single fault zone (see also Figure 5.4), using the findings of the existing literature, especially the results for the Pisia fault, published by Mechernich et al. (2018), in which the author of this thesis contributed in fieldwork.

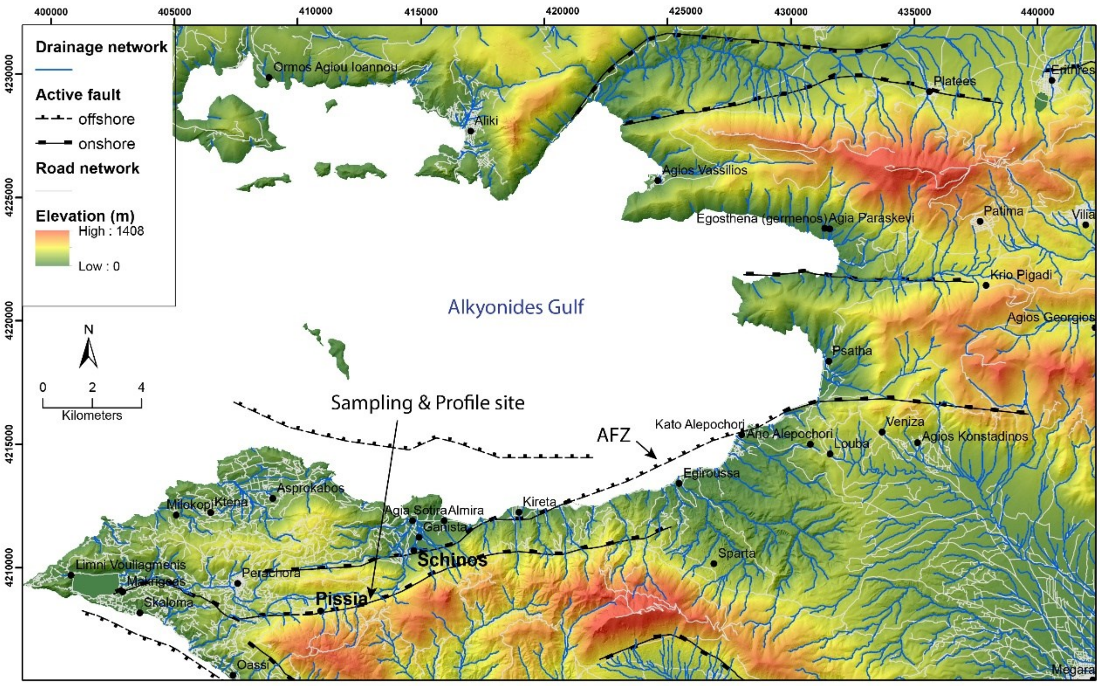

Figure 6.56: The NW dipping South Alkyonides fault zone (AFZ, id = 8 on Table 6.1), spanning from the Perachora peninsula in the West to Psatha in the East. This zone includes several faults and fault segments, with the Schinos (north) and Pisia (south) faults being the most important ones (see also Mechernich et al., 2018), but it was modelled as a single fault zone (see also Figure 5.4) for the seismic hazard assessment. Note the small and linear drainage basins with small catchments flowing towards NW, perpendicular to the fault. In addition, 78% of the Megara basin (SE part of the map) is drained towards SE, into the Saronikos Gulf. The drainage divide is shifted towards the Alkyonides Gulf due to the ongoing uplift of the South Alkyonides fault zone. ^{36}Cl sampling and topographic profiling site (P6) is located in the Pisia fault scarp.

The Pisia fault is best exposed in its central section (8–17 km from its western tip), where it crosses Triassic to Lower Jurassic carbonates of the Boeotian zone (Bornovas et al., 1981). After the February 1981 earthquake sequence, surface ruptures along the pre-existing fault scarp exhumed an additional 50 – 110 cm of fresh fault plane, which is still visible today (Figure 6.57)

Figure 6.57: The Pisia fault scarp at location P7 just 19 m east of P6. Note the dark grey stripe which was created after the 1981 rupture and the consequent exhumation of the free face. White paper elongated stripe length in the middle of the photograph is 1 m.

Wiatr et al. (2015) were the first to use t-Lidar globally for identifying paleoevents on limestone fault scarps, and they used the Pisia fault as the case study. They based their outcomes on the different smoothness across the fault plane that relates to different exposure time to weathering phenomena (the concept was first tested by Stewart (1996), but without success, due to spatial resolution constraints). Mechernih et al. (2018) confirmed the above findings and performed a similar study on another site along the Pisia fault. They used terrestrial laser scanning, coupled with analyses of colour changes, lichen colonization, and karstic features, to identify differentially weathered stripes across the exposed Pissia fault plane and identified 6 – 8 paleoearthquakes, including the latest in 1981. These results were coupled with cosmogenic ^{36}Cl measurements, to define the absolute ages of each exhumation. The cosmogenic ^{36}Cl dating has been widely used to date paleoearthquakes for several limestone fault scarps in Greece (e.g. Benedetti et al., 2002, 2003; Mechernich et al., 2018; Iezzi et al. (submitted for publication)) and in Italy (Palumbo et al., 2004; Benedetti et al., 2013; Cowie et al., 2017; Schlagenhauf et al*.,* 2011).

The sampling location is shown in Figure 6.56. The samples were partly taken continuously and partly with a gap of up to 45 cm depending on the surface preservation, in the best-preserved line on the fault plane at a bearing of 351°, which deviates from the average orientation of the striation by only 4°. Additionally, the buried portion of the fault plane (-1.95 to 0 m) was sampled at a bearing of 347°, parallel to local striations (Figure 6.58). These subsurface samples are required to allow a precise analysis of the ^{36}Cl pre-exposure concentrations (Schlagenhauf et al., 2010).

Figure 6.58: Sampling ladder at the subsurface part of the Pisia fault scarp, in order to define the ^{36}Cl pre-exposure concentrations. Each sample is 5 cm high. The total pit depth is 1.95 m.

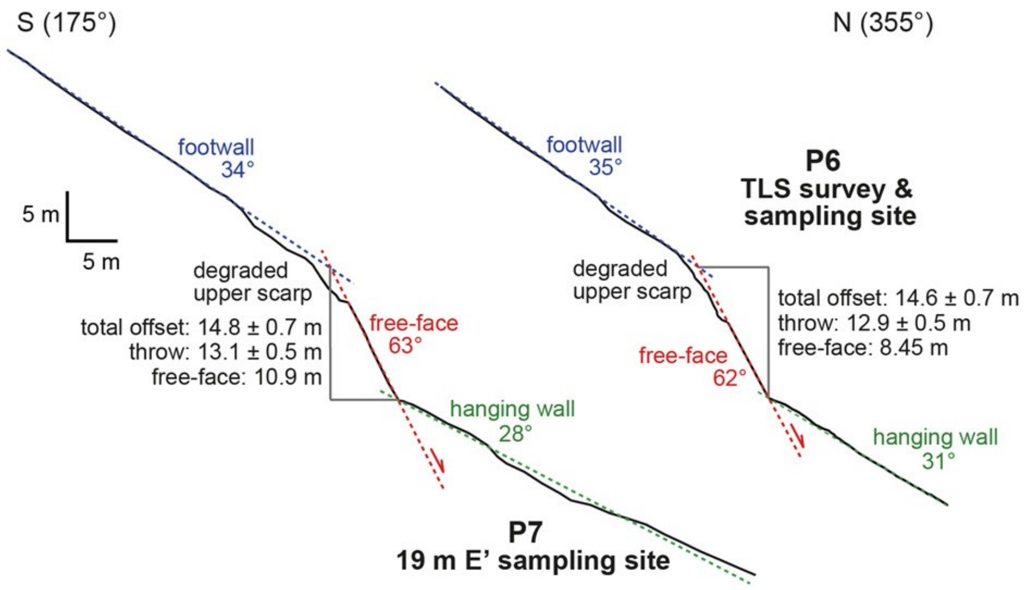

Figure 6.59: Topographic profiles at sites P6 (same location with the ^{36}Cl sampling site) and P7, just 19 m East of P6, obtained from measurements using a clinometer and a 1 m long scalebar (see also Papanikolaou et al., 2005 for details in methodology). The profiles reveal the fault scarp height and geometry, which are used as input parameters for the cosmogenic nuclide modelling and the throw rate calculation. Figure modified after Mechernich et al., 2018.

In order to measure the fault scarp and constrain the ^{36}Cl results, 2 topographic profiles were obtained across the Pissia fault scarp, at locations P6 and P7 (Figure 6.59). The profiles reveal a total throw of ~ 13 m (see also Mechernich et al., 2018).

The final results show a maximum slip rate of 2.3 mm/y at the early Holocene. The slip rate associated with the last 6-8 earthquakes (Late Holocene) that occurred during the last 7.3 ± 0.7 kyr, including the 1981 rupture, is calculated at 0.5-0.6 mm/y (Figure 6.60). However, both Skinos and Pissia faults are most likely linked at depth (Roberts, 1996), and since Mechernich et al. (2018) interpreted an age range of 1.4–2.5 kyr for the penultimate event on the Pisia fault, at least three of the reported paleoearthquakes by Collier et al. (1998) on the Skinos fault were not accompanied with surface ruptures of the Pisia fault. The latter implies that the Pissia and Skinos faults are not always activated simultaneously, as happened in 1981. Furthermore, the Skinos fault seems to have increased activity during the Late Holocene, as revealed from the paleoseismic trenching in Vamvakies alluvial fan (Pantosti et al., 1996; Collier et al., 1998). As a result, the maximum value of 2.3 mm/y was used as a slip-rate value for the South Alkyonides fault zone.

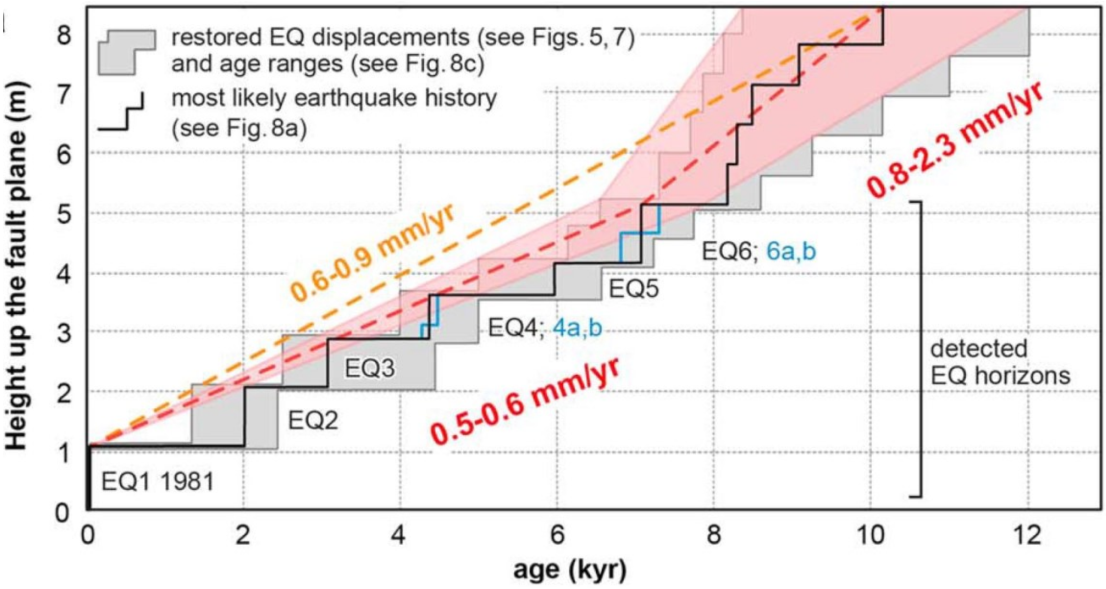

Figure 6.60: The exhumation history of the free-face at site P6, after Mechernich et al., 2018. The slip rate was 0.5–0.6 mm/yr for the last ~7.3 kyr (1.1–5.15 m). For the upper part of the free-face (5.15–8.45 m; hypothetical earthquake offsets) the exhumation occurred at a significantly higher rate. Please note that the apparent slip history of the degraded scarp and the scarp age are hypothetical due to significant erosion, sedimentation at the scarp base, and a lack of cosmogenic data. Figure modified after Mechernich et al., 2018.

6.2.9. The Loutraki fault

The Loutraki fault has two parallel segments approximately 1.5km apart (Figure 6.61). The main segment is offshore, bounding the Loutraki basin, but it is also traced onshore in the northern margin of the Loutraki basin (e.g. Sakellariou et al., 2007; Roberts et al., 2009; Moretti et al., 2016). The second (upper) segment exhibits a postglacial scarp at about 550 m altitude (Figure 6.62, close view of the degraded upper scarp shown in Figure 6.63). The Loutraki Fault is active as it offsets a slope formed during periglacial activity in the last glacial maximum (~18 ka) and deforms sediments from the last glacial maximum exposed in a small quarry on the roadside near Osios Potapios Monastery (Roberts et al., 2011).

A detailed fault scarp profile crossing the upper Loutraki degraded fault scarp (Figure 6.64) reveals a post-glacial throw of 9 m. This is in agreement with the two upper scarp profiles presented by Roberts et al. (2011), implying that the Loutraki fault has a throw rate of approximately 0.5 mm/yr.

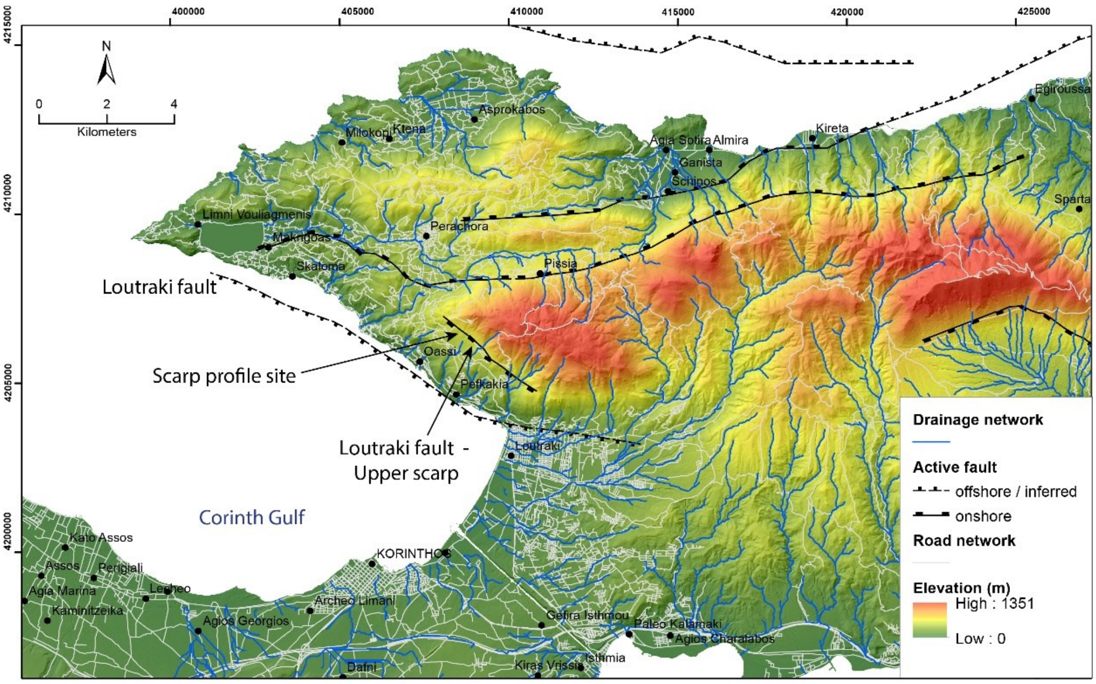

Figure 6.61: The offshore Loutraki fault in W Attica (id = 10 on Table 6.1) and the Upper Loutraki fault scarp. The Loutraki fault continues onshore, bounding the Loutraki basin in the north, although there is no fault scarp preserved. The Upper Loutraki fault′s postglacial scarp is continuous for approximately 3.5 km and has a total throw of 9 m (see also Figure 6.64).

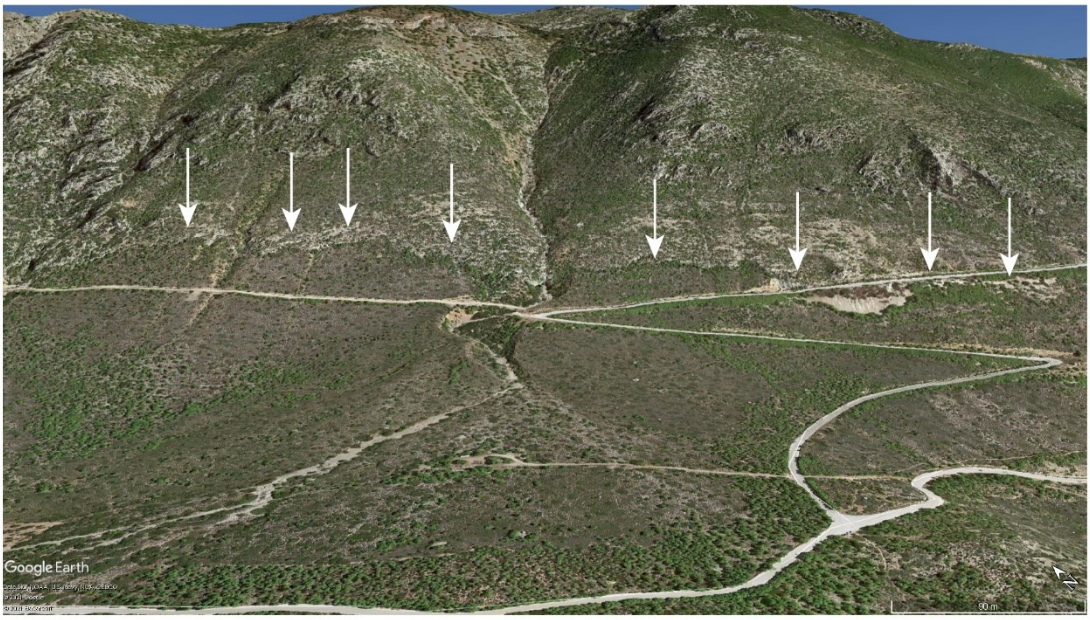

Figure 6.62: The Loutraki fault degraded scarp, as seen from a distance (Google Earth imagery)

Figure 6.63: Close up view of the Loutraki Upper fault scarp. The Upper Loutraki fault's postglacial scarp is continuous, and a total throw of 9 m is recorded (see also Figure 6.64).

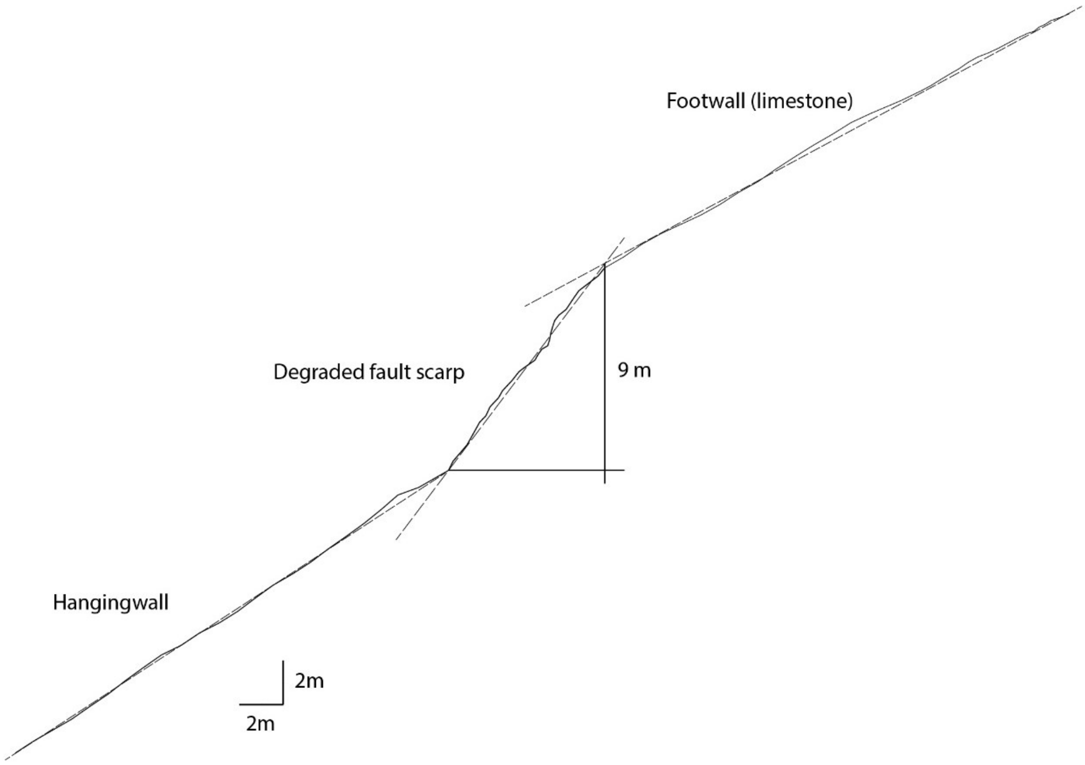

Figure 6.64: Detailed profile perpendicular to the Upper Loutraki fault scarp. Measurements obtained using a clinometer and a foldable meter scale (see also Papanikolaou et al., 2005 for details in methodology). The profiles reveal the fault scarp height and geometry, which are used for the throw rate calculation. The location of the fault scarp profile is shown in Figure 6.61.

6.2.10. The Kakia Skala fault

The Kakia Skala fault is an approximately 20 km long, NW – SE trending, SW dipping normal fault (Figure 6.65). The central and northwestern part of the fault bounds the southern flanks of the Geraneia mountain, while the eastern part of the fault continues at the coastal Saronic Gulf. Its footwall comprises mainly Triassic limestone, while the footwall consists of Pleistocene talus cones and fluvioterrestrial deposits, which are locally covered by recent Holocene deposits (Gaitanakis et al., 1981 & 1982; Gaitanakis et al., 1981).

The fault was first studied by Goldsworthy and Jackson (2000), who referred to it as Saros fault, and characterized it as active, based on a qualitative river incision assessment. Rondoyianni and Marinos (2008) assessed the old Athens – Corinth highway and the rail fault crossing and estimated a potential 50 cm coseismic displacement in case of seismic rupture. On the other hand, Mack et al. (2009) argued that the Saros fault might have been inactice since late Pleistocene.

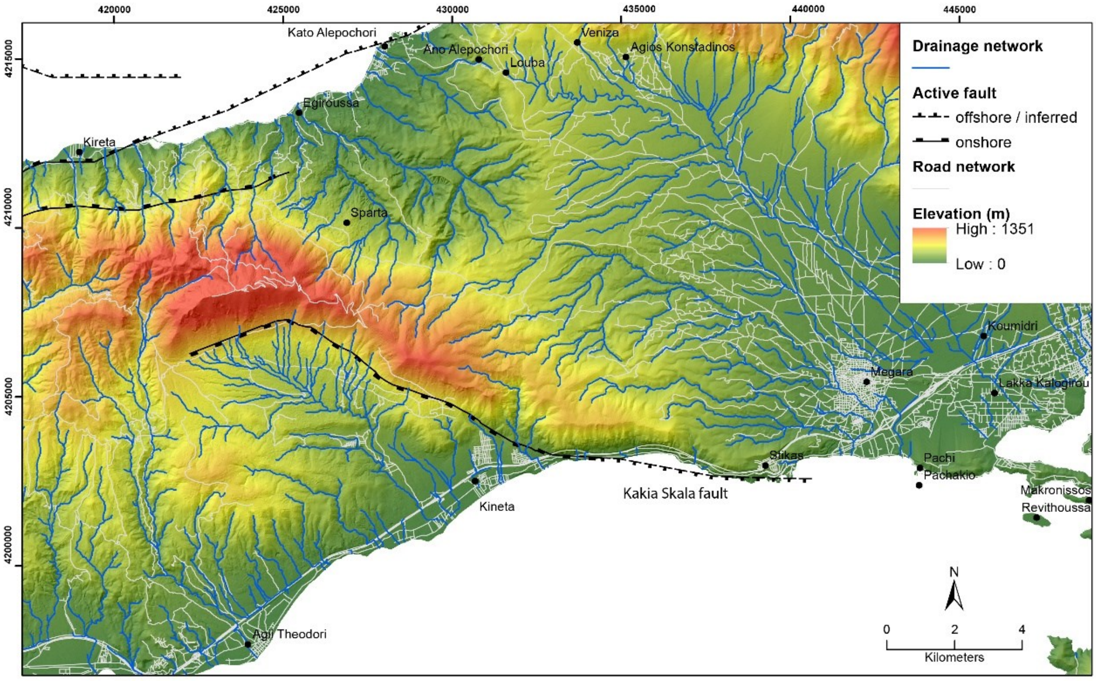

Figure 6.65: The SW dipping Kakia Skala fault in NW Attica (id = 13 on Table 6.1) and the main drainage network.

The steepest slope gradients along the Kakia Skala fault (<45°) occur mainly in the central part of the fault (Figure 6.66). A swath topographic profile in a fault-parallel direction reveals a maximum 570 m elevation difference between the footwall and the hanging wall. The shape of the local relief curve indicates that the footwall is highly incised by the fluvial network (Figure 6.67). However, it is important to note that the stripe of the swath profiles does not expand to the coastal segment or the Gerania mountain top due to technical reasons related to DTM errors. The maximum elevation difference is manually measured at approximately 800 m in the NW.

Two swath topographic profiles within fault perpendicular stripes (Figure 6.68, see Figure 6.69 for the profiles locations) show convex reaches right over the fault. The enhanced Transverse Hypsometric Integral (THi*) was calculated at 0.85 for P1 and 0.7 for P2. This implies a young transient landscape and an active uplift.

An average slip-rate of 0.3 mm/y is assigned, taking into account a conservative assessment of 800 m total throw and Pleistocene age of fault activity, based on the oldest basin fill (Ganas et al., 2005).

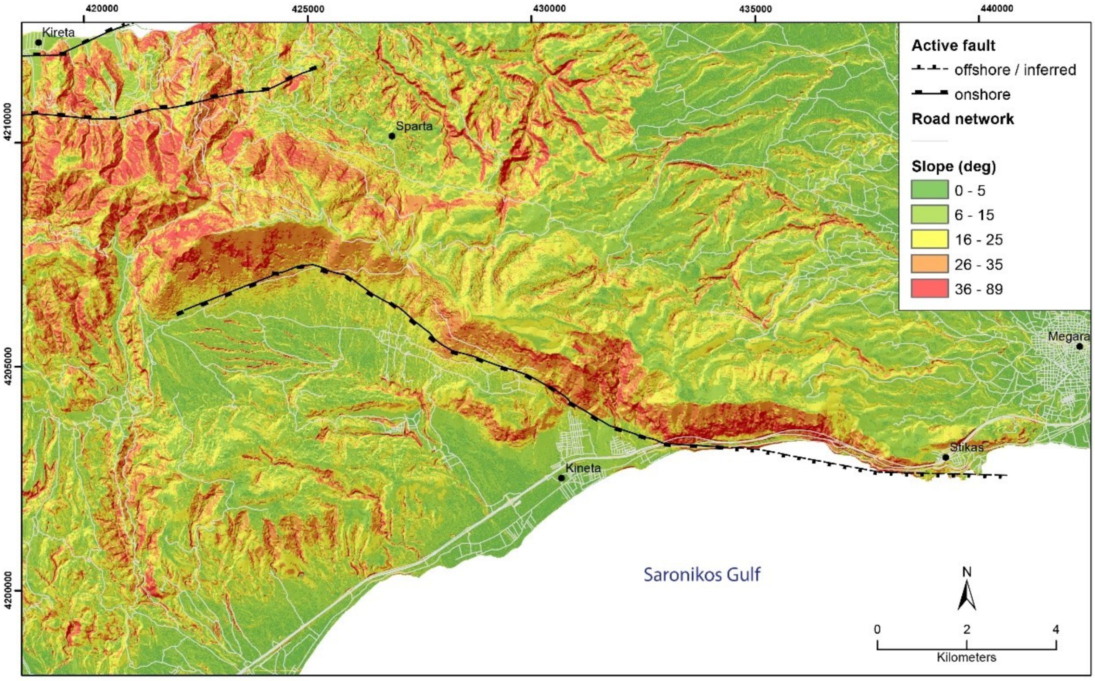

Figure 6.66: Slope map showing the abrupt slopes in the Kakia Skala fault footwall. The highest slope values (> 45°) appear on the central part of the fault's footwall. Nearly vertical slopes occur near the coastline. Note the mild slopes in the adjacent Megara basin in the NE, which is now inactive (Bentham et al., 1991)

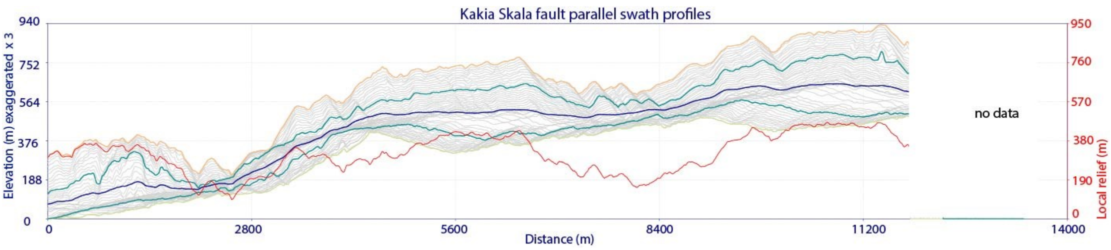

Figure 6.67: Swath topographic profiles within the Kakia Skala fault parallel stripe. Fault located at the middle of the stripe. The stripe width is 1000 m. Y-axis is exaggerated about three times. View looking towards SW (the right part of the graph is located at the NW tip of the fault). DTM artefacts resulted in zero elevation values for the NW tip of the fault. Orange line represents the maximum elevation, light green line represents the lower elevation, blue line represents the mean elevation, dark green lines represent the Q1 and Q3 quartiles, red line represents the local relief (maximum elevation minus minimum elevation at the same distance along the fault line).

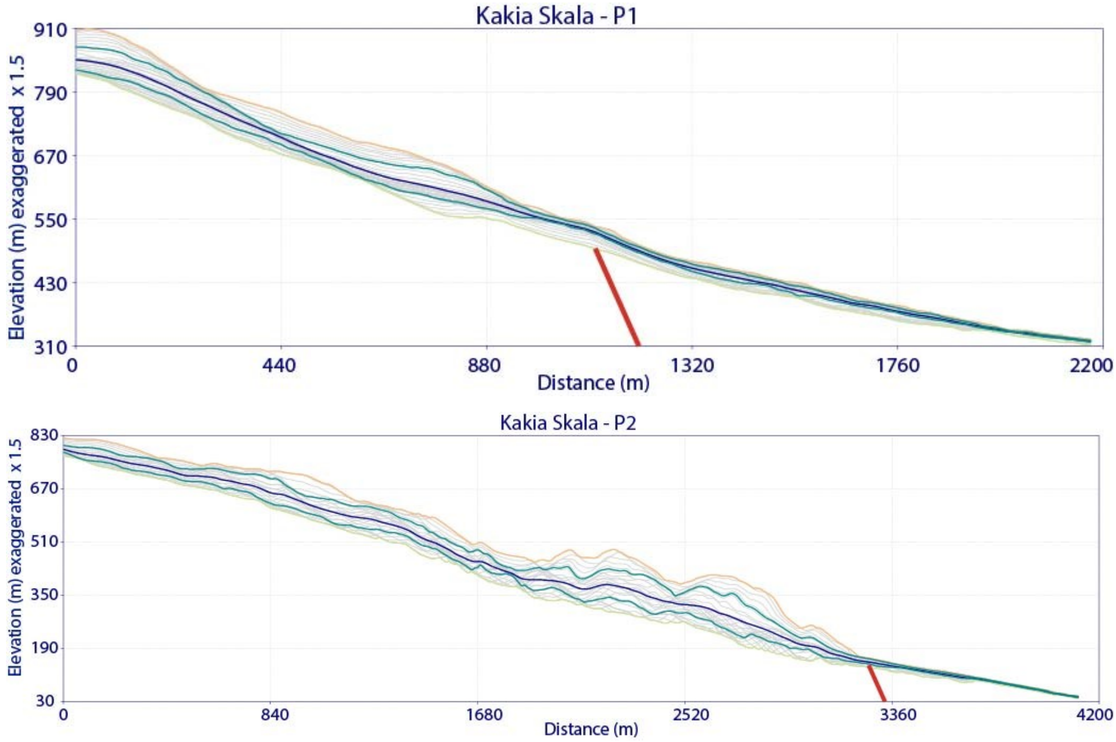

Figure 6.68: Swath topographic profiles within a fault perpendicular stripe, following the drainage network flowing perpendicular to the Kakia Skala fault. Stripe axis location shown in Figure 6.69. Stripe width is 500 m. Y-axis is exaggerated about 1.5 times. View looking towards East. Orange line represents the maximum elevation, light green line represents the lower elevation, blue line represents the mean elevation, dark green lines represent the Q1 and Q3 quartiles. The red line represents the Kakia Skala fault.

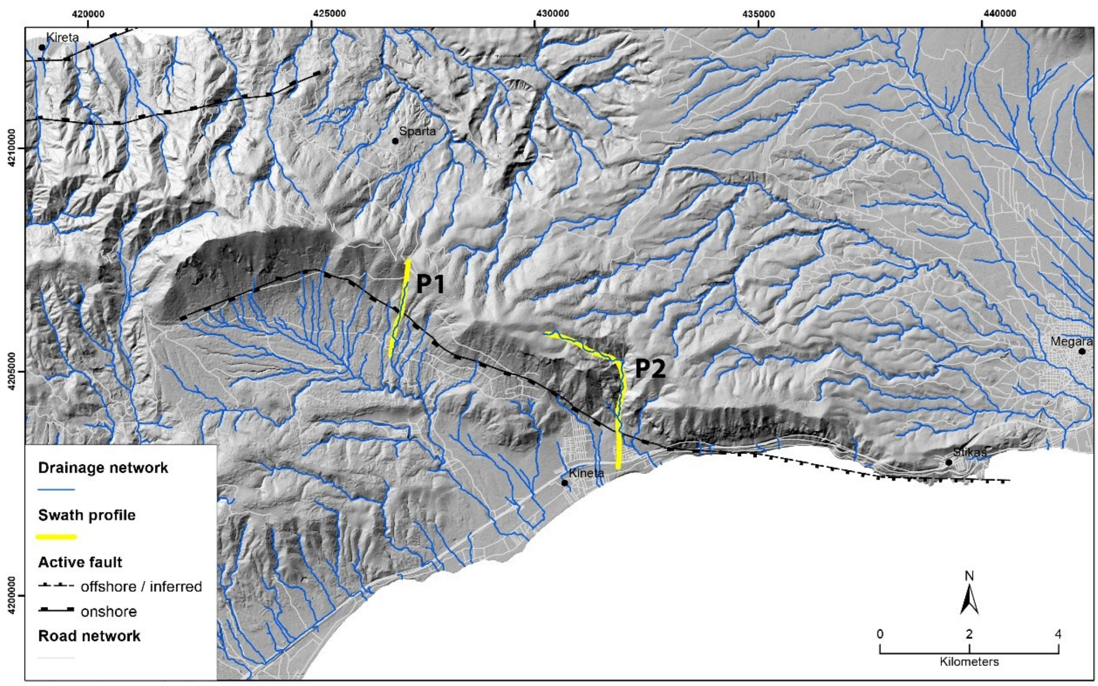

Figure 6.69: Shaded relief map of the Kakia Skala fault, showing the main drainage network and the location of the fault – perpendicular swath profiles (P1 and P2).

6.2.11. Thriassio & Fili faults

The Thriassio and Fili faults are two parallel, NW-SE trending, SW dipping normal faults. Both were examined after the Athens 1999 Mw=5.9 earthquake event by many researchers (see also Section 3.2.2 and references therein) who tried to assign the epicentre either to the Thriassio (e.g. Papadimitriou et al., 2002) or to the Fili fault (e.g. Pavlides et al., 2002). The Thriassio fault is a 16.5 km long structure that bounds the SW flanks of the Parnitha mountain and defines the Thriassio plain boundary. The Fili fault is cutting through the Thriassio footwall, uplifting the main Parnitha mountain to the northeast (Figure 6.70).

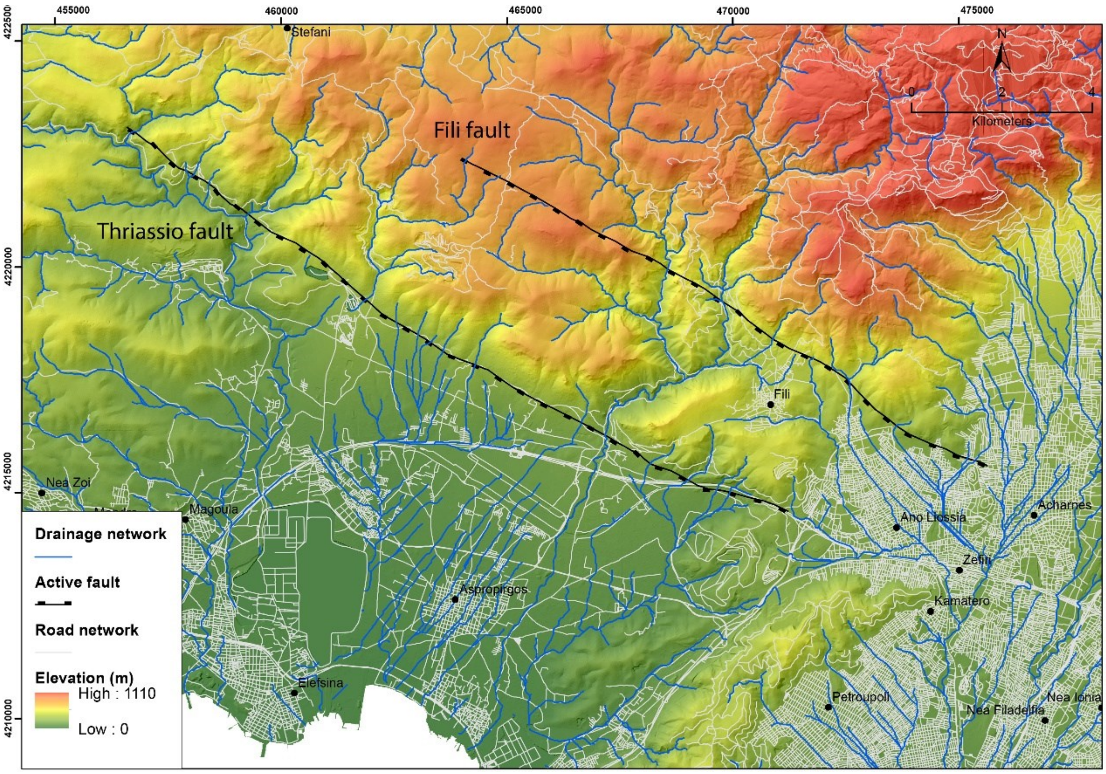

Figure 6.70: The SW dipping Thriassio and Fili faults west of the Athens basin (id = 14 & 15 respectively, on Table 6.1) and the main drainage network. Base map shows the Digital Terrain Model (DTM) from the National Cadastre with 5 m spatial resolution.

Both faults have uplifted the Triassic - Upper Cretaceous limestone of the Pelagonian zone (s.l.) in their footwall. However, the Thriassio fault's hanging wall comprises Holocene scree and alluvial fans in the immediate vicinity of the fault, while Plio - Pleistocene sediments are present at the Thriassio plain (Katsikatsos et al., 1986). The total thickness of the Plio - Pleistocene sediments reaches up to 350 m, with an additional 5-10 m of recent Holocene deposits. The Quaternary sediments consist of Plio – Pleistocene marls, clay, marly limestone and carbonate breccia/conglomerate, overlaid by Holocene clay, sands and gravels. This is also supported by the existence of multiple aquifers (Hermides et al., 2020 and references therein).

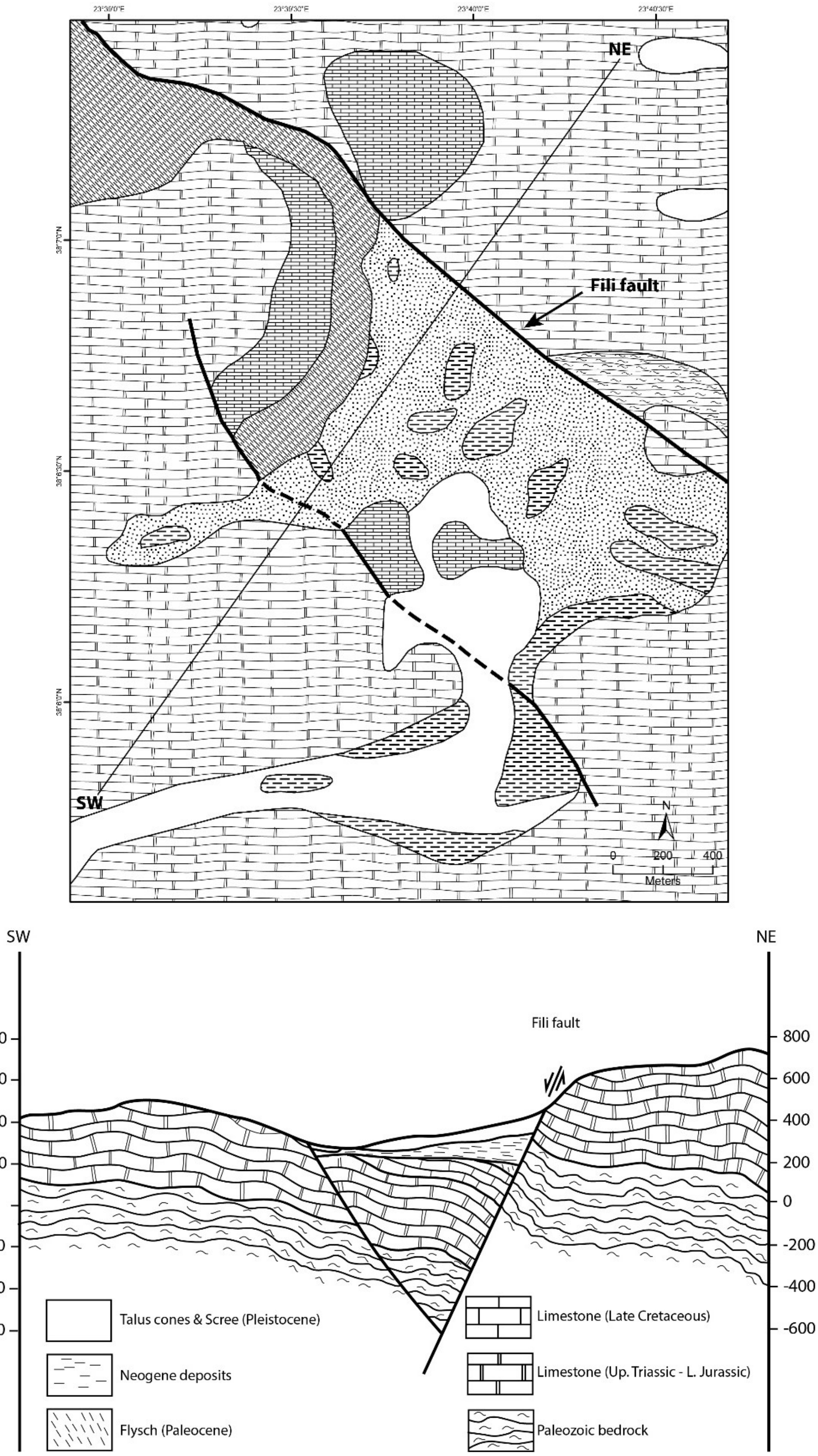

Figure 6.71: Top: Geology of the Fili fault and the surroundings (geology modified after Katsikatsos et al., 1986). SW–NE line marks the cross-section. Bottom: Cross-section based on the Geological Map of Katsikatsos et al., 1986. The total throw of the Fili Fault is 600 ± 150 m.

Most importantly, Foumelis (2019) determined strain tensors across the Thriassio fault, using geodetic data. Apart from a single tensor at the fault's centroid, he also calculated strain over several uniformly distributed points along the fault zone. As a result, he reports an overall extensional rate of 1.30 ± 0.78 μstrain/yr at a NE – SW direction, which is almost perpendicular to the Thriassio fault trace. He also calculated extensional rates reaching 1.68 ± 0.02 μstrain/yr at the Thriasio Basin, which are the highest in the broad Athens basin area.

On the other hand, the Fili fault uplifts the Pelagonian Zone (s.l.) limestones against the Paleocene flysch of the same unit. At the central part of the fault, a Neogene basin is mapped by Katsikatsos et al. (1986) (see also Figure 6.71). The absence of more recent sediments in the Fili fault's hanging wall may imply small displacement or small erosional processes (Ganas et al., 2004). Indeed, a total throw of 600 ± 150 m is observed based on the geological cross-section based on Katsikatsos et al. (1986) geological map (Figure 6.71), which is nearly half, compared to the NE dipping Malakasa fault, which is the northern boundary of Parnitha (see also Figure 6.23).

Steep slope gradients occur in the immediate footwall of the Thriassio fault, reaching up to 40° in the central part, where deeply incised channels cutting through the footwall are visible. The same holds for the Fili fault, with slope gradients up to 42° at the immediate footwall (Figure 6.72).

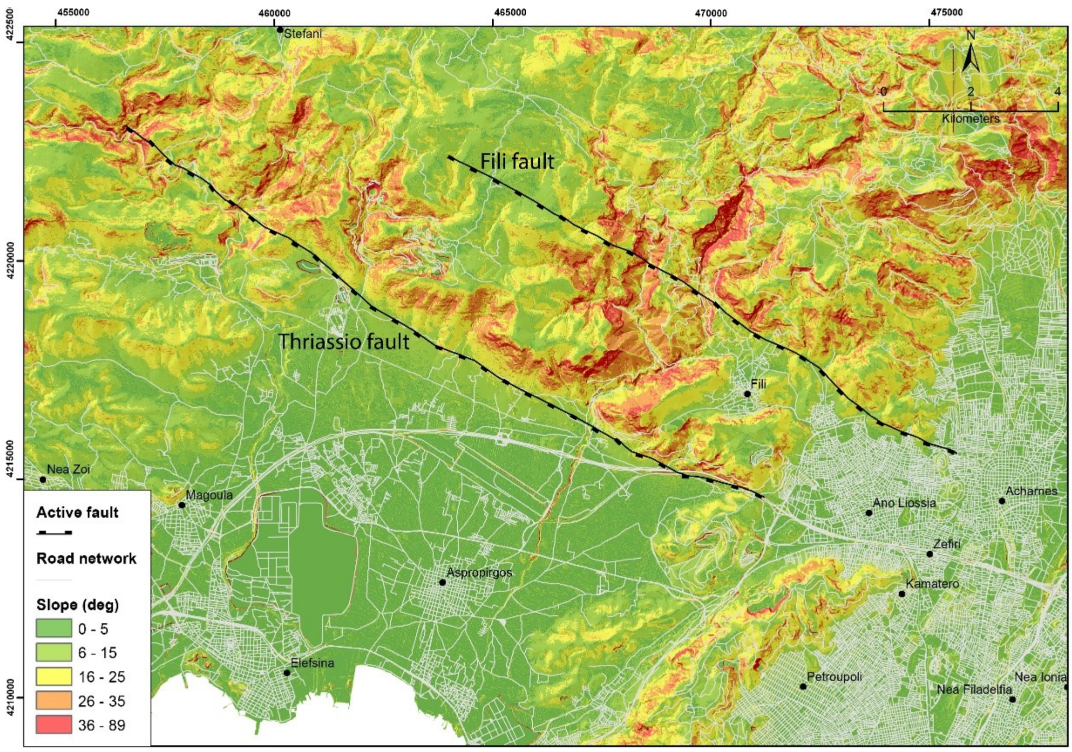

Figure 6.72: Slope map showing the slope changes in the Thriassio and Fili faults footwall, as well as the difference in both faults hanging walls. Thriassio fault has a nearly planar hanging wall (Thriassion plain), while the Fili fault's hanging wall is deeply insised, due to the uplift caused by the Thriassio fault. Highest slope values (> 45°) appear on the central part of the fault's footwall.

The fault parallel swath topographic profiles for the Fili fault shows a triangular pattern, with higher altitude differences in the central part of the fault. On the other hand, the Thriassio fault displays an eroded relief, with deep incisions in the central part of the fault (Figure 6.73). However, all valleys are V shaped and the Vf values are extremely low, spanning from 0.022 at the NW part of the Thriassio fault (3400 m in Figure 6.73) up to 0.15 in the SE part. This implies an active tectonic environment (see also Koukouvelas et al., 2018).

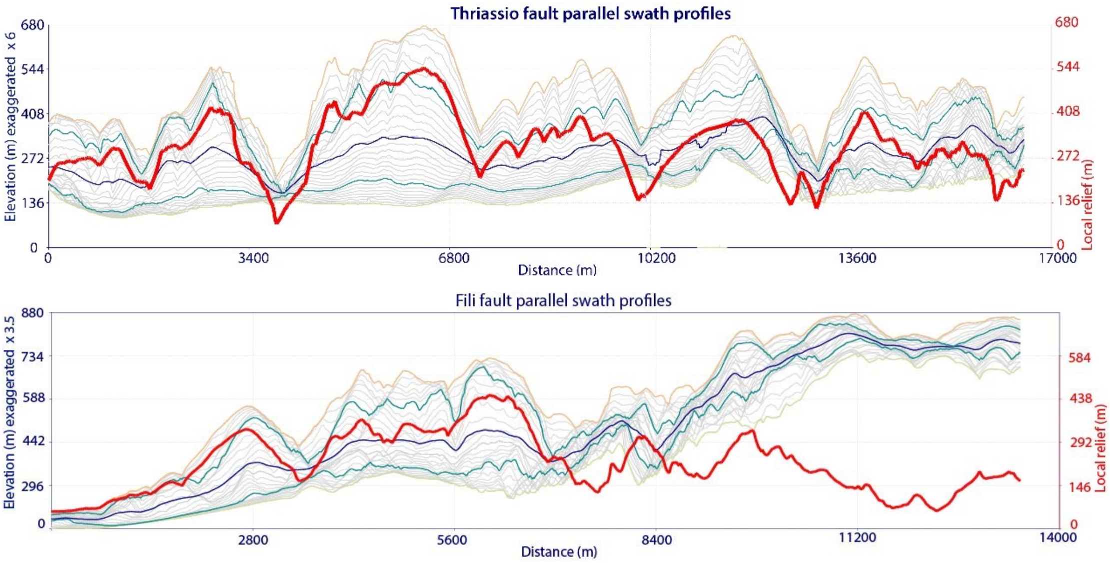

Figure 6.73: Swath topographic profiles within Thriassio (top) and Fili (bottom) fault parallel stripes. Faults located at the middle of the stripes. Stripes' width is 2000 m. Y-axis is exaggerated about 6 times for Thriassio and 3.5 times for Fili fault. View looking to the South. Orange line represents the maximum elevation, light green line represents the lower elevation, blue line represents the mean elevation, dark green lines represent the Q1 and Q3 quartiles, red line represents the local relief (maximum elevation minus minimum elevation at the same distance along the fault line).

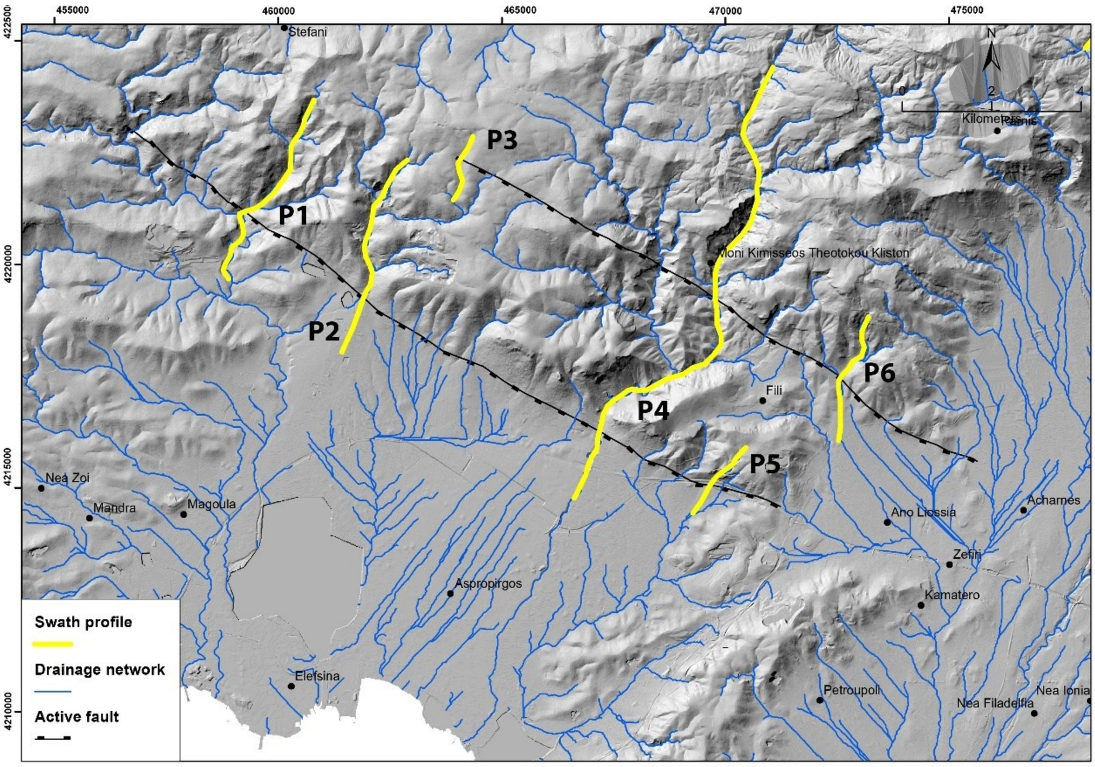

Figure 6.74: Shaded relief map of the Thriassio and Fili faults, showing the main drainage network and the location of the fault – perpendicular swath profiles (P1 – P6).

Six swath topographic profiles within fault perpendicular stripes were plotted in both faults. The locations of the profiles are shown in Figure 6.75. P1 and P2 follow deeply incised valleys in the Thriassio footwall near the NW end of the fault. P5 follows a small catchment flowing perpendicular to the easternmost Thriassio fault tip. P3 and P6 follow catchments flowing perpendicular to the Fili fault ends. P4 is the only profile that runs through both Fili and Thriassio footwalls and ends in Thriassio plain (Figure 6.75). All profiles show convex reaches right on the fault trace, with P2 and P4 being the most characteristic. The THi* values are all above 0.5, with the higher values in P3 and P5 (0.75) and the lower value in P6 (0.55). The THi* values for P1, P2, and P4 are all 0.6. This implies that the landscape in both faults is in a transient state (Pérez-Peña et al., 2017).

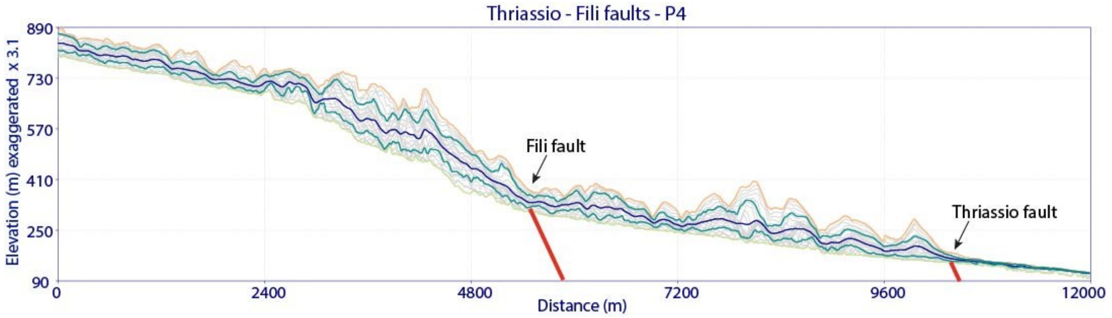
Thriassio - Fili faults - P4
Elevation (m) exaggerated x 3.1
890
730
570
410
250
90
Fili fault
Thriassio fault
0
2400
4800
7200
9600
12000
Distance (m)

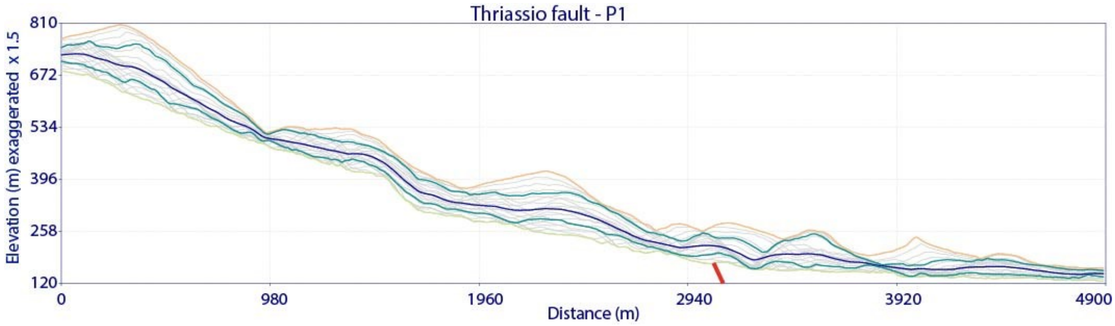
Thriassio fault - P1
Elevation (m) exaggerated x 1.5
810
672
534
396
258
120
0
980
1960
2940
3920
4900
Distance (m)

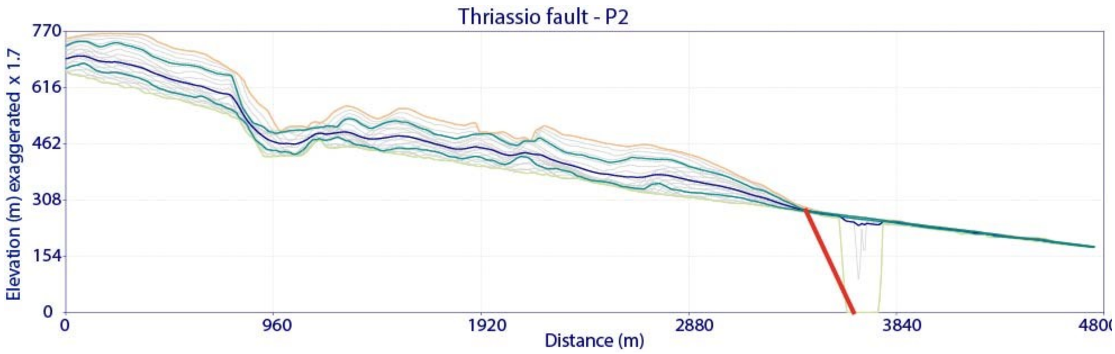
Thriassio fault - P2
Elevation (m) exaggerated x 1.7
770
616
462
308
154
0
0
960
1920
2880
3840
Distance (m)

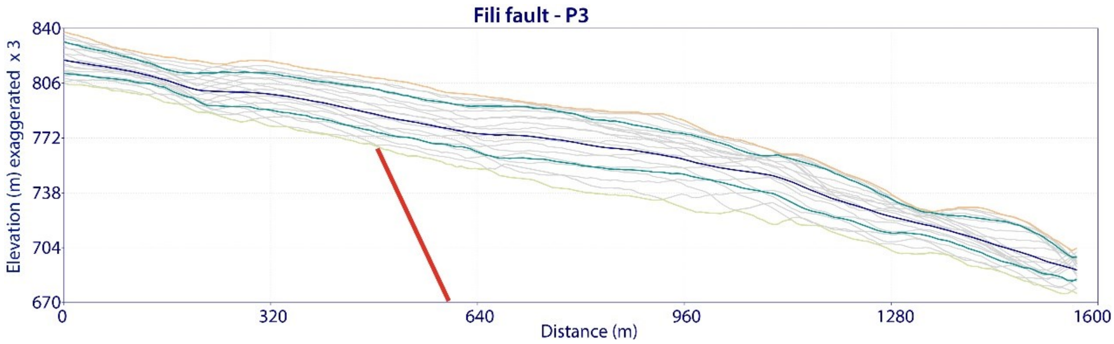
Fili fault - P3
Elevation (m) exaggerated x 3
840
806
772
738
704
670
0
320
640
960
1280
1600
Distance (m)

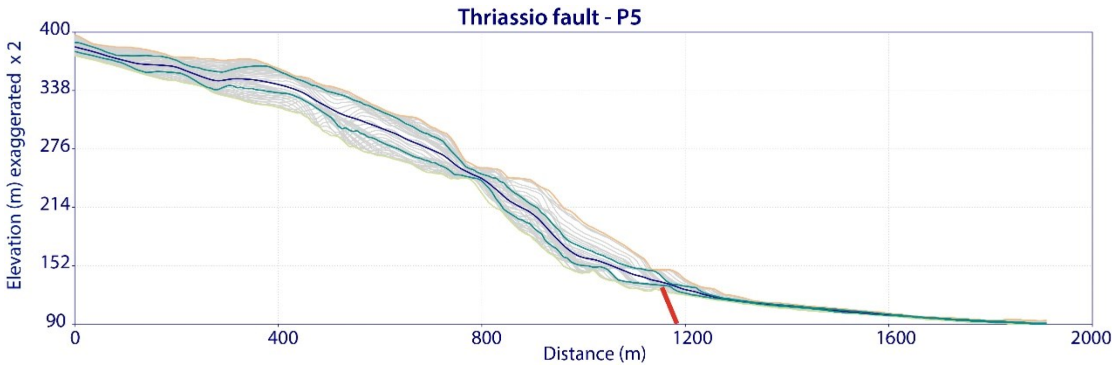
Thriassio fault - P5
Elevation (m) exaggerated x 2
400
338
276
214
152
90
0
400
800
1200
1600
2000
Distance (m)

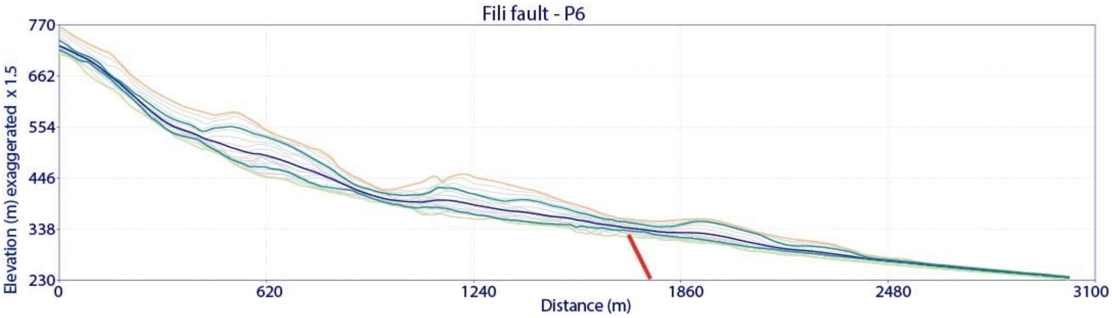

Figure 6.75: Swath topographic profiles within fault perpendicular stripes, following drainage network flowing perpendicular to the Thriassio fault (P1, P1, P5) and Fili fault (P3, P6). Stripe axes locations are displayed in Figure 6.74. Stripe width is 500 m. Y-axes are exaggerated. P4 shows a swath profile crossing perpendicular both faults. View looking towards East. Orange line represents the maximum elevation, light green line represents the lower elevation, blue line represents the mean elevation, dark green lines represent the Q1 and Q3 quartiles. The red line represents the faults.

In addition, a 3d model of the Fili fault scarp was developed (Figure 6.76), using a handheld 12 mp camera, and multiple 10 x 10 cm cartboards as ground control points with known relevant distances. In total, 94 images were acquired in oblique and nadir views, and were processed using Structure from Motion photogrammetry, in Agisoft Metashape Professional v 1.5. This process resulted to a model with measurable distances with an error of 1 cm. The slip was measured at 2.5 m, which confirmed the total slip measurements along the fault scarp in the field.

Regarding the slip rates of both faults, Ganas et al. (2004 & 2005) suggest a 0.17 mm/y slip rate for Fili fault, which is also supported by the 2.5 m slip along the fault scarp (Figure 6.77), as measured in the field. They also estimate a 0.27 mm/y slip rate for the Thriassio fault, which is reasonable, judging from the impact of the fault in the topography and the elevation variations.

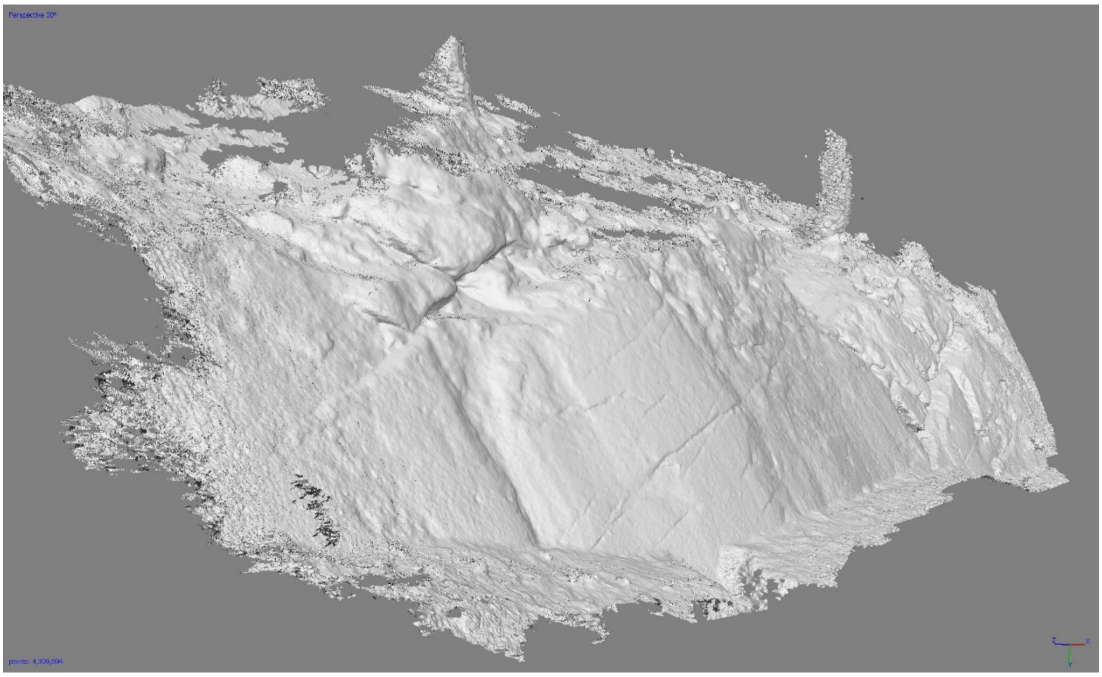

Figure 6.76: Oblique perspective view of a dense point cloud representing the Fili fault scarp. Solution flutes and small cracks are visible in the free face. 94 images acquired by a handheld 12 mp camera. The photogrammetric processing was carried out using Agisoft Metashape v1.5.0. Distances within the model are measureable with an error of 1 cm, based on the measured distances between control points. The maximum fault slip along the free face was measured at 2.5 m.

Figure 6.77: The Fili fault postglacial scarp. The slip along the free face is measured at 2.5 m.

6.2.12. The Kehriai fault

The Kehriai fault (or Kechriaie or Kechries or Kechriai or Kenchriaie in modern Greek : Κεχριές) is located at the farthest distance from the Attica region among all other faults. However, due to its proven activity and the fact that it is possibly related to repeated earthquake activity in the area over the recent past (Ambraseys, 2009; Tsapanos et al., 2010; Koukouvelas et al., 2017; Copley et al., 2018), it is included in the current fault database. The Kehriai fault is an E-W trending north dipping normal fault, which bounds the northern flanks of the Oneia Mt (Koukouvelas et al., 2017) (Figure 6.78). Abrupt slopes occur in the central and eastern part of the Oneia mt flanks, but a lower gradient is present in the western part, where the fault seems to terminate (Figure 6.79). The footwall comprises Middle Triassic – Lower Jurassic limestone, and the hanging wall consists of Plio – Pleistocene formations (Bornovas et al., 1969; Koukouvelas et al., 2017).

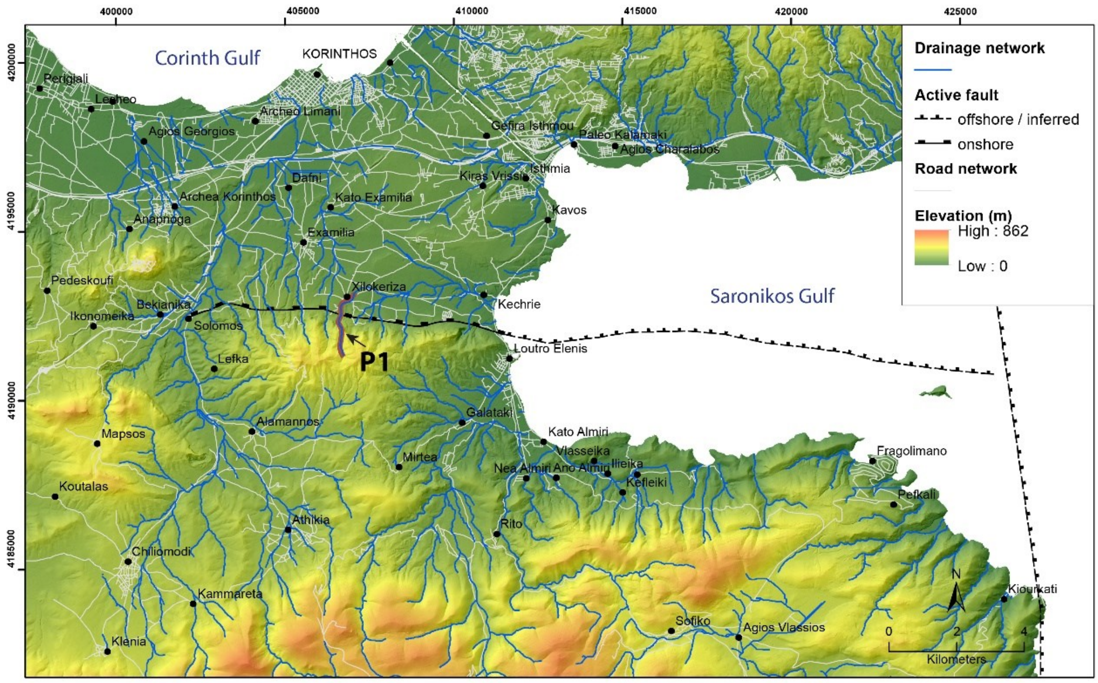

Figure 6.78: The SW dipping Kakia Skala fault in NW Attica (id = 13 on Table 6.1) and the main drainage network.

The fault parallel swath topographic profiles for the Kehriai fault reveals a triangular pattern, with higher altitude differences in the central part of the fault (Figure 6.80). A minimum total throw of 420 m is observed without considering the thickness of the sediments in the hanging wall. The high local relief values at the easternmost part of the swath profile may indicate that the fault continues to the east. One swath topographic profile following a small catchment flowing perpendicular to the fault trace reveals a considerable convexity (Figure 6.81) related to tectonic uplift at the central part of the fault.

Jackson et al. (1982) were the first to describe the Kehriai fault escarpment briefly and connected it to the deposition of the Neogene and Quaternary sediments, although they suggested that the fault activity is diminished. At the same time, they also related it with the subsidence of the ancient Kehriai harbour, which lies on the immediate hanging wall, as did Goldsworthy and Jackson (2001). Until recently, the activity of the Kehriai fault was unclear. For example, Dia et al. (1999) suggested that the fault is now inactive, and the absence of a clear post-glacial fault scarp (Papanikolaou et al., 2015) implied a very low slip-rate. However, there is a clear continuation of the fault towards the east, into the Saronikos Gulf, where it forms a clear rupture zone and offsets recent sediments (Papanikolaou et al., 1988 & 1989; Foutrakis & Anastasakis, 2020).

In 2017, Koukouvelas et al. presented the onshore fault's Quaternary slip history by applying a series of geomorphic indices and by conducting paleoseismic trenching at the immediate footwall of the fault. They suggested that the Kechriai Fault has a 0.15 mm/y slip-rate, with a recurrence interval ranging between 1300 and 4700 years and a maximum offset of 0.6 m per event. Considering that the fault continues offshore for several kilometres (Papanikolaou et al., 1988 & 1989; Foutrakis & Anastasakis, 2020) and that this fault is modelled as a single structure in the current study, the slip rate has been slightly increased to 0.2 mm/y.

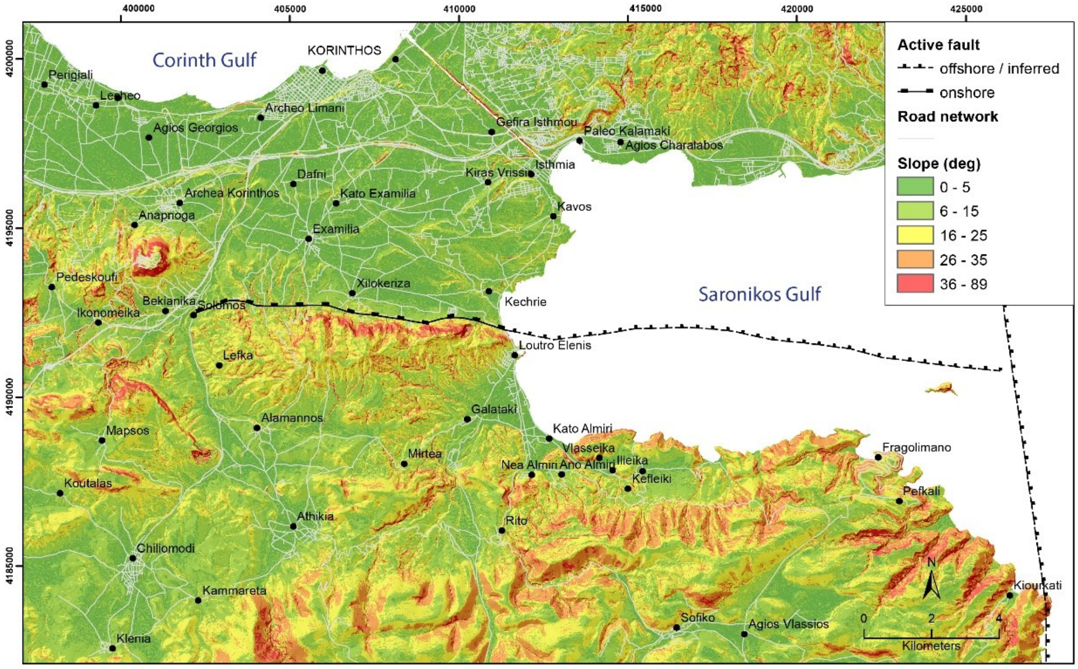

Figure 6.79: Slope map showing the slope changes related to Kehries fault (id = 19 on Table 6.1). Steeper slopes are observed at the footwall on the onshore part of the fault, which has created an E-W elongated abrupt slope that reaches the coastline.

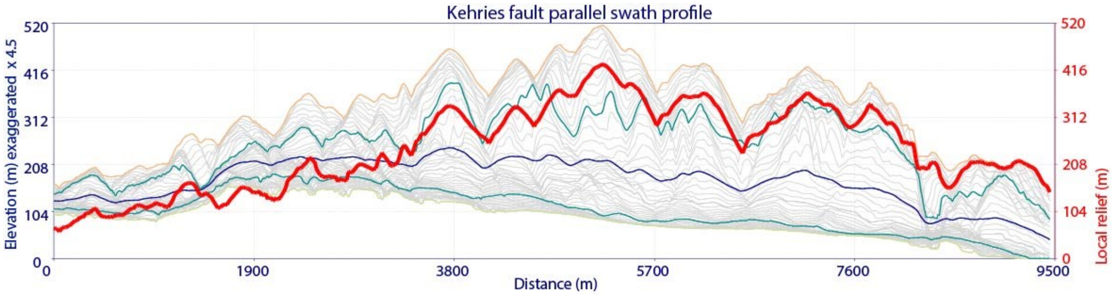

Figure 6.80: Swath topographic profile within a Kehries fault parallel stripe. Fault located at the middle of the stripe. Stripe width is 1600 m. Y-axis is exaggerated about 4.5 times. View looking towards the North (right part of the graph is located at the east tip of the fault). Orange line represents the maximum elevation, light green line represents the lower elevation, blue line represents the mean elevation, dark green lines represent the Q1 and Q3 quartiles, red line represents the local relief (maximum elevation minus minimum elevation at the same distance along the fault line). Note that the local relief is still high at the east fault tip (right end of the graph), possibly implying an eastward offshore continuation.

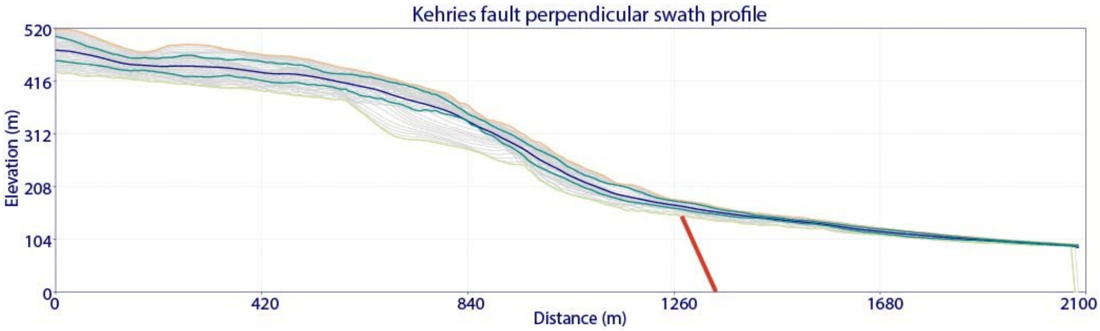

Figure 6.81: Swath topographic profiles within a fault perpendicular stripe, following drainage network flowing perpendicular to the Kehries fault. Stripe axis location shown in Figure 6.78. Stripe width is 500 m. View looking towards West. Orange line represents the maximum elevation, light green line represents the lower elevation, blue line represents the mean elevation, dark green lines represent the Q1 and Q3 quartiles. The red line represents the Kehries fault.

6.2.13. The Dafni fault

The Dafni fault, also known as Dafnes (Tsodoulos et al., 2008) or Dafnoula fault (Ganas et al., 2005), is a NE- SW trending NW dipping normal fault that forms the southeast boundary of the Asopos river basin (Figure 6.82). Its footwall comprises Triassic limestones, and the hanging wall is filled with Pliocene sediments and recent Holocene deposits (Dounas, 1971). The fault extends until the Erythres town towards SW where it seems to terminate. The adjacent Erythres fault (see also Section 6.2.6) is traced further South, a couple of kilometres away. The NE tip of the Dafni fault coincides with a protuberance of the bedrock, and there is no visible sign of continuation further NE. Abrupt slopes appear only in the central part of the fault (Figure 6.83), where the drainage network has deeply incised the exposed bedrock. It is possible that Erythres (Section 6.2.6) and Dafni faults may form a larger fault zone. However, the morphology of the north dipping boundary of the Asopos basin implies that two different segments exist. Furthermore, there is no clear evidence of simultaneous rupture during an earthquake event. As a result, Erythres and Dafni faults are studied separately.

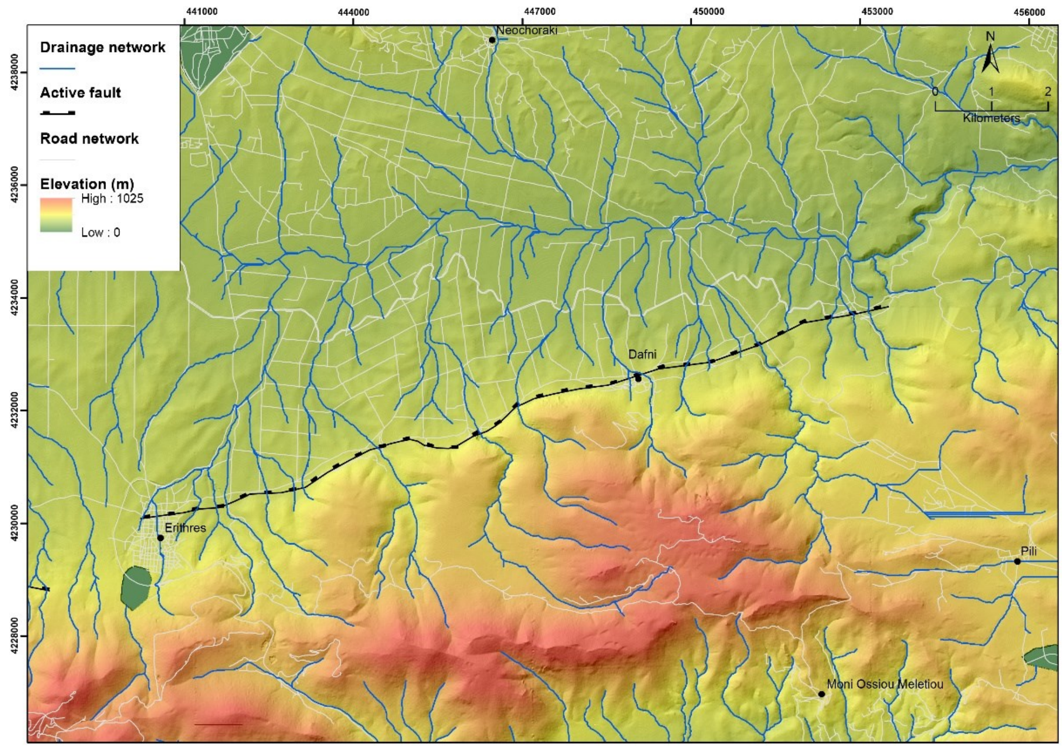

Figure 6.82: The NW dipping Dafni fault in NW Attica (id = 13 on Table 6.1) and the main drainage network.

A swath profile in a fault-parallel direction shows a triangular shape of the local relief curve, with the maximum elevation differences occurring in the central part of the fault (Figure 6.84), although the footwall is deeply incised. The elevation difference between the footwall and the hanging wall is up to 360 m. The activity of the fault is also supported by the convexities in the swath topographic profiles within fault perpendicular stripes at the centre and the tips of the fault (see Figure 6.86 for swath profile locations and Figure 6.85 for the profiles). The shape of the profiles reveals higher uplift rates at the central part of the fault. However, part of the topographic differences could be attributed to the different lithology (see also Whittaker et al., 2008).

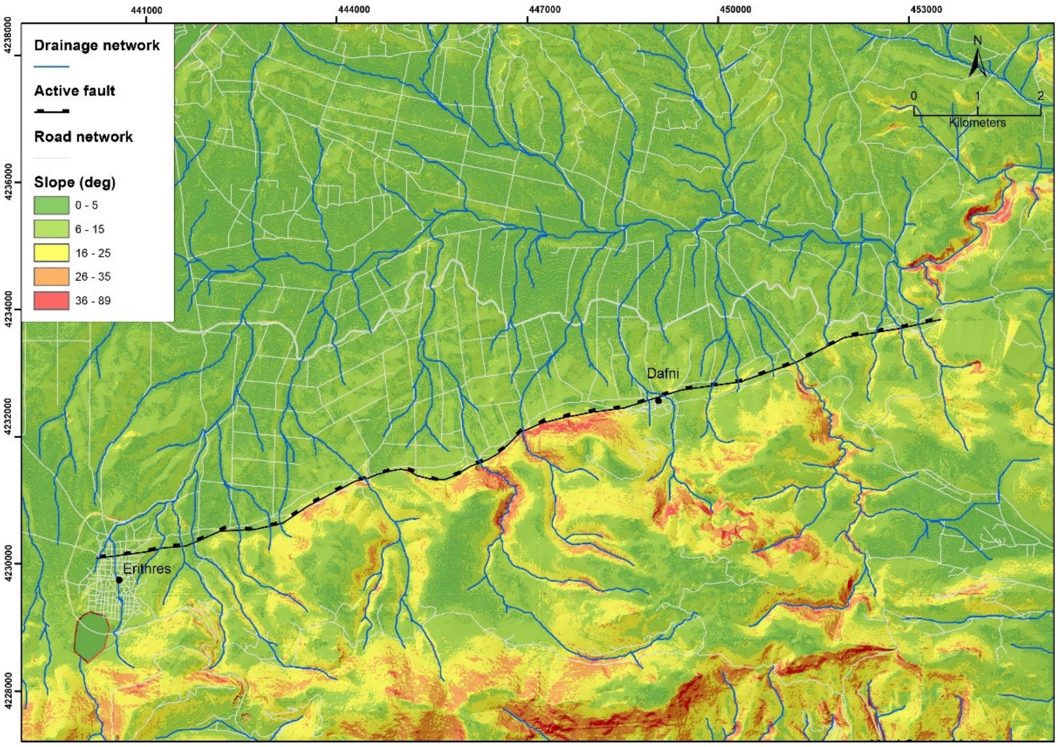

Figure 6.83: Slope map showing the abrupt slopes and deep river incision in the central part of the Dafni fault footwall. The fault's hanging wall has a gentle slope towards NW.

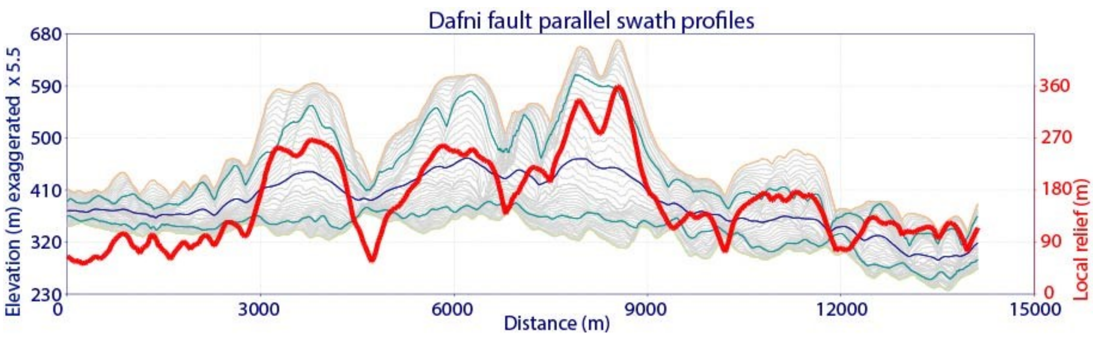

Figure 6.84: Swath topographic profiles within a Dafni fault parallel stripe. Fault located at the middle of the stripe. The stripe width is 2000 m. Y-axis is exaggerated about 5.5 times. View looking towards the North (right part of the graph is located at the east tip of the fault). The orange line represents the maximum elevation, the light green line represents the lower elevation, the blue line represents the mean elevation, dark green lines represent the Q1 and Q3 quartiles, the red line represents the local relief (maximum elevation minus minimum elevation at the same distance along the fault line).

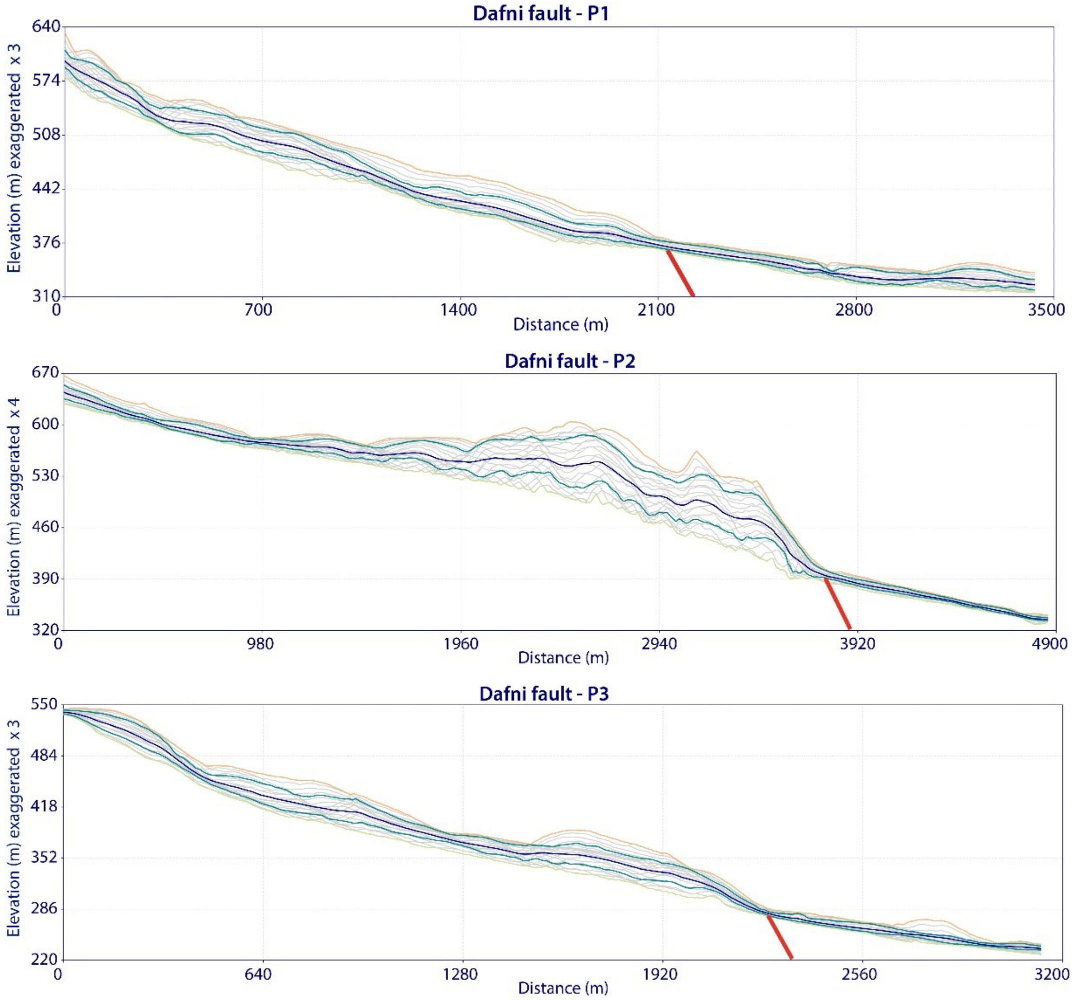

Figure 6.85: Swath topographic profiles within a fault perpendicular stripe, following drainage network flowing perpendicular to the Dafni fault. The stripe axis location is shown in Figure 6.86. The stripe width is 400 m. Y-axis is exaggerated about 3 times for P1&P1 and 4 times for P2. View looking towards SW. Orange line represents the maximum elevation, the light green line represents the lower elevation, the blue line represents the mean elevation, dark green lines represent the Q1 and Q3 quartiles. The red line represents the Dafni fault.

The fault is 14 km long and exhibits a postglacial scarp for several kilometres, even if it is intensely eroded and degraded in most cases. Well preserved but possibly older fault scarp with a height of several meters is found in higher altitudes at the central part of the fault. A fresh scarp free face outcrops in the vicinity of the Dafnes village, approximately 170 m north of the northern border of the limestone, implying a possible migration towards the north.

Four locations were selected for detailed fault scarp topographic profiles to measure the fault's postglacial throw. The locations of the profiles are shown in Figure 6.86. TP1 (Figure 6.87) is located in a fault bend close to the western tip of the Dafni fault. TP2 is near the central part of the Dafni fault and represents two distinct locations, namely TP2-a (Figure 6.88) and TP2-b (Figure 6.90), approximately 20 m apart. TP3 (Figure 6.91) is located near the East tip of the fault.

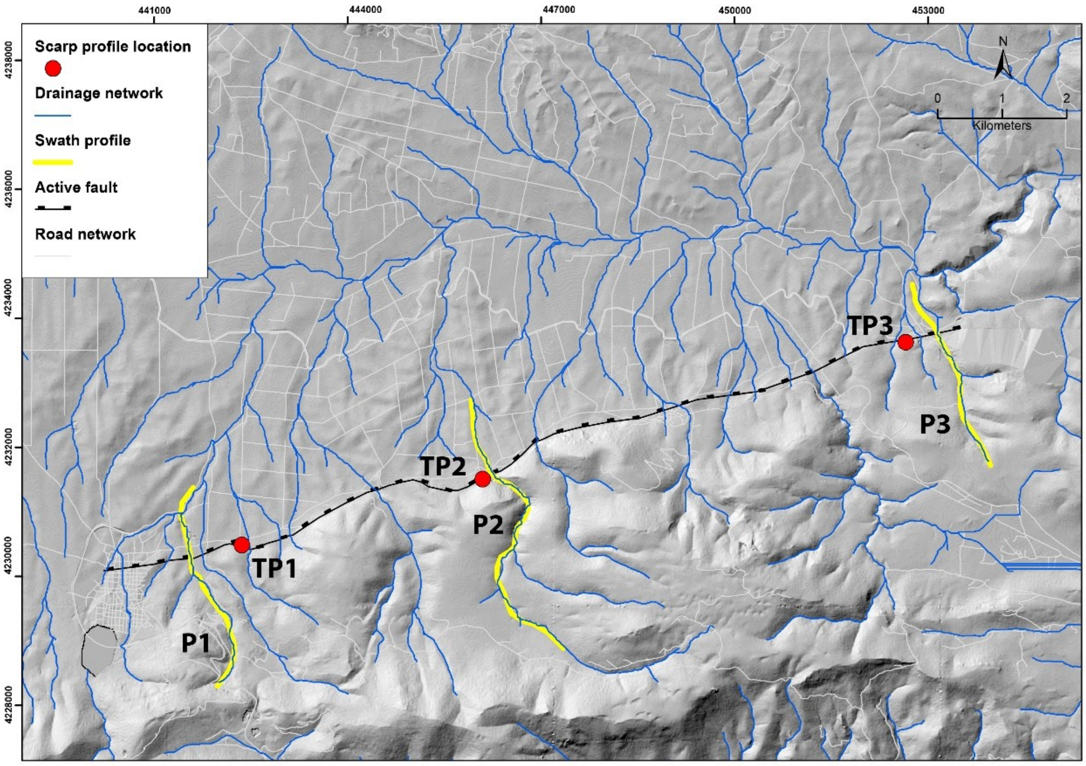

Figure 6.86: Shaded relief map of the Dafni fault area, showing the main drainage network, the location of the fault – perpendicular swath profiles (P1 – P3) and the locations where a topographic scarp profile was made.

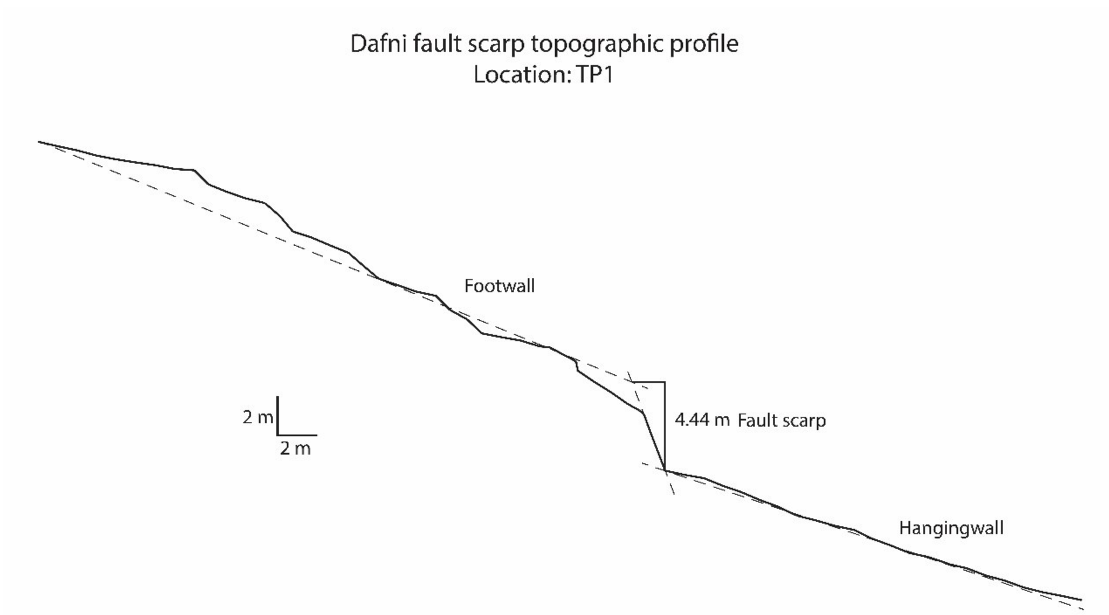

Figure 6.87: Topographic profile crossing the Dafni fault scarp at location TP1. Measurements obtained using a clinometer and a 1 m stick (see also Papanikolaou et al., 2005 for details in methodology). The profile reveals the fault scarp height and geometry. The total throw is measured at 4.44 m. Location of the profile is shown in Figure 6.86.

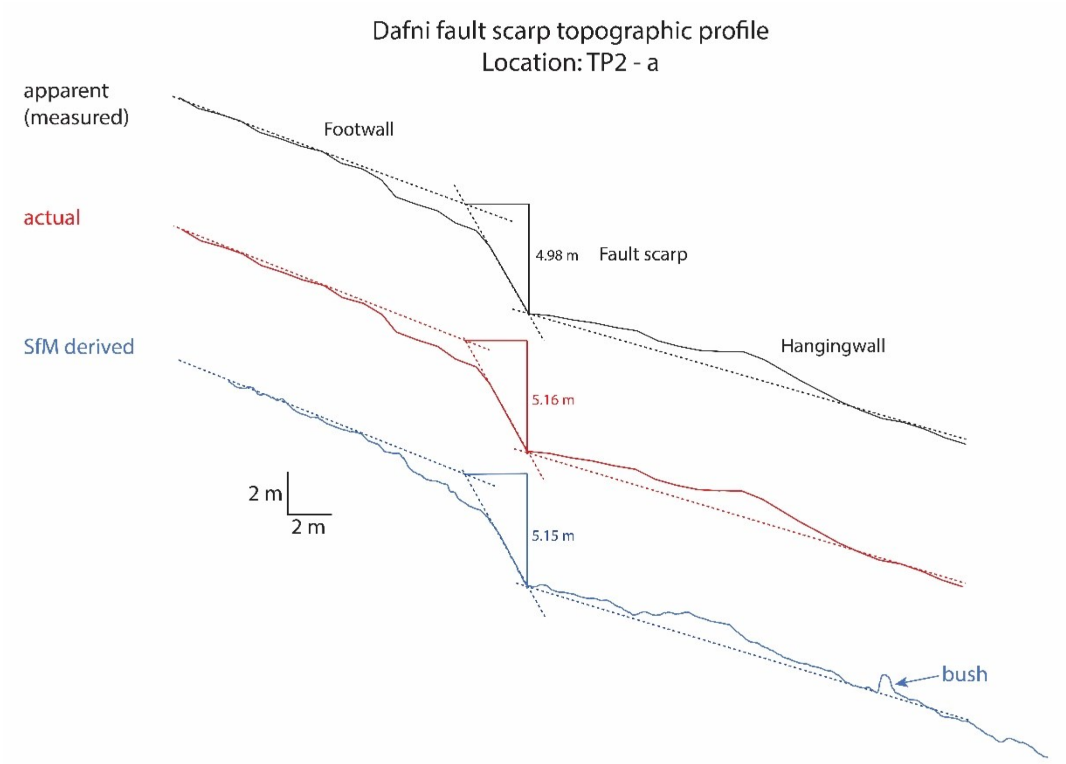

Figure 6.88: Topographic profiles crossing the Dafni fault scarp at location TP2-a. Top measurement (black) obtained using a clinometer and a 1 m stick. Middle profile (red) represents the profile after the angles corrections (see text for details). Lower profile (blue) produced from SfM derived DSM. The total throw is measured at 5.16 m. Profile location is shown in Figure 6.86.

All profiles were measured using a 1 m long stick and a clinometer, in a fault perpendicular direction. At the location TP2-a, a high-resolution DSM was constructed (Figure 6.89), using Structure from Motion photogrammetry (see also Alexiou et al., 2021). An autonomous UAV flight was used, with an 80% image overlapping and custom made ground control points (GCPs) with known distances from each other. This resulted to an estimated error of 5 cm, based on the GCP distances as measured within the model. The orthomosaic of the area revealed that the actual direction of the manmade profile was oblique to the fault strike (75^{o} instead of 90^{o}). As a result, the initial profile had an apparent throw, which was corrected by applying simple trigonometric rules.

Furthermore, a new profile was constructed in GIS environment, this time using the high - resolution DSM which was extracted from the SfM photogrammetry. As shown in Figure 6.88, there are slight differences among the throw values in the three profiles, of the order of a few centimetres, which do not affect the final throw rate values. All three profiles are presented together in Figure 6.88.

The maximum measured throw is 7.2 m in TP2-b, which implies a postglacial throw rate of 0.48 mm/y.

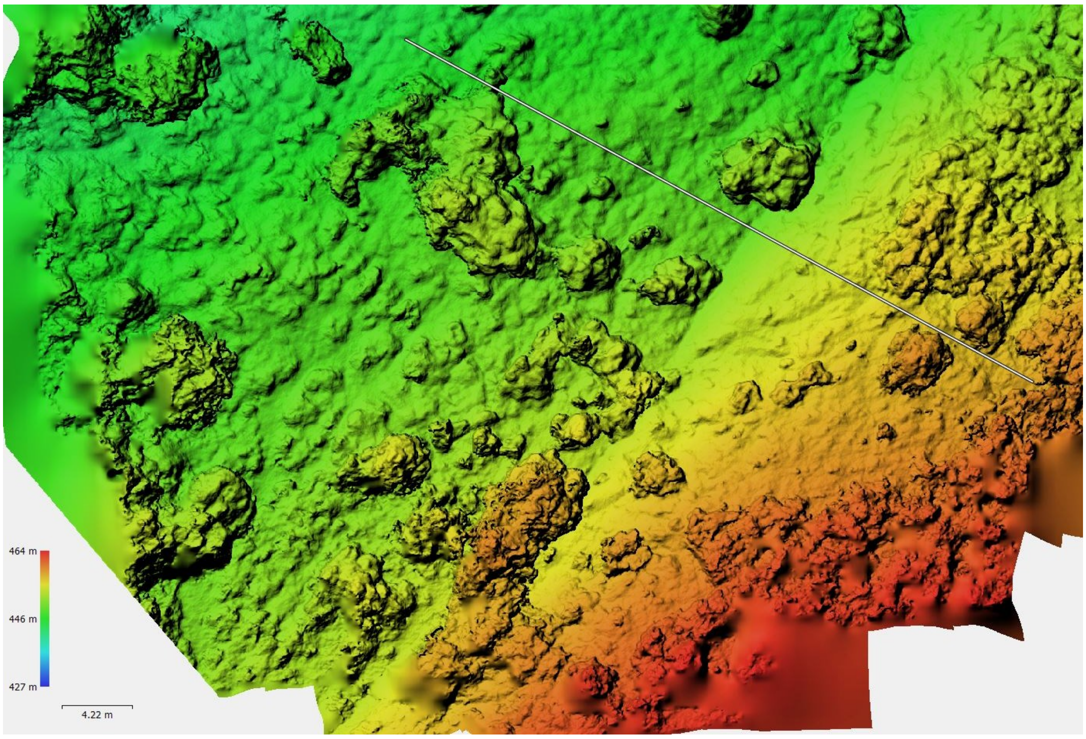

Figure 6.89: High resolution (4.35 cm/px) Digital Surface Model of the TP2-a location. 101 images with 80% overlapping were acquired by a small UAV with a 12 mp camera. The photogrammetric processing was carried out using Agisoft Metashape v1.5.0. The vegetation was extracted in the final stage of the profile processing, except for a bush in the hanging wall (lower profile in Figure 6.88), which was intentionally kept as a reference. The thin grey line represents the profile axis.

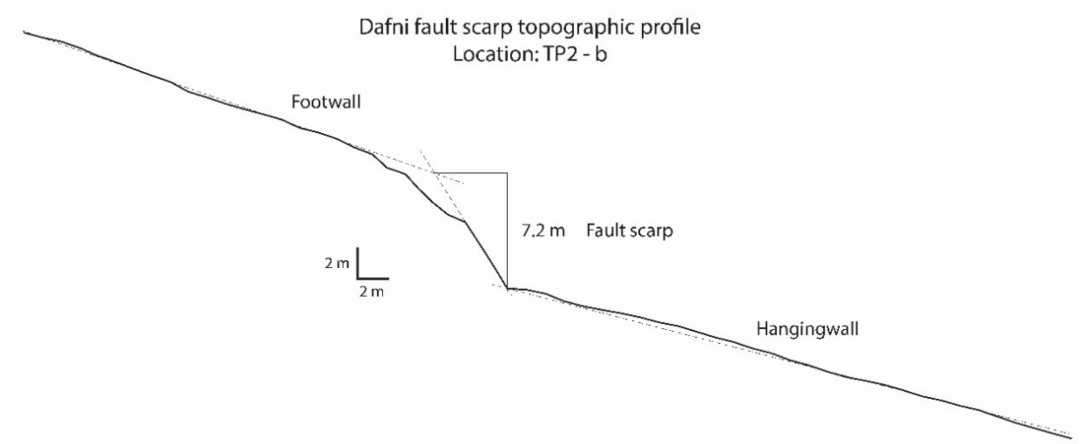

Figure 6.90: Topographic profiles crossing the Dafni fault scarp at location TP2 – b, approximately 25 m west of TP2 – a. Measurements obtained using a clinometer and a 1 m stick (see also Papanikolaou et al., 2005 for details in methodology). The profile reveals the fault scarp height and geometry. The total throw is measured at 7.2 m. Profile location is shown in Figure 6.86.

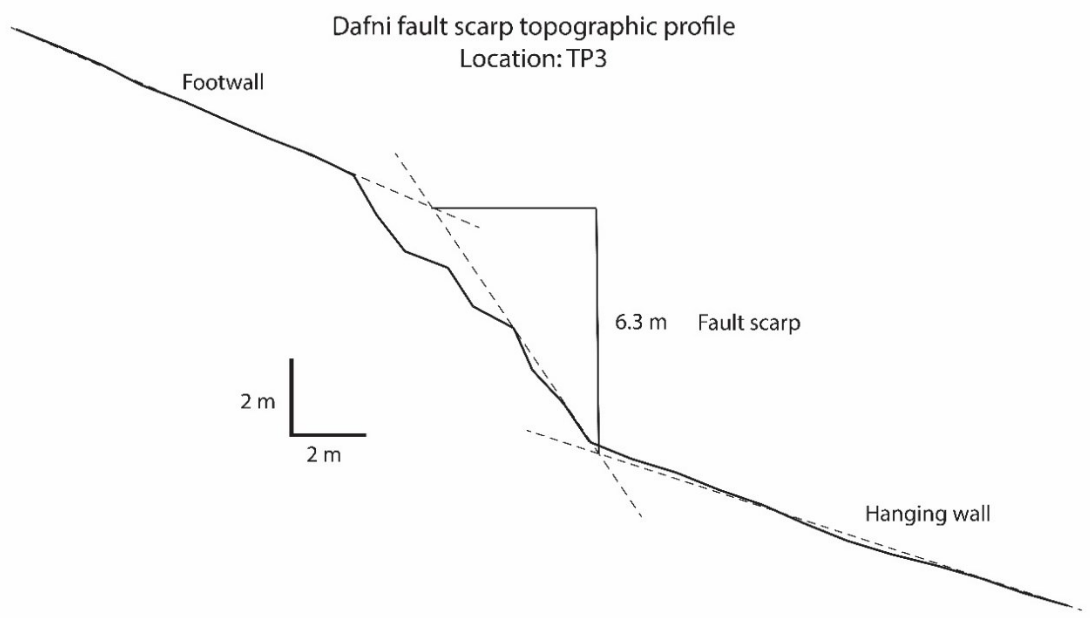

Figure 6.91: Topographic profiles crossing the Dafni fault scarp at location TP3. Measurements obtained using a clinometer and a 1 m stick (see also Papanikolaou et al., 2005 for details in methodology). The profile reveals the fault scarp height and geometry. The total throw is measured at 6.3 m. Profile location is shown in Figure 6.86.

6.3. Active faults database for the Attica mainland

The active faults database contains 24 faults that: a) are long enough to produce surface ruptures and b) can sustain damage in the Attica mainland in case of earthquake rupture (Figure 6.92).

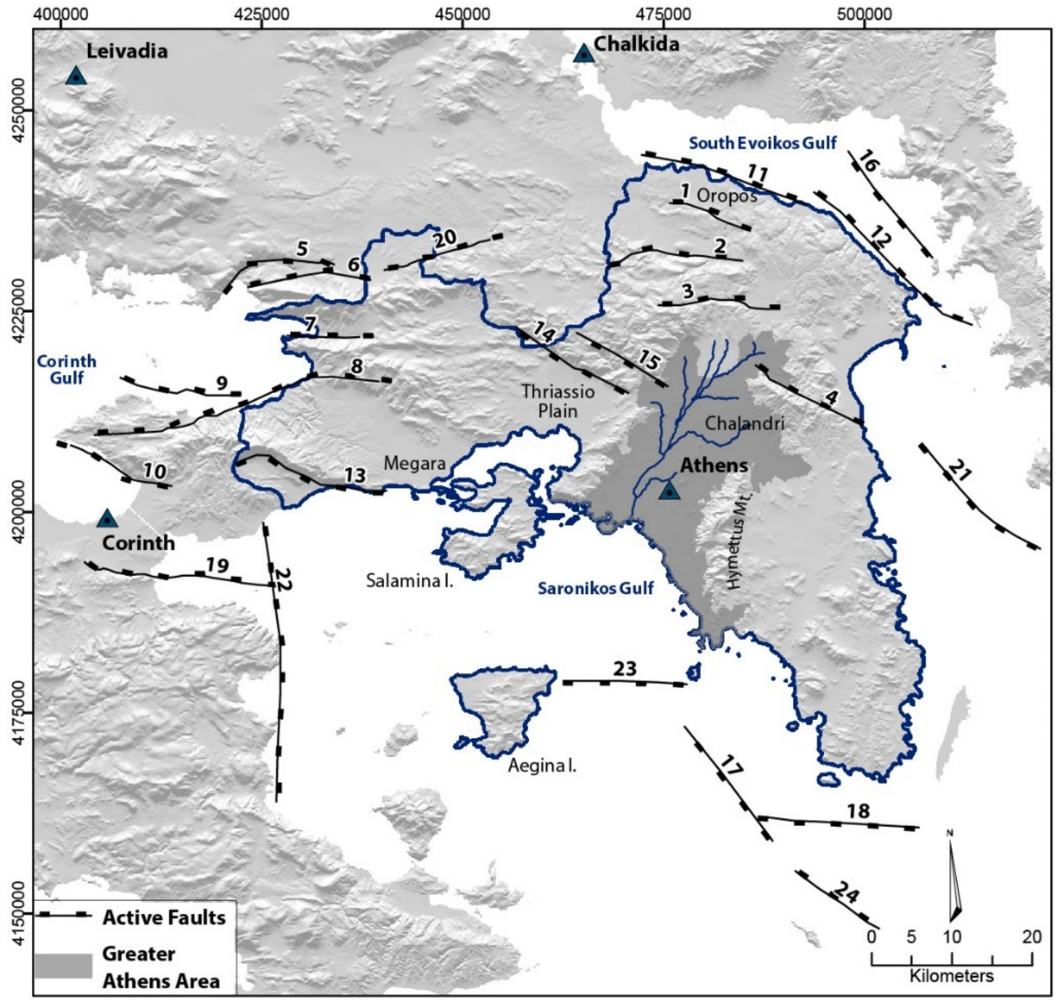

Figure 6.92: Map of active faults that can sustain damage within the region of Attica. No faults are located in the Athens Plain, except for the southeastern tip of the Fili fault (id = 15 on Table 6.1), but with low slip rate faults (see Figure 6.93b). Fault labels refer to the Id numbers on (Table 6.1).

Fault lengths and their characteristics regarding their kinematics and slip rates are shown in Table 6.1.

The average expected earthquake magnitude is Mw 6.5, based on empirical relationships between rupture lengths and earthquake magnitudes. However, these faults are located away from the Athens plain, except for the southeastern tip of the Fili fault (id = 15 in Table 6.1, see Figure 6.92). Overall, active faults are mostly located outside the Athens basin and most faults that are proximal to the basin are dipping away from it (e.g. id 3, id 4, id 23). As a result, seismic hazard and earthquake effects within the Athens basin are expected to be less severe and governed also by the bedrock geology characteristics. Moreover, most of the densely inhabited areas in the Greater Athens Area lay on the footwall of the neighbouring active faults (id = 3, 4 on Table 6.1, see Figure 6.92 and Figure 6.93). Fault lengths vary from 9 up to 35km. Faults that exceed 30 km in length were assumed to rupture in floating earthquakes of magnitude Ms = 6.65±0.15. As a result, the expected earthquake magnitude of the South Alkyonides Fault system (id = 8 in Table 6.1) is not proportional to its length (Roberts, 1996). Instead, floating earthquakes of magnitude 6.7 along the strike of the fault are modelled, which is in agreement with the 1981 earthquake (Jackson et al., 1982).

The majority of the active faults that affect the region of Attica do not exceed the relatively low slip-rate values of 0.3mm/yr, which also agrees with Ganas et al. (2005) findings. However, the faults activated during the 1981 earthquakes events (South Alkyonides Fault segments) reach or exceed slip-rate values of 2mm/yr, thus the mean slip-rate value of the faults that affect Attica is ~0.35mm/y (Figure 6.93b). This low mean slip-rate implies large reccurence intervals between earthquakes and highlights the importance of fault based approaches.

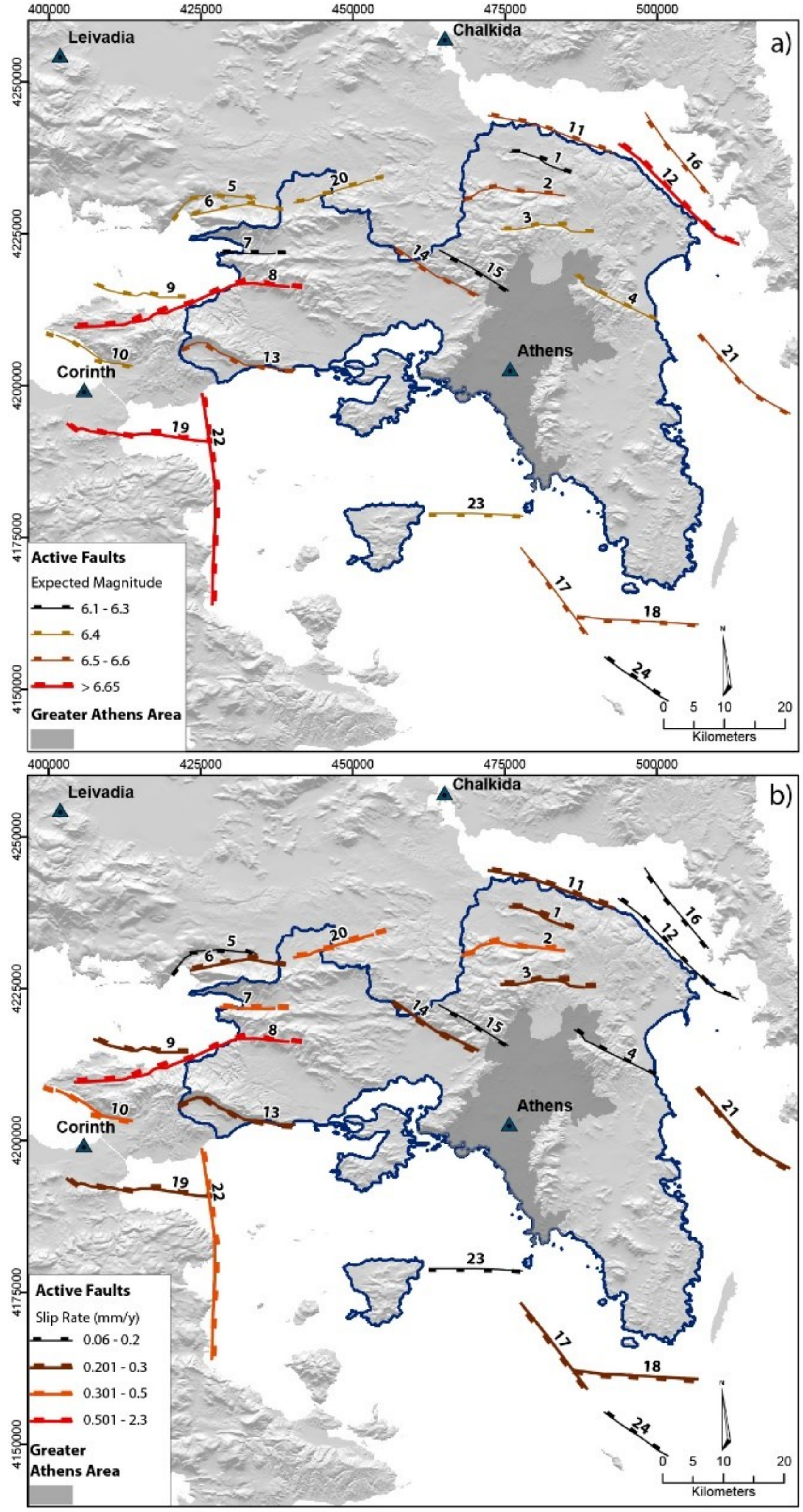

Figure 6.93: Map of active faults that can sustain damage within the region of Attica. a) Different fault symbols represent the maximum expected magnitude that these faults can generate. b) Different fault symbols represent different slip-rate categories. Slip rates govern earthquake recurrence. As slip rates increase, average earthquake recurrence intervals tend to decrease.

Table 6.1: Fault characteristics used for extracting the earthquake recurrence per site over the last 15 kyrs. Expected Magnitude and Maximum Displacement per Event values are based on Wells and Coppersmith (1994) equations. Slip rate column refers to short term where available, or long term slip rate values, induced from published papers and neotectonic maps (see text for details). *Id* numbers refer to the map displayed in Figure 6.92. Fault characteristics are based on the following sources (numbers correspond to the "Source" column): *1)* Papanikolaou et al., 1988; *2)* Official Neotectonic map of Saronikos Gulf (Papanikolaou et al., 1989); *3)* Official Neotectonic map of South Evoikos Gulf (Papanikolaou et al., 1989) ; *4)* Official Neotectonic map of East Attica (Papanikolaou et al., 1995); *5)*Pantosti et al., 1996; *6)*Collier et al., 1998; *7)*Morewood and Roberts, 1999; *8)*Morewood and Roberts, 2001; *9)*Pavlides et al., 2002; *10)*Goldsworthy et al., 2002; *11)*Benedetti et al., 2003; *12)*Ganas et al., 2004; *13)*Chatzipetros et al., 2005; *14)*Ganas et al., 2005; *15)*Kokkalas et al., 2007; *16)*Papanikolaou and Papanikolaou, 2007b; *17)*Sakellariou et al. 2007; *18)*Rontoyianni and Marinos, 2008; *19)*Tsodoulos et al., 2008; *20)*Roberts et al., 2009; *21)*Roberts et al., 2011; *22)* Foutrakis, 2016, *23)* Grützner et *al*., *2016* and *24)* Mechernich et al., 2018. *f*: fieldwork findings.

Id	Length (km)	Postglacial Throw (m)	Expected Magnitude	Slip Rate (mm/y)	Maximum Displacement per Event (m)	Source	Fault name
1	9.7	4.5	6.2	0.30	0.32	*10,16,23, f*	Milesi
2	17.7	6.0	6.5	0.40	0.80	*10,12,14, 16, f*	Malakasa
3	14.2	4.5	6.4	0.30	0.58	*12,16*	Afidnes
4	14.8	1.4	6.4	0.10	0.61	*16, f*	Dionysos
5	14.5	3.0	6.4	0.20	0.59	*11,13,15, 19,20*	Kaparelli
6	15.7	4.5	6.4	0.30	0.67	*19, f*	Erythres
7	9.2	7.5	6.1	0.50	0.30	*14, f*	Aigosthena
8	32.8	34.5	6.7	2.30	2.04	*5,6,7,8,20,21,24,f*	South Alkyonides FZ
9	15.1	4.5	6.4	0.30	0.63	*17*	Strava
10	13.9	7.5	6.4	0.50	0.56	*21, f*	Loutraki
11	21.8	4.5	6.6	0.30	1.10	*16*	Oropos
12	26.2	1.5	6.7	0.10	1.45	*3,4*	S.Evoikos 1
13	19.6	4.5	6.6	0.30	0.94	*14,18*	Kakia Skala
14	16.5	4.1	6.5	0.27	0.72	*9,14*	Thriassio
15	13.3	2.6	6.3	0.17	0.52	*9,14,f*	Fili
16	17.0	2.4	6.5	0.16	0.76	*3,4*	S.Evoikos 2
17	18.1	4.4	6.5	0.29	0.83	*1,2,22*	Saronikos 1
18	19.3	3.7	6.6	0.25	0.92	*1,2,22*	Saronikos 2
19	23.7	4.4	6.7	0.20	1.25	*21*	Kehries
20	13.9	7.0	6.4	0.48	0.56	*f*	Dafni
21	19.6	4.4	6.6	0.29	0.93	*3,4*	Petalioi
22	35.0	3.3	6.7	0.22	2.25	*1,2,22*	Saronikos 3
23	15.5	1.0	6.4	0.06	0.66	*1,2,22*	Aigina
24	12.8	1.5	6.3	0.10	0.49	*1,2,22*	Saronikos 4

7. Fault specific seismic hazard maps

Two different types of fault specific seismic hazard maps were developed during this PhD. The first type represents fault seismic hazard maps which are based on a single fault, and forms the simple case study. This applies to the Sparta fault, which was analysed in Section 6.1. Four detailed seismic hazard maps were compiled for the region of Attica, one for each of the intensities VII – X (MM), based on all 24 faults presented in Section 6.3. These maps are much more complicated than the single-fault ones, since they offer the cumulative impact from all seismic sources in each specific locality. They offer a locality specific shaking recurrence record, which represents the long-term shaking record in a more complete way than the historical/instrumental catalogue since they incorporate several seismic cycles of the active faults. In addition, two maps showing the maximum expected intensity and maximum recurrences distribution offer information for the worst-case scenario and the locations of high shaking frequencies respectively.

7.1. Seismic hazard maps for the Sparta fault

A high spatial resolution fault specific seismic hazard map for the Sparta fault was created, showing the intensity IX recurrence in each locality close to the fault. The input data came from interpretations on geological and morphological conditions of the Sparta Basin and important work already available in the literature. Moreover, the tectonic geomorphologic analysis in Section 6.1 provided a useful tool for the fault delineation and the conclusion of the actual fault length.

The town of Sparta lies closer to the centre of the Sparta fault hangingwall and is founded on Quaternary sediments, whereas surrounding villages are founded on alluvial fans and triangular facets. The maximum expected intensities based on the surface geology and assuming earthquakes of expected magnitudes M=7 are shown in Figure 7.1.

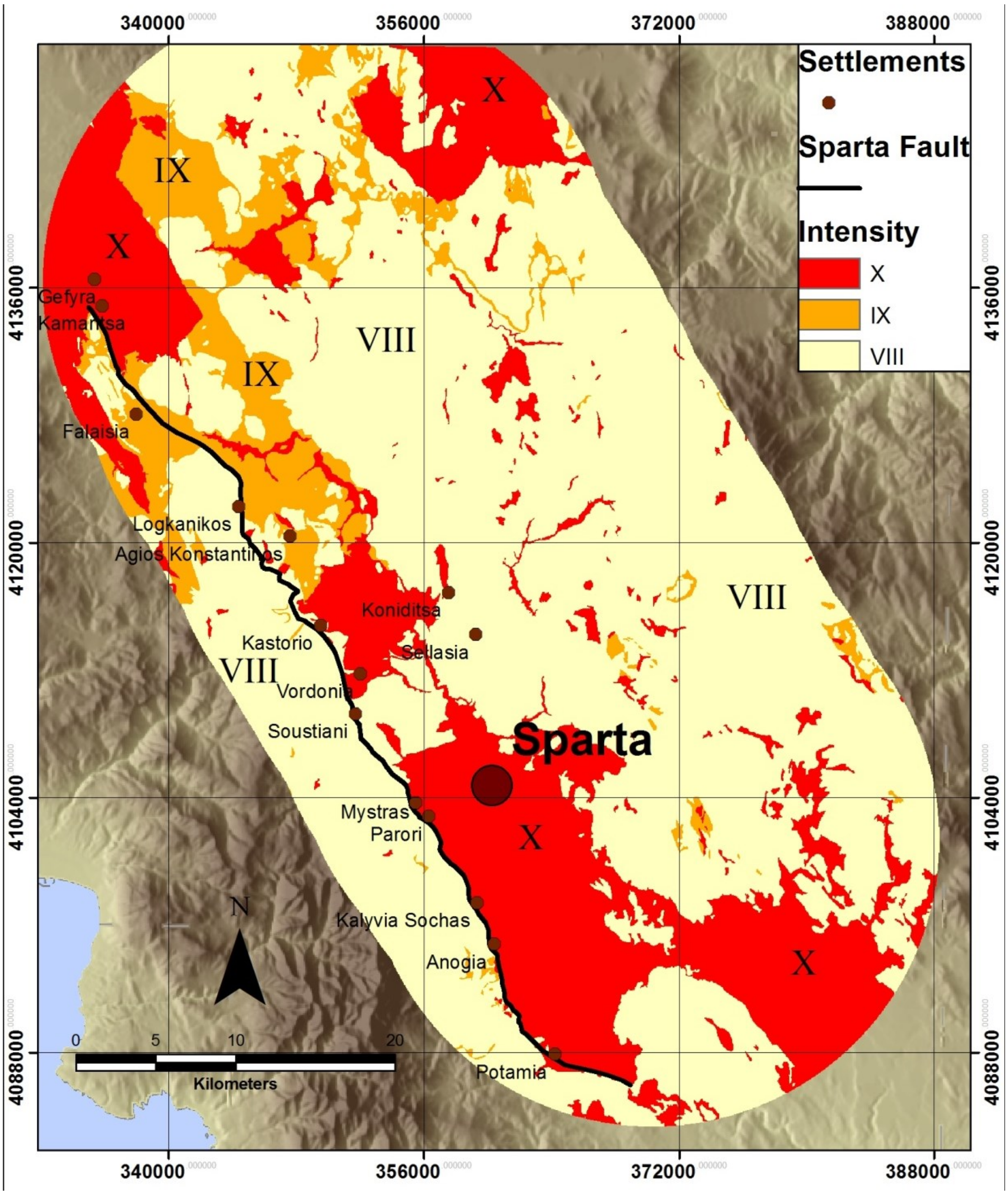

Figure 7.1: Map for the Sparta Basin showing the maximum expected intensities distribution. The maximum intensity locations are defined by the proximity to the Sparta fault and the bedrock geology. Figure reproduced after Papanikolaou et al., 2013

The addition of the recurrence intervals resulted in a new map that shows how many times each location has been shaken at a certain intensity value over a fixed time period (e.g. since the last glaciation), which can be easily transformed into a map of recurrence intervals. The value of the initially used intensity is IX, with a radius of 18 km, as calculated using Theodulidis (1991) equations. However, average changes in intensity associated with different types of surface geology are taken into account so that the maximum expected intensity reaches the value of X in the Quaternary and Pliocene deposits, while remains IX for flysch/foredeep formations and reduces to VIII for the bedrock.

Since the recurrence of the maximum expected intensities for the last 15±3kys is calculated using the intensity value IX, a new seismic hazard map was constructed. In this map, the same interaction of surface geology with the isoseismals is used, but the resulting intensity VIII, which comes out from the combination of alpine bedrock and intensity IX, is now eliminated. This results in a seismic hazard map displaying the localities that will receive enough energy to shake at intensities ≥ IX over 15±3kys (Figure 7.2).

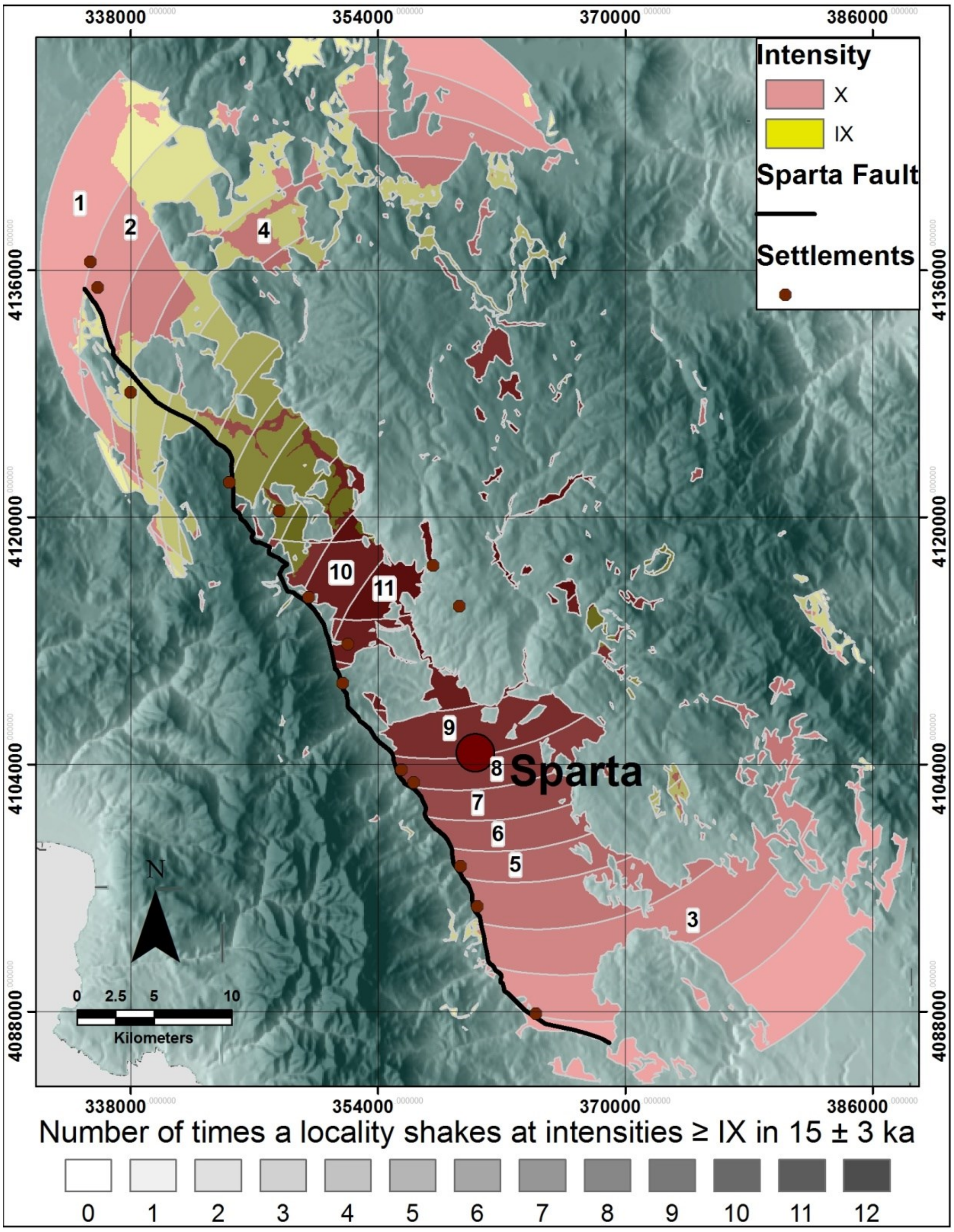

Figure 7.2: Seismic hazard map for the Sparta Basin, showing how many times a locality receives enough energy to shake at intensities ≥IX in 15±3kyrs, after considering the bedrock geology and assuming a circular pattern of energy release, with a 18 km radius of isoseismal IX. Figure reproduced after Papanikolaou et al., 2013.

As shown in Figure 7.2, the recurrence of intensity ≥ IX increases towards the center of the Sparta fault. This agrees with the assumed triangular throw profile of the fault and the observation of maximum throw in the fault centre. The town of Sparta is located closer to the hangingwall centre and is founded on Quaternary sediments. Thus it has received enough energy to shake at intensity X for 8 or 9 times over the 15±3kys.

The GIS construction of this high spatial resolution seismic hazard map allows files transformations and exchange through different files formats. Since this mapping method is implemented in real conditions, a visualization of this map in a satellite view is very useful, combining the high spatial analysis with the existing situation. The easiest application for such visualizations is the Google Earth. The conversion of ArcGIS shapefiles to Keyhole Markup Language (kml) files was achieved using the free online Geospatial Data Converter (Geoconverter) and the result was the seismic hazard map overlay on the Google Earth Globe map (Figure 7.3). This is also important because both the public and decision makers are familiar with Google Earth.

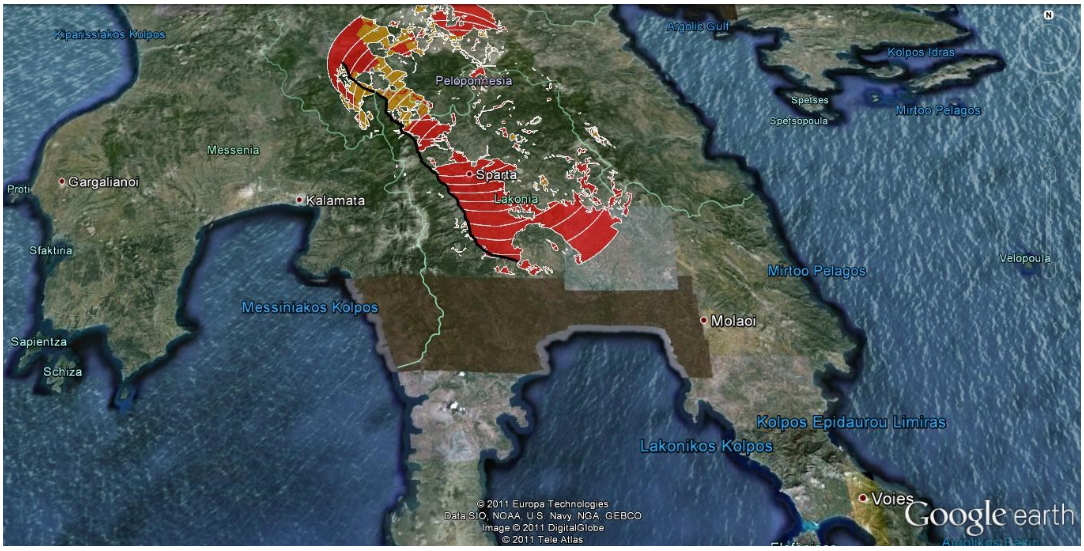

Figure 7.3: Seismic hazard map for the Sparta Fault, overlaid in the Globe map, provided by Google Earth.

This also allows the interpretation of the existing manmade constructions, such as towns and village boundaries (e.g. buildings stock) and road networks and other critical infrastructures, in relation to the maximum expected intensities and their recurrence over 15±3kyrs (Figure 7.4).

Figure 7.4: Detailed map detail of the overlaid seismic hazard layer of the Sparta fault in the Google Earth environment. High spatial analysis of the seismic hazard map provides detailed visualization in relation to the variations of recurrence and intensities affecting manmade constructions, such as the Sparta city boundaries and road network. The northern part of the town of Sparta has a higher recurrence of intensity X over 15±3kyrs.

The town of Sparta is situated in Quaternary deposits, and is expected to receive a X macroseismic intensity for M = 7, which is in agreement with the historical record. However, as shown in Figure 7.2 and in greater detail in Figure 7.4, the number of times it receives this intensity over 15±3 kyrs varies, depending on the different parts of the city. The location where the central part of the town is now located is expected to receive enough energy to shake at intensity X, 8 times over 15±3kyrs, while the northern part is expected to receive one more time (9 times over 15±3 kyrs).

For the whole Sparta Basin, this information can be easily transformed into recurrence intervals, which is the main input data for the probabilistic seismic hazard analysis. Simple calculations show that the town of Sparta experiences a destructive event similar to 464 B.C., approximately every 1792 ± 458 years (Papanikolaou, et al., 2013).

7.2. Seismic hazard maps for the Attica region

Six high spatial resolution fault specific seismic hazard maps for the Attica region are presented. Section 7.2.1 offers a seismic hazard map that displays the maximum expected intensities without showing information about their recurrences. Sections 7.2.2 - 7.2.5 present separate seismic hazard maps for each intensity (VII – X), with the corresponding recurrence values, so that they can be used for probabilistic seismic hazard assessment. Section 7.2.6 offers the distribution of the maximum recurrences for each intensity across the Attica region.

7.2.1. Maximum expected intensity map

Figure 7.5 shows a combination of the intensity layers, providing information for the maximum expected intensities for each locality in the Attica mainland. It is important to note that this map contains no information about the intensity recurrences. Instead, it displays the maximum ground motions that any locality seems to have experienced over 15 kyrs, even if they had occurred only once. As a result, this map is valuable for defining the worst-case scenario in terms of the maximum ground motions expected.

Higher intensities (IX – X) are observed proximal to the large active faults, mostly in the northern and western parts of the Attica mainland. Intensity X seems to occur in areas covered by loose sediments that are close to major faults. Localities that are also covered by loose sediments but lie in a further distance from large faults or close to smaller faults, seem to have at least once been shaken at intensity IX. It is important to note that many localities in the Greater Athens Area seem to have received enough energy to shake at intensity IX over the last 15 kyrs. On the other hand, it seems that the largest part of the Greater Athens has not experienced destructive ground motions and the maximum expected intensities are VIII or VII.

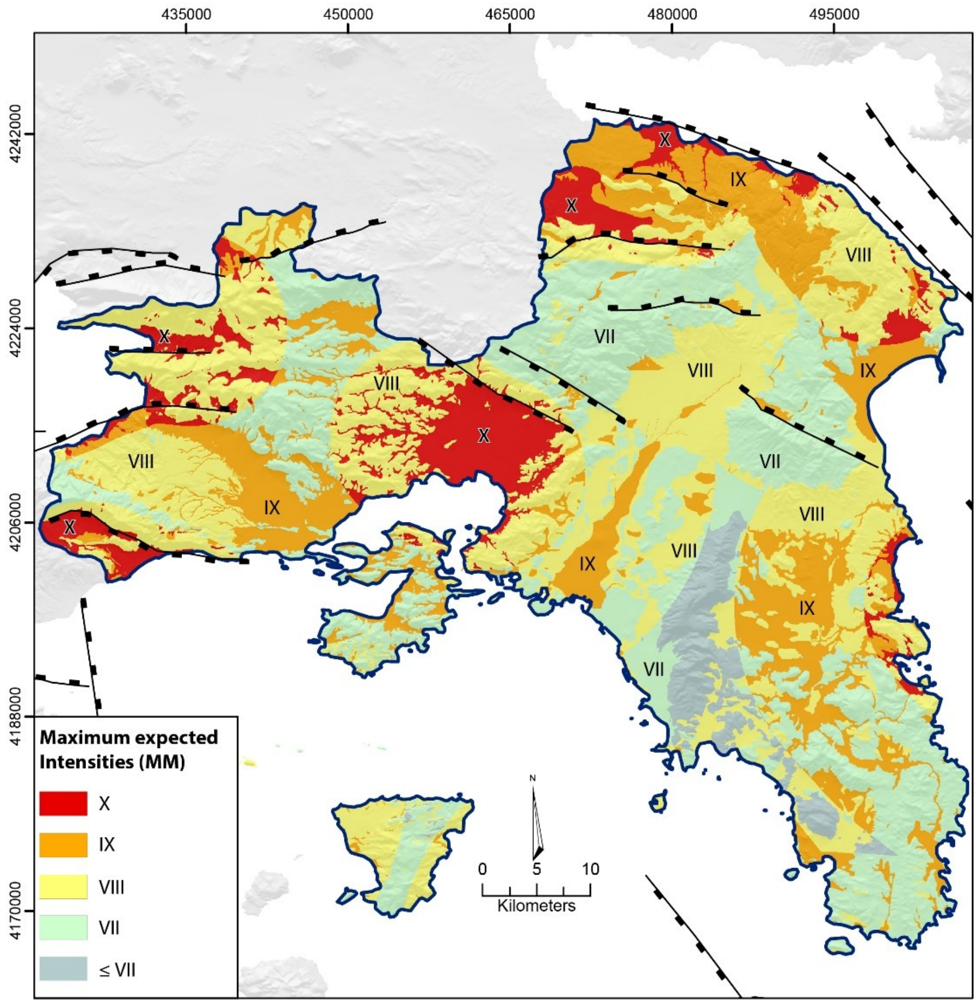

Figure 7.5: Maximum expected intensities distribution for each locality in the Attica mainland. They are defined by the proximity to the active faults and the surface geology. Figure reproduced from Deligiannakis et al., 2018a.

7.2.2. Intensity X

Intensity X is mostly observed in limited areas in the hanging wall of large faults, covered by loose sediments (Figure 7.6). Surface geology plays the most critical role for the intensity X occurrence, as it increases by a single value the calculated isoseismals of intensity IX that only larger faults can produce in case of seismic rupture. The highest recurrence of intensity X (>20 times in the past 15 kyrs) is observed only in the western part of Attica, close to the Corinth Gulf. This is attributable to the high slip rate value of the fault that ruptured during the 1981 earthquake (South Alkyonides Fault system), which is capable of producing earthquakes of magnitude M = 6.7. A second peak (11 times in the past 15 kyrs) in recurrence is observed in the northern coastal zone (Oropos area). This area is affected by two significant faults (faults n.2 and 11 on Table 6.1) and is also covered by loose alluvial and Plio – Pleistocene sediments. Large areas are expected to have been shaken in such intensities in the Thriassio plain, west of the Greater Athens Area, but their recurrence is relatively low, due to the low slip rates of the neighbouring faults. No intensity X is expected for the

Greater Athens Area, as it is located far away or in the footwall of potentially damaging long faults (id = 2, 8, 11, 12, 14 on Table 6.1).

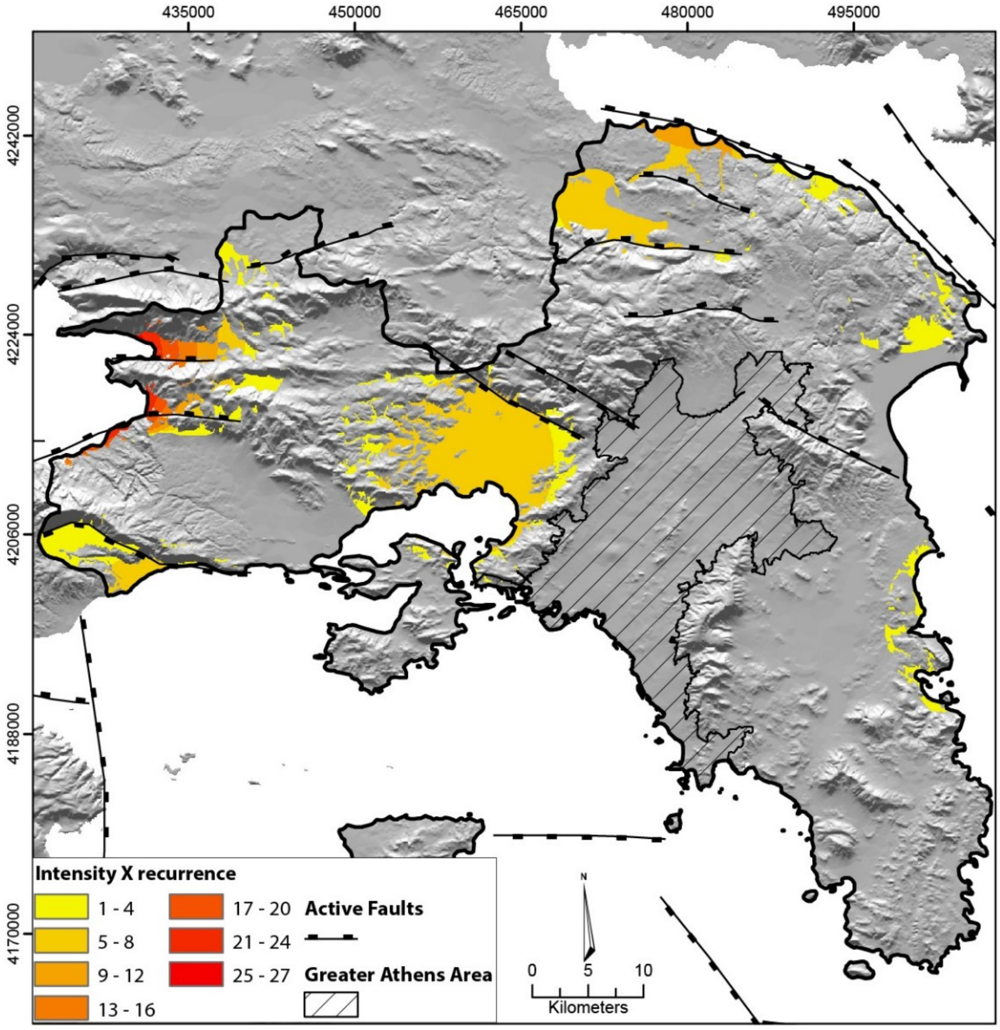

Figure 7.6: Seismic hazard map of Attica, showing the estimated site-specific recurrence for intensities X (MM). The Greater Athens Area is not expected to have experienced such intensities during the last 15 kyrs. Figure reproduced from Deligiannakis et al., 2018a.

7.2.3. Intensity IX

Intensity IX is expected to have occurred in larger areas of Attica and in higher recurrence levels, compared to intensity X (Figure 7.7). This is attributed to the fact that the calculated isoseismals of the shorter faults (< 16 km) are also taken into account in the modeling procedure. Intensity VIII isoseismals are amplified by one value when applied to loose sediments and are then added to the larger faults impact. Even though recurrence values are relatively low, it is important to note that intensity IX is expected up to 11 times in the western parts of the Greater Athens Area and only 2 times in sparse areas in the eastern parts of the Athens plain. The loose alluvial sediments of the Kifissos River which flows near the centre of Athens, along with the Upper Pliocene – Lower Pleistocene lake sediments at Chalandri and surrounding areas (Papanikolaou et al., 2004, see Figure 6.92 for locations) increase the intensity values. Severe damages were inflicted during the Athens 1999 Mw 5.9 earthquake in such geological formations

(Lekkas, 2000). The highest recurrence (77 times, or nearly 195 year return period) is observed in the western part of Attica, due to the highly active South Alkyonides Fault. Moreover, the seismic hazard is also increased close to the Saronic Gulf coastline, which is expected to experience intensity IX with a minimum return period of 288 years. The northern part of Attica is mostly affected by Afidnai, Avlonas – Malakasa, Milessi and Oropos faults (faults nos 3, 2, 1 and 11 respectively in Table 6.1), which explains the relatively high intensity IX recurrence (up to 37 times, or 405 year return period).

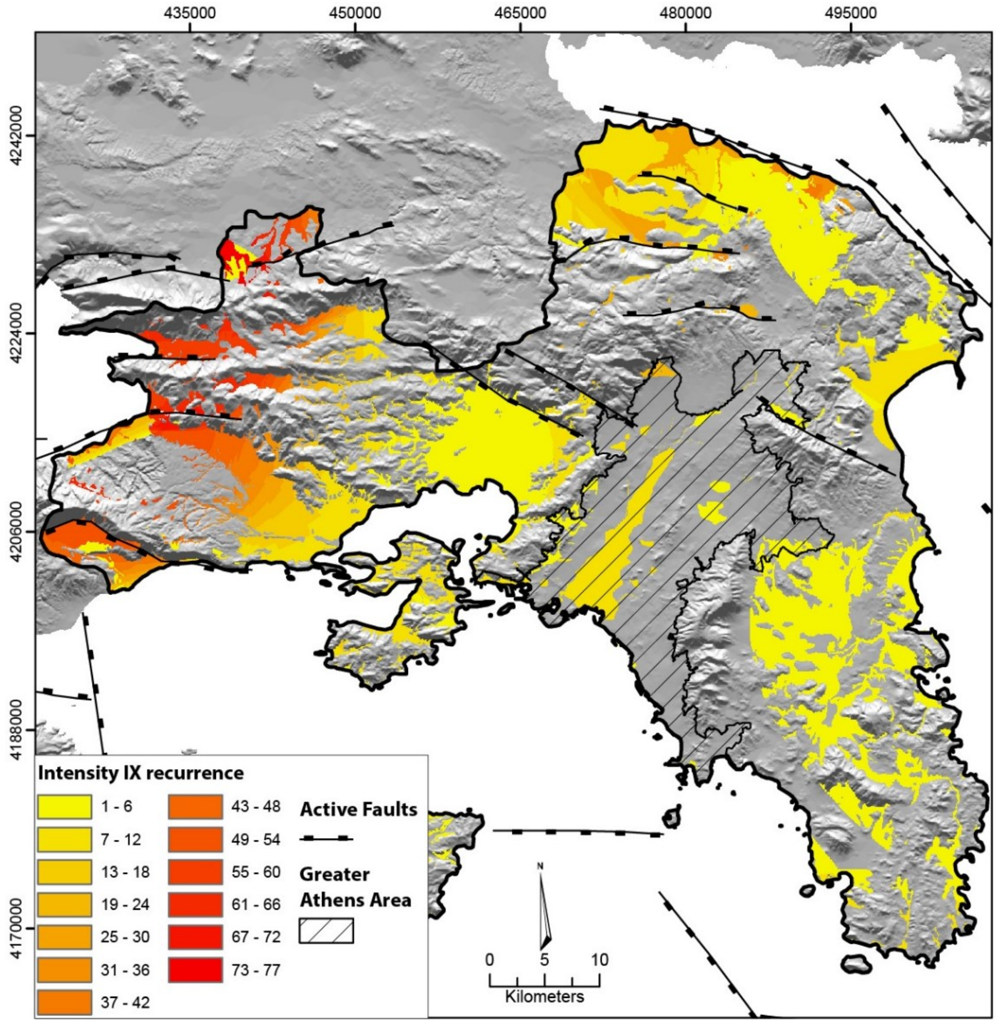

Figure 7.7: Seismic hazard map of Attica, showing the estimated site-specific recurrence for intensities IX (MM). Figure reproduced from Deligiannakis et al., 2018a.

However, as also indicated in the intensity X spatial distribution (Figure 7.6), it seems that the central Athens area is not expected to have experienced high intensities during the last 15 kyrs, which is in agreement with Ambraseys and Psycharis (2012) conclusions for lack of evidence for destructive events in the ancient and historical old part of the town for the last 2300 years. Nevertheless, the expansion of the city through the last decades has increased both the vulnerability and the hazard in particular areas with poor geotechnical conditions.

7.2.4. Intensity VIII

Intensity VIII covers larger areas in the Attica mainland because of the larger isoseismals for intensity VIII on the larger faults. As a result, there is also an increase in intensity VIII recurrence in the Attica mainland, compared to the intensities X and IX (Figure 7.8). The highest recurrence, outreaching 100 the times over 15 kyrs, seems to have occurred in the Megara basin, NW of the Salamina island, mostly because this area is now partly affected by the highly active South Alkyonides fault system, as intensity VIII occurs in the distance between 11 and 25 km from the large faults (see Table 5.1). Indeed, during the 1981 event, when this fault system ruptured, Megara basin suffered serious damage, assessed as intensity VIII (Ambraseys and Jackson, 1981; Carydis et al., 1982; Antonaki et al., 1988; Papanikolaou et al., 2009). Moreover, the majority of the central and the western part of the Greater Athens Area seems to have experienced intensity VIII, 20 times during the last 15 kyrs on average, due to the low slip rates of the faults that affect this part of Attica.

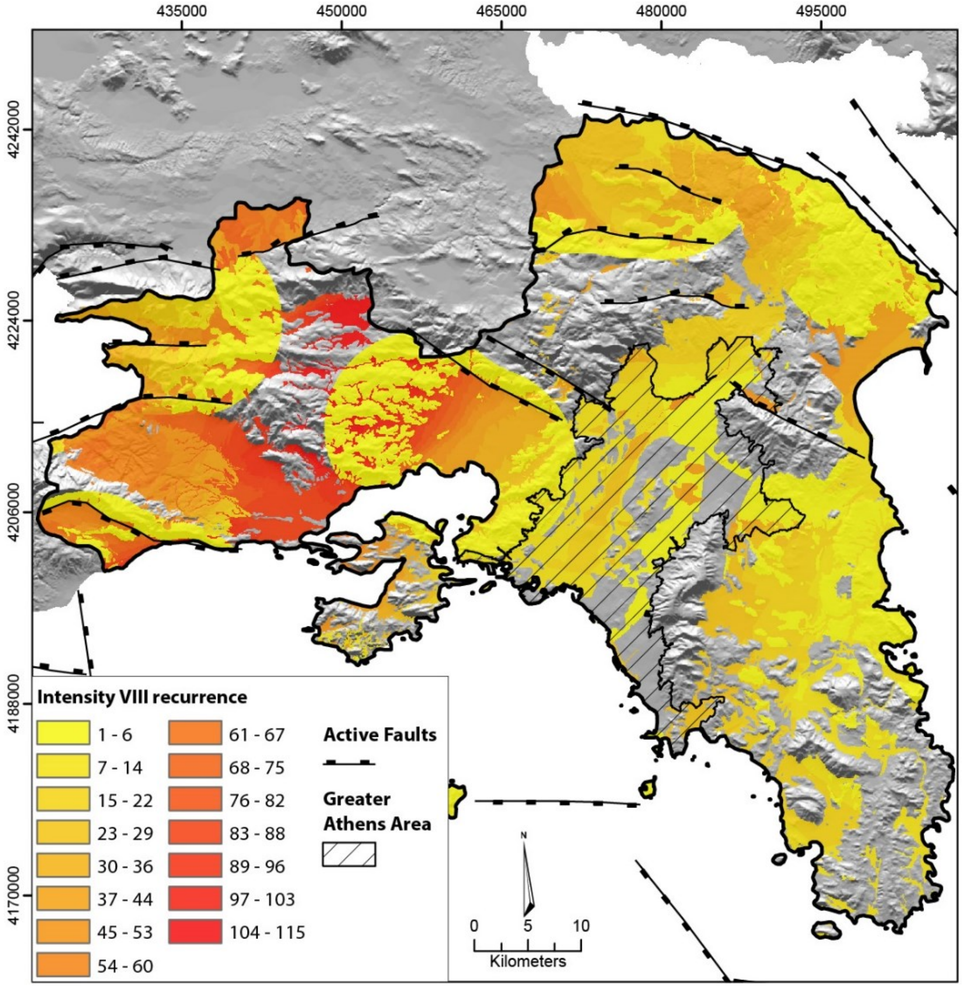

Figure 7.8: Seismic hazard map of Attica, showing the estimated site specific recurrence for intensities VIII (MM). Figure reproduced from Deligiannakis et al., 2018a.

7.2.5. Intensity VII

Almost every part of the Attica mainland seems to have experienced intensity VII at least once during the last 15 kyrs, except for the Hymettus Mountain, which seems that it has not experienced intensity VII due to its bedrock geology (mostly marbles and schists) and its considerable distance from active faults (Figure 7.9). Recurrence levels in the Attica mainland reach up to 150 times, mostly observed in the centre of the Greater Athens Area in an NNE – SSW general direction. Even distant faults seem to affect this part of Attica, which lies in conjunction with the majority of the active faults' lower intensities isoseismals. The seismic risk is increased in this densely inhabited area, although small industries and warehouses are also located near the Kifissos River. It is noteworthy that during the Athens 1999 Mw 5.9 earthquake, severe and moderate damages were recorded in the northern parts of the Kifissos riverbed, in an NNE – SSW general direction of the intensity contours (Lekkas, 2001). In addition, intensities of VII and in some districts, VIII, were assessed during the February 1981 earthquake sequence.

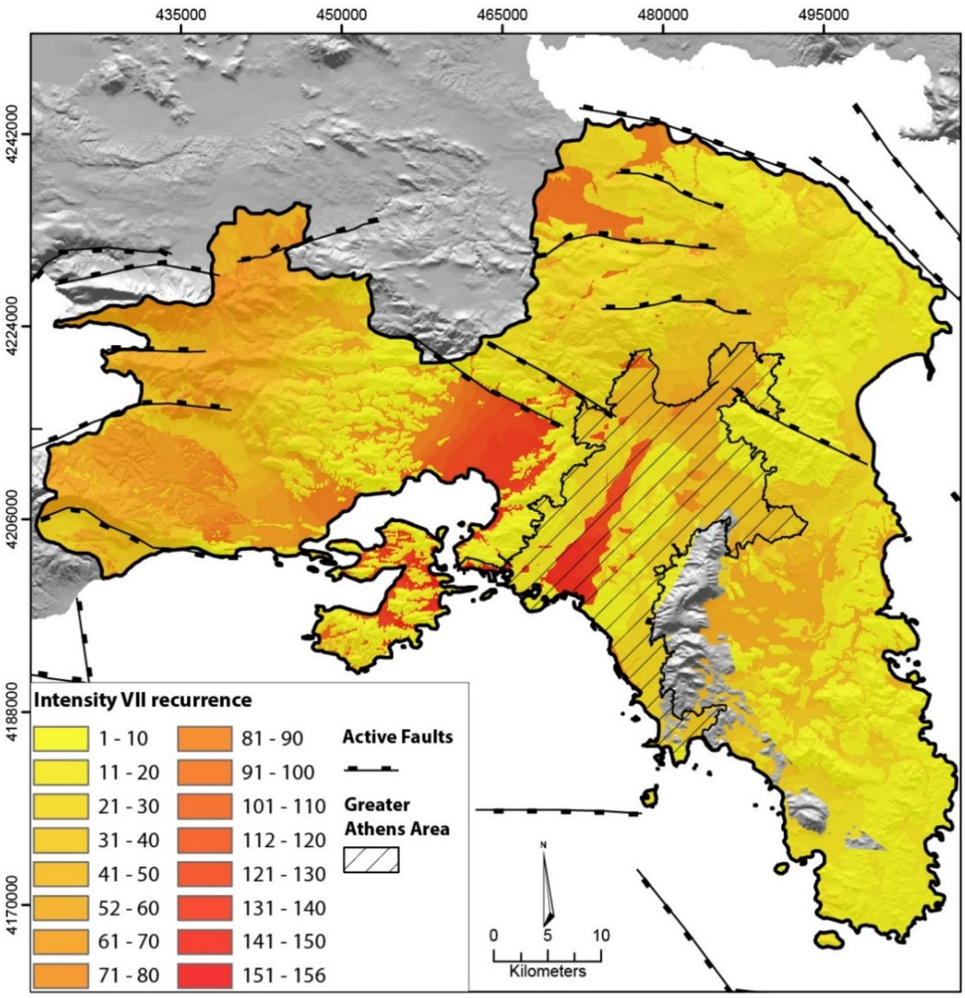

Figure 7.9: Seismic hazard map of Attica, showing the estimated site-specific recurrence for intensities VII (MM). Nearly every suburb of the Greater Athens Area has experienced such intensities in the past 15 kyrs, including the recent 1981 earthquake sequence and the 1999 event. Figure reproduced from Deligiannakis et al., 2018a.

7.2.6. Maximum recurrences distribution

The top quintile of the intensities VII – X recurrences is displayed in Figure 7.10. This map shows the highest (top 20%) recurrences from each intensity and the corresponding spatial distribution in different colours. Thus, it depicts the locations where the peak recurrences of each intensity are observed, rather than the most hazardous areas in terms of maximum expected intensities. For example, the southern suburbs of the Greater Athens Area seem to have experienced intensity VII more times than the rest of the Athens plain. However, this is not the maximum expected intensity for this area.

The peak recurrences for every intensity are observed in the western part of the Attica mainland. The top 20% intensity X recurrence (22-27 times over 15 kyrs) is constrained in a small area, only at the loose sediments of the western Attica coastline, in the Corinth Gulf, close to the highly active South Alkyonides fault system. The highest intensity IX recurrence (62-77 times over 15 kyrs) is observed on a broader area, in the westernmost parts of the Attica mainland. As intensities decrease, their peak recurrences seem to move towards the centre of Attica. Intensity VIII seems to occur in its maximum recurrence (92-115 times over 15 kyrs) between the Corinth and the Saronikos Gulfs, while the top 20% of the intensity VII recurrence is observed in the eastern part of the Thriassio plain, the NW part of the Greater Athens Area and Salamina Island in the Saronic Gulf. However, the distribution of the top 20% recurrences for intensities VIII and VII in the western part of Attica may be underestimated because active faults located farther offshore in the Corinth Gulf are not included in the model. Furthermore, fault specific seismic hazard maps are able to model events of magnitude M>6.0, and as such, they tend to underestimate intensity VIII and predominantly intensity VII recurrence. Overall, the locations of the peak recurrence values vary significantly per intensity. Interestingly, the peak recurrence values are gradually shifted from the western part, where the highest fault slip-rates are recorded towards the centre of the Athens Plain as the intensity values decrease.

Apart from the South Alkyonides fault, it is evident that more faults contribute to the total recurrence for intensities lower than X. As the intensities decrease, the isoseismals increase and more faults contribute to seismic hazard. However, as expected, the highest recurrences seem to be highly affected by the high slip rates of the South Alkyonides fault.

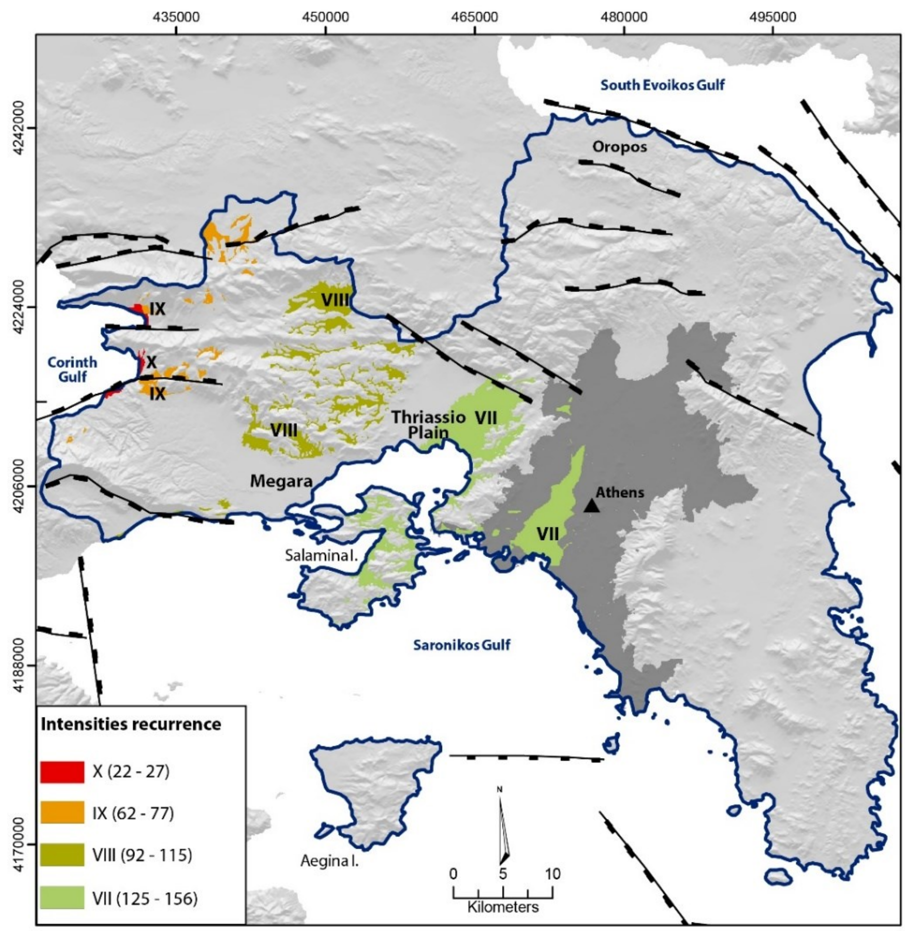

Figure 7.10: Top quintile (top 20%) for the recurrences of the intensities VII – X. Figure reproduced from Deligiannakis et al., 2018a.

The recurrence values in each locality of the fault specific hazard maps (Figure 7.6 - Figure 7.9) can be used as input for calculating probabilities of strong ground shaking in high spatial resolution, over a specific time period (Deligiannakis et al., 2018a). Since the historical seismic record is incomplete for the majority of the active faults, the stationary Poisson model can be utilized for the calculation of locality specific probabilities (see also Papanikolaou et al., 2013) for each locality of the Attica mainland, based on the average recurrence intervals of the intensities VII - X. If λ is the rate of occurrence of certain seismic events within a time *t*, the probability that *n* events take place within such interval is $Poisson = \frac{\lambda^n e^{-\lambda}}{n}$. If the occurrence of events follows a Poisson distribution, then the intervals of time t between consecutive events have an exponential distribution (Udias, 1999). In this case, the equation for the probability density function is: $P(n) = \lambda e^{-\lambda \delta t}$, whereas the cumulative distribution function is $P = 1 - e^{-\lambda t}$ (Papoulis, 1991; Udias, 1999). This model is usually applied when no information other than the mean rate of earthquake production is known (WGCEP, 1999).

The high spatial resolution of the maps allows an assignment of the λ value in different scales, varying from building blocks to Postal Code or Municipality level (e.g.

in Figure 7.11). Using the Poisson model and the λ values derived from the intensity recurrence, a time-independent probability of shaking at intensities VII - X can be calculated for every desired area in the map for a given period. The recurrence values for each Postal Code of the Attica region is presented in Annex I. Annex IIoffers the λ values for use in the Poisson cumulative distribution function.

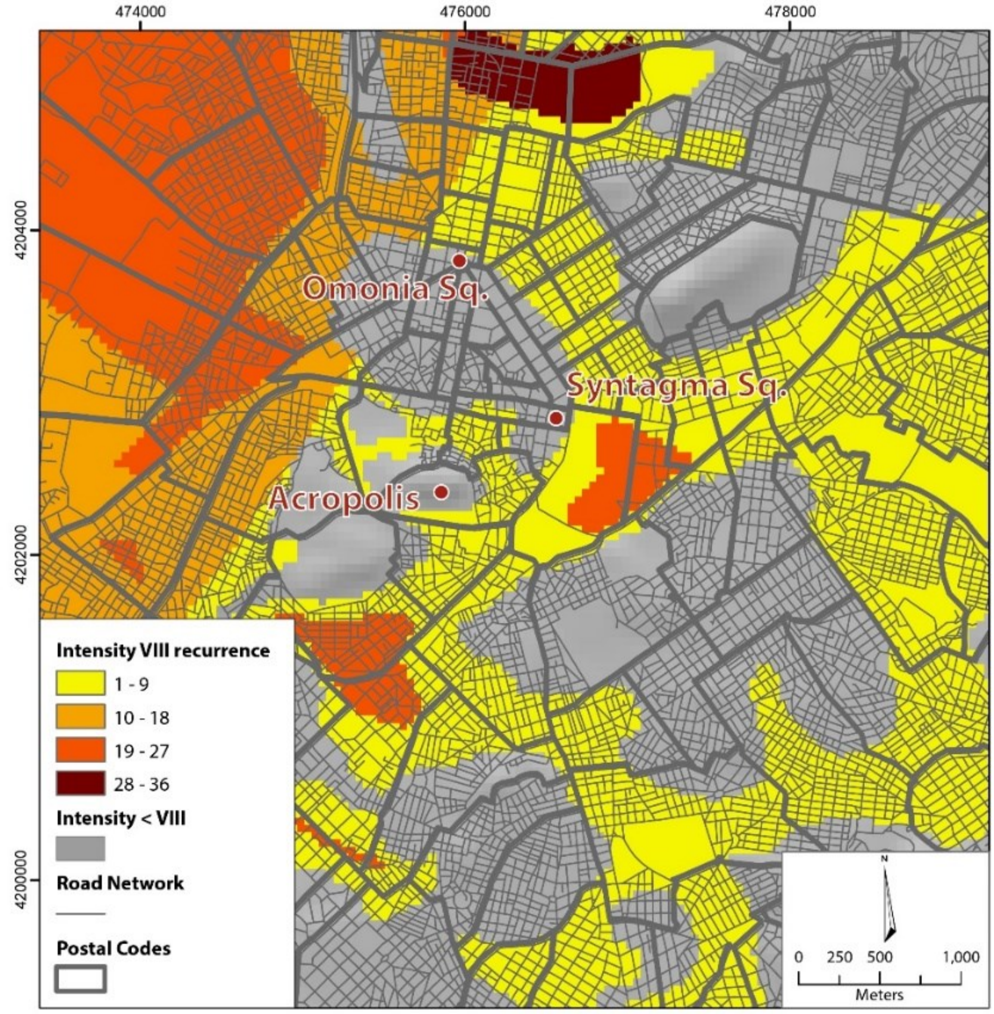

Figure 7.11: Fault Specific Seismic hazard map of the Athens centre. Tonal variations show how many times these localities have received enough energy to shake at intensity VIII over the past 15kyrs. This map offers a high spatial resolution of the intensity distribution and recurrence. Therefore it allows a detailed calculation of λ values at Postal Code or even building block level. Figure reproduced from Deligiannakis et al., 2018a.

8. Earthquake Catastrophe model

8.1. Insured loss estimation (Loss Reserves Calculation)

The loss reserves calculation on buildings portfolio combines the probability of specific intensities occurrence within the Postal Codes, with the building's characteristics, such as the building construction type and the insured value.

The first step is the development of a Table based on the building characteristics (e.g. Table 8.1).

Table 8.1: Building characteristics for each insurance policy

Building Characteristics							
Policy Serial No.	**Postal Code**	**Construction Value (x_1)**	**Insured Value (x_2)**	**Construction Type (x_3)**	**Building Age (x_4)**	**Number of floors (x_5)**	**Use of Property (x_6)**
1	10431						
2	10431						
...	...						
n	19600						

The "Construction Type" categories and relative losses in case of intensities occurrences are displayed in Table 8.2.

Table 8.2: Construction type in relation to average loss in case of intensities VII – X occurrence, after Sauter & Shah (1978) and Degg (1992).

Building Characteristics	**Construction Type (x_3)**	**Average loss (%)**			
		VII (y_1)	**VIII (y_2)**	**IX (y_3)**	**X (y_4)**
Adobe	1	22%	50%	100%	100%
Non seismic design unreinforced masonry	2	14%	40%	80%	100%
Reinforced concrete frames non seismic design	3	11%	33%	70%	100%
Reinforced concrete frames seismic design	4	4%	13%	33%	58%
Shear wall structures seismic design	5	2.3%	7%	17%	30%
Wooden structures seismic design	6	2.8%	8%	15%	23%
Steel frames seismic design	7	2%	7%	20%	40%
Reinforced masonry high quality seismic design	8	1.5%	5%	13%	25%

A standard approach for the reserves calculation K(t) is used, for a specific time period, which can be any time span from 1 up to several hundreds of years:

$$\boldsymbol{K(t)} = \frac{\boldsymbol{x_2}}{\boldsymbol{x_1}} \cdot \left[\boldsymbol{x_1} \cdot \boldsymbol{y_1} \cdot \boldsymbol{P_{1(t)}} + \boldsymbol{x_1} \cdot \boldsymbol{y_2} \cdot \boldsymbol{P_{2(t)}} + \boldsymbol{x_1} \cdot \boldsymbol{y_3} \cdot \boldsymbol{P_{3(t)}} + \boldsymbol{x_1} \cdot \boldsymbol{y_4} \cdot \boldsymbol{P_{4(t)}}\right]$$

K(t) is a function of the probabilities of occurrence for the seismic intensities VII – X. $P_{1(t)} - P_{4(t)}$ represent the probabilities of occurrence for intensities VII - X for the same period, x_1 represents the value of the building, x_2 represents the insured value and $y_1 - y_4$ represent the characteristics of the building, such as the construction type, age, height and use of property (see also Table 8.1 & Table 8.2). The x_2/x_1 ratio can be modified to cover any other insurance policy or restriction desired.

For example, assuming:

a) a portfolio worth 4bn € for the buildings of the whole region of Attica,

b) that all buildings are constructed under the old seismic code (i.e. built before the 1992 seismic code)

c) that every postal code has the same building value insured (the 4bn € portfolio is equally divided to each postal code),

a graph was created showing the calculated expected loss curve for the *K(t)* over various return periods (Figure 8.1, Table 8.3).

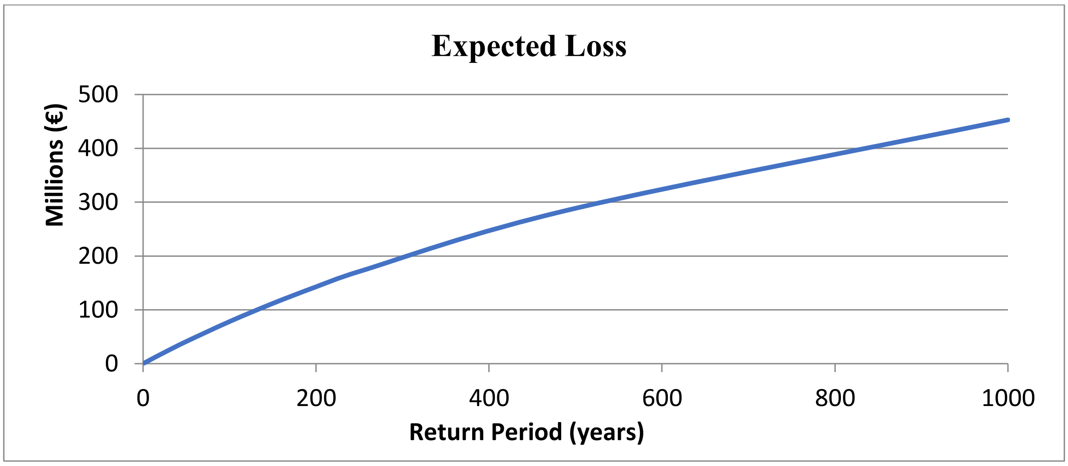

Figure 8.1: Example of the expected losses over various return periods. Assumptions are explained in the text.

Table 8.3: Expected losses over selected return periods for a 4 billion euros demo portfolio. Assumptions are explained in the text

RETURN PERIOD	Loss Estimate (milion €)
1	1
5	4
10	9
25	21
50	41
100	**78**
150	111
200	**142**
250	171
500	288
1000	452

8.2. Earthquake Catastrophe model for the SCR calculation

Deligiannakis et al. (submitted for publication, see also Deligiannakis et al., 2018b) developed a fully functional earthquake catastrophe model that is compatible with the Solvency II requirements (see also European Union, 2009) for risk profile determination, management of earthquake risk, and full transparency on the SCR calculation process. The model comprises four separate modules; Hazard, Vulnerability, Exposure and Loss modules. The details regarding the inputs and outputs of each module are shown in the following subsections.

8.2.1. Hazard Module

The Hazard module contains all 24 active faults included in the Active Fault Database presented in Section 6.3. Consequently, it analyzes earthquakes of magnitude M≥6 (Deligiannakis et al., 2018b). This threshold on magnitudes is twofold: First, since the purpose of this model is to accurately estimate the extreme earthquake events and the corresponding catastrophes for the insurance companies, it is essential to isolate and better analyze the significant earthquake events. M≥6.0 earthquakes can cause damages to buildings and general infrastructure, as they could produce seismic intensity VIII or even IX (Deligiannakis et al., 2018a). Second, the use of active fault analysis only allows for accurate analysis of the significant magnitude events. Events with a lower magnitude (M<6.0) rarely produce surface ruptures or are connected to blind faults that have no surface expression and thus are not taken into account using a fault specific approach.

In addition to that, in order to capture the full damage pattern over the insured building stock, it was necessary to include the existing earthquake catalogues. This way, the use of background seismicity, as well as the deep subduction zone related earthquakes, could refine the risk assessment. Therefore, the module also includes a combination of the two most accurate catalogues for the Greek territory, namely the NOA-UOA and AUTH catalogues (Papazachos et al., 2000; Makropoulos et al., 2012), for earthquakes of magnitude M≥5.0. Lower magnitude earthquakes would vastly increase the number of calculations and would not add any meaningful information regarding building damages. In order to extract the final catalogue with epicentres originating from the fault analysis and the existing catalogues, the latter is compared versus the projection of the fault planes on the ground surface (Figure 8.2) and the earthquake events that are related to the faults' activity are excluded.

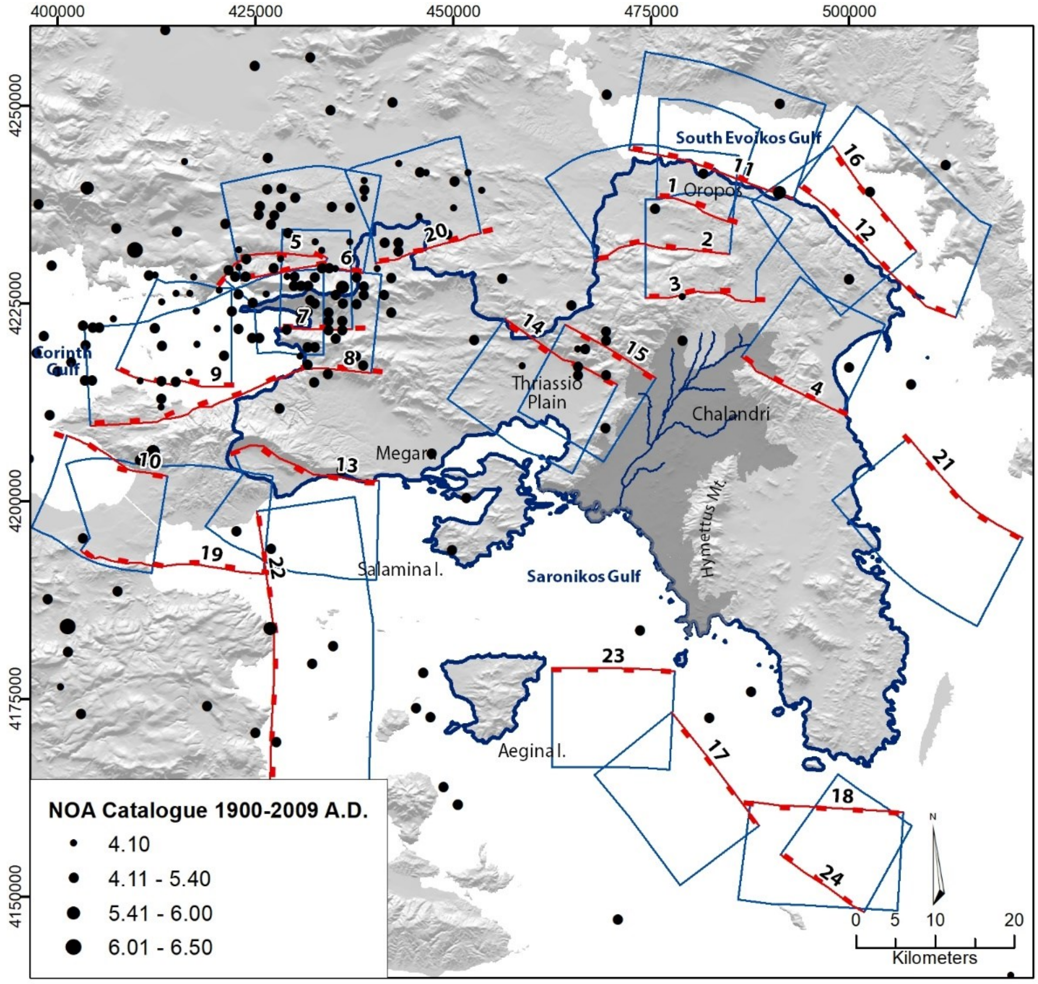

Figure 8.2: Projected fault planes on the horizontal surface, vs the recorded earthquakes of magnitude M>4.1 for the Attica region, between 1900 – 2009 (catalogue source: Makropoulos et al., 2012).

This process resulted in a synthetic catalogue that is considered complete for the past 15 kyrs for magnitudes M≥6. For lower magnitudes, the completeness is similar to the traditional models, hence not exceeding a few tens of years (Papazachos and Papazachou, 2003). Since this synthetic catalogue comprise the most precise and complete representation of the past earthquakes, it was stochastically simulated in order to assess the future earthquake events. These simulations included the location, magnitude, depth, and recurrence for each event. The spatial distribution of future events followed the two-dimensional beta distribution, which indicated the probability of each earthquake to occur in specific locations based on the existing catalogue and active fault traces. The Beta distribution provides enough flexibility regarding the modelling of loss from natural hazards (Woo,1999). We then divided the Attica region into 100 x 100 m (or 0.001 degrees) microcells and calculated the Poisson λ parameter for each cell, according to the corresponding number of events that fall within each cell. This 100m cell dimension is regarded as adequate since it corresponds more or less to the accuracy of the geological boundaries of the 1:25.000 and 1:50.000 scale geological maps. We then used this parameter to simulate the number of future events for each year. For each event, we simulated the three-dimensional coordinates within the microcell, using the bivariate variable that determines whether the simulated earthquake is shallow or deep. We used this approach as the research about the precise determination of earthquake’s depth is quite recent and certainly not fully explored (Florez & Prieto, 2017).

Furthermore, the magnitudes of the simulated earthquakes followed a beta distribution, as is the common practice in catastrophe models (Lallemant & Kiremidjian, 2014). Still, there is an option for future research, in order to test the Gutenberg – Richter distribution, using the *a* and *b* values proposed for the Greek territory by various researchers (e.g., Papazachos, 1999; Papaioannou & Papazachos, 2000; Vamvakaris et al., 2016). However, these area sources are rather granular. In particular, the Attica region is covered by up to only four different areal sources for the greatest part of Attica (see also Papaioannou & Papazachos, 2000) and thus the spatial resolution of the hazard assessment would be relatively poor. In any case, the upper extreme magnitude values were adjusted so that they could not exceed the maximum seismic potential of the active faults. In the Attica region, this threshold is set at M6.7 (Deligiannakis et al., 2018a).

The earthquake intensity distribution was based on the Theodulidis’ (1991) attenuation relationships, as was the case with the development of the seismic hazard maps (see also Chapter 7). Similarly, the input for the effect of the surface geology was based on the same principles, as described in Chapter 7.

The final output of the Hazard module is a large set of earthquake events, and their corresponding intensity distributions plotted using a high resolution 45 x 45 m grid. Figure 8.3 illustrates a simulated M6.6 earthquake event related to an active fault offshore eastern Attica. Depending on the portfolio structure and the level of detail regarding the location of each policy, an intensity value per contract and earthquake event is assigned, or the results are aggregated in Postal Code level, creating a table of intensities occurrence for each simulated event per Postal Code.

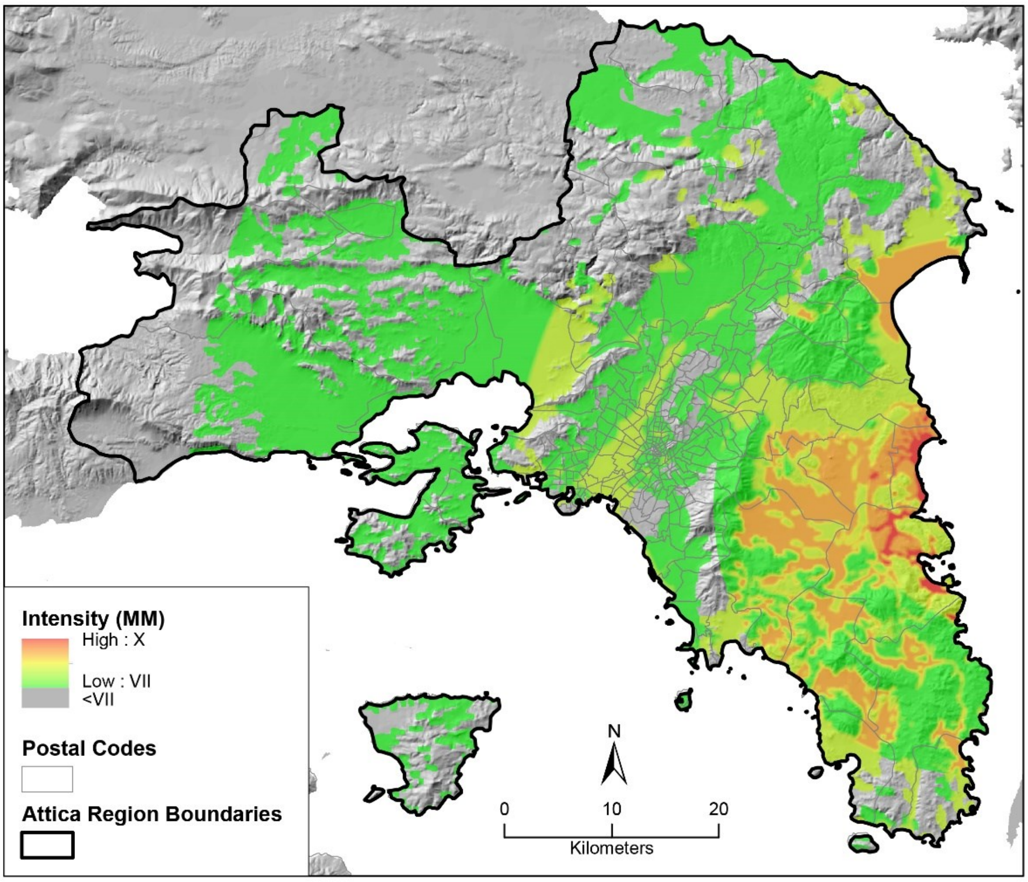

Figure 8.3: Spatial distribution of MM intensity after a simulated earthquake event of magnitude M6.6. The modelled epicentre is related to an active fault offshore eastern Attica.

8.2.2. Vulnerability module

The actual values that were used in this module are based on existing earthquake–loss susceptibility data by Sauter & Shah (1978) and Degg (1992). These data are compatible in general with the already published loss and damage patterns (e.g., Kappos et al., 1998; Kappos et al., 2007; Kappos & Panagopoulos, 2010), which represent the Greek building inventory more accurately. However, higher loss ratios are attributed for adobe, unreinforced masonry and buildings without seismic design, for a more conservative approach. Figure 8.4 shows the corresponding vulnerability curves for eight different construction types for Adobe, Concrete, Wooden, and Steel buildings that are used in the model.

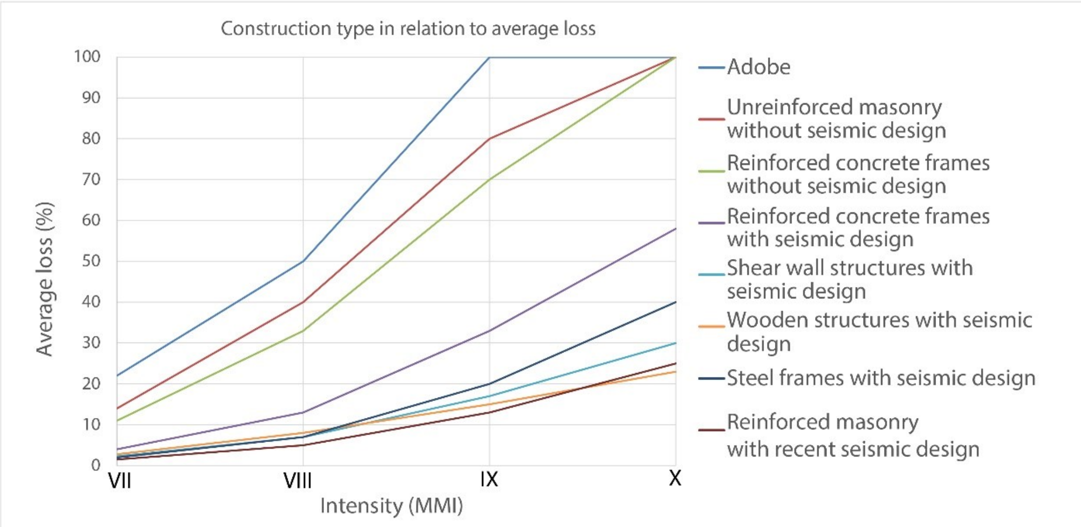

Figure 8.4: Vulnerability curves per construction type, concerning average damage in case of intensities VII – X occurrence, modified after Degg, 1992.

8.2.3. Exposure module

A demo portfolio for insured buildings was developed in order to be used as input in the different model runs. A total sum insured value of €100 bn for the Greek territory was set as a fixed value, and then the portfolio was split by the Greek Postal Codes, using the Industry Exposure Database (IED) values that were provided by the Bank of Greece, exclusively for this test. Each Postal Code was separated into 3 different parts, assigning each cluster according to the proportion of buildings built under new, old, or no seismic design, based on statistical data from the most representative industry data. Subsequently, each Postal Code was represented three times in the exposure module, each time with a different sum insured value, according to the building construction year. Furthermore, the Postal Codes that lie outside of the Attica region were excluded, and the final Total Sum Insured was 41,559,673,152 €, which emulates the distribution of the insured buildings in the Attica region in the most accurate way. The Input Table for the model included the Postal Code value, Contract Number, Construction Year, Construction Type, Building Insured Value, Interior Insured Value, Deductible for Building, Deductible for Interior, and Co-insurance percentage. The Construction Type was set to reinforced concrete, which represents almost 95% of the insured buildings in Greece. The input values related to the building interior were set to zero, as there are no statistical data available for the Greek territory.

8.2.4. Loss module

According to the "Solvency II" regulatory framework, every year, each insurance company specifies the required capital *K*, which would potentially be consumed by unexpected loss events, occurring with a probability of 0.5% or less in a one–year period (Mittnik, 2011). In other words, the insurance company would be insolvent (thus, the capital *K* would be insufficient for full damage coverage of its own retention) with a probability of 0.5%, which is equivalent to capital K inefficacy once every 200 years (European Commission, 2009).

For the SCR calculation, it is assumed that the insured portfolio consists of n buildings, and X_i is a random variable, representing the amount of the annual own retained loss for the ith building, where $i=1,2,\dots,n$. The total annual own retained loss amount S for the insurance company can be described as follows:

$$S= X_1+X_2+\cdots X_n \qquad (1)$$

The following equation typically describes the Solvency II requirement:

$$Pr[S<K]=99.5\% \qquad (2)$$

Since S represents a sum of random variables, it is also a random variable. Equation (2) could be solved for K, if an analytical formula could compute the distribution of the S random variable (Kaas et al., 2008). As this is not feasible, special simulation techniques are used for the definition of the random variable S.

Since a synthetic stochastic model for the future earthquake events is already developed, a large number (e.g., N, where $N=10,000$) of different values for the random variable S (e.g., S_1, S_2,...$S_{9,999}$, $S_{10,000}$) is reproduced. This way, an events table is created, using all simulated earthquakes. These events are related to their corresponding damages, after applying the attenuation relationships, local site conditions, vulnerability values, insurance, and reinsurance policies, which were already described in the relevant modules.

For the calculation of the capital K, the random variable S values are sorted in descending order (e.g., $S(1)$, $S(2)$,...$S(9,999)$, $S(10,000)$), then select the number ω arranged value, where:

$$\omega=N\times 0.05 \qquad (3)$$

and calculate the capital K based on the corresponding value from the sorted random variables S, that is:

$$K= S(\omega) \qquad (4)$$

The workflow for the process is shown in Figure 8.5.

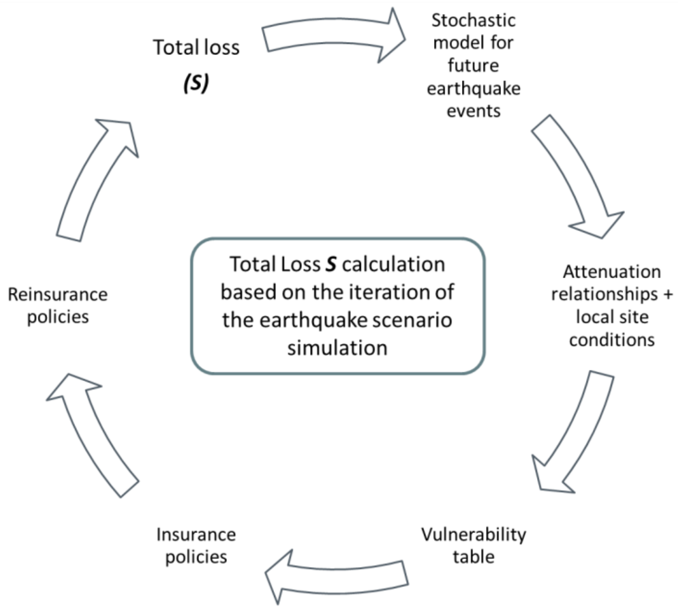

Figure 8.5: Flow diagram showing the sequence for the calculation of the Total Loss. This process iterates for a large number of event years to develop the Events Table.

8.2.5. SCR calculation for a demo portfolio in Attica region

The annual SCR for the region of Attica was calculated, using the demo portfolio that was developed in the Exposure module. Attica region is divided into 297 Postal Codes, which, when aggregated by the first two digits, yield 10 CRESTA zones (that is CRESTA zone 10 up to 19). Several runs of the model were made in the postal code level, each time with separate relativity scenarios for the CRESTA zones of Attica.

Scenario No1 assumes a one-CRESTA exposure per run or zero exposure to the other CRESTA zones of Attica. Using this scenario, we calculate the total SCR using the following equation:

$$SCR_{total} = SCR_{10} + SCR_{11} + \ldots + SCR_{19}$$

Where SCR_x represents the calculated SCR for each CRESTA zone (10-19)

The final SCR value for the € 41,559,673,152 insured value is € 1,313,113,651 with an average 3.16% risk premium (Table 8.4).

Table 8.4: 1/200 loss to insured value for each CRESTA Zone in the Attica region, assuming single CRESTA zone exposure for each model run

CRESTA zone	Building Sum Insured	$Loss_{99,5\%}$	Risk premium
10	€ 3,096,717,275	€ 105,001,003	3.39%
11	€ 3,978,840,862	€ 88,814,524	2.23%
12	€ 1,701,478,391	€ 60,514,798	3.56%
13	€ 2,818,568,890	€ 98,882,904	3.51%
14	€ 5,136,921,166	€ 133,530,322	2.60%
15	€ 6,277,049,505	€ 183,199,273	2.92%
16	€ 3,712,381,814	€ 65,528,378	1.77%
17	€ 3,644,449,934	€ 106,461,434	2.92%
18	€ 5,303,004,906	€ 164,988,845	3.11%
19	€ 5,890,260,409	€ 306,192,171	5.20%
TOTAL	**€ 41,559,673,152**	**€ 1,313,113,652**	**3.16%**

Scenario No2 assumes exposure throughout the whole Attica region. The total SCR for the same insured value is € 1,258,210,333, with an average 3.03% risk premium (Table 8.5). Under this scenario, the $Loss_{95\%}$ is € 319,053,282 and the $Loss_{99.9\%}$ is € 1,879,283,251, which represents the most extreme Loss scenario.

Table 8.5: 1/200 loss to insured value in the Attica region, assuming exposure in every CRESTA zone.

CRESTA zone	Building Sum Insured	$Loss_{99,5\%}$	Risk premium
10	€ 3,096,717,275	€ 104,001,003	3.36%
11	€ 3,978,840,862	€ 89,106,910	2.24%
12	€ 1,701,478,391	€ 60,293,709	3.54%
13	€ 2,818,568,890	€ 45,030,241	1.60%
14	€ 5,136,921,166	€ 36,943,332	0.72%
15	€ 6,277,049,505	€ 169,535,806	2.70%
16	€ 3,712,381,814	€ 192,158,660	5.18%
17	€ 3,644,449,934	€ 112,345,051	3.08%
18	€ 5,303,004,906	€ 190,300,871	3.59%
19	€ 5,890,260,409	€ 258,494,750	4.39%
TOTAL	**€ 41,559,673,152**	**€ 1,258,210,333**	**3.03%**

The SCR and the corresponding risk premium values are further decreased when applying a 2% deductible policy in each demo contract. In this case, the SCR is € 677,319,349, which results in an overall risk premium of 1.63% (Table 8.6). Considering that a 2% deductible is the commonest policy for earthquake insurance in

Greece, then this scenario is considered the most representative of the Greek Insurance market.

Table 8.6: 1/200 loss to insured value in the Attica region, assuming exposure in every CRESTA zone and applying a 2% deductible policy.

CRESTA zone	**Building Sum Insured**		**$Loss_{99,5\%}$**		**Risk premium**
10	€	3,096,717,275	€	41,538,232	1.34%
11	€	3,978,840,862	€	23,798,473	0.60%
12	€	1,701,478,391	€	23,215,666	1.36%
13	€	2,818,568,890	€	65,679,992	2.33%
14	€	5,136,921,166	€	128,099,540	2.49%
15	€	6,277,049,505	€	75,739,925	1.21%
16	€	3,712,381,814	€	9,493,523	0.26%
17	€	3,644,449,934	€	58,496,327	1.61%
18	€	5,303,004,906	€	80,177,678	1.51%
19	€	5,890,260,409	€	171,079,994	2.90%
TOTAL	**€**	**41,559,673,152**	**€**	**677,319,349**	**1.63%**

Regarding the granularity of the risk assessment, the high spatial resolution of the hazard module across the Attica region allows for loss and risk premium calculations in the Postal Code level, or in even higher resolution. Figure 8.6 shows the distribution of the 1/200 loss in comparison to the exposure within each Postal Code of the Attica region. There is significant variability within each Cresta Zone, thus the model can map local peculiarities and provide essential insights within each Zone.

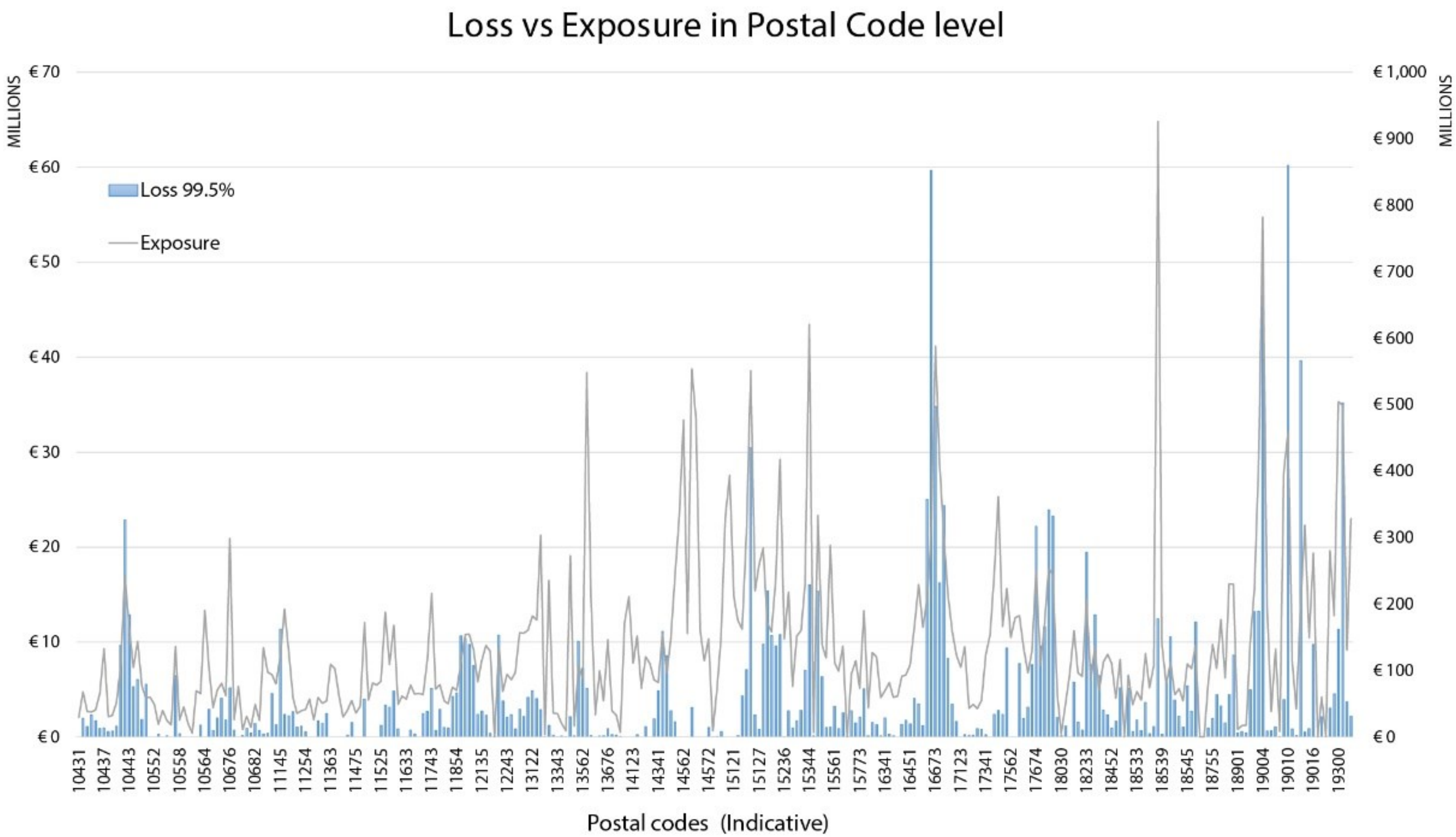

Figure 8.6: 1/200 Loss, compared to the exposure of each Postal Code in the Attica region.

9. Discussion

9.1. Assessment of the fault specific seismic hazard mapping method

9.1.1. Advantages

A method of seismic hazard mapping is presented in this thesis, that is based only on geological fault slip-rate data. Geological data can extend the history of earthquakes on a fault back many thousands of years (Yeats and Prentice and 1996). As a result, geological fault slip-rate data include numerous seismic cycles and establish the most critical tools required to assess seismic hazard (Papanikolaou, 2003).

Existing seismic hazard maps exhibit five major disadvantages, which are presented in Section 2.3. The method applied in this thesis tries to address them sufficiently and also offers some additional capabilities that can be useful for seismic hazard assessment purposes.

In particular, this method presented in this thesis:

a) offers a hazard map and site-specific shaking recurrence intervals for every location in the Sparta basin and in the Attica Region over the past 15 kyrs, a period which is long enough to eliminate both the incompleteness of the historical record and the temporal clustering problems that could lead to erroneous conclusions about the seismicity of an area. The site-specific shaking recurrence is of particular importance for: i) areas such as Attica where multiple seismic faults can generate damage in one locality and ii) lower intensities (VII- VIII) whose isoseismals extend to a broader area.

b) offers maps that demonstrate the influence of geologic formations on the intensity distribution and can incorporate different attenuation/amplification scenarios, in contrast to existing seismic hazard maps that can only handle an average local site condition.

c) quantifies the hazard variability along-strike every fault, providing a more realistic hazard interpretation.

d) offers locality specific hazard maps that either incorporate the seismic hazard associated with one fault (e.g. Sparta fault - Section 7.1) or integrate the hazard related to multiple faults with different slip-rates (e.g. Attica region – Section 7.2), thus providing a much more complex hazard assessment.

e) provides a high spatial resolution of hazard with earthquake shaking frequencies changing every few hundreds of meters, not only because of the relevant distance from seismic sources, but also because of their geometry (fault plane dipping direction, as well as variations in strike) and local geological conditions.

f) it offers hazard maps that are not based on subjective judgement regarding the delineation of seismic source zones.

g) provides recurrence intervals averaged over 15 kyrs, which can be used for the calculation of time-independent probabilities for every intensity between VII and X. In combination with the knowledge of the timing of the last earthquake event, conditional time-dependent probabilities can be calculated for desired periods. Indeed, Papanikolaou et al. (2013) calculated the time-dependent probabilities for the town of Sparta to be shaken in intensities ≥ IX (3.0% for the next 30 years and 4.9% over the next 50 years based on a Coefficient of Variation (COV) =0.5), since the last rupture of the Sparta fault occurred in 464 B.C.

h) provides a map showing the maximum expected intensity for each location, which is highly important for disaster prevention and insurance underwriting. In particular, this qualitative approach is useful for identifying areas of low seismic hazard

i) the outcome is capable of supporting an earthquake catastrophe model and can provide the maximum spatial resolution desired, estimate losses from geocoding level to Postal Codes and CRESTA zones level.

9.1.2. Limitations

Although the presented method of fault specific hazard mapping has certain advantages compared to the traditional seismic hazard maps based on historical earthquake catalogues, still there are limitations that pose new challenges for future research.

First, this method is applied only to normal faults, with the associated geometry and the projection of the epicentres in the hanging wall. Further modifications are needed in order to incorporate strike-slip and reverse faults.

Second, it requires well defined seismic sources that are not always feasible to define accurately, particularly for low slip-rate faults. New methods of data collection, especially the high-resolution DTMs obtained by UAV-based photogrammetry, can support more detailed fault mapping and source definition. However, it can be challenging for low slip-rate faults, where erosional processes outpace fault slip-rates. In these cases, no topographic effect of the fault activity would be maintained. The latter support why other techniques such as paleoseismic trenching studies are always crucial for tracing such faults.

Third, it requires the knowledge of fault slip-rates, which can be challenging to collect, especially in cases where the footwall geology does not support the presence of post-glacial scarps or marine terraces. Geomorphic indices that could also support an approximation of fault slip rates can prove valuable in such cases.

Last, it incorporates faults that are large enough to break the surface and produce earthquakes of M≥6. Although blind faults or faults that do not break the surface can generate only moderate earthquakes (Ms=5.5-6.0), they sometimes can cause considerable damage.

9.2. Errors and major assumptions in fault specific seismic hazard maps development

Seismic hazard maps incorporate uncertainties as their predictions vary significantly, depending on the choice of many poorly known parameters (Stein et al., 2012). The analysis of the active faults and the geologic conditions in the Attica mainland aims at reducing the major uncertainties attributed to the historic earthquake catalogues. However, assumptions made in key methodology aspects are connected to: a) faults determination and fault geometry, b) fault slip rates, c) surface geology and d) intensity attenuation relationships.

a) Both qualitative and quantitative assumptions were made for the delineation of the fault database. The presented active faults are constrained in a way that literature findings and personal fieldwork are in agreement with the tectonic activity regime in Attica. Regarding fault lengths, the error parameters are well communicated in the corresponding literature, where applicable (see Benedetti et al, 2003; Ganas et al., 2005; Papanikolaou and Papanikolaou, 2007b; Sakellariou et al., 2007; Roberts et al., 2009; Grützner et al, 2016;). Fault lengths are estimated around ±10%, whereas faults derived from 1:100000 neotectonic maps may also include a maximum spatial error of the order of 400 m. Fieldwork findings were based on 1:50,000 geological maps and crosschecked using slope maps, based on the high resolution DSMs of the Greek Cadastre, with a nominal accuracy of 25 m in the XY axes. Through the completion of this thesis, Greek Cadastral DTM (5 m cell size) was used in order to measure geomorphic indices and to refine the previous outcomes.

One of the major questions is whether all active faults have been traced and included in the database. Considering that Attica is a well-studied area with major infrastructure, all major active faults that are capable of producing magnitudes M ≥ 6 and surface ruptures are included in this thesis. Fault zone traces have been used to cope with divergences in fault traces between literature and this thesis (e.g. Kaparelli fault, South Alkyonides fault zone, Erythres fault). However, six potential active fault structures are not taken into account in the modelling procedure (see faults P1 – P6 in Figure 9.1 for approximate locations). It is not clear whether these are active structures due to considerably unclear indications about their existence and level of activity. Indications in neotectonic maps of East Attica (Papanikolaou et al., 1995) and the South Evoikos submarine neotectonic map (Papanikolaou et al., 1989b) are not clear about the existence and throw rate regarding the P1 probable fault. In fact, the neotectonic map of East Attica suggests that P1 is probably an inactive structure, with an overall small amount of finite throw. It seems that P1 is a WNW – ESE trending structure, parallel to the Oropos fault, dipping towards the center of the South Evoikos Gulf. In addition, geomorphic and geologic signs about P2 and P3 faults suggest that these structures need further analysis. Antoniou (2010) argues that small faults like P2 (Figure 9.1) may act as active boundaries on the existing basins in east Attica. However, these structures were characterized by Papanikolaou et al. (1995) as “mostly inactive”. Regarding P3, there is some evidence for neotectonic activity, according to Mariolakos and Theocharis (2001) and Theocharis and Fountoulis (2002). Moreover, this structure seems to be related to an offshore WNW – ESE trending fault zone with a noticeably small total throw, rupturing Mesozoic sedimentary rocks and Plio-Quaternary sediments (Papanikolaou et al., 1989a). Similarly, Papanikolaou et al. (1998) describe the P4 fault in Aegina Island as a SW-NE trending structure. This fault seems to have an offshore prolongation with a small amount of throw in the northeastern submarine area (Papanikolaou et al., 1989a) and forms small scarps throughout the sedimentary and volcanic formations in the surface of Aegina. However, Foutrakis and Anastasakis (2020) suggest that no offshore prolongation is traced. Papanikolaou et al. (1989a) and Foutrakis and Anastasakis (2020) also indicate two offshore E-W trending structures; the north dipping P5, which lies between Salamina and Aegina Islands and the south-dipping P6, NE of Aegina Island. These faults seem to rupture Mesozoic and even Middle and Upper Pleistocene sedimentary formations; however, they present a noticeably small total throw.

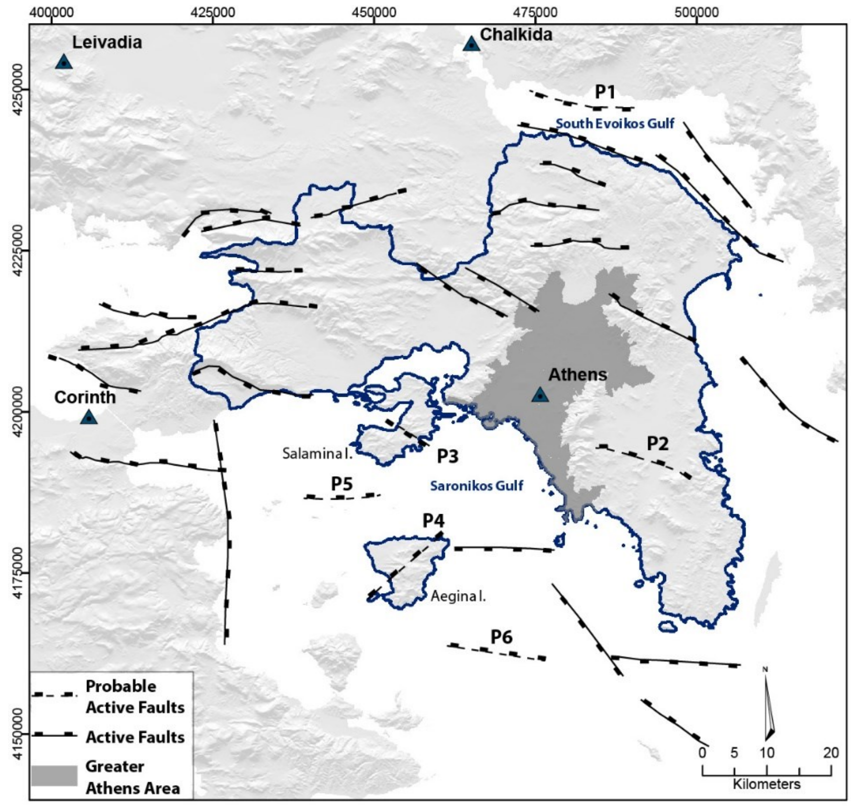

Figure 9.1: Probable active fault structures (dashed lines) in Attica region. These faults are not taken into account in seismic hazard mapping as they are either antithetic structures of major fault zones (e.g. P1 and P6), or it is unclear whether they are active or not. If these faults were incorporated to the analysis, their impact to seismic hazard would be insignificant compared to the active structures already analyzed.

Consequently, no significant changes would occur in the hazard maps if these faults had been included in the seismic hazard mapping of the Attica region, as their slip rate values would be less than 0.1mm/y, judging from their finite throw. This implies an earthquake recurrence of less than 3-4 times over 15 kyrs, making no considerable difference to the total recurrence values. However, since this is a GIS-based methodology, new data or updated data on the already analyzed faults can be incorporated in seismic hazard scenarios, should any more information for these faults occur in the future.

It is also important to note that only active faults capable of producing earthquakes of magnitude Ms > 6.0, with evident surface ruptures, are modelled. Indeed, earthquakes with magnitude Ms < 5.5 are unlikely to break the surface (Michetti et al., 2000) and earthquakes of magnitude < Ms 6.0 are usually poorly expressed at the surface, as discontinuous traces or fractures (e.g. Bonilla et al., 1984; Darragh and Bolt, 1987). Furthermore, intermediate and deep earthquake events (150-200 km depth) whose epicenters are plotted in Attica, generated from the Hellenic subduction zone, are excluded from the analysis. Such events will not affect the vast majority of may buildings in Attica. They may affect only high-rise buildings in Athens. However, the behavior of such buildings and the expected hazard pattern remain largely unknown since modern Athens has not experienced such an event.

b) Fault slip rate values dominate the intensity recurrences of the fault specific seismic hazard maps. It is of decisive importance that errors in slip rate measurements are reduced in a way that they do not affect the final earthquake recurrence values. Already published slip rate values for active faults included information about the error or minimum and maximum values (e.g. Ganas et al., 2005). Both in this case, and in case of neotectonic maps, the average slip rate values or the average finite throws and sediments thickness were used. The latter were applied on faults derived from the official neotectonic maps, where long term slip rate values were extracted by combining both. Value ranges for both sediments thickness and faults total throw have a maximum variation of ±100m, which results in ±0.04mm/y on long term fault slip rate values. Slip rate characteristics for faults derived from fieldwork depended on errors in scarp height measurements. A scarp height variation of ± 20% (see also Roberts et al., 2004) is assumed, which results to ± 0.2 mm/y for a fault with a slip rate of 1 mm/y.

c) Geological maps at 1:50,000 scale often include a maximum error of 200 m. Maximum spatial error on 1:100.000 scale neotectonic maps is up to 400 m. Except for the exact fault location and length, these uncertainties affect the accuracy of the spatial distribution of the strong ground motions since surface geology amplifies or attenuates the calculated intensities. For the spatial distribution of the modelled intensities, the official 1:50,000 Geological Maps of IGME and the 1:25,000 map of E.P.P.O. (Marinos et al., 1999a) were used. These maps provide an adequate spatial analysis regarding surface geology and the corresponding attenuation or amplification of the strong ground motion. Furthermore, they can offer critical information about earthquake-induced secondary effects, such as landslides and liquefactions.

Expected intensity at certain localities is highly sensitive to the relationships that calculate the attenuation of strong ground motion with distance from the epicentre. Final results can be drastically affected by the uncertainties incorporated in the fault geometry (and thus in the epicenters location) and in the attenuation relationships that are based in the traditional intensity scales. For example, Papanikolaou (2011) quantified errors in both spatial distribution and recurrence intervals of the expected intensities in the Apennines and showed that they can significantly outreach the aforementioned 20% error of the fault slip rates. Therefore, the attenuation relationships used, form a major source of uncertainty and in several cases they overshadow all the other factors of uncertainty, even fault slip-rates, which directly affect the calculated earthquake recurrences.

9.3. Constraints and limitations in the tectonic geomorphological analysis

The tectonic geomorphological analysis in this thesis was used a) for the definition of the Sparta fault segmentation and the determination of the total length to be modelled, b) to challenge new techniques and confirm the level of activity for the faults that could potentially affect the Attica region, from a qualitative point of view.

Tectonic geomorphological analysis of stream long profiles crossing active faults has recently been used systematically for uplift rate interpretations in actively deforming areas (e.g. Whipple and Tucker 2002; Kirby et al., 2003; Duval et al., 2004; Vassilakis et al., 2007; Whittaker et al., 2008; Boulton and Wittaker, 2009; Papanikolaou et al., 2013; Geurts et al., 2020). Such analysis has been performed in nine catchments crossing perpendicular the Sparta Fault and has given interesting results regarding fault slip variations and strike the fault. The results were also calibrated and confirmed by analyzing long profiles of two catchments crossing the antithetic structure of the Sparta fault, along with three catchments flowing in localities that no fault exists (see also Papanikolaou et al., 2013)

Overall, long profile convexities can be revealed in all but one (Agios Konstantinos) rivers crossing the Sparta Fault. Moreover, the documented large-scaled along-strike variations show that the central part of the Sparta Fault system appears to have undergone an increase in relative uplift rate compared to the north and southern part of the fault, indicating that the uplift rate diminishes as approaching the tips of the fault. The latter is also confirmed from the k_{sn} differences between the outer (k_s<83) and central parts (121<k_{sn}<138) of the Sparta Fault. Moreover, the heights of the convex reaches are much greater in channels profiles at the centre of the fault, indicating that the Sparta Fault has been tectonically active as one hard-linked structure probably for the last few hundred thousand years. This is important for the seismic hazard analysis since the fault was modelled as one seismic source.

A different approach was adopted for the analysis of faults and drainage network in Attica. Swath topographic profiles were primarily used to examine the topography affected by the active faults qualitatively, as they summarize elevation data of a complex landscape into a single profile (Andreani et al., 2014). This is a common approach in tectonic geomorphology, as topographic patterns are effectively used for the assessment of regional tectonics (e.g. Clark & Royden, 2000; Molin et al., 2004 & 2012; Andreani et al., 2014) or in smaller domains (e.g. Ponza et al., 2010; Fernández-Blanco et al., 2019). Such analyses were performed for all the onshore faults included in the seismic hazard model to confirm the topography pattern along the fault lines, visualize the drainage incision form perpendicular to the footwalls, and interpret possible irregularities along fault lines.

The swath topographic profiles along the Milesi, Dionissos, Fili, Kehries and Dafni faults showed a triangular relief pattern, with the highest relief values occurring at the central part of the faults. Afidnes fault also presents higher relief values towards the fault centre, although the whole structure is tilted towards the East. The swath profiles along the other faults reveal varying relief values along the fault direction. In cases such as the Malakasa fault, the triangular relief pattern is interrupted by deep river incisions, as shown from the high enhanced transverse hypsometry index (THi*) values in the fault proximity. The same holds with the Thriassio fault, which presents an overall triangular relief pattern in the fault parallel swath profile, but with a deeply incised footwall, as also confirmed by the extremely low V_f values. On the other hand, the Kaparelli fault zone swath profile indicates that there is a strong possibility that the Livadostra segment continues further south and may have an offshore prolongation. Regarding the Kakia Skala, Aigosthena and Erythres faults, technical constraints related to DTM artefacts didn't allow for full coverage of the fault-related anaglyph. However, for the Kakia Skala fault, the maximum THi* values reach up to 0.8, indicating that it is active. The activity of the Aigosthena fault is also confirmed by the degraded scarp and the fault parallel drainage basin. The latter is asymmetrical, as indicated from the A_f value (66.6), which implies a southward tilting towards the fault. Regarding the Erythres fault, the swath rectangle based on the fault trace did not yield a complete set of profiles. However, clear geomorphic indications, such as triangular facets and wineglass valleys, support the characterization of the fault as active.

Overall, the fault parallel swath profiles proved a valuable tool for a qualitative assessment of the deformation pattern along strike the faults. However, there are limitations in the application related to the extent of the swath and the quality of the DTM. For instance, the stripe needs to be as wide as it takes to reach the drainage divide at the footwall. However, there are cases where there are topographic flexures at the hangingwall, which may not be related to the fault activity, but if included in the swath profile, they might affect the outcome. This is one of the reasons why the topographic swath profiles were primarily used for a qualitative assessment of the deformation pattern. They were used for throw rate estimations only in cases where there was no other option.

Regarding the fault perpendicular swath profiles, they also provided an indication for transient landscapes. Since low slip rates characterize the majority of the analyzed faults, the fault perpendicular swath profiles are expected to have small topographic flexures and concavities just over the fault or in higher altitudes, especially in profiles running through the centre of the fault (see also Papanikolaou et al., 2013 and Section 6.1). It is important to note that the fault – perpendicular swath profiles are indicators of the general topography and do not clearly represent the contrast between uplift and river incision, as river profiles do.

With regards to the Loutraki fault, there was no swath profile constructed because the main fault is offshore. However, the fault activity is well constrained, and the throw rate was extracted from the postglacial scarps detailed profiles. This is also the case for the Alkyonides fault zone, which is one of the most well-examined faults in Greece, with a well-constrained activity level.

9.4. Comparison with existing macroseismic intensity data from historic earthquake events

The difficulties and constraints on the comparison of the results with the available macroseismic data rest on two major factors. Firstly, the deficiencies in spatial resolution of the macroseismic intensity, especially for past events, affect the comparison regarding the intensity distribution. Secondly, the incompleteness of the existing earthquake catalogues makes it difficult to compare the recurrence values over long periods of time, even for lower intensities (VIII or VII). Moreover, fault specific seismic hazard maps are able to model events of magnitude M>6.0 and as such they tend to underestimate intensity VIII and predominantly intensity VII recurrence. Indeed, events of lower magnitude are associated with the background seismicity and can sustain moderate damage in a limited area. However, they cannot produce intensities as high as IX on the Modified Mercalli Scale. Also it is possible that the fault specific based recurrences for intensities VIII and VII in the western part of Attica are underestimated, because active faults located farther offshore in the Corinth Gulf are not included in the model. In any case, there could be a comparison of the fault specific seismic hazard maps with the existing descriptions of the damage distributions for recent earthquake events.

Four earthquake events affecting parts of the Attica region are recent enough to provide data for macroseismic intensity distributions. The 1938 Mw 6.0 Oropos is reported as an intensity VIII (MM) event in areas close to the epicentre, at Northern Attica (Ambraseys and Jackson, 1990). The central and southern parts, including Athens, experienced lower intensities (VI) during the same event. During the February Alkyonides earthquake sequence in the Corinth Gulf (Ms = 6.7, Ms = 6.4), intensity VIII occurred in the town of Megara at the western parts of Attica, while the Greater Athens Area experienced similar or lower intensities (VIII – VII). During the March 1981 event (Ms = 6.3), intensity VII occurred near the Athens Basin (also known as the Greater Athens Area) (Antonaki et al., 1988). A more detailed picture of the intensity distribution during the Athens 1999 Mw 5.9 earthquake is available in Lekkas (2001). He shows that the highest intensity values (VIII – IX) were observed in a limited zone over the northern parts of the Kifissos River sediments, mostly in NNE-SSW orientation (see also Figure 3.7). These areas fit well to the ones that are shown to have experienced maximum intensities of VIII – IX in Figure 7.10. Although the observed intensities were recorded using the E.M.S.-1998 scale, they were directly converted to the MM Intensity scale for comparison purposes, according to Musson et al. (2010).

Regarding the recurrence values, the historic earthquake catalogues are considered complete for less than 200 years for such events. However, based on these historic events, a minimum return period of 100 years is observed for intensity VII in the Greater Athens Area and for intensity VIII in the western parts of Attica. A minimum 200 years return period is observed for intensity VIII in the northern Attica and in limited zones in the Greater Athens Area. Intensity IX is also observed in sparse locations in the Greater Athens Area and in the westernmost parts of Attica mainland. The findings for intensity VII in Athens agree with Papaioannou and Papazachos (2000), who suggest that this area shakes at such intensities every 110 years. However, there is a large difference for intensity VIII, as they suggest that the return period exceeds 1000 years.

Based on the fault specific seismic hazard maps, the same localities that experienced intensity VII during the 1981 series of 3 earthquakes (February - March) and the 1999 event show a return period from 200 years (western Attica) and 170 years (Megara), to 106 years (central part of the Greater Athens Area, see also Figure 7.5 and Figure 9.2). For the areas that have experienced intensity VIII during the February – March events, the return periods vary from 240 years in the western part of Attica, to more than 280 years in the central part and 440 years for the northern part of Attica (Figure 7.9). Intensity IX seems to have a return period that varies from 714 to 1360 years in the same areas that were shaken in such intensities during the 1999 earthquake event and as low as 230 years for the westernmost part of Attica. The findings for intensities VII and VIII agree with Papaioannou and Papazachos (2000) for the recurrence of intensity VII in Athens. However, there is a large difference on higher intensities, as they suggest a 1000 year return period of intensity VIII in Athens, which is more than double compared to the results of the fault specific hazard maps in most localities of the Greater Athens Area.

Table 9.1: A comparison between the return periods and the observed intensities of historical earthquakes in certain locations versus the fault specific seismic hazard maps outputs (cells in colour). AB stands for Athens Basin (also known as the Greater Athens Area). WA stands for West Attika. N/O stands for No Occurrence, indicating that there are still areas where no such intensity occurred. PP stands for Papaioannou and Papazachos (2000), regarding the city of Athens. The Maximum return period column shows the lowest recurrence within either the Athens basin or the rest of the Attica. However, in all cases, there are even small localities that have not shaken in intensities ≥ VII (Figure 9.2). The differences between the historical catalogues and the fault specific seismic hazard maps indicate the need for longer observation time periods and higher spatial resolution in seismic hazard assessment.

Intensity	**Historical earthquakes**	**Athens basin**		**Rest of the Attica**	
	Min return period (yrs)	Min return period (yrs)	No Occurrence extent (%)	Min return period (yrs)	Max return period (yrs)
VII	100 (AB) 110 (PP)	96	2%	100	15000 (N/O)
VIII	100 (WA) 200 (AB) >1000 (PP)	272	30%	130	15000 (N/O)
IX	Sparse locations during 1999	652	84%	195	15000 (N/O)
X	Sparse locations during 1999	15000	99.6%	555	15000 (N/O)

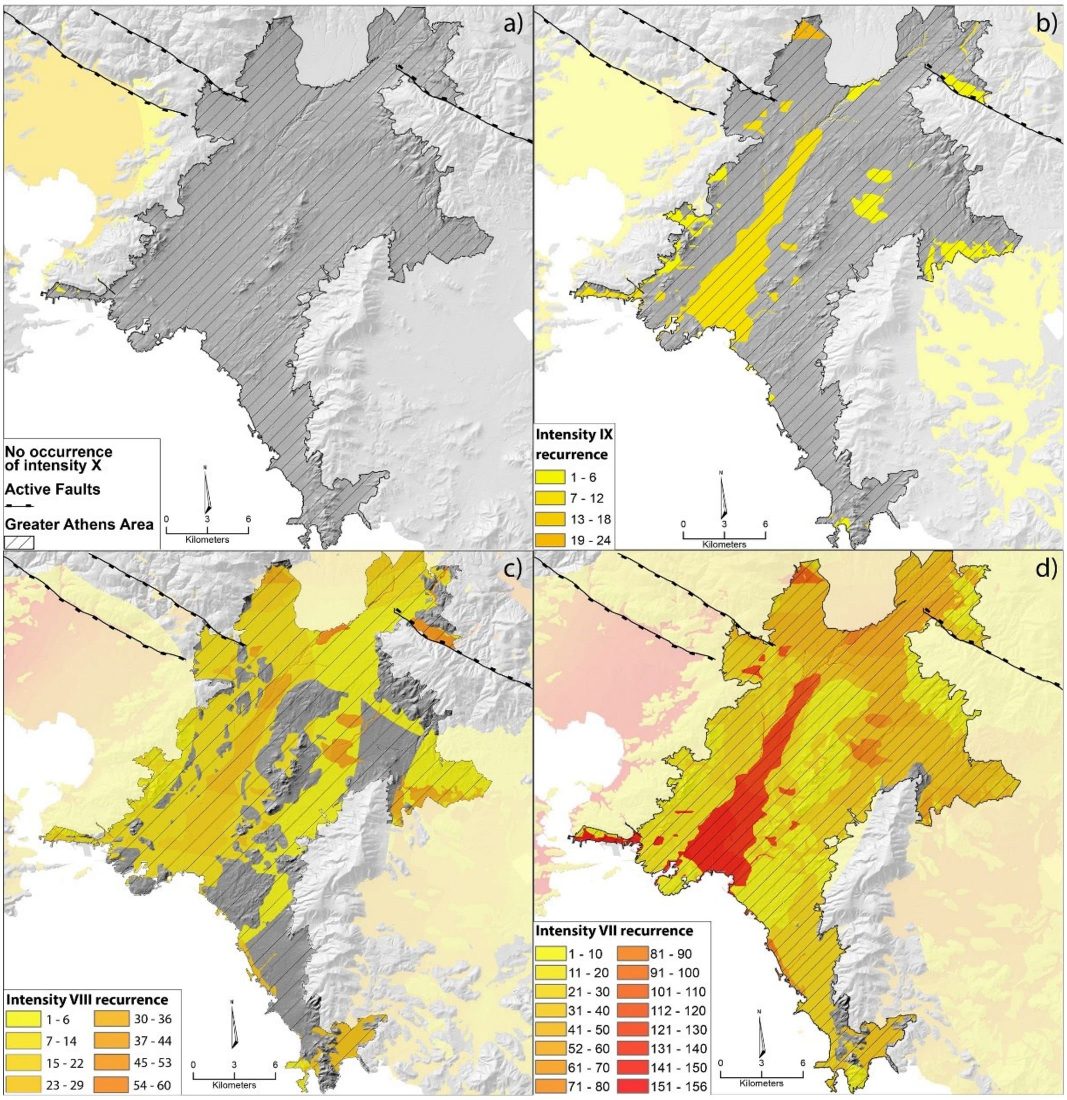

Figure 9.2: Recurrences of a) intensity X (no occurrence), b) intensity IX (maximum 23 times over 15 kyrs, or 652 y minimum return period), c) intensity VIII (maximum 55 times over 15 kyrs or 272 y minimum return period), and d) intensity VII (maximum 156 times over 15 kyrs, or 96 y return period), at the Athens basin. The Greater Athens Area boundaries were digitized using the OpenStreetMap road network.

9.5. Uncertainties in intensity distribution

The largest uncertainty in seismic hazard mapping lies on the attenuation relationships, based on the traditional intensity scales. From one point of view, this is an inevitable assumption that has to be made when intending to examine damages in the built environment. On the other hand, Earthquake Environmental Effects (EEE) are objective criteria indicating the severity or ground shaking in the non-built environment. Since they are not influenced by human parameters, they overstep problems that are inherited in traditional intensity scales, which tend to reflect mainly the economic development and the cultural setting of the area that experienced the earthquake, instead of its “strength” (Serva, 1994). The Environmental Intensity Scale - ESI 2007 (Michetti et al., 2007) incorporates the advantages of Earthquake Geology and uses EEE for the determination of seismic intensity (Michetti et al., 2007; Silva et al., 2008; Reicherter et al., 2009). Moreover, it can define the intensities above VII degree with a high level of accuracy as also shown in several recent and historic earthquakes worldwide (e.g. Serva et al., 2007; Tatevosian, 2007; Papanikolaou et al., 2009). Papanikolaou et al. (2009) implemented the ESI 2007 intensity scale for the 1981 Alkyonides earthquake sequence in the Corinth Gulf (Ms = 6.7, Ms = 6.4, Ms =6.3) and showed that it allows accurate assessment in sparsely populated areas. This implies that ESI 2007 could be used outside of the Greater Athens Area for modelling the ground shaking distribution with higher accuracy than the traditional intensity scales

New attenuation relationships for the ESI 2007 intensity scale would remarkably reduce the error incorporated in the existing seismic hazard maps. Such attenuation relationships have been partly developed for Greece and the Med (Papanikolaou and Melaki 2017). They define the relationship between earthquake magnitude and the estimated ESI Intensity based on 35 events, but the dataset is not large enough (8 events) for defining accurately the attenuation with distance. Ferrario et al. (2020) provide such preliminary attenuations with distance for selected Italian earthquakes (14 events). Following these remarks in the upcoming years, it might be possible to use the ESI intensity as well as input data for such maps in order to reduce the large uncertainty in the attenuation relationships imposed by human parameters.

9.6.Historical seismic record compared to geological fault slip data

The analysis of the active faults that can sustain damage (intensities ≥VII on the Modified Mercalli intensity scale) in the Attica region in case of seismic rupture aims to address the problems related to the incompleteness of the historical records since geological data sample much greater periods of time. The historical seismic record can be used for the seismic hazard analysis where smaller or blind faults can cause moderate earthquakes up to magnitude 6, with potentially damaging effects on older buildings. It is clear though that the official seismic zonation in Greece (E.P.P.O.) is based only on the historical earthquake catalogue and does not consider a fault specific approach.

Despite the inconsistencies and inhomogeneity in historic earthquake catalogues, the majority of the recorded events lie in the hanging wall of the hereby modelled active faults. Among them, there are few recorded strong events that could cause considerable damage, especially in the eastern part of the Attica Region (Figure 9.3). However, large uncertainties regarding the position of the instrumentally recorded epicentres are evident even for recent earthquake events. For example, the most recent 1999 Mw 5.9 is recorded in both NOA-UOA (National Observatory of Athens – University of Athens) and AUTH (Aristotle University of Thessaloniki) catalogues, but the epicentral localities lay more than 5 km apart. This uncertainty is magnified more than two times for the 1938 Mw 6.0 Oropos event, where the distance between the epicentres from these two catalogues is 12km. Larger uncertainties result for the older events approximate epicentral locations. For the period 1901-1964, the errors can be up to 30 km, but they can reach up to 50km for the older events (before 1900) when the number of available macroseismic information points is less than 5. Stucchi et al. (2012) also observe uncertainties larger than 50km for regional catalogues that cover the time window 1000 – 1899 in the Broad Aegean area. Regarding the errors in magnitude, Papazachos et al. (2000) suggest a ± 0.25 interval for the instrumental period (1911-1999). They also attribute an ± 0.35 error for the historical data, when the number of available macroseismic observations (number of places where the intensity is known) is ≥ 10, otherwise, the magnitude errors reach up to a half of the magnitude unit. Furthermore, focal depths are not available for many events recorded in the historic earthquake catalogues, thus there is a strong possibility that some of the epicenters displayed in Figure 9.3 are actually attributed to the subduction zone. Regarding the total number of historic earthquake events, there seems to be no consistency, as there are events that don't exist in either catalogues.

In total, 9 events affecting the Attica region could be related to the analyzed faults. Large uncertainties occur for 5 of them, as there are large variabilities regarding their location and depth and as a result, they can not be correlated with a known fault trace. In contrast, 4 major events can be related to specific faults with lower uncertainties. The 1981 Alkyonides earthquake sequence in the Corinth Gulf (Ms = 6.7, Ms = 6.4, Ms = 6.3) can be attributed to South Alkyonides and Kapareli faults (id No 5 and 8 in Table 6.1) (Jackson et al., 1982). Moreover, the 1938 Oropos event (Ms = 6.0) could have probably ruptured the Oropos offshore fault (id No 11 in Table 6.1, see also

Papanikolaou and Papanikolaou, 2007b), causing considerable damage in the north part of Attika (Ambraseys and Jackson, 1990). Other events, like 1705 (Fig. 12b) have large uncertainties in their location, or even are not included in both catalogues. For example, Papadopoulos et al. (2002) argue that the 1705 event could be located at a distance of about 30 km from the center of Athens; however, the little macroseismic information available makes their epicentral locations very uncertain. Papazachos and Papazachou (2003) suggest an epicentral location in North Attica, accompanied by minor damages in Athens and Chalkida. Ambraseys and Jackson (1997) fitted significant damage in Athens and to the north of the town to the 1705 event, while for other events there were no clear reports for serious damage in Athens or in other areas in Attica.

Eventually, 4 major events can be attributed to the fault database, suggesting that due to low slip rates, the majority of the active faults may have not ruptured during the last 200 or 500 years, which is the time period when historic seismic catalogues are considered to be complete for earthquakes of $M \geq 6.5$ and $M \geq 7.3$ respectively.

As a result, there is an overall spatial concurrence between the fault database and the existing earthquake catalogues, for recent earthquake events. On the other hand, the historic earthquake catalogues are inadequate for displaying the full extent of seismic hazard, due to the lack of temporal and spatial resolution.

The large differences between the two catalogues shown in Figure 9.3 also indicate that the information for recorded earthquakes, even for the most recent events like the Athens 1999 earthquake, is not consistent. Thus, the association of the recorded events with the known active faults needs verification through further palaeoseismological research.

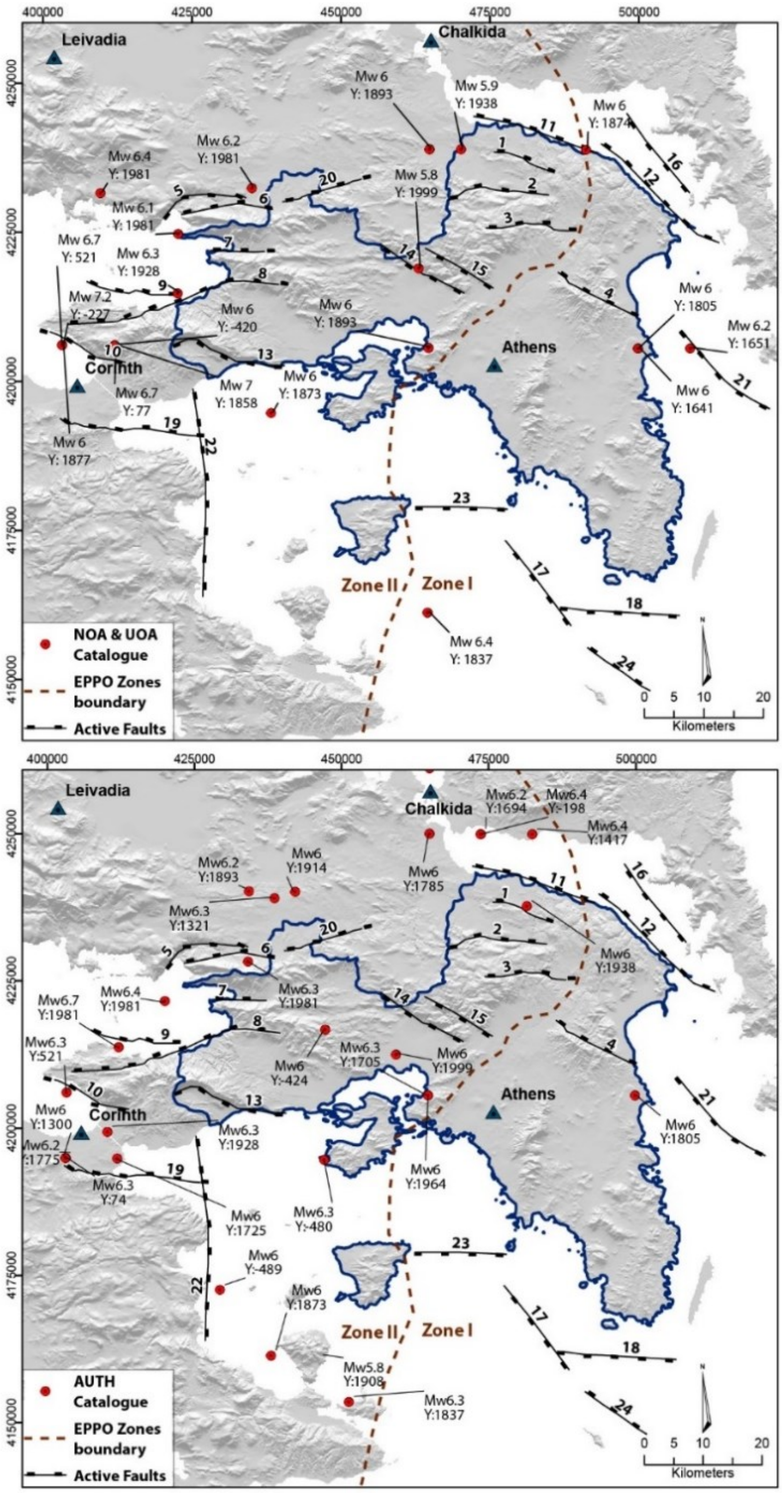

Figure 9.3: Historical earthquake record from a) the National Observatory and University of Athens (NOA&UOA) and b) the Aristotle University of Thessaloniki, for shallow earthquakes of magnitudes Mw>6 in comparison to active faulting in the Attica Region. The Athens 1999 and Oropos 1938 events are displayed in the NOA& UOA catalogue, although they are recorded as Mw5.8 and Mw5.9 events respectively. Focal depths are not available for the majority of the events in both catalogues, thus events with focal depth >20km might be also displayed. Both catalogues are complete for events Mw≥7.3 since 1500 and for Mw≥6.5 since 1845. As a result, active faults with no rupture history during the last 200 years may have not been included in the seismic hazard zonation of Greece, as shown in the map. Zone I represents the lowest seismic hazard and Zone II the intermediate hazard.

9.7. The role of the Miocene detachment in fault activity and intensities distribution

A major, now inactive, NNE-SSW striking fault system characterizes the geological structure of Attica. It trends northeast and separates metamorphic rocks to the south (Cycladic and Attica units) from non-metamorphosed units of the internal Hellenides to the north (Papanikolaou and Royden, 2007). Although this zone acted during the early and late Miocene time (Papanikolaou and Royden, 2007), it causes significant local variations of strain rates. The southeastern part of Athens plain seems to be under minor deformation rates, in contrast to the northwestern part, where higher strain rates are observed, indicating the control of the inactive detachment on the current deformation field of the region (Foumelis et al., 2013). Moreover, this detachment separates the E-W trending faults towards the western part of Attica from the NW-SE trending less active faults towards the eastern part (Papanikolaou and Papanikolaou, 2007b). The detachment also influences the seismicity pattern, as it coincides with the line that separates zone I (lowest category of seismic risk) from zone II (intermediate zone) of the national seismic building code (EAK-2003, see Figure 9.3), which has been compiled based on the seismicity level (Papanikolaou and Papanikolaou, 2007b).

Eastern Attica (the area east of the zone) lies primarily on metamorphic rocks, such as marbles and schists, that compose a massive, westward-dipping body. The area west of the detachment (Western Attica) is mainly comprised of sedimentary rocks, such as limestones and clastic formations. Recent post-alpine sediments, such as talus cones and scree, that cover areas of lower altitude or even the slopes of the mountain fronts, are often being used as the commonest foundation soils for urban structure (Lekkas, 2000).

Apart from the significant effect of the Miocene detachment on the neotectonic structure of Attica, influencing the geometry, style and intensity of deformation (Papanikolaou and Papanikolaou, 2007b), it seems to have played a fundamental role in the intensity distribution of earthquake events. During the Athens 1999 Mw=5.9 earthquake, the distribution of the strong ground motions and the heavy building damages were concentrated in NNE-SSW oriented zones. These zones coincide with or are parallel to the Miocene detachment, which seems to have performed passively from the coastline of the Greater Athens Area, up to its northernmost borders. High intensities, that were restricted in the areas west of the detachment, were abruptly blocked and didn't enter the eastern suburbs (Papanikolaou et al., 1999; Marinos et al., 1999b; Lekkas, 2001).

In this thesis, two parameters attributed to the effects of the detachment influenced the intensity distribution. The first parameter has to do with the loose sediments along the Kifissos riverbed, that flows parallel to and near the detachment. This part of Attica seems to have been shaken several times at intensities from VII to IX, while the intensity distribution is in agreement with the observed values during the Athens 1999 earthquake event. The second parameter has to do with the different fault orientation and activity on either side of the detachment. Higher intensities and recurrence values are observed in the western parts of the Attica mainland due to higher fault slip rate values. In contrast, lower intensities and longer recurrence intervals occur towards the eastern part of the Greater Athens Area or even the easternmost parts of Attica.

9.8. Topographic amplification factor

The implementation of the topographic amplification factor in the modeling procedure, as described in Eurocode 8 for the European Union (Bisch et al., 2012), could potentially increase the accuracy of the intensity distribution in the final seismic hazard maps. This factor incorporates slope instability effects, usually observed on isolated cliffs and ridges with crests and can be applied on Seismic Hazard Analysis based on Peak Ground Acceleration (PGA) values (values are multiplied by 1.2 to 1.4). However, according to Wald et al. (1999) and Paolucci (2002), an increase of PGA by a factor ranging from 1.2 to 1.4, implies an increase of MMI ranging from 0.29 to 0.53, which is less than the increase (or decrease) derived from the incorporation of geological conditions. Furthermore, a test regarding the impact of the topographic gradient in the Greater Athens Area was performed. It showed that less than 0.4km^2 of inhabited areas (or ~ 0.1% of the Greater Athens Area) meet the landscape parameters for the application of the topographic amplification factor, thus the final maps would have imperceptible changes. This parameter can be incorporated in more detailed micro zonation studies.

9.9. Major assumptions on the Catastrophe model

9.9.1. Hazard module

The most ordinary approach is to analyze the existing seismic catalogues and apply sophisticated simulations in order to capture future catastrophic events. The problem with this approach is that historical earthquake catalogues are too short (e.g. Speidel and Mattson 1997), covering a period of time that is much shorter than the average seismic cycle of the active faults which rupture at a recurrence interval from a few hundred years to several thousands of years (Goes, 1996; Yeats & Prentice, 1996; Machette, 2000). It should be considered that the completeness period is usually a small fraction of the period covered by the historical record and ranges from only 100 yrs (e.g. central America and New Zealand) up to 500 yrs (in parts of Europe) for M≥5.8, but is essential since it is used as input data in the probabilistic seismic hazard assessment (Papanikolaou et al., 2015).

Therefore, it is clear that a large number of faults would not have ruptured during the completeness period of the historical record, so the statistical sample would be clearly incomplete (Papanikolaou et al., 2015; Grützner et al., 2016). Indeed, in the Attica region where 24 active faults have been mapped, only four major historical earthquake events can be attributed to the active faults of the Hazard Module and five other strong historical events have major epicentral uncertainties and can not be correlated to specific faults (Deligiannakis et al., 2018a). In the offshore settings the incompleteness problem becomes even more evident. For example, in the Skyros Basin, Northern Aegean, Greece, out of the 19 major active faults, only three have been ruptured during the period covered by the historical seismicity (Papanikolaou et al., 2019). Sufficient historical information at an adequate granular level is a prerequisite for insurance undertakings, even for the calculation of premium provisions for non-life obligations (EIOPA, 2014b). Thus, in Attica, because faults have mostly low slip-rates, the majority of the active sources would not have ruptured during the last 500 years or even 200 years, which is the time period when historic seismic catalogues are considered to be complete for earthquakes of M≥6.5 and M≥7.3 respectively (Papazachos et al., 2000). Consequently, there is an overall spatial concurrence between the fault database and the existing earthquake catalogues for recent earthquake events. On the other hand, the earthquake catalogues that cover the Attica region are inadequate for displaying the full extent of seismic hazard, due to the lack of temporal and spatial resolution. Overall, the European Seismic Catalogue from 1000 up to 1899 A.D., holds large uncertainties regarding both the epicentral localities (approx. 40-50 km) and the estimated paleomagnitudes (mostly around 0.3-0.6 of Mw) of historical events (Stucchi et al., 2013).

The whole Hazard Module input is based on the slip-rate of the active faults that affect the Attica region. Slip rates provide the information for the level of activity and the frequency each fault ruptures through the period of time (Roberts et al., 2004). The extraction of the anticipated earthquake frequency based on the fault slip rates serves the need to quantify the earthquake hazard in a long term period.

A considerable uncertainty in seismic hazard mapping lies on the attenuation relationships, based on the traditional intensity scales. Indeed, Papanikolaou (2011) demonstrated that the attenuation relationships of traditional intensities form a major source of uncertainty in seismic hazard assessment and in several cases they overshadow all the other factors of uncertainty, even fault slip-rates, which govern the earthquake occurrence. Still, this is a particular assumption that has to be made when intending to examine earthquake damages in the built environment. On the other hand, since catastrophic earthquakes are rare events, the only way to evaluate the attenuation relationships is to compare them with existing macroseismic data or to select the most appropriate ones for the region in question. However, such a comparison is difficult to be performed and suffers from two main constraints. First, it is difficult to compare the recurrence values over extended periods because of the incompleteness of the existing earthquake catalogues, even for magnitudes that are related to lower intensities (VIII or VII). Second, the uncertainty on the spatial resolution of the intensity, especially for past events, affects the comparison with the modelled spatial distribution. However, Section 9.4 (see also Deligiannakis et al., 2018a) confirms the accuracy of the proposed method for the spatial distribution of the macroseismic intensities VII up to IX and corresponding damages to the building stock.

9.9.2. Vulnerability Module

The use of the vulnerability tables that combine the intensity values is adopted in the current model for two reasons. First, the intensity values represent by default the actual effects of the strong ground motions to the built environment. As such, they describe the damages to buildings in an accurate way, especially when there is a need to apply the damage estimation to a large number of buildings, as is the case with the portfolios of the insurance companies. Second, there are specific characteristics of buildings that need to be inserted in a vulnerability curve in order to yield an accurate result regarding the expected damage. In most cases, such data are not available at the Greek insurance companies' portfolios, where it is unusual that the insured buildings are classified in a formal building code based on their actual characteristics. As a result, it is argued that the use of the Modified Mercalli intensity values and the simplistic attenuation functions are adequate for this model and for the type of information that is available in the insured portfolios. However, the use of PGA, PGV, or SA based curves is easy to be integrated into the Vulnerability module in case the insurance market provides more detailed information regarding the building construction types.

Another important aspect is related to the actual fragility curves and the corresponding costs after damaging earthquakes. According to Kappos et al. (2006), one common way to develop fragility curves is to follow empirical rules, which in turn are based on statistical data for different intensity values (e.g., Lagomarsino & Giovinazzi, 2006). While there is enough information for smaller and more frequent earthquake events, the resulting intensities are usually not able to cause significant and costly damages to the building stock. In addition to that, the major earthquake events with intensities more than IX are rare in Europe, and thus the building damage data are insufficient for statistical evaluation (Kappos et al., 2006). On the other hand, the usage of existing damage-to-loss models that have not been adjusted to the appropriate construction types may lead to an erroneous estimation of the vulnerability (Martins et al., 2014). Methods that use both statistical data from past earthquakes and non-linear analysis of typical structures (e.g., Kappos et al., 1998; Kappos et al., 2006) can provide considerably better results regarding the expected building damages and repair costs (Kappos & Panagopoulos, 2010). While they are useful for risk assessment at a city level (e.g., for the cities of Volos and Grevena, by Kappos et al. 2002; 2009), they require specific characteristics of the structural system that are unavailable in the typical insurance companies portfolios.

Additionally, the fragility curves in terms of the PGA are combined with microzonation data for more accurate results, which are not available in large scale geographic exposure, such as the Attica region. A solution to this problem would be to make use of the insured losses that are connected to damages of known building types, after damaging earthquakes in Greece, or in countries with similar geotectonic conditions and building stock characteristics. In this case, the statistical sample is inadequate, primarily because the majority of the large earthquakes in Greece had minimal insured losses due to the reduced penetration of the Greek insurance companies in the market during the previous decades (EAEE, 2019). To this end, it is argued that the vulnerability table that was used represents an average damage ratio, which yields more conservative yet satisfactory results since it incorporates statistics from a large number of building damages of older building design codes. Nevertheless, the vulnerability curves could be refined in the future particularly when a fault specific approach is developed regarding the expected PGA or damage pattern (e.g. Mavroeidis & Papageorgiou, 2010; Spudich et al., 2013).

9.9.3. Exposure module

The exposure module represents the input data on behalf of the insurance company. The relevant assumptions include the building type, location, construction date, and use. For this test, a rather conservative approach was adopted, knowing that the market penetration of the Greek insurance companies is targeted to particular risks, mostly driven by the obligatory fire and earthquake risk insurance for each new building mortgage. As a result, nearly all insured residential buildings are constructed under the new or older seismic code. In contrast, the commercial and industrial buildings are considered to have a more even spread over the various seismic codes. Having kept every parameter unchanged in the other three modules, tests with actual portfolios from the insurance vendors were conducted. These tests showed that actually, the SCR is at least an additional 15% lower compared to the demo portfolio.

Another aspect is that the location data for each contract usually include the Postal Code, rather than the actual street address of the exact coordinates of the risk. The actual location of every risk is essential in order to define the proximity to the active faults and the attenuation or amplification of strong ground motion due to the local site conditions (see also Papanikolaou et al., 2013). The exposure module is able to function with geocoded contracts, as long as they are available.

9.9.4. Events table

The primary assumption in the Loss module is that the compiled Events table is large enough to simulate all extreme earthquake events that are expected in the near or far future. To put this to the right perspective, it is important to see what the number of events actually represents. The common practice in the commercial sector suggests that the Events table includes tens of thousands of simulated events, which correspond to tens of thousands of years forward, using Monte Carlo simulations (Crowley and Bommer, 2006). However, since these simulations are based on the existing catalogues, it is possible that they have questionable credibility in terms of accuracy and ability to include every location and every magnitude explicitly. This happens simply because areas with no major earthquake events during the past 200 years may have low or zero probability of occurrence for new earthquake events. For instance, in the Attica region, only four significant events can be attributed to the 24 active faults that are included in the model (Deligiannakis et al., 2018a), which means that there are at least 20 faults that will eventually rupture since they are active. Still, the Monte Carlo simulations based on the existing catalogues may not be able to take them into account. At the same time, localities that suffered earthquake damages within this period usually present an overestimated hazard. This is also the case for the Attica region, which experienced the expensive damages of the Athens 1999 Mw5.9 earthquake event. In any case, the model structure supports as-if scenarios for past earthquake events based on the insured portfolio for Vulnerability and Loss validations. It can also use claims data from previous events to calibrate and validate the vulnerability curves or adopt new ones.

9.10. Comparison of the SCR calculation with the EIOPA's SF.

According to the Solvency II directive (European Union, 2009) the starting point for the adequacy of the quantitative requirements in the insurance sector is the Solvency Capital Requirement. The Standard Formula (SF) is intended to reflect the risk profile of most insurance and reinsurance undertakings. However, there may be some cases where the standardized approach does not adequately reflect the very specific risk profile of an undertaking. This happens because the SF aims to capture the material quantifiable risks that most undertakings are exposed to. As a result, it is by default a standardized calculation method, and is therefore not tailored to the individual risk profile of a specific undertaking. For this reason, in some cases, the standard formula might not reflect the risk profile of a specific undertaking and consequently the level of own funds it needs (EIOPA, 2014b). The use of the SF for the SCR calculation is very common among the Greek insurance companies. This happens because it is easy to use, it is approved by the supervising authority as an alternative solution and it can be run without any additional computing sources. However, this section will show that there is a significant overestimation of the SCR when using the Standard Formula, compared to the proposed model.

The herein proposed earthquake catastrophe model' results were compared with the EIOPA SF outputs for the same demo portfolio, using the 2016 values for the Greek Country Factor, Zonal Relativities, and Aggregation Matrix (EIOPA, 2014a). At first, the SF is widely used by the European insurance vendors, as it is the most convenient, efficient and widely accepted benchmark for the ORSA, and SCR calculations. Second, the combined use of the Standard Approach with the commercial catastrophe models is also being used as a basis for the reinsurance treaties in the Greek insurance industry.

The results show an overall 19.3% overestimation by the SF, compared to the proposed model, for the SCR calculation in the Attica Region, without even applying the deductibles in the demo portfolio, thus implying a much higher overestimation. However, more significant variations resulted when modelling separate CRESTA Zones within Attica. In 7 out of 10 CRESTA Zones, the SCR calculated by the SF was from 2.69% up to 133.57 % higher, while in 3 cases, it was 16.28% – 32.97% lower. These variations result from the differences in the spatial analysis, the local site conditions, and the variations in seismic intensity recurrences throughout the same CRESTA Zone.

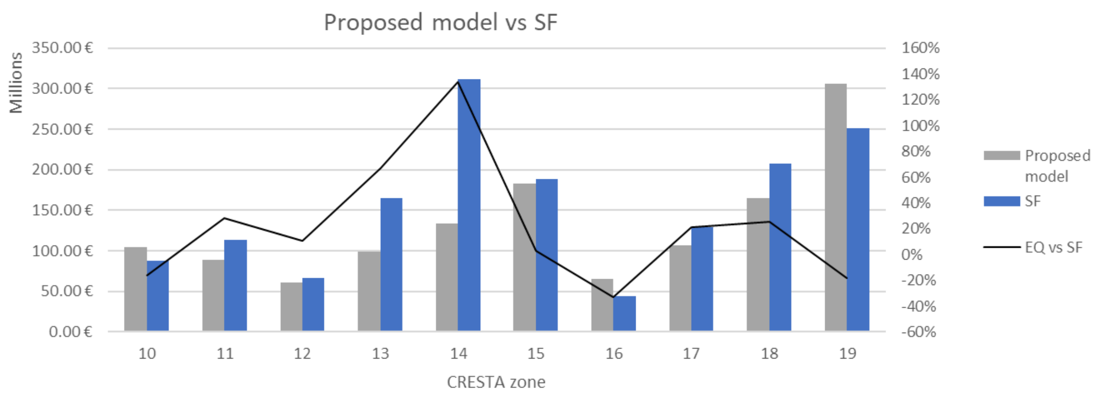

Figure 9.4: SCR calculations per CRESTA Zone for the Attica region without taking into account any deductible in the proposed model (EQ). The SF overestimates the SCR for the majority of the cases, with the most prominent differences occurring in Zone 14 (see text for explanation).

In general, the need to develop an algorithm for the SF that fits every country inherits some default assumptions that may impede the ability to produce accurate results for each insurance company. For example, the calibration of the SF is based on average conditions for any given country-peril combination (EIOPA, 2014b). This means that the SF may ignore the local peculiarities for each country and each country region. Additionally, the vulnerability is calculated on average for every peril-country combination, along with the other insurance policies (EIOPA, 2014b). For example, there is no option for different building construction types, the number of stories or different seismic codes that drastically affect the vulnerability and response of buildings in strong ground motions (e.g. Kappos et al., 2007; Kappos et al., 2008; Pomonis & Gaspari, 2014). Furthermore, although there is an underlying assumption for an average deductible, there is no option for the distinction of policies and lines of business. On this comparison, one scenario that takes into account a 2% deductible for all policies is also added. For the other two model runs and main comparisons, no deductibles were used, since it is not clear what is the average deductible that the SF uses.

It is important to note that even if the deductible usually refers to such a small percentage of the insured claims for earthquake insurance contracts, it has an unproportionally large impact at the final compensation. For example, the latest Elassona – Tyrnavos Mw6.3 and Mw5.9 earthquake sequence on 3rd - 4th of March 2021 (Tolomei et al., 2021), caused an insured loss of 1.7 million euros. However, with the application of the deductible policies, the actual payments on behalf of the insurance companies dropped to 0.8 million euros, nearly 50% less than the initial claims projection (EAEE, 2021). This happens because the deductible policy applies to the initial insured value. For example, a 2% deductible on a 100,000 € contract results to 2,000 € that would be deducted from any payment. Moreover, if the claim is equal or below 2,000 € there will be no compensation (see also Goda et al., 2014). As a result, in case of small damages there will be small or even zero payments on behalf of the insurance companies.

The adaptation of the SF on a country level is based on three critical parameters for the SCR calculation. These are the Country Factor, the Zonal Relativities, and the Aggregation Matrix. The Zonal Relativities are connected to the 1 in 200-year loss of each CRESTA zone, and the Aggregation Matrix shows the correlation between the CRESTA zones at the 1 in 200-year loss level (EIOPA, 2014b). Similarly, the Country Factor for the earthquake risk represents the maximum amount that the insurer pays on a 1 in a 200-year loss basis, as a ratio of the total sums insured. The Country Factors are based on the best estimates provided by expert judgment, but at the same time, the Zonal Relativities and the Aggregation matrix rely on several underlying, stochastic event-based catastrophe risk models (EIOPA, 2014b). It is noteworthy that these catastrophe models provide significantly different results. Indeed, four vendor models were tested by Petseti & Nektarios (2012) and the PML as % of total sum insured 1 in 200 years (0.5%) ranged from 1,03 up to 3,80%. Since these models are not available for review, it is assumed that they utilize the existing historical earthquake catalogues as an input for their hazard modules. In their latest versions, they might also incorporate incomplete or preliminary active fault databases, such as the ones used in the SHARE project (Woessner et al., 2015), or the Global Earthquake Model, which include only six faults for the Attica region. However, this means that the algorithms of the SF incorporate the corresponding temporal and spatial uncertainties of the catalogues (see also Deligiannakis et al., 2018b). The importance of complete input data is also indicated by EIOPA (2014a, 2018) since they signify the need to assess whether they include sufficient historical information to evaluate the characteristics of the underlying risks.

Although there is limited academic research regarding the assessment of the SF in non-life catastrophe risk, it is evident that the standardised method could benefit from further adjustments (Doff, 2008). The SCR calculation algorithms for non-life underwriting risk are highly affected by the aggregation matrices (Bermúdez et al., 2013), while the uncertainty in the prediction of the trend in ultimate claim amounts affects the SCR substantially (Alm, 2015). Similarly, regarding credit and market risks, the portfolio characteristics strongly affect the SCR calculations (Gatzert and Martin, 2012).

The following examples show the high spatial resolution of the proposed model for the Intensity VIII distribution over the last 15000 years for the northern and southern suburbs of Athens. In Figure 9.5, it is evident that the largest part of CRESTA Zone ‘14’ is not expected to experience such intensities. Indeed, 6 out of 26 postal codes within the Zone will not experience Intensity VIII at all, while the others will be shaken at such intensities with a very low recurrence. In this CRESTA Zone, the postal codes with low or zero intensity VIII recurrence are the ones with the largest insured values, and thus, the SF estimates a 133.57% higher SCR than the proposed model.

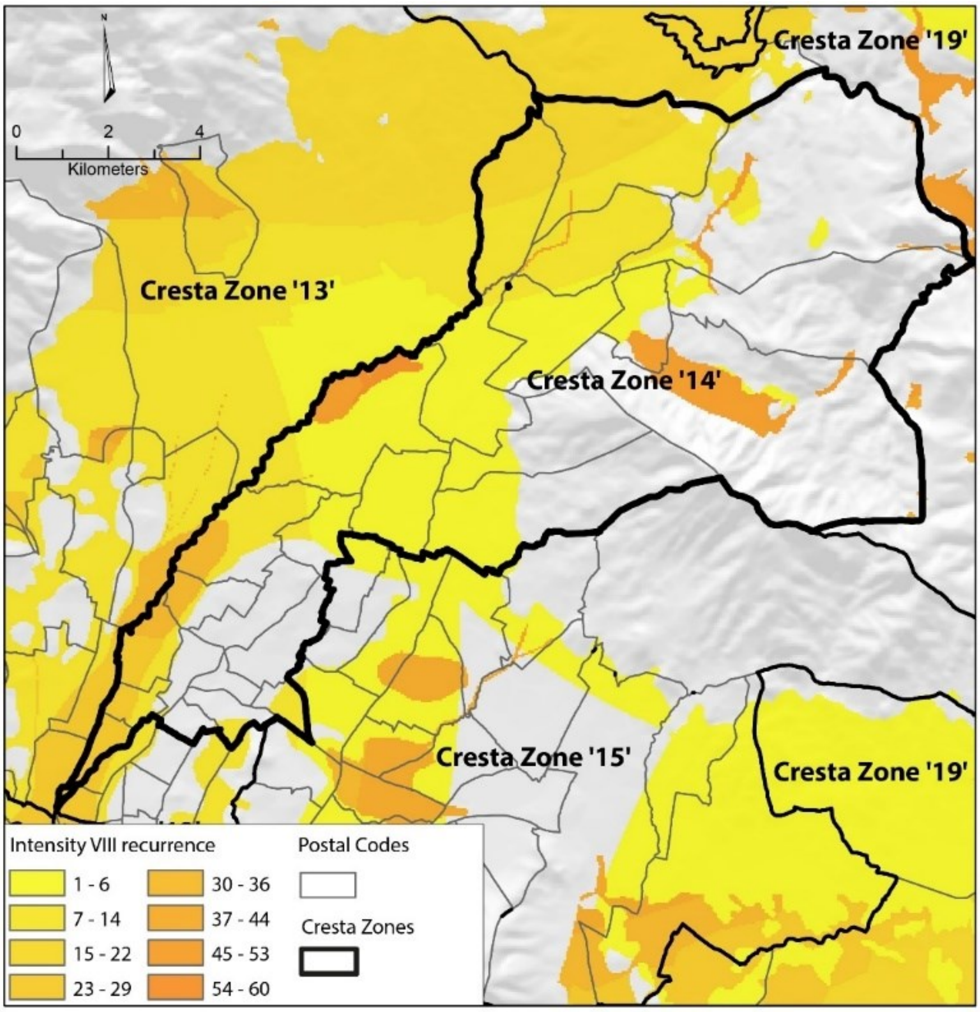

Figure 9.5: The Fault Specific Seismic hazard map on the CRESTA Zone '14', see Deligiannakis et al. (2018b) for details. Colour variations show how many times the localities in the map have received enough energy to shake at intensity VIII over the past 15kyrs. This map offers a high spatial resolution of the intensities' distribution and recurrence, which allows for increased accuracy on the SCR calculations.

Similarly, the proposed earthquake catastrophe model calculates the smallest SCR for the CRESTA Zone '16', compared to the other CRESTA Zones of Attica. Nevertheless, 5 out of 19 Postal Codes within that Zone have experienced intensity VIII and even IX in low recurrence (Figure 9.6). However, this CRESTA Zone is attributed to an extremely low CRESTA relativity factor (0.6), which seems to result in an SCR 32.97% lower than the proposed model. These variations illustrate the importance of spatial granularity in the hazard analysis, in contrast to the assumption of homogenous exposure and hazard throughout the entire CRESTA zone.

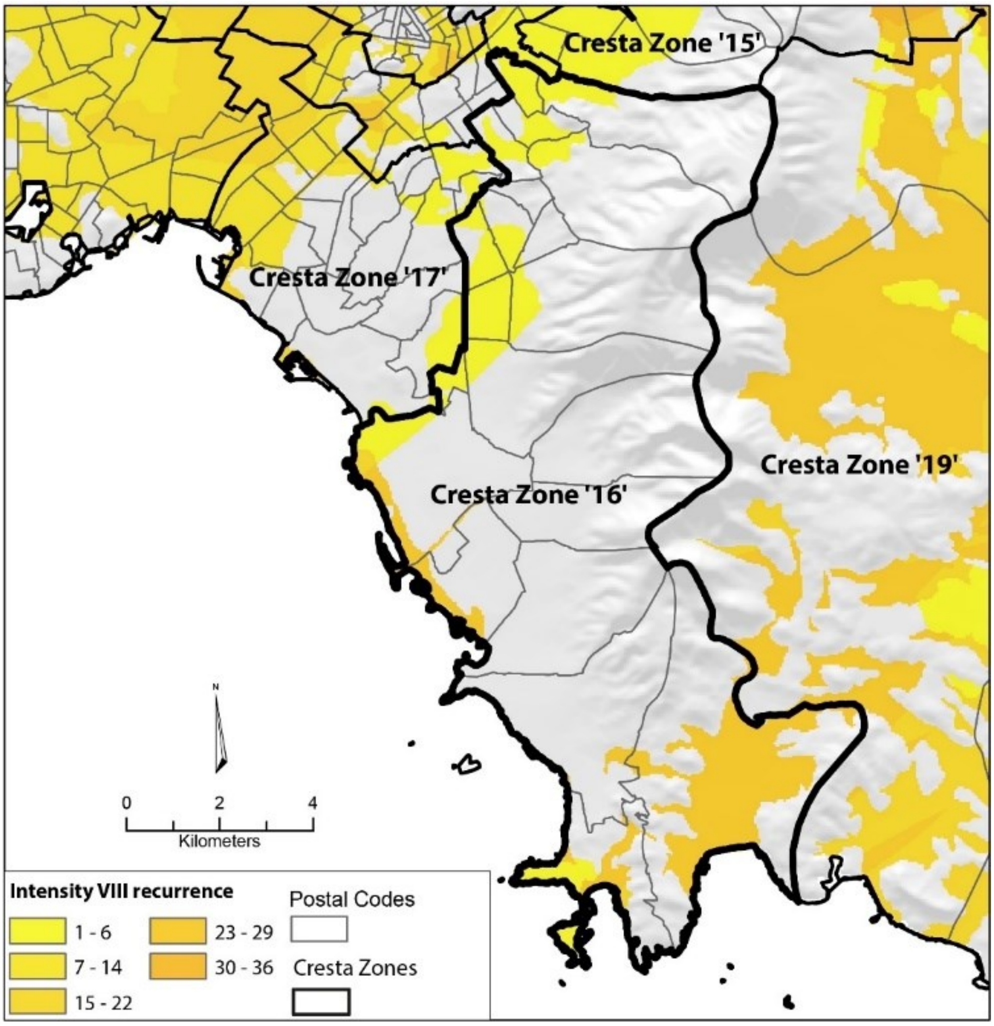

Figure 9.6: The Fault Specific Seismic hazard map on the CRESTA Zone '16', see Deligiannakis et al. (2018b) for details. Colour variations show how many times the localities in the map have received enough energy to shake at intensity VIII over the past 15kyrs.

One could argue that the seismic hazard maps would act as the most accurate tool for underwriting and exposure planning. Although this is the general picture, there is a distinction regarding the SCR calculation, which relies on the simulated events table. In this case, the event year, which represents the 99.5% loss, could include earthquake events that have different damage distribution compared to the high-risk areas, based on the seismic hazard maps. This is the reason why the geographic diversification of the portfolio plays such an important role. In any case, this indicates the importance of transparent processes throughout every step of the model. Furthermore, no matter how sophisticated the analysis of earthquake catalogues is, there is a considerable probability that large earthquake events will fall out of the models' projections. It has already happened on past events (e.g., Swiss Re Institute, 2019a) and insurance vendors have already realized the need to integrate academic research in the hazard modules. Besides, the 3rd Pillar of the Solvency II regulation requires insurers to adopt transparent procedures and avoid "black box" risk assessment techniques.

Indeed, the results of the herein proposed model runs and the comparison with the SF were shared with the EIOPA's Catastrophe Risk Subgroup of the Insurance and Reinsurance Stakeholder Group. The differences in risk premiums and, most importantly, the evidence for overestimation of the SCR by the SF in the Attica region lead to suggestions for modifications of the SF. In detail, the EIOPA's second set of advice to the European Commission (EIOPA, 2018) includes suggestions for recalibration of country factor (1.75% from 1.85%), zonal weights and aggregation matrices, especially those referring to the Attica CRESTA zones.

Apart from the calculation of the SCR, there are two other ways that the current thesis can provide valuable help from an insurance company point of view, especially for policy planning, undertaking and portfolio diversification.

First, the visualization of the potential seismic hazard in high-resolution seismic hazard maps is an important tool for decision making, regarding insurance penetration strategies, portfolio expansion and diversification. Second, the high-resolution fault specific seismic hazard maps can be used to calculate probabilities of occurrence for the desired intensities in a required time period. Section 8.1 provides a method for future losses calculation, other than the SCR. The latter is currently the main input that insurance companies have for the awareness of the underlying seismic hazard. Until now, variations on hazard are only visible through consecutive model runs, either using the Standard Formula (SF), or any other commercial model. The final output of such runs is a map showing the anticipated losses, usually at a postal code level. As a result, there is no clear view of the potential hazard regardless of the exposure, which is something that high resolution fault specific hazard maps can provide.

10. Conclusions

This thesis has combined geological and tectonic geomorphological data in order to define active faults parameters to be used for seismic hazard assessment. Fault specific seismic hazard maps with high spatial resolution have been developed for the Attica Region (multiple faults case), based on fault characteristics and local site conditions. In the case of the Attica region, an Earthquake Catastrophe model is developed based on a fault specific Hazard module. This model can be used for the calculation of the Solvency Capital Requirements for insurance companies.

Two different types of fault specific seismic hazard maps were developed in this thesis. The first type includes fault seismic hazard maps which are based on a single fault and forms a simple case study. This applies to the Sparta fault, which was activated in 464 B.C., devastating the city of Sparta. The second type represents much more complicated maps than the single-fault ones since they offer the cumulative impact from all seismic sources in each specific locality. This method is applied to the region of Attica, which is the most densely inhabited area in Greece, as nearly half of the country's population lives in Athens and its surrounding suburbs.

Tectonic geomorphological methods are used to examine the properties and characteristics of each onshore fault that is modelled in both types of maps. With regards to the Sparta fault, qualitative analysis of catchments profiles shows a significant difference in longitudinal convexity between the central and both the south and north parts of the fault system, leading to the conclusion of varying uplift rate along strike. Quantitative analysis shows that catchments are sensitive in differential uplift, as is observed by the calculated differences of the steepness index ($k_{sn)}$ between the outer (k_{sn}<83) and central parts (121<k_{sn}<138) of the Sparta Fault along strike the fault system. As a result, the Sparta fault segments are considered hard linked, and thus it could be modelled as a single structure for seismic hazard assessment.

Detailed information is presented for 14 onshore faults that lie within or in short distances from the Attica region boundaries and can cause damage in case of earthquake rupture. Swath topographic profiles along the 6 faults show a triangular relief pattern, as expected in actively uplifting environments. The swath profiles along the other faults reveal varying relief values along the fault direction, caused by river incision or possible fault segmentation. Tectonic geomorphological indices, such as the enhanced transverse hypsometry index (THi*), the Asymmetry factor (Af) and the Valley floor to valley high ratio (Vf), along with geomorphological observations, help define the level of fault activity in other cases. Finally, a database of 24 active faults that could cause damage to Attica in case of seismic rupture is developed, including information regarding the offshore faults located in short distances from the Attica region boundaries. This database is used for the development of 4 fault specific seismic hazard maps for the Attica Region. The majority of these faults have relatively low slip rates and the Greater Athens Area lies mostly on the active faults footwall. The spatial distribution of hazard depends on soil conditions for intensities X and IX and is governed by the distance from faults for intensities VIII and VII.

Four fault specific seismic hazard maps are developed for the Attica region, one for each of the intensities VII – X (MM), showing their recurrence at each locality in the map. The Attica mainland seems to have been exposed to intensity X for more than 20 times in the last 15 kyrs, along the west coastline, in Corinth Gulf. Maximum intensity X recurrences (25-29/15kyrs, or a 517 year return period) are observed near the South Alkyonides fault system. The maximum recurrences for intensity IX (73-77/15kyrs, or a 195 year return period) are observed in the westernmost parts of the Attica mainland. The highest recurrences for intensity VIII (115 times over 15 kyrs, or up to a 130 year return period) are expected in the western part of Attica. The highest recurrences for intensity VII (151-156 times over 15 kyrs, or up to a 96 year return period) are observed in the densely populated central part of the Athens basin. Regarding the seismicity record, there is an overall spatial concurrence between the fault database and the existing earthquake catalogues for recent earthquake events. On the other hand, the historic earthquake catalogues are inadequate for displaying the full extent of seismic hazard due to the lack of temporal resolution, highlighting the necessity for fault specific seismic hazard assessment.

An earthquake catastrophe model that calculates the SCR using a hazard module that combines active fault analysis with traditional seismic catalogue information is proposed in this thesis. It is applied in the Attica region, which hosts 41.6% of the insured buildings in Greece. Results show a risk premium from 1.63% up to 3.16% for the residential buildings. A comparison between the SF and the proposed model shows that the SF overestimates the SCR by 19.3% in the Attica region. The addition of 2% deductible in the exposure policies results to an SCR 56.8% lower than the SF. For 7 out of 10 CRESTA zones, the overestimation varies from 2.7% up to 133.57%, while for the three remaining zones, the SF underestimates the SCR by 16.28 – 32.97%.

11. References

Abercrombie, R.E.: 1991, Earthquake Rupture Dynamics and Neotectonics in the Aegean Region, Ph.D. thesis, University of Reading, UK.

Akçar, N., Tikhomirov, D., Özkaymak, Ç., Ivy-Ochs, S., Alfimov, V., Sözbilir, H., Uzel, B., Schlüchter, C., 2012. 36Cl exposure dating of paleoearthquakes in the Eastern Mediterranean: First results from the western Anatolian Extensional Province, Manisa fault zone, Turkey. Bull. Geol. Soc. Am. 124, 1724–1735. https://doi.org/10.1130/B30614.1

Alexiou, S., Deligiannakis, G., Pallikarakis, A., Papanikolaou, I., Psomiadis, E., Reicherter, K., 2021. Comparing High Accuracy t-LiDAR and UAV-SfM Derived Point Clouds for Geomorphological Change Detection. ISPRS Int. J. Geo-Inf. 2021, 10(6), 367; https://doi.org/10.3390/ijgi10060367.

Alexopoulos, A., Moraiti, E., Lekkas, S., 1998. On the occurrence of a non metamorphic upper Eocene -lower Oligocene clastic sequence, wedged between the allochthon and the relative autochthon system of Attiki (Greece). Bulletin of the Geological Society of Greece Proceedings of the 8th International Congress, Patras, XXXII, 79-84.

Algermissen, S.T., Perkins, D.M., Thenhaus, P.C., Hanson, S.L., Bender, B.L., 1982. Probabilistic estimates of maximum acceleration and velocity in rock in the contiguous United States. U.S. Geol. Surv. Open-File Report, pp. 82–1033.

Alm, J., 2015. A simulation model for calculating solvency capital requirements for non-life insurance risk. Scand. Actuar. J. 2015, 107–123. https://doi.org/10.1080/03461238.2013.787367

Ambraseys, N., 1999. Material for the investigation of the seismicity of central Greece. (http://emidius.irrs.mi.cnr. it/RHISE/ii_lamb//ii_lamb.html).

Ambraseys, N., 2009. Earthquakes in the East Mediterranean and the Middle East - A multidisciplinary study of Seismicity up to 1900, 1st Publication. Cambridge University Press, New York.

Ambraseys, N.N. & Psycharis, I.N., 2012. Assessment of the long-term seismicity of Athens from two classical columns, Bull. Earthq. Eng., 10, 1635–1666.

Ambraseys, N.N., Jackson, J.A., 1981. Earthquake hazard and vulnerability in the northeastern Mediterranean: the Corinth earthquake sequence of February-March 1981. Disasters 5, 355-368

Ambraseys, N.N., Jackson, J.A., 1990. Seismicity and associated strain of central Greece between 1890 and 1988. Geophys. J. Int. 101, 663–708. https://doi.org/10.1111/j.1365-246X.1990.tb05577.x

Ambraseys, N.N., Jackson, J.A., 1997. Seismicity and associated strain in the Gulf of Korinth (Greece) since 1694. Journal of Earthquake Engineering 1, 433-474.

Andreani, L., Stanek, K., Gloaguen, R., Krentz, O., Domínguez-González, L., 2014. DEM-

Based Analysis of Interactions between Tectonics and Landscapes in the Ore Mountains and Eger Rift (East Germany and NW Czech Republic). Remote Sens. 6, 7971–8001. doi:10.3390/rs6097971

Andronopoulos, V., Eleftheriou, A., Koukis, G., Rozos, D. and Angelidis, Ch., 1981. Macroseismic, geological and tectonic observations in the area affected by the earthquakes of the Corinthian Gulf (February--March 1981). International Symposium on the Hellenic Arc and Trench (H.E.A.T.), 1: 19--34.

Angster, S., Wesnousky, S., Huang, W.L., Kent, G., Nakata, T., Goto, H., 2016. Application of UAV photography to refining the slip rate on the Pyramid Lake fault zone, Nevada. Bull. Seismol. Soc. Am. 106, 785–798. https://doi.org/10.1785/0120150144

Antonaki, R., Vlachos, I., Staurakakis, G., Taflambas, I., Tokas, Chatziandreou, S., Smpokos, I., Karydis, P., and Kaleuras, B., 1988. Earthquake economic impact – Insurance. Report in Earthquake Planning and Protection Organization (in Greek) 233pp.

Antoniou,V., 2010. Anaglyph analysis and geotechnical structure of East Attica. Ph.D. Thesis. Agricultural University of Athens, Athens, Greece, 304 pp (in Greek).

Armijo, R., Lacassin, R., Coudurier-Curveur, A., Carrizo, D., 2015. Coupled tectonic evolution of Andean orogeny and global climate. Earth-Science Rev. 143, 1–35. https://doi.org/10.1016/j.earscirev.2015.01.005

Armijo, R., Tapponnier, P., 1986. Quaternary extension in southern Tibet: Field observations and tectonic implications. J. Geophys. Res. 91, 13.803-13.872.

Atzori, S., Manunta, M., Fornaro, G., Ganas, A., Salvi, S., 2008. Postseismic displacement of the 1999 Athens earthquake retrieved by the Differential Interferometry by Synthetic Aperture Radar time series. J. Geophys. Res. Solid Earth 113, 1–14. https://doi.org/10.1029/2007JB005504

Bacun, W.H., 1999. Seismic activity of the San Francisco Bay region. Bull. Seismol. Soc. Am. 89, 764-784

Barberio, M.D., Barbieri, M., Billi, A., Doglioni, C., Petitta, M., 2017. Hydrogeochemical changes before and during the 2016 Amatrice-Norcia seismic sequence (central Italy). Sci. Rep. 7, 1–12. https://doi.org/10.1038/s41598-017-11990-8

Baumont, D., Courboulex, F., Scotti, O., Melis, N.S., Stavrakakis, G., 2002. Slip distribution of the MW 5.9, 1999 Athens earthquake in- verted from regional seismological data, Geophys. Res. Lett. 29, doi 10.1029/2001GL014261.

Baziotis, I., 2008. Petrological and Geochemical study of the metamorphic rocks from east Attica. Ph.D. Thesis, National Technical University of Athens, Greece.

Bell, F.G., 1999. Geological Hazards, Their assessment, avoidance and mitigation. ENFN SPON, Routledge.

Bellier, O., Bourles, D.L., Beaudouin, T., Braucher, R., 1999. Cosmic Ray Exposure (CRE) dating in a wet tropical domain: Late Quaternary fan emplacements in central Sulawesi (Indonesia). Terra Nov. 11, 174–180. https://doi.org/10.1046/j.1365-3121.1999.00242.x

Bemis, S.P., Micklethwaite, S., Turner, D., James, M.R., Akciz, S., T. Thiele, S., Bangash, H.A., 2014. Ground-based and UAV-Based photogrammetry: A multi-scale, high-resolution mapping tool for structural geology and paleoseismology. J. Struct. Geol. 69, 163–178. https://doi.org/10.1016/j.jsg.2014.10.007

Bender, B., and Perkins, D.M., 1993. Treatment of parameter uncertainty and variability for a single seismic hazard map. Earthquake Spectra 9, 165-194

Benedetti, L., Finkel, R., King, G., Armijo, R., Papanastassiou, D., Ryerson, F.J., Flerit, F., Farber, D., Stavrakakis, G., 2003. Motion on the Kaparelli fault (Greece) prior to the 1981 earthquake sequence determined from 36Cl cosmogenic dating. Terra Nov. 15, 118–124. https://doi.org/10.1046/j.1365-3121.2003.00474.x

Benedetti, L., Finkel, R., Papanastassiou, D., King, G., Armijo, R., Ryerson, F., Farber, D., Flerit, F., 2002. Post-glacial slip history of the Sparta fault (Greece) determined by 36Cl cosmogenic dating: Evidence for non-periodic earthquakes. Geophys. Res. Lett. 29, 1–4. https://doi.org/10.1029/2001gl014510

Benedetti, L., Manighetti, I., Gaudemer, Y., Finkel, R., Malavieille, J., Pou, K., et al. 2013. Earthquake synchrony and clustering on Fucino faults (Central Italy) as revealed from in situ 36Cl exposure dating. Journal ofGeophysical Research: Solid Earth, 118, 4948–4974. https://doi.org/ 10.1002/jgrb.50299

Bentham, P., Collier, R.E.L., Gawthorpe, R.L., Leeder, M.R., Prossor, S., Stark, C., 1991. Tectono-sedimentary development of an extensional basin: The Neogene Megara Basin, Greece. J. Geol. Soc. London. 148, 923–934. https://doi.org/10.1144/gsjgs.148.5.0923

Bermúdez, L., Ferri, A., Guillén, M., 2013. A correlation sensitivity analysis of non-life underwriting risk in solvency capital requirement estimation. ASTIN Bull. 43, 21–37. https://doi.org/10.1017/asb.2012.1

Billiris, H., Paradissis, D., Veis, G., England, P., Featherstone, W., Parsons, B., Cross, P., Rands, P., Rayson, M., Sellers, P., Ashkenazi, V., Davison, M., Jackson, J., Ambraseys, N., 1991. Geodetic determination of tectonic deformation in central Greece from 1900 to 1988. Nature 350, 124–129. https://doi.org/10.1038/350124a0

Bisch, P., Carvalho, E., Fajfar, P., Fardis, M., Franchin, P., Kreslin, M., Pecker, A., Pinto, P., Plumier, A., Somja, H., Tsionis, G., 2012. Eurocode 8 : Seismic Design of Buildings Worked examples. Luxembourg. https://doi.org/10.2788/91658

Bolt, B.A., 1999. Earthquakes. W.H. Freeman and Company, New York, 366pp

Bommer, J., Spence, R., Erdik, M., Tabuchi, S., Aydinoglu, N., Booth, E., Del Re, D., Peterken, O., 2002. Development of an earthquake loss model for Turkish catastrophe insurance. J. Seismol. 6, 431–446.

Boncio, P., Lavecchia, G., Pace, B., 2004. Defining a model of 3D seismogenic sources for Seismic Hazard Assessment applications: The case of central Apennines (Italy). J. Seismol. 8, 407–425. https://doi.org/10.1023/B:JOSE.0000038449.78801.05

Bonilla, M.G., Mark, R.K., Lienkaemper, J.J., 1984. Statistical relations among earthquake magnitude, surface rupture length, and surface fault displacement. Bull. Seismol. Soc.

Am. 74, 2379–2411.

Boore, D.M., Skarlatoudis, A.A., Margaris, B.N., Costas, B.P., Ventouzi, C., 2009. Along-Arc and Back-Arc Attenuation, Site Response, and Source Spectrum for the Intermediate-Depth 8 January 2006 M 6.7 Kythera, Greece, Earthquake. Bull. Seismol. Soc. Am. 99, 2410–2434. https://doi.org/10.1785/0120080229

Bornovas, J. Lalechos, N., Filippakis, N., 1969. 1:50000 Geological Map "Korinthos". IGME, Athens.

Bornovas, J., Eleftheriou, A., Gaitanakis. P., Rontogianni, Th., Simeaki, K., Mettos, A., 1981. 1:50000 Geological Map "Kaparellion". IGME, Athens.

Bouckovalas, G.D., Kouretzis, G.P., 2001. Stiff soil amplification effects in the 7 September 1999 Athens (Greece) earthquake. Soil Dyn. Earthq. Eng. 21, 671–687. https://doi.org/10.1016/S0267-7261(01)00045-8

Boulton, S.J., Whittaker, A.C., 2009. Quantifying the slip rates, spatial distribution and evolution of active normal faults from geomorphic analysis: field examples from an oblique-extensional graben, southern Turkey. Geomorphology 104, 299–316.

Brecht, H., Deichmann, U., Wang, H.G., 2013. A Global Urban Risk Index, Policy Research Working Paper, 6506.

Briole, P., Rigo, A., Lyon-Caen, H., Ruegg, J.-C., Papazissi, K., Mitsakaki, C., Balodimou, A., Veis, G., Hatzfeld, A., 2000. Active deformation of the Corinth rift, Greece: results from repeated Global Positioning System surveys between 1990 and 1995. J. Geophys. Res. 105, 25605–25625.

Bull, W.B., 2009. Tectonically Active Landscapes. Wiley-Blackwell, Oxford.

Bull, W.B., McFadden, L., 1977. Tectonic geomorphology North and South of the Garlock fault, California. In: Dohering, D.O. (Ed.), Geomorphology in Arid Regions. Publ. in Geomorphol- ogy, State University of New York, Binghamton, pp. 115–138.

Caputo, R., Monaco, C., Tortorici, L., 2006. Multiseismic cycle deformation rates from Holocene normal fault scarps on Crete (Greece). Terra Nova 18, 181-190

Carydis, P., Tilford, N., Brandow, G., Jirsa, J., 1982. The Central Greece Earthquakes of February-March 1981, The Central Greece Earthquakes of February-March 1981. https://doi.org/10.17226/19598

Chandler, A.M., Jones, E.J.W., Patel, M.H., 2001. Property Loss Estimation for Wind and Earthquake Perils. Risk Anal. 21, 235–250. https://doi.org/10.1111/0272-4332.212108

Chartier, T., Scotti, O., Lyon-Caen, H., 2019. SHERIFS: Open-source code for computing earthquake rates in fault systems and constructing hazard models. Seismol. Res. Lett. 90, 1678–1688. https://doi.org/10.1785/0220180332

Chatzipetros, A., Kokkalas, S., Pavlides, S., Koukouvelas, I., 2005. Palaeoseismic data and their implication for active deformation in Greece. J. Geodyn. 40, 170–188. https://doi.org/10.1016/j.jog.2005.07.005

Chatzipetros, A., Pavlides, S., 1998. A quantitative morphotectonic approach to the study of active faults, Mygdonia basin, northern Greece. Bull. Geol. Soc. Greece 32, 155–164.

Chen, W.P., Molnar, P., 1983. Focal depths of intracontinental and intraplate earthquakes and their implications for the thermal and mechanical properties of the lithosphere. Journal of Geophysical Research 88(B5), 4183-4214.

Childs C., Nicol A., Walsh J.J. & Watterson J. 2003. The growth and propagation of synsedimentary faults. Journal of Structural Geology, 25, 633–648.

Christoulas, S.G., Tsiampaos, G.K., Sabatakakis, N.S., 1985. Engineering geological conditions and the effects of the 1981 earthquake in Athens, Greece. Eng. Geol. 22. https://doi.org/10.1016/0013-7952(85)90044-4

Collier, R.E.L., Pantosti, D., D'Addezio, G., De Martini, P.M., Masana, E., Sakellariou, D., 1998. Paleoseismicity of the 1981 Corinth earthquake fault: Seismic contribution to extensional strain in central Greece and implications for seismic hazard. J. Geophys. Res. Solid Earth 103, 30001–30019. https://doi.org/10.1029/98jb02643

Comninakis, P.E. and Papazachos, B.C., 1986. A catalogue of earthquakes in Greece and surrounding area for the period 1901-1985. Laboratory Publication, University of Thessaloniki, 1, 167 pp.

Copley, A., Grützner, C., Howell, A., Jackson, J., Penney, C., Wimpenny, S., 2018. Unexpected earthquake hazard revealed by Holocene rupture on the Kenchreai Fault (central Greece): Implications for weak sub-fault shear zones. Earth Planet. Sci. Lett. 486, 141–154.

Coppersmith, K.J., Youngs, R.R., 2000. Data needs for probabilistic fault displacement hazard analysis. J. Geodyn. 29, 329–343. https://doi.org/10.1016/S0264-3707(99)00047-2

Cornell, C.A., 1968. Engineering seismic risk analysis. Bull. Seismol. Soc. Am. 58, 1583–1606. https://doi.org/http://dx.doi.org/10.1016/0167-6105(83)90143-5

Cornell, C.A., 1972, Bayesian Statistical Decision Theory and Reliability-Based Design, Proceedings of the International Con- ference on Structural Safety and Reliability, A.M. Freundenthal, Editor, April 9–11, Washington, D.C., Smithsonian Institute, pp. 47–66.

Corradetti, A., McCaffrey, K., De Paola, N., Tavani, S., 2017. Evaluating roughness scaling properties of natural active fault surfaces by means of multi-view photogrammetry. Tectonophysics 717, 599–606. https://doi.org/10.1016/j.tecto.2017.08.023

Cowie, P. A., and G. P. Roberts, 2001. Constraining slip rates and spacings for active normal faults, *J. Struc. Geol.*, 23, 1901– 1915.

Cowie, P.A., Phillips, R.J., Roberts, G.P., McCaffrey, K., Zijerveld, L.J.J., Gregory, L.C., Faure Walker, J., Wedmore, L.N.J., Dunai, T.J., Binnie, S.A., Freeman, S.P.H.T., Wilcken, K., Shanks, R.P., Huismans, R.S., Papanikolaou, I., Michetti, A.M., Wilkinson, M., 2017. Orogen-scale uplift in the central Italian Apennines drives episodic behaviour of earthquake faults. Sci. Rep. 7. https://doi.org/10.1038/srep44858

Cowie, P.A., Shipton, Z.K., 1998. Fault tip displacement gradients and process zone dimensions. Journal of Structural Geology 20, 983-997.

CRED - UNISDR, 2017. Economic Losses, Poverty and Disasters 1998 - 2017.

Crone, A. J. & Hailer, K. M. 1991. Segmentation and the coseismic behaviour of basin and range normal faults: Examples from east- central Idaho and southwestern Montana, U.S.A. J. Struct. Geol. 13, 151-164.

Crowley, H., Bommer, J.J., 2006. Modelling seismic hazard in earthquake loss models with spatially distributed exposure. Bull. Earthq. Eng. 4, 249–273. https://doi.org/10.1007/s10518-006-9009-y

Crowley, H., Pinho, R., 2011. Global Earthquake Model : Community-Based Seismic Risk Assessment. https://doi.org/10.1007/978-94-007-1448-9

Cummins, J.D., 2008. CAT bonds and other risk-linked securities: State of the market and recent developments. Risk Manag. Insur. Rev. 11, 23–47. https://doi.org/10.1111/j.1540-6296.2008.00127.x

Darragh, R.B., Bolt, B.A., 1987. A comment on the statistical regression relation between earthquake magnitude and fault rupture length. Bull. Seismol. Soc. Am. 77, 1479–1484.

Degg, M.R. 1992. The ROA Earthquake Hazard Atlas project: recent work from the Middle East. In: *Geohazards: Natural and man-made*, McCall, G.J.H., Laming, D.J.C., Scott, S.C. (eds). Chapman and Hall, London, pp. 93-104

Deligiannakis G., Papanikolaou I., Zimbidis A. and Kakouris I., 2018b. Earthquake CAT Risk model for the Region of Attica, Greece, based on a fault specific hazard module. 9th International INQUA Meeting on Paleoseismology, Active Tectonics and Archeoseismology (PATA), 25 – 27 June, 2018, Possidi, Greece

Deligiannakis, G., Papanikolaou, I.D., Roberts, G., 2018a. Fault specific GIS based seismic hazard maps for the Attica region, Greece. Geomorphology 306, 264–282. https://doi.org/10.1016/j.geomorph.2016.12.005

Deligiannakis, G., Zimbidis, A., Papanikolaou, I.D. (submitted for publication). Earthquake loss and Solvency Capital Requirement calculation using a fault specific catastrophe model. (Submitted for publication)

Dewey, J. W., 1987. Instrumental seismicity of central Idaho. Bulletin of the Seismological Society of America, 77, 819-836.

Dia, A.N., Cohen, A.S., O'Nions, R.K., Jackson, J.A., 1997. Rates of uplift investigated through Th dating in the Gulf of Corinth (Greece). Chem. Geol. 138, 171–184. https://doi.org/10.1016/S0009-2541(97)00010-7

Dilalos, S., Alexopoulos, J., Lozios, S., 2019. New insights on subsurface geological and tectonic structure of the Athens basin (Greece), derived from urban gravity measurements. Journal of Applied Geophysics, 167, 73-105, ISSN 0926-9851, doi.org/10.1016/j.jappgeo.2019.04.024.

Doff, R., 2008. A critical analysis of the solvency II proposals. Geneva Pap. Risk Insur. Issues Pract. 33, 193–206. https://doi.org/10.1057/gpp.2008.2

Dounas, A., 1971. 1:50000 Geological Map "Erythrai". IGME, Athens

Drakatos, G., Karastathis,V., Makris, J., Papoulia, J. &Stavrakakis, G., 2005. 3D crustal structure in the neotectonic basin of the Gulf of Saronikos (Greece), Tectonophysics, 400, 55–65.

Duval, A., Kirby, E., Burbank, D., 2004. Tectonic and lithologic controls on bedrock chan- nel profiles and processes in coastal California. Journal of Geophysical Research 109 (F03002), 1–18.

EAEE (Hellenic Association of Insurance Companies), 2019. Natural catastrophes in Greece 1993-2018. Athens.

EAEE (Hellenic Association of Insurance Companies), 2021. Earthquake losses after Thessaly earthquake sequence of 3-4 March, 2021. Athens.

EAK (2000). Greek Seismic Code, edited by: Earthquake Planning & Pro- tection Organizatin. Athens – Greece, 72 pp., 7 appendixes, 2000 (in Greek).

EAK (2003). Greek Seismic Code, edited by: Earthquake Planning & Pro- tection Organizatin. Athens – Greece, 72 pp., 7 appendixes, 2003 (in Greek).

EIOPA, 2014a. Annexes to the Technical Specification for Preparatory Phase (Part I). Brussells.

EIOPA, 2014b. The underlying assumptions in the standard formula for the Solvency Capital Requirement calculation. Brussels.

EIOPA, 2014c. Final Report on Public Consultation No . 14 / 036 on Guidelines on valuation of technical provisions 1–95.

EIOPA, 2018. EIOPA's second set of advice to the European Commission on specific items in the Solvency II Delegated Regulation (EIOPA-BoS-18/075).

Eliet, P.P., Gawthorpe, R.L., 1995. Drainage development and sediment supply within rifts, examples from the Sperchios basin, central Greece. Journal of the Geological Society of London 152, 883–893

Ellsworth, W.L., Matthews, M.V., Nadeau, R.M., Nishenko, S.P., Reasenberge, P.A., Simpson, R.W., 1999. A physically-based earthquake recurrence model for estima- tion of long-term earthquake probabilities. U.S. Geological Survey Open File Report 99-552. 23p.

ELSTAT, 2015. Buildings Inventory 2011. Athens, Greece.

Esper, P. and Tachibanak, E., 1998. The lesson of Kobe earthquake. In Geohazards and Engineering Geology. Engineering Geology Special Publications 14, Geological Society London.

Esteva, L. (1970). Seismic Risk and Seismic Design Decisions, in: Seismic Design for Nuclear Power Plants, edited by: Hansen, R. J., Mas- sachusetts Inst. of Tech. Press, Cambridge, MA, USA, 142–82.

European Commission, 2010. QIS5 technical specifications, Annex to Call for Advice from CEIOPS on QIS5. Brussells.

European Union, 2009. Solvency II Directive, Official journal of the European Union. European Union, Strasbourg.

Evernden, J. F. and Thomson, J. M. 1985. Predicting seismic intensities, U.S. Geological Survey Professional Paper 1360, 151–202.

Faure Walker, J., Boncio, P., Pace, B., Roberts, G., Benedetti, L., Scotti, O., Visini, F., Peruzza, L., 2021. Fault2SHA Central Apennines database and structuring active fault data for seismic hazard assessment. Sci. Data 8, 87. https://doi.org/10.1038/s41597-021-00868-0

FEMA, 1989. Estimating Losses From Future Earthquakes (No. 50), Earthquake hazards reduction series.

FEMA, 1992. A benefit-cost model for the seismic rehabilitation of buildings, Fema 227.

FEMA, 2018. FEMA P-58-1: Seismic Performance Assessment of Buildings. Volume 1 – Methodology.

Fernández-Blanco, D., de Gelder, G., Lacassin, R., Armijo, R., 2019. A new crustal fault formed the modern Corinth Rift. Earth-Science Rev. 199, 102919. https://doi.org/10.1016/j.earscirev.2019.102919

Ferrario, M.F., Livio, F., Capizzano, S.S., Michetti, A.M., 2020. Developing the first intensity prediction equation based on the environmental scale intensity: A case study from strong normal-faulting earthquakes in the Italian Apennines. Seismological Research Letters 91, 2611-2623.

Fielding, E., Isacks, B., Barazangi, M., and Duncan, C.C., 1994. How flat is Tibet? Geology, v. 22, p. 163–167.

Florez, M. A., & Prieto, G. A. (2017). Precise relative earthquake depth determination using array processing techniques. Journal of Geophysical Research: Solid Earth, 122(6), 4559–4571. https://doi.org/10.1002/2017JB014132

Foumelis, M., 2019. Velocity field and crustal deformation of broader Athens plain (Greece) from a dense geodetic network. Journal of Applied Geodesy 13, 305-316.

Foumelis, M., Fountoulis, I., Papanikolaou, I.D., Papanikolaou, D., 2013. Geodetic evidence for passive control of a major Miocene tectonic boundary on the contemporary deformation field of Athens (Greece). Ann. Geophys. 56. https://doi.org/10.4401/ag-6238

Foumelis, M., Parcharidis, I., Lagios, E., Voulgaris, N., 2009. Evolution of post-seismic ground deformation of the Athens 1999 earthquake observed by SAR interferometry. J. Appl. Geophys. 69, 16–23. https://doi.org/10.1016/j.jappgeo.2009.02.007

Foutrakis, P., 2016. Marine geological evolution of Saronikos Gulf during the Quaternary (in Greek). Ph.D. Thesis. National and Kapodistrian University of Athens, Athens, 326 pp.

Foutrakis, P.M., Anastasakis, G., 2020. Quaternary continental shelf basins of Saronikos Gulf, Aegean Sea. Geo-Marine Lett. 40, 629–647. https://doi.org/10.1007/s00367-020-00653-9

Frankel, A., 1995. Mapping seismic hazard in the central and Eastern United States, Seismological Research Letters 66, 8-21

Gaitanakis, I., 1978. 1:50000 Geological Map “Megara”. IGME, Athens.

Gaitanakis, I., 1982. 1:50000 Geological Map “Athina-Peiraias”. IGME, Athens.

Gaitanakis, I., Mettos, A., Fytikas, M. 1981. 1:50000 Geological Map “Sofiko”. IGME, Athens

Galanakis, D., Antonarakou, A., Ch, G., Drinia, H., 2004. Brittle tectonic , sedimentation and morphological alteration of Megara basin, in: 5th International Symposium on Eastern Mediterranean Geology. Thessaloniki, pp. 3–6.

Galanopoulos, A., 1961. A Catalogue of Shocks with Io ≥VII for the Years Prior to 1800. National Observatory of Athens, Seismological Institute.

Ganas, A., Papadopoulos, G., Pavlides, S.B., 2001. The 7 September 1999 Athens 5.9 Ms earthquake: Remote sensing and digital elevation model inputs towards identifying the seismic fault. Int. J. Remote Sens. 22, 191–196. https://doi.org/10.1080/014311601750038938

Ganas, A., Papoulia, I., 2000. High-resolution, digital mapping of the seismic hazard within the Gulf of Evia Rift, Central Greece using normal fault segments as line sources. Nat. Hazards 22, 203–223. https://doi.org/10.1023/A:1008159904873

Ganas, A., Pavlides, S., Karastathis, V., 2005. DEM-based morphometry of range-front escarpments in Attica, central Greece, and its relation to fault slip rates. Geomorphology 65, 301-319.

Ganas, A., Pavlides, S.B., Sboras, S., Valkaniotis, S., Papaioannou, S., Alexandrisb, G.A., Plessa, A., Papadopoulos, G.A. 2004. Active fault geometry and kinematics in Parnitha Mountain, Attica, Greece. Journal of Structural Geology 26, 2103-2118.

Gatzert, N., Martin, M., 2012. Quantifying credit and market risk under Solvency II: Standard approach versus internal model. Insur. Math. Econ. 51, 649–666. https://doi.org/10.1016/j.insmatheco.2012.09.002

Gawthorpe, R.L., Hurst, J.M., 1993. Transfer zones in extensional basins: their structural style and influence on drainage development and stratigraphy. Journal of the Geological Society of London 150, 1137–1152

Gawthorpe, R.L., Leeder, M.R., 2000. Tectono-sedimentary evolution of active extensional basins. Basin Res. 12, 195–218. https://doi.org/10.1111/j.1365-2117.2000.00121.x

Gazetas, G., Kallou, P. V., Psarropoulos, P.N., 2002. Topography and soil effects in the Ms 5.9 Parnitha (Athens) earthquakes: The case of Adámes. Nat. Hazards 27, 133–169. https://doi.org/10.1023/A:1019937106428

Geurts, A.H., Whittaker, A.C., Gawthorpe, R.L., Cowie, P.A., 2020. Transient landscape and stratigraphic responses to drainage integration in the actively extending central Italian Apennines. Geomorphology 353, 107013. https://doi.org/10.1016/j.geomorph.2019.107013

Giardini D (1999) The Global Seismic Hazard Assessment Program (GSHAP)—1992/1999. Ann di Geofis 42:957–974. doi:10.1111/j.1365-3121.1992.tb00609.x

Giraudi, C., Frezzotti, M., 1997. Late Pleistocene glacial events in the Central Apennines, Italy. Quaternary Research 48, 280-290.

Gkimprixis, A., Douglas, J., Tubaldi, E., 2021. Seismic risk management through insurance and its sensitivity to uncertainty in the hazard model. Nat. Hazards. https://doi.org/10.1007/s11069-021-04748-z

Goda, K., Hong, H.P., 2010. Insurer's solvency under catastrophic seismic risk. Safety, Reliab. Risk Struct. Infrastrcutures Eng. Syst. 3439–3446.

Goda, K., Wenzel, F., Daniell, J., 2014. Insurance and Reinsurance Models for Earthquake, in: Beer, M., Kougioumtzoglou, I.A., Patelli, E., Au, I.S.-K. (Eds.), Encyclopedia of Earthquake Engineering. Springer Berlin Heidelberg, Berlin, Heidelberg, pp. 1–24. https://doi.org/10.1007/978-3-642-36197-5_261-1

Goes, S.D.B., 1996. Irregular recurrence of large earthquakes: an analysis of historic and paleoseismic catalogs. Journal of Geophysical Research 101, 5739–5749

Goldsworthy, M., Jackson, J., 2000. Active normal fault evolution in Greece revealed by geomorphology and drainage patterns. J. Geol. Soc. London. 157, 967–981. https://doi.org/10.1144/jgs.157.5.967

Goldsworthy, M., Jackson, J., 2001. Migration of activity within normal fault systems: Examples from the Quaternary of mainland Greece. J. Struct. Geol. 23, 489–506. https://doi.org/10.1016/S0191-8141(00)00121-8

Goldsworthy, M., Jackson, J., Haines, J., 2002. The continuity of active fault systems in Greece. Geophys. J. Int. 148, 596–618.

Grossi, P., Kleindorfer, P., Kunreuther, H., 1999. The Impact of Uncertainty in Earthquake Frequency and, Wharton Financial Institution Center.

Grossi, P., Kunreuther, H., Windeler, D., 2005. An Introduction to Catastrophe Models and Insurance, in: Patel, C.C. (Ed.), Catastrophe Modeling: A New Approach to Managing Risk. Springer. https://doi.org/10.1007/b100669

Grunthal, G., GSHAP Working Group Region 3, 1999. Seismic hazard assessment for Central, North and Northwest Europe: GSHAP Region 3. Ann di Geofis 42

Grunthal, G., Wahlstrom, R. (2000). Probabilistic seismic hazard assessment (horizontal PGA) for Sweden, Finland and Denmark using different logic tree approaches. Soil Dyn Earthq Eng 20:45–58.

Grützner, C., Carson, E., Walker, R.T., Rhodes, E.J., Mukambayev, A., Mackenzie, D., Elliott, J.R., Campbell, G., Abdrakhmatov, K., 2017. Assessing the activity of faults in continental interiors: Palaeoseismic insights from SE Kazakhstan. Earth Planet. Sci. Lett. 459, 93–104. https://doi.org/10.1016/j.epsl.2016.11.025

Grützner, C., Schneiderwind, S., Papanikolaou, I., Deligiannakis, G., Pallikarakis, A., Reicherter, K., 2016. New constraints on extensional tectonics and seismic hazard in northern Attica, Greece: The case of the Milesi Fault. Geophys. J. Int. 204, 180–199. https://doi.org/10.1093/gji/ggv443

Grützner, Ch., Barba, S., Papanikolaou, I., Perez-Lopez, R., 2013. Earthquake Geology: science, society and critical facilities. Annals of Geophysics 56, doi: 10.4401/ag-6503.

Gutenberg, B. and C. F. Richter, 1944. Frequency of earthquakes in California, Bull. Seism. Soc. Am. 34, 185-188.

Hadjian, A.H. 1993. The Spitak, Armenia earthquake of 7 December 1988 — why so much destruction. Soil Dynamics and Earthquake Engineering, 12 (1)

Hatzfeld, D. 1999. The present-day tectonics of the Aegean as deduced from seismicity. Geol Soc Spec Publ 156:415–426. https://doi.org/ 10.1144/GSL.SP.1999.156.01.19

Hatzidimitriou, P.M., Papadimitriou, E.E., Mountrakis, D.M., Papazachos, B.C., 1985. The seismic parameter b of the frequency-magnitude relation and its association with the geological zones in the area of Greece. Tectonophysics 120, 141–151. https://doi.org/10.1016/0040-1951(85)90092-7

Hermides, D., Kyriazis, D., Makri, P., Ermidou, A., 2020. Geochemical evolution of the Thriassion Plain groundwaters, Attica, Greece. Environ. Monit. Assess. 192. https://doi.org/10.1007/s10661-020-08491-z

Hippolyte, J.C., Brocard, G., Tardy, M., Nicoud, G., Bourlès, D., Braucher, R., Ménard, G., Souffaché, B., 2006. The recent fault scarps of the Western Alps (France): Tectonic surface ruptures or gravitational sackung scarps? A combined mapping, geomorphic, levelling, and 10Be dating approach. Tectonophysics 418, 255–276. https://doi.org/10.1016/j.tecto.2006.02.009

Hodge, M., Biggs, J., Fagereng, Å., Elliott, A., Mdala, H., Mphepo, F., 2019. A semi-automated algorithm to quantify scarp morphology (SPARTA): Application to normal faults in southern Malawi. Solid Earth 10, 27–57. https://doi.org/10.5194/se-10-27-2019

Hofer, L., Zanini, M.A., Gardoni, P., 2020. Risk-based catastrophe bond design for a spatially distributed portfolio. Struct. Saf. 83, 101908. https://doi.org/10.1016/j.strusafe.2019.101908

Hsu, W.K., Chiang, W.L., Xue, Q., Hung, D.M., Huang, P.C., Chen, C.W., Tsai, C.H., 2013. A probabilistic approach for earthquake risk assessment based on an engineering insurance portfolio. Nat. Hazards 65, 1559–1571. https://doi.org/10.1007/s11069-012-0425-9

Hubert, A., King, G.C.P., Armijo, R., Meyer, B. and D. Papanastassiou, 1996. Fault reactivation, stress interaction and rupture propagation in the 1981 Corinth earthquake sequence, Earth Planet. Sci. Lett., 142, 573–585, doi:10.1016/0012-821X(96)00108-2

IAEA, 2015. The Contribution of Palaeoseismology to Seismic Hazard Assessment in Site Evaluation for Nuclear Installations. International Atomic Energy Agency, Vienna. https://doi.org/10.13140/RG.2.1.3042.9289

Iezzi, F., Roberts, G., Faure Walker, J., Papanikolaou, I., Ganas, A., Deligiannakis, G., Beck, J., Wolfers, S., Gheorghiu, D. (submitted for publication) Temporal and spatial earthquake clustering revealed through comparison of millennial strain-rates from 36Cl cosmogenic exposure dating and decadal GPS strain-rate.

Ioakim, Ch., Rondoyanni, Th., and Mettos, A., 2005. The Miocene basins of Greece (Eastern Mediterranean) from a paleoclimatic perspective, Revue de Paleobiologe, 24, 735-748.

Jackson, J. A., J. Gagnepain, G. Houseman, G. C. P. King, P. Papadimitriou, C. Soufleris, and J. Virieux, 1982. Seismicity, normal faulting and the geomor- phological development of the Gulf of Corinth (Greece): the Cotinth earthquakes of February and March 1981, Earth Planet. Sci. Lett., 57, 377–397.

Jenny, S., Goes, S., Giardini, D., Kahle, H.G., 2004. Earthquake recurrence parameters from seismic and geodetic strain rates in the eastern Mediterranean. Geophys. J. Int. 157, 1331–1347. https://doi.org/10.1111/j.1365-246X.2004.02261.x.

Jessica Weinkle, 2015. A Public Policy Evaluation of Florida's Citizens Property Insurance Corporation. J. Insur. Regul. 34, 31–62.

Jimenez MJ, Giardini D, Gru¨nthal G et al., 2001. Unified seismic hazard modelling throughout the Mediterranean region. Boll Di Geofis Teor Ed Appl 42:3–18

Johnson, K., Nissen, E., Saripalli, S., Arrowsmith, J.R., McGarey, P., Scharer, K., Williams, P., Blisniuk, K., 2014. Rapid mapping of ultrafine fault zone topography with structure from motion. Geosphere 10, 969–986. https://doi.org/10.1130/GES01017.1

Kappos, A., Pitilakis, K., Morfidis, K., Hatzinikolaou, N. 2002). Vulnerability and risk study of Volos (Greece) metropolitan area. Proceedings of the 12th ECEE, London, UK, Sep. 2002

Kappos, A.J. & Panagopoulos, G. (2010). Fragility curves for reinforced concrete buildings in Greece. Structure and Infrastructure Engineering, 6(1), 39 – 53.

Kappos, A.J., Lekidis, V., Panagopoulos, G., Sous, I., Theodulidis, N., Karakostas, C., Anastasiadis, T., Salonikios, T., Margaris, B., 2007. Analytical estimation of economic loss for buildings in the area struck by the 1999 Athens earthquake and comparison with statistical repair costs. Earthq. Spectra 23, 333–355. https://doi.org/10.1193/1.2720366

Kappos, A.J., Panagopoulos, G., Panagiotopoulos, C., Penelis, G., 2006. A hybrid method for the vulnerability assessment of R/C and URM buildings. Bull. Earthq. Eng. 4, 391–413. https://doi.org/10.1007/s10518-006-9023-0

Kappos, A.J., Panagopoulos, G., Penelis, G.G., 2008. Development of a seismic damage and loss scenario for contemporary and historical buildings in Thessaloniki, Greece. Soil Dyn. Earthq. Eng. 28, 836–850. https://doi.org/10.1016/j.soildyn.2007.10.017

Kappos, A.J., Stylianidis, K.C., Pitilakis, K., 1998. Development of seismic risk scenarios based on a hybrid method of vulnerability assessment. Nat. Hazards 17, 177–192. https://doi.org/10.1023/A:1008083021022

Kappos, A.J., Stylianidis, K.C., Sextos, A.G., Papaikolaou, V.K., Panagopoulos, G., Koyris, L. & Goutzika, E. (2009). Seismic risk scenarios for the building stock in Grevena. 16th Hellenic Conference on Concrete, Paphos, Cyprus.

Katsikatsos, G., 1991. 1:50000 Geological Map "Rafina". IGME, Athens.

Katsikatsos, G., 2000. 1:50000 Geological Map "Eretria". IGME, Athens

Katsikatsos, G., 2002. 1:50000 Geological Map "Kifissia". IGME, Athens.

Katsikatsos, G., Mettos, A., Vidakis, M., Dounas, A., 1986. 1:50000 Geological Map "Athina-

Elefsis”. IGME, Athens

Keller, E.A., Pinter, N., 2002. Active tectonics (2nd Ed). Prentice Hall, New Jersey.

Kerr, R.A., 2011. Seismic crystal ball proving mostly cloudy around the world. Science https://doi.org/10.1126/science.332.6032.912

Kirby, E., and Whipple K.X., 2001. Quantifying differential rock-uplift rates via stream profile analysis. *Geology* 108, pp.415-418.

Kirby, E., Whipple, K.X., Tang, W., Chen, Z., 2003. Distribution of active rock uplift along the eastern margin of the Tibetan Plateau: inferences from bedrock channel longitu- dinal profiles. J. Geophys. Res. 108, B42217

Kircher, C.A., Whitman, R. V., Holmes, W.T., 2006. HAZUS Earthquake Loss Estimation Methods. Nat. Hazards Rev. 7, 45–59. https://doi.org/10.1061/(asce)1527-6988(2006)7:2(45)

Kokkalas, S., Pavlides, S., Koukouvelas, I., Ganas, A., Stamatopoulos, L., 2007. Paleoseismicity of the Kaparelli fault (eastern Corinth Gulf): Evidence for earthquake recurrence and fault behavior. Boll. della Soc. Geol. Ital. 126, 387–395.

Konstantinou, K.I., Mouslopoulou, V., Saltogianni, V., 2020. Seismicity and Active Faulting around the Metropolitan Area of Athens, Greece. Bull. Seismol. Soc. Am. 1–18. https://doi.org/10.1785/0120200039

Kontoes, C., Elias, P., Sykioti, O., Briole, Pierre, Sachpazi, Maria, Briole, P, Remy, D., Sachpazi, M, Veis, G., Kotsis, I., 2000. Displacement field and fault model for the September 7, 1999 Athens earthquake inferred from ERS2 satellite radar interferometry. Geophys. Res. Lett. 27, 3989–3992. https://doi.org/10.1029/2000GL008510ï

Koravos, G.C., Main, I.G., Tsapanos, T.M., Musson, R.M.W., 2003. Maximum earthquake magnitudes in the Aegean area constrained by tectonic moment release rates. Geophys. J. Int. 152, 94–112. https://doi.org/10.1046/j.1365-246X.2003.01825.x

Koukouvelas, I.K., Stamatopoulos, L., Katsonopoulou, D., Pavlides, S., 2001. A palaeoseismological and geoarchaeological investigation of the Eliki fault, Gulf of Corinth, Greece. J. Struct. Geol. 23 (2–3), 531–543.

Koukouvelas, I.K., Zygouri, V., Nikolakopoulos, K., Verroios, S., 2018. Treatise on the tectonic geomorphology of active faults: The significance of using a universal digital elevation model. J. Struct. Geol. 116, 241–252. https://doi.org/10.1016/j.jsg.2018.06.007

Koukouvelas, I.K., Zygouri, V., Papadopoulos, G.A., Verroios, S., 2017. Holocene record of slip-predictable earthquakes on the Kenchreai Fault, Gulf of Corinth, Greece. J. Struct. Geol. 94, 258–274. https://doi.org/10.1016/j.jsg.2016.12.001

Krohe, A., Mposkos, E., Diamantopoulos, A., Kaouras, G., 2010. Formation of basins and mountain ranges in Attica (Greece): The role of Miocene to Recent low-angle normal detachment faults. Earth-Science Rev. 98, 81–104. https://doi.org/10.1016/j.earscirev.2009.10.005

Lallemant, D & Kiremidjian, A., 2014. A Beta Distribution Model for Characterizing

Earthquake Damage State Distribution. *Earthquake Spectra,* DOI: 10.1193/012413EQS013M

Latsoudas, Ch., 1992. 1:50000 Geological Map “Koropi-Plaka”. IGME, Athens

Leeder, M.R., Portman, C., Andrews, J.E., Collier, R.E.L., Finch, E., Gawthorpe, R.L., McNeill, L.C., Pérez-Arlucea, M., Rowe, P., 2005. Normal faulting and crustal deformation, Alkyonides Gulf and Perachora peninsula, eastern Gulf of Corinth rift, Greece. J. Geol. Soc. London. 162, 549–561. https://doi.org/10.1144/0016-764904-075

Leeder, M.R., Seger, M.J., Stark, C.P., 1991. Sedimentation and tectonic geomorphology adjacent to major active and inactive normal faults, southern Greece. J. Geol. Soc. London. 148, 331–343. https://doi.org/10.1144/gsjgs.148.2.0331

Lekkas, E. 1996. Pyrgos earthquake damages (based on E.M.S.-1992) in relation with geological and geo- technical conditions. Soil Dynamics and Earthquake Engineering, 15, 61–68

Lekkas, E., 2001. The Athens earthquake (7 September 1999): intensity distribution and controlling factors. Eng. Geol. 59, 297–311.

Lekkas, E., Fountoulis, I., Lozios, S., Kranis, C., Adanopoulou, E., 1996. Neotectonic implications of Grevena-Kozani earthquake (May 13, 1995, W. Macedonia, Greece). In: International Meeting on Results of the May 13 1995 Earthquake of West Macedonia: One Year after, pp. 76e80.

Lekkas, S. & Lozios, S., 2000. Tectonic structure of Mt. Hymmittos (Attica — Greece). Annales Géologiques des Pays Hélléniques 38, 47–62.

Ley-Borrás, R. and Fox, B. (2015) Using probabilistic models to appraise and decide on sovereign disaster risk financing and insurance. Financing and Insurance Policy Research Working Papers. World Bank Group, Washington, DC.

Liati A., Skarpelis N., Fanning C.M., 2013. Late Permian–Early Triassic igneous activity in the Attic Cycladic Belt (Attica): New geochronological data and geodynamic implications. Tectonophysics, 595–596, 140-147. doi.org/10.1016/j.tecto.2012.05.009.

Louvari, E., Kiratzi, A., 2001. Source parameters of the 7 September 1999 Athens (Greece) earthquake based on teleseismic data. J. Balk. Geophys. Soc. 4, 51–60.

Maccaferri, S., Cariboni, F., Campolongo, F., 2012. Natural Catastrophes : Risk relevance and Insurance Coverage in the EU. JRC Sci. Tech. Reports 1–132. https://doi.org/10.2788/93626

Machette, M., 2000. Active, capable, and potentially active faults – a paleoseismic perspective. *Journal of Geodynamics*, 29, pp. 387-392

Mahdyiar, M., Porter, B., 2005. Chapter 3 – The Risk Assessment Process : The Role of Catastrophe Modeling in Dealing with Natural, in: Grossi, P., Kunreuther, H. (Eds.), Catastrophe Modeling: A New Approach to Managing Risk. Springer, pp. 45–68.

Main, I., 1996. Statistical Physics, Seismogenesis and seismic hazard. Reviews of Geophysics 34, 433-462.

Makris, J., Papoulia, J., Drakatos, G., 2004. Tectonic deformation and microseismicity of the Saronikos Gulf, Greece. Bull. Seismol. Soc. Am. 94, 920–929. https://doi.org/10.1785/0120020209.

Makropoulos, K., Kaviris, G., Kouskouna, V., 2012. An updated and extended earthquake catalogue for Greece and adjacent areas since 1900. Nat. Hazards Earth Syst. Sci. 12, 1425–1430. https://doi.org/10.5194/nhess-12-1425-2012

Makropoulos, K.C., Burton, P.W., 1985. Seismic hazard in Greece. I. Magnitude recurrence. Tectonophysics 117. https://doi.org/10.1016/0040-1951(85)90273-2

Marco, S., M. Stein, A. Agnon, and H. Ron, 1996. Long-term earthquake clustering: A 50,000-year paleoseismic record in the Dead Sea graben, J. Geophys. Res. 101, 6179–6191.

Marinos, G., Petraschek, W.E., 1956. Laurium. Geological and Geophysical Research, Special Issue 1–247.

Marinos, P., Bouckovalas, G., Tsiambaos, G., Sabatakakis, N., Antoniou, A., 2001. Ground zoning against seismic hazard in Athens, Greece. Eng. Geol. 62, 343–356. https://doi.org/10.1016/S0013-7952(01)00035-7

Marinos, P., Boukouvalas, G., Tsiambaos, G., Pronotarios, G., Sabatakakis, N.,1999b. Damage distribution in the western part of Athens after the 7-9-99 earthquake. Newsletter of E.C.P.F.E., Council of Europe, Athens, pp. 37-39.

Marinos, P., Boukovalas, G., Tsiambaos, G., Protonotarios, G. & Sabatakakis, N. (1999a). Preliminary geological - geotechnical study of the disaster area (of Athens earthquake of Sept 7th, 1999) in NW Athens Basin (in Greek). E.P.P.O., Athens, 13 pp.

Marioakos, I., Fountoulis, I., Mariolakos, D., Andreadakis, E., Georgakopoulos, A., 2000. Geodynamic phenomena observed during the Athens earthquake (Ms=5.9) 7-9-99. Ann. Geol. des Pays Hell. 38, 175–186.

Mariolakos and Theocharis 2001. Shifting shores in the Saronic Gulf during the last 18,000 years and the Kychreia paleolimni. Proceedings ofthe 9th International Conference, Athens, Bulletin of Hellenic Geological Society XXXVI 1: 405-413.

Mariolakos, I. & Papanikolaou, D. 1982. The neogene Basins of the Aegean Arc from the Paleogeographic and the Geodynamic point of view. Intern Symp. Hell. Arc and Trench, Proceedings 1, p. 383-399, Athens.

Mariolakos, I. & Papanikolaou, D., 1982. The Neogene basins of the Aegean arc from paleographic and geodynamic point of view. Int. Symp. Hellen. Arc and Trench (HEAT), April 1981, Proceedings 383-399, Athens

Mariolakos, I., Fountoulis, I., 2000. The Athens earthquake September 7, 1999: The Neotectonic regime of the affected area. Ann. Geol. Pays Hell. 38, 165–174.

Mariolakos, I., Fountoulis, I., Mariolakos, D., Andreadakis, E., Georgakopoulos, A., 2000. Geodynamic phenomena observed during the Athens earthquake. Ann. Geol. des Pays Hell. 38, 175–186.

Mariolakos, I., Papanikolaou, D., Symeonidis, N., Lekkas, S., Karotsieris, Z., Sideris, CH.,

1981. The deformation of the area around the Eastern Corinthian Gulf, affected by the earthquakes of February-March 1981. In Proceedings HEAT Symposium, v. 1, p. 400-420, Athens.

Mariolakos, I., Papanikolaou, D., Symeonidis, N., Lekkas, S., Karotsieris, Z., Sideris, CH., 1982. The deformation of the area around the eastern Korinthian gulf, affected by the earthquakes of February–March 1981. Proceedings of International Symposium on the Hellenic Arc and Trench (H.E.A.T.), 1. National Technical University, Athens, 400–420.

Martins, L., Silva, V., Marques, M., Crowley, H., Delgado, R., 2014. Evaluation of Analytical Fragility and Damage-To- Loss Models for Reinforced Concrete Buildings. Second Eur. Conf. Earthq. Eng. Seismol. Istanbul 3–4. https://doi.org/10.13140/2.1.3001.9842

Mason, J., Schneiderwind, S., Wiatr, T., Reicherter, K., Pallikarakis, A., Papanikolaou, I., Mechernich, S., Wiatr, T., 2016. Fault structure and deformation rates at the Lastros-Sfaka Graben, Crete. Tectonophysics 683. https://doi.org/10.1016/j.tecto.2016.06.036

Mavroeidis, G.P., Papageorgiou, A.S., 2010. Effect of fault rupture characteristics on near-fault strong ground motions. Bull. Seismol. Soc. Am. 100, 37–58. https://doi.org/10.1785/0120090018

McCalpin, J.P., 2009. Paleoseismology, 2nd ed. Elsevier, San Diego.

McClusky, S., Balassanian, S., Barka, A., Demir, C., Ergintav, S., Georgiev, I., Gurkan, O., Hamburger, M., Hurst, K., Kahle, H., Kastens, K., Kekelidze, G., King, R., Kotzev, V., Lenk, O., Mahmoud, S., Mishin, A., Nadariya, M., Ouzounis, A., Paradissis, D., Peter, Y., Prilepin, M., Reilinger, R., Sanli, I., Seeger, H., Tealeb, A., Toksöz, M.N., Veis, G., 2000. Global Positioning System constraints on plate kinematics and dynamics in the eastern Mediterranean and Caucasus. J. Geophys. Res. Solid Earth 105, 5695–5719. https://doi.org/10.1029/1999jb900351

McGuire, R.K., 1976. FORTRAN computer program for seismic risk analysis. USGS Open-File Rep. 76, 90.

McGuire, R.K., 1993. Computations of seismic hazard. Annali di Geofisica XXXVI, 181-200.

Mechernich, S., Schneiderwind, S., Mason, J., Papanikolaou, I.D., Deligiannakis, G., Pallikarakis, A., Binnie, S.A., Dunai, T.J., Reicherter, K., 2018. The Seismic History of the Pisia Fault (Eastern Corinth Rift, Greece) From Fault Plane Weathering Features and Cosmogenic 36Cl Dating. J. Geophys. Res. Solid Earth 123, 4266–4284. https://doi.org/10.1029/2017JB014600

Mercier, J. L., Sorel, D., Vergeley, P., and Simeakis, C., 1989. Extensional tectonic regimes in the Aegean basins during the Cenozoic, Basin Res., 2, 49–71,.

Michetti, A. M., Esposito, E. et al. 2007. Intensita` scale ESI 2007. In: Guerrieri, L. & Vittori, E. (eds) Memorie Descrittive della. Carta Geologica d'Italia, 74, Servizio Geologico d'Italia, Dipartimento Difesa del Suolo, APAT, Rome.

Michetti, A.M., Audemard M., F.A., Marco, S., 2005. Future trends in paleoseismology: Integrated study of the seismic landscape as a vital tool in seismic hazard analyses. Tectonophysics 408, 3–21. https://doi.org/10.1016/j.tecto.2005.05.035

Michetti, A.M., Brunamonte, F., Serva, L., 1995. Paleoseismologi- cal evidence in the epicentral area of the January 13, 1968, Belice (SW Sicily) earthquake. In: Serva, L., Slemmons, D.B. (Eds.), Perspectives in Paleoseismology, Bulletin of the Asso- ciation of Engineering Geologists. Special Publication, vol. 6, pp. 127–139

Michetti, A.M., Ferreli, L., Esposito, E., Porfido, S., Blumetti, A.M., Vittori, E., Serva, L., Roberts, G.P., 2000. Ground effects during the 9 September 1998, MW = 5.6, Lauria earthquake and the seismic potential of the "aseismic" Pollino region in Southern Italy. Seismol. Res. Lett. 71, 31–46. https://doi.org/10.1785/gssrl.71.1.31

Mitchell, S. G., A. Matmon, P. R. Bierman, Y. Enzel, M. Caffee, and D. Rizzo, 2001. Displacement history of a limestone normal fault scarp, northern Israel, from cosmogenic 36Cl, J. Geophys. Res. 106, no. B106, 4247–4264.

Mitchell-Wallace, K., Jones, M., Hillier, J., Foote, M., 2017. Natural catastrophe risk management and modelling, 1st ed, Natural catastrophe risk management and modelling. John Wiley & Sons Ltd All, Hoboken, NJ. https://doi.org/10.1002/9781118906057

Moretti, I., Sakellariou, D., Lykousis, V., & Micarelli, L. , 2003. The Gulf of Corinth: an active half graben? Journal of Geodynamics, 36(1-2), 323–340. doi:10.1016/s0264-3707(03)00053-x

Morewood, N.C., Roberts, G.P., 1999. Lateral propagation of the surface trace of the South Alkyonides normal fault segment, central Greece: Its impact on models of fault growth and displacement-length relationships. J. Struct. Geol. 21, 635–652. https://doi.org/10.1016/S0191-8141(99)00049-8

Morewood, N.C., Roberts, G.P., 2001. Comparison of surface slip and focal mechanism slip data along normal faults: An example from the eastern Gulf of Corinth, Greece. J. Struct. Geol. 23, 473–487. https://doi.org/10.1016/S0191-8141(00)00126-7

Moro, M., Saroli, M., Stramondo, S., Bignami, C., Albano, M., Falcucci, E., Gori, S., Doglioni, C., Polcari, M., Tallini, M., Macerola, L., Novali, F., Costantini, M., Malvarosa, F., Wegmüller, U., 2017. New insights into earthquake precursors from InSAR. Sci. Rep. 7, 1–11. https://doi.org/10.1038/s41598-017-12058-3

Mposkos, E., Krohe, A., Diamantopoulos, A., Baziotis, I., 2007. Late and post-Miocene geodynamic evolution of the Mesogea basin (East Attica, Greece): constraints from sediments, petrography and structures. Bulletin of the Geological Society of Greece, 40 (1), 399-411

Munich Re Group, 2019. NatCatSERVICE Relevant natural loss events wordlwide 2007 – 2017 [WWW Document]. Munich Re. URL http://natcatservice.munichre.com/topten/1?filter=eyJ5ZWFyRnJvbSI6MTk4MCwieWVhclRvIjoyMDE2fQ%3D%3D&type=1 (accessed 4.2.20).

Murphy, A. H. \,1993. What is a good forecast? An essay on the nature of goodness in weather forecasting, Weather Forecast. 8, 281–293.

Mylonakis, G., Voyagaki, E., Price, T., 2003. Damage potential of the 1999 Athens, Greece, Accelerograms. Bull. Earthq. Eng. 1, 205–240. https://doi.org/10.1023/A:1026380608133

Ogata, Y., 1999. Estimating the hazard of rupture using uncertain occurrence times of paleoearthquakes. Journal of Geophysical Research 104, 17995–18014.

Pace, B., Peruzza, L., Lavecchia, G., Boncio, P., 2006. Layered seismogenic source model and probabilistic seismic-hazard analyses in central Italy. Bull. Seismol. Soc. Am. 96, 107–132. https://doi.org/10.1785/0120040231

Pace, B., Peruzza, L., Visini, F., 2010. LASSCI2009.2: Layered earthquake rupture forecast model for central Italy, submitted to the CSEP project. Ann. Geophys. 53, 85–97. https://doi.org/10.4401/ag-4847

Pace, B., Visini, F., Peruzza, L., 2016. FiSH: MATLAB Tools to Turn Fault Data into Seismic-Hazard Models. Seismol. Res. Lett. 87, 374–386. https://doi.org/10.1785/0220150189

Palumbo, L., Benedetti, L., Bourlès, D., Cinque, A., Finkel, R., 2004. Slip history of the Magnola fault (Apennines, Central Italy) from 36Cl surface exposure dating: Evidence for strong earthquakes over the Holocene. Earth Planet. Sci. Lett. 225, 163–176. https://doi.org/10.1016/j.epsl.2004.06.012

Pantosti, D., Collier, R., D'Addezio, G., Masana, E., Sakellariou, D., 1996. Direct geological evidence for prior earthquakes on the 1981 Corinth Fault (central Greece). Geophys. Res. Lett. 23, 3795–3798. https://doi.org/10.1029/96GL03647

Pantosti, D., De Martini, P., Papanastassiou, D., Lemeille, N., Palyvos, D., Stavrakakis, G.., 2004. Palaeoseismological trenching accros the Atalanti fault; evidence for the ancestors of the 1894 earthquake during the middle ages and Roman times, Bull. Seism. Soc. Am., 94, 531–549.

Panza, G., Kossobokov, V.G., Peresan, A., Nekrasova, A., 2014. Why are the Standard Probabilistic Methods ofEstimating Seismic Hazard and Risks Too Often Wrong, Earthquake Hazard, Risk and Disasters. Elsevier Inc. https://doi.org/10.1016/B978-0-12-394848-9.00012-2

Paolucci, R., 2002. Amplification of earthquake ground motion by steep topographic irregularities. Earthq. Eng. Struct. Dyn. 31, 1831–1853. https://doi.org/10.1002/eqe.192

Papadimitriou, P., Voulgaris, N., Kassaras, I., Kaviris, G., Delibasis, N., Makropoulos, K., 2002. The M w = 6.0, 7 September 1999 Athens Earthquake, Natural Hazards.

Papadopoulos, G.A., 2002. The Athens, Greece, earthquake (Ms 5.9) of 7 September 1999: An event triggered by the İzmit, Turkey, 17 August 1999 earthquake? Bull. Seismol. Soc. Am. 92, 312–321. https://doi.org/10.1785/0120000805

Papadopoulos, G.A., Drakatos, G., Papanastassiou, D., Kalogeras, I., Stavrakakis, G., 2000. Preliminary results about the catastrophic earthquake of 7 September 1999 in Athens, Greece. Seismol. Res. Lett. https://doi.org/10.1785/gssrl.71.3.318

Papadopoulos, T.D., Goulty, N., Voulgaris, N.S., Alexopoulos, J.D., Fountoulis, I., Kambouris, P., Karastathis, V., Peirce, C., Chailas, S., Kassaras, J., Pirli,M., 2007. Tectonic structure of Central-Western Attica (Greece) based on geophysical investigations-preliminary results. Bull. Geol. Soc. Greece 40 (3), 1207–1218. https://doi.org/10.12681/bgsg.16873

Papagiannaki, Diakakis, Kotroni, Lagouvardos, Andreadakis, 2019. Hydrogeological and

Climatological Risks Perception in a Multi-Hazard Environment: The Case of Greece. Water 11, 1770. https://doi.org/10.3390/w11091770

Papaioannou, C.A., Papazachos, B.C., 2000. Time-independent and time-dependent seismic hazard in Greece based on seismogenic sources. Bull. Seismol. Soc. Am. 90, 22–33. https://doi.org/10.1785/0119980023

Papaioannou, Ch. A., 1984. Attenuation of seismic intensities and seismic hazard assessment in Greece and the surrounding area. Ph.D. Thessaloniki: University of Thessaloniki

Papanikolaou, D., Bassi, E.-K., Kranis, Ch., Danamos, G., 2004 b. Paleogeographic evolution of the Athens basin from Late Miocene up to present. Bulletin of the Geological Society of Greece XXXVI, 816–825

Papanikolaou, D., Chronis, G., Likousis, V., Pavlakis, P., 1989a. Submarine Neotectonic Map of Saronikos Gulf, 1:100,000. Athens, Greece.

Papanikolaou, D., Chronis, G., Likousis, V., Pavlakis, P., with the contribution of Roussakis, G., Syskakis, D., 1989b. Submarine Neotectonic Map of South Evoikos Gulf, 1:100,000. Athens, Greece.

Papanikolaou, D., Lekkas, E., Lozios, S., Papoulia, I., Vassilopoulou, S., 1995. Neotectonic Map of Eastern Attica. Use and Applications with the Geographical Information System, in: 4th Congress of the Geographical Society of Greece. Athens, Greece, pp. 240–262.

Papanikolaou, D., Lozios, S., Soukis, K., Skourtsos, M., 2004a. The geological structure of the allocthonus "Athens Schists". Bulletin of the Geological Society of Greece, XXXVI, 1550–1559.

Papanikolaou, D., Lykoussis, V., Chronis, G., Pavlakis, P., 1988. A comparative study of neotectonic basins across the Hellenic arc: the Messiniakos, Argolikos, Saronikos and Southern Evoikos Gulfs. Basin Res. 1, 167–176.

Papanikolaou, D., Mpasi, E.K., Kranis, C., Danamos, G., 2004. Paleogeographic evolution of the Athens Basin from Upper Miocene to Present. Bull. Geol. Soc. Greece 36, 816–825. https://doi.org/10.1017/CBO9781107415324.004

Papanikolaou, D., Nomikou, P., Papanikolaou, I., Lampridou, D., Rousakis, G., Alexandri, M., 2019. Active tectonics and seismic hazard in Skyros Basin, North Aegean Sea, Greece. Mar. Geol. 407, 94–110. https://doi.org/10.1016/j.margeo.2018.10.001

Papanikolaou, D., Papanikolaou, I., 2007b. Geological, Geomorphological and Tectonic Structure of Ne Attica and Seismic Hazard Implications for the Northern Edge of the Athens Plain. Bull. Geol. Soc. Greece 40, 425. https://doi.org/10.12681/bgsg.16634

Papanikolaou, D.I., 2021. The Geology of Greece, Regional Geology Reviews. Springer International Publishing, Cham. https://doi.org/10.1007/978-3-030-60731-9

Papanikolaou, D.I., Lekkas, E., Sideris, C., Fountoulis, I., Danamos, G., Kranis, C., Lozios, L., 1999. Geology and tectonics of Western Attica in relation to the 7-9-99 earthquake.

Papanikolaou, D.I., Mariolakos, I.D., Lekkas, E.L., Lozios, S.G., 1988. Morphotectonic observations on the Asopos Basin and the Coastal zone of Oropos. Contribution to the

Neotektonics of Northern Attica. Bull. Geol. Soc. Greece 20, 251–267.

Papanikolaou, D.J., Royden, L.H., 2007. Disruption of the Hellenic arc: Late Miocene extensional detachment faults and steep Pliocene-Quaternary normal faults - Or what happened at Corinth? Tectonics 26, 1–16. https://doi.org/10.1029/2006TC002007

Papanikolaou, I. D., Roberts, G. P., & Michetti, A. M., 2005. Fault scarps and deformation rates in Lazio-Abruzzo, Central Italy: Comparison between geological fault slip-rate and GPS data. Tectonophysics, 408(1-4), 147–176. https://doi.org/10.1016/j.tecto.2005.05.043

Papanikolaou, I., and Melaki, M., 2017. The Environmental Seismic Intensity Scale (ESI 2007) in Greece, newly added events and its relationship with Magnitude; Preliminary attenuation relationships for the Mediterranean. Quaternary International 451, 37-55.

Papanikolaou, I.D., 2003. Generation of high resolution seismic hazard maps through integration of earthquake geology, fault mechanics theory and GIS techniques in extensional tectonic settings. Unpublished Ph.D thesis, University of London, 437pp

Papanikolaou, I.D., 2011. Uncertainty in intensity assignment and attenuation relationships: How seismic hazard maps can benefit from the implementation of the Environmental Seismic Intensity scale (ESI 2007). Quat. Int. 242, 42–51. https://doi.org/10.1016/j.quaint.2011.03.058

Papanikolaou, I.D., Papanikolaou, D.I., 2007a. Seismic hazard scenarios from the longest geologically constrained active fault of the Aegean. Quat. Int. 171–172, 31–44. https://doi.org/10.1016/j.quaint.2007.03.020

Papanikolaou, I.D., Papanikolaou, D.I., Lekkas, E.L., 2009. Advances and limitations of the Environmental Seismic Intensity scale (ESI 2007) regarding near-field and far-field effects from recent earthquakes in Greece: Implications for the seismic hazard assessment. Geol. Soc. Spec. Publ. 316, 11–30. https://doi.org/10.1144/SP316.2

Papanikolaou, I.D., Roberts, G.P., Deligiannakis, G., Sakellariou, A., Vassilakis, E., 2013. The Sparta fault, southern Greece: From segmentation and tectonic geomorphology to seismic hazard mapping and time dependent probabilities. Tectonophysics 597–598, 85–105. https://doi.org/10.1016/j.tecto.2012.08.031

Papanikolaou, I.D., Triantaphyllou, M., Pallikarakis, A., Migiros, G., 2015b. Active faulting at the Corinth Canal based on surface observations, borehole data and paleoenvironmental interpretations. Passive rupture during the 1981 earthquake sequence? Geomorphology 237, 65–78. https://doi.org/10.1016/j.geomorph.2014.10.036.

Papanikolaou, I.D., Van Balen, R., Silva, P.G., Reicherter, K., 2015a. Geomorphology of active faulting and seismic hazard assessment: New tools and future challenges. Geomorphology 237, 1–13. https://doi.org/10.1016/j.geomorph.2015.02.024

Papazachos, B. C., Comninakis, P. E., Hatzidimitriou, P. M., Kiriakidis, E. C., Kiratzi, A. A., Panagiotopoulos, D. G., Papadimitriou, E. E., Papaioannou, Ch. A., Pavlides, S. B., and Tzanis, E. P., 1982. Atlas of lsoseismal Maps Earthquakes in Greece, 1902-1981, Publ. University of Thessaloniki, Geophysical Laboratory, No. 4.

Papazachos, B. C., Karakaisis, G.F., Papadimitriou, E.E.,. Pappaioannou, Ch.A (1997). The regional time and magnitude predictable model and its application to the Alpine-Himalayan belt, Tectonophysics 271, 295–323

Papazachos, B.C., 1980. Seismicity rates and long-term earthquake predic- tion in the Aegean area, Quaterniones Geodaesiae, 3, 171–190.

Papazachos, B.C., Comninakis, P.E., 1971. Geophysical and tectonic features of the Aegean Arc. J. Geophys. Res. 76, 8517–8533. https://doi.org/10.1029/jb076i035p08517

Papazachos, B.C., Comninakis, P.E., Karakaisis, G.F., Karakostas, B.G., Papaioannou, C.A., Papazachos, C.B., Scordilis, E.M., 2000. A catalogue of earthquakes in Greece and surrounding area for the period 550BC-1999. Thessaloniki.

Papazachos, B.C., Comninakis, P.E., Papadimitriou, E.E., Scordilis, E.M., 1984. Properties of the February-March 1981 seismic sequence in the Alkyonides gulf of central Greece. Ann. Geophys. 2, 537–544. https://doi.org/10.1007/BF00879574

Papazachos, B.C., Comninakis, P.E., Papadimitriou, E.E., Scordilis, E.M., 1984. Properties of the February-March 1981 seismic sequence in the Alkyonides gulf of central Greece. Ann. Geophys. 2, 537–544. https://doi.org/10.1007/BF00879574

Papazachos, B.C., Dimitriadis, S.T., Panagiotopoulos, D.G., Papazachos, C.B., Papadimitriou, E.E., 2005. Deep structure and active tectonics of the southern Aegean volcanic arc, in: Fytikas, M., Vougioukalakis, G.E. (Eds.), The South Aegean Active Volcanic Arc. Elsevier B.V., pp. 47–64. https://doi.org/10.1016/S1871-644X(05)80032-4

Papazachos, B.C., Papaioannou, C.A., 1993. Long-term earthquake prediction in the Aegean area based on a time and magnitude predictable model. Pure Appl. Geophys. PAGEOPH 140, 593–612. https://doi.org/10.1007/BF00876578

Papazachos, B.C., Papaioannou, C.A., Papastamatiou, D.J., Margaris, B.N., Theodulidis, N.P., 1990. On the reliability of different methods of seismic hazard assessment in Greece. Nat. Hazards 3, 141–151. https://doi.org/10.1007/BF00140428

Papazachos, B.C., Papaioannou, C.P., 1997. Seismic hazard in Greece based on new seismotectonic data. In: IASPEI 29th General Assembly, Thessaloniki, 18–30 August 1997

Papazachos, B.C., Papazachou, C., 2003. The earthquakes of Greece. Ziti Publications, Thessaloniki.

Papazachos, C., 1999. An Alternative Method for a Reliable Estimation of Seismicity with an Application in Greece and the Surrounding Area. Bull. Seismol. Soc. Am. 89, 111–119.

Papazachos, C.B., Karakostas, B.G., Karakaisis, G.F., Papaioannou, Ch.A., 2001. The Athens 1999 mainshock (MW5.9) and the evolution of its aftershock sequence, in Proc. of the 9th Int. Conf. of the Geological Society of Greece, September 2001, Athens, 1581– 1586.

Papoulia, J., Stavrakakis, G., Papanikolaou, D., 2001. Bayesian estimation of strong earthquakes in the Inner Messiniakos fault zone, southern Greece, based on seismological and geological data. J. Seismol. 5, 233–242. https://doi.org/10.1023/A:1011491103922

Parginos, D., Mavridis, A., Bornovas, I., Mettos, A., Katsikatsos, G., Koukis, G., 2007. 1:50000

Geological Map “Chalkida”. IGME, Athens.

Park, S., Elrick, S., 1998. Predictions of shear wave velocities in southern California using surface geology. Bulletin of the Seismological Society of America 88, 677–685.

Pavlides, S., 1996. First palaeoseismological results from Greece. Ann. Geofis. 34, 545–555.

Pavlides, S., Caputo, R., 2004. Magnitude versus faults’ surface parameters: quantitative relationships from the Aegean Region. Tectonophysics 380, 159-188.

Pavlides, S., Papadopoulos G.A, Ganas, A., 1999. The 7th September 1999 unexpected earthquake oί" Athens: Preliminary results οη the seismotectonic environment, 1st Conf Advances in Natural Hazards Mitigation: Experiencesjrom Europe and Japan, Progrαιnme-Abstracts-Reports, Athens, 3-4 November, 1999, 80-85

Pavlides, S., Tsapanos, T., Zouros, N., Sboras, S., Koravos, G., Chatzipetros, A., 2009. Using active fault data for assessing seismic hazard: a case study from NE Aegean sea, Greece. Earthq. Geotech. Eng. Satell. Conf. XVIIth Int. Conf. Soil Mech. Geotech. Eng. 2–3.

Pavlides, S.B., Papadopoulos, G., Ganas, A., 2002. The fault that caused the Athens September 1999 Ms = 5.9 earthquake: Field observations. Nat. Hazards 27, 61–84. https://doi.org/10.1023/A:1019927302304

Pavlopoulos, K., Kotabasi, Ch., Skedos, A., 2005. Geomorphological evolution of the basin of Athens. Bulletin of the Geological Society of Greece, [S.l.], v. 38, p. 1-13, sep. 2005. ISSN 2529-1718. https://doi.org/10.12681/bgsg.18351

Pérez-Peña, J. V., Al-Awabdeh, M., Azañón, J.M., Galve, J.P., Booth-Rea, G., Notti, D., 2018. SwathProfiler and NProfiler: Two new ArcGIS Add-ins for the automatic extraction of swath and normalized river profiles. Comput. Geosci. 104, 135–150. https://doi.org/10.1016/j.cageo.2016.08.008

Petersen, M.D., Bryant, W.A., Cramer, C.H., Reuchle, M.S., Real, C.R., 1997. Seismic ground-motion hazard mapping incorporating site effects for Los Angeles, Orange, and Ventura Counties, California: a geographic information system application. Bulletin of the Seismological Society of America 87, 249–255

Petseti, A., Nektarios, M., 2012. Proposal for a national earthquake insurance programme for Greece. Geneva Pap. Risk Insur. Issues Pract. 37, 377–400. https://doi.org/10.1057/gpp.2012.12

Petseti, A., Nektarios, M., 2013. Earthquake insurance for Greece: comparative analysis and pricing issues. J. Risk Financ. 14, 251–265. https://doi.org/10.1108/JRF-11-2012-0082

Photiades, A., and Carras, N., 2001. Stratigraphy and geological structure of the Lavrion area, Bulletin Geological Society of Greece, XXXIV/1, 103-109

Plastino, W., Povinec, P.P., De Luca, G., Doglioni, C., Nisi, S., Ioannucci, L., Balata, M., Laubenstein, M., Bella, F., Coccia, E., 2010. Uranium groundwater anomalies and L’Aquila earthquake, 6th April 2009 (Italy). J. Environ. Radioact. 101, 45–50. https://doi.org/10.1016/j.jenvrad.2009.08.009

Pomonis, A., Gaspari, M., 2014. Earthquake loss estimation and benefit-cost analysis of mitigation measures for buildings in Greece: Case study of Pylos town. Boll. di Geofis. Teor. ed Appl. 55, 535–560. https://doi.org/10.4430/bgta0072

Pope, R.J., Wilkinson, K.N., Millington, A.C., 2003. Human and climatic impact on Late Quaternary deposition in the Sparta Basin piedmont: evidence from alluvial fan systems. Geoarcheology: An International Journal 18, 685–724.

PreventionWeb, 2020. Greece – Disaster & Risk profile. [Online]. Available at: https://www.preventionweb.net/countries/grc/data/

Psycharis, I., Papastamatiou, D., Taflambas, I., Carydis, P., 1999. The Athens, Greece Earthquake of September 7, 1999. Athens, Greece.

Rao, G., He, C., Chen, H., Yang, X., Shi, X., Chen, P., Hu, J., Yao, Q., Yang, C.-J., 2020. Use of small unmanned aerial vehicle (sUAV)-acquired topography for identifying and characterizing active normal faults along the Seerteng Shan, North China. Geomorphology 107168. https://doi.org/10.1016/j.geomorph.2020.107168

Reicherter, K., Michetti, A.M., Silva Barroso, P.V., 2009. Paleoseismology: historical and prehistorical records of earthquake ground effects for seismic hazard assessment. Special Publication of the Geological Society of London 316, 1-10

Reid, H.F., 1910. The mechanics of the earthquake. In: The CaZ~forn~ earthquake ofApril 18, 1906. Rept. State Earthquake Invest. Comm.,Carnegie Inst., Washington, D.C., 192 pp.

Reilinger, R., McClusky, S., Vernant, P., Lawrence, S., Ergintav, S., Cakmak, R., Ozener, H., Kadirov, F., Guliev, I., Stepanyan, R., Nadariya, M., Hahubia, G., Mahmoud, S., Sakr, K., ArRajehi, A., Paradissis, D., Al-Aydrus, A., Prilepin, M., Guseva, T., Evren, E., Dmitrotsa, A., Filikov, S. V., Gomez, F., Al-Ghazzi, R., Karam, G., 2006. GPS constraints on continental deformation in the Africa-Arabia-Eurasia continental collision zone and implications for the dynamics of plate interactions. J. Geophys. Res. Solid Earth 111, 1–26. https://doi.org/10.1029/2005JB004051

Reiter, L., 1990. Earthquake hazard analysis. Columbia University Press, New York, 254p.

Reiter, L., 1990. Earthquake Hazard Analysis. Issues and Insights. New York: Columbia University Press 254 pp.

Rikitake T. 1991. Assessment of earthquake hazard in the Tokyo area, Japan, Tectonophysics, 199, 121-131.

Rivas-Medina, A., Benito, B., Miguel Gaspar-Escribano, J., 2018. Approach for combining fault and area sources in seismic hazard assessment: Application in south-eastern Spain. Nat. Hazards Earth Syst. Sci. 18, 2809–2823. https://doi.org/10.5194/nhess-18-2809-2018

Roberts, G. P., 1996. Noncharacteristic normal faulting surface ruptures from the Gulf of Corinth, Greece. Journal of Geophysical Research, 101(B11), 25,255–25,267. https://doi.org/10.1029/96JB02119

Roberts, G. P. and Gawthorpe, R. L., 1995. Strike variation in deformation and diagenesis along segmented normal faults: an example from the eastern Gulf of Corinth, Greece. In Hydrocarbon Habitat in Rift Basins, ed J. J. Lambiase. Geol. Sot. Sp. Publ. 80, 57-74.

Roberts, G. P., 1996. Variation in fault-slip directions along active and segmented normal fault systems. Journal of Structural Geology 18, 835-845.

Roberts, G., Papanikolaou, I., Vött, A., Pantosti, D., Hadler, H., 2011. Active Tectonics and Earthquake Geology of the Perachora Peninsula and the Area of the Isthmus, Corinth Gulf, Greece. In: Roberts, G., Papanikolaou, I., Vött, A., Pantosti, D., Hadler, H. (eds). INQUA - TERPRO Focurs Area on Paleoseismology and Active Tectonics & IGCP-567 Earthquake Archaeology, Athens, 40 pp

Roberts, G.P., Cowie, P., Papanikolaou, I., Michetti, A.M., 2004. Fault scaling relationships, deformation rates and seismic hazards: An example from the Lazio-Abruzzo Apennines, central Italy. J. Struct. Geol. 26, 377–398. https://doi.org/10.1016/S0191-8141(03)00104-4

Roberts, G.P., Houghton, S.L., Underwood, C., Papanikolaou, I., Cowie, P.A., Van Calsteren, P., Wigley, T., Cooper, F.J., McArthur, J.M., 2009. Localization of quaternary slip rates in an active rift in 105 years: An example from central Greece constrained by 234U-230Th coral dates from uplifted paleoshorelines. J. Geophys. Res. Solid Earth 114, 1–26. https://doi.org/10.1029/2008JB005818

Roberts, G.P., Koukouvelas, I., 1996. Structural and seismological segmentation of the Gulf of Corinth fault system: implications for models of fault growth. Ann. Geophys. 39. https://doi.org/https://doi.org/10.4401/ag-3996

Rondoyanni, T., Marinos, P., 2008. The Athens-Corinth highway and railway crossing a tectonically active area in Greece. Bull. Eng. Geol. Environ. 67, 259–266. https://doi.org/10.1007/s10064-008-0134-5

Roubanis, B.S., 1961. Geological research on the Parnes mountain range, Annales Géologiques des Pays Helléniques, 12, 18-104.

Roumelioti, Z., Kiratzi, A., Theodoulidis, N., Kalogeras, I., Stavrakakis, G., 2003. Rupture directivity during the September 7, 1999 (Mw 5.9) Athens (Greece) earthquake inferred from forward modeling of strong ground motion. Pure Appl. Geophys. 160, 2301–2318. https://doi.org/10.1007/s00024-003-2395-z

Roumelioti, Z., Kiratzi, A., Theodulidis, N., 2004. Stochastic strong ground-motion simulation of the 7 September 1999 Athens (Greece) earthquake. Bull. Seismol. Soc. Am. 94, 1036–1052. https://doi.org/10.1785/0120030219

Royden LH, Papanikolaou DJ. Slab segmentation and late Cenozoic disruption of the Hellenic arc. Geochem. Geophys. Geosyst. 2011;12:Q03010

Sakellariou, D., Lykousis, V., Alexandri, S., Kaberi, H., Rousakis, G., Nomikou, P., Georgiou, P., Ballas, D., 2007. Faulting, seismic-stratigraphic architecture and late quaternary evolution of the gulf of alkyonides Basin-East Gulf of Corinth, Central Greece. Basin Res. 19, 273–295. https://doi.org/10.1111/j.1365-2117.2007.00322.x

Sargeant, S.L., Burton, P.W., Douglas, A., Evans, J.R., 2002. The source mechanism of the Athens earthquake, September 7, 1999, estimated from P seismograms recorded at long range. Nat. Hazards 27, 35–45. https://doi.org/10.1023/A:1019924508035

Sauter, F. & Shah, H.C. (1978). Studies on earthquake insurance. Proceedings of the Central American Conference on Earthquake Engineering, San Salvador.

Schlagenhauf, A., Gaudemer, Y., Benedetti, L., Manighetti, I., Palumbo, L., Schimmelpfennig, I., et al., 2010. Using in situ Chlorine-36 cos- monuclide to recover past earthquake histories on limestone normal fault scarps: A reappraisal of methodology and interpretations. Geophysical Journal International, 182,36–72. https://doi.org/10.1111/j.1365-246X.2010.04622.x

Schlagenhauf, A., Manighetti, I., Benedetti, L., Gaudemer, Y., Finkel, R., Malavieille, J. &Pou, K., 2011. Earthquake supercycles in central Italy in- ferred from 36Cl exposure dating, Earth planet. Sci. Letts., 307, 487–500, doi:10.1016/j.epsl.2011.05.022.

Scholz, C.H., 2002. The Mechanics of Earthquakes and Faulting. Cambridge University Press, Cambridge, 471 pp.

Scholz, C.H., 2019. The Mechanics of Earthquakes and Faulting, 3rd ed, The Mechanics of Earthquakes and Faulting. Cambridge University Press, Cambridge. https://doi.org/10.1017/9781316681473

Scholz, C.H., Sykes, L.R., Aggarwal, Y.P., 1973. American Association for the Advancement of Science. Science (80-.). 181, 803–810. https://doi.org/10.1126/science.os-2.57.341-a

Schwartz, David P. & Coppersmith, K.J., 1986. Seismic Hazards: New Trends in Analysis Using Geologic Data, in: Active Tectonics: Impact on Society (1986). The National Academies Press., Washington, DC, pp. 215–230. https://doi.org/10.17226/624

Serva, L., 1994. Ground effects in the intensity scales. Terra Nova 6, 414-416

Serva, L., Esposito, E., Guerrieri, L., Porfido, S., Vittori, E., Commerci, V., 2007. Environmental effects from five historical earthquakes in southern Apennines (Italy) and macroseismic intensity assessment: Contribution to INQUA EEE Scale project. Quaternary International 173-174, 30-44

Shaw, B., Jackson, J., 2010. Earthquake mechanisms and active tectonics of the Hellenic subduction zone. Geophys. J. Int. 181, 966–984. https://doi.org/10.1111/j.1365-246X.2010.04551.x

Shearer, P.M., Stark, P.B., 2012. Global risk of big earthquakes has not recently increased. Proc. Natl. Acad. Sci. U. S. A. 109, 717–721. https://doi.org/10.1073/pnas.1118525109

Shimazaki, K., and Nakata, 1989. Time predictable reccurrence model for large earthquakes. Geophysical Research Letters 7, 279-282

Sibson, R.H., 1984. Roughness at the base of the seismogenic zone: contributing factors. Journal of Geophysical Research 89, 5791-5799.

Sieh, K .. Stuiver. M., and Brillinger, D., 1989. A more precise chronology of earthquakes produced by the San Andreas fault in southern California, J. Geophys. Res. 94, 603-623.

Silva, P.G., Goy, J.L., Zazo, C., Bardají, T., 2003. Faulth-generated mountain fronts in southeast Spain: Geomorphologic assessment of tectonic and seismic activity. Geomorphology 50, 203–225. https://doi.org/10.1016/S0169-555X(02)00215-5

Silva, P.G., Rodriguez Pascua, M.A., Giner Robles, J.L., Perez Lopez, R., Lario Gomez, L., Perucha Atienza, M.A., Bardaji Azcarate, T., Huerta Hurtado, P., Roquero Garcia-Casal, E., Bautista Davila, M.B., 2008. Catalogación de los efectos geologicos y ambientales de los terremotos en Espana en la escala ESI-2007 y su aplicación a los estudios paleosismologicos. Geotemas 6, 1063-1066.

Singh, S.K., Mena, E., and Castro, R.,1988. Some aspects of source characteristics of the 19 September 1985 Michoacan earthquake and ground motion amplification in and near Mexico City from strong motion data. Bulletin of Seismological Society of America 78, 451-477.

Skarlatoudis, A.A., Papazachos, C.B., Margaris, B.N., Ventouzi, C., Kalogeras, I., 2013. Ground-motion prediction equations of intermediate-depth earthquakes in the Hellenic arc, southern Aegean subduction area. Bull. Seismol. Soc. Am. 103, 1952–1968. https://doi.org/10.1785/0120120265

Speidel, D.H., and Mattson, P.H., 1997. Problems for probabilistic seismic hazard analysis. Natural Hazards 16, 165-179.

Spudich, P., Bayless, J.R., Baker, J., Chiou, B.S.J., Rowshandel, B., Shahi, S., Somerville, P., 2013. Final Report of the NGA-West2 Directivity Working Group, Pacific Engineering Research Center Report. Berkeley.

Stavrakakis, G. and Drakopoulos, J., 1995, Bayesian probabilities ofearthquake occurrences in Greece and surrounding areas, Pure Appl. Geophys. 144(2), 307–319.

Stavrakakis, G. and Tselentis, G.A., 1987, Bayesian probabil- istic prediction of strong earthquakes in the main seismogenic zones of Greece, Bolletino di Geofisica Teorica et Applicata XXIX(113), 51–63.

Stavrakakis, G.N., Chouliaras, G., Panopoulou, G., 2002. Seismic source parameters for the ML = 5.4 Athens earthquake (7 September 1999) from a new telemetric broad band seismological network in Greece. Nat. Hazards 27, 47–60. https://doi.org/10.1023/A:1019939628612

Stein, R.S., 2002. Parkfield's unfulfilled promise. Nature 419, 257–258.

Stein, S., Geller, R.J., Liu, M., 2012. Why earthquake hazard maps often fail and what to do about it. Tectonophysics 562–563, 1–25. https://doi.org/10.1016/j.tecto.2012.06.047

Stein, S., Spencer, B.D., Brooks, E.M., 2015. Metrics for assessing earthquake-hazard map performance. Bull. Seismol. Soc. Am. 105, 2160–2173. https://doi.org/10.1785/0120140164

Steinbrugge, K. V., 1982. Earthquakes, Volcanoes, and Tsunamis: An Anatomy of Hazards. Skandia America Group: New York, New York.

Stewart, I. and Hancock, P., 1991. Scales of structural heterogeneity within neotectonic normal fault zones in the Aegean region, J. Struct. Geol., 13, 191–204,

Stewart, I.S., 1996. A rough guide to limestone fault scarps. J. Struct. Geol. 18, 1259–1264

Stirling, M., McVerry, G., Gerstenberger, M., Litchfield, N., Van Dissen, R., Berryman, K., Barnes, P., Wallace, L., Villamor, P., Langridge, R., Lamarche, G., Nodder, S., Reyners, M., Bradley, B., Rhoades, D., Smith, W., Nicol, A., Pettinga, J., Clark, K., Jacobs, K., 2012. National seismic hazard model for New Zealand: 2010 update. Bull. Seismol. Soc. Am. 102, 1514–1542. https://doi.org/10.1785/0120110170

Stirling, M.W., McVerry, G.H., and Berryman K.R., 2002. A new seismic Hazard model for New Zealand. Bulletin of the Seismological Society of America 92, 1878-1903.

Stover CW, Coffman JL., 1993. Seismicity of the United States, 1568–1989 (revised). United States Govern- ment Printing Office, Washington

Stucchi, M., Rovida, A., Gomez Capera, A.A., Alexandre, P., Camelbeeck, T., Demircioglu, M.B., Gasperini, P., Kouskouna, V., Musson, R.M.W., Radulian, M., Sesetyan, K., Vilanova, S., Baumont, D., Bungum, H., Fäh, D., Lenhardt, W., Makropoulos, K., Martinez Solares, J.M., Scotti, O., Živčić, M., Albini, P., Batllo, J., Papaioannou, C., Tatevossian, R., Locati, M., Meletti, C., Viganò, D., Giardini, D., 2013. The SHARE European Earthquake Catalogue (SHEEC) 1000-1899. J. Seismol. 17, 523–544. https://doi.org/10.1007/s10950-012-9335-2

Swafford, L., Stein, S., 2007. Limitations of the short earthquake record for seismicity and seismic hazard studies. In: Stein, S., Mazzotti, S. (Eds.), Continental Intraplate Earthquakes, Special Paper, 425. GSA, Boulder, CO, pp. 49–58.

Swiss Re Institute, 2019a. A decade of major earthquakes : lessons for business, October 2019.

Swiss Re Institute, 2019b. Natural catastrophes and man-made disasters in 2018: "secondary" perils on the frontline. Sigma 2, 1–36.

Tataris, A., Kounis, G., Maragkoudakis, N., 1966. 1:50000 Geological Map "Thivai". IGME, Athens.

Tatevosian, R.E., 2007. The Verny, 1887, earthquake in Central Asia: Application of the INQUA scale, based on coseismic environmental effects. Quaternary International 173-174, 23-29.

Taymaz, T., J. Jackson, and R. Westaway, 1990. Earthquake mechanisms in the Hellenic trench near Crete, Geophys. J. Int. 102, 695–731.

Taymaz, T., Jackson, J. & McKenzie, D., 1991. Active tectonics ofthe north and central Aegean Sea, Geophys. J. Int., 106, 433–490

Tesson, J., Pace, B., Benedetti, L., Visini, F., Delli Rocioli, M., Arnold, M., et al. 2016. Seismic slip history of the Pizzalto fault (central Apennines, Italy) using in situ-produced 36Cl cosmic ray exposure dating and rare earth element concentrations. Journal of Geophysical Research: Solid Earth, 121, 1983–2003. https://doi.org/10.1002/2015JB012565

Theodulidis, N. P., 1991. Contribution to strong ground motion study in Greece. Ph.D. Thesis. Aristotle University of Thessaloniki, Thessaloniki, Greece, 500 pp (in Greek).

Theocharis, D., Fountoulis, I., 2002. Morphometric indices and active tectonic structures. The case of Salamis Island (Greece), in: Proceedings of the 6th Panhellenic Conference of the Greek Geological Society. Athens, pp. 97–106.

Tolomei, C., Caputo, R., Polcari, M., Famiglietti, N.A., Maggini, M., Stramondo, S., 2021. The use of interferometric synthetic aperture radar for isolating the contribution of major shocks: The case of the march 2021 thessaly, greece, seismic sequence. Geosci. 11. https://doi.org/10.3390/geosciences11050191

Toth, L., Gyori, E., Monus, P., Zsiros, T., 2004. Seismicity and seismic hazard in the Pannonian basin. Proc. NATO Ad. Res. Worksh.: The Adria microplate, pp. 119–123.

Trichopoulos, D., Zavitsanos, X., Katsouyanni, K., Tzonou, A., Dalla-Vorgia, P., 1983. Psychological Stress and Fatal Heart Attack: the Athens (1981) Earthquake Natural Experiment. Lancet 321, 441–444. https://doi.org/10.1016/S0140-6736(83)91439-

Tripathi, B., Bob, 2001. Earthquake Loss Estimation Methodology For Prioritizing Seismic Mitigation At Federally Owned Facilities, in: Transactions, SMiRT 16,. Washington, DC, pp. 1–7.

Tsapanos, T., Koravos, G., Zygouri, V., Tsapanos, M., Kortsari, A., Kijko, A., Kalogirou, E., 2010. Deterministic seismic hazard analysis for the city of Corinth- central Greece. J. Balkan Geophys. Soc. 14, 1e14.

Tsapanos, T.M., Mäntyniemi, P., Kijko, A., 2004. A probabilistic seismic hazard assessment for Greece and the surrounding region including site-specific considerations. Ann. Geophys. 47, 1678–1688. https://doi.org/10.4401/ag-3367

Tselentis, G., Zahradnik, J., 2000a. Aftershock Monitoring of the Athens Earthquake of 7 September 1999. Seismol. Res. Lett. 71, 330–337.

Tselentis, G., Zahradnik, J., 2000b. The Athens Earthquake of 7 September 1999. Bull. Seismol. Soc. Am. 1143–1160. https://doi.org/10.1785/0119990168

Tselentis, G.A., Danciu, L., 2010. Probabilistic seismic hazard assessment in Greece – Part 1: Engineering ground motion parameters. Nat. Hazards Earth Syst. Sci. 10, 51–59.

Tsodoulos, I.M., Koukouvelas, I.K., Pavlides, S., 2008. Tectonic geomorphology of the easternmost extension of the Gulf of Corinth (Beotia, Central Greece). Tectonophysics 453, 211–232. https://doi.org/10.1016/j.tecto.2007.06.015

Tucker, G., McCoy, S.W., Whittaker, C.A., Roberts, G.P., Lancaster, S.T., Phillips, R., 2011. Geomorphic significance of postglacial bedrock scarps on normal-fault footwalls. Journal of Geophysical Research 116, doi:10.1029/2010JF001861.

UNISDR, 2017. Words into Action Guidelines: National Disaster Risk Assessment - Hazard Specific Risk Assessment. https://doi.org/10.1029/2001GC000252.2

Vamvakaris, D.A., Papazachos, C.B., Papaioannou, C.A., Scordilis, E.M., Karakaisis, G.F., 2016. A detailed seismic zonation model for shallow earthquakes in the broader Aegean area. Nat. Hazards Earth Syst. Sci. 16, 55–84. https://doi.org/10.5194/nhess-16-55-2016

Vassilakis, E., Skourtsos, E., Kranis, E. 2007. Estimation of tectonic uplift rate using quantified morphometric indices. Proceedings of the 8th Pan-Hellenic Geographical Conference of the Greek Geographical Society, pp. 17-26.

Wald, D.J., Quitoriano, V., Heaton, T.H., Kanamori, H., 1999. Relationships between peak ground acceleration, peak ground velocity, and modified mercalli intensity in California. Earthq. Spectra 15, 557–564. https://doi.org/10.1193/1.1586058

Wallace, R.E. (1978) Geometry and rates of changes of fault- generated range fronts, north-central Nevada. United States. Geol. Survey J. Res., 6, 637–650

Wells, D.L., Coppersmith, K., 1994. New Empirical Relationships among Magnitude, Rupture Length, Rupture Width, Rupture Area, and Surface Displacement. Bulletin of the Seismological Society of America 84, 974-1002.

Wensnousky, S.G., 1994. The Gutenberg-Richter or characteristic earthquake distribution, which is it? Bulletin of the Seismological Society of America (1994) 84 (6): 1940–1959

Wesnousky, S.G.,1987. Geological Data and Seismic Hazard Analysis: Past and Future, Proceedings of Conference XXXIX, Directions in Paleoseismology, U.S.G.S. Open-File Report 87-673, pp. 418-427.

Whipple, K.X. and Tucker, G.E., 1999. Dynamics of the stream-power river incision model: Implications for height limits of mountain ranges, landscape response timescales, and research needs. *Journal of Geophysical Research* 104,(B8), pp.17,661-17,674.

Whipple, K.X. and Tucker, G.E., 2002. Implications of sediment-flux-dependent river incision models for landscape evolution. *Journal of Geophysical Research* 107, pp. 1-20.

Whipple, K.X., Wobus, C., Krosby, B., Kirby, E., Sheehan, D., 2007. New Tools for Quantitative Geomorphology: Extraction and Interpretation of Stream Profiles from Digital Topographic Data. GSA Short Course: #506.

Whittaker, A.C., Attal, M., Cowie, P.A., Tucker, G.E., Roberts, G., 2008. Decoding temporal and spatial patterns of fault uplift using transient river long profiles. *Geomorphology* 100, pp.506-526.

Wiatr, T., Papanikolaou, I., Fernández-Steeger, T., Reicherter, K., 2015. Bedrock fault scarp history: Insight from t-LiDAR backscatter behaviour and analysis of structure changes. Geomorphology 228, 421–431. https://doi.org/10.1016/j.geomorph.2014.09.021

Wobus, C., Whipple, K.X., Kirby, E., Synder, N., Johnson, J., Spyropolou, K., Crosby, B.T., Sheehan, D., 2006. Tectonics from topography: Procedures, promise, and pitfalls, in: Willett, S.D., Hovius, N., Brandon, M.T., Fisher, D.M. (Eds.), Tectonics, Climate and Landscape Evolution. Geology Society of America Spetial Papers, pp. 55–74. doi:10.1130/2006.2398(04)

Woessner, J., Laurentiu, D., Giardini, D., Crowley, H., Cotton, F., Grünthal, G., Valensise, G., Arvidsson, R., Basili, R., Demircioglu, M.B., Hiemer, S., Meletti, C., Musson, R.W., Rovida, A.N., Sesetyan, K., Stucchi, M., 2015. The 2013 European Seismic Hazard Model: key components and results. Bull. Earthq. Eng. 13, 3553–3596. https://doi.org/10.1007/s10518-015-9795-1

Woith, H., Petersen, G.M., Hainzl, S., Dahm, T., 2018. Review: Can animals predict earthquakes? Bull. Seismol. Soc. Am. 108, 1031–1045. https://doi.org/10.1785/0120170313

Woo, G. (1999). The mathematics of natural catastrophes (1st ed.). Imperial College Press, London.

Working Group on California Earthquake Probabilites (WGCEP), 1990. Probabilities of large earthquakes in the San Fransisco Bay region, California. U.S. Geol. Surv. Circ., 1053, 51pp.

Working Group on California Earthquake Probabilities (WGCEP), 1999. Preliminary report: Earthquake Probabilities in the San Francisco Bay Region: 2000-2030- A Summary of Findings. USGS Open-File Report 99-517.

Working Group on California Earthquake Probabilities (WGCEP), 2002. Earthquake probabilities in the San Francisco bay region: 2002-2031. USGS Open-File Report 03-214.

Working Group on California Earthquake Probabilities (WGCEP), 2007. Uniform California Earthquake Rupture Forecast 2 Final Report.

Xypolias, P., Kokkalas, S., Skourlis, K., 2003. Upward extrusion and subsequent trans- pression as a possible mechanism for the exhumation of HP/LT rocks in Evia island, Aegean sea, Greece. Journal of Geodynamics 35, 303–332.

Yeats, R.S., Sieh, K., Allen, C.R., 1997. The Geology of Earth- quakes. Oxford University Press, New York (568 pp.).

Yeats, S., Prentice, S., 1996. Introduction to special section : Paleoseismology Corvallis A proverb states 101, 5847–5853.

Yomogida, K., Yoshizawa, K., Koyama, J., Tsuzuki, M., 2011. Along-dip segmentation of the 2011 off the Pacific coast of Tohoku Earthquake and comparison with other megathrust earthquakes. Earth, Planets and Space 63, 697–701.

Zimbidis, A.A., Frangos, N.E., Pantelous, A.A., 2007. Modeling Earthquake Risk via Extreme Value Theory and Pricing the Respective Catastrophe Bonds. ASTIN Bull. 37, 163–183. https://doi.org/10.2143/ast.37.1.2020804

Zreda, M. and Noller, J., 1998. Ages of prehistoric earthquakes revealed by cosmogenic chlorine-36 in a bedrock fault scarp at Hebgen Lake. Science, 282, 1097–1099.

List of Tables

Table 1.1: Number of insured claims, claim amount and average claim per disaster type in Greece, from 1993 up to 2018 (reproduced by EAEE, 2019). 20
Table 5.1: Radii of the isoseismals for the active faults in Attica, based on the Theodulidis (1991) attenuation relationships. Intensity IX is not expected in firm sediments affected by faults shorter than 16km...82
Table 5.2: Average intensity changes depending on different types of surface geology, proposed by Sauter and Shah (1978), and Degg (1992). 85
Table 6.1: Fault characteristics used for extracting the earthquake recurrence per site over the last 15 kyrs. Expected Magnitude and Maximum Displacement per Event values are based on Wells and Coppersmith (1994) equations. Slip rate column refers to short term where available, or long term slip rate values, induced from published papers and neotectonic maps (see text for details). *Id* numbers refer to the map displayed in Figure 6.92. Fault characteristics are based on the following sources (numbers correspond to the "Source" column): *1)* Papanikolaou et al., 1988; *2)* Official Neotectonic map of Saronikos Gulf (Papanikolaou et al., 1989); *3)* Official Neotectonic map of South Evoikos Gulf (Papanikolaou et al., 1989) ; *4)* Official Neotectonic map of East Attica (Papanikolaou et al., 1995); *5)*Pantosti et al., 1996; *6)*Collier et al., 1998; *7)*Morewood and Roberts, 1999; *8)*Morewood and Roberts, 2001; *9)*Pavlides et al., 2002; *10)*Goldsworthy et al., 2002; *11)*Benedetti et al., 2003; *12)*Ganas et al., 2004; *13)*Chatzipetros et al., 2005; *14)*Ganas et al., 2005; *15)*Kokkalas et al., 2007; *16)*Papanikolaou and Papanikolaou, 2007b; *17)*Sakellariou et al. 2007; *18)*Rontoyianni and Marinos, 2008; *19)*Tsodoulos et al., 2008; *20)*Roberts et al., 2009; *21)*Roberts et al., 2011; *22)* Foutrakis, 2016, *23)* Grützner et *al*., *2016* and *24)* Mechernich et al., 2018. *f*: fieldwork findings...171
Table 8.1: Building characteristics for each insurance policy 187
Table 8.2: Construction type in relation to average loss in case of intensities VII – X occurrence, after Sauter & Shah (1978) and Degg (1992)................................187
Table 8.3: Expected losses over selected return periods for a 4 billion euros demo portfolio. Assumptions are explained in the text 189
Table 8.4: 1/200 loss to insured value for each CRESTA Zone in the Attica region, assuming single CRESTA zone exposure for each model run 198
Table 8.5: 1/200 loss to insured value in the Attica region, assuming exposure in every CRESTA zone..198
Table 8.6: 1/200 loss to insured value in the Attica region, assuming exposure in every CRESTA zone and applying a 2% deductible policy. 199
Table 9.1: A comparison between the return periods and the observed intensities of historical earthquakes in certain locations versus the fault specific seismic hazard maps outputs (cells in colour). AB stands for Athens Basin (also known as the Greater Athens Area). WA stands for West Attika. N/O stands for No Occurrence, indicating that there are still areas where no such intensity occurred. PP stands for Papaioannou and Papazachos (2000), regarding the city of Athens. The Maximum return period column shows the lowest recurrence within either the Athens basin or the rest of the Attica. However, in all cases, there are even small localities that have not shaken in intensities ≥ VII (Figure 9.2). The differences between the historical catalogues and the fault specific seismic hazard maps indicate the need

for longer observation time periods and higher spatial resolution in seismic hazard assessment...210

List of Figures

Figure 1.1: Number of fatalities due to geophysical and climate – related natural disasters worldwide, between 1998 and 2017 (reproduced by CRED - UNISDR, 2017). Three major earthquakes (2004 Sumatra – Andaman Mw 9.1earthquake and tsunami, 2008 Sichuan Mw 7.9, 2010 Haiti Mw 7.0 earthquake) resulted in more than 500,000 fatalities...15
Figure 1.2: Impact of natural disasters worldwide, between 1998 and 2017 (reproduced by CRED - UNISDR, 2017). Although the earthquakes events were considerably less than the climate-related disasters (i.e. floods and storms), they caused the vast majority of fatalities within this period. In addition, in terms of economic loss, earthquakes rank 2nd after storms. 16
Figure 1.3: Number of claims and the total claim amount per year for all types of natural disasters in Greece, from 1993 up to 2018 (reproduced by (EAEE, 2019). The largest amount of claims and damage compensations were recorded in 1999, when the Athens Mw 5.9 earthquake occurred. 21
Figure 2.1: A characteristic example of the subjective delination of seismic zones. The spatial distribution of the seismic zones in the North Aegean Basin, Greece, is delineated by different research groups. This figure shows that the definition of zone boundaries, within which seismicity rates are assumed to be uniform, is rather subjective. Image reproduced from Papanikolaou & Papanikolaou (2007). 31
Figure 2.2: Mean-value analysis results (black dots) plotted along with recurrence curves obtained from probabilistic hazard analysis (Cornel, 1968), for Athens and Corinth. The mean-value analysis, which incorporates historical data for macroseismic intensities, results to higher values for the mean-value method. Indeed, at the time of this publication, Corinth had already experienced the 1981 Alkyonides earthquake sequence, but the Athens 1999 Mw5.9 earthquake had not occurred. Image reproduced from Papazachos et al. (1990)...............................34
Figure 2.3: The 69 shallow earthquake sources proposed by Papazachos and Papaioannou (1993). Note that there are extended areas in Northern Greece, Attica and the north Cyclades, where no seismic source is constrained, as there was no historical or instrumental seismicity recorded yet. Image reproduced from Papazachos and Papaioannou (1993)..35
Figure 2.4: The 67 shallow earthquake sources proposed by Papaioannou and Papazachos (2000). Note that after the Kozani Grevena 1996 and Athens 1999 earthquakes, there are no aseismic areas and each location on the map belongs to a source zone. Image reproduced from Papazachos and Papaioannou (2000). ...36
Figure 2.5: Seismic hazard map for the Aegean domain, by Tselentis and Danciu (2010), representing hazard using points mesh with 0.1° interval. Each point corresponds to a PGA value with 10% probability of exceedance for the following 50 years. 37
Figure 2.6: The first seismic hazard map issued by the Earthquake Planning and Protection Organization in 1984. It divided Greece into 4 different seismic hazard zones, showing the expected PGA with a 10% probability of exceedance in 50 years. Note that the central Aegean, parts of Attica, Western Macedonia and parts of Thrace belong to the lower hazard zone...38
Figure 2.7: The second seismic hazard map issued by the Earthquake Planning and Protection Organization (EAK 2000). Kozani and Grevena cities are now included in Zone II, after the 1995 Kozani-Grevena earthquake. 38

Figure 2.8: The third seismic hazard map issued by the Earthquake Planning and Protection Organization (EAK, 2003). The previous Zone I is now ommited and the lowest hazard Zone (Zone II) represents 0.16g with 10% probability of exceedance in 50 years. 39
Figure 2.9: The Tohoku 2011 mega-earthquake (star and blue band) struck far north of the zone considered to have the greatest seismic hazard (depicted in red colour). Reproduced by Kerr, 2011. 42
Figure 2.10: Two different seismic hazard maps for Hungary and the surrounding area, showing PGA expected at 10% probability in 50 years (Swafford and Stein, 2007). The GSHAP model (bottom), based only on historic and recorded seismicity, predicts more concentrated hazard near sites of earlier earthquakes, compared to a different model (top) including geological data that predicts more diffuse hazard (Toth et al., 2004). Image reproduced by Stein et al. (2012). 43
Figure 3.1: Simplified map of the Hellenic system by Papanikolaou and Royden (2007) showing active thrust faults (black lines with barbs), active normal faults (black lines with tick marks), and arc-parallel extensional detachment faults of Miocene age (grey lines with arrows, St, Strymon detachment; OC, Olympos-Cyclades detachment; EP, East Peloponnesus Detachment). 48
Figure 3.2: Schematic geological cross-section of the central part of Attica, in a NW – SE direction including the Athens basin. The NW dipping Miocene detachment separates the non-metamorphic bedrock in the west, from the metamorphic formations in the east. Image modified from Papanikolaou et al., 1999. 50
Figure 3.3: Map showing the topography in the Attica Region, including the most important mountains and basins. Road network source: OpenStreetMap 2019. .53
Figure 3.4: Map showing locations of subsided and uplifted coastline, primary surface ruptures and focal mechanisms after the 24 – 25 February and 4 March major earthquakes that struck west Attica in 1981. Sketch reproduced from Papanikolaou et al., 2009). 57
Figure 3.5: Map showing the Modified Mercalli Intensity distribution after the two earthquakes on 24 and 24 of February (reproduced from Carydis et al., 1982) ..58
Figure 3.6: The inferred epicentre locations after the Athens 1999 M5.9 earthquake in West Attica. Note that the epicencers of AUTH and NOA lie in a distance of about 12 km apart from each other. Reproduced after Papanikolaou et al., 2015a. 61
Figure 3.7: Distribution of buildings damages after the Athens 1999 earthquake. Left: MMI distribution after Lekkas (1999), Right: Damages distribution and categorization after Marinos et al., 2000. Note that in both cases damages were constrained by the Kifissos river, which possibly flows over the Miocene detachment. 62
Figure 4.1: An example of an EP (Exceedance Probability) curve from Hsu et al. (2012) which displays the loss loss ratio versus return period. The loss ratio is 3.5 % in case A and greater than 2.65 % in case B for an event loss of 500 return periods. Figure reproduced from Hsu et al. (2012). 66
Figure 5.1: 2 km wide swath profiles for Sierra Alhamilla mountain range, modified after Pérez-Peña et al., 2017. 72
Figure 5.2: Helium balloon with a camera mount on the belly side, at the Lastros fault postglacial scarp in Lasithi, Crete. 76
Figure 5.3: Left: The small drone (DJI Phantom 4) from the Mineralogy – Geology Laboratory (Agricultural University of Athens), which was used to create high resolution DSM. The Dafni fault postglacial scarp is visible in the background.

Right: GCP number 7, printed on an A4 paper, and installed in the upper part of the fault scarp, on the profiling axis (thin white line at the center of the image laying in the hanging wall). 77
Figure 5.4: Schematic representation for the construction of the hazard map, modified after Papanikolaou (2003) and Roberts et al., (2004). a) The concept of the methodology for one of the 24 faults in Attica (South Alkyonides Fault). Assuming a triangular throw profile for the faults and ruptures and that the maximum throw is observed at the centre of the fault, the number of surface faulting earthquakes of Ms=6.7 can be calculated. b) Throw in this profile represents the slip that the fault has accumulated during the post-glacial period (since 15 kyr ago±3 kyr). c) Mathematical formula describing the earthquake distribution along strike each active fault. The distance (x) of each earthquake point from the tip of the fault is calculated. Each fault is divided in two halves (triangles A and B) and the corresponding formula is applied for each one of them. d) Epicentres are plotted 7 km away from the fault in the hanging wall and circles with 11 km radius of intensity IX (representing "isoseismals") are added. Geology is not yet taken into account. 83
Figure 5.5: Simplified geological map of the area of Attica, based on 1:50,000 scale geological maps of IGME and the 1:25,000 scale Earthquake Planning and Protection Organization (E.P.P.O.) detailed geotechnical map for the Athens Metropolitan Area (Marinos et al., 1999a). 85
Figure 5.6: The basic modules of the Earthquake Catastrophe model. The Hazard Module has the most critical role, as the whole model is based on its outputs. The final results are extracted from the Loss module, which calculates both direct (meaning cost to repair or replace construction) and indirect (meaning business interruption) losses, but it also integrates other significant policy characteristics, such as deductibles and coverage limits, reinsurance coverage, etc. 87
Figure 5.7: The main processes within the proposed Hazard module. The primary input is the fault specific modelling results, which vastly increases the earthquakes sample for magnituted M≥6. 89
Figure 6.1: Map view of the the Sparta fault. It trends NNW-SSE and has a length of 64km. 93
Figure 6.2: Drainage basins and main branches for 9 catchments crossing the Sparta fault, two crossing the antithetic structure and three crossing no fault. 94
Figure 6.3: Comparison of 5 catchment long profiles crossing the Sparta fault. Agios Konstantinos - F7 (northern part) catchment is the only one to appear with concave up long profile, while Potamia -F9 (southern part) profile is the less steep. Figure reproduced from Papanikolaou et al., 2013. 95
Figure 6.4: Long profiles of rivers crossing perpendicular the Sparta Fault near the Potamia, Anogia, Kalyvia-Sochas, Parori, Soystianoi, Kastorio, Ag. Konstantinos, Logkanikos and Falaisia villages, respectively. Locality names are shown geographically in Figure 6.2. Figure modified from Papanikolaou et al., 2013. . 97
Figure 6.5: Long profiles of rivers crossing the antitethic Sparta Fault as well as rivers that cross no active fault near the Sellasia, Koniditsa and Kollinaitiko villages. Locality names are shown geographically in Figure 6.2. Figure modified after Papanikolaou et al., 2013. 98
Figure 6.6: Diagram showing the convex height variability of the catchments along strike the fault system, with higher values towards its centre that diminish towards its tips. Error bar represents the 100 m convex height that can be attributed to

differential erosion. Agios Konstantinos profile is missing, due to the convexity that is attributed to the lithology. Figure modified after Papanikolaou et al., 2013. 98
Figure 6.7: Normalized steepness index (k_{sn}) for each of the 9 catchments crossing the Sparta Fault. Higher values appear in the centre of the fault. Dashed line separates the northern 14 km fault segment. 99
Figure 6.8: The Milesi and Oropos faults plotted against the Mw=6.0, 1938 Oropos event, which is retrieved from the two earthquake catalogues of NOA (UoA) and AUTH. Both epicentres are located 12 km away from each other and on the footwall of the Oropos fault, rather than its hangingwall. Image reproduced from Papanikolaou et al., 2015. 101
Figure 6.9: The NW-SE striking and NE dipping Milesi fault in NE Attica (id = 1 on Table 6.1) and the main drainage network flowing towards the South Evoikos Gulf. Base map shows the Digital Terrain Model (DTM) from the National Cadastre with 5 m spatial resolution. 102
Figure 6.10: Slope map showing the break of slope related to the Milesi fault (id = 1 on Table 6.1). Steeper slopes are observed at the footwall centre, where the maximum displacement is observed. 102
Figure 6.11: Zoomed map showing 2 windgaps and one possible windgap, at the center of the fault. The second order stream in tle lower right part of the map is flowing towards NE but seems to be diverted towards NW, parallel to the fault strike. 103
Figure 6.12: Swath topographic profiles within a Milesi fault-parallel stripe. Fault located at the centre of the stripe. Stripe width is 2600 m. Y-axis is exaggerated about 5.5 times. View looking towards NE. Orange line represents the maximum elevation, light green line represents the lower elevation, blue line represents the mean elevation, dark green lines represent the Q1 and Q3 quartiles, red line represents the local relief (maximum elevation minus minimum elevation at the same distance along the fault line). 103
Figure 6.13: Swath topographic profiles within fault perpendicular stripes, following drainage network branches close to the center and both ends of the fault. Stripe axes locations shown in Figure 6.14. Stripe width is 500 m. Y-axis is exaggerated about 2.5 times for P1 & P2, and 4 times for P3. View looking towards E. X-axis is not on the same scale in each profile. Orange line represents the maximum elevation, light green line represents the lower elevation, blue line represents the mean elevation, dark green lines represent the Q1 and Q3 quartiles. The red line represents the Milesi fault. Note the prominent convex profile on the footwall in P2, which indicates higher uplift rates towards the centre of the fault. 104
Figure 6.14: Shaded relief map of the Milesi fault, showing tha main drainage network, the locations of paleoseismic trench and fault scarp profile, as well as the location of the fault – perpendicular swath profiles (P1, P2 and P3). 105
Figure 6.15: a) Geology of the Milesi Fault and the surroundings (geology modified after Katsikatsos 2000; map and cross-section after Grützner et al., 2016). C–C' marks the cross-section in (b). (b) Cross-section based on the Geological Map (Katsikatsos 2000). The total throw of the Milesi Fault is 1050 ± 500 m. 106
Figure 6.16: Photo mosaic of the trench wall (top) and interpretation of the main units (bottom) after Grützner et al., 2016. Grid width is 1 m. Note the buried palaeosol close to the surface and a second one at 1–2 m depth. SA: Sample location. 30°/30°: dip direction and dip angle of the second palaeosol. A retrodeformation

with 4 up to 5 earthquake events that led to the present day geometry, along with the dating results are presented in Grützner et al., 2016. 107

Figure 6.17: Topographic scarp profile of the weathered large fault plane above the trench site, after Grützner et al. (2016). This fault plane dips with 38º to the NNE (30 º /038º) and has a vertical throw of 3.9 m as derived from the profiling by means of a yardstick and an inclinometer. For methodology see Papanikolaou et al. (2005). Coordinates indicate the upper and lower ends of the profile. Image reproduced from Grützner et al., 2016. 108

Figure 6.18: The E-W striking and North dipping Malakasa fault in NE Attica (id = 2 on Table 6.1) and the main drainage network of the area. 109

Figure 6.19: Slope map showing the abrupt slopes in the Malakasa fault footwall. Highest slope values (> 45º) appear on the central part of the footwall. 110

Figure 6.20: Swath topographic profiles within a Malakasa fault parallel stripe. Fault located at the center of the stripe. Stripe width is 2000 m. View looking towards North. Y-axis is exaggerated about 8 times. Orange line represents the maximum elevation, light green line represents the lower elevation, blue line represents the mean elevation, dark green lines represent the Q1 and Q3 quartiles, red line represents the local relief (maximum elevation minus minimum elevation at the same distance along the fault line). 110

Figure 6.21: Swath topographic profiles within a fault perpendicular stripe, following drainage network branch near the Western tip of the Malakasa fault. Stripe axis location shown in Figure 6.22. Stripe width is 500 m. View looking towards NE. Y-axis is exaggerated. Orange line represents the maximum elevation, light green line represents the lower elevation, blue line represents the mean elevation, dark green lines represent the Q1 and Q3 quartiles. The red line represents the Malakasa fault. 111

Figure 6.22: Shaded relief map of the Malakasa fault area, showing the main drainage network and the location of the fault – perpendicular swath profiles (P1 - P4). 112

Figure 6.23: Geological cross-section at the central part of the Malakasa fault (previous page), based on the 1:50.000 geological map of HSGME (Figure 6.25) (Gaitanakis, 1982; Parginos et al., 2007). The total throw of the Malakasa Fault 1200+/-300 m. Although it is not depicted in the current 1:50.000 scale geological map, it's clear that there is at least one older structure further upwards because of the limestone sequence that is exposed in the footwall (Late Cretaceous limestone right on the fault, then Triassic - Jurassic limestone and Late Cretaceous limestone again in the upper parts) and of the morphology. The latter is also supported by the swath profile P2. This structure is now inactive, and today's fault location is an example of fault scarp's hanging wall migration. 113

Figure 6.24: Geology of the Malakasa Fault and the surroundings (geological map compiled and modified after Gaitanakis, 1982; Parginos et al., 2007). The dashed line represents the secondary, probably older fault, further upwards. The Straight SSW NNE black line represents the geological cross-section profile (Figure 6.26). 114

Figure 6.25: Orthomosaic of part of the post-glacial scarp on Malakasa fault. The potential occurrence of differentially weathered horizontal stripes is visible. Stripe thickness is measured at 86 ± 1.6 cm. The orthomosaic was developed using Structure from Motion photogrammetry through Agisoft Metashape Professional. In total, 26 mages were acquired using a Nikon D7200 camera with an 18 mm

lens, and were photogrammetrically processed in Agisoft Metashape Professional v1.5.0. Relative accuracy was achieved by setting control points within 1 m distance from each other. Image location is shown in Figure 6.22. It is important to note that the photogrammetric processing at the Malakasa fault aimed on the determination of possible horizontal stripes, and not for the total throw measurement. 115
Figure 6.26: Topographic profile crossing the Malakasa fault scarp. Measurements obtained using a clinometer and a foldable meter scale (see also Papanikolaou et al., 2005 for details in methodology). The profiles reveal the fault scarp height and geometry, which are used for the throw rate calculation. Location of the profile is shown in Figure 6.22. 116
Figure 6.27: The E-W striking and North dipping Afidnes fault in NE Attica (id =3 on Table 6.1) and the main drainage network flowing towards the Athens Basin. 117
Figure 6.28: Slope map showing the slope changes related to Afidnes fault (id = 3 on Table 6.1). Steeper slopes are observed at the footwall, in parallel to the Afidnes fault. 118
Figure 6.29: Swath topographic profiles within an Afidnes fault parallel stripe. Fault located at the centre of the stripe. Stripe width is 1500 m. Y-axis is exaggerated about 4 times. View looking towards North. The orange line represents the maximum elevation; the light green line represents the lower elevation, the blue line represents the mean elevation, dark green lines represent the Q1 and Q3 quartiles, the red line represents the local relief (maximum elevation minus minimum elevation at the same distance along the fault line). 118
Figure 6.30: Swath topographic profiles within 3 fault perpendicular stripes, following catchments flowing perpendicular to the Afidnes fault. Stripe axis location shown in Figure 6.31. Stripe width is 500 m. Relief is exaggerated about 2 times for P2. View looking towards NE. Y-axis is exaggerated 2 times in P2. Orange line represents the maximum elevation, light green line represents the lower elevation, blue line represents the mean elevation, dark green lines represent the Q1 and Q3 quartiles. The red line represents the Malakasa fault....................................... 119
Figure 6.31: Shaded relief map of the Afidnes fault area, showing the main drainage network and the location of the fault – perpendicular swath profiles (P1 - P3). Note the asymmetry on the drainage basin of the river flowing towards the east, parallel to the fault. The Af is calculated at 35.6, indicating a tilt towards the south. 120
Figure 6.32: The NW-SE striking and NE dipping Dionysos fault in NE Attica (id =4 on Table 6.1) and the main drainage network. The fault bounds the NE facing flanks of the Penteli mountain. 121
Figure 6.33: Slope map showing the slope changes related to Dionysos fault (id = 4 on Table 6.1). Steeper slopes are observed at the footwall, parallel to the fault, especially in the central and northern part. 122
Figure 6.34: Swath topographic profiles within a Dionysos fault parallel stripe. Fault located at the center of the stripe. Stripe width is 1500 m. Y-axis is exaggerated about 4 times. View looking towards NE. Orange line represents the maximum elevation, light green line represents the lower elevation, blue line represents the mean elevation, dark green lines represent the Q1 and Q3 quartiles, red line represents the local relief (maximum elevation minus minimum elevation at the same distance along the fault line)... 122

Figure 6.35: Swath topographic profiles within a fault perpendicular stripe, following drainage network flowing perpendicular to the Dionysos fault. Stripe axis location shown in Figure 6.36.Stripe width is 500 m. Y-axis is exaggerated about 1.5 times for P1 and P2 and 2 times for P3 and P2. View looking towards SE. Orange line represents the maximum elevation, light green line represents the lower elevation, blue line represents the mean elevation, dark green lines represent the Q1 and Q3 quartiles. The red line represents the Dionysos fault. 123
Figure 6.36: Shaded relief map of the Dionysos fault area, showing tha main drainage network and the location of the fault – perpendicular swath profiles (P1 - P3). Note the prominent triangular facets at the NW and the SE tips of the fault. .. 124
Figure 6.37: Topographic profile crossing the Dionisos fault scarp. Measurements obtained using a clinometer and a foldable meter scale (see also Papanikolaou et al., 2005 for details in methodology). The profiles reveal the fault scarp height and geometry, which are used for the throw rate calculation. Location of the profile is shown in Figure 6.22. 124
Figure 6.38: The SE dipping Kaparelli fault zone in NW Attica (id = 5 on Table 6.1) and the main drainage network. 125
Figure 6.39: Slope map showing the slope changes related to the Kaparelli fault (id = 5 on Table 6.1). Steeper slopes are observed at the footwall in the Livadostras fault segment (see text for explanation). 126
Figure 6.40: Swath topographic profiles within a fault parallel stripe. Fault located at the center of the stripe. Stripe width is 1500 m. Relief is exaggerated about 9 times. View looking towards north. Orange line represents the maximum elevation, light green line represents the lower elevation, blue line represents the mean elevation, dark green lines represent the Q1 and Q3 quartiles, red line represents the local relief (maximum elevation minus minimum elevation at the same distance along the fault line). 126
Figure 6.41: Swath topographic profiles within fault perpendicular stripes, following drainage network flowing perpendicular to the Kaparelli fault. Stripe axis location shown in Figure 6.42. Stripe width is 500 m. Relief is exaggerated about 1.5 times. View looking towards East. Orange line represents the maximum elevation, light green line represents the lower elevation, blue line represents the mean elevation, dark green lines represent the Q1 and Q3 quartiles. The red line represents the Kaparelli fault. 127
Figure 6.42: Shaded relief map of the Kaparelli fault area, showing the main drainage network and the location of the fault – perpendicular swath profiles (P1 & P2). 127
Figure 6.43: The north dipping Erythres fault in NW Attica (id = 6 on Table 6.1) and the main drainage network. Note that first order elongated catchments flow perpendicular to the Erythres fault, which forms the northern flanks of Kithaironas mountain. 129
Figure 6.44: Slope map showing the slope changes related to Erythres fault (id = 6 on Table 6.1). 130
Figure 6.45: Oblique view of the north flanks of Kithaironas mountain, which is bounded by the Erythres fault. Wineglass valleys and triangular facets are visible, implying quaternary tectonic activity (Armijo et al., 1986). Image modified from Goole Earth. View looking South. 130
Figure 6.46: Swath topographic profiles within the Erythres fault parallel stripe. Fault located at the center of the stripe. Stripe width is 1000 m for the upper graph and

9000 m for the lower graph. Y-axis is exaggerated 8 times for the upper and 3.5 times for the lower graph. View looking towards South. Orange line represents the maximum elevation, light green line represents the lower elevation, blue line represents the mean elevation, dark green lines represent the Q1 and Q3 quartiles, red line represents the local relief (maximum elevation minus minimum elevation at the same distance along the fault line). 131
Figure 6.47: Shaded relief map of the Erythres fault area, showing the main drainage network and the location of the fault – perpendicular swath profiles (P1 – P3). 131
Figure 6.48: Swath topographic profiles within a fault perpendicular stripe, following drainage network flowing perpendicular to the Erythres fault. Stripe axis location shown in Figure 6.47.Stripe width is 200 m. Y-axis is sligthtly exaggerated for P2. View looking towards West. Orange line represents the maximum elevation, light green line represents the lower elevation, blue line represents the mean elevation, dark green lines represent the Q1 and Q3 quartiles. The red line represents the Erythres fault. 132
Figure 6.49: The North dipping Aigosthena fault in W Attica (id = 7 on Table 6.1) and the main drainage network. The base map shows the Digital Terrain Model (DTM) from the National Cadastre with 5 m spatial resolution. The fault continues offshore. 133
Figure 6.50: Slope map showing the slope changes related to Aigosthena fault (id = 7 on Table 6.1). Steeper slopes are observed at the footwall, in parallel to the Aigosthena fault. 134
Figure 6.51: Swath topographic profiles within the Aigosthena fault parallel stripe. Fault located at the northern edge of the stripe. The stripe width is 500 m. Y – axis exaggerated about 2 times. View looking towards South. Orange line represents the maximum elevation, the light green line represents the lower elevation, blue line represents the mean elevation, dark green lines represent the Q1 and Q3 quartiles, red line represents the local relief (maximum elevation minus minimum elevation at the same distance along the fault line). 134
Figure 6.52: Swath topographic profiles within a fault perpendicular stripe, following drainage network flowing perpendicular to the Aigosthena fault. Stripe axes locations shown in Figure 6.53. The stripe width is 200 m. Y-axis is exaggerated about 1.3 times for P1. View looking towards West. The red line represents the Aigosthena fault. 135
Figure 6.53: Shaded relief map of the Aigosthena fault area, showing the main drainage network and the location of the fault – perpendicular swath profiles (P1 – P3). Note the asymmetry on the drainage basin of the river flowing towards the west, parallel to the fault. 136
Figure 6.54: Distant (top) and close (bottom) view of the degraded fault scarp at the central part of the Aigosthena fault next to P3 profile (see location in Figure 6.53). The visually estimated throw is 7-8 m. 137
Figure 6.55: The Aigosthena fault scarp remnants, at the easternmost tip of the fault. Scarp height is 1.5 m. 137
Figure 6.56: The NW dipping South Alkyonides fault zone (AFZ, id = 8 on Table 6.1), spanning from the Perachora peninsula in the West to Psatha in the East. This zone includes several faults and fault segments, with the Schinos (north) and Pisia (south) faults being the most important ones (see also Mechernich et al., 2018), but it was modelled as a single fault zone (see also Figure 5.4) for the seismic

hazard assessment. Note the small and linear drainage basins with small catchments flowing towards NW, perpendicular to the fault. In addition, 78% of the Megara basin (SE part of the map) is drained towards SE, into the Saronikos Gulf. The drainage divide is shifted towards the Alkyonides Gulf due to the ongoing uplift of the South Alkyonides fault zone. ^{36}Cl sampling and topographic profiling site (P6) is located in the Pisia fault scarp. 139
Figure 6.57: The Pisia fault scarp at location P7 just 19 m east of P6. Note the dark grey stripe which was created after the 1981 rupture and the consequent exhumation of the free face. White paper elongated stripe length in the middle of the photograph is 1 m..140
Figure 6.58: Sampling ladder at the subsurface part of the Pisia fault scarp, in order to define the ^{36}Cl pre-exposure concentrations. Each sample is 5 cm high. The total pit depth is 1.95 m...141
Figure 6.59: Topographic profiles at sites P6 (same location with the ^{36}Cl sampling site) and P7, just 19 m East of P6, obtained from measurements using a clinometer and a 1 m long scalebar (see also Papanikolaou et al., 2005 for details in methodology). The profiles reveal the fault scarp height and geometry, which are used as input parameters for the cosmogenic nuclide modelling and the throw rate calculation. Figure modified after Mechernich et al., 2018..............................142
Figure 6.60: The exhumation history of the free-face at site P6, after Mechernich et al., 2018. The slip rate was 0.5–0.6 mm/yr for the last ~7.3 kyr (1.1–5.15 m). For the upper part of the free-face (5.15–8.45 m; hypothetical earthquake offsets) the exhumation occurred at a significantly higher rate. Please note that the apparent slip history of the degraded scarp and the scarp age are hypothetical due to significant erosion, sedimentation at the scarp base, and a lack of cosmogenic data. Figure modified after Mechernich et al., 2018. 143
Figure 6.61: The offshore Loutraki fault in W Attica (id = 10 on Table 6.1) and the Upper Loutraki fault scarp. The Loutraki fault continues onshore, bounding the Loutraki basin in the north, although there is no fault scarp preserved. The Upper Loutraki fault's postglacial scarp is continuous for approximately 3.5 km and has a total throw of 9 m (see also Figure 6.64). 144
Figure 6.62: The Loutraki fault degraded scarp, as seen from a distance (Google Earth imagery)...145
Figure 6.63: Close up view of the Loutraki Upper fault scarp. The Upper Loutraki fault's postglacial scarp is continuous, and a total throw of 9 m is recorded (see also Figure 6.64). 145
Figure 6.64: Detailed profile perpendicular to the Upper Loutraki fault scarp. Measurements obtained using a clinometer and a foldable meter scale (see also Papanikolaou et al., 2005 for details in methodology). The profiles reveal the fault scarp height and geometry, which are used for the throw rate calculation. The location of the fault scarp profile is shown in Figure 6.61. 146
Figure 6.65: The SW dipping Kakia Skala fault in NW Attica (id = 13 on Table 6.1) and the main drainage network...147
Figure 6.66: Slope map showing the abrupt slopes in the Kakia Skala fault footwall. The highest slope values (> 45°) appear on the central part of the fault's footwall. Nearly vertical slopes occur near the coastline. Note the mild slopes in the adjacent Megara basin in the NE, which is now inactive (Bentham et al., 1991)............148
Figure 6.67: Swath topographic profiles within the Kakia Skala fault parallel stripe. Fault located at the middle of the stripe. The stripe width is 1000 m. Y-axis is

exaggerated about three times. View looking towards SW (the right part of the graph is located at the NW tip of the fault). DTM artefacts resulted in zero elevation values for the NW tip of the fault. Orange line represents the maximum elevation, light green line represents the lower elevation, blue line represents the mean elevation, dark green lines represent the Q1 and Q3 quartiles, red line represents the local relief (maximum elevation minus minimum elevation at the same distance along the fault line)...148
Figure 6.68: Swath topographic profiles within a fault perpendicular stripe, following the drainage network flowing perpendicular to the Kakia Skala fault. Stripe axis location shown in Figure 6.69. Stripe width is 500 m. Y-axis is exaggerated about 1.5 times. View looking towards East. Orange line represents the maximum elevation, light green line represents the lower elevation, blue line represents the mean elevation, dark green lines represent the Q1 and Q3 quartiles. The red line represents the Kakia Skala fault...149
Figure 6.69: Shaded relief map of the Kakia Skala fault, showing the main drainage network and the location of the fault – perpendicular swath profiles (P1 and P2). 149
Figure 6.70: The SW dipping Thriassio and Fili faults west of the Athens basin (id = 14 & 15 respectively, on Table 6.1) and the main drainage network. Base map shows the Digital Terrain Model (DTM) from the National Cadastre with 5 m spatial resolution. 150
Figure 6.71: Top: Geology of the Fili fault and the surroundings (geology modified after Katsikatsos et al., 1986). SW–NE line marks the cross-section. Bottom: Cross-section based on the Geological Map of Katsikatsos et al., 1986. The total throw of the Fili Fault is 600 ± 150 m. 151
Figure 6.72: Slope map showing the slope changes in the Thriassio and Fili faults footwall, as well as the difference in both faults hanging walls. Thriassio fault has a nearly planar hanging wall (Thriassion plain), while the Fili fault’s hanging wall is deeply insised, due to the uplift caused by the Thriassio fault. Highest slope values (> 45°) appear on the central part of the fault’s footwall.......................152
Figure 6.73: Swath topographic profiles within Thriassio (top) and Fili (bottom) fault parallel stripes. Faults located at the middle of the stripes. Stripes’ width is 2000 m. Y-axis is exaggerated about 6 times for Thriassio and 3.5 times for Fili fault. View looking to the South. Orange line represents the maximum elevation, light green line represents the lower elevation, blue line represents the mean elevation, dark green lines represent the Q1 and Q3 quartiles, red line represents the local relief (maximum elevation minus minimum elevation at the same distance along the fault line)...153
Figure 6.74: Shaded relief map of the Thriassio and Fili faults, showing the main drainage network and the location of the fault – perpendicular swath profiles (P1 – P6)...154
Figure 6.75: Swath topographic profiles within fault perpendicular stripes, following drainage network flowing perpendicular to the Thriassio fault (P1, P1, P5) and Fili fault (P3, P6). Stripe axes locations are displayed in Figure 6.74. Stripe width is 500 m. Y-axes are exaggerated. P4 shows a swath profile crossing perpendicular both faults. View looking towards East. Orange line represents the maximum elevation, light green line represents the lower elevation, blue line represents the mean elevation, dark green lines represent the Q1 and Q3 quartiles. The red line represents the faults. 156

Figure 6.76: Oblique perspective view of a dense point cloud representing the Fili fault scarp. Solution flutes and small cracks are visible in the free face. 94 images acquired by a handheld 12 mp camera. The photogrammetric processing was carried out using Agisoft Metashape v1.5.0. Distances within the model are measureable with an error of 1 cm, based on the measured distances between control points. The maximum fault slip along the free face was measured at 2.5 m. 157
Figure 6.77: The Fili fault postglacial scarp. The slip along the free face is measured at 2.5 m. 157
Figure 6.78: The SW dipping Kakia Skala fault in NW Attica (id = 13 on Table 6.1) and the main drainage network. 158
Figure 6.79: Slope map showing the slope changes related to Kehries fault (id = 19 on Table 6.1). Steeper slopes are observed at the footwall on the onshore part of the fault, which has created an E-W elongated abrupt slope that reaches the coastline. 159
Figure 6.80: Swath topographic profile within a Kehries fault parallel stripe. Fault located at the middle of the stripe. Stripe width is 1600 m. Y-axis is exaggerated about 4.5 times. View looking towards the North (right part of the graph is located at the east tip of the fault). Orange line represents the maximum elevation, light green line represents the lower elevation, blue line represents the mean elevation, dark green lines represent the Q1 and Q3 quartiles, red line represents the local relief (maximum elevation minus minimum elevation at the same distance along the fault line). Note that the local relief is still high at the east fault tip (right end of the graph), possibly implying an eastward offshore continuation. 160
Figure 6.81: Swath topographic profiles within a fault perpendicular stripe, following drainage network flowing perpendicular to the Kehries fault. Stripe axis location shown in Figure 6.78. Stripe width is 500 m. View looking towards West. Orange line represents the maximum elevation, light green line represents the lower elevation, blue line represents the mean elevation, dark green lines represent the Q1 and Q3 quartiles. The red line represents the Kehries fault. 160
Figure 6.82: The NW dipping Dafni fault in NW Attica (id = 13 on Table 6.1) and the main drainage network. 161
Figure 6.83: Slope map showing the abrupt slopes and deep river incision in the central part of the Dafni fault footwall. The fault's hanging wall has a gentle slope towards NW. 162
Figure 6.84: Swath topographic profiles within a Dafni fault parallel stripe. Fault located at the middle of the stripe. The stripe width is 2000 m. Y-axis is exaggerated about 5.5 times. View looking towards the North (right part of the graph is located at the east tip of the fault). The orange line represents the maximum elevation, the light green line represents the lower elevation, the blue line represents the mean elevation, dark green lines represent the Q1 and Q3 quartiles, the red line represents the local relief (maximum elevation minus minimum elevation at the same distance along the fault line). 162
Figure 6.85: Swath topographic profiles within a fault perpendicular stripe, following drainage network flowing perpendicular to the Dafni fault. The stripe axis location is shown in Figure 6.86. The stripe width is 400 m. Y-axis is exaggerated about 3 times for P1&P1 and 4 times for P2. View looking towards SW. Orange line represents the maximum elevation, the light green line represents the lower

elevation, the blue line represents the mean elevation, dark green lines represent the Q1 and Q3 quartiles. The red line represents the Dafni fault. 163
Figure 6.86: Shaded relief map of the Dafni fault area, showing the main drainage network, the location of the fault – perpendicular swath profiles (P1 – P3) and the locations where a topographic scarp profile was made. 164
Figure 6.87: Topographic profile crossing the Dafni fault scarp at location TP1. Measurements obtained using a clinometer and a 1 m stick (see also Papanikolaou et al., 2005 for details in methodology). The profile reveals the fault scarp height and geometry. The total throw is measured at 4.44 m. Location of the profile is shown in Figure 6.86. 164
Figure 6.88: Topographic profiles crossing the Dafni fault scarp at location TP2-a. Top measurement (black) obtained using a clinometer and a 1 m stick. Middle profile (red) represents the profile after the angles corrections (see text for details). Lower profile (blue) produced from SfM derived DSM. The total throw is measured at 5.16 m. Profile location is shown in Figure 6.86. 165
Figure 6.89: High resolution (4.35 cm/px) Digital Surface Model of the TP2-a location. 101 images with 80% overlapping were acquired by a small UAV with a 12 mp camera. The photogrammetric processing was carried out using Agisoft Metashape v1.5.0. The vegetation was extracted in the final stage of the profile processing, except for a bush in the hanging wall (lower profile in Figure 6.88), which was intentionally kept as a reference. The thin grey line represents the profile axis. 166
Figure 6.90: Topographic profiles crossing the Dafni fault scarp at location TP2 – b, approximately 25 m west of TP2 – a. Measurements obtained using a clinometer and a 1 m stick (see also Papanikolaou et al., 2005 for details in methodology). The profile reveals the fault scarp height and geometry. The total throw is measured at 7.2 m. Profile location is shown in Figure 6.86...........................166
Figure 6.91: Topographic profiles crossing the Dafni fault scarp at location TP3. Measurements obtained using a clinometer and a 1 m stick (see also Papanikolaou et al., 2005 for details in methodology). The profile reveals the fault scarp height and geometry. The total throw is measured at 6.3 m. Profile location is shown in Figure 6.86. 167
Figure 6.92: Map of active faults that can sustain damage within the region of Attica. No faults are located in the Athens Plain, except for the southeastern tip of the Fili fault (id = 15 on Table 6.1), but with low slip rate faults (see Figure 6.93b). Fault labels refer to the Id numbers on (Table 6.1)..168
Figure 6.93: Map of active faults that can sustain damage within the region of Attica. a) Different fault symbols represent the maximum expected magnitude that these faults can generate. b) Different fault symbols represent different slip-rate categories. Slip rates govern earthquake recurrence. As slip rates increase, average earthquake recurrence intervals tend to decrease..170
Figure 7.1: Map for the Sparta Basin showing the maximum expected intensities distribution. The maximum intensity locations are defined by the proximity to the Sparta fault and the bedrock geology. Figure reproduced after Papanikolaou et al., 2013 173
Figure 7.2: Seismic hazard map for the Sparta Basin, showing how many times a locality receives enough energy to shake at intensities ≥IX in 15±3kyrs, after considering the bedrock geology and assuming a circular pattern of energy release,

with a 18 km radius of isoseismal IX. Figure reproduced after Papanikolaou et al., 2013. 174
Figure 7.3: Seismic hazard map for the Sparta Fault, overlaid in the Globe map, provided by Google Earth. 175
Figure 7.4: Detailed map detail of the overlaid seismic hazard layer of the Sparta fault in the Google Earth environment. High spatial analysis of the seismic hazard map provides detailed visualization in relation to the variations of recurrence and intensities affecting manmade constructions, such as the Sparta city boundaries and road network. The northern part of the town of Sparta has a higher recurrence of intensity X over 15±3kyrs. 176
Figure 7.5: Maximum expected intensities distribution for each locality in the Attica mainland. They are defined by the proximity to the active faults and the surface geology. Figure reproduced from Deligiannakis et al., 2018a. 178
Figure 7.6: Seismic hazard map of Attica, showing the estimated site-specific recurrence for intensities X (MM). The Greater Athens Area is not expected to have experienced such intensities during the last 15 kyrs. Figure reproduced from Deligiannakis et al., 2018a. 179
Figure 7.7: Seismic hazard map of Attica, showing the estimated site-specific recurrence for intensities IX (MM). Figure reproduced from Deligiannakis et al., 2018a. 180
Figure 7.8: Seismic hazard map of Attica, showing the estimated site specific recurrence for intensities VIII (MM). Figure reproduced from Deligiannakis et al., 2018a. 181
Figure 7.9: Seismic hazard map of Attica, showing the estimated site-specific recurrence for intensities VII (MM). Nearly every suburb of the Greater Athens Area has experienced such intensities in the past 15 kyrs, including the recent 1981 earthquake sequence and the 1999 event. Figure reproduced from Deligiannakis et al., 2018a. 182
Figure 7.10: Top quintile (top 20%) for the recurrences of the intensities VII – X. Figure reproduced from Deligiannakis et al., 2018a. 184
Figure 7.11: Fault Specific Seismic hazard map of the Athens centre. Tonal variations show how many times these localities have received enough energy to shake at intensity VIII over the past 15kyrs. This map offers a high spatial resolution of the intensity distribution and recurrence. Therefore it allows a detailed calculation of λ values at Postal Code or even building block level. Figure reproduced from Deligiannakis et al., 2018a. 185
Figure 8.1: Example of the expected losses over various return periods. Assumptions are explained in the text. 188
Figure 8.2: Projected fault planes on the horizontal surface, vs the recorded earthquakes of magnitude M>4.1 for the Attica region, between 1900 – 2009 (catalogue source: Makropoulos et al., 2012). 192
Figure 8.3: Spatial distribution of MM intensity after a simulated earthquake event of magnitude M6.6. The modelled epicentre is related to an active fault offshore eastern Attica. 194
Figure 8.4: Vulnerability curves per construction type, concerning average damage in case of intensities VII – X occurrence, modified after Degg, 1992. 195
Figure 8.5: Flow diagram showing the sequence for the calculation of the Total Loss. This process iterates for a large number of event years to develop the Events Table. 197

Figure 8.6: 1/200 Loss, compared to the exposure of each Postal Code in the Attica region. 200
Figure 9.1: Probable active fault structures (dashed lines) in Attica region. These faults are not taken into account in seismic hazard mapping as they are either antithetic structures of major fault zones (e.g. P1 and P6), or it is unclear whether they are active or not. If these faults were incorporated to the analysis, their impact to seismic hazard would be insignificant compared to the active structures already analyzed. 204
Figure 9.2: Recurrences of a) intensity X (no occurrence), b) intensity IX (maximum 23 times over 15 kyrs, or 652 y minimum return period), c) intensity VIII (maximum 55 times over 15 kyrs or 272 y minimum return period), and d) intensity VII (maximum 156 times over 15 kyrs, or 96 y return period), at the Athens basin. The Greater Athens Area boundaries were digitized using the OpenStreetMap road network. 211
Figure 9.2: Historical earthquake record from a) the National Observatory and University of Athens (NOA&UOA) and b) the Aristotle University of Thessaloniki, for shallow earthquakes of magnitudes Mw>6 in comparison to active faulting in the Attica Region. The Athens 1999 and Oropos 1938 events are displayed in the NOA& UOA catalogue, although they are recorded as Mw5.8 and Mw5.9 events respectively. Focal depths are not available for the majority of the events in both catalogues, thus events with focal depth >20km might be also displayed. Both catalogues are complete for events Mw≥7.3 since 1500 and for Mw≥6.5 since 1845. As a result, active faults with no rupture history during the last 200 years may have not been included in the seismic hazard zonation of Greece, as shown in the map. Zone I represents the lowest seismic hazard and Zone II the intermediate hazard. 215
Figure 9.3: SCR calculations per CRESTA Zone for the Attica region without taking into account any deductible in the proposed model (EQ). The SF overestimates the SCR for the majority of the cases, with the most prominent differences occurring in Zone 14 (see text for explanation). 224
Figure 9.4: The Fault Specific Seismic hazard map on the CRESTA Zone ‘14’, see Deligiannakis et al. (2018b) for details. Colour variations show how many times the localities in the map have received enough energy to shake at intensity VIII over the past 15kyrs. This map offers a high spatial resolution of the intensities' distribution and recurrence, which allows for increased accuracy on the SCR calculations. 226
Figure 9.5: The Fault Specific Seismic hazard map on the CRESTA Zone '16', see Deligiannakis et al. (2018b) for details. Colour variations show how many times the localities in the map have received enough energy to shake at intensity VIII over the past 15kyrs. 227

Annexes

Annex I

Recurrences of Intensities VII – X per Postal Code, for the region of Attica, estimated over a time period of 15000 years.

ID	POSTAL CODE	MUNICIPALITY	VII	VIII	IX	X
1	10431	ATHINAION	26,20	3,35	0,27	0,00
2	10432	ATHINAION	34,22	8,56	0,27	0,00
3	10433	ATHINAION	35,76	8,80	0,27	0,00
4	10434	ATHINAION	75,43	17,37	4,49	0,00
5	10435	ATHINAION	48,77	10,78	1,87	0,00
6	10436	ATHINAION	29,45	6,43	0,27	0,00
7	10437	ATHINAION	27,91	4,73	0,27	0,00
8	10438	ATHINAION	32,67	8,74	0,27	0,00
9	10439	ATHINAION	31,03	6,28	0,27	0,00
10	10440	ATHINAION	34,75	7,97	0,39	0,00
11	10441	ATHINAION	100,00	15,98	7,55	0,00
12	10442	ATHINAION	110,00	18,40	7,97	0,00
13	10443	ATHINAION	88,48	17,90	6,22	0,00
14	10444	ATHINAION	62,79	12,89	3,42	0,00
15	10445	ATHINAION	53,62	10,34	2,75	0,00
16	10446	ATHINAION	36,52	9,56	0,37	0,00
17	10447	ATHINAION	110,00	15,91	7,90	0,00
18	10551	ATHINAION	24,45	2,22	0,27	0,00
19	10552	ATHINAION	24,45	2,22	0,27	0,00
20	10553	ATHINAION	29,83	5,58	0,41	0,00
21	10554	ATHINAION	25,11	2,68	0,27	0,00
22	10555	ATHINAION	28,03	4,70	0,27	0,00
23	10556	ATHINAION	31,31	6,70	0,27	0,00
24	10557	ATHINAION	51,33	10,33	1,99	0,00
25	10558	ATHINAION	29,03	4,96	0,27	0,00

ID	POSTAL CODE	MUNICIPALITY	VII	VIII	IX	X
26	10559	ATHINAION	24,45	2,22	0,27	0,00
27	10560	ATHINAION	24,45	2,22	0,27	0,00
28	10561	ATHINAION	24,38	2,22	0,27	0,00
29	10562	ATHINAION	24,16	2,22	0,27	0,00
30	10563	ATHINAION	26,57	3,80	0,27	0,00
31	10564	ATHINAION	24,25	2,22	0,27	0,00
32	10671	ATHINAION	32,54	6,91	0,27	0,00
33	10672	ATHINAION	30,26	5,54	0,27	0,00
34	10673	ATHINAION	33,54	7,42	0,27	0,00
35	10674	ATHINAION	63,55	13,07	3,06	0,00
36	10675	ATHINAION	37,26	7,76	0,65	0,00
37	10676	ATHINAION	31,59	5,84	0,27	0,00
38	10677	ATHINAION	33,95	8,28	0,27	0,00
39	10678	ATHINAION	32,52	7,30	0,27	0,00
40	10679	ATHINAION	30,13	5,87	0,27	0,00
41	10680	ATHINAION	33,27	7,60	0,27	0,00
42	10681	ATHINAION	33,02	7,67	0,27	0,00
43	10682	ATHINAION	35,60	8,52	0,27	0,00
44	10683	ATHINAION	34,95	8,25	0,27	0,00
45	11141	ATHINAION	25,74	2,42	0,27	0,00
46	11142	ATHINAION	26,37	3,05	0,27	0,00
47	11143	ATHINAION	57,79	13,37	2,80	0,00
48	11144	ATHINAION	30,97	5,98	0,27	0,00
49	11145	ATHINAION	98,44	19,77	7,50	0,00
50	11146	GALATSIOU	30,07	4,75	0,27	0,00
51	11147	GALATSIOU	32,13	5,58	0,27	0,00
52	11251	ATHINAION	48,59	11,71	1,57	0,00
53	11252	ATHINAION	37,18	9,72	0,27	0,00
54	11253	ATHINAION	35,10	8,63	0,27	0,00

ID	POSTAL CODE	MUNICIPALITY	VII	VIII	IX	X
55	11254	ATHINAION	29,74	5,07	0,27	0,00
56	11255	ATHINAION	25,17	2,22	0,27	0,00
57	11256	ATHINAION	27,33	3,39	0,27	0,00
58	11257	ATHINAION	40,32	9,29	0,50	0,00
59	11361	ATHINAION	36,50	7,64	0,27	0,00
60	11362	ATHINAION	45,41	9,94	1,22	0,00
61	11363	ATHINAION	24,66	2,38	0,27	0,00
62	11364	ATHINAION	24,51	2,24	0,27	0,00
63	11471	ATHINAION	23,73	2,22	0,27	0,00
64	11472	ATHINAION	23,89	2,22	0,27	0,00
65	11473	ATHINAION	29,60	4,67	0,27	0,00
66	11474	ATHINAION	47,16	9,61	1,85	0,00
67	11475	ATHINAION	23,89	2,27	0,27	0,00
68	11476	ATHINAION	24,05	2,34	0,27	0,00
69	11521	ATHINAION	32,20	5,41	0,27	0,00
70	11522	ATHINAION	23,27	2,22	0,27	0,00
71	11523	ATHINAION	23,17	2,39	0,27	0,00
72	11524	ATHINAION	22,84	2,22	0,27	0,00
73	11525	ATHINAION	31,33	3,50	0,27	0,00
74	11526	ATHINAION	33,20	4,34	0,27	0,00
75	11527	ATHINAION	40,85	4,72	0,27	0,00
76	11528	ATHINAION	36,34	5,79	0,27	0,00
77	11631	ATHINAION	30,62	4,80	0,27	0,00
78	11632	ATHINAION	22,17	2,22	0,27	0,00
79	11633	ATHINAION	22,12	2,24	0,27	0,00
80	11634	ATHINAION	25,88	3,34	0,27	0,00
81	11635	ATHINAION	24,18	2,90	0,27	0,00
82	11636	ATHINAION	23,89	2,65	0,27	0,00
83	11741	ATHINAION	48,48	8,22	1,89	0,00

ID	POSTAL CODE	MUNICIPALITY	VII	VIII	IX	X
84	11742	ATHINAION	32,48	6,70	0,27	0,00
85	11743	ATHINAION	30,67	5,61	0,27	0,00
86	11744	ATHINAION	28,39	4,61	0,32	0,00
87	11745	ATHINAION	45,59	8,73	1,48	0,00
88	11851	ATHINAION	29,73	6,90	0,27	0,00
89	11852	ATHINAION	34,05	8,56	0,52	0,00
90	11853	ATHINAION	68,68	11,95	3,65	0,00
91	11854	ATHINAION	78,11	13,31	4,67	0,00
92	11855	ATHINAION	110,00	14,93	7,97	0,00
93	12131	PERISTERIOU	74,98	15,05	4,49	0,00
94	12132	PERISTERIOU	76,09	15,75	4,76	0,00
95	12133	PERISTERIOU	62,86	13,06	3,49	0,00
96	12134	PERISTERIOU	35,52	9,81	0,27	0,00
97	12135	PERISTERIOU	33,55	8,65	0,27	0,00
98	12136	PERISTERIOU	30,94	6,61	0,27	0,00
99	12137	PERISTERIOU	26,21	3,53	0,30	0,00
100	12241	AIGALEO	95,13	12,14	6,19	0,00
101	12242	AIGALEO	66,37	12,41	3,62	0,00
102	12243	AIGALEO	31,18	8,27	0,27	0,00
103	12244	AIGALEO	28,00	9,69	0,27	0,00
104	12351	AGIAS BARBARAS	25,99	4,89	0,29	0,00
105	12461	CHAIDARIOU	40,87	6,78	1,14	0,84
106	12462	CHAIDARIOU	29,17	5,63	0,71	0,12
107	13121	ILIOU (NEON LIOSION)	34,55	9,31	0,27	0,00
108	13122	ILIOU (NEON LIOSION)	38,70	8,90	0,84	0,00
109	13123	ILIOU (NEON LIOSION)	35,12	8,31	0,30	0,00
110	13231	PETROUPOLIS	30,65	5,44	0,40	0,00

ID	POSTAL CODE	MUNICIPALITY	VII	VIII	IX	X
111	13341	ANO LIOSION	65,48	13,42	1,91	0,00
112	13342	ANO LIOSION	59,39	10,47	1,62	0,40
113	13343	ANO LIOSION	46,89	5,27	0,53	0,00
114	13344	ANO LIOSION	50,67	7,60	1,11	0,23
115	13345	FULIS	52,85	7,05	1,12	0,12
116	13451	KAMATEROU	35,23	6,11	0,36	0,00
117	13561	AGION ANARGURON	100,00	19,93	7,61	0,00
118	13562	AGION ANARGURON	90,48	18,49	6,53	0,00
119	13671	ACHARNON	56,00	11,62	2,15	0,00
120	13672	ACHARNON	54,57	8,64	0,88	0,00
121	13673	ACHARNON	56,38	10,49	0,51	0,00
122	13674	ACHARNON	59,43	11,18	0,81	0,00
123	13675	ACHARNON	46,08	9,35	0,79	0,00
124	13676	THRAKOMAKEDON ON	67,05	16,51	3,73	0,00
125	14121	IRAKLEIOU	23,21	2,22	0,27	0,00
126	14122	IRAKLEIOU	23,80	2,22	0,27	0,00
127	14123	LUKOBRUSEOS	38,51	4,58	0,27	0,00
128	14231	NEAS IONIAS	25,94	2,76	0,27	0,00
129	14232	NEAS IONIAS	25,19	2,47	0,27	0,00
130	14233	NEAS IONIAS	27,80	3,79	0,27	0,00
131	14234	NEAS IONIAS	24,42	2,22	0,27	0,00
132	14235	NEAS IONIAS	36,47	5,66	0,27	0,00
133	14341	NEAS FILADELFEIAS	66,72	14,43	3,98	0,00
134	14342	NEAS FILADELFEIAS	81,27	18,90	5,84	0,00
135	14343	NEAS CHALKIDONOS	98,26	19,84	7,54	0,00

ID	POSTAL CODE	MUNICIPALITY	VII	VIII	IX	X
136	14451	METAMORFOSEOS	49,16	10,09	2,82	0,00
137	14452	METAMORFOSEOS	52,12	11,08	1,90	0,00
138	14561	KIFISIAS	49,91	4,03	0,27	0,00
139	14562	KIFISIAS	31,32	2,82	0,27	0,00
140	14563	KIFISIAS	28,49	2,62	0,27	0,00
141	14564	KIFISIAS	62,30	12,36	0,86	0,00
142	14565	AGIOU STEFANOU	62,25	13,72	0,53	0,00
143	14568	KRUONERIOU	62,61	14,49	0,55	0,00
144	14569	ANOIXEOS	67,38	10,17	0,65	0,00
145	14572	DROSIAS	46,03	12,49	1,21	0,00
146	14574	RODOPOLEOS	24,28	2,84	0,32	0,00
147	14575	STAMATAS	36,33	4,89	0,55	0,00
148	14576	DIONUSOU	24,52	6,56	0,79	0,00
149	14578	EKALIS	60,58	7,15	0,38	0,00
150	14671	NEAS ERUTHRAIAS	58,01	5,43	0,38	0,00
151	15121	PEUKIS	30,40	3,00	0,27	0,00
152	15122	AMAROUSIOU	25,51	2,54	0,27	0,00
153	15123	AMAROUSIOU	41,85	5,62	0,36	0,00
154	15124	AMAROUSIOU	47,30	6,28	0,41	0,00
155	15125	AMAROUSIOU	54,43	14,43	0,66	0,00
156	15126	AMAROUSIOU	47,37	3,62	0,27	0,00
157	15127	MELISSION	29,01	3,28	0,28	0,00
158	15231	CHALANDRIOU	45,53	6,84	0,40	0,00
159	15232	CHALANDRIOU	67,79	26,41	1,61	0,00
160	15233	CHALANDRIOU	58,99	17,49	1,07	0,00
161	15234	CHALANDRIOU	48,91	6,73	0,45	0,00
162	15235	BRILISSION	44,69	2,76	0,27	0,00
163	15236	PENTELIS	21,34	2,27	0,27	0,00
164	15237	FILOTHEIS	30,00	4,37	0,42	0,00

ID	POSTAL CODE	MUNICIPALITY	VII	VIII	IX	X
165	15341	AGIAS PARASKEUIS	28,26	2,29	0,27	0,00
166	15342	AGIAS PARASKEUIS	35,53	2,22	0,27	0,00
167	15343	AGIAS PARASKEUIS	44,73	3,43	0,28	0,00
168	15344	GERAKA	36,27	4,78	0,31	0,00
169	15349	ANTHOUSAS	37,92	3,05	0,27	0,00
170	15351	PALLINIS	43,06	9,06	0,58	0,00
171	15451	NEOU PSUCHIKOU	27,33	2,86	0,27	0,00
172	15452	PSUCHIKOU	24,53	2,62	0,27	0,00
173	15561	CHOLARGOU	43,40	3,57	0,27	0,00
174	15562	CHOLARGOU	27,20	2,51	0,27	0,00
175	15669	PAPAGOU	32,72	2,89	0,27	0,00
176	15771	ZOGRAFOU	36,74	5,33	0,27	0,00
177	15772	ZOGRAFOU	27,74	2,90	0,27	0,00
178	15773	ZOGRAFOU	37,84	4,45	0,27	0,00
179	16121	KAISARIANIS	36,18	5,02	0,27	0,00
180	16122	KAISARIANIS	20,62	2,41	0,27	0,00
181	16231	BURONOS	28,20	3,10	0,27	0,00
182	16232	BURONOS	27,40	3,16	0,27	0,00
183	16233	BURONOS	19,88	2,32	0,27	0,00
184	16341	ILIOUPOLIS	33,64	2,92	0,27	0,00
185	16342	ILIOUPOLIS	20,26	2,28	0,27	0,00
186	16343	ILIOUPOLIS	19,36	2,24	0,27	0,00
187	16344	ILIOUPOLIS	19,31	2,22	0,27	0,00
188	16345	ILIOUPOLIS	26,11	2,60	0,27	0,00
189	16346	ILIOUPOLIS	29,11	3,00	0,27	0,00
190	16451	ARGUROUPOLIS	24,52	2,28	0,27	0,00
191	16452	ARGUROUPOLIS	31,40	2,85	0,27	0,00
192	16561	GLUFADAS	25,74	2,22	0,27	0,00
193	16562	GLUFADAS	22,05	2,22	0,27	0,00

ID	POSTAL CODE	MUNICIPALITY	VII	VIII	IX	X
194	16671	BOULIAGMENIS	27,91	5,13	0,34	0,00
195	16671	BOULIAGMENIS	27,91	5,13	0,34	0,00
196	16672	BARIS	27,96	8,76	0,27	0,00
197	16672	BARIS	27,96	8,76	0,27	0,00
198	16673	BOULAS	25,32	2,68	0,27	0,00
199	16674	GLUFADAS	26,07	2,22	0,27	0,00
200	16674	GLUFADAS	26,07	2,22	0,27	0,00
201	16675	GLUFADAS	36,96	4,86	0,27	0,00
202	16777	ELLINIKOU	37,14	4,22	0,29	0,00
203	17121	NEAS SMURNIS	35,14	5,20	0,91	0,00
204	17122	NEAS SMURNIS	37,47	3,42	1,17	0,00
205	17123	NEAS SMURNIS	22,55	2,40	0,27	0,00
206	17124	NEAS SMURNIS	22,79	2,51	0,27	0,00
207	17234	DAFNIS	23,38	2,65	0,27	0,00
208	17235	DAFNIS	22,76	2,51	0,27	0,00
209	17236	UMITTOU	27,52	3,51	0,27	0,00
210	17237	UMITTOU	30,42	4,27	0,27	0,00
211	17341	AGIOU DIMITRIOU	21,85	2,46	0,27	0,00
212	17342	AGIOU DIMITRIOU	19,55	2,23	0,27	0,00
213	17343	AGIOU DIMITRIOU	23,54	2,98	0,27	0,00
214	17455	ALIMOU	23,42	2,82	0,35	0,00
215	17456	ALIMOU	25,63	2,57	0,27	0,00
216	17561	PALAIOU FALIROU	53,71	5,25	1,99	0,00
217	17562	PALAIOU FALIROU	21,75	2,22	0,27	0,00
218	17563	PALAIOU FALIROU	21,13	2,22	0,27	0,00
219	17564	PALAIOU FALIROU	72,54	6,85	3,08	0,00
220	17671	KALLITHEAS	28,42	5,45	0,27	0,00
221	17672	KALLITHEAS	35,69	8,11	0,62	0,00
222	17673	KALLITHEAS	71,92	7,02	3,31	0,00

ID	POSTAL CODE	MUNICIPALITY	VII	VIII	IX	X
223	17674	KALLITHEAS	110,00	9,41	5,97	0,00
224	17675	KALLITHEAS	110,00	10,83	6,93	0,00
225	17676	KALLITHEAS	84,22	12,54	4,96	0,00
226	17778	TAUROU	110,00	13,39	7,76	0,00
227	18010	AIGINAS	68,39	8,16	0,87	0,00
228	18010	AGKISTRIOU	68,39	8,16	0,87	0,00
229	18120	KORUDALLOU	31,49	9,92	0,68	0,00
230	18121	KORUDALLOU	28,08	6,18	0,45	0,00
231	18122	KORUDALLOU	28,16	4,55	0,61	0,00
232	18233	AGIOU IOANNOU RENTI	120,00	11,66	7,96	0,00
233	18344	MOSCHATOU	120,00	7,84	7,17	0,00
234	18345	MOSCHATOU	120,00	10,68	7,27	0,00
235	18346	MOSCHATOU	110,00	12,82	7,43	0,00
236	18450	NIKAIAS	30,50	9,37	0,60	0,00
237	18451	NIKAIAS	26,60	6,90	0,28	0,00
238	18452	NIKAIAS	26,44	5,16	0,55	0,00
239	18453	NIKAIAS	26,57	9,92	0,27	0,00
240	18454	NIKAIAS	44,67	9,81	1,78	0,00
241	18531	PEIRAIOS	60,68	8,51	3,45	0,00
242	18532	PEIRAIOS	23,95	6,71	0,27	0,00
243	18533	PEIRAIOS	48,73	5,18	2,13	0,00
244	18534	PEIRAIOS	25,31	3,03	0,45	0,00
245	18535	PEIRAIOS	36,48	8,97	1,25	0,00
246	18536	PEIRAIOS	32,52	3,93	0,87	0,00
247	18537	PEIRAIOS	28,05	2,71	0,60	0,00
248	18538	PEIRAIOS	46,77	3,57	1,88	0,00
249	18539	PEIRAIOS	24,54	2,22	0,27	0,00
250	18540	PEIRAIOS	95,27	7,30	5,91	0,00

ID	POSTAL CODE	MUNICIPALITY	VII	VIII	IX	X
251	18541	PEIRAIOS	120,00	8,94	7,97	0,00
252	18542	PEIRAIOS	65,60	10,45	3,53	0,00
253	18543	PEIRAIOS	44,45	6,64	1,80	0,00
254	18544	PEIRAIOS	25,88	6,64	0,27	0,00
255	18545	PEIRAIOS	61,59	8,47	3,25	0,00
256	18546	PEIRAIOS	38,30	6,35	1,30	0,00
257	18547	PEIRAIOS	120,00	7,29	7,37	0,00
258	18648	DRAPETSONAS	29,56	3,53	0,63	0,00
259	18755	KERATSINIOU	35,54	4,63	1,17	0,00
260	18756	KERATSINIOU	54,57	8,05	2,60	0,00
261	18757	KERATSINIOU	28,96	6,63	0,46	0,00
262	18758	KERATSINIOU	35,37	5,10	1,11	0,01
263	18863	PERAMATOS	44,91	5,74	1,65	0,35
264	18900	SALAMINAS	87,50	18,15	3,17	0,19
265	18902	AMPELAKION	83,49	11,05	2,80	0,00
266	18903	SALAMINAS	80,82	12,77	1,92	0,00
267	19001	KERATEAS	23,79	3,72	0,84	0,00
268	19001	KERATEAS	23,79	3,72	0,84	0,00
269	19001	KERATEAS	23,79	3,72	0,84	0,00
270	19002	PAIANIAS	40,09	10,92	1,41	0,00
271	19003	MARKOPOULOU MESOGAIAS	28,83	5,28	1,19	0,14
272	19004	SPATON-LOUTSAS	39,01	9,80	1,83	0,00
273	19005	NEAS MAKRIS	29,02	6,51	0,85	0,00
274	19006	NEAS PERAMOU	100,00	46,63	4,50	0,39
275	19007	MARATHONOS	35,93	12,52	1,83	0,13
276	19008	ERUTHRON	74,02	30,16	12,07	0,22
277	19009	RAFINAS	35,04	6,07	0,50	0,00

ID	POSTAL CODE	MUNICIPALITY	VII	VIII	IX	X
278	19010	KALUBION THORIKOU	29,59	6,16	1,11	0,00
279	19011	AULONOS	61,86	17,23	5,48	1,87
280	19012	OINOIS	91,13	26,94	11,80	2,51
281	19012	VILION	91,13	26,94	11,80	2,51
282	19013	ANABUSSOU	24,99	5,79	0,97	0,00
283	19014	KAPANDRITIOU	49,32	15,96	2,43	0,11
284	19015	OROPION	54,50	21,11	8,20	1,89
285	19016	ARTEMIDOS	32,39	5,48	1,33	0,30
286	19100	MEGAREON	110,00	39,59	8,76	0,44
287	19200	ELEUSINOS	99,01	36,85	3,48	5,08
288	19300	ASPROPURGOU	85,73	22,27	2,75	3,39
289	19400	KROPIAS	34,19	9,46	0,77	0,00
290	19500	LAUREOTIKIS	21,79	3,61	0,73	0,00
291	19600	MANDRAS	54,64	20,10	3,04	0,71

Annex II

λ values for Intensities VII – X per Postal Code, for the region of Attica.

ID	POSTAL CODE	MUNICIPALITY	VII	VIII	IX	X
1	10431	ATHINAION	0,001747	0,000223	0,000018	6,66667E-12
2	10432	ATHINAION	0,002281	0,000571	0,000018	6,66667E-12
3	10433	ATHINAION	0,002384	0,000587	0,000018	6,66667E-12
4	10434	ATHINAION	0,005029	0,001158	0,000299	6,66667E-12
5	10435	ATHINAION	0,003251	0,000719	0,000125	6,66667E-12
6	10436	ATHINAION	0,001963	0,000429	0,000018	6,66667E-12
7	10437	ATHINAION	0,00186	0,000315	0,000018	6,66667E-12
8	10438	ATHINAION	0,002178	0,000583	0,000018	6,66667E-12
9	10439	ATHINAION	0,002069	0,000419	0,000018	6,66667E-12
10	10440	ATHINAION	0,002317	0,000531	0,000026	6,66667E-12
11	10441	ATHINAION	0,006667	0,001065	0,000503	6,66667E-12
12	10442	ATHINAION	0,007333	0,001227	0,000531	6,66667E-12
13	10443	ATHINAION	0,005899	0,001193	0,000415	6,66667E-12
14	10444	ATHINAION	0,004186	0,000859	0,000228	6,66667E-12
15	10445	ATHINAION	0,003574	0,000689	0,000183	6,66667E-12
16	10446	ATHINAION	0,002435	0,000637	0,000025	6,66667E-12
17	10447	ATHINAION	0,007333	0,001061	0,000527	6,66667E-12
18	10551	ATHINAION	0,00163	0,000148	0,000018	6,66667E-12
19	10552	ATHINAION	0,00163	0,000148	0,000018	6,66667E-12
20	10553	ATHINAION	0,001989	0,000372	0,000027	6,66667E-12
21	10554	ATHINAION	0,001674	0,000179	0,000018	6,66667E-12
22	10555	ATHINAION	0,001869	0,000313	0,000018	6,66667E-12
23	10556	ATHINAION	0,002087	0,000447	0,000018	6,66667E-12
24	10557	ATHINAION	0,003422	0,000689	0,000133	6,66667E-12
25	10558	ATHINAION	0,001935	0,000331	0,000018	6,66667E-12
26	10559	ATHINAION	0,00163	0,000148	0,000018	6,66667E-12

ID	POSTAL CODE	MUNICIPALITY	VII	VIII	IX	X
27	10560	ATHINAION	0,00163	0,000148	0,000018	6,66667E-12
28	10561	ATHINAION	0,001625	0,000148	0,000018	6,66667E-12
29	10562	ATHINAION	0,001611	0,000148	0,000018	6,66667E-12
30	10563	ATHINAION	0,001771	0,000253	0,000018	6,66667E-12
31	10564	ATHINAION	0,001617	0,000148	0,000018	6,66667E-12
32	10671	ATHINAION	0,002169	0,000461	0,000018	6,66667E-12
33	10672	ATHINAION	0,002018	0,000369	0,000018	6,66667E-12
34	10673	ATHINAION	0,002236	0,000495	0,000018	6,66667E-12
35	10674	ATHINAION	0,004236	0,000871	0,000204	6,66667E-12
36	10675	ATHINAION	0,002484	0,000517	0,000043	6,66667E-12
37	10676	ATHINAION	0,002106	0,000389	0,000018	6,66667E-12
38	10677	ATHINAION	0,002264	0,000552	0,000018	6,66667E-12
39	10678	ATHINAION	0,002168	0,000487	0,000018	6,66667E-12
40	10679	ATHINAION	0,002009	0,000391	0,000018	6,66667E-12
41	10680	ATHINAION	0,002218	0,000507	0,000018	6,66667E-12
42	10681	ATHINAION	0,002201	0,000511	0,000018	6,66667E-12
43	10682	ATHINAION	0,002373	0,000568	0,000018	6,66667E-12
44	10683	ATHINAION	0,00233	0,00055	0,000018	6,66667E-12
45	11141	ATHINAION	0,001716	0,000161	0,000018	6,66667E-12
46	11142	ATHINAION	0,001758	0,000203	0,000018	6,66667E-12
47	11143	ATHINAION	0,003853	0,000891	0,000187	6,66667E-12
48	11144	ATHINAION	0,002065	0,000399	0,000018	6,66667E-12
49	11145	ATHINAION	0,006563	0,001318	0,000500	6,66667E-12
50	11146	GALATSIOU	0,002004	0,000317	0,000018	6,66667E-12
51	11147	GALATSIOU	0,002142	0,000372	0,000018	6,66667E-12
52	11251	ATHINAION	0,003239	0,000781	0,000105	6,66667E-12
53	11252	ATHINAION	0,002479	0,000648	0,000018	6,66667E-12
54	11253	ATHINAION	0,00234	0,000575	0,000018	6,66667E-12
55	11254	ATHINAION	0,001983	0,000338	0,000018	6,66667E-12

ID	POSTAL CODE	MUNICIPALITY	VII	VIII	IX	X
56	11255	ATHINAION	0,001678	0,000148	0,000018	6,66667E-12
57	11256	ATHINAION	0,001822	0,000226	0,000018	6,66667E-12
58	11257	ATHINAION	0,002688	0,000619	0,000033	6,66667E-12
59	11361	ATHINAION	0,002433	0,000509	0,000018	6,66667E-12
60	11362	ATHINAION	0,003027	0,000663	0,000081	6,66667E-12
61	11363	ATHINAION	0,001644	0,000159	0,000018	6,66667E-12
62	11364	ATHINAION	0,001634	0,000149	0,000018	6,66667E-12
63	11471	ATHINAION	0,001582	0,000148	0,000018	6,66667E-12
64	11472	ATHINAION	0,001592	0,000148	0,000018	6,66667E-12
65	11473	ATHINAION	0,001973	0,000311	0,000018	6,66667E-12
66	11474	ATHINAION	0,003144	0,000641	0,000123	6,66667E-12
67	11475	ATHINAION	0,001593	0,000151	0,000018	6,66667E-12
68	11476	ATHINAION	0,001603	0,000156	0,000018	6,66667E-12
69	11521	ATHINAION	0,002147	0,000361	0,000018	6,66667E-12
70	11522	ATHINAION	0,001552	0,000148	0,000018	6,66667E-12
71	11523	ATHINAION	0,001545	0,000159	0,000018	6,66667E-12
72	11524	ATHINAION	0,001523	0,000148	0,000018	6,66667E-12
73	11525	ATHINAION	0,002088	0,000233	0,000018	6,66667E-12
74	11526	ATHINAION	0,002214	0,000289	0,000018	6,66667E-12
75	11527	ATHINAION	0,002724	0,000315	0,000018	6,66667E-12
76	11528	ATHINAION	0,002423	0,000386	0,000018	6,66667E-12
77	11631	ATHINAION	0,002041	0,00032	0,000018	6,66667E-12
78	11632	ATHINAION	0,001478	0,000148	0,000018	6,66667E-12
79	11633	ATHINAION	0,001475	0,000149	0,000018	6,66667E-12
80	11634	ATHINAION	0,001725	0,000223	0,000018	6,66667E-12
81	11635	ATHINAION	0,001612	0,000193	0,000018	6,66667E-12
82	11636	ATHINAION	0,001593	0,000177	0,000018	6,66667E-12
83	11741	ATHINAION	0,003232	0,000548	0,000126	6,66667E-12
84	11742	ATHINAION	0,002165	0,000447	0,000018	6,66667E-12

ID	POSTAL CODE	MUNICIPALITY	VII	VIII	IX	X
85	11743	ATHINAION	0,002045	0,000374	0,000018	6,66667E-12
86	11744	ATHINAION	0,001893	0,000307	0,000021	6,66667E-12
87	11745	ATHINAION	0,003039	0,000582	0,000099	6,66667E-12
88	11851	ATHINAION	0,001982	0,00046	0,000018	6,66667E-12
89	11852	ATHINAION	0,00227	0,000571	0,000035	6,66667E-12
90	11853	ATHINAION	0,004579	0,000797	0,000243	6,66667E-12
91	11854	ATHINAION	0,005207	0,000887	0,000311	6,66667E-12
92	11855	ATHINAION	0,007333	0,000995	0,000531	6,66667E-12
93	12131	PERISTERIOU	0,004998	0,001003	0,000299	6,66667E-12
94	12132	PERISTERIOU	0,005072	0,00105	0,000317	6,66667E-12
95	12133	PERISTERIOU	0,004191	0,000871	0,000233	6,66667E-12
96	12134	PERISTERIOU	0,002368	0,000654	0,000018	6,66667E-12
97	12135	PERISTERIOU	0,002237	0,000577	0,000018	6,66667E-12
98	12136	PERISTERIOU	0,002063	0,000441	0,000018	6,66667E-12
99	12137	PERISTERIOU	0,001747	0,000235	0,000020	6,66667E-12
100	12241	AIGALEO	0,006342	0,000809	0,000413	6,66667E-12
101	12242	AIGALEO	0,004425	0,000827	0,000241	6,66667E-12
102	12243	AIGALEO	0,002078	0,000551	0,000018	6,66667E-12
103	12244	AIGALEO	0,001867	0,000646	0,000018	6,66667E-12
104	12351	AGIAS BARBARAS	0,001733	0,000326	0,000019	6,66667E-12
105	12461	CHAIDARIOU	0,002725	0,000452	0,000076	0,000056
106	12462	CHAIDARIOU	0,001945	0,000375	0,000047	0,000008
107	13121	ILIOU (NEON LIOSION)	0,002303	0,000621	0,000018	6,66667E-12
108	13122	ILIOU (NEON LIOSION)	0,00258	0,000593	0,000056	6,66667E-12
109	13123	ILIOU (NEON LIOSION)	0,002341	0,000554	0,000020	6,66667E-12
110	13231	PETROUPOLIS	0,002044	0,000363	0,000027	6,66667E-12
111	13341	ANO LIOSION	0,004366	0,000895	0,000127	6,66667E-12
112	13342	ANO LIOSION	0,003959	0,000698	0,000108	2,66667E-05
113	13343	ANO LIOSION	0,003126	0,000351	0,000035	6,66667E-12

ID	POSTAL CODE	MUNICIPALITY	VII	VIII	IX	X
114	13344	ANO LIOSION	0,003378	0,000507	0,000074	1,53333E-05
115	13345	FULIS	0,003523	0,00047	0,000075	0,000008
116	13451	KAMATEROU	0,002349	0,000407	0,000024	6,66667E-12
117	13561	AGION ANARGURON	0,006667	0,001329	0,000507	6,66667E-12
118	13562	AGION ANARGURON	0,006032	0,001233	0,000435	6,66667E-12
119	13671	ACHARNON	0,003733	0,000775	0,000143	6,66667E-12
120	13672	ACHARNON	0,003638	0,000576	0,000059	6,66667E-12
121	13673	ACHARNON	0,003759	0,000699	0,000034	6,66667E-12
122	13674	ACHARNON	0,003962	0,000745	0,000054	6,66667E-12
123	13675	ACHARNON	0,003072	0,000623	0,000053	6,66667E-12
124	13676	THRAKOMAKEDONON	0,00447	0,001101	0,000249	6,66667E-12
125	14121	IRAKLEIOU	0,001547	0,000148	0,000018	6,66667E-12
126	14122	IRAKLEIOU	0,001587	0,000148	0,000018	6,66667E-12
127	14123	LUKOBRUSEOS	0,002567	0,000305	0,000018	6,66667E-12
128	14231	NEAS IONIAS	0,001729	0,000184	0,000018	6,66667E-12
129	14232	NEAS IONIAS	0,001679	0,000165	0,000018	6,66667E-12
130	14233	NEAS IONIAS	0,001854	0,000253	0,000018	6,66667E-12
131	14234	NEAS IONIAS	0,001628	0,000148	0,000018	6,66667E-12
132	14235	NEAS IONIAS	0,002431	0,000377	0,000018	6,66667E-12
133	14341	NEAS FILADELFEIAS	0,004448	0,000962	0,000265	6,66667E-12
134	14342	NEAS FILADELFEIAS	0,005418	0,00126	0,000389	6,66667E-12
135	14343	NEAS CHALKIDONOS	0,006551	0,001323	0,000503	6,66667E-12
136	14451	METAMORFOSEOS	0,003278	0,000673	0,000188	6,66667E-12
137	14452	METAMORFOSEOS	0,003474	0,000739	0,000127	6,66667E-12
138	14561	KIFISIAS	0,003328	0,000269	0,000018	6,66667E-12
139	14562	KIFISIAS	0,002088	0,000188	0,000018	6,66667E-12
140	14563	KIFISIAS	0,001899	0,000175	0,000018	6,66667E-12
141	14564	KIFISIAS	0,004153	0,000824	0,000057	6,66667E-12
142	14565	AGIOU STEFANOU	0,00415	0,000915	0,000035	6,66667E-12

ID	POSTAL CODE	MUNICIPALITY	VII	VIII	IX	X
143	14568	KRUONERIOU	0,004174	0,000966	0,000037	6,66667E-12
144	14569	ANOIXEOS	0,004492	0,000678	0,000043	6,66667E-12
145	14572	DROSIAS	0,003069	0,000833	0,000081	6,66667E-12
146	14574	RODOPOLEOS	0,001619	0,000189	0,000021	6,66667E-12
147	14575	STAMATAS	0,002422	0,000326	0,000037	6,66667E-12
148	14576	DIONUSOU	0,001634	0,000437	0,000053	6,66667E-12
149	14578	EKALIS	0,004039	0,000477	0,000025	6,66667E-12
150	14671	NEAS ERUTHRAIAS	0,003867	0,000362	0,000025	6,66667E-12
151	15121	PEUKIS	0,002027	0,0002	0,000018	6,66667E-12
152	15122	AMAROUSIOU	0,001701	0,000169	0,000018	6,66667E-12
153	15123	AMAROUSIOU	0,00279	0,000375	0,000024	6,66667E-12
154	15124	AMAROUSIOU	0,003153	0,000419	0,000027	6,66667E-12
155	15125	AMAROUSIOU	0,003629	0,000962	0,000044	6,66667E-12
156	15126	AMAROUSIOU	0,003158	0,000241	0,000018	6,66667E-12
157	15127	MELISSION	0,001934	0,000219	0,000019	6,66667E-12
158	15231	CHALANDRIOU	0,003035	0,000456	0,000027	6,66667E-12
159	15232	CHALANDRIOU	0,00452	0,001761	0,000107	6,66667E-12
160	15233	CHALANDRIOU	0,003932	0,001166	0,000071	6,66667E-12
161	15234	CHALANDRIOU	0,003261	0,000449	0,000030	6,66667E-12
162	15235	BRILISSION	0,002979	0,000184	0,000018	6,66667E-12
163	15236	PENTELIS	0,001422	0,000151	0,000018	6,66667E-12
164	15237	FILOTHEIS	0,002	0,000291	0,000028	6,66667E-12
165	15341	AGIAS PARASKEUIS	0,001884	0,000153	0,000018	6,66667E-12
166	15342	AGIAS PARASKEUIS	0,002369	0,000148	0,000018	6,66667E-12
167	15343	AGIAS PARASKEUIS	0,002982	0,000229	0,000019	6,66667E-12
168	15344	GERAKA	0,002418	0,000319	0,000021	6,66667E-12
169	15349	ANTHOUSAS	0,002528	0,000203	0,000018	6,66667E-12
170	15351	PALLINIS	0,002871	0,000604	0,000039	6,66667E-12
171	15451	NEOU PSUCHIKOU	0,001822	0,000191	0,000018	6,66667E-12

ID	POSTAL CODE	MUNICIPALITY	VII	VIII	IX	X
172	15452	PSUCHIKOU	0,001635	0,000175	0,000018	6,66667E-12
173	15561	CHOLARGOU	0,002893	0,000238	0,000018	6,66667E-12
174	15562	CHOLARGOU	0,001813	0,000167	0,000018	6,66667E-12
175	15669	PAPAGOU	0,002181	0,000193	0,000018	6,66667E-12
176	15771	ZOGRAFOU	0,002449	0,000355	0,000018	6,66667E-12
177	15772	ZOGRAFOU	0,001849	0,000193	0,000018	6,66667E-12
178	15773	ZOGRAFOU	0,002523	0,000297	0,000018	6,66667E-12
179	16121	KAISARIANIS	0,002412	0,000335	0,000018	6,66667E-12
180	16122	KAISARIANIS	0,001375	0,000161	0,000018	6,66667E-12
181	16231	BURONOS	0,00188	0,000207	0,000018	6,66667E-12
182	16232	BURONOS	0,001827	0,000211	0,000018	6,66667E-12
183	16233	BURONOS	0,001325	0,000155	0,000018	6,66667E-12
184	16341	ILIOUPOLIS	0,002243	0,000195	0,000018	6,66667E-12
185	16342	ILIOUPOLIS	0,00135	0,000152	0,000018	6,66667E-12
186	16343	ILIOUPOLIS	0,001291	0,000149	0,000018	6,66667E-12
187	16344	ILIOUPOLIS	0,001288	0,000148	0,000018	6,66667E-12
188	16345	ILIOUPOLIS	0,001741	0,000173	0,000018	6,66667E-12
189	16346	ILIOUPOLIS	0,001941	0,0002	0,000018	6,66667E-12
190	16451	ARGUROUPOLIS	0,001635	0,000152	0,000018	6,66667E-12
191	16452	ARGUROUPOLIS	0,002093	0,00019	0,000018	6,66667E-12
192	16561	GLUFADAS	0,001716	0,000148	0,000018	6,66667E-12
193	16562	GLUFADAS	0,00147	0,000148	0,000018	6,66667E-12
194	16671	BOULIAGMENIS	0,001861	0,000342	0,000023	6,66667E-12
195	16671	BOULIAGMENIS	0,001861	0,000342	0,000023	6,66667E-12
196	16672	BARIS	0,001864	0,000584	0,000018	6,66667E-12
197	16672	BARIS	0,001864	0,000584	0,000018	6,66667E-12
198	16673	BOULAS	0,001688	0,000179	0,000018	6,66667E-12
199	16674	GLUFADAS	0,001738	0,000148	0,000018	6,66667E-12
200	16674	GLUFADAS	0,001738	0,000148	0,000018	6,66667E-12

ID	POSTAL CODE	MUNICIPALITY	VII	VIII	IX	X
201	16675	GLUFADAS	0,002464	0,000324	0,000018	6,66667E-12
202	16777	ELLINIKOU	0,002476	0,000281	0,000019	6,66667E-12
203	17121	NEAS SMURNIS	0,002343	0,000347	0,000061	6,66667E-12
204	17122	NEAS SMURNIS	0,002498	0,000228	0,000078	6,66667E-12
205	17123	NEAS SMURNIS	0,001503	0,00016	0,000018	6,66667E-12
206	17124	NEAS SMURNIS	0,001519	0,000167	0,000018	6,66667E-12
207	17234	DAFNIS	0,001558	0,000177	0,000018	6,66667E-12
208	17235	DAFNIS	0,001517	0,000167	0,000018	6,66667E-12
209	17236	UMITTOU	0,001835	0,000234	0,000018	6,66667E-12
210	17237	UMITTOU	0,002028	0,000285	0,000018	6,66667E-12
211	17341	AGIOU DIMITRIOU	0,001457	0,000164	0,000018	6,66667E-12
212	17342	AGIOU DIMITRIOU	0,001303	0,000149	0,000018	6,66667E-12
213	17343	AGIOU DIMITRIOU	0,001569	0,000199	0,000018	6,66667E-12
214	17455	ALIMOU	0,001562	0,000188	0,000023	6,66667E-12
215	17456	ALIMOU	0,001708	0,000171	0,000018	6,66667E-12
216	17561	PALAIOU FALIROU	0,00358	0,00035	0,000133	6,66667E-12
217	17562	PALAIOU FALIROU	0,00145	0,000148	0,000018	6,66667E-12
218	17563	PALAIOU FALIROU	0,001409	0,000148	0,000018	6,66667E-12
219	17564	PALAIOU FALIROU	0,004836	0,000457	0,000205	6,66667E-12
220	17671	KALLITHEAS	0,001895	0,000363	0,000018	6,66667E-12
221	17672	KALLITHEAS	0,002379	0,000541	0,000041	6,66667E-12
222	17673	KALLITHEAS	0,004794	0,000468	0,000221	6,66667E-12
223	17674	KALLITHEAS	0,007333	0,000627	0,000398	6,66667E-12
224	17675	KALLITHEAS	0,007333	0,000722	0,000462	6,66667E-12
225	17676	KALLITHEAS	0,005615	0,000836	0,000331	6,66667E-12
226	17778	TAUROU	0,007333	0,000893	0,000517	6,66667E-12
227	18010	AIGINAS	0,00456	0,000544	0,000058	6,66667E-12
228	18010	AGKISTRIOU	0,00456	0,000544	0,000058	6,66667E-12
229	18120	KORUDALLOU	0,0021	0,000661	0,000045	6,66667E-12

ID	POSTAL CODE	MUNICIPALITY	VII	VIII	IX	X
230	18121	KORUDALLOU	0,001872	0,000412	0,000030	6,66667E-12
231	18122	KORUDALLOU	0,001877	0,000303	0,000041	6,66667E-12
232	18233	AGIOU IOANNOU RENTI	0,008	0,000777	0,000531	6,66667E-12
233	18344	MOSCHATOU	0,008	0,000523	0,000478	6,66667E-12
234	18345	MOSCHATOU	0,008	0,000712	0,000485	6,66667E-12
235	18346	MOSCHATOU	0,007333	0,000855	0,000495	6,66667E-12
236	18450	NIKAIAS	0,002033	0,000625	0,000040	6,66667E-12
237	18451	NIKAIAS	0,001774	0,00046	0,000019	6,66667E-12
238	18452	NIKAIAS	0,001762	0,000344	0,000037	6,66667E-12
239	18453	NIKAIAS	0,001771	0,000661	0,000018	6,66667E-12
240	18454	NIKAIAS	0,002978	0,000654	0,000119	6,66667E-12
241	18531	PEIRAIOS	0,004045	0,000567	0,000230	6,66667E-12
242	18532	PEIRAIOS	0,001597	0,000447	0,000018	6,66667E-12
243	18533	PEIRAIOS	0,003248	0,000345	0,000142	6,66667E-12
244	18534	PEIRAIOS	0,001688	0,000202	0,000030	6,66667E-12
245	18535	PEIRAIOS	0,002432	0,000598	0,000083	6,66667E-12
246	18536	PEIRAIOS	0,002168	0,000262	0,000058	6,66667E-12
247	18537	PEIRAIOS	0,00187	0,000181	0,000040	6,66667E-12
248	18538	PEIRAIOS	0,003118	0,000238	0,000125	6,66667E-12
249	18539	PEIRAIOS	0,001636	0,000148	0,000018	6,66667E-12
250	18540	PEIRAIOS	0,006352	0,000487	0,000394	6,66667E-12
251	18541	PEIRAIOS	0,008	0,000596	0,000531	6,66667E-12
252	18542	PEIRAIOS	0,004373	0,000697	0,000235	6,66667E-12
253	18543	PEIRAIOS	0,002964	0,000443	0,000120	6,66667E-12
254	18544	PEIRAIOS	0,001725	0,000443	0,000018	6,66667E-12
255	18545	PEIRAIOS	0,004106	0,000565	0,000217	6,66667E-12
256	18546	PEIRAIOS	0,002553	0,000423	0,000087	6,66667E-12
257	18547	PEIRAIOS	0,008	0,000486	0,000491	6,66667E-12

ID	POSTAL CODE	MUNICIPALITY	VII	VIII	IX	X
258	18648	DRAPETSONAS	0,001971	0,000235	0,000042	6,66667E-12
259	18755	KERATSINIOU	0,002369	0,000309	0,000078	6,66667E-12
260	18756	KERATSINIOU	0,003638	0,000537	0,000173	6,66667E-12
261	18757	KERATSINIOU	0,00193	0,000442	0,000031	6,66667E-12
262	18758	KERATSINIOU	0,002358	0,00034	0,000074	6,66667E-12
263	18863	PERAMATOS	0,002994	0,000383	0,000110	2,33333E-05
264	18900	SALAMINAS	0,005833	0,00121	0,000211	1,26667E-05
265	18902	AMPELAKION	0,005566	0,000737	0,000187	6,66667E-12
266	18903	SALAMINAS	0,005388	0,000851	0,000128	6,66667E-12
267	19001	KERATEAS	0,001586	0,000248	0,000056	6,66667E-12
268	19001	KERATEAS	0,001586	0,000248	0,000056	6,66667E-12
269	19001	KERATEAS	0,001586	0,000248	0,000056	6,66667E-12
270	19002	PAIANIAS	0,002672	0,000728	0,000094	6,66667E-12
271	19003	MARKOPOULOU MESOGAIAS	0,001922	0,000352	0,000079	9,33333E-06
272	19004	SPATON-LOUTSAS	0,0026	0,000653	0,000122	6,66667E-12
273	19005	NEAS MAKRIS	0,001935	0,000434	0,000057	6,66667E-12
274	19006	NEAS PERAMOU	0,006667	0,003109	0,000300	0,000026
275	19007	MARATHONOS	0,002395	0,000835	0,000122	8,66667E-06
276	19008	ERUTHRON	0,004935	0,002011	0,000805	1,46667E-05
277	19009	RAFINAS	0,002336	0,000405	0,000033	6,66667E-12
278	19010	KALUBION THORIKOU	0,001973	0,000411	0,000074	6,66667E-12
279	19011	AULONOS	0,004124	0,001149	0,000365	0,000124667
280	19012	OINOIS	0,006075	0,001796	0,000787	0,000167333
281	19012	VILION	0,006075	0,001796	0,000787	0,000167333
282	19013	ANABUSSOU	0,001666	0,000386	0,000065	6,66667E-12
283	19014	KAPANDRITIOU	0,003288	0,001064	0,000162	7,33333E-06
284	19015	OROPION	0,003633	0,001407	0,000547	0,000126
285	19016	ARTEMIDOS	0,002159	0,000365	0,000089	0,00002

ID	POSTAL CODE	MUNICIPALITY	VII	VIII	IX	X
286	19100	MEGAREON	0,007333	0,002639	0,000584	2,93333E-05
287	19200	ELEUSINOS	0,0066	0,002457	0,000232	0,000334533
288	19300	ASPROPURGOU	0,005715	0,001485	0,000183	0,000226
289	19400	KROPIAS	0,002279	0,000631	0,000051	6,66667E-12
290	19500	LAUREOTIKIS	0,001453	0,000241	0,000049	6,66667E-12
291	19600	MANDRAS	0,003643	0,00134	0,000203	4,73333E-05